# Design and development of an electrochemical and infrared spectroscopic medical device for serum-based cancer diagnostics

A thesis submitted in fulfilment of the requirements for the degree of

Doctor of Engineering in Medical Devices

Christopher Rinaldi M. Eng

**Centre for Doctoral Training in Medical Devices & Health Technologies**

**Department of Biomedical Engineering**

**University of Strathclyde**

**2019**

This thesis is the result of the author's original research. It has been composed by the author and has not been previously submitted for examination which has led to the award of a degree.



Signed: Date:

**Acknowledgements**

Firstly, I would like to express my sincere gratitude to my academic supervisors, Dr Lynn Dennany and Dr Matthew Baker, for your guidance and support throughout my dissertation. Lynn, your patience and easy-going approach, and Matt your eternal optimism and enthusiasm for the research, have together helped me enormously over the past three years, and I am genuinely very grateful for all your support.

Similarly, I would like to express my sincere gratitude to Dr Damion Corrigan for his role in the project, for his patience and for the countless discussions and suggestions on how to overcome numerous issues in the lab over the past eighteen months.

I would also like to thank all the other members of our research group for putting up with me over the past three years, and for the entertaining chats over morning coffee. I would especially like to thank Julien for putting up with my constant moaning and for making my life much easier in the lab on a near daily basis.

I would like to dedicate this dissertation to my family; my three brothers, sister, mother, Karen, and fiancé Kirsty for their love, laughter and continual support, and without whom this dissertation would not have been possible. I would also like to say a special thank you to Kirsty for everything over the past few years, as I genuinely would not have been able to achieve this without your love and support and I am forever grateful.

**Abstract**

Development of an integrated electrochemical and spectroscopic serum diagnostic device would have significant potential as a triage tool for brain cancer and Hodgkin's lymphoma in primary care settings to better inform clinical decisions and facilitate prompt referral to secondary care, whilst reducing financial and practical constraints placed on current diagnostic modalities. Additionally, the ability to detect IDH1 molecular status from serum samples would have significant clinical value to patients and clinicians alike, ultimately allowing earlier diagnosis and improved planning of surgery and treatment therapeutics. To this extent, the medical device has demonstrated the ability to electrochemically detect the biomarker CCL17/TARC at 387-50,000pg/ml concentrations with $R^2 = 0.979$ and limit of detection of 387pg/ml in spiked buffer samples. Thereafter, the medical device demonstrated successful diagnosis of Hodgkin's lymphoma in all 11 tested clinical patient samples. Additionally, ATR-FTIR discriminated between Hodgkin's lymphoma and healthy controls in 200 patient samples with sensitivity of 83.2 ± 6.6% and specificity of 85.3 ± 8.1% with Random Forest classification, highlighting differences in protein secondary structures within clinical serum samples. The integrated diagnostic platform further demonstrated the ability to electrochemically detect IDH1-R132H proteins in spiked buffer samples at 0.05-10,000ng/ml concentrations with $R^2 = 0.958$. However, it was not subsequently possible to detect IDH1 mutant proteins in clinical serum samples. Nevertheless, ATR-FTIR demonstrated the ability to discriminate between IDH1 molecular status in 104 glioma patients through consideration of the global molecular signatures of serum samples with sensitivity of 89.0 ± 11.3% and specificity of 88.2 ± 10.1% with PLS classification.

**Publications & Presentations**

Finlayson, D., Rinaldi, C., Baker, M. J. (2019) Is Infrared Spectroscopy Ready for the Clinic? *Anal. Chem*. 91, 19, 12117-12128

BioMedEng19, Imperial College London, 5-6 September 2019. *Poster Presentation.*

BioMedEng18, Imperial College London, 6-7 September 2019. *Poster Presentation.*

SPEC2018, University of Strathclyde, 10-15 June 2018. *Poster & Flash Presentation*.

CLIRCON 2017, University of Manchester, 2-5 April 2017. *Poster Presentation.*

**Contents**

**Chapter 2: Theoretical Background**



**Chapter 3: Development of Silicon IRE Device for Combined Spectroscopic and Electrochemical Analysis**

# Chapter 1: Introduction

## *1.1 Cancer Overview*

Today, an individual will receive a confirmatory cancer diagnosis every two minutes in the UK, which equates to ~1000 new cancer patients per day (Cancer Research UK, 2019). Concurrently, cancer claims an individual's life every four minutes in the UK, and equates to over a quarter of mortalities in the UK per year, highlighting the immense destruction the disease causes to society (Cancer Research UK, 2019). Worryingly, the incidence of cancer has risen by 6% in the UK over the past ten year period, primarily attributed to the ageing population, such that presently a person has a 50% probability of receiving a cancer diagnosis over the course of their life (Cancer Research UK, 2019). From an economic perspective, the impact of cancer on wider UK society is marked at £18.3billion per year, with direct healthcare costs to NHS England of ~£5billion per year (Department of Health & Social Care, 2019). With latest forecasts predicting a funding shortfall of ~£20billion in NHS England by 2022/23, in conjunction with a 2% rise in the incidence of cancer by 2035, it is clear the health service is under tremendous strain to deliver cancer services (The Kings Fund, 2017; Cancer Research UK, 2019). Nevertheless, considerable progress has been realised to improve patient outcomes that provide optimism for the future, with overall cancer survival at 5-years shown to have significantly increased from 28.9% in 1971/72 to 54.2% in 2010/11 (Quaresma et al, 2015). However, 5-year survival rates remain poor for difficult to diagnose cancers, such as pancreatic, lung and brain cancer, at 3.3-18.5%, whilst over half of all cancers are currently diagnosed at a clinically late stage, associated with poorer patient outcomes and significantly increased health care costs (Quaresma et al, 2015). Hence, early diagnosis of cancer has become a key

strategy for health services as outlined in the current "The NHS Long Term Plan" report, particularly since no country has achieved the current cancer "62-day" patient waiting time targets in the UK, emphasising the need for development of novel strategies to facilitate timely cancer diagnosis (NHS England, 2019; Cancer Research UK, 2019).

## *1.2 Biological Overview of Cancer*

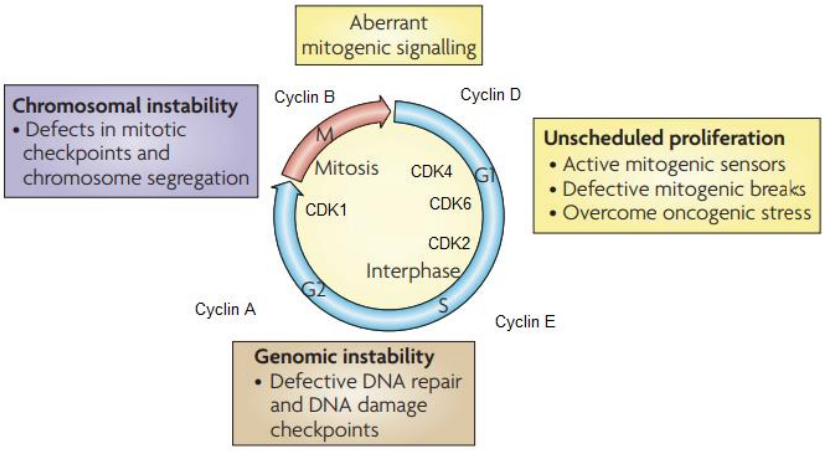


*Figure 1.1: Overview of cell cycle and CDK's implicated in cancer. Adapted. (Malumbres et al, 2009).*

Cancer encompasses a heterogeneous collection of >100 diseases characterised by genetic mutations that facilitate unregulated cell proliferation. The process of cellular division is represented by the cell cycle, and instigated upon transition from G1 to S phase, which in healthy individuals is regulated by the G1 checkpoint, as indicated in Figure 1.1. The G1 checkpoint evaluates whether cellular growth and DNA content is appropriate for DNA synthesis in S phase, and is determined by the activity of proto-oncogenes and tumour suppressant genes, which produce proteins that promote or inhibit cell cycle progression respectively (Malumbres et al, 2009). Hence, the G1 checkpoint is regulated by molecular signals, in particular, two distinct, interdependent

pathways, controlled by attachment of cyclins to cyclin dependent kinases (CDK's) and detachment of retinoblastoma (pRB), p107 and p130 proteins from E2F molecules respectively. The interplay between these two mechanisms ensures that cellular division is controlled in healthy individuals and only proceeds if the cellular environment is sufficient, hence, if deemed unsuitable, proliferation is prevented to restrict transcription of damaged DNA content.

Briefly, these molecular pathways are activated during an early period of G1 phase where cyclin D binds to CDK4 and CDK6, which causes incomplete phosphorylation of pRB, p107 and p130 proteins, and consequently increases production of cyclin E (Malumbres et al, 2009). Thereafter, at a later period during G1 phase, elevated cyclin E binds to CDK2, which causes complete phosphorylation of pRB, p107 and p130 proteins and their detachment from respective E2F molecules (Malumbres et al, 2009). Consequently, activation of E2F transcription factors enables expression of a variety of genes and proteins responsible for transition to S phase (Bertoli et al, 2013). Conversely, the G1 checkpoint may prevent transition to S phase in the presence of DNA damage, primarily through activation of ATM/ARM, CHK1/CHK2 and p53 pathways (Kastan et al, 2004; Malumbres et al, 2009). Ultimately, these protection mechanisms, commonly referred to as DNA damage checkpoints, once active increase the production of specific proteins, such as p16 and p21, that prevent both the progression of the cyclin-CDK pathway and detachment of pRB from E2F molecules (Malumbres et al, 2009). Additionally, increased levels of the p53 protein may promote either DNA repair or apoptosis where the cell is subjected to programmed cell death (Sherr et al, 2002). Overall, these molecular events occur in healthy

individuals to prevent replication of damaged DNA during S phase, which is recognised as a fundamental component in the development of cancers.

The process of cellular division subsequently requires successful progression through S and G2 phases where cells must duplicate their entire DNA profiles and grow to synthesise structures, such as microtubules, necessary for mitosis. In healthy individuals, such cellular events are strictly monitored by additional molecular checkpoints, S and G2 checkpoints respectively, which similarly operate through the cyclin-CDK pathway. Firstly, the S checkpoint evaluates the transcription process regarding replication of DNA through regulation of cyclin A and CDK2 activity, which may permit progression to G2 phase (Malumbres et al, 2009). Likewise, the G2 checkpoint assesses suitability of cellular growth and DNA content synthesised in S phase for mitosis, which is determined by the interaction of cyclin B with CDK1 proteins, and is a pre-requisite mechanism for promotion of mitosis (Malumbres et al, 2009). Specifically, binding of cyclin B to CDK1 produces a series of molecular events that ultimately promotes certain proteins, which prevent inhibition of cyclin B-CDK1 pathways; thereby enabling progression to mitosis (Malumbres et al, 2009). At both checkpoints, DNA damage is similarly regulated by ATM/ATR, CHK1/CHK2 and p53 pathways, which identify, repair and/or permanently remove damaged DNA prior to progression to the mitotic cycle (Kastan et al, 2004). Overall, the widespread nature of these protective mechanisms, found at all three respective cell checkpoints within interphase, highlights their importance for the regulated proliferation of cells in healthy individuals.

Mutations to proto-oncogenes and tumour suppressant genes have been widely observed in various cancers and have been shown to negatively interfere with molecular pathways associated with G1, S and G2 checkpoints. In particular, mutations in proto-oncogenes responsible for activity of CDK4 and CDK6 proteins during G1 phase have been found in numerous cancers, including glioma and lymphoma cancers (Malumbres et al, 2009). Similarly, mutations in proto-oncogenes, commonly referred to as oncogenes, have been recognised to alter production of cyclins, p16, and pRB proteins, associated with over stimulation of the cyclin-CDK pathway in cancer (Malumbres et al, 2001; Malumbres et al, 2009). Likewise, mutations in tumour suppressant genes have been identified in cancers, especially regarding expression of the p53 protein, which is thought to occur in >50% of cancers (Osaki et al, 2011; Hollstein et al, 1991; Soussi et al, 2007; Parrales et al, 2015). Consequently, the change in functionality of p53 prevents activation of DNA repair mechanisms and instigation of apoptosis, which together form pivotal roles at all checkpoints in healthy individuals to ensure damaged DNA does not progress through the cell cycle (Sherr et al, 2002). Similarly, mutations in other tumour suppressant genes, such as pRB and p16, have been identified in cancers (Sherr et al, 2002), which ultimately hinder the functionality of the G1 checkpoint, reiterating the importance of checkpoints in healthy individuals in preventing cancer development.

The ability for cells to evade molecular checkpoints and the resultant uncontrollable proliferation of cells promotes accumulation of cells that over a variable period of time

comprise tissue. The growth of abnormal tissue, referred to as a tumour, may either be categorised as benign or malignant depending on growth activity and tendency to invade surrounding healthy tissues. Benign tumours describe the slow development of abnormal tissues characterised by minimal interference with normal tissues and may be identified histologically by the integrity of the basal membrane (Baba, 2007). Benign tumours do not possess the ability to spread to other locations in the body, and often may be completely removed through surgical resection if deemed necessary; hence, benign tumours do not pose significant health risks to life. Conversely, malignant tumours represent the fast growth of abnormal tissues that may be difficult to distinguish from surrounding tissue due to tumour invasiveness and may be identified histologically by alterations to the basal membrane, differences in the nucleus, development of blood vessel capillaries, and expression of molecules on cell membranes (Baba, 2007; Hanahan et al, 2011). Malignant tumours have the ability to permeate the circulatory or lymphatic system, interfering with other healthy tissues at different physiological sites in the body, with potential to form secondary metastatic tumours, associated with poorer patient outcomes (Qian et al, 2017). Additionally, malignant tumours may return following radiation therapy, surgical resection and/or completion of drug therapeutics, with tumour recurrence associated with poorer patient outcomes (Qian et al, 2017). Hence, malignant tumours pose immediate and critical health risks to an individual's life, and must be identified and treated at the earliest opportunity, with early detection recognised to improve patient outcomes.

Malignant tumours may be categorised with regards to the cellular type and initial physiological location of the abnormal tissue. Carcinomas constitute epithelial cells

that encompass internal organs and comprise skin, and represents 85% of all cancers in the UK (Cancer Research UK, 2019). Next, lymphomas describe abnormal proliferation of lymphocytes of the lymphatic system, and correspond to 5% of all cancers in the UK (Cancer Research UK, 2019). Similarly, leukaemia describes abnormalities of white blood cells, in particular leukocytes, found in the circulatory system and accounts for 3% of cancers in the UK (Cancer Research UK, 2019). Then, brain cancers constitute glial cells of the central nervous system that comprise 3% of all cancers in the UK (Cancer Research UK, 2019). Lastly, sarcomas describe unregulated proliferation of mesenchymal cells that form the basis of connective tissue, and in general is a less prevalent cancer, accounting for only 1% of all cancers in the UK (Cancer Research UK, 2019).

Malignancies may further be categorised with reference to tumour stage commonly determined clinically by the TNM staging system. Briefly, the components of the TNM staging system entail assessment of the size of the malignant growth, and subsequently the degree of interaction with lymph nodes close to the proximity of the tumour, and lastly the degree of metastases and the aggressive nature of invasion to surrounding healthy tissues. All three respective letters in the TNM staging system are assigned numeric values where greater numbers for letters correspond to increased tumour severity. The TNM staging system is commonly employed to form the basis of evaluation of overall tumour stage, with cancer severity represented by four distinct stages, numerically assigned from I to IV. Briefly, stage I represents presence of a small malignancy that does not demonstrate evidence of significant invasion to surrounding healthy tissue. Conversely, stages II and III characterise malignancies of

increased volume that display higher degrees of invasiveness of healthy tissue and interaction with neighbouring lymph nodes. Lastly, stage IV describes malignancies of significant growth that have entered the circulatory and/or the lymphatic system, leading to metastases and the presence of a secondary tumour. As before, the greater number employed to describe tumour activity indicates increased cancer severity. Hence, the assigned tumour stage reflects the pathophysiology of the cancer in patients, which interestingly often corresponds with the presence of specific biological molecules, and thus provides an opportunity to target such molecules through development of a diagnostic device to evaluate cancer severity in patients.

*1.3 Comparison of Cancer in the UK with Other Countries Worldwide*

Clinical performance of delivering effective cancer services in the UK has recently been scrutinised, and has consistently found to perform unfavourably compared to other high-income countries around the world. Globally, ~18.1 million patients received a cancer diagnosis in 2018, and in the same year an astonishing ~9.56 million patients died as a consequence of cancer (WHO, 2018). Future predictions anticipate that ~21.6 million persons will receive a cancer diagnosis by 2030, and given that worldwide cancer costs in 2010 were estimated at US$1.16 trillion, it is clear that the significant challenge society faces to improve cancer services whilst remaining economically viable is not confined to the UK and is a matter of global concern (WHO, 2016). Nevertheless, the UK has been found to perform below the European average of 5-year survival for 9 out of 10 common cancers when compared to 25 other European countries, in a recent study of >10 million cancer patients between 2000-07 (De Angelis et al, 2014). In particular, 5-year survivals in the UK for lung, colon and

breast cancer were 24th, 18th and 16th out of 25 European countries respectively, with significant disparity observed in relation to other high-income countries (De Angelis et al, 2014). These findings have been echoed by another, larger report of ~25million cancer patients across 67 countries, where 5-year survival for the UK between 2000-05 for colon, breast and prostate cancers were 18th, 15th and 16th out of 27 European countries respectively (Allemani et al, 2015). Worldwide, the story is similar, the UK performed poorly in a recent study of >37million patients across 71 countries, with significantly reduced 5-year survival between 2010-14 for numerous cancers, including pancreatic, colon, breast and brain, compared to several high-income countries, not limited to Australia, Canada, USA, Japan, Sweden, Spain, Italy, Germany and France (Allemani et al, 2018). Poorer 5-year survival statistics in the UK have primarily been attributed to late diagnosis of cancer patients, with a study showing that 5,000-10,000 lives could be saved over the time period in England alone for breast, colorectal and lung cancer with earlier diagnostics (Richards, 2009), and re-iterates the need for careful consideration of the current diagnostic pathway.

*1.4 Cancer Diagnostic Pathway in the UK: State of Play*

Current diagnostic pathway guidelines for suspected cancers were revised by the National Institute for Health and Care Excellence (NICE) in 2015 with the aim to achieve earlier cancer diagnoses, and corresponds to a key strategy of the NHS 2015-2020 cancer roadmap for improving cancer patient outcomes (NHS England, 2016). Presently, patients that present in primary care with suspected cancers should urgently be referred by general practitioners (GP's) to consultants in secondary care within a two-week time period, commonly referred to as the "two-week wait" pathway. At

clinical evaluation in secondary care settings, patients often require imaging to assess the presence of cancer, in the form of either Magnetic Resonance Imaging (MRI), Computed Tomography (CT), X-Ray, Positron Emission Tomography (PET) and ultrasound, depending on the suspected malignancy. In other cases, suspected patients may require specialist diagnostic modalities, such as a colonoscopies or investigative tissue biopsies, depending on cancer type. Currently, the diagnostic pathway is assessed by the "62-day" waiting time target, which advocates that patients should begin treatment within 62 days of initial GP referral. Furthermore, the treatment process is evaluated by the "31-day" waiting time target, which states that patients should initiate cancer treatment within 31 days of receiving confirmatory diagnosis.

The clinical effectiveness of the current cancer pathway in the UK may be realised with reference to both the route of diagnosis and response to waiting time targets. Presently, only 34% of cancer patients in England were referred to secondary care through the "two-week wait" pathway to confirm their malignancy, although 57% of these patients were identified with low-grade cancers (Cancer Research UK, 2019). Conversely, 21% of all cancer patients received diagnosis in an emergency setting, where 65% attend Accident and Emergency (A&E) departments, with remaining patients referred as emergencies within primary or secondary care settings (Cancer Research UK, 2019). Crucially, 77% of emergency patients received diagnoses of high-grade cancers, associated with poorer patient outcomes, which emphasises the importance of early diagnosis (Cancer Research UK, 2019). To this extent, NHS England has achieved the current 93% "two-week wait" target for prompt consultation in secondary care (Cancer Research UK, 2019). However, the "62-day" waiting time

target has not been achieved by any country in the UK, whilst the "31-day" waiting time target has been achieved only by England and Scotland in the UK (Cancer Research UK, 2019). Thus, current statistics strongly suggest bottlenecks in the diagnostic pathway that delay initiation of cancer treatments, which ultimately translates to poorer outcomes for cancer patients.

One of the key challenges for GP's that often prevents early diagnosis through the "two-week wait" pathway is recognising possible malignancies in difficult to detect cancers, where patients present with non-specific symptoms often mistaken for common illnesses. In such cases, patients often have to visit their GP on several occasions, which may delay referral through the "two-week wait" pathway, or prevent referral with patients presenting through emergency routes. A classic example of the prolonged diagnostic process is in brain cancer where patients often present with non-specific, general symptoms, such as headache, that significantly delays time to referral, recognised between 3-12 months, where patients on average visit their GP five times prior to secondary care referral (Gray et al, 2018). One possible solution to facilitate earlier diagnosis would be to extend screening programmes, currently employed for breast, cervical and bowel cancers, to several other difficult to detect cancers. However, such screening programmes incur huge costs, with breast, cervical and bowel screening costs calculated to be £169 million, £185 million and £211 million per year respectively (NHS England, 2016). Furthermore, the significant majority of patients screened will not have cancer, for example in breast cancer 1.8 million females are screened per year with a total of ~18,000 cancers identified (NHS England, 2019). Hence, screening is not economical for all cancer types, particularly those with very

large numbers of patients that present with common symptoms associated with a low positive predictive value (PPV), inclusive of brain cancer (Gray et al, 2018; Schmidt-Hansen et al, 2015). Hence, there is a strong case in these cancers for development of low-cost, rapid diagnostic tools to aid clinical decision-making in primary care settings, and ultimately ensure, where appropriate, prompt patient referral to secondary care.

Another major challenge in the diagnostic pathway that contributes to clinical delay and significant economic expense is the current demand for diagnostic imaging modalities. Currently, findings show that the quantity of imaging tests conducted in NHS England in 2016/17 to determine the presence of cancer in suspected patients increased by 2.3% in comparison to the previous year, with a total of ~11 million tests now performed annually (NHS England, 2017). In particular, use of MRI and CT modalities through GP referrals for suspected cancers increased significantly in 2016/17, with 12.6% growth in MRI and 15.5% growth in CT scans compared to the previous 5-year period (NHS England, 2017). Additionally, overall use of both MRI and CT modalities not necessarily related to cancer increased substantially in NHS England in 2016/17, with 8.9% and 7.9% growth respectively compared to the previous 5-year period (NHS England, 2017). Given that latest figures show the UK ranks 25$^{th}$ and 26$^{th}$ out of 27 European countries for the number of MRI and CT scanners (OECD/EU, 2018), and with the cost of MRI and CT per scan at £164 and £85 respectively (Gray et al, 2018), it is unsurprising patients with non-specific symptoms visit GP's repeatedly before gaining access to these tools. Unfortunately, this situation is likely to get worse in future years, barring significant investment, since

current NICE guidelines state that GP's should instigate referral at a reduced PPV cancer risk of 3% compared to previous guidelines at 5%, with the view of promoting early diagnosis (NICE, 2015). Hence, there is an argument for development of rapid, low-cost diagnostic tools that provisionally identify cancers, which would allow patient triage and facilitate earlier referral of high-risk patients to imaging for confirmatory diagnosis in secondary care.

*1.5 Brain Cancer*

*1.4.1 Introduction*

Today, 32 individuals will receive a confirmatory diagnosis of a brain tumour in the UK, equivalent to ~12,000 persons per year, or 3% of all patients diagnosed with cancer per year (Cancer Research UK, 2019). Over 100,000 persons are believed to be living with a brain tumour in the UK today, with the demographic comprised of 53% female and 47% male patients, with increased incidence amongst elderly persons, as indicated in Figure 1.2. Astonishingly, brain cancer incidence has soared by 36% over the previous thirty-year period in the UK, and forecast to rise by a further 6% by 2035 (Cancer Research UK, 2019). Implications for patients and families are tragic, brain cancer is responsible for >5,000 mortalities per year in the UK, with 20.1 mean years of life lost to the disease per patient, which is greater than any other cancer (Cancer Research UK, 2019; Burnet et al, 2005). Long-term survival is equally dismal, less than half of individuals survive primary brain cancer longer than one year, whilst 19% of patients survive 5 years and 14% of patients survive 10 years (Cancer Research UK, 2019). However, survival rates in the UK are less than several other European countries for brain cancer, not limited to Norway, Sweden, Italy, Ireland and Germany

(Allemani et al, 2018). In fact, evidence suggests that >300 primary brain cancer mortalities could be prevented every year in the UK if survival rates corresponded to the European average, and serves as motivation to find diagnostic strategies to improve patient outcomes (Abdel-Rahman et al, 2009; Hamdan et al, 2013). Additionally, economic costs of brain tumours on health services are significant, and were estimated to cost the UK £29,406 per patient in 2010, equivalent to £766 million for 2010 alone (Gustavsson et al, 2011), with significantly more spent unnecessarily on imaging for patients who do not have brain tumours (Gray et al, 2018). To this extent, a recent health economic study suggested a low-cost, blood-based diagnostic test for early brain tumour diagnosis may be cost saving to NHS services if employed to triage patients for medical imaging in primary and secondary care settings. In particular, the study found that a test would provide cost savings to the NHS in primary and secondary care provided test sensitivity and specificity were above 80% and at a cost per test below £40 (Gray et al, 2018), and provides additional motivation to develop an economical blood test for early diagnosis of brain tumours.

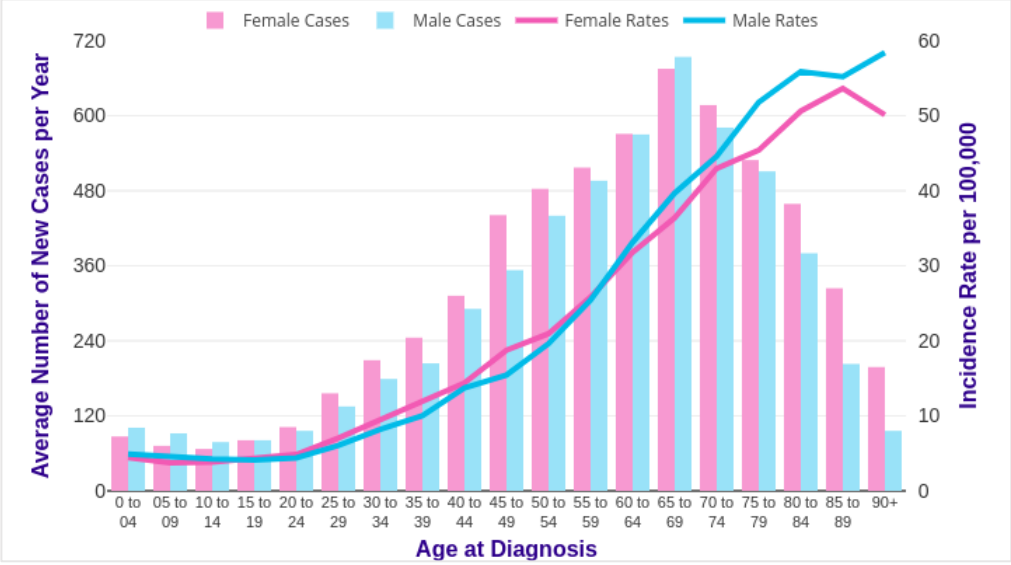


Figure 1.2: Brain cancer incidence in the UK for males and females 2014-2016. Reproduced (Cancer Research UK, 2019)

*1.4.2 Anatomy of the Brain*

The architecture of the human brain is comprised of three primary constituents, namely the cerebrum, cerebellum and brain stem, together responsible for controlling functions fundamental to our very existence. The cerebrum position is superior to the cerebellum and brain stem and comprises two cerebral hemispheres attached to the corpus callosum that facilitates transfer of electrical signals between right and left sides of the brain. Individual cerebral hemispheres may be further sub-categorised in to four distinct regions, namely the frontal, temporal, parietal and occipital lobes, that exhibit particular functions, as indicated in Figure 1.3. The cerebellum is situated inferior to the cerebrum and similarly consists of two hemispheres attached to the vermis with respective hemispheres constructed of three lobes. The function of the cerebellum is predominantly to determine motor response and is associated with the fine control of movement, coordination, balance and speech. The brain stem is located anterior to the cerebellum and may be categorised in to three regions known as the mesencephalon, metencephalon and the medulla oblongata, which together serve functions critical for life. Specifically, the brain stem is recognised to regulate aspects of the cardiovascular system with control of heartbeat, respiration and blood pressure, and is further associated with other vital functions, such as hearing, sight, sleeping and swallowing. The main structures of the brain are encompassed by the meninges that comprise three layers of connective tissue of different thickness called the dura, arachnoid and pia mater. The meninges primarily function as a protective barrier for the central nervous system where the dura mater, which is positioned superior to the arachnoid and pia mater, connects with the cranium that further provides structural protection to the brain.

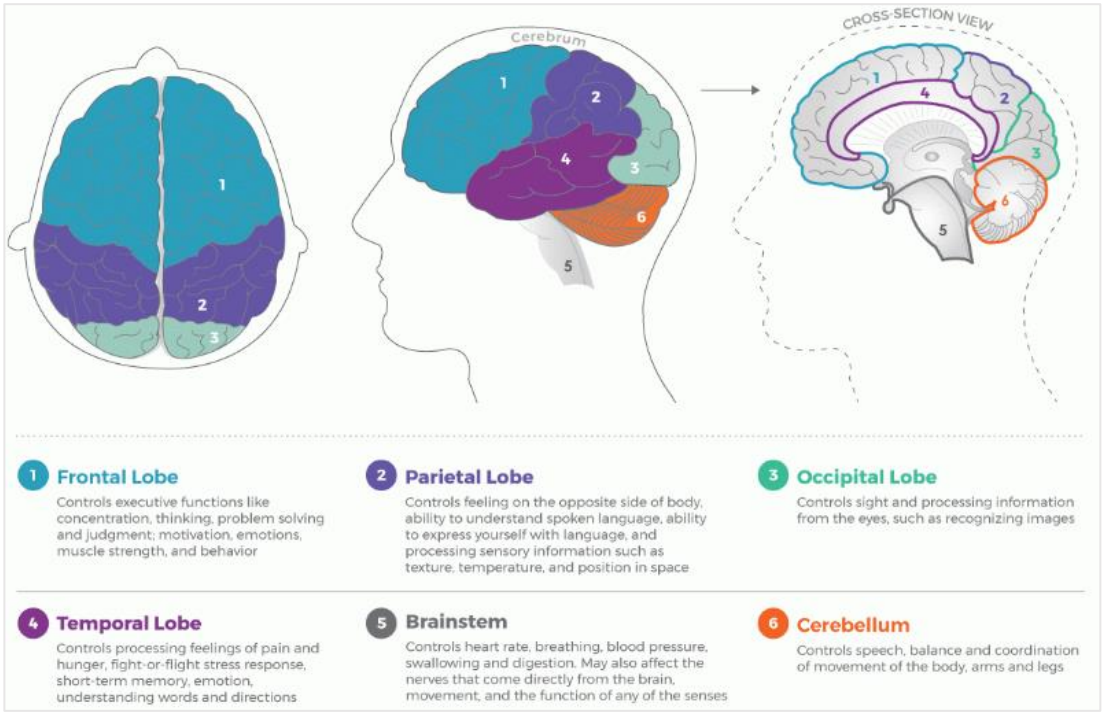


*Figure 1.3: Anatomy of the human brain. Reproduced. (National Cancer Institute Center for Cancer Research, 2019)*

The structure of the human brain may also be described according to cellular composition where neurons and glial cells represent grey matter and myelinated axons represent white matter that together form the architectures of the brain. Neurons describe cells that possess electrical conduction capabilities where the production of action potentials facilitates communication with other parts of the brain and body. Conversely, glial cells do not conduct electrical signals and primarily consist of astrocytes and oligodendrocytes that structurally support neurons and participate in myelination of the axons of neurons respectively. Overall, quantities of neuron and glial cells in the brain are estimated to be in the region of 100 billion cells respectively (von Bartheld et al, 2016), although it is the glial cells that are most commonly implicated in brain tumours as outlined in subsequent sections.

### *1.4.3 Primary Brain Tumours*

#### *1.4.3.1 Meningioma*

Meningioma's represent the most frequent neoplasm in the patient group and describe the development of cancer in the connective tissues of meninges that encompass the central nervous system. Meningioma's originate in the brain in ~90% of the patient group and account for ~35% of all primary brain tumours, yet the substantial majority, ~90%, are benign growths (Holleczek et al, 2019; Zhou et al, 2016; Larjavaara et al, 2008; Claus et al, 2005). Consequently, benign meningioma's, also commonly referred to as WHO grade I meningioma's, have significant 5-year and 10-year survival in patients of 92% and 81% respectively (van Alkemade et al, 2012). Conversely, malignant meningioma's, also known as WHO grade III meningioma's, comprise 1-5% of all cases of the disease, with a reduced 5-year and 10-year survival of 50% and 23% respectively (Lim et al, 2013; Claus et al, 2005; Larjavaara et al, 2008; Holleczek et al, 2019). However, given the fact that the overwhelming minority of patients have malignant neoplasms, meningioma's will not be considered during the project.

#### *1.4.3.2 Glioma*

Gliomas represent a heterogeneous group of neoplasms that describe the unregulated proliferation of glial cells. Presently, it is estimated that gliomas comprise ~30-40% of all primary brain tumours but, crucially, constitute 75-80% of total malignant brain tumours diagnosed in the patient group (Schneider et al, 2010; Lapointe et al, 2018). The majority of glial cells, ~70%, are located in the cerebrum of the brain where the population of glial cells far exceeds the number of neurons with a ratio of 1.48

respectively (Azevedo et al, 2009). Conversely, the cerebellum is predominantly populated with neurons and contains only 19% of total glial cells of the brain (Azevedo et al, 2009). Hence, unsurprisingly gliomas are primarily located in the cerebrum, and estimated to represent over 90% of all gliomas diagnosed in the patient group (Schneider et al, 2010; Grant, 2004). Gliomas may originate from glial cells in any four anatomical lobes of the cerebral hemispheres, either frontal, temporal, parietal or occipital, which have been listed in terms of prevalence in the patient group (Davis, 2016).

Gliomas may be classified according to glial cell type and the invasive nature of cancerous cells relative to surrounding healthy grey and white matter in the brain. Gliomas primarily originate from astrocyte cells in three quarters of all cases and are commonly referred to as astrocytoma's and assigned a specific tumour grade (Grier et al, 2006). Thereafter, oligodendrocyte cells comprise the next most frequently observed glioma by cell type, which are commonly referred to as oligodendroglioma's and assigned a specific tumour grade (Ohgaki et al, 2005). The WHO classification of tumours of the central nervous system strictly employed by clinicians describes grade I astrocytoma's as slow growth tumours that do not invade nearby healthy tissue. Therefore, grade I astrocytoma's are considered benign and patients routinely curable following surgical resection with high survival rates over 90% at 5 and 10 years (Lapointe et al, 2018, Grier et al, 2006). Conversely, grade II, III and IV astrocytoma's show different degrees of invasion of surrounding healthy tissues, and may be classed as malignant. Specifically, grade II astrocytoma's are considered "low-grade" malignancies that slowly progress over time, whilst grade III and IV astrocytoma's are

recognised as "high grade" malignancies with fast growth over time (Lapointe et al, 2018; Wesseling et al, 2018). Furthermore, oligodendroglioma's may either be categorised as grade II "low-grade" malignancies, or grade III "high-grade" malignancies, defined by tumour growth and invasion of nearby healthy tissue (Wesseling et al, 2018; Louis et al, 2016) .

Patients suffering from "low-grade" gliomas represent ~30% of diagnosed gliomas and have median 5-year survival of 50% and 81% for grade II astrocytoma and oligodendroglioma respectively (Ostrom et al, 2017; Lapointe et al, 2018). However, over a variable period of time, patients with grade II "low-grade" gliomas will inevitably progress to "high-grade" gliomas, ultimately leading to premature death. Indeed, patients with "high-grade" gliomas have significantly poorer long-term prognosis, with median 5-year survival of 30% and 57% for grade III astrocytoma's and oligodendroglioma's respectively (Lapointe et al, 2018). Furthermore, patients suffering from grade IV astrocytoma, commonly referred to as glioblastoma multiforme (GBM), representative of ~56% of all glioma patients, have a shocking median survival of 15 months and 5-year survival of 5.5% (Ostrom et al, 2017; Thakkar et al, 2014; Davis, 2016; Lapointe et al, 2018).

*1.4.3.3 Ependymoma*

Ependymoma's describe the development of a primary brain tumour arising from ependymocyte cells in the brain and spinal cord that play a major role in the production and movement of cerebrospinal fluid around the central nervous system. Interestingly,

ependymoma's predominantly originate in the spinal cord in ~60% of adult patients, whilst the overwhelming majority of children, ~90%, present with ependymoma's in the brain (Armstrong et al, 2010; Persaud-Sharma et al, 2017). Ependymoma's may be classed as either WHO grade I, grade II or grade III, with "low grade" tumours the most prevalent in the patient group accounting for 88% of neoplasms compared to ~12% of "high grade" malignancies (Armstrong et al, 2010). Patient survival of "low-grade" and "high-grade" ependymoma is significantly greater compared to glioma malignancies, with 5-year survival at 73.7% and 65.9% and 10-year survival at 60.9% and 41.8% respectively (Mansur et al, 2005). Overall, ependymoma's may be classed as a rare sub-type of malignancies that represent 2-4% of all primary brain cancers (Metellus et al, 2010; Persaud-Sharma et al, 2017), and, given the rarity of the disease will not be considered during the course of this project.

### 1.4.4 Secondary Brain Tumour

The presence of secondary brain tumours in patients is representative of metastases where cancerous cells from primary tumour sites traverse the circulatory blood and/or lymphatic system, enter the central nervous system and continue to uncontrollably proliferate, thereby producing additional malignancies in the central nervous system. Commonly, primary neoplasms responsible for metastasis are found in close proximity to the circulatory system, and primarily constitute lung cancer in over half of all secondary brain metastases, then breast cancer that contributes a fifth of cases, with smaller contributions from melanoma and colon cancer (Eichler et al, 2007; Nathoo, 2005). Entry of cancerous cells into the central nervous system is facilitated by an

impaired blood-brain barrier in patients that allows cells to invade cerebrospinal fluid, circulate the brain and interact with tissues. Since the largest anatomical feature of the brain comprises the cerebrum, it is unsurprising that secondary brain tumours originate in the cerebrum in 80% of patients, followed by 15% in the cerebellum, with 5% prevalence in the brain stem (Eichler et al, 2007). Cancerous cells may either invade healthy tissue in one location, reported in 30-40% of cases, or spread to multiple tissues within the brain, reported by another study in 80-90% of patients (Wong et al, 2008; Patchell, 2003). Therefore, prognosis is devastatingly poor, especially since metastases is indicative of an aggressive "high-grade" primary cancer, with median survival of 6 months in the patient group (Wong et al, 2008). Overall, it is believed primary neoplasms have a 20-40% probability of transforming in to brain metastases throughout the course of malignancy, and as a result the quantity of secondary brain tumours in the population is estimated at 10 times that of primary brain tumours (Wong et al, 2008; Nathoo, 2005; Patchell, 2003). Furthermore, these statistics are anticipated to escalate given the increase in survival rates of numerous cancers combined with projected increases in cancer incidence in future years.

### 1.4.5 Brain Cancer Symptoms

Symptoms of primary and secondary brain tumours largely depend on the position of the glioma with reference to the architecture of the brain and, thus, symptoms are often diverse amongst patients. The most prevalent symptom of brain cancer at presentation is epileptic seizures associated with ~25-35% of glioma patients, predominantly in "low-grade" over "high-grade" gliomas with prevalence at 65-90% and 30-62%

respectively (Davis, 2016; IJzerman-Korevaar et al, 2018; Kerkhof et al, 2013; Armstrong et al, 2016; Vecht et al, 2014). Epileptic seizures have been reported to be the first medical symptom of brain tumours at presentation in 70-90% of "low-grade" glioma patients where high prevalence amongst the patient cohort is believed to be attributable to disease pathophysiology (Kerkhof et al, 2013; Armstrong et al, 2016). In particular, epileptic seizures correlate with presence of specific molecular markers, D-2-Hydroxyglutarate (D2HG) and Isocitrate dehydrogenase 1 (IDH1) mutations, with only 18-34% of IDH1 wild-type patients suffering from epileptic seizures compared to 59-74% for IDH1 mutated patients (Chen et al, 2017). Overall, the clinical utility of epileptic seizures in contributing to glioma diagnoses exceeds all other common patient symptoms and is associated with improved patient outcomes due to correlation with "low-grade" gliomas (Gray et al, 2018; Vecht et al, 2014). However, the probability of a suspected patient with epileptic seizures suffering from a brain tumour is rare with a PPV of 1.2% (Hamilton, 2007). The second most prevalent symptom of glioma at presentation is cognitive deficit, such as deterioration in attention, memory or language function, and is recognised in ~36% of the patient group (IJzerman-Korevaar et al, 2018). The proportion of patients presenting with cognitive deficit is believed to be greater for "high-grade" gliomas compared to "low-grade" gliomas, with heightened impairment for "high-grade" patients due to the interaction of tumours with specific architectures of the brain (van Kessel et al, 2017; Miotto et al, 2011). Furthermore, identification of cognitive deficit in suspected patients with brain cancer is currently the primary criteria for referral of patients to secondary care through the "two-week wait" cancer pathway, as outlined by NICE 2015 guidelines. The third most prevalent symptom of glioma at presentation is headache with an

estimated prevalence of ~21-31% in the patient group, although this statistic is found to vary between different studies from 12.5% up to 60% for glioma patients (IJzerman-Korevaar et al, 2018; Comelli et al, 2017; Russo et al, 2017; Schankin et al, 2007). The probability of a person with headache suffering from brain cancer is extremely rare in primary care settings with a PPV of 0.09%, although when reported with an additional neurological or behavioural symptom, which was more common than headache alone, PPV increased slightly to 0.39% (Hamilton et al, 2007; Ozawa et al, 2018). Other notable patient symptoms of glioma include impairment of motor functions, dizziness, drowsiness and aphasia, with prevalence estimated to be ~22%, ~23.5%, 15% and 20.1% respectively in the patient group (IJzerman-Korevaar et al, 2018). Overall, patient symptoms for brain tumours may be described as diverse, non-specific, subjective and in cases of neurological function may mirror ageing processes. Consequently GP's face significant challenges in accurately assessing whether patients may have a suspected malignancy or whether symptoms simply correspond with commonly observed ailments in the population.

### 1.4.6 Brain Cancer Diagnostics

#### *1.4.6.1 Clinical Assessment*

The diagnostic pathway for a suspected brain tumour is most frequently initiated through patient interaction with a GP in a primary care setting where the GP must evaluate possible causes of symptoms at presentation within allocated time (Ozawa et al, 2018). The GP will consider patient age, medical history and conduct a physical and neurological examination prior to clinical assessment. The GP may refer to revised

NICE 2015 guidelines in cases of suspected malignancy that specifies the necessary conditions for patient referral through the "two-week wait" cancer pathway. Current NICE guidance recommends adult patients should be referred for direct access to medical imaging techniques within two weeks if the patient presents with "progressive, sub-acute loss of central neurological function". Previous NICE guidance recommended referral within a two-week period in cases of "progressive neurological deficit, mental changes and new-onset seizures" and/or "headache of recent onset accompanied by features suggestive of raised intracranial pressure". Given it is estimated that a GP will experience patients with brain tumours on 4 to 5 occasions over the length of their career, alongside time constraints and the subjective nature of current guidelines, it is unsurprising that GP referrals through the "two-week wait" cancer pathway account for ~1% of glioma diagnoses (Grant, 2004; Osawa et al, 2018).

*1.4.6.2 Magnetic Resonance Imaging (MRI)*

The pre-operative diagnosis of glioma is primarily performed with MRI imaging through analysis of the spin state of protons within tissue volumes in response to application of magnetic fields and microwave signals. MRI is currently the preferred imaging modality for tumour identification in the UK, where soft tissue contrast allows characterisation of anatomical structures of the human brain and identification of suspected malignancies. The presence of "low-grade" glioma may be characterised by no enhancement on T1-weighted and enhancement on T2-weighted images of the suspected tumour volume, and minimal enhancement when contrast agents such as

gadolinium have been utilised (Guillevan et al, 2014). Similarly, "high-grade" gliomas show equivalent enhancement on respective T-weighted images, with additional ring enhancement in T2 images characteristic of necrosis, and enhancement when performed with gadolinium contrast agents (Pope et al, 2018; Davis, 2016). Nevertheless, detection of specific tumour grade is a significant clinical challenge for neuro-radiologists with notable intra-observer variability, further highlighted by one study where MRI and CT imaging techniques failed to predict tumour grade in 45% of 20 patients with primary brain tumours (Guillevin et al, 2014; Pope et al, 2018; Kondziolka et al, 1993). Additionally, distinction between astrocytoma and oligodendroglioma "low-grade" tumour types is not possible with MRI (Pope et al, 2018). Similarly, the differentiation between primary brain tumour and secondary metastases is not trivial with MRI, highlighted by one study that showed neuro-radiologists could not distinguish between the two tumour types in >10% of patients (Pope et al, 2018; Patchell et al, 1990). Hence, it is recognised that MRI is susceptible to a degree of diagnostic error, particularly between glioma grades, where sensitivity and specificity ranged from 47.8-82.8% and 90.3-97.6% respectively in >700 patients (Yan et al, 2016). Consequently, suspected malignancies identified through MRI imaging must be confirmed by histopathology of resected tissue during surgery. From an economic perspective, MRI equipment is expensive; estimated cost of a typical unit with magnets of 1.5 to 3 Tesla is $1 million per Tesla, attributed to high magnet costs and need for cooling with liquid helium (Sarracanie et al, 2015). High instrumentation cost inevitably translates to high cost per single test of £164 for a MRI scan in the UK (Gray et al, 2018), and ultimately restricts testing to patients with high suspicion of malignancy based on symptoms at presentation.

*1.4.6.3 Computed Tomography (CT)*

CT may also perform the pre-operative diagnosis of glioma when MRI is contra-indicated according to current NICE guidelines and functions on the principle of the acquisition of multiple X-ray's at specific distance intervals to form a detailed image of the anatomical structure. The resultant CT image indicates the presence of a brain tumour in cases of concentrated enhancement relative to healthy tissue that reflects the increased density of tumour cells. Commonly, the brain tumour is encompassed by a non-enhanced region if the tumour is "high-grade" glioma characteristic of edema (Ahmed et al, 2014; Johnson et al, 2015). CT may also be performed with a contrast agent to increase signal intensity, however, regardless, sensitivity of CT is inferior to MRI for evaluation of soft tissue. To this extent, it was reported that ~10% of patients in a Scottish audit with glioma were originally given a negative diagnoses through CT scans (Grant, 2004). Furthermore, CT was found to have accuracies of 61%, 83% and 82% for "high-grade", "low-grade" and metastases respectively when neuro-radiologist assessment was compared to subsequent histology in 222 patients (Grant, 2004). From an economic perspective, the expense of a CT scan is significant to health services at £85 per scan in the UK (Gray et al, 2018), which similar to MRI is cost prohibitive for extended, wide-scale screening of suspected brain cancer patients.

*1.4.6.4 Histopathology*

Histopathology is performed in the diagnostic pathway following positive diagnoses with medical imaging through stereotactic biopsies or surgical resection to confirm

and grade suspected primary brain tumours. Traditionally, histopathological investigation of primary brain tumours were performed solely with a microscope and haematoxylin and eosin agents that stain nuclei purple and extracellular matrix pink respectively, ultimately allowing inspection of cell morphology and tissue architecture. However, histopathological analysis of cancerous tissue is recognised to be difficult and subjective with significant intra-observer and inter-observer variability reported in the literature (Raab et al, 2005; Gilles et al, 2008). Therefore, the WHO classification for gliomas has recently been revised to allow the integration of classical histopathology with detection of specific biomarkers, namely IDH mutations and 1p/19q status, which together inform clinical diagnoses. Tissue characteristics represent a benign grade I glioma when cellular proliferation is minimal and the tumour boundary is clearly established with no invasion of surrounding healthy tissue (Lapointe et al, 2018, Grier et al, 2006). Pathologist's may identify grade II gliomas when tissue shows signs of increased cell proliferation and infiltration of healthy tissue with poorly defined tumour boundaries (Maher et al, 2001). Additionally, presence of an IDH mutation is highly indicative of a "low-grade" glioma and may be performed through immunohistochemical staining with IDH mutant antibodies that stain cytoplasm and nuclei of mutant cells (Louis et al, 2016; Wesseling et al, 2018). Similarly, grade III gliomas may be identified by presence of IDH mutations and histological inspection where cells show increased proliferation, poor differentiation and significant disruption of surrounding tissue (Wesseling et al, 2018; Maher et al, 2001). Lastly, grade IV primary GBM may be identified by a pathologist when tissue sections display a dense cell population, poor differentiation, tissue necrosis and proliferation of endothelial cells with evidence of a microvascular environment

(Maher et al, 2001). Crucially, primary grade IV GBM's do not display IDH mutations whereas secondary grade IV GBM's, although histologically identical, routinely display IDH mutations, thereby allowing distinction between both tumour types (Louis et al, 2016; Reifenberger et al, 2016; Wesseling et al, 2018). Overall, revised WHO guidelines for glioma classification may be summarised in Figure 1.4, alongside the current histopathology decision pathway in Figure 1.5, which shows the importance of molecular signatures, such as IDH mutations, for glioma diagnosis.

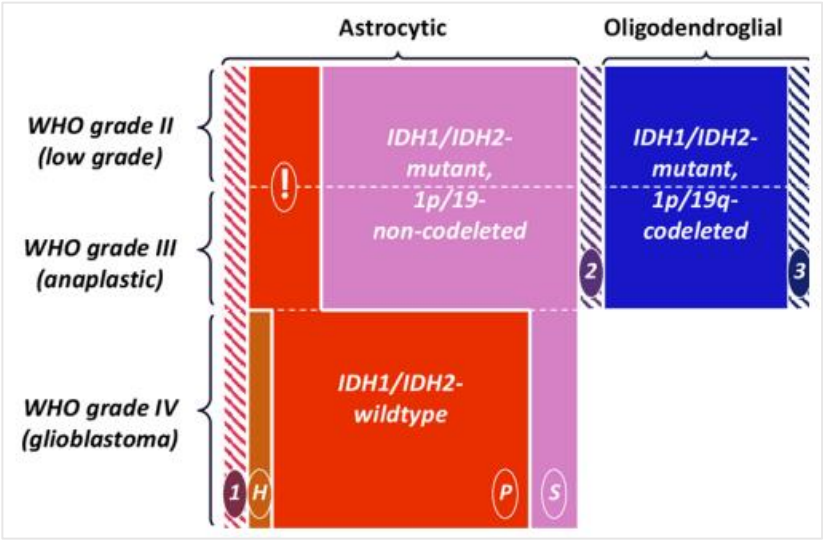


Figure 1.4: WHO Classification for glioma with biomarkers for tumour types. Reproduced (Wesseling et al, 2018).

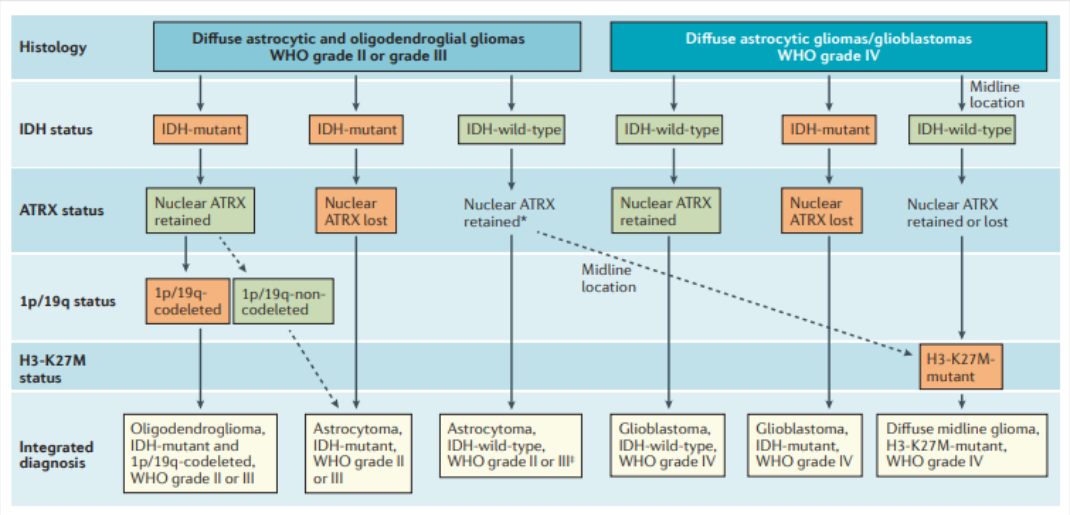


*Fig 1.5: Clinical diagnostic pathway based on molecular biomarkers. Reproduced. (Reifenberger et al, 2016)*

### *1.4.7 Current Diagnostic Molecular Biomarkers*

#### *1.4.7.1 IDH1/IDH2 Mutations*

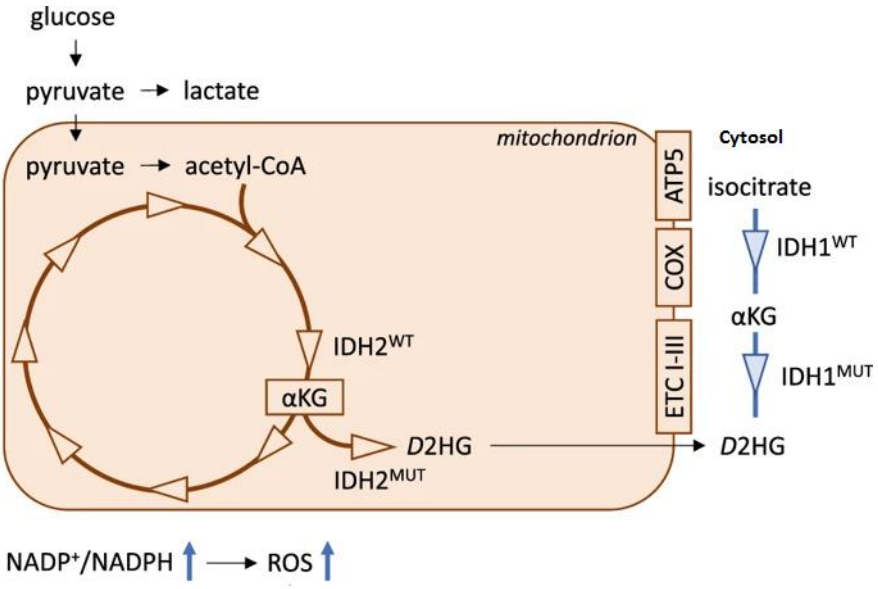


*Fig 1.6: IDH1/IDH2 participation in the Kreb's cycle. Adapted. (Molenaar et al, 2018).*

Identification of point mutations in IDH1/IDH2 proteins is crucial for the accurate characterisation and grading of glioma patients. The IDH1 gene encodes for the IDH1

wild-type enzymatic protein found in the cytoplasm and peroxisomes of cells. The IDH1 wild-type protein facilitates conversion of isocitrate to alpha-ketoglutarate, and reduction of NADH to NADHP in the citric acid cycle, as indicated in Figure 1.6 (Cairns et al, 2013). However, somatic codon 132 mutations of the IDH1 gene encode for mutant IDH1 proteins, with prevalence of IDH1-R132H recognised in >90% of patients, with the remaining IDH1-R132C, IDH1-R132S, IDH1-R132G, IDH1-R132L and R132V mutations identified in significantly less of the population (Balss et al, 2008). The IDH1-R132H mutant protein features a single arginine to histidine amino acid substitution, which causes significant reductions in alpha-ketoglutarate and NADPH, and substantial production of the onco-metabolite D-2-hydroxyglutarate, associated with oxidative damage, DNA methylation and MGMT expression in the early stages of gliomagenesis (Yang et al, 2012). Consequently, IDH1 mutations were found to have strong correlation with grade II astrocytomas (68%), grade II/III oligodendrogliomas (69%), grade II/III oligoastrocytomas (78%) and secondary glioblastomas (88%), in contrast to primary glioblastomas (7%) (Balss et al, 2008). Current detection of IDH1 mutations predominantly rely on immunohistochemistry of tissue samples for IDH1-R132H detection and subsequent genetic testing, such as Sanger and pyro-sequencing, for cases where the test does not identify IDH1-R132H or IDH1-wild type in patients (Picca et al, 2018). Glioma patients with mutations of the IDH2 gene are much less commonly observed clinically and estimated to occur in 2-3% of patients with gliomas (Wang et al, 2016; Cohen et al, 2013). Therefore, only the IDH1-R132H mutation will be considered throughout the course of the project as it is by far the most clinically tested IDH1/IDH2 mutation and covers the overwhelming majority of glioma patients with IDH1/IDH2 mutated status.

*1.4.7.2 ATRX*

The ATRX protein is a tumour suppressant protein influential in chromatin remodelling and production of histone 3.3 for telomeres that ultimately regulates gene expression and helps protect against DNA damage respectively. The loss of function of ATRX arises from alterations in specific genetic content in patients and identification of ATRX is commonly employed in histopathology to determine glioma grade when previous IDH testing has confirmed the presence of an IDH mutation. In particular, loss of function of ATRX in conjunction with IDH mutated status in patients confirms the presence of grade II or III astrocytoma or secondary grade IV glioblastoma. Therefore, loss of ATRX in patients is an important diagnostic biomarker for glioma classification and corresponds with improved patient prognosis when compared to patients with intact ATRX and IDH mutated status (Wiestler et al, 2013; Nandakumar et al, 2017).

*1.4.7.3 1p/19q*

The identification of missing genetic information in chromosomes 1 and 19 is routinely employed on cells of glioma tissue in histopathology when clinicians have suspicions that a patient may have an oligodendroglioma brain tumour. In particular, the 1p/19q test is current standard practice in situations where prior molecular testing indicates IDH mutations and retention of ATRX function in patients. The identification of 1p/19q co-deletion is confirmation of an oligodendroglioma in patients and is associated with improved patient outcomes compared to solely IDH1 mutated or IDH1

wild-type patients (Brat et al, 2015). Furthermore, a positive 1p/19q co-deletion finding in patients has shown to benefit from procarbazine/lomustine/vincristine (PVC) chemotherapy alongside radiotherapy with improved treatment responses (van den Bent et al, 2006). Hence, 1p/19q is an important biomarker in histopathology with significant diagnostic, prognostic and predictive value for patients with oligodendroglioma tumours.

### *1.4.8 Current Problems with Brain Cancer Diagnostic Pathway*

Currently, a mere 1% of patients with primary brain tumours were referred by GP's through the "two-week wait" pathway, as identified in the only long-term study to date assessing referrals from 2002 to 2011 (Hamdan et al, 2013). Of 85 patients suspected of brain cancer referred through the "two-week wait" programme, only 18 individuals received a positive diagnosis. Conversely, ~98% of patients were referred by GP's to secondary care outpatient departments, equivalent to 43,332 referrals, where 1093 brain tumours were later diagnosed. These results were in agreement to previous findings by Pengiran et al where a 9-month retrospective study in Nottingham and Derby between 2000 and 2001 found that 4 of 43 patients referred through the "two-week wait" pathway received a brain tumour diagnosis, whilst at least 69 patients received diagnosis of brain tumours through other pathways (Pengiran et al, 2003). In both studies, GP's were found to adhere to diagnostic referral guidelines in 59% and 70% of cases respectively. However, adherence to clinical guidelines resulted in only 20 out of 80 patients receiving positive diagnoses, whilst strict guideline adherence would have prevented positive diagnosis of two brain tumours, highlighting the

difficulty in finding a predictive diagnosis for brain cancer. To compound matters, patient symptoms are often non-specific, and may include headache, anxiety, depression, confusion and memory loss, all symptoms of numerous other conditions and therefore have low associated PPV's of less than 1% for brain cancer (Hamilton et al, 2007; Schmidt-Hansen et al, 2015). Incidence in the UK for patients attending primary care with symptoms of headache is 4.4% per year, which far outweighs the incidence of brain tumours in the UK at 0.01-0.06% per year, thereby producing a low PPV for headache of 0.09% (Suwanwela et al, 1994; Hamilton et al, 2007). Yet, a recent study found that ~21% of brain tumour patients that initially presented at primary care stated headache as their most common symptom, and under current guidelines would not be considered for immediate referral to medical imaging, unless suffering from additional, well-defined decline of neurological function. Consequently, such patients visit their GP practice on average 3-5 times prior to referral to secondary care, leading to significant diagnostic delays that varied between studies, from 30-75 mean days and up to 86-166 days for a quarter of the patient group (Ozawa et al, 2018; Lyratzopoulos et al, 2013). Other clinical experts believe the total time a patient spends in primary care is anywhere between 3-12 months (Gray et al, 2018). Heightened patient symptoms often translates to presentation in emergency settings, where >60% of brain cancer patients currently receive diagnosis, with reduced overall and one-year survival compared to diagnosis through non-emergency pathways (Penfold et al, 2017; Aggarwal et al, 2014). Therefore, there is a clear need to identify suspected brain cancer patients early in the primary care setting pathway to prevent patients with non-specific symptoms incurring considerable diagnostic delay.

Presently, a notable issue is the lack of available and low-cost diagnostic tests that could provide assistance to GP's to help determine whether a patient may be suffering from brain cancer or simply has a common illness. Recently, it has been demonstrated in a large population-based study that out of 2,938 patients referred to direct access CT by GP's for suspected brain tumours, only 42 patients were diagnosed with a malignant brain tumour, equating to 1.43% of patients (Zienius et al, 2019). Hence, introduction of an extended, widespread screening programme for patients with current medical imaging modalities for earlier detection is not economically viable given the ~£100 per scan costs as previously described, and emphasises the significant avoidable cost to the NHS for medical imaging of persons that do not have brain tumours. Therefore, development of rapid, low-cost platforms in primary care to triage patients for medical imaging may reduce diagnostic delay whilst potentially providing cost-saving or cost-effective infrastructures for health care providers. Interestingly, a recent study found GP's were of the opinion that ~30% of diagnostic delays experienced by patients in primary care may have been preventable, whilst one fifth of GP's advocated that tools allowing timely clinical assessment may have benefited patients (Osawa et al, 2018).

Presently, identification of patients with a "low-grade" glioma is a challenge in the clinical pathway as slow tumour growth often translates to less notable symptoms at presentation compared to "high-grade" gliomas, thereby contributing to significant pre-clinical delays for patients (Bouwen et al, 2018; Arnautovic et al, 2016). In particular, "low-grade" glioma patients commonly present with epileptic seizures of wide-ranging severity in ~70-90% of cases, although, crucially, show markedly

reduced prevalence of other common brain cancer symptoms, including neurological deficit, 2-30%, and elevated intracranial pressure, ~10%; both requirements for secondary care referral through "two-week wait" cancer pathways (Jooma et al, 2019; Wessels et al, 2003). To this extent, it has been estimated that ~10% of patients with "low-grade" glioma are diagnosed unexpectedly through imaging of other clinical events, and emphasises the difficulty of prompt diagnosis for some patients (Jooma et al, 2019; Potts et al, 2012). Furthermore, whilst MRI generally allows accurate identification of brain tumours, it is significantly poorer at determining tumour grade, where one study found that approximately a third of primary brain tumours diagnosed as "low-grade" through MRI were in fact "high-grade" malignancies (Scott et al, 2002). Therefore, development of a rapid and low-cost platform to accurately detect "low-grade" primary brain tumours for patients presenting with often overlooked symptoms would be beneficial for GP's and patients to facilitate referral from primary care settings.

Prolonged time to diagnosis and treatment for "low-grade" glioma patients risks the acceleration of brain tumour progression to a "high-grade" tumour, with poorer patient outcomes and reduced overall survival (Lapointe et al, 2018). Consequently, survival rates for "low-grade" glioma patients at 5-years varies significantly from 27% to 85% in the patient group, in part determined by prompt diagnosis and access to treatment (Wessels et al, 2003). Traditionally, "low-grade" glioma patients were deemed at risk of accelerated progression to "high-grade" malignancies when over 40 years of age, whilst patients below 40 years of age represented lower risk for rapid tumour growth (Geurts et al, 2018). However, recent emergence of molecular biomarkers, namely

IDH mutations, ATRX and 1p/19q co-deletions, have demonstrated substantial predictive and prognostic capabilities for glioma patients (Sanson et al, 2009; Hartmann et al, 2011). In particular, it has been acknowledged that early and maximal surgical resection in "low-grade" patients with particular molecular profiles provides significantly increased chances of long-term survival (Hardesty et al, 2012; Jooma et al, 2019; Jakola et al, 2012; Jakola et al, 2017), particularly with regards to IDH1 mutations (Wijnenga et al, 2017). Similarly, IDH1 mutations in glioblastoma patients were associated with significantly improved patient survival following surgery in comparison to IDH1 wild-type patients (Beiko et al, 2013). Presently, guidelines suggest a sequential testing approach for detection of molecular biomarkers that starts with immunohistochemistry of IDH1 mutations and ATRX on resected tissue samples post-surgery followed by genetic testing of 1p/19q co-deletions with fluorescence in-situ hybridization (FISH) (Sepúlveda-Sánchez et al, 2018). The immunohistochemistry and FISH protocols are time-consuming and consequently denies neurosurgeons the status of molecular biomarkers in patients intra-operatively (Livermore et al, 2019). This has negative implications for neuro-oncology since absence of biomarker status means neuro-surgeons cannot evaluate the benefit of maximal resection against possible side-effects of surgery with knowledge of predicted patient outcomes based on molecular signatures. Hence, development of tests that enable molecular biomarkers to be identified in patients either prior to surgery or intra-operatively would be beneficial to neurosurgeons and inform surgical decisions during surgery. Furthermore, it has been shown that molecular biomarkers, including IDH1 mutations and 1p/19q co-deletion, may predict patient response to chemotherapy in the case of low-grade gliomas and oligodendrogliomas respectively

(Huang et al, 2019; van den Bent et al, 2013; Koriyama et al, 2018). Therefore, detection of biomarkers in patients prior to surgery would facilitate effective treatment planning and timely initiation of drug therapeutics for patients.

### *1.4.9 Human Blood Serum*

Blood is fundamental to physiological function of all cells and their perpetual interaction provides a rich source of endogenous molecules that may inform a person's disease status. Cancer represents a host of genetic and epigenetic changes in cells, and since one gene has potential to produce ~100 proteins, numerous, distinct protein signatures undoubtedly exist within cancer cells and the tumour microenvironment (Ponomarenko et al, 2016). Recently, changes in function of specific intracellular proteins, namely ARF and RAB, which together influence cellular secretion, have been observed for numerous cancers, including glioma, leading to over stimulation of the classical secretion pathway, as indicated in Figure 1.7 (Bonnin et al, 2018; Casalou et al, 2016; Kim et al, 2014). Similarly, the four distinct mechanisms that comprise the non-classical secretion pathway, namely plasma membrane, ABC transporter, autophagosome and Golgi bypass mechanisms, have all been implicated in many cancers in response to cellular stresses, thereby over stimulating the non-classical secretion pathway (Bonnin et al, 2018). Extracellular vesicles comprised of exosomes and micro-vesicles have also been recognised to play an increasingly important role in tumorigenesis, and ultimately facilitate the transfer of oncoproteins, metabolites, lipids and nucleic acid content from cancer cells to the tumour microenvironment. Furthermore, death of cancerous cells causes the release of nucleic acid content,

referred to as circulating tumour DNA (ctDNA), into the blood circulatory system (Bonnin et al, 2018). Consequently, a plethora of molecules that reflect biochemical events of malignancy and tumour growth may be present in blood, and therefore represents an attractive and promising sample medium for the early identification of cancerous events.

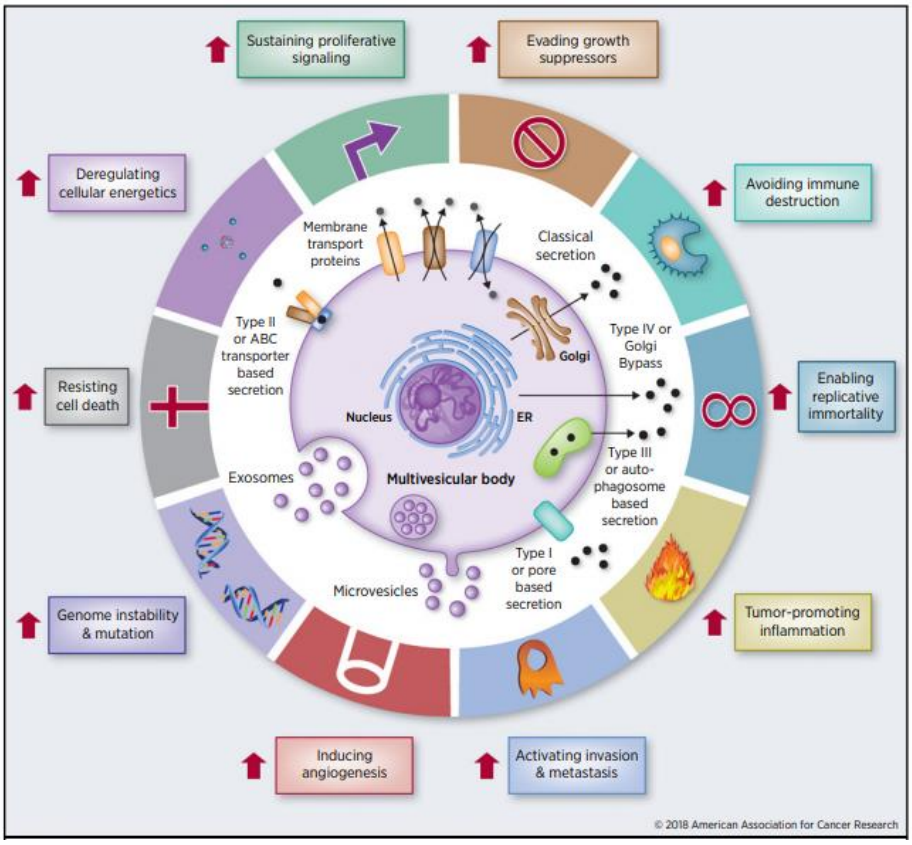


*Fig 1.7: Cellular secretion pathways implicated during tumorigenesis. Reproduced. (Bonnin et al, 2018).*

The detection of biomolecules implicated in cancer with a blood-based diagnostic scheme would be advantageous in the clinical environments for both patients and clinicians alike. Blood serum represents the fraction of blood that contains no red or white blood cells, coagulating factors or fibrinogen, but that contains a multitude of proteins, lipids, carbohydrates, nucleic acids, hormones, antigens and antibodies that reflect various physiological functions of an individual. In particular, blood serum is

overwhelmingly comprised of high molecular weight albumin and immunoglobulin proteins, where the remaining lower molecular weight proteins present in smaller quantities describe the "peptidome" of an individual thought to be important for disease diagnostics (Bonnier et al, 2016). Indeed, protein biomarkers, such as CA125, prostate specific antigen and α-fetoprotein, already inform diagnosis of certain cancers within current health care practices. Hence, the concept of detecting biomolecules in blood serum to inform clinical decision-making is well established, and its present wide-spread employment in clinical biofluid laboratories may facilitate easier clinical translation. Similarly, the collection of blood from suspected patients is familiar, minimally invasive, rapid and cost-effective, with subsequent blood fractionation to obtain blood serum already well established in clinical laboratories through centrifugation processes. Therefore, employment of blood serum as a screening diagnostic tool for early cancer detection is attractive for the clinic from both practical and economical perspectives.

It is widely recognised that cancers display a high degree of intra- and inter-patient tumour heterogeneity and therefore one of the criticisms of a blood-based approach is that identification of a single biomarker may not be representative of a patients malignancy and health status (Mayeux, 2004). To this extent, we believe that the combination of infrared spectroscopy and electrochemistry may allow improved detection capabilities to account for tumour heterogeneity. Specifically, infrared spectroscopy provides qualitative interrogation of all infrared active macromolecular constituents of serum, and has previously demonstrated detection of cancers with high sensitivities and specificities as discussed in depth later. Conversely, electrochemistry

provides direct or indirect quantitative detection of specific biomolecules and has previously demonstrated significant potential for detection of cancer biomarkers as detailed later. Together, we believe that the combination of both techniques would provide significantly more diagnostic information on serum samples, which may ultimately translate to an accurate, representative serum diagnostic test to inform clinical decisions.

#### *1.4.6.6 Potential Serum Biomarkers for Brain Cancer*

The detection of blood-based biomarkers would represent a paradigm shift in the current clinical diagnostic pathway for brain cancer where molecular status of a patient is often established at a late stage of cancer progression and following invasive surgical procedures. Currently, the only biomarkers clinically accepted to support clinicians in diagnosis and grading of primary brain cancer are IDH mutations, 1p/19q and ATRX, which are detected from resected tissue samples as previously mentioned. However, various biomarkers present in blood fractions of glioma patients have been shown to correlate with presence of brain tumours, and deserve consideration as target biomarkers for the proposed device. Glial fibrillary acidic protein (GFAP) molecules were found present in 40 out of 50 grade IV glioblastoma patients at significantly higher concentrations in comparison to grade III astrocytoma, oligodendroglioma and healthy volunteer patients (Jung et al, 2007). However, other findings have found that GFAP is a protein biomarker that may correlate with neurological trauma rather than tumorigenesis, since concentration was shown to rise considerably from 52% to 96% in glioma patients following surgery irrespective of tumour grade (Husain et al, 2012).

These observations have been confirmed in another study that showed GFAP concentration increased with the severity of traumatic brain injury (Lei et al, 2015). Several proteins of angiogenesis related to blood vessel formation and tumour progression have been targeted as prognostic biomarkers in the serum of glioma patients. In particular, both vascular endothelial growth factor (VEGF) and basic fibroblast growth factor (bFGF) were evaluated in 50 patients during a clinical trial of angiogenesis factors, where serum concentrations did not correlate with disease progression (Kesari et al, 2008). Furthermore, VEGF concentrations were not found to decrease upon temozolomide and radiation treatment therapies and therefore did not reflect prognostic outlook for patients (Demirici et al, 2012). Similarly, overexpression of two other related angiogenic factors, epidermal growth factor receptor (EGFR) and EGFR mutant vIII (EGFRvIII), are widely identified to be important in progression of "high-grade" gliomas but elevated levels of these molecules did not translate to significant differences in overall survival, and, hence, exhibited poor prognostic utility (Chen et al, 2015). Another major issue with discussed angiogenic factors is their lack of specificity to glioma cancers. Changes in concentrations of VEGF, bFGF, EGFR and EGFRvIII have been found in various cancers, not limited to breast and lung cancer, and other neurological conditions, such as Alzheimer's disease and stroke, ultimately yielding poor diagnostic significance for screening tests (Kros et al, 2015; Shim et al, 2018; Gan et al, 2013). Another proposed protein biomarker, YKL-40, is widely recognised to be secreted in to the circulatory system from macrophages and has been found to be present at elevated levels in blood serum of glioma patients in numerous studies (Hormigo et al, 2006; Bernardi et al, 2011). Notably, one large-scale prospective study on 1740 samples found that elevated YKL-40 in serum facilitated

stratification of "low-grade" and "high-grade" gliomas and correlated with worse overall patient survival (Iwamoto et al, 2011). However, YKL-40 has similarly been identified in a host of other cancers, such as melanoma, colon and prostate cancer, as well as cardiovascular disease and diabetes, and therefore represents a poor biomarker for screening (Schmidt et al, 2006; Johansen et al, 2009; Rathcke et al, 2009). The significant challenge in identifying well-established proteins specific to glioma is further highlighted by raised serum levels of several cytokines. In particular, interleukin-6 and interleukin-10, have been reported in blood serum of glioma patients, but their presence has similarly been recognised in the pathophysiology of various other diseases given the prominent role of cytokines in inflammatory pathways. (Shan et al, 2015; Burmeister et al, 2018).

The characteristics of ctDNA may provide improved biomarker specificity given that these nucleic acid strands are directly secreted from cancer cells upon apoptosis and cell necrosis. Previous studies have shown detection of ctDNA associated with p16, p73, p15INK4B, p14ARF and MGMT genes in blood plasma and serum of glioma patients with variable test performance, with a range of sensitivities and specificities at 11.8-60.0% and 75.0-95.0% respectively (Majchrzak-Celińska et al, 2013; Weaver et al, 2006; Wakabayashi et al, 2009; Balana et al, 2011). Increased specificity is unsurprising given that these ctDNA targets represent mutated tumour suppressant genes that are heavily involved in unregulated cellular proliferation that is a hallmark of cancer. However, findings should be considered with caution as studies were conducted on between 10 and 20 individuals. Furthermore, reported ctDNA tests represent mutations in tumour suppressant genes that participate in a variety of

cancers, hence, test specificity may be significantly reduced for screening of the general population where individuals may present with other malignancies (Kim et al, 2011, Lee et al, 2009). Interestingly, detection of ctDNA for IDH1 has also been reported in blood plasma of glioma patients harbouring the IDH1-R132H mutation and may represent an improved diagnostic strategy given IDH1 mutations are directly involved in gliomagenesis for certain astrocytoma tumour types (Boisselier et al, 2012). Whilst the study found detection of ctDNA for IDH1-R132H correlated with tumour volume and had a test specificity of 100%, test sensitivity was only 60% from 25 patients, and consequently total ctDNA content was not found to be significantly different from healthy controls. Poor test sensitivity is a common feature for ctDNA diagnostic schemes that may be attributed to the small concentration of ctDNA fragments relative to total circulating free DNA (cfDNA) (Elazezy et al, 2018). In particular, percent fraction of mutant ctDNA in cfDNA is strongly correlated with tumour volume, and it is estimated that 0.01% ctDNA in total cfDNA is likely the lowest detectable concentration with current diagnostic approaches, which equates to a tumour volume of 12.5mm diameter (Diamandis et al, 2017). Hence, it is argued that patients with tumours <12.5mm diameter would not be detectable in plasma extracted from standard 10ml blood draws (Diamandis et al, 2017). This may in part explain poor sensitivities of previously reported results and poses significant challenges for clinical translation of ctDNA platforms for glioma since previous health economics studies have indicated sensitivity must be ≥80% to be economically viable as a screening tool within health services.

Therefore, it was decided through discussions with our clinical collaborators that it was imperative to target biomarkers that were not only specific to gliomagenesis but that could actively participate in the current diagnostic pathway for glioma classification. To this extent, a possible biomarker target deemed worthy of investigation was the IDH1-R132H mutant protein. To date, no studies have been published regarding the detection of IDH1 mutant proteins in the circulatory system. However, given the IDH1-R132H protein resides in the cytosol of cells and that over stimulation of classical and secondary secretion pathways is heavily implicated in gliomagenesis as previously described, it has been deemed feasible that IDH1-R132H proteins may translate to the extracellular environment during gliomagenesis. Furthermore, recent identification of nucleic acid content of IDH1-R132H proteins in blood serum has demonstrated that the mutant variant protein interacts to some capacity with the circulatory system. The IDH1-R132H protein has significant relevance to clinicians and detection in blood serum of glioma patients has potential to redefine the current diagnostic pathway, where by the molecular status of patients would be accessible to clinicians prior to invasive surgical procedures, ultimately allowing accurate prognosis and improved surgery and treatment planning for patients.

### *1.4.7 Hodgkin's Lymphoma*

#### *1.4.7.1 Introduction*

Today, approximately six individuals will receive a confirmatory diagnosis of Hodgkin's lymphoma in the UK, equivalent to ~2,100 persons in one year in the UK (Cancer Research UK, 2019). Hodgkin's lymphoma describes unregulated

proliferation of a particular white blood cell, namely B type lymphocytes, pertinent to the lymphatic system. The lymphoproliferative disorder may be further categorised as either classical or nodular lymphocyte-predominant Hodgkin's lymphoma, with >90% of patients diagnosed with classical Hodgkin's lymphoma (Cancer Research UK, 2019; Shanbhag et al, 2018). To date, incidence of Hodgkin's lymphoma has risen dramatically by 36% over the past thirty-year period, and is predicted to rise by a further 5% by 2035 (Cancer Research UK, 2019). The disease displays a bi-modal age distribution with highest incidence in 20-25 and 75-85 age groups, and affects more males than females at 57% and 43% respectively in the UK, as indicated in Figure 1.8. (Cancer Research UK, 2019). Presently, one-person dies from Hodgkin's lymphoma per day in the UK, which translates to ~330 mortalities per year in the UK, with a 5-year and 10-year survival rate of ~85% and ~80% respectively (Cancer Research UK, 2019). The outlook for patients suffering from Hodgkin's lymphoma has improved immensely over the past fifty years with a 30% increase in 5-year survival attributed to improved treatment therapeutics and is now considered a highly remediable malignancy (Cancer Research Uk, 2019; ). However, significant delays in the diagnostic pathway for some patients prevents timely initiation of treatment and correlates with poorer progression-free and overall survival (Brooks et al, 2015). Additionally, the recurrence of disease or unresponsiveness to chemotherapy or radiation treatments occur in 5-20% of "low-grade" patients and 15-40% of "high-grade" patients, who then require salvage chemotherapy prior to high dose therapy and autologous stem cell transplants (Nikolaenko et al, 2017; Byrne et al, 2007; Brice, 2018). In both scenarios, patient outcomes and prognosis is poor with second attempt treatments curing only half of recurred or refractory patients (Gopas et al, 2016;

Ahmadzadeh et al, 2014; von Tresckow et al, 2016). Hence, there is a real clinical need to identify patients that may not respond to chemotherapy agents or may be at increased risk of disease recurrence. To this extent, positron emission tomography (PET) imaging in conjunction with CT imaging is currently employed to grade malignancies, to confirm chemotherapy effectiveness at treatment onset and to confirm disease remission upon successful chemotherapy treatment. Overall, PET shows high sensitivity and specificity for imaging of Hodgkin's lymphoma at 93% and 88% respectively, although is extremely costly at £750-1000 per scan, with significant additional infrastructure costs for PET scanners estimated to be >£10 million ultimately limiting wide-spread use in secondary care (Isasi et al, 2005; Brush et al, 2011; Medical Research Council, 2017). Furthermore, it has recently been shown that molecular biomarkers may provide considerable potential to identify possible refracted Hodgkin's lymphoma patients earlier than PET scans throughout assessment of chemotherapy treatment (Farina et al, 2014). Therefore, the development of a low-cost, molecular based diagnostic device for early detection and monitoring of classical Hodgkin's lymphoma throughout treatment would have significant benefits to patients, clinicians and health care services alike, and serves as a primary source of motivation for the project.

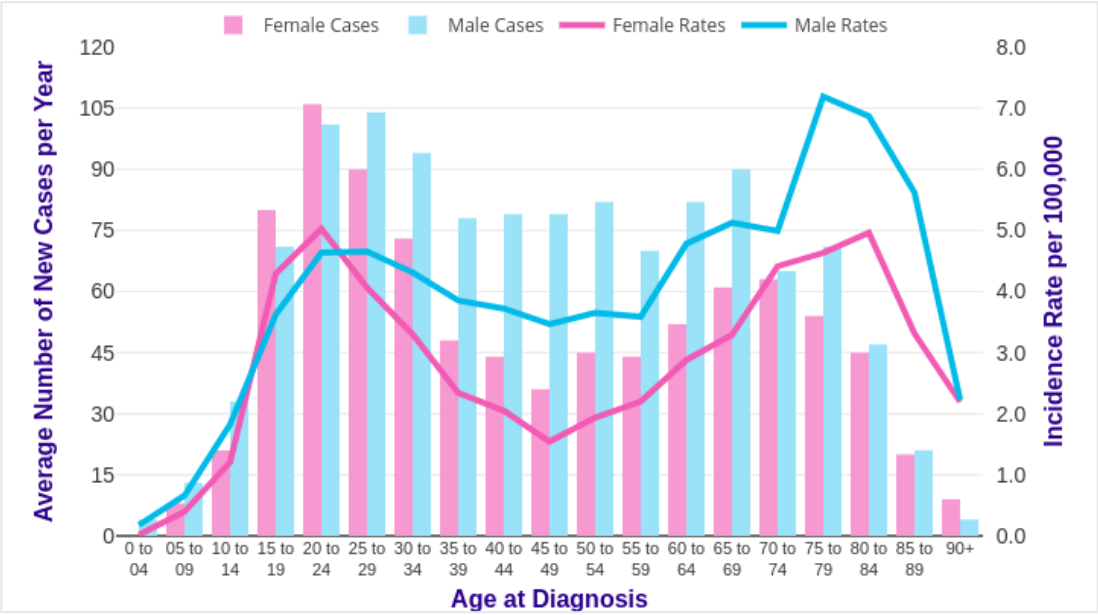


*Fig 1.8: Hodgkin's lymphoma incidence in UK for males and females 2014-2016. Reproduced (Cancer Research UK, 2019).*

### *1.4.7.2 Anatomy of Lymphatic System*

The lymphatic system is comprised of a vast network of lymphatic vessels and nodes that transport lymph fluid around the human body and primarily functions to remove various organisms and cellular waste products to protect against ill health. The lymphatic system maintains protective functions in the body in part through the production of both T-lymphocytes in the thymus and several white and red blood cells in bone marrow. Similarly, the spleen provides rich populations of lymphocytes and replenishes blood cells in the circulatory system. Likewise, recent evidence suggests that tonsils may also produce T-lymphocytes that serve to protect against entry of foreign organisms during inhalation (McClory et al, 2012). Together, these anatomical features are commonly referred to as lymphatic organs and play important roles in production of lymphocytes that contribute to the immune system of an individual. Subsequently, lymph nodes provide storage of both T-lymphocytes and B-

lymphocytes within the lymphatic system that filter lymph fluid, provide intra-cellular protection against organisms, and produce antibodies respectively. The distribution of lymph nodes throughout the human body is widespread, however, high populations are present in the groin, armpit, abdomen and pelvic regions, with ~10% of total lymph nodes further located in the neck (Ramadas et al, 2017), as indicated in Figure 1.9. Hodgkin's lymphoma primarily originates in lymph nodes of the neck in ~70% of the patient group, and in the spleen in ~30% of cases, with smaller prevalence reported in lungs, bone marrow and liver of patients (Cancer Research UK, 2019).

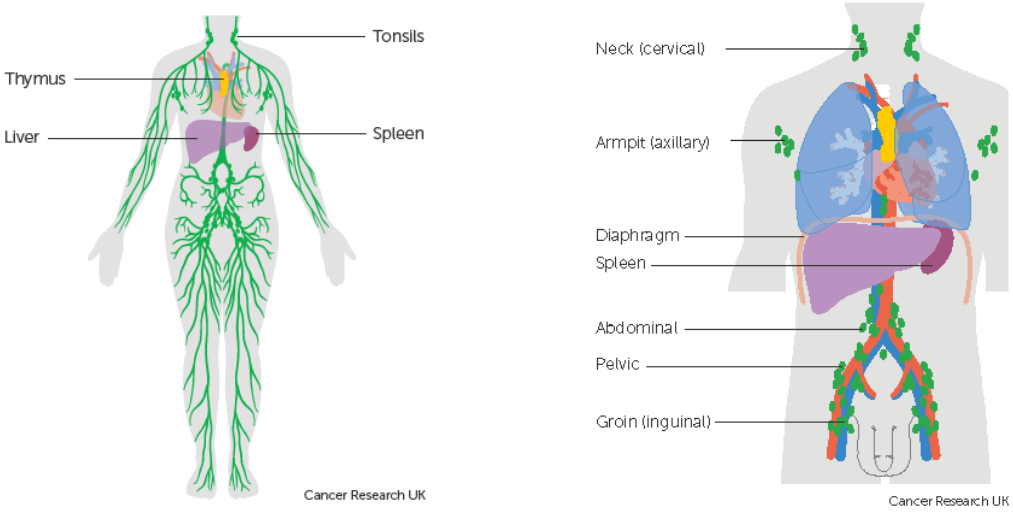


*Fig 1.9: Anatomy of the lymphatic system. Reproduced. (Cancer Research UK, 2019).*

### *1.4.7.3 Biology Overview of classical Hodgkin's Lymphoma*

Hodgkin's lymphoma is characterised by the existence of a small quantity of Reed-Sternberg and Hodgkin cells, ~1-10%, encompassed by a large population, ~90-99%, of molecules and cells associated with inflammatory responses (Hnatkova et al, 2009; Kuppers et al, 2008). Reed-Sternberg cells arise from unintentional proliferation of mutated B-lymphocytes in lymphatic tissue with the Epstein-Barr virus also believed

to contribute to malignant transformation in 40-50% of individuals (Kuppers et al, 2012; Hnatkova et al, 2009). Reed-Sternberg cells represent large cells with multiple nuclei that secrete a host of signalling molecules that promote progressive growth of the tumour microenvironment. Specifically, Reed-Sternberg cells express chemokines, such as CCL17/TARC, which primarily target the protein receptor CD4 on cell membranes of T-lymphocytes that encourage their activation and migration to malignant sites (Kuppers et al, 2012; Hnatkova et al, 2009). Additionally, Reed-Sternberg cells secrete a multitude of cytokines, carbohydrate binding proteins and interleukin molecules that to a lesser extent also attract other white blood cells, such as eosinophils, neutrophils and macrophages, and connective tissue cells, such as fibroblasts and mast cells, as indicated in Figure 1.10 (Hnatkova et al, 2009; Kuppers, 2008; Kuppers et al, 2012). The accumulation of inflammatory cells that encompass Reed-Sternberg and Hodgkin cells primarily function to support proliferation and stability of malignant cells through release of chemokines and cytokines, such as CD28 and CD40L, that promote tumorigenesis (Kuppers et al, 2012). Ultimately, the complex interplay between malignant and inflammatory cells promotes abnormal growth of lymphatic tissue that may have devastating consequences for patients if not diagnosed and treated with chemotherapy agents promptly.

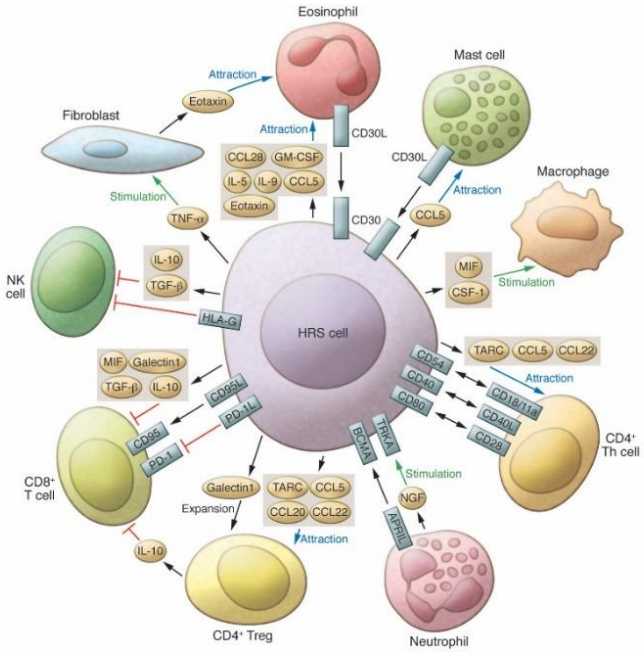


*Fig 1.10: Overview of biological molecules involved in Hodgkin's lymphoma. Reproduced. (Kuppers et al, 2012)*

### *1.4.7.4 Types of Hodgkin's Lymphoma*

#### *1.4.7.4.1 Classical Hodgkin's Lymphoma*

Classical Hodgkin's lymphoma is exclusively diagnosed through identification of Reed-Sternberg cells and may be further categorised in to four disease sub-types relative to the architecture of both malignant cells and the tumour microenvironment. Nodular sclerosis Hodgkin's lymphoma is clinically prevalent representing ~70-75% of classical Hodgkin's lymphoma patients and describes extensive fibrous tissue that encompasses morphologically distinct Reed-Sternberg cells (Agostinelli et al, 2014, Shanbhag et al, 2018). Nodular sclerosis Hodgkin's lymphoma predominantly appears in lymph nodes located in the neck, collarbone or lung regions, and typically represents "low-grade" malignancies of grade I or II status, therefore, is associated with favourable prognosis with ~80% progression-free survival (Ansell, 2015; Derenzini et

al, 2011). Nodular sclerosis Hodgkin's lymphoma is generally not related to positive Epstein-Barr virus cases and predominantly affects adolescents and young adults <30 years of age (Shanbhag et al, 2018; Derenzini et al, 2011). Mixed cellularity Hodgkin's lymphoma is the next most prevalent representative of 20-25% of the patient group and constitutes Reed-Sternberg cells surrounded by diverse populations of inflammatory cells (Shanbhag et al, 2018). The disease predominantly affects young adults <30 years of age and elderly individuals ≥50 years of age and is strongly linked with patients of positive Epstein-Barr and HIV infected status, and, therefore, has poorer patient prognosis (Shanbhag et al, 2018; Derenzini et al, 2011). Lymphocyte rich Hodgkin's lymphoma is a less prevalent form of the disease that affects ~5-6% of patients and is characteristic of Reed-Sternberg cells distributed within a tumour microenvironment composed of high numbers of lymphocytes. Generally, lymphocyte rich Hodgkin's lymphoma primarily affects older individuals' ≥50 years of age, where high frequencies of "low-grade" malignancies translates to favourable prognosis amongst patients (Shanbhag et al, 2018; Agostinelli et al, 2014). Lastly, lymphocyte depleted Hodgkin's lymphoma is the least clinically prevalent disease form affecting ~1% of patients and involves Reed-Sternberg cells within a scarce inflammatory environment (Shanbhag et al, 2018). Consequently, the disease does not present with enlarged lymph nodes and typically affects elderly patients with positive HIV status that results in poor patient outcomes (Shanbhag et al, 2018; Ansell, 2015).

*1.4.7.4.2 Nodular Lymphocyte-Predominant Hodgkin's Lymphoma (NLPHL)*

NLPHL does not concern the presence of Reed-Sternberg cells and instead describes a fundamentally different disease pathophysiology centred around the abnormal growth of lymphocyte-predominant cells. Malignant lymphocyte-predominant cells have distinct molecular signatures and morphologies that display slower rates of growth in comparison to Reed-Sternberg cells, which ultimately translates to significantly improved patient outcomes (Kuppers et al, 2012). Overall, the incidence of NLPHL is extremely low in the general population at 0.1 to 0.2 per 100,000 persons, equivalent to ~5% of all Hodgkin's lymphoma cases (Eichenauer et al, 2017), and, therefore, NLPHL shall not be considered in the project given the rarity and prognosis of the disease.

#### *1.4.7.4 Symptoms of classical Hodgkin's Lymphoma*

Symptomatic clinical presentation has been observed in ~90% of Hodgkin's lymphoma patients where the vast majority of individuals, ~70%, experience painless lymphadenopathy in the neck (Shepard et al, 2015; Cancer Research UK, 2019). Additionally, Hodgkin's lymphoma patients may also present with painless lymphadenopathy in the chest region in ~60% of cases (Shanbhag et al, 2018; Townsend et al, 2012). Furthermore, general, non-specific symptoms commonly referred to as B-symptoms have been routinely clinically reported in ~25-33% of patients (Pileri et al, 2002; Glass, 2008). B-symptoms describe systemic, non-specific symptoms that may include high temperature, night sweats and/or weight loss, which appear more common in elderly individuals and correlate with poorer patient outcomes (Glass, 2008). High prevalence of general, non-specific symptoms is similarly

observed with tiredness and was reported as the second most common reported symptom in one study after lymphadenopathy (Howell et al, 2013). Overall, it is recognised that ~50-65% of all Hodgkin's lymphoma patients initially present with "low-grade" malignancies (Shamoon et al, 2018; Pileri et al, 2002), which provides considerable optimism that, in some instances, earlier diagnosis may improve long-term patient outcomes.

#### *1.4.7.4 Classical Hodgkin's Lymphoma Diagnostics*

##### *1.4.7.4.1 Clinical Assessment*

Clinical evaluation of suspected patients routinely encompasses a review of patient medical history to establish the presence of B-symptoms and a physical examination to identify the presence of potential lymphadenopathy or swollen spleen or liver. Additionally, blood may be taken from the patient and sent to clinical laboratories with request of a full blood count and erythrocyte sedimentation rate (ESR) in cases where the patients describes B-symptoms. Current NICE guidelines further suggest that patients should be considered for referral through the "two-week wait" cancer pathway in situations where patients may present with unexplained lymphadenopathy accompanied with either B-symptoms, alcohol induced lymph node pain or shortness of breath (NICE, 2015).

##### *1.4.7.4.1 Exploratory Imaging with X-Ray & Computed Tomography (CT)*

X-ray and CT is routinely employed as exploratory imaging tools for Hodgkin's lymphoma depending on the location of the suspected malignancy. Currently, X-ray is used to assess possible swollen lymph nodes located in the chest region. Similarly, CT is used to assess the thorax of a patient as well as the pelvis and abdomen and neck in cases of cervical lymphadenopathy (NHS England, 2011).

*1.4.7.4.1 Confirmatory Diagnosis with Lymph Node Biopsies*

Patients must receive a lymph node biopsy in secondary care to confirm the presence of suspected Hodgkin's lymphoma where excised cells are subjected to immunohistochemical staining to identify Reed-Sternberg cells. Immunohistochemistry analysis utilises a panel of antibodies for identification of CD30, CD15 and CD20 biomarkers present on formalin fixed, paraffin embedded tissue samples (Pileri et al, 2002; Karnik et al, 2003). Fine-needle aspiration is not currently recommended for diagnosis of Hodgkin's lymphoma in health practice as the low quantity of Reed-Sternberg cells combined with reduced sampling size may cause misdiagnosis in patients (Hehn et al, 2004).

*1.4.7.4.1 Grading with CT, Positron Emission Scanning (PET) & Blood Chemistry*

Tumour grading is mandatory upon a confirmatory diagnosis of Hodgkin's lymphoma to establish the spread of malignancy and allow accurate assessment of proposed treatment therapeutics. Currently, PET in conjunction with CT is the gold standard imaging modality for grading where radioactive labels, 18-fluoro-2-deoxy-D-glucose, show increased uptake by cancerous cells that allows improved detail compared to CT

alone. In particular, it has been recognised that PET/CT has the capacity to identify additional malignant features in up to ~30% of Hodgkin's lymphoma patients (Subocz et al, 2017). Hence, PET/CT performance is superior for grading with sensitivities of 73% and 92% for extra-nodal and nodal characterisation of lymphatic tissue in comparison to 37% and 83% for CT respectively (Hutchings et al, 2006). The capability of PET/CT is also sufficient for evaluation of bone marrow during grading and has been found to be more sensitive than conventional bone marrow biopsies (Hassan et al, 2017). Hence, bone marrow biopsies are no longer required as part of grading procedures provided PET/CT scans have been conducted. Overall, PET/CT scanning is recommended prior to initiation of chemotherapy and radiotherapy treatments, during chemotherapy to assess treatment response and to confirm remission following successful treatment response. Patient's blood must also be evaluated during tumour grading with a full blood count, erythrocyte sedimentation rate, C-reactive protein, albumin and liver function tests performed in conjunction with infectious disease tests including hepatitis B, hepatitis C and human immunodeficiency virus (Eichenauer et al, 2018).

*1.4.7.4.1 Ann Arbor Classification of Hodgkin's Lymphoma Grade*

The neoplastic lymphatic tissue is assigned a tumour grade based on the Ann Arbor classification scheme and is evaluated based on clinical findings of PET/CT and blood chemistry investigations. Hodgkin's lymphoma may be clinically classified as grade I or II when the malignancy is isolated to one or two lymph node regions respectively. The lymph nodes must both be positioned either superior or inferior to the diaphragm

for grade II, otherwise the malignancy is graded III with lymph nodes located on either side of the diaphragm. Hodgkin's lymphoma may also be classed grade IV when there is indication that the cancer has metastasised and spread to other organs out with the lymphatic system, commonly the liver, lungs and bone. The Ann Arbor classification system further assigns one of four letters, either A or B, S, E and X, after respective grade numbers to provide additional clinical information. Clinicians assign the letters A or B to patients to allow identification of whether the patient has suffered from B-symptoms that is often associated with poorer patient outcomes. Similarly, clinicians may assign letters S, E and X to describe whether the malignancy is located in the spleen, metastasised or measured larger than 10cm at initial diagnosis respectively. Lastly, the tumour may be categorised as "low-grade" for grades I and IIa or "high-grade" for grades IIb, III and IV malignancies. Ultimately, the Ann Arbor grade will determine the number of chemotherapy cycles prior to patient treatment and thus represents an integral part of the diagnostic process.

.

*1.4.7.4.1 Current Problems in Hodgkin's Lymphoma Diagnostic Pathway*

Currently, ~35% of patients with Hodgkin's lymphoma receive primary care referrals for clinical evaluation in secondary care through the "two-week wait" cancer pathway (Cancer Research UK, 2019). However, ~10% of lymphoma patients still experience significant diagnostic delays in excess of 90 days, and in particular ~42% of patients with Hodgkin's lymphoma visit their GP on three or more occasions prior to referral to secondary care (Lyratzopoulos et al, 2012; Swann et al, 2017). Furthermore, Hodgkin's lymphoma patients are deemed less likely to receive referral through the

"two-week" cancer pathway than numerous other cancers, not limited to breast, lung, colon and melanoma (Zhou et al, 2017). Consequently, ~17%, of patients currently present through emergency settings, where ~60% of such patients visit accident and emergency departments, recognised to correspond with disease progression and reduced overall survival (Cancer Research UK, 2019; Howell et al, 2019).

Presently, a significant challenge that prevents timely diagnosis in the younger demographic of Hodgkin's lymphoma patients is the misinterpretation of a malignant cervical lymphadenopathy for routine infections such as tonsillitis and glandular fever (Lake et al, 2018). Currently, unexplained lymphadenopathy is a routine observation in primary care with overall incidence of 0.6% per year (Gaddey et al, 2016). However, only 0.4% of younger patients that present with unexplained lymphadenopathy receive a cancer diagnosis, and therefore the symptom represents a poor diagnostic indicator given the quantity of infectious disease involving the neck amongst younger individuals (Gaddey et al, 2016). Yet, cervical unexplained lymphadenopathy is the most common symptom in patients with Hodgkin's lymphoma, with the disease more prevalent in younger patients at ~7 cases per 100,000 persons (Cancer Research UK, 2019). Current guidelines recommend a 6-week watchful wait approach for unexplained lymphadenopathy, which often translates to considerable diagnostic delay, particularly for younger individuals, where a quarter of the patient group experienced a median time to diagnosis of 166 days (Howell et al, 2013). For patients >40 and >60 years of age, presence of an unexplained lymphadenopathy has increased diagnostic significance for Hodgkin's lymphoma, with associated PPV scores of 4.0% and 5.6% respectively (Gaddey et al, 2016; Shephard et al, 2015). Yet, a proportion of

the elderly population still experience diagnostic delays, with a greater quantity of patients >60 years of age presenting as an emergency relative to younger patients classed as <50 years of age in the study (National Cancer Registration & Analysis Service, 2016). Therefore, the development of an early diagnostic tool for primary care to identify suspected Hodgkin's lymphoma patients and accelerate patients for lymph node biopsies would have significant benefit for younger and elderly patients alike in situations where prompt diagnosis is not forthcoming.

Presently, a secondary challenge in the clinical assessment of Hodgkin's lymphoma patients concerns the accurate evaluation of an individual's response to chemotherapy treatment. Currently, PET/CT may be employed after two to four chemotherapy cycles as a prognostic tool to measure treatment response. However, ~15% of Hodgkin's lymphoma patients fail initial chemotherapy treatments, ~40% of such patients then fail secondary salvage chemotherapy and autologous stem cell transplant, and long-term survival amongst patients who then receive allogenic stem cell transplants is as low as 20-30% (Jauhari et al, 2016; Eichenauer et al, 2008; Farina et al, 2014). Recently, it has been shown that molecular biomarkers for Hodgkin's lymphoma have potential to inform treatment response after one cycle of chemotherapy, which would allow earlier identification of refractory patients compared to PET/CT imaging (Plattel et al, 2011). Furthermore, biomarkers have been shown to more accurately represent treatment response compared to PET/CT imaging, which is recognised to be susceptible to chemotherapy-induced false positives that may ultimately lead to increased future toxicity in affected patients (Plattel et al, 2011, Weihrauch et al, 2005; Sauer et al, 2012; Jauhari et al, 2016). Indeed, biomarkers have recently been viewed

as a way to assess and tailor chemotherapy treatment to minimise chemotherapy-induced toxicity in patients, which is known to cause organ damage and secondary cancers (Byrne et al, 2006; Sauer et al, 2012). However, no devices currently exist within clinical practice to assess treatment response with biomarkers from Hodgkin's lymphoma patients, hence; the development of a low-cost, molecular based diagnostic device would have significant potential as a prognostic tool within secondary care settings.

#### *1.4.7.4.1 Serum Biomarkers for Hodgkin's Lymphoma*

Blood serum represents an attractive, highly accessible, minimally invasive sample medium for earlier diagnosis and continued monitoring of Hodgkin's lymphoma patients in both primary and secondary care. Currently, standard blood chemistry is performed on patients prior to diagnosis and grading but tested biomolecules do not directly correspond to disease pathophysiology and instead provide a snap-shot of a patient's health status. Recently, it has been shown that several molecular biomarkers may be present in blood of Hodgkin's lymphoma patients that actively participate in disease pathophysiology, and, therefore, may provide specific and significant insights in to patient tumorigenesis. In particular, numerous chemokines and cytokines produced by Reed-Sternberg cells and the inflammatory tumour microenvironment hold significant diagnostic and prognostic potential, and, hence, shall be considered for the current project.

To date, Reed-Sternberg cells have been found to secrete Galectin-1 in to blood serum of Hodgkin's lymphoma patients at high concentrations, ~90ng/ml, which correlated with tumour grade and patient outcomes (Ouyang et al, 2013). However, a separate study found that Galectin-1 was present in only 67% of Hodgkin's lymphoma blood samples and, although decreased after treatment, was not found to correspond to treatment outcomes (Plattel et al, 2016). The abundance of macrophage cells in the tumour microenvironment were found to produce high concentrations, ~1-2ng/ml, of soluble CD163 proteins in blood serum samples that correlated with response to chemotherapy treatment (Jones et al, 2012). However, in a separate study CD163 was only identified in blood plasma of a small sub-population, 21%, of patients, and was unresponsive to chemotherapy treatment (Plattel et al, 2016). Additionally, Reed-Sternberg cells known to express the protein CD30 in blood serum to elevated concentrations, ~5ng/ml, did not correlate with treatment outcomes (Plattel et al, 2016). However, in a separate study, the detection of CD30 in blood serum of patients prior to chemotherapy showed considerable prognostic significance with ability to predict 5-year patient survival in patients assigned to four distinct cohorts (Casasnovas et al, 2007). The discrepancies between studies may be due to disparate sample populations or findings may indicate that CD30 only has prognostic value prior to initiation of chemotherapy. Other molecules of the tumour microenvironment detected in blood serum of Hodgkin's lymphoma patients include cell membrane proteins, I-CAM1 and V-CAM1, at high concentrations of ~725ng/ml and ~1000ng/ml respectively, which were found to facilitate the diagnosis and grading of Hodgkin's lymphoma (Gruss et al, 1993; Pizzolo et al, 1993; Christiansen et al, 1998). Interestingly, inflammatory cytokines of the tumour microenvironment, such as

interleukin-6 and -10, have been found in small concentrations, ~1-4pg/ml, in blood serum of Hodgkin's lymphoma patients in the 1-2 year period prior to confirmatory clinical diagnosis, thus making them attractive for earlier diagnosis (Levin et al, 2017). However, identified interleukins play integral roles to several inflammatory pathways and consequently are implicated in numerous cancers and infectious diseases, inclusive of severe glandular fever (Ma et al, 2008; Leão et al, 2015; Ahmad et al, 2018).

Recently, the chemokine, CCL17/TARC secreted from malignant Reed-Sternberg cells has gained considerable research attention as a candidate specific biomarker for Hodgkin's lymphoma. Specifically, CCL17/TARC has been found in two studies to be significantly elevated in 82-93% of Hodgkin's lymphoma patients with a median serum concentration of 13,670/54,161pg/ml compared to healthy volunteers at 395/134pg/ml, where the large differences in concentration is attractive for diagnostic purposes (Niens et al, 2008; Plattel et al, 2016). Serum concentrations of CCL17/TARC also correlated with tumour grade and dramatically decreased in 95 out of 96 patients that received successful chemotherapy, and, therefore, represents a promising prognostic biomarker for monitoring treatment response (Niens et al, 2008; Plattel et al, 2016). To this extent, elevated serum CCL17/TARC was observed to decrease after one cycle of chemotherapy and has demonstrated the ability to identify relapsed Hodgkin's lymphoma patients, as well as individuals unresponsive to allogenic stem cell transplant (Plattel et al, 2011; Weihrauch et al, 2005; Farina et al, 2014). Therefore, following discussions with clinical collaborators, CCL17/TARC was deemed to represent the ideal diagnostic and prognostic biomarker that would be

targeted throughout development of a molecular-based medical diagnostic device for Hodgkin's lymphoma.

### *1.4.8 Infrared Spectroscopy for Serum Cancer Diagnostics*

Infrared spectroscopy represents an attractive analytical tool for translation to clinical diagnostic applications since the technique offers a rapid, economical and non-destructive platform that requires minimal sample preparation and negates the need for costly labels and reagents (Baker et al, 2014). Infrared spectroscopy provides qualitative information on all infrared active sample constituents where the resultant vibrational molecular fingerprint contains vast quantities of biochemical information. Hence, infrared spectroscopy has demonstrated significant potential for cancer diagnostics of numerous malignancies, not limited to lung (Lewis et al, 2010), oesophageal (Ingham et al, 2019), colon (Song et al, 2019), ovarian (Grzelak et al, 2018), breast (Pilling et al, 2017), prostate (Baker et al, 2008) and brain (Hands et al, 2016) cancers. Furthermore, different spectroscopic sampling modalities have facilitated the development of a wide range of future medical technologies for cancer diagnostics within the healthcare landscape, including spectral histopathology (Bird et al, 2012), stainless staining (Mayerich et al, 2015), spectral cytopathology (Diem et al, 2016) and synchrotron FTIR for cancer biomarker discovery (Pijanka et al, 2009). Similarly, infrared spectroscopy has demonstrated immense clinical potential for a wide range of biofluid applications, not limited to clinical testing of serum (Hands et al, 2016), with infrared technologies now maturing and on the cusp of clinical translation. Recent emergence of commercial clinical infrared ventures, such as

Clinspec Diagnostics Ltd and Biotech Resources, further highlights the potential of infrared biofluid technologies for diagnostic screening of various cancers and infectious diseases respectively.

Infrared spectroscopy for serum diagnostics is an ever-evolving field that has demonstrated significant analytical capabilities for cancer diagnostics. Previously, Backhaus showed detection of breast cancer using 1µL of blood serum with high sensitivity, 96-98%, and high specificity, 93-95%, from 196 clinical samples in transmission and trans-flection mode (Backhaus et al, 2010). Furthermore, Backhaus showed acquired spectral fingerprints were robust and specific to the characteristic molecular profile of breast cancer when evaluated in the presence of over 3,000 patients associated with 11 other disease states. Similarly, Elmi utilised transmission mode FTIR to distinguish between 43 breast cancer patients and 43 healthy controls with high diagnostic accuracy of ~80%, noting molecular differences in protein and lipid content (Elmi et al, 2017). However, a critical challenge for transmission mode infrared spectroscopy for clinical serum diagnostic applications is the ability to dry samples in a timely and reproducible fashion to maintain a constant optical path length for analyses (Dubois et al, 2004). Presently, sample drying has been considered a pre-requisite for infrared serum diagnostics since the strong dipole moment of water dominates the infrared spectrum and often obscures infrared bands of diagnostic importance (Dubois et al, 2004). Similarly, infrared spectroscopy in trans-flection mode has been subject of recent scrutiny where the combination of the electric field standing wave effect and sample thickness variability makes the technique susceptible to analytical error (Hughes et al, 2014; Mayerhofer et al, 2018). Nevertheless, Ollesch

attempted to overcome the technological barriers of transmission mode infrared spectroscopy with great success, through design of a robotic piezoelectric spotter that enabled increased precision of sample depositions in a high-throughput 386-well plate format (Ollesch et al, 2013). Thereafter, Ollesch demonstrated detection of bladder cancer from a large sample population of over 200 patients versus non-cancerous individuals with other routinely observed clinical conditions, and reported high sensitivities of 93-78% and specificities of 86-81% respectively with a Random Forest classifier (Ollesch et al, 2014). Another approach reported extensively in the literature for serum-based cancer diagnostics concerns the use of attenuated total reflectance-Fourier transform infrared spectroscopy (ATR-FTIR).

ATR-FTIR represents an attractive sampling modality for a blood serum diagnostic device since the production of evanescent waves at the substrate interface allows the optical sample path length to remain constant between measurements irrespective of small deviations in sample thickness (Dubois et al, 2004). Previously, Gajjar demonstrated the diagnostic capability of ATR-FTIR for ovarian and endometrial cancers from clinical plasma and serum patient samples versus healthy controls with classification accuracies of 96.7% and 81.2% respectively (Gajjar et al, 2013). Ghimire further showed that ATR-FTIR has diagnostic significance for other cancers where mouse model studies found discriminant molecular signatures in protein, lipid and nucleic acid signatures characteristic of non-Hodgkin's lymphoma and subcutaneous melanoma (Ghimire et al, 2017). Similarly, Neves showed that ATR-FTIR has the capacity to diagnose pre-cancerous cervical lesions from clinical plasma samples and the ability to grade malignancies according to clinical classification schemes with high

sensitivities up to 94% and specificities up to 100% respectively (Neves et al, 2016). Hands showed comprehensively in one of the largest studies in the field with 433 patient samples that the detection capabilities of ATR-FTIR could further extend to not only diagnose and grade brain cancers with high diagnostic accuracies but also allowed differentiation between primary and secondary metastatic tumours (Hands et al, 2016). Interestingly, Hands further demonstrated the analytical tool could distinguish between glioma and meningioma tumour types as well as low-grade and high-grade gliomas with mean sensitivities and specificities of 81.1/80.9% and 66.7/48.5% respectively, which makes a compelling case for detection of specific biomarkers that contribute to these distinct molecular signatures with ATR-FTIR spectroscopy. To this extent, Uckermann recently showed that ATR-FTIR could determine the IDH status of patients based on five pertinent spectroscopic signatures in the 1100-1550cm-1 region that significantly contributed to accurate glioma classification (Uckermann et al, 2017). Whilst the study by Uckermann was demonstrated on resected tissue samples, many others have demonstrated the applicability of ATR-FTIR for identification of biomarkers from serum samples for a variety of disease states (Lima et al, 2015; Spalding et al, 2018). Interestingly, Bonnier recently showed that centrifugal filtration of serum samples facilitated a 50 times increase in sensitivity for detection of low molecular weight molecules and may represent an effective diagnostic strategy for identification of biomarkers in the current project (Bonnier et al, 2016).

Whilst ATR-FTIR has demonstrated significant clinical utility for cancer diagnostics in previously described proof-of-principle studies, a major limitation preventing

clinical translation is dependence on existing internal reflection elements (IRE's). Fundamentally, IRE's facilitate the production of evanescent waves based on the refractive index of the substrate and commonly comprise diamond, germanium, KRS-5 and zinc selenide materials. Hence, the currently utilised IRE's have high component costs and limited throughput capabilities, and are thus not conducive to high-volume point-of-care diagnostics where an economical test platform is paramount. However, Schumacher and Karabudak have both demonstrated that silicon wafers could be micro-fabricated to feature V-shaped grooves thereby allowing silicon substrates to perform as IRE components (Schumacher et al, 2010; Karabudak et al, 2012). Recently, our group have further developed a silicon IRE component that has a reduced sample path length to minimise inherent silicon vibrations and is attractive from both economical and scale-up perspectives for clinical translation (Butler et al, 2019). Therefore, the silicon component will be employed throughout the course of the project and evaluated with regards to suitability for the diagnosis of brain cancer and Hodgkin's lymphoma.

### *1.4.9 Electrochemical Immunsensors for Serum Cancer Diagnostics*

Electrochemical immunosensors encompass a wide range of sensor technologies that fundamentally characterise and translate antibody-antigen interactions in to quantifiable electrical signals. Electrochemical immunosensors have received considerable research attention of late and offer the possibility of a relatively low-cost, disposable, simple, miniaturised, rapid and scalable analytical tool for point-of-care cancer diagnostics in the clinical setting (Hammond et al, 2016). Previously, Emami

has demonstrated the ability to detect the clinically important prognostic biomarker, HER-2, from clinical serum samples of breast cancer patients with an "unlabelled" electrochemical sensor (Emami et al, 2014). In particular, gold nano-particle electrodes were functionalised with thiols creating a self-assembled monolayer that provided a platform for attachment of nano-particles conjugated with primary antibodies through EDC/NHS coupling chemistry. Impressively, Emami showed that the "unlabelled" detection scheme measured a decrease in the voltammetric signal with differential pulsed voltammetry (DPV) upon antigen binding with equivalent detection capabilities when compared to standard enzyme-linked immunosorbent assay (ELISA) methods with a limit of detection of 0.995pg/ml. Similarly, Li showed the ability to detect another important biomarker for breast cancer as well as ovarian cancer, namely CA-125, from patient serum samples with graphene-ferrocene composite electrodes that were electrochemically reduced to allow the coupling of gold nano-particles (Li et al, 2014). Thereafter, primary antibodies were simply attached to electrode surfaces through physical absorption and antigen binding was measured with DPV by assessing the reduction in peak current with baseline measurements. Li demonstrated detection of the biomarker CA-125 with a limit of detection of 0.015U/mL and patient sample results were validated with ELISA methods. Overall, both studies highlight the applicability of voltammetric methods for quantitative detection of protein biomarkers using "unlabelled" assay formats.

Electrochemical immunosensors have also been reported extensively in "labelled" formats where secondary labelled antibodies allow detection of antigen binding with amperometry methods. Recently, Biscay showed the potential of immunosensors for

detection of another clinically relevant biomarker, prostate specific antigen (PSA), with an electrochemical "sandwich" biosensor (Biscay et al, 2015). In this work, carbon screen-printed electrodes were functionalised with magnetic nano-particles that were modified with streptavidin enabling attachment of biotinylated antibodies through the streptavidin-biotin affinity interaction. Thereafter, Biscay employed secondary antibodies to negate non-specific binding and an enzymatic label, horseradish peroxidase, to generate signals proportional to antigen concentration in clinical serum samples. This approach has shown great promise with a limit of detection of 1.86ng/ml and a linear range of 5-100ng/ml that successfully allowed quantification of clinical samples and was comparable to ELISA techniques. Similarly, Xiong illustrated the potential of a "labelled" electrochemical immunosensor for detection of the cancer biomarker, α-fetoprotein, routinely employed for diagnosis of the primary liver cancer hepatocellular carcinoma (Xiong et al, 2012). In this work, Xiong employed gold electrodes functionalised with gold nano-particles and self-assembled monolayers of thiolated protein G molecules to capture primary antibodies. Interestingly, protein G displays affinity interactions with the Fc region of antibodies that enables precise control of antibody orientation, and highlights another strategy for coupling antibodies to electrodes. Xiong also employed a "sandwich" assay format for detection of α-fetoprotein where the amperometric signal showed an improved limit of detection of 0.002ng/ml and successfully identified the clinical biomarker in all patient serum samples. Overall, amperometric "sandwich" immunosensors have been reported by numerous research groups for a variety of biomarkers and offers the primary advantage of overcoming non-specific binding

effects of dominant molecules in blood serum that often translates to improved assay sensitivity and reproducibility.

Electrochemical immunosensors comprised of "unlabelled" assay formats may also be evaluated for antibody-antigen affinity interactions with electrochemical impedance spectroscopy (EIS). Recently, Aydin demonstrated the potential of the EIS technique for "unlabelled" cancer diagnostic approaches for detection of the p53 protein implicated in various cancers, such as colorectal cancer, that formed the basis of the research (Aydin et al, 2018). In particular, indium-tin oxide (ITO) electrodes were functionalised with a star-shape polymer that allowed covalent attachment of primary antibodies and were subsequently exposed to antigenic patient serum samples. EIS successfully characterised p53 binding at electrodes by measuring the charge transfer resistance before and after incubation with antigenic solutions, and was found to be highly sensitive with a limit of detection of 0.02pg/ml and assay linearity of $R^2 = 0.998$. Similarly, Soares recently employed EIS for the early diagnosis of pancreatic cancer through identification of the biomarker CA19-9 from clinical serum samples (Soares et al, 2017). Specifically, polymer nanofiber electrodes were functionalised with carbon nano-tubes and gold nano-particles in two separate experiments with primary antibodies subsequently covalently attached through EDC/NHS coupling chemistry. Thereafter, impedance was evaluated after incubation with target antigen solutions with respect to baseline measurements and produced limits of detection of 1.57-1.84U/mL, whilst CA19-9 was successfully identified in clinical serum samples. In a separate approach, a member of our research group demonstrated the utility of an EIS detection scheme for diagnosis of sepsis biomarkers, TREM-1, MMP-9 and HSL,

through covalent cross-linking of primary antibodies to gold electrode surfaces with a heterobifunctional cross-linker (Ciani et al, 2012). This work similarly calculated differences in charge transfer resistance before and after antibody-antigen interactions where the resultant signals displayed linearity over a large concentration range from 10,000-0.1ng/ml and limits of detection of 3.3pM, 1.1nM and 1.4nM respectively. Recently, our research group has since employed the heterobifunctional cross-linker assay on micro-electrodes for the clinically important biomarker interleukin-6 and showed sensitive and specific detection of the cytokine at 25pg/ml within 2.5 minutes from spiked blood serum samples (Russell et al, 2018). Overall, countless immunosensors utilising EIS detection schemes have been reported in the literature with the primary advantage of reduced assay time and complexity and the potential to perform "unlabelled" sensing that would integrate easier in to clinical workflows. In conclusion, a vast quantity of electrochemical immunosensors have demonstrated clinical potential through proof-of-concept studies where devices feature a range of electrode substrates, immobilisation chemistries and detection schemes, highlighting the breadth of the field and the versatility of electrochemical immunosensor platforms.

### *1.4.10 Combined Infrared Spectroscopic and Electrochemical Diagnostics*

The integration of infrared spectroscopic and electrochemical techniques into a medical device would facilitate introduction of a device with extended diagnostic capabilities. Specifically, infrared spectroscopy permits molecular classification of sample components based on infrared active vibrational modes. Hence, infrared spectroscopy provides the capacity for qualitative detection of all infrared active

biochemical components of a blood serum sample, producing a biochemical fingerprint representative of all the different macromolecular constituents of blood serum. The ability to provide information rich biochemical fingerprints of a blood serum sample would have significant benefits in a clinical environment where the analysis of single biomarkers is often elusive on further clinical investigation due to the heterogeneous nature of numerous diseases, including cancerous malignancies. However, a well-recognised current limitation of infrared spectroscopy is the inability to provide quantitative detection of specific biochemical signals within complex sample mediums at low-level biological concentrations (Bonnier et al, 2016). The inclusion of an electrochemical technique in the medical device would circumvent such issues and facilitate quantitative detection of specific biomarkers at biologically relevant concentrations based on redox activities of biomolecules, electrochemical probes or conjugated labels (Kaim et al, 2009; O'Reilly et al, 2015). Therefore, an integrated device, that performs both infrared spectroscopic and electrochemical analysis, would provide significantly more diagnostic information, enabling detection of specific biomarkers as well as rich global biochemical signatures of patient blood serum samples. Furthermore, simultaneous infrared spectroscopic and electrochemical analysis would enable *in-situ* elucidation of the structural changes of electro-active species when in reduced and oxidised states, thereby allowing inspection of complex molecules for clinical scenarios, for instance anti-cancer drug compounds (Enache et al, 2008) and cancer pathogenesis (Omole et al, 2009). Ultimately, a combined spectroscopic and electrochemical approach would permit acquisition of qualitative, quantitative, kinetic and thermodynamic information characteristic of sample

components (Kobrina et al, 2010; Zhai et al, 2018), allowing the acquisition of advanced molecular content on biofluids inaccessible by either technique alone.

### *1.4.11 Overall Research Aims*

- Development of an integrated silicon component and fabricated sample cell with the capacity to perform electrochemical and spectroscopic measurements on model systems and biomarkers at clinically relevant concentrations.

- Development of an electrochemical and spectroscopic platform for brain cancer diagnostics that demonstrates capabilities to identify the clinically relevant IDH1-R132H molecular status of an individual from spiked and clinical patient samples.

- Development of an electrochemical and spectroscopic platform for Hodgkin's lymphoma diagnostics that demonstrates capabilities to detect the presence of Hodgkin's lymphoma and identify the clinically relevant biomarker, CCL17/TARC, in spiked and clinical patient samples.

# *1 References*


Abdel-Rahman M , Stockton D , Rachet B , Hakulinen T , Coleman MP . What if cancer survival in Britain were the same as in Europe: how many deaths are avoidable? Br J Cancer 2009 ; 101 : S115 – 24 .

Aggarwal, A., Herz, N., Arkush, L., Short, S., & Rees, J. (2014). *OP30 * DIAGNOSTIC DELAY AND SURVIVAL IN HIGH GRADE GLIOMAS - EVIDENCE OF THE "WAITING TIME PARADOX." Neuro-Oncology, 16(suppl 6), vi21–vi21*. doi:10.1093/neuonc/nou251.28

Agostinelli, C., & Pileri, S. (2014). Pathobiology of hodgkin lymphoma. *Mediterranean journal of hematology and infectious diseases*, *6*(1), e2014040. doi:10.4084/MJHID.2014.040

Ahmad, N., Ammar, A., Storr, S. J., Green, A. R., Rakha, E., Ellis, I. O., & Martin, S. G. (2018). IL-6 and IL-10 are associated with good prognosis in early stage invasive breast cancer patients. *Cancer immunology, immunotherapy : CII*, *67*(4), 537–549. doi:10.1007/s00262-017-2106-8

Ahmadzadeh, A., Yekaninejad, M. S., Jalili, M. H., Bahadoram, M., Efazat, M., Seghatoleslami, M., … Saki, N. (2014). Evaluating the Survival Rate and the Secondary Malignancies after Treating Hodgkin's Lymphoma Patients with Chemotherapy Regimens. *International journal of hematology-oncology and stem cell research*, *8*(2), 21–26.

Ahmed, R., Oborski, M. J., Hwang, M., Lieberman, F. S., & Mountz, J. M. (2014). Malignant gliomas: current perspectives in diagnosis, treatment, and early response assessment using advanced quantitative imaging methods. *Cancer management and research*, *6*, 149–170. doi:10.2147/CMAR.S54726

Allemani, C., Matsuda, T., Di Carlo, V., Harewood, R., Matz, M., Nikšić, M., … Estève, J. (2018). *Global surveillance of trends in cancer survival 2000–14 (CONCORD-3): analysis of individual records for 37 513 025 patients diagnosed with one of 18 cancers from 322 population-based registries in 71 countries. The Lancet, 391(10125), 1023–1075*. doi:10.1016/s0140-6736(17)33326-3

Allemani, C., Weir, H. K., Carreira, H., Harewood, R., Spika, D., Wang, X.-S., … Coleman, M. P. (2015). *Global surveillance of cancer survival 1995–2009: analysis of individual data for 25 676 887 patients from 279 population-based registries in 67 countries (CONCORD-2). The Lancet, 385(9972), 977–1010*. doi:10.1016/s0140-6736(14)62038-9

Almiron Bonnin, D. A., Havrda, M. C., & Israel, M. A. (2018). *Glioma Cell Secretion: A Driver of Tumor Progression and a Potential Therapeutic Target. Cancer Research*. doi:10.1158/0008-5472.can-18-0345

Ansell, S. M. (2015). *Hodgkin Lymphoma: Diagnosis and Treatment. Mayo Clinic Proceedings, 90(11), 1574–1583*. doi:10.1016/j.mayocp.2015.07.005

Armstrong, T. S., Grant, R., Gilbert, M. R., Lee, J. W., & Norden, A. D. (2016). Epilepsy in glioma patients: mechanisms, management, and impact of anticonvulsant therapy. *Neuro-oncology*, *18*(6), 779–789. doi:10.1093/neuonc/nov269

Armstrong, T.; Vera-Bolanos, E.; Bekele, B.; Aldape, K.; Gilbert, M. Adult ependymal tumors: Prognosis and the M. D. Anderson Cancer Center experience. *Neuro Oncol.* **2010**, *12*, 862–870.

Arnautovic, A., Billups, C., Broniscer, A., Gajjar, A., Boop, F., & Qaddoumi, I. (2015). Delayed diagnosis of childhood low-grade glioma: causes, consequences, and potential solutions. *Child's nervous system : ChNS : official journal of the International Society for Pediatric Neurosurgery*, *31*(7), 1067–1077. doi:10.1007/s00381-015-2670-1

Aydın, M., Aydın, E. B., & Sezgintürk, M. K. (2018). *A disposable immunosensor using ITO based electrode modified by a star-shaped polymer for analysis of tumor suppressor protein p53 in human serum. Biosensors and Bioelectronics, 107, 1–9*. doi:10.1016/j.bios.2018.02.017

Azevedo, F. A. C., Carvalho, L. R. B., Grinberg, L. T., Farfel, J. M., Ferretti, R. E. L., Leite, R. E. P., … Herculano-Houzel, S. (2009). *Equal numbers of neuronal and nonneuronal cells make the human brain an isometrically scaled-up primate brain. The Journal of Comparative Neurology, 513(5), 532–541*. doi:10.1002/cne.21974

Baba, A. I. (2007) Comparative Oncology. Chapter 3: Tumor Cell Morphology. Publishing House of the Romanian Academy, 2007. ISBN 9732714573, 9789732714577

Backhaus, J., Mueller, R., Formanski, N., Szlama, N., Meerpohl, H.-G., Eidt, M., & Bugert, P. (2010). *Diagnosis of breast cancer with infrared spectroscopy from serum samples. Vibrational Spectroscopy, 52(2), 173–177*. doi:10.1016/j.vibspec.2010.01.013

Baker, M. J., Gazi, E., Brown, M. D., Shanks, J. H., Gardner, P., & Clarke, N. W. (2008). *FTIR-based spectroscopic analysis in the identification of clinically aggressive prostate cancer. British Journal of Cancer, 99(11), 1859–1866*. doi:10.1038/sj.bjc.6604753

Baker, M. J., Trevisan, J., Bassan, P., Bhargava, R., Butler, H. J., Dorling, K. M., … Martin, F. L. (2014). Using Fourier transform IR spectroscopy to analyze biological materials. *Nature protocols*, *9*(8), 1771–1791. doi:10.1038/nprot.2014.110

Balañá, C., Carrato, C., Ramírez, J. L., Cardona, A. F., Berdiel, M., Sánchez, J. J., … Rosell, R. (2011). *Tumour and serum MGMT promoter methylation and protein expression in glioblastoma patients. Clinical and Translational Oncology, 13(9), 677–685*. doi:10.1007/s12094-011-0714-x

Balss, J., Meyer, J., Mueller, W., Korshunov, A., Hartmann, C., & von Deimling, A. (2008). *Analysis of the IDH1 codon 132 mutation in brain tumors. Acta Neuropathologica, 116(6), 597–602*. doi:10.1007/s00401-008-0455-2

Beiko, J., Suki, D., Hess, K. R., Fox, B. D., Cheung, V., Cabral, M., … Cahill, D. P. (2013). *IDH1 mutant malignant astrocytomas are more amenable to surgical resection and have a survival benefit associated with maximal surgical resection. Neuro-Oncology, 16(1), 81–91*. doi:10.1093/neuonc/not159

Bernardi, D., Padoan, A., Ballin, A., Sartori, M., Manara, R., Scienza, R., … Della Puppa, A. (2011). *Serum YKL-40 following resection for cerebral glioblastoma. Journal of Neuro-Oncology, 107(2), 299–305*. doi:10.1007/s11060-011-0762-7

Bertoli, C., Skotheim, J. M., & de Bruin, R. A. M. (2013). Control of cell cycle transcription during G1 and S phases. Nature Reviews Molecular Cell Biology, 14(8), 518–528. doi:10.1038/nrm3629

Bird, B., Miljković, M., Remiszewski, S., Akalin, A., Kon, M., & Diem, M. (2012). *Infrared spectral histopathology (SHP): a novel diagnostic tool for the accurate classification of lung cancer. Laboratory Investigation, 92(9), 1358–1373*. doi:10.1038/labinvest.2012.101

Biscay, J., González García, M. B., & García, A. C. (2015). *Determination of Total PSA Using Magnetic Beads and a Re-usable Screen Printed Carbon Electrode Array. Electroanalysis, 27(12), 2773–2777*. doi:10.1002/elan.201500351

Boisselier, B., Gallego Perez-Larraya, J., Rossetto, M., Labussiere, M., Ciccarino, P., Marie, Y., … Sanson, M. (2012). *Detection of IDH1 mutation in the plasma of patients with glioma. Neurology, 79(16), 1693–1698*. doi:10.1212/wnl.0b013e31826e9b0a

Bonnier, F., Brachet, G., Duong, R., Sojinrin, T., Respaud, R., Aubrey, N., … Chourpa, I. (2016). *Screening the low molecular weight fraction of human serum using ATR-IR spectroscopy. Journal of Biophotonics, 9(10), 1085–1097*. doi:10.1002/jbio.201600015

Bouwen, B. L. J., Pieterman, K. J., Smits, M., Dirven, C. M. F., Gao, Z., & Vincent, A. J. P. E. (2018). *The Impacts of Tumor and Tumor Associated Epilepsy on Subcortical Brain Structures and Long Distance Connectivity in Patients With Low Grade Glioma. Frontiers in Neurology, 9*. doi:10.3389/fneur.2018.01004

Brat D, Verhaak R, et al (2015). Comprehensive, Integrative Genomic Analysis of Diffuse Lower-Grade Gliomas. New England Journal of Medicine, 372(26), 2481–2498. doi:10.1056/nejmoa1402121

Brice, P. (2018). Refractory Hodgkin lymphoma: time for targeted therapies? Blood, 131(11), 1156–1157. doi:10.1182/blood-2017-12-824136

Brooks, E. G., Connors, J. M., Sehn, L. H., Gascoyne, R. D., Savage, K. J., Shenkier, T. N., … Villa, D. (2015). *Impact of time from diagnosis to initiation of curative-intent chemotherapy on clinical outcomes in patients with classical Hodgkin lymphoma. Leukemia & Lymphoma, 57(4), 872–879*. doi:10.3109/10428194.2015.1086919

Brush, J., Boyd, K., Chappell, F., Crawford, F., Dozier, M., Fenwick, E., … Dunlop, M. (2011). *The value of FDG positron emission tomography/computerised tomography (PET/CT) in pre-operative staging of colorectal cancer: a systematic review and economic evaluation. Health Technology Assessment, 15(35)*. doi:10.3310/hta15350

Burmeister, A. R., & Marriott, I. (2018). *The Interleukin-10 Family of Cytokines and Their Role in the CNS. Frontiers in Cellular Neuroscience, 12*. doi:10.3389/fncel.2018.00458

Burnet, N. G., Jefferies, S. J., Benson, R. J., Hunt, D. P., & Treasure, F. P. (2005). *Years of life lost (YLL) from cancer is an important measure of population burden — and should be considered when allocating research funds. British Journal of Cancer, 92(2), 241–245*. doi:10.1038/sj.bjc.6602321

Butler, H. J., Brennan, P. M., Cameron, J. M., Finlayson, D., Hegarty, M. G., Jenkinson, M. D., … Baker, M. J. (2019). *Development of high-throughput ATR-FTIR technology for rapid triage of brain cancer. Nature Communications, 10(1)*. doi:10.1038/s41467-019-12527-5

Byrne, B. J., & Gockerman, J. P. (2007). *Salvage Therapy in Hodgkin's Lymphoma. The Oncologist, 12(2), 156–167*. doi:10.1634/theoncologist.12-2-156

Cairns, R. A., & Mak, T. W. (2013). *Oncogenic Isocitrate Dehydrogenase Mutations: Mechanisms, Models, and Clinical Opportunities. Cancer Discovery, 3(7), 730–741*. doi:10.1158/2159-8290.cd-13-0083

Cancer Research UK, Cancer Research UK Website. Accessed October 2019. https://www.cancerresearchuk.org/health-professional/cancer-statistics-for-the-uk#heading-Zero

Cancer Research UK, Cancer Research UK Website. Accessed October 2019. https://www.cancerresearchuk.org/what-is-cancer/how-cancer-starts/types-of-cancer

Cancer Research UK, Cancer Research UK Website. Accessed October 2019. https://www.cancerresearchuk.org/health-professional/cancer-statistics/statistics-by-cancer-type/hodgkin-lymphoma#heading-Zero

Casalou, C., Faustino, A., & Barral, D. C. (2016). *Arf proteins in cancer cell migration. Small GTPases, 7(4), 270–282*. doi:10.1080/21541248.2016.1228792

Casasnovas, R.-O., Mounier, N., Brice, P., Divine, M., Morschhauser, F., Gabarre, J., … Salles, G. (2007). *Plasma Cytokine and Soluble Receptor Signature Predicts Outcome of Patients With Classical Hodgkin's Lymphoma: A Study From the Groupe d'Etude des Lymphomes de l'Adulte. Journal of Clinical Oncology, 25(13), 1732–1740.* doi:10.1200/jco.2006.08.1331

Chen, H., Judkins, J., Thomas, C., Wu, M., Khoury, L., Benjamin, C. G., … Horbinski, C. (2017). Mutant IDH1 and seizures in patients with glioma. *Neurology*, *88*(19), 1805–1813. doi:10.1212/WNL.0000000000003911

Chen, J.-R., Xu, H.-Z., Yao, Y., & Qin, Z.-Y. (2015). *Prognostic value of epidermal growth factor receptor amplification and EGFRvIII in glioblastoma: meta-analysis. Acta Neurologica Scandinavica, 132(5), 310–322.* doi:10.1111/ane.12401

Christiansen, I., SundstrÖm, C., Enblad, G., & Tötterman, T. H. (1998). *Soluble vascular cell adhesion molecule-1 (sVCAM-1) is an independent prognostic marker in Hodgkin's disease. British Journal of Haematology, 102(3), 701–709*. doi:10.1046/j.1365-2141.1998.00840.x

Ciani, I., Schulze, H., Corrigan, D. K., Henihan, G., Giraud, G., Terry, J. G., … Mount, A. R. (2012). *Development of immunosensors for direct detection of three wound infection biomarkers at point of care using electrochemical impedance spectroscopy. Biosensors and Bioelectronics, 31(1), 413–418.* doi:10.1016/j.bios.2011.11.004

Claus, E. B., Bondy, M. L., Schildkraut, J. M., Wiemels, J. L., Wrensch, M., & Black, P. M. (2005). *Epidemiology of Intracranial Meningioma. Neurosurgery, 57(6), 1088–1095.* doi:10.1227/01.neu.0000188281.91351.b9

Cohen, A. L., Holmen, S. L., & Colman, H. (2013). IDH1 and IDH2 mutations in gliomas. *Current neurology and neuroscience reports*, *13*(5), 345. doi:10.1007/s11910-013-0345-4

Comelli, I., Lippi, G., Campana, V., Servadei, F., & Cervellin, G. (2017). Clinical presentation and epidemiology of brain tumors firstly diagnosed in adults in the Emergency Department: a 10-year, single center retrospective study. *Annals of translational medicine*, *5*(13), 269. doi:10.21037/atm.2017.06.12

Davis M. E. (2016). Glioblastoma: Overview of Disease and Treatment. *Clinical journal of oncology nursing, 20*(5 Suppl), S2–S8. doi:10.1188/16.CJON.S1.2-8

De Angelis, R., Sant, M., Coleman, M. P., Francisci, S., Baili, P., Pierannunzio, D., … Capocaccia, R. (2014). *Cancer survival in Europe 1999–2007 by country and age: results of EUROCARE-5—a population-based study. The Lancet Oncology, 15(1), 23–34*. doi:10.1016/s1470-2045(13)70546-1

Demirci, U., Yaman, M., Buyukberber, S., Coskun, U., Baykara, M., Uslu, K., … Bagriacik, E. U. (2012). *Prognostic importance of markers for inflammation, angiogenesis and apoptosis in high grade glial tumors during temozolomide and radiotherapy. International Immunopharmacology, 14(4), 546–549*. doi:10.1016/j.intimp.2012.08.007

Derenzini, E., & Younes, A. (2011). *Predicting treatment outcome in classical Hodgkin lymphoma: genomic advances. Genome Medicine, 3(4), 26*. doi:10.1186/gm240

Diamandis, E. P., & Fiala, C. (2017). Can circulating tumor DNA be used for direct and early stage cancer detection?. *F1000Research*, *6*, 2129. doi:10.12688/f1000research.13440.1

Diem, M., Miljković, M., Bird, B., Mazur, A. I., Schubert, J. M., Townsend, D., … Old, O. (2016). *Cancer screening via infrared spectral cytopathology (SCP): results for the upper respiratory and digestive tracts. The Analyst, 141(2), 416–428*. doi:10.1039/c5an01751c

Dubois, J., & Shaw, R. A. (2004). *Peer Reviewed: IR Spectroscopy in Clinical and Diagnostic Applications. Analytical Chemistry, 76(19), 360 A–367 A.* doi:10.1021/ac041647v

Eichenauer, D. A., & Engert, A. (2017). Nodular lymphocyte-predominant Hodgkin lymphoma: a unique disease deserving unique management. *Hematology. American Society of Hematology. Education Program, 2017*(1), 324–328. doi:10.1182/asheducation-2017.1.324

Eichenauer, D. A., Fuchs, M., Borchmann, P., & Engert, A. (2008). *Hodgkin's lymphoma: current treatment strategies and novel approaches. Expert Review of Hematology, 1(1), 63–73.* doi:10.1586/17474086.1.1.63

Eichler, A. F., & Loeffler, J. S. (2007). Multidisciplinary Management of Brain Metastases. The Oncologist, 12(7), 884–898. doi:10.1634/theoncologist.12-7-884

Elazezy, M., & Joosse, S. A. (2018). Techniques of using circulating tumor DNA as a liquid biopsy component in cancer management. *Computational and structural biotechnology journal*, *16*, 370–378. doi:10.1016/j.csbj.2018.10.002

Elmi, F., Movaghar, A. F., Elmi, M. M., Alinezhad, H., & Nikbakhsh, N. (2017). *Application of FT-IR spectroscopy on breast cancer serum analysis. Spectrochimica Acta Part A: Molecular and Biomolecular Spectroscopy, 187, 87–91*. doi:10.1016/j.saa.2017.06.021

Enache, M., Bendic, C., & Volanschi, E. (2008). Spectroelectrochemistry of the redox activation of anti-cancer drug mitoxantrone. Bioelectrochemistry, 72(1), 10–20.doi:10.1016/j.bioelechem.2007.10.001

Emami, M., Shamsipur, M., Saber, R., & Irajirad, R. (2014). *An electrochemical immunosensor for detection of a breast cancer biomarker based on antiHER2–iron oxide nanoparticle bioconjugates. The Analyst, 139(11), 2858–2866*. doi:10.1039/c4an00183d

Farina, L., Rezzonico, F., Spina, F., Dodero, A., Mazzocchi, A., Crippa, F., … Corradini, P. (2014). *Serum Thymus and Activation-Regulated Chemokine Level Monitoring May Predict Disease Relapse Detected by PET Scan after Reduced-Intensity Allogeneic Stem Cell Transplantation in Patients with Hodgkin Lymphoma. Biology of Blood and Marrow Transplantation, 20(12), 1982–1988*. doi:10.1016/j.bbmt.2014.08.016

Gaddey, H. L., Riegel, A. M. (2016) Unexplained Lymphadenopathy: Evaluation and Differential Diagnosis. *Am Fam Physician.* 94(11):896-903.

Gajjar, K., Trevisan, J., Owens, G., Keating, P. J., Wood, N. J., Stringfellow, H. F., … Martin, F. L. (2013). *Fourier-transform infrared spectroscopy coupled with a classification machine for the analysis of blood plasma or serum: a novel diagnostic approach for ovarian cancer. The Analyst, 138(14), 3917.* doi:10.1039/c3an36654e

Gan, H. K., Cvrljevic, A. N., & Johns, T. G. (2013). *The epidermal growth factor receptor variant III (EGFRvIII): where wild things are altered. FEBS Journal, 280(21), 5350–5370.* doi:10.1111/febs.12393

Geurts, M., & van den Bent, M. J. (2018). *On high-risk, low-grade glioma: What distinguishes high from low? Cancer*. doi:10.1002/cncr.31834

Ghimire, H., Venkataramani, M., Bian, Z., Liu, Y., & Perera, A. G. U. (2017). *ATR-FTIR spectral discrimination between normal and tumorous mouse models of lymphoma and melanoma from serum samples. Scientific Reports, 7(1)*. doi:10.1038/s41598-017-17027-4

Gilles, F. H., Tavaré, C. J., Laurence, E. B., Burger, P. C., Yates, A. J., Pollack, I. F., & Finlay, J. L. (2008). Pathologist Interobserver Variability of Histologic Features in Childhood Brain Tumors: Results from the CCG-945 Study. *Pediatric and Developmental Pathology, 11*(2), 108–117. https://doi.org/10.2350/07-06-0303.1

Glass, c. (2008) Role of the primary care physician in Hodgkin lymphoma. *Am Fam Physician.* 2008 Sep 1;78(5):615-622.

Gopas, J., Stern, E., Zurgil, U., Ozer, J., Ben-Ari, A., Shubinsky, G., … Livneh, E. (2016). Reed-Sternberg cells in Hodgkin's lymphoma present features of cellular senescence. *Cell death & disease, 7*(11), e2457. doi:10.1038/cddis.2016.185

Grant, R. (2004). *Overview: brain tumour diagnosis and management/Royal College of Physicians guidelines. Journal of Neurology, Neurosurgery & Psychiatry, 75(suppl_2), ii18–ii23*. doi:10.1136/jnnp.2004.040360

Gray E, Butler HJ, Board R, et al. Health economic evaluation of a serum-based blood test for brain tumour diagnosis: exploration of two clinical scenarios. BMJ Open 2018;8:e017593. doi:10.1136/ bmjopen-2017-017593

Grier, J. T. (2006). *Low-Grade Gliomas in Adults. The Oncologist, 11(6), 681–693.* doi:10.1634/theoncologist.11-6-681

Gruss HJ, Dölken G, Brach MA, Mertelsmann R, Herrmann F. Serum levels of circulating ICAM-1 are increased in Hodgkin's disease. Leukemia [01 Aug 1993, 7(8):1245-1249]

Grzelak, M. M., Wróbel, P. M., Lankosz, M., Stęgowski, Z., Chmura, Ł., Adamek, D., … Castillo-Michel, H. (2018). *Diagnosis of ovarian tumour tissues by SR-FTIR spectroscopy: A pilot study. Spectrochimica Acta Part A: Molecular and Biomolecular Spectroscopy, 203, 48–55*. doi:10.1016/j.saa.2018.05.070

Guillevin, R., Herpe, G., Verdier, M., & Guillevin, C. (2014). *Low-grade gliomas: The challenges of imaging. Diagnostic and Interventional Imaging, 95(10), 957–963.* doi:10.1016/j.diii.2014.07.005

Gustavsson, A., Svensson, M., Jacobi, F., Allgulander, C., Alonso, J., Beghi, E., … Olesen, J. (2011). *Cost of disorders of the brain in Europe 2010. European Neuropsychopharmacology, 21(10), 718–779*. doi:10.1016/j.euroneuro.2011.08.008

Hamdan, A., & Mitchell, P. (2013). *The two-week wait guideline for suspected CNS tumours: a decade analysis. British Journal of Neurosurgery, 27(5), 642–645.* doi:10.3109/02688697.2013.771725

Hamilton, W., & Kernick, D. (2007). Clinical features of primary brain tumours: a case-control study using electronic primary care records. *The British journal of general practice : the journal of the Royal College of General Practitioners, 57*(542), 695–699.

Hammond, J. L., Formisano, N., Estrela, P., Carrara, S., & Tkac, J. (2016). Electrochemical biosensors and nanobiosensors. *Essays in biochemistry*, *60*(1), 69–80. doi:10.1042/EBC20150008

Hanahan, D., & Weinberg, R. A. (2011). *Hallmarks of Cancer: The Next Generation. Cell, 144(5), 646–674*. doi:10.1016/j.cell.2011.02.013

Hands, J. R., Clemens, G., Stables, R., Ashton, K., Brodbelt, A., Davis, C., … Baker, M. J. (2016). *Brain tumour differentiation: rapid stratified serum diagnostics via attenuated total reflection Fourier-transform infrared spectroscopy. Journal of Neuro-Oncology, 127(3), 463–472.* doi:10.1007/s11060-016-2060-x

Hardesty DA, Sanai N (2012) The value of glioma extent of resection in the modern neurosurgical era. Front Neurol 3:140

Hartmann C, Hentschel B, Tatagiba M, Schramm J, Schnell O, Seidel C, Stein R, Reifenberger G, Pietsch T, von Deimling A, Loeffler M, Weller M. German Glioma Network. Molecular markers in low-grade gliomas: Predictive or prognostic? Clin Cancer Res 2011; 17: 4588– 99

Hartwell, L., & Kastan, M. (1994). *Cell cycle control and cancer. Science, 266(5192), 1821–1828*. doi:10.1126/science.7997877

Hassan, A., Siddique, M., Bashir, H., Riaz, S., Wali, R., Mahreen, A., & Nawaz, M. K. (2017). *18F-FDG PET-CT imaging versus bone marrow biopsy in pediatric Hodgkin's lymphoma: a quantitative assessment of marrow uptake and novel insights into clinical implications of marrow involvement. European Journal of Nuclear Medicine and Molecular Imaging, 44(7), 1198–1206*. doi:10.1007/s00259-017-3647-y

Hehn, S. T., Grogan, T. M., & Miller, T. P. (2004). *Utility of Fine-Needle Aspiration As a Diagnostic Technique in Lymphoma. Journal of Clinical Oncology, 22(15), 3046–3052*. doi:10.1200/jco.2004.02.104

Hnátková, M., Mociková, H., Trnený, M., Zivný, J. (2009) The biological environment of Hodgkin's lymphoma and the role of the chemokine CCL17/TARC. *Prague Med Rep*. 2009;110(1):35-41.

Holleczek, B., Zampella, D., Urbschat, S., Sahm, F., von Deimling, A., Oertel, J., & Ketter, R. (2019). *Incidence, mortality and outcome of meningiomas: A population-based study from Germany. Cancer Epidemiology, 62, 101562.* doi:10.1016/j.canep.2019.07.001

Hollstein, M., Sidransky, D., Vogelstein, B., & Harris, C. (1991). *p53 mutations in human cancers. Science, 253(5015), 49–53*. doi:10.1126/science.1905840

Hormigo, A., Gu, B., Karimi, S., Riedel, E., Panageas, K. S., Edgar, M. A., … Holland, E. C. (2006). *YKL-40 and Matrix Metalloproteinase-9 as Potential Serum Biomarkers for Patients with High-Grade Gliomas. Clinical Cancer Research, 12(19), 5698–5704.* doi:10.1158/1078-0432.ccr-06-0181

Howell, D. A., Smith, A. G., Jack, A., Patmore, R., Macleod, U., Mironska, E., & Roman, E. (2013). Time-to-diagnosis and symptoms of myeloma, lymphomas and leukaemias: a report from the Haematological Malignancy Research Network. *BMC hematology*, *13*(1), 9. doi:10.1186/2052-1839-13-9

Huang, J., Yu, J., Tu, L., Huang, N., Li, H., & Luo, Y. (2019). *Isocitrate Dehydrogenase Mutations in Glioma: From Basic Discovery to Therapeutics Development. Frontiers in Oncology, 9*. doi:10.3389/fonc.2019.00506

Hughes, C., Brown, M., Clemens, G., Henderson, A., Monjardez, G., Clarke, N. W., & Gardner, P. (2014). *Assessing the challenges of Fourier transform infrared spectroscopic analysis of blood serum. Journal of Biophotonics, 7(3-4), 180–188*. doi:10.1002/jbio.201300167

Husain, H., Savage, W., Grossman, S. A., Ye, X., Burger, P. C., Everett, A., … Holdhoff, M. (2012). *Pre- and post-operative plasma glial fibrillary acidic protein levels in patients with newly diagnosed gliomas. Journal of Neuro-Oncology, 109(1), 123–127*. doi:10.1007/s11060-012-0874-8

Hutchings, M., Loft, A., Hansen, M., Pedersen, LM., Berthelsen, AK., Keiding, S., D'Amore, F., Boesen, AM., Roemer, L., Specht, L. (2006) Position emission tomography with or without computed tomography in the primary staging of Hodgkin's lymphoma. *Haematologica*. 91(4):482-9.

IJzerman-Korevaar, M., Snijders, T. J., de Graeff, A., Teunissen, S. C. C. M., & de Vos, F. Y. F. (2018). *Prevalence of symptoms in glioma patients throughout the disease trajectory: a systematic review. Journal of Neuro-Oncology*. doi:10.1007/s11060-018-03015-9

Ingham, J., Pilling, M. J., Martin, D. S., Smith, C. I., Ellis, B. G., Whitley, C. A., … Barrett, S. (2019). *A novel FTIR analysis method for rapid high-confidence discrimination of esophageal cancer. Infrared Physics & Technology, 102, 103007.* doi:10.1016/j.infrared.2019.103007

Isasi, C. R., Lu, P., & Blaufox, M. D. (2005). *A metaanalysis of 18F-2-deoxy-2-fluoro-D-glucose positron emission tomography in the staging and restaging of patients with lymphoma. Cancer, 104(5), 1066–1074.* doi:10.1002/cncr.21253

Iwamoto, F. M., Hottinger, A. F., Karimi, S., Riedel, E., Dantis, J., Jahdi, M., … Hormigo, A. (2011). *Serum YKL-40 is a marker of prognosis and disease status in high-grade gliomas. Neuro-Oncology, 13(11), 1244–1251.* doi:10.1093/neuonc/nor117

Jakola, A. S., Myrmel, K. S., Kloster, R., Torp, S. H., Lindal, S., Unsgård, G., & Solheim, O. (2012). *Comparison of a Strategy Favoring Early Surgical Resection vs a Strategy Favoring Watchful Waiting in Low-Grade Gliomas. JAMA, 308(18), 1881.* doi:10.1001/jama.2012.12807

Jakola, A. S., Skjulsvik, A. J., Myrmel, K. S., Sjåvik, K., Unsgård, G., Torp, S. H., … Solheim, O. (2017). Surgical resection versus watchful waiting in low-grade gliomas. *Annals of oncology : official journal of the European Society for Medical Oncology, 28*(8), 1942–1948. doi:10.1093/annonc/mdx230

Jauhari, S., & Nasta, S. D. (2016). PET/CT in the Evaluation of Relapsed or Refractory Hodgkin Lymphoma. *American journal of hematology/oncology, 12*(9), 8–13.

Johansen, J. S., Bojesen, S. E., Mylin, A. K., Frikke-Schmidt, R., Price, P. A., & Nordestgaard, B. G. (2009). Elevated Plasma YKL-40 Predicts Increased Risk of Gastrointestinal Cancer and Decreased Survival After Any Cancer Diagnosis in the General Population. Journal of Clinical Oncology, 27(4), 572–578. doi:10.1200/jco.2008.18.8367

Johnson, D. R., Fogh, S. E., Giannini, C., Kaufmann, T. J., Raghunathan, A., Theodosopoulos, P. V., & Clarke, J. L. (2015). *Case-Based Review: newly diagnosed glioblastoma. Neuro-Oncology Practice, 2(3), 106–121.* doi:10.1093/nop/npv020

Jones, K., Vari, F., Keane, C., Crooks, P., Nourse, J. P., Seymour, L. A., … Gandhi, M. K. (2012). *Serum CD163 and TARC as Disease Response Biomarkers in Classical Hodgkin Lymphoma. Clinical Cancer Research, 19(3), 731–742.* doi:10.1158/1078-0432.ccr-12-2693

Jooma, R., Waqas, M., & Khan, I. (2019). Diffuse Low-Grade Glioma - Changing Concepts in Diagnosis and Management: A Review. *Asian journal of neurosurgery, 14*(2), 356–363. doi:10.4103/ajns.AJNS_24_18

Jung, C. S., Foerch, C., Schanzer, A., Heck, A., Plate, K. H., Seifert, V., … Sitzer, M. (2007). *Serum GFAP is a diagnostic marker for glioblastoma multiforme. Brain, 130(12), 3336–3341.* doi:10.1093/brain/awm263

K Zienius, Ip Chak-Lam, J Park, M Ozawa, W Hamilton, D Weller, D Summers, L Porteous, S Mohiuddin, E Keeney, W Hollingworth, Y Ben-Shlomo, R Grant, PM Brennan (2019) Direct access CT for suspicion of brain tumour: an analysis of referral pathways in a population-based patient group. *BMC Family Practice*. 20:118. https://doi.org/10.1186/s12875-019-1003-y

Kaim, W., & Fiedler, J. (2009). Spectroelectrochemistry: the best of two worlds. Chemical Society Reviews, 38(12), 3373.doi:10.1039/b504286k

Karabudak, E., Kas, R., Ogieglo, W., Rafieian, D., Schlautmann, S., Lammertink, R. G. H., … Mul, G. (2012). Disposable Attenuated Total Reflection-Infrared Crystals from Silicon Wafer: A Versatile Approach to Surface Infrared Spectroscopy. Analytical Chemistry, 85(1), 33–38. doi:10.1021/ac302299g

Karnik, S., Srinivasan, B., & Nair, S. (2003). *Hodgkin's lymphoma: immunohistochemical features and its association with EBV LMP-1. Experience from a South Indian hospital. Pathology, 35(3), 207–211.* doi:10.1080/0031302031000123164

Kastan, M. B., & Bartek, J. (2004). *Cell-cycle checkpoints and cancer. Nature, 432(7015), 316–323.* doi:10.1038/nature03097

Kerkhof, M., & Vecht, C. J. (2013). *Seizure characteristics and prognostic factors of gliomas. Epilepsia, 54, 12–17.* doi:10.1111/epi.12437

Kesari, S., Schiff, D., Henson, J. W., Muzikansky, A., Gigas, D. C., Doherty, L., … Wen, P. Y. (2008). *Phase II study of temozolomide, thalidomide, and celecoxib for newly diagnosed glioblastoma in adults. Neuro-Oncology, 10(3), 300–308.* doi:10.1215/15228517-2008-005

Kim, J.-K., Lee, S.-Y., Park, C.-W., Park, S.-H., Yin, J., Kim, J., … Kim, S.-C. (2014). *Rab3a promotes brain tumor initiation and progression. Molecular Biology Reports, 41(9), 5903–5911.* doi:10.1007/s11033-014-3465-2

Kim. (2010). *Polymorphisms in genes involved in folate metabolism and plasma DNA methylation in colorectal cancer patients. Oncology Reports, 25(1).* doi:10.3892/or_00001057

Kobrina, Y., Isaksson, H., Sinisaari, M., Rieppo, L., Brama, P. A., van Weeren, R., … Saarakkala, S. (2010). Infrared spectroscopy reveals both qualitative and quantitative differences in equine subchondral bone during maturation. Journal of Biomedical Optics, 15(6), 067003.doi:10.1117/1.3512177

Kondziolka, D., Lunsford, L. D., & Martinez, A. J. (1993). *Unreliability of contemporary neurodiagnostic imaging in evaluating suspected adult supratentorial (low-grade) astrocytoma. Journal of Neurosurgery, 79(4), 533–536.* doi:10.3171/jns.1993.79.4.0533

Koriyama, S., Nitta, M., Kobayashi, T., Muragaki, Y., Suzuki, A., Maruyama, T., … Kawamata, T. (2018). *A surgical strategy for lower grade gliomas using intraoperative molecular diagnosis. Brain Tumor Pathology, 35(3), 159–167.* doi:10.1007/s10014-018-0324-1

Kros, J. M., Mustafa, D. M., Dekker, L. J., Sillevis Smitt, P. A., Luider, T. M., & Zheng, P. P. (2015). Circulating glioma biomarkers. *Neuro-oncology*, *17*(3), 343–360. doi:10.1093/neuonc/nou207

Küppers, R. (2008). *The biology of Hodgkin's lymphoma. Nature Reviews Cancer, 9(1), 15–27.* doi:10.1038/nrc2542

Küppers, R., Engert, A., & Hansmann, M.-L. (2012). *Hodgkin lymphoma. Journal of Clinical Investigation, 122(10), 3439–3447*. doi:10.1172/jci61245

Lake, A., Nixon, I. J., Beattie, P., Ah-See, K., Culligan, D., Heaney, N., McKay, P., Hilmi, O. J., Jarret, R. F. (2018) P031 (0145) EVALUATION OF CCL17 (TARC) AS A DIAGNOSTIC BIOMARKER FOR CLASSICAL HODGKIN LYMPHOMA. *HemaSphere*. Volume 2 - Issue S3 - p 14–15 doi:10.1097/01.HS9.0000547881.48587.85

Lapointe, S., Perry, A., & Butowski, N. A. (2018). *Primary brain tumours in adults. The Lancet, 392(10145), 432–446*. doi:10.1016/s0140-6736(18)30990-5

Larjavaara, S., Haapasalo, H., Sankila, R., Helén, P., & Auvinen, A. (2008). Is the incidence of meningiomas underestimated? A regional survey. *British journal of cancer*, *99*(1), 182–184. doi:10.1038/sj.bjc.6604438

Laurent James Livermore, Martin Isabelle, Ian Mac Bell, Connor Scott, John Walsby-Tickle, Joan Gannon, Puneet Plaha, Claire Vallance, Olaf Ansorge, Rapid intraoperative molecular genetic classification of gliomas using Raman spectroscopy, *Neuro-Oncology Advances*, Volume 1, Issue 1, May-December 2019, vdz008, https://doi.org/10.1093/noajnl/vdz008

Leão, S. C., Leal, I. O., do Nascimento Rocha, H. M., & Rodrigues, T. M. de A. (2015). *Evaluation of cytokines produced by β-hemolytic streptococcus in acute pharyngotonsillitis. Brazilian Journal of Otorhinolaryngology, 81(4), 402–407*. doi:10.1016/j.bjorl.2015.05.003

Lee, B. B., Lee, E. J., Jung, E. H., Chun, H.-K., Chang, D. K., Song, S. Y., … Kim, D.-H. (2009). *Aberrant Methylation of APC, MGMT, RASSF2A, and Wif-1 Genes in Plasma as a Biomarker for Early Detection of Colorectal Cancer. Clinical Cancer Research, 15(19), 6185–6191.* doi:10.1158/1078-0432.ccr-09-0111

Lei, J., Gao, G., Feng, J., Jin, Y., Wang, C., Mao, Q., & Jiang, J. (2015). Glial fibrillary acidic protein as a biomarker in severe traumatic brain injury patients: a prospective cohort study. *Critical care (London, England)*, *19*, 362. doi:10.1186/s13054-015-1081-8

Levin, L. I., Breen, E. C., Birmann, B. M., Batista, J. L., Magpantay, L. I., Li, Y., … Martínez-Maza, O. (2017). *Elevated Serum Levels of sCD30 and IL6 and Detectable IL10 Precede Classical Hodgkin Lymphoma Diagnosis. Cancer Epidemiology Biomarkers & Prevention, 26(7), 1114–1123.* doi:10.1158/1055-9965.epi-16-1012

Li, C., Qiu, X., Deng, keqin, & Hou, Z. (2014). *Electrochemical co-reduction synthesis of Au/ferrocene–graphene nanocomposites and their application in an electrochemical immunosensor of a breast cancer biomarker. Anal. Methods, 6(22), 9078–9084.* doi:10.1039/c4ay01838a

Lim, Y. S., Kim, M. K., Park, B. J., Kim, T. S., & Lim, Y. J. (2013). *Long Term Clinical Outcomes of Malignant Meningiomas. Brain Tumor Research and Treatment, 1(2), 85.* doi:10.14791/btrt.2013.1.2.85

Lima, K. M. G., Gajjar, K. B., Martin-Hirsch, P. L., & Martin, F. L. (2015). *Segregation of ovarian cancer stage exploiting spectral biomarkers derived from blood plasma or serum analysis: ATR-FTIR spectroscopy coupled with variable selection methods. Biotechnology Progress, 31(3), 832–839.* doi:10.1002/btpr.2084

Louis, D. N., Perry, A., Reifenberger, G., von Deimling, A., Figarella-Branger, D., Cavenee, W. K., … Ellison, D. W. (2016). *The 2016 World Health Organization Classification of Tumors of the Central Nervous System: a summary. Acta Neuropathologica, 131(6), 803–820.* doi:10.1007/s00401-016-1545-1

Lyratzopoulos, G., Abel, G. A., McPhail, S., Neal, R. D., & Rubin, G. P. (2013). *Measures of promptness of cancer diagnosis in primary care: secondary analysis of national audit data on patients with 18 common and rarer cancers. British Journal of Cancer, 108(3), 686–690.* doi:10.1038/bjc.2013.1

Ma, C., Wong, C. K., Wong, B. C. K., Chan, K. C. A., Lun, S. W. M., Lee, N., … Tang, J. W. (2008). *Cytokine responses in a severe case of glandular fever treated successfully with foscarnet combined with prednisolone and intravenous immunoglobulin. Journal of Medical Virology, 81(1), 99–105*. doi:10.1002/jmv.21383

Maher, E. A. (2001). *Malignant glioma: genetics and biology of a grave matter. Genes & Development, 15(11), 1311–1333*. doi:10.1101/gad.891601

Majchrzak-Celińska, A., Paluszczak, J., Kleszcz, R., Magiera, M., Barciszewska, A.-M., Nowak, S., & Baer-Dubowska, W. (2013). *Detection of MGMT, RASSF1A, p15INK4B, and p14ARF promoter methylation in circulating tumor-derived DNA of central nervous system cancer patients. Journal of Applied Genetics, 54(3), 335–344.* doi:10.1007/s13353-013-0149-x

Malumbres, M., & Barbacid, M. (2001). *To cycle or not to cycle: a critical decision in cancer. Nature Reviews Cancer, 1(3), 222–231.* doi:10.1038/35106065

Malumbres, M., & Barbacid, M. (2009). Cell cycle, CDKs and cancer: a changing paradigm. Nature Reviews Cancer, 9(3), 153–166. doi:10.1038/nrc2602

Mansur, D. B., Perry, A., Rajaram, V., Michalski, J. M., Park, T. S., Leonard, J. R., … Simpson, J. R. (2005). *Postoperative radiation therapy for grade II and III intracranial ependymoma. International Journal of Radiation Oncology*Biology*Physics, 61(2), 387–391.* doi:10.1016/j.ijrobp.2004.06.002

Mayerhöfer, T. G., & Popp, J. (2018). *The electric field standing wave effect in infrared transflection spectroscopy. Spectrochimica Acta Part A: Molecular and Biomolecular Spectroscopy, 191, 283–289.* doi:10.1016/j.saa.2017.10.033

Mayerich, D., Walsh, M. J., Kadjacsy-Balla, A., Ray, P. S., Hewitt, S. M., & Bhargava, R. (2015). Stain-less staining for computed histopathology. *Technology*, *3*(1), 27–31. doi:10.1142/S2339547815200010

Mayeux R. (2004). Biomarkers: potential uses and limitations. *NeuroRx : the journal of the American Society for Experimental NeuroTherapeutics*, *1*(2), 182–188. doi:10.1602/neurorx.1.2.182

McClory, S. Hughes, T. Freud, A. G., Briercheck, L. G., Martin, L., Trimboli, A. J., Yu, J., Zhang, X., Leone, G., Nuovo, G., Caligiuri, M. A. (2012) Evidence for a stepwise program of extrathymic T cell development within the human tonsil. J Clin Invest. 2012;122(4):1403–1415. doi:10.1172/JCI46125.

Medical research council (2017) MRC Review of Positron Emission Tomography (PET) within The Medical Imaging Research Landscape 2017. Accessed October 2019
https://mrc.ukri.org/publications/browse/review-of-pet-within-the-medical-imaging-landscape

Metellus, P., Guyotat, J., Chinot, O., Durand, A., Barrie, M., Giorgi, R., … Figarella-Branger, D. (2010). Adult intracranial WHO grade II ependymomas: long-term outcome and prognostic factor analysis in a series of 114 patients. *Neuro-oncology*, *12*(9), 976–984. doi:10.1093/neuonc/noq047

Miotto, E. C., Silva Junior, A., Silva, C. C., Cabrera, H. N., Machado, M. A. R., Benute, G. R. G., … Teixeira, M. J. (2011). *Cognitive impairments in patients with low grade gliomas and high grade gliomas. Arquivos de Neuro-Psiquiatria, 69(4), 596–601.* doi:10.1590/s0004-282x2011000500005

Molenaar, R. J., Maciejewski, J. P., Wilmink, J. W., & van Noorden, C. J. F. (2018). *Wild-type and mutated IDH1/2 enzymes and therapy responses. Oncogene, 37(15), 1949–1960.* doi:10.1038/s41388-017-0077-z

Nandakumar, P., Mansouri, A., & Das, S. (2017). The Role of ATRX in Glioma Biology. *Frontiers in oncology*, *7*, 236. doi:10.3389/fonc.2017.00236

Nathoo, N. (2005). *Pathobiology of brain metastases. Journal of Clinical Pathology, 58(3), 237–242.* doi:10.1136/jcp.2003.013623

National Cancer Registration and Analysis Service. Routes to Diagnosis 206-2016. Worksheet A.
http://www.ncin.org.uk/publications/routes_to_diagnosis Accessed October 2019

Neves, A. C. O., Silva, P. P., Morais, C. L. M., Miranda, C. G., Crispim, J. C. O., & Lima, K. M. G. (2016). *ATR-FTIR and multivariate analysis as a screening tool for cervical cancer in women from northeast Brazil: a biospectroscopic approach. RSC Advances, 6(102), 99648–99655.* doi:10.1039/c6ra21331f

NHS England Birmingham, Guideline for the Management of Classical Hodgkin's Lymphoma in Adults 2011. Accessed October 2019
https://www.uhb.nhs.uk/Downloads/pdf/CancerPbClassicalHodgkinsLymphoma.pdf Accessed October 2019

NHS England, Achieving World-Class Cancer Outcomes: A Strategy for England 2015-2020, Progress Report 2016-2017. Accessed October 2019.
https://www.england.nhs.uk/wp-content/uploads/2017/10/national-cancer-transformation-programme-2016-17-progress.pdf

NHS England, Diagnostic Imaging Dataset Annual Statistical Release 2017/18. Accessed October 2019. https://www.england.nhs.uk/statistics/wp-content/uploads/sites/2/2018/11/Annual-Statistical-Release-2017-18-PDF-1.6MB-1.pdf

NHS England, NHS Screening Programmes in England 2016-2017. Accessed October 2019.
https://assets.publishing.service.gov.uk/government/uploads/system/uploads/attachment_data/file/661677/NHS_Screening_Programmes_in_England_2016_to_2017_web_version_final.pdf

NHS England, The NHS Long Term Plan 2019. Accessed October 2019.
https://www.longtermplan.nhs.uk/publication/nhs-long-term-plan/

Niens, M., Visser, L., Nolte, I. M., van der Steege, G., Diepstra, A., Cordano, P., … van den Berg, A. (2008). *Serum chemokine levels in Hodgkin lymphoma patients: highly increased levels of CCL17 and CCL22. British Journal of Haematology, 140(5), 527–536.* doi:10.1111/j.1365-2141.2007.06964.x

Nikolaenko, L., Chen, R., & Herrera, A. F. (2017). Current strategies for salvage treatment for relapsed classical Hodgkin lymphoma. *Therapeutic advances in hematology, 8*(10), 293–302. doi:10.1177/2040620717728000

Ohgaki, H., & Kleihues, P. (2005). *Epidemiology and etiology of gliomas. Acta Neuropathologica, 109(1), 93–108*. doi:10.1007/s00401-005-0991-y

Ollesch, J., Drees, S. L., Heise, H. M., Behrens, T., Brüning, T., & Gerwert, K. (2013). *FTIR spectroscopy of biofluids revisited: an automated approach to spectral biomarker identification. The Analyst, 138(14), 4092*. doi:10.1039/c3an00337j

Ollesch, J., Heinze, M., Heise, H. M., Behrens, T., Brüning, T., & Gerwert, K. (2014). *It's in your blood: spectral biomarker candidates for urinary bladder cancer from automated FTIR spectroscopy. Journal of Biophotonics, 7(3-4), 210–221*. doi:10.1002/jbio.201300163

Omole, M. A., Noah, N., Zhou, L., Almaletti, A., Sadik, O. A., Asemota, H. N., … Gilchrist, J. (2009). Spectroelectrochemical characterization of pain biomarkers. Analytical Biochemistry, 395(1), 54–60. doi:10.1016/j.ab.2009.07.038

O'Reilly, E. J., Conroy, P., Keyes, T. E., O'Kennedy, R., Forster, R. J., Dennany, L. (2015) Combining recombinant Antibody technology and highly sensitive electrochemiluminescence for the detection of the Cardiac Biomarker C-Reactive protein at sub fg Limits of Detection. RSC Advances. 5:68874-67877.

Ostrom, Q. T., Gittleman, H., Liao, P., Vecchione-Koval, T., Wolinsky, Y., Kruchko, C., & Barnholtz-Sloan, J. S. (2017). *CBTRUS Statistical Report: Primary brain and other central nervous system tumors diagnosed in the United States in 2010–2014. Neuro-Oncology, 19(suppl_5), v1–v88.* doi:10.1093/neuonc/nox158

Ouyang, J., Plutschow, A., von Strandmann, E. P., Reiners, K. S., Ponader, S., Rabinovich, G. A., … Shipp, M. A. (2013). *Galectin-1 serum levels reflect tumor burden and adverse clinical features in classical Hodgkin lymphoma. Blood, 121(17), 3431–3433.* doi:10.1182/blood-2012-12-474569

Ozaki, T., & Nakagawara, A. (2011). *Role of p53 in Cell Death and Human Cancers. Cancers, 3(1), 994–1013*. doi:10.3390/cancers3010994

Ozawa, M., Brennan, P. M., Zienius, K., Kurian, K. M., Hollingworth, W., Weller, D., … Ben-Shlomo, Y. (2018). *Symptoms in primary care with time to diagnosis of brain tumours. Family Practice.* doi:10.1093/fampra/cmx139

Parrales, A., & Iwakuma, T. (2015). *Targeting Oncogenic Mutant p53 for Cancer Therapy. Frontiers in Oncology, 5*. doi:10.3389/fonc.2015.00288

Patchell, R. A. (2003). *The management of brain metastases. Cancer Treatment Reviews, 29(6), 533–540*. doi:10.1016/s0305-7372(03)00105-1

Patchell, R. A., Tibbs, P. A., Walsh, J. W., Dempsey, R. J., Maruyama, Y., Kryscio, R. J., … Young, B. (1990). *A Randomized Trial of Surgery in the Treatment of Single Metastases to the Brain. New England Journal of Medicine, 322(8), 494–500*. doi:10.1056/nejm199002223220802

Penfold, C., Joannides, A. J., Bell, J., & Walter, F. M. (2017). *Diagnosing adult primary brain tumours: can we do better? British Journal of General Practice, 67(659), 278–279.* doi:10.3399/bjgp17x691277

Pengiran Tengah, D. S. N. ., Byrne, P. ., & Wills, A. . (2003). *Urgent 2-week Referrals for CNS/Brain Tumours: a Retrospective Audit. Clinical Oncology, 15(1), 7–9*. doi:10.1053/clon.2002.0133

Persaud-Sharma, D., Burns, J., Trangle, J., & Moulik, S. (2017). *Disparities in Brain Cancer in the United States: A Literature Review of Gliomas. Medical Sciences, 5(3), 16.* doi:10.3390/medsci5030016

Picca, A., Berzero, G., Di Stefano, A. L., & Sanson, M. (2018). *The clinical use of IDH1 and IDH2 mutations in gliomas. Expert Review of Molecular Diagnostics.* doi:10.1080/14737159.2018.1548935

Pijanka, J. K., Kohler, A., Yang, Y., Dumas, P., Chio-Srichan, S., Manfait, M., … Sulé-Suso, J. (2009). *Spectroscopic signatures of single, isolated cancer cell nuclei using synchrotron infrared microscopy. The Analyst, 134(6), 1176.* doi:10.1039/b821112d

Pileri SA, Ascani S, Leoncini L, *et al.*. (2002) Hodgkin's lymphoma: the pathologist's viewpoint. *Journal of Clinical Pathology* 2002;**55:**162-176.

Pilling, M. J., Henderson, A., & Gardner, P. (2017). *Quantum Cascade Laser Spectral Histopathology: Breast Cancer Diagnostics Using High Throughput Chemical Imaging. Analytical Chemistry, 89(14), 7348–7355*. doi:10.1021/acs.analchem.7b00426

Pizzolo, G., Vinante, F., Nadali, G., Ricetti, M. M., Morosato, L., Marrocchella, R., … Chilosi, M. (1993). *ICAM-1 tissue overexpression associated with increased serum levels of its soluble form in Hodgkin's disease. British Journal of Haematology, 84(1), 161–162*. doi:10.1111/j.1365-2141.1993.tb03040.x

Plattel, W. J., Alsada, Z. N. D., van Imhoff, G. W., Diepstra, A., van den Berg, A., & Visser, L. (2016). *Biomarkers for evaluation of treatment response in classical Hodgkin lymphoma: comparison of sGalectin-1, sCD163 and sCD30 with TARC. British Journal of Haematology, 175(5), 868–875*. doi:10.1111/bjh.14317

Plattel, W. J., van den Berg, A., Visser, L., van der Graaf, A.-M., Pruim, J., Vos, H., … van Imhoff, G. W. (2011). *Plasma thymus and activation-regulated chemokine as an early response marker in classical Hodgkin's lymphoma. Haematologica, 97(3), 410–415*. doi:10.3324/haematol.2011.053199

Ponomarenko, E. A., Poverennaya, E. V., Ilgisonis, E. V., Pyatnitskiy, M. A., Kopylov, A. T., Zgoda, V. G., … Archakov, A. I. (2016). The Size of the Human Proteome: The Width and Depth. *International journal of analytical chemistry*, *2016*, 7436849. doi:10.1155/2016/7436849

Pope, W. B., & Brandal, G. (2018). Conventional and advanced magnetic resonance imaging in patients with high-grade glioma. *The quarterly journal of nuclear medicine and molecular imaging : official publication of the Italian Association of Nuclear Medicine (AIMN) [and] the International Association of Radiopharmacology (IAR), [and] Section of the Society of...*, *62*(3), 239–253. doi:10.23736/S1824-4785.18.03086-8

Potts, M. B., Smith, J. S., Molinaro, A. M., & Berger, M. S. (2012). *Natural history and surgical management of incidentally discovered low-grade gliomas. Journal of Neurosurgery, 116(2), 365–372*. doi:10.3171/2011.9.jns111068

Qian, C. N., Mei, Y., & Zhang, J. (2017). Cancer metastasis: issues and challenges. *Chinese journal of cancer*, *36*(1), 38. doi:10.1186/s40880-017-0206-7

Quaresma, M., Coleman, M. P., & Rachet, B. (2015). 40-year trends in an index of survival for all cancers combined and survival adjusted for age and sex for each cancer in England and Wales, 1971–2011: a population-based study. The Lancet, 385(9974), 1206–1218. doi:10.1016/s0140-6736(14)61396-9

Raab, S. S., Grzybicki, D. M., Janosky, J. E., Zarbo, R. J., Meier, F. A., Jensen, C., & Geyer, S. J. (2005). *Clinical impact and frequency of anatomic pathology errors in cancer diagnoses. Cancer, 104(10), 2205–2213*. doi:10.1002/cncr.21431

Ramadas, A. A., Jose, R., Varma, B., & Chandy, M. L. (2017). Cervical lymphadenopathy: Unwinding the hidden truth. *Dental research journal*, *14*(1), 73–78. Ramadas, A. A., Jose, R., Varma, B., & Chandy, M. L. (2017). Cervical lymphadenopathy: Unwinding the hidden truth. *Dental research journal*, *14*(1), 73–78.

Rathcke, C. N., & Vestergaard, H. (2009). *YKL-40 - an emerging biomarker in cardiovascular disease and diabetes. Cardiovascular Diabetology, 8(1), 61*. doi:10.1186/1475-2840-8-61

Reifenberger, G., Wirsching, H.-G., Knobbe-Thomsen, C. B., & Weller, M. (2016). *Advances in the molecular genetics of gliomas — implications for classification and therapy. Nature Reviews Clinical Oncology, 14(7), 434–452*. doi:10.1038/nrclinonc.2016.204

Richards, M. A. (2009). *The size of the prize for earlier diagnosis of cancer in England. British Journal of Cancer, 101(S2), S125–S129*. doi:10.1038/sj.bjc.6605402

Russell, C., Ward, A. C., Vezza, V., Hoskisson, P., Alcorn, D., Steenson, D. P., & Corrigan, D. K. (2018). Development of a needle shaped microelectrode for electrochemical detection of the sepsis biomarker interleukin-6 (IL-6) in real time. Biosensors and Bioelectronics. doi:10.1016/j.bios.2018.11.053

Russo, M., Villani, V., Taga, A., Genovese, A., Terrenato, I., Manzoni, G. C., … Pace, A. (2017). *Headache as a presenting symptom of glioma: A cross-sectional study. Cephalalgia, 38(4), 730–735*. doi:10.1177/0333102417710020

Sanson M, Marie Y, Paris S, Idbaih A, Laffaire J, Ducray F, El Hallani S, Boisselier B, Mokhtari K, Hoang-Xuan K, Delattre JY. Isocitrate dehydrogenase 1 codon 132 mutation is an important prognostic biomarker in gliomas. J Clin Oncol 2009; 27: 4150–49

Sarracanie, M., LaPierre, C. D., Salameh, N., Waddington, D., Witzel, T., & Rosen, M. S. (2015). Low-Cost High-Performance MRI. *Scientific reports*, *5*, 15177. doi:10.1038/srep15177

Sauer, M., Plütschow, A., Jachimowicz, R. D., Kleefisch, D., Reiners, K. S., Ponader, S., … von Strandmann, E. P. (2012). *Baseline serum TARC levels predict therapy outcome in patients with Hodgkin lymphoma. American Journal of Hematology, 88(2), 113–115*. doi:10.1002/ajh.23361

Schankin, C., Ferrari, U., Reinisch, V., Birnbaum, T., Goldbrunner, R., & Straube, A. (2007). *Characteristics of Brain Tumour-Associated Headache. Cephalalgia, 27(8), 904–911*. doi:10.1111/j.1468-2982.2007.01368.x

Schmidt, H., Johansen, J. S., Gehl, J., Geertsen, P. F., Fode, K., & von der Maase, H. (2006). *Elevated serum level of YKL-40 is an independent prognostic factor for poor survival in patients with metastatic melanoma. Cancer, 106(5), 1130–1139*. doi:10.1002/cncr.21678

Schmidt-Hansen, M., Berendse, S., & Hamilton, W. (2015). Symptomatic diagnosis of cancer of the brain and central nervous system in primary care: a systematic review. Family Practice, 32(6), 618–623. doi:10.1093/fampra/cmv075

Schneider, T., Mawrin, C., Scherlach, C., Skalej, M., & Firsching, R. (2010). Gliomas in adults. *Deutsches Arzteblatt international, 107*(45), 799–808. doi:10.3238/arztebl.2010.0799

Schumacher, H., Künzelmann, U., Vasilev, B., Eichhorn, K.-J., & Bartha, J. W. (2010). *Applications of Microstructured Silicon Wafers as Internal Reflection Elements in Attenuated Total Reflection Fourier Transform Infrared Spectroscopy. Applied Spectroscopy, 64(9), 1022–1027*. doi:10.1366/000370210792434404

Scott, J. N., Brasher, P. M. A., Sevick, R. J., Rewcastle, N. B., & Forsyth, P. A. (2002). *How often are nonenhancing supratentorial gliomas malignant? A population study. Neurology, 59(6), 947–949*. doi:10.1212/wnl.59.6.947

Sepúlveda-Sánchez, J. M., Muñoz Langa, J., Arráez, M. Á., Fuster, J., Hernández Laín, A., Reynés, G., … Gallego, Ó. (2018). SEOM clinical guideline of diagnosis and management of low-grade glioma (2017). *Clinical & translational oncology : official publication of the Federation of Spanish Oncology Societies and of the National Cancer Institute of Mexico , 20*(1), 3–15. doi:10.1007/s12094-017-1790-3

Shamoon, R. P., Ali, M. D., & Shabila, N. P. (2018). Overview and outcome of Hodgkin's Lymphoma: Experience of a single developing country's oncology centre. *PloS one, 13*(4), e0195629. doi:10.1371/journal.pone.0195629

Shan, Y., He, X., Song, W., Han, D., Niu, J., & Wang, J. (2015). Role of IL-6 in the invasiveness and prognosis of glioma. *International journal of clinical and experimental medicine, 8*(6), 9114–9120.

Shanbhag, S., & Ambinder, R. F. (2018). Hodgkin lymphoma: A review and update on recent progress. *CA: a cancer journal for clinicians, 68*(2), 116–132. doi:10.3322/caac.21438

Shephard, E. A., Neal, R. D., Rose, P. W., Walter, F. M., & Hamilton, W. T. (2015). Quantifying the risk of Hodgkin lymphoma in symptomatic primary care patients aged ≥40 years: a case-control study using electronic records. *The British journal of general practice : the journal of the Royal College of General Practitioners, 65*(634), e289–e294. doi:10.3399/bjgp15X684805

Sherr, C. J., & McCormick, F. (2002). *The RB and p53 pathways in cancer. Cancer Cell, 2(2), 103–112*. doi:10.1016/s1535-6108(02)00102-2

Shim, J., & Madsen, J. (2018). *VEGF Signaling in Neurological Disorders. International Journal of Molecular Sciences, 19(1), 275*. doi:10.3390/ijms19010275

Soares, J. C., Iwaki, L., Soares, A. C., Rodrigues, V. C., Melendez, M. E., Fregnani, J., … Oliveira, O. N., Jr (2017). Immunosensor for Pancreatic Cancer Based on Electrospun Nanofibers Coated with Carbon Nanotubes or Gold Nanoparticles. *ACS omega, 2*(10), 6975–6983. doi:10.1021/acsomega.7b01029

Song, C. L., Vardaki, M. Z., Goldin, R. D., & Kazarian, S. G. (2019). *Fourier transform infrared spectroscopic imaging of colon tissues: evaluating the significance of amide I and C–H stretching bands in diagnostic applications with machine learning. Analytical and Bioanalytical Chemistry*. doi:10.1007/s00216-019-02069-6

Soussi, T., & Wiman, K. G. (2007). *Shaping Genetic Alterations in Human Cancer: The p53 Mutation Paradigm. Cancer Cell, 12(4), 303–312*. doi:10.1016/j.ccr.2007.10.001

Spalding, K., Bonnier, F., Bruno, C., Blasco, H., Board, R., Benz-de Bretagne, I., … Baker, M. J. (2018). *Enabling quantification of protein concentration in human serum biopsies using attenuated total reflectance – Fourier transform infrared (ATR-FTIR) spectroscopy. Vibrational Spectroscopy, 99, 50–58*. doi:10.1016/j.vibspec.2018.08.019

Subocz, E., Hałka, J., & Dziuk, M. (2017). *The role of FDG-PET in Hodgkin lymphoma. Współczesna Onkologia, 2, 104–114*. doi:10.5114/wo.2017.68618

Suwanwela, N., Phanthumchinda, K., & Kaoropthum, S. (1994). *Headache in Brain Tumor: A Cross-Sectional Study. Headache: The Journal of Head and Face Pain, 34(7), 435–438*. doi:10.1111/j.1526-4610.1994.hed3407435.x

Swann, R., McPhail, S., Witt, J., Shand, B., Abel, G. A., … Hiom, S. (2017). *Diagnosing cancer in primary care: results from the National Cancer Diagnosis Audit. British Journal of General Practice, 68(666), e63–e72*. doi:10.3399/bjgp17x694169

*Thakkar JP, Dolecek TA, Horbinski C, Ostrom QT, Lightner DD, Barnholtz-Sloan JS, Villano JL. (2014) Cancer Epidemiol Biomarkers Prev. 23(10):1985-96.*

The Kings Fund, The Autumn Budget: Joint Statement on Health and Social Care 2017. Accessed October 2019. https://www.kingsfund.org.uk/sites/default/files/2017-11/The%20Autumn%20Budget%20-%20joint%20statement%20on%20health%20and%20social%20care%2C%20Nov%202017.pdf

The National Institute for Health and care Excellence. Suspected Cancer: Recognition and Referral 2015. Accessed October 2019. https://www.nice.org.uk/guidance/ng12/chapter/Introduction

Townsend, W., & Linch, D. (2012). *Hodgkin's lymphoma in adults. The Lancet, 380(9844), 836–847*. doi:10.1016/s0140-6736(12)60035-x

Uckermann, O., Juratli, T. A., Galli, R., Conde, M., Wiedemuth, R., Krex, D., … Kirsch, M. (2017). *Optical Analysis of Glioma: Fourier-Transform Infrared Spectroscopy Reveals theIDH1Mutation Status. Clinical Cancer Research, 24(11), 2530–2538*. doi:10.1158/1078-0432.ccr-17-1795

UK Government Department of health and social care, Policy Paper: 2010 to 2015 Government Policy: Cancer Research and Treatment. Updated 2015. Accessed October 2019. https://www.gov.uk/government/publications/2010-to-2015-government-policy-cancer-research-and-treatment/2010-to-2015-government-policy-cancer-research-and-treatment

Van Alkemade, H., de Leau, M., Dieleman, E. M. T., Kardaun, J. W. P. F., van Os, R., Vandertop, W. P., … Stalpers, L. J. A. (2012). *Impaired survival and long-term neurological problems in benign meningioma. Neuro-Oncology, 14(5), 658–666*. doi:10.1093/neuonc/nos013

Van den Bent, M. J., Brandes, A. A., Taphoorn, M. J. B., Kros, J. M., Kouwenhoven, M. C. M., Delattre, J.-Y., … Hoang-Xuan, K. (2013). Adjuvant Procarbazine, Lomustine, and Vincristine Chemotherapy in Newly Diagnosed Anaplastic Oligodendroglioma: Long-Term Follow-Up of EORTC Brain Tumor Group Study 26951. Journal of Clinical Oncology, 31(3), 344–350. doi:10.1200/jco.2012.43.2229

van Kessel, E., Baumfalk, A. E., van Zandvoort, M., Robe, P. A., & Snijders, T. J. (2017). Tumor-related neurocognitive dysfunction in patients with diffuse glioma: a systematic review of neurocognitive functioning prior to anti-tumor treatment. *Journal of neuro-oncology, 134*(1), 9–18. doi:10.1007/s11060-017-2503-z

Vecht, C. J., Kerkhof, M., & Duran-Pena, A. (2014). Seizure prognosis in brain tumors: new insights and evidence-based management. *The oncologist, 19*(7), 751–759. doi:10.1634/theoncologist.2014-0060

von Bartheld, C. S., Bahney, J., & Herculano-Houzel, S. (2016). The search for true numbers of neurons and glial cells in the human brain: A review of 150 years of cell counting. *The Journal of comparative neurology, 524*(18), 3865–3895. doi:10.1002/cne.24040

von Tresckow, B., & Moskowitz, C. H. (2016). Treatment of relapsed and refractory Hodgkin Lymphoma. *Seminars in hematology, 53*(3), 180–185. doi:10.1053/j.seminhematol.2016.05.010

Wakabayashi, T., Natsume, A., Hatano, H., Fujii, M., Shimato, S., Ito, M., … Yoshida, J. (2009). *P16 PROMOTER METHYLATION IN THE SERUM AS A BASIS FOR THE MOLECULAR DIAGNOSIS OF GLIOMAS. Neurosurgery, 64(3), 455–462*. doi:10.1227/01.neu.0000340683.19920.e3

Wang, H.-Y., Tang, K., Liang, T.-Y., Zhang, W.-Z., Li, J.-Y., Wang, W., … Zhang, S.-Z. (2016). *The comparison of clinical and biological characteristics between IDH1 and IDH2 mutations in gliomas. Journal of Experimental & Clinical Cancer Research, 35(1)*. doi:10.1186/s13046-016-0362-7

Weaver, K. D., Grossman, S. A., & Herman, J. G. (2006). *Methylated Tumor-Specific DNA as a Plasma Biomarker in Patients with Glioma. Cancer Investigation, 24(1), 35–40*. doi:10.1080/07357900500449546

Weihrauch, M. R., Manzke, O., Beyer, M., Haverkamp, H., Diehl, V., Bohlen, H., … Schultze, J. L. (2005). *Elevated Serum Levels of CC Thymus and Activation-Related Chemokine (TARC) in Primary Hodgkin's Disease: Potential for a Prognostic Factor. Cancer Research, 65(13), 5516–5519*. doi:10.1158/0008-5472.can-05-010

Wesseling, P., & Capper, D. (2018). WHO 2016 Classification of gliomas. Neuropathology and Applied Neurobiology, 44(2), 139–150. doi:10.1111/nan.12432

Wessels, P. H., Weber, W. E., Raven, G., Ramaekers, F. C., Hopman, A. H., & Twijnstra, A. (2003). *Supratentorial grade II astrocytoma: biological features and clinical course. The Lancet Neurology, 2(7), 395–403*. doi:10.1016/s1474-4422(03)00434-4

WHO. (2016) Cancer prevention and control in the context of an integrated approach: report by the Secretariat. Geneva: World Health Organization, 2016.

Wiestler, B., Capper, D., Holland-Letz, T., Korshunov, A., von Deimling, A., Pfister, S. M., … Wick, W. (2013). *ATRX loss refines the classification of anaplastic gliomas and identifies a subgroup of IDH mutant astrocytic tumors with better prognosis. Acta Neuropathologica, 126(3), 443–451*. doi:10.1007/s00401-013-1156-z

Wijnenga, M. M. J., French, P. J., Dubbink, H. J., Dinjens, W. N. M., Atmodimedjo, P. N., Kros, J. M., … van den Bent, M. J. (2017). *The impact of surgery in molecularly defined low-grade glioma: an integrated clinical, radiological, and molecular analysis. Neuro-Oncology, 20(1), 103–112.* doi:10.1093/neuonc/nox176

Wong, J., Hird, A., Kirou-Mauro, A., Napolskikh, J., & Chow, E. (2008). Quality of life in brain metastases radiation trials: a literature review. *Current oncology (Toronto, Ont.), 15*(5), 25–45.

World Health Organisation (WHO) 2018, Latest global cancer data: Cancer burden rises to 18.1 million new cases and 9.6 million cancer deaths in 2018. Accessed October 2019. https://www.who.int/cancer/PRGlobocanFinal.pdf

Xiong, P., Gan, N., Cao, Y., Hu, F., Li, T., & Zheng, L. (2012). An Ultrasensitive Electrochemical Immunosensor for Alpha-Fetoprotein Using an Envision Complex-Antibody Copolymer as a Sensitive Label. *Materials*, *5*(12), 2757–2772. doi:10.3390/ma5122757

Yan, P.-F., Yan, L., Zhang, Z., Salim, A., Wang, L., Hu, T.-T., & Zhao, H.-Y. (2016). *Accuracy of conventional MRI for preoperative diagnosis of intracranial tumors: A retrospective cohort study of 762 cases. International Journal of Surgery, 36, 109–117.* doi:10.1016/j.ijsu.2016.10.023

Yang, H., Ye, D., Guan, K. L., & Xiong, Y. (2012). IDH1 and IDH2 mutations in tumorigenesis: mechanistic insights and clinical perspectives. Clinical cancer research : an official journal of the American Association for Cancer Research, 18(20), 5562–5571. doi:10.1158/1078-0432.CCR-12-1773

Zhai, Y., Zhu, Z., Zhou, S., Zhu, C., & Dong, S. (2018). Recent advances in spectroelectrochemistry. Nanoscale, 10(7), 3089–3111. doi:10.1039/c7nr07803j

Zhou, Y., Mendonca, S. C., Abel, G. A., Hamilton, W., Walter, F. M., Johnson, S., … Lyratzopoulos, G. (2017). *Variation in "fast-track" referrals for suspected cancer by patient characteristic and cancer diagnosis: evidence from 670 000 patients with cancers of 35 different sites. British Journal of Cancer, 118(1), 24–31.* doi:10.1038/bjc.2017.381

## Chapter 2: Theoretical Background

### 2.1 Introduction

This chapter will provide an overview of the fundamental principles of infrared spectroscopy, and will describe how such principles can be applied to the study of blood serum samples, through implementation of appropriate sampling techniques, instrumentation, pre-processing and statistical data analysis methods. Thereafter, this chapter will detail the fundamental priniciples of electrochemistry, and will describe how voltammetry and electrochemical impedance spectroscopy may be utilised to characterise redox-active molecules and biomarkers of blood serum samples.

### 2.2 Infrared Spectroscopy

#### 2.2.1 Electromagnetic Radiation

Electromagnetic radiation consists of a mutually perpendicular electric and magnetic field component that oscillate sinusoidally with time to form a self-propagating transverse wave that travels at the speed of light in a vacuum. Electromagnetic waves arise from the acceleration of charged particles and their behaviour can be described, in classical terms, by Maxwell's equations (Krey et al, 2007). A charged particle, both before and after acceleration, exhibits a radial electric field distribution where the electric field magnitude is equivalent at each point on the Gaussian surface, in accordance with Maxwell's first equation, Gauss's law (Krey et al, 2007). However, when the charged particle is subjected to a momentary instantaneous acceleration, the electric field lines must transition between the radial electric field distributions characteristic of the point charge at constant velocity. Consequently, the electric field

lines propagate outwards at the speed of light perpendicular to the direction of motion of the charged particle, and represents the electric field component of an electromagnetic wave, as depicted in Figure 2.1 (Misner et al, 2017).

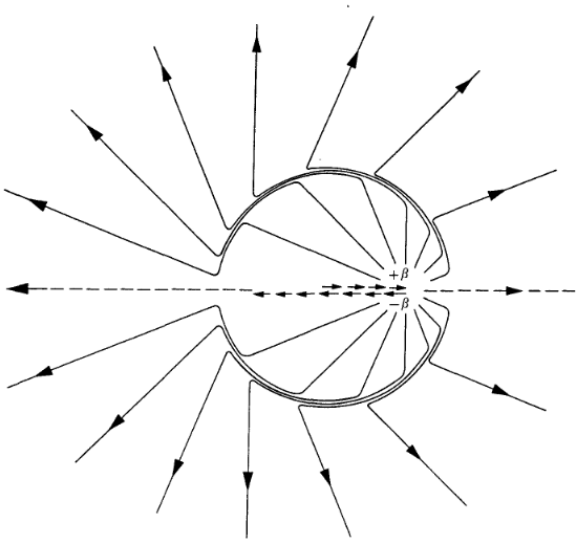


*Figure 2.1: Production of electromagnetic radiation from the acceleration of a point charge. Reproduced. (Misner et al, 2017).*

The electric field component of an electromagnetic wave oscillates sinusoidally with time giving rise to an encompassing magnetic field component with zero divergence, in accordance with Maxwell's second and fourth equation; Gauss's law of magnetism and Ampere's law respectively (Krey et al, 2007). Similarly, the magnetic field component of an electromagnetic wave oscillates sinusoidally with time which induces a time-varying electric field component, in accordance with Maxwell's third equation, Faraday's law (Krey et al, 2007). Therefore, in-phase electric and magnetic field components perpetually induce one another to form a self-propagating transverse

wave, depicted in Figure 2.2, which may be characterised by the wavelength, $\lambda$, and frequency, $\nu$, of the electromagnetic wave in relation to the speed of light, $c$.

$$c = \nu\lambda \qquad \text{(eq 2.1)}$$

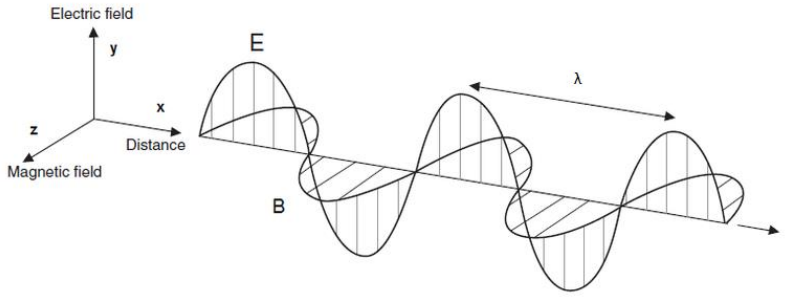


*Figure 2.2: Schematic of an electromagnetic wave with an oscillating electric and magnetic field component. Adapted. (Lusch, 1999)*

Given the wave-particle duality of electromagnetic waves, radiation may alternatively be represented in quantum mechanical terms, as a series of discrete packets of photons of quantised energy that propagate at the speed of light in a vacuum. Photons representative of electromagnetic radiation arise as a consequence of spontaneous emission where transitions in the charged particles quantum states, specifically from an excited state to a lower energy state, gives rise to an oscillating electric dipole moment, resulting in photon emission of quantised energy (Prasad, 2004). The photons energy is equivalent to the difference in energy between quantised energy states and may be determined by the Planck-Einstein relation, where the energy of the photon, *E*, is a function of its frequency, $\nu$, and Planck's proportionality constant, *h*, and may also

be expressed in terms of the wavelength, $\lambda$, of the electromagnetic wave (Griffiths et al, 2007).

$$E = h\nu = \frac{hc}{\lambda} \quad \text{(eq 2.2)}$$

Infrared spectroscopy concerns the interaction of electromagnetic waves with molecules where the energy of applied radiation is commonly expressed in terms of wavenumber, $\tilde{\nu}$, which describes the number of wavelengths per unit distance, and is determined from the inverse of the electromagnetic waves wavelength, $\lambda$.

$$\tilde{\nu} = \frac{1}{\lambda} \quad \text{(eq 2.3)}$$

The electromagnetic spectrum characterises electromagnetic waves according to their energies where infrared radiation has a wavelength range greater than and below the visible and microwave region respectively. The infrared region of the electromagnetic spectrum can further be divided in to the near, mid and far infrared region, with the mid-infrared wavenumber range of 4000-400cm$^{-1}$ pertinent to the molecular classification of biological samples.

### 2.2.2 Molecular Vibrations

Irradiation of infrared light on matter promotes transitions in quantised energy states of the fundamental modes of vibration characteristic of the atomic composition of a molecule. A molecule comprising N atoms in three-dimensional space exhibits 3N

degrees of freedom representative of the vibrational, translational and rotational nuclear motions of an atom (Griffiths et al, 2007). Hence, a non-linear molecule, whose constituent atoms form chemical bonds at angles other than 180°, exhibits six degrees of freedom attributed to three translational and rotational motions in the X, Y and Z-plane, equating to 3N – 6 fundamental modes of vibration (Griffiths et al, 2007). Conversely, a linear molecule whose constituent atoms form chemical bonds at angles equal to 180° has one rotational degree of freedom omitted, as rotation about the axis of the bond does not induce displacement of atoms, resulting in 3N – 5 fundamental modes of vibration (Griffiths et al, 2007). In all molecules, each mode of fundamental vibration represents one discrete vibrational motion of two constituent atoms with the superposition of individual modes representative of the complete vibration of the molecule.

Consideration of a diatomic heteronuclear covalent molecule allows understanding of the inherent vibrational motion of a molecule and its subsequent behaviour upon interaction with infrared radiation. The two atoms, in order to obtain a stable outer electron arrangement, share one or more pairs of valence electrons when their atomic orbitals overlap, forming a covalent bond (Kelter et al, 2008). The electronegativity of the atoms defines their ability to attract bonding electrons when their atomic orbitals overlap and therefore determines the polarity of the covalent bond. If the atoms electronegativity values differ by 0.5-2.0 on the Pauling scale, a polar covalent bond is formed where bonding electrons experience greater affinity to the nucleus of the atom with increased electronegativity (Kelter et al, 2008). Consequently, an uneven charge distribution exists in the molecule with one atom having a partial positive

charge and the other having a partial negative charge which produces a bond dipole moment. The magnitude of the bond dipole moment is the product of the total charge separation and distance between partial charges. Conversely, an electronegativity difference between the two atoms of 0-0.5 on the Pauling scale describes a non-polar covalent bond where bonding electrons experience mutual attraction to respective nuclei, causing an equal sharing of bonding electrons and, hence, no net dipole moment exists (Kelter et al, 2008). The electronegativity of the respective atoms thus determines the presence of bond dipole moments in molecules, which in turn influences their ability to absorb infrared radiation, given that spectroscopic transitions arise following fluctuations in the electric dipole moment of a molecule. However, it should be stressed that molecules do not strictly require permanent bond dipoles to observe absorption bands on infrared spectra provided its zero bond dipole moment changes upon vibrational motion (Griffiths et al, 2007).

The two atoms upon forming a covalent bond establish an equilibrium inter-nuclear distance where attractive electrostatic interactions between oppositely charged bonding electrons and nuclei balance repulsive electrostatic interactions between charged non-bonding electrons and charged nuclei. The two atoms' thermal energies induce a continuous state of vibrational motion where respective nuclei invariably deviate from their equilibrium inter-nuclear distance. Consequently, the molecule experiences a fluctuating electric dipole moment where the electric field vector oscillates in sinusoidal fashion at a frequency corresponding to that of the molecular vibration. The electric field may interact with the electric field of a propagating electromagnetic wave if the frequency of applied radiation corresponds to the natural

frequency of the molecular vibration, ultimately causing the molecule to absorb photons of quantised energy (Pavia et al, 2008). Consequently, the amplitude of vibration increases independently of the natural frequency of the molecule, allowing absorption bands to be observed on infrared spectra, where the band intensity is proportional to the magnitude of the change in the electric dipole moment of the molecule (Pavia et al, 2008).

The interaction of vibrational modes in any molecule with infrared energy can similarly be described by stretching or bending vibrations, which constitute the two principal motions, as depicted in Figure 2.3. Stretching vibrations, both symmetric and asymmetric, describe a change in the inter-atomic distance relative to the bond axis and are, generally, observed at higher wavenumbers on infrared spectra (Pavia et al, 2008). Bending vibrations, categorised as either twisting, wagging, scissoring or rocking motions, describe a change in bond angle between two atoms and are, generally, observed at lower wavenumbers on infrared spectra (Pavia et al, 2008).

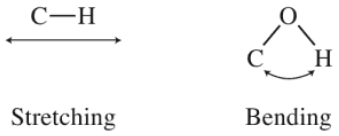


*Figure 2.3: Principal vibrational modes in infrared spectroscopy. Reproduced. (Pavia et al, 2008)*

Consideration of symmetry further allows determination of the molecules infrared active vibrational modes and the number of absorption bands present on an infrared

spectrum. Molecules that display low symmetry with reference to point group theory have vibrational modes that are typically both infrared and Raman active (Larkin, 2011). Conversely, molecules that exhibit high symmetry with a centre of inversion strictly only have either infrared or Raman active vibrational modes, in accordance with the principle of mutual exclusion (Larkin, 2011). In general, an increase in the symmetry of the molecule results in a decrease in the number of absorption bands observed on an infrared spectrum, as a consequence of required degeneracy (Larkin, 2011). Required degeneracy occurs in molecules that display a three-fold or greater axis of symmetry, causing two or more vibrational modes to absorb infrared energy at identical frequencies, therefore producing only one absorption band for these vibrational modes (Larkin, 2011).

The vibrational motion of a diatomic hetero-nuclear covalent molecule can be approximated by Hooke's law where the constituent atoms and adjoining chemical bond are modelled as two masses and a massless spring respectively (Smith, 1998, Baker et al, 2016). The natural vibration of the molecule causes continuous displacement of the constituent atoms, or masses, from their equilibrium inter-nuclear distance. Consequently, perpetual extension and contraction of the covalent bond, or spring, from its equilibrium position subjects the masses to a proportional linear elastic restoring force, as defined by Hooke's law.

$$F = -kx \qquad \text{(eq 2.4)}$$

Where $F$ is the restoring force, $k$ is the spring constant, $x$ is the displacement of the spring.

The masses experience simple harmonic motion about their equilibrium position with each sinusoidal oscillation having a constant amplitude and resonant frequency. The resonant frequency of the molecule is characteristic of its atomic composition and independent of the energy imposed on the atoms and, therefore, may be determined from the reduced mass and bond strength of the two atoms.

$$v = \frac{1}{2\pi}\sqrt{\frac{k}{\mu}} \qquad \text{(eq 2.6)}$$

Where $v$ is the vibrational frequency, $k$ is the force constant, and μ is the reduced mass.

The reduced mass of the two atoms, μ, is calculated from their respective masses, m1 and m2,.

$$\mu = \frac{m1m2}{m1+m2} \qquad \text{(eq 2.7)}$$

The total energy in a harmonic oscillator is the summation of potential and kinetic energy where the conservative nature of the system permits continual transfer of energy between both states relative to the atoms position. The displacement of two atoms from their equilibrium position produces a proportional increase in potential energy that is equivalent to the total vibrational energy at maximum displacement. The two atoms subsequent return towards their equilibrium inter-nuclear distance produces a proportional increase in kinetic energy that corresponds to the total vibrational

energy at their equilibrium position. Thus, the displacement of atoms are confined to the quadratic potential surface of the harmonic oscillator, for each quantised energy level, where potential energy of the atoms can be expressed as a function of the force constant and displacement of the spring.

$$V\ (x) = \frac{1}{2}kx^2 \qquad \text{(eq 2.8)}$$

Where $V$ is the potential energy, $k$ is the spring constant and $x$ is the displacement of the atom.

The atoms in a molecule, at room temperature, primarily populate the lowest quantised vibrational energy state, referred to as the ground state, in accordance with Boltzmann' distribution law (Sathyanarayana, 2015). The atoms may transition to the first excited energy state, referred to as a fundamental transition, upon absorption of a photon of quantised energy provided the quantum corresponds to the difference in energy between the molecules ground and first vibrational quantum energy states.

$$V_j = \left(\mathrm{v_j} + \frac{1}{2}\right)\nu_j h \qquad \text{(eq 2.9)}$$

Where $V_j$ is an integer value representing the vibrational energy state at a characteristic frequency, $h$ is Planck's constant, $\mathrm{v_j}$, is the discrete quantum number of the $j$th mode and, $\nu_j$, is the characteristic frequency of the mode of vibration.

The vibrational selection rules must also be satisfied for transitions to occur between vibrational quantum energy states. Firstly, the gross selection rule states that such transitions can only occur when the absorption of quantised energy induces a net change in the molecules electric dipole moment (Sathyanarayana, 2015). Secondly, the specific selection rule states that molecules can only transition to the next vibrational quantum state in the harmonic oscillator model where all vibrational energy levels are equidistant (Sathyanarayana, 2015).

$$\Delta v_j = \pm 1 \tag{10}$$

Where $v_j$ represents the quantum number of the $j$th mode.

The vibrational motion of real molecules can only be approximated to the harmonic oscillator model at low vibrational quantum states where the atoms experience small displacements from their equilibrium position. The harmonic oscillator does not accurately represent molecular motion at high vibrational quantum energy states because it does not account for the finite length of the chemical bond (Sasic et al, 2011). In reality, the displacement of atoms increases with increasing vibrational quantum energy states to a maximum position where subsequent displacement causes the molecular bond to break and its atoms dissociate. Thus, real molecules behave as

non-linear oscillators and may be represented by the anharmonic oscillator model, depicted in Figure 2.4.

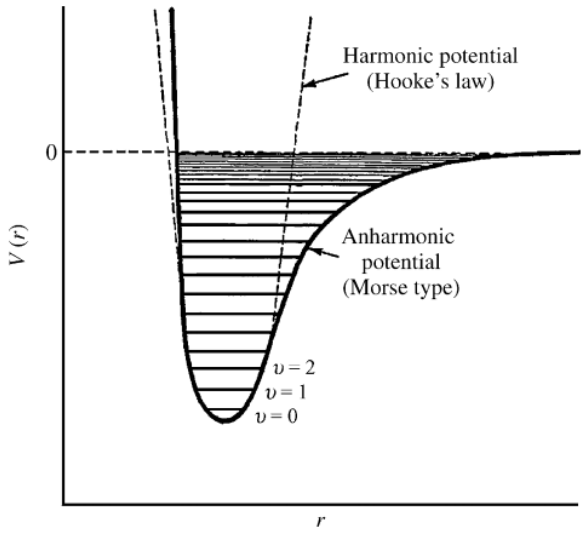


*Figure 2.4: A vibrating molecule represented by harmonic and anharmonic oscillator models. Reproduced. (Griffiths et al, 2007)*

The anharmonic oscillator does not obey Hooke's law and distinctions can be observed between its potential energy curve and the parabolic curve of the harmonic oscillator. Firstly, the gradient of the anharmonic oscillators potential curve is more profound at smaller inter-nuclear distances because of the inclusion of the atoms repulsive electrostatic interactions which act in the direction of the restoring force. Secondly, the gradient of the anharmonic oscillators potential curve decreases with increasing inter-nuclear distance and tends asymptotically towards zero at large displacements. The potential energy of the atoms in an anharmonic oscillator can be represented by the Morse potential, in conjunction with the Schrodinger equation, to describe the vibrational motion of real life molecules (Baker et al, 2016).

$$V_j = \left(v_j + \frac{1}{2}\right) v_j h + \left(v_j + \frac{1}{2}\right)^2 v_j h x_j \qquad \text{(eq 2.11)}$$

Where $V_j$ is an integer value representing the vibrational energy state at a characteristic frequency, $h$ is Planck's constant, $v_j$, is the discrete quantum number of the $j$th mode, $v_j$, is the characteristic frequency of the mode of vibration and, $x_j$, is the anharmonicity constant.

The anharmonic oscillators vibrational energy levels converge with increasing quantum numbers and thus the specific selection rule is no longer strictly valid (Baker et al, 2016; Griffiths et al, 2007). The molecule may transition, for example, from an initially excited state to higher energy states upon absorption of additional photons, with these transitions referred to as hot bands. The intensity of hot bands depend on the probability of atoms initially populating an excited energy state which is significantly reduced at room temperature and with increasing frequency, in accordance with Boltzmann' distribution law (Sathyanarayana, 2015; Baker et al, 2016). Similarly, the molecule may transition from ground state energy to vibrational energy states above the first excited state with such transitions referred to as overtone bands (Pavia et al, 2008; Baker et al, 2016). Thus, the specific selection rule must be revised to account for the higher order transitions of hot bands and overtones observed in the anharmonic oscillator.

$$\Delta v_j = \pm 1, \pm 2, \pm 3 \ldots \qquad \text{(eq 2.12)}$$

Where $v_j$ represents the quantum number of the $j$th mode.

Overtone bands represent the higher resonant frequencies of a vibrational mode and are observed on infrared spectra at lower frequencies and lower intensities than multiples of the fundamental transition, reflecting the decrease in energy between adjacent vibrational states with successive quantum numbers. The most identifiable overtones are first and second overtone bands that describe transitions from ground state energy to the second and third excited state respectively. In general, the intensity of overtone absorption bands decrease with higher order transitions from ground state energy, in accordance with Boltzmann' distribution law (Sathyanarayana, 2015).

The anharmonic oscillator permits coupling of individual modes of vibration in polyatomic molecules. Combination bands arise from simultaneous excitation of multiple modes of vibration from ground state energy to the first excited state and occur at frequencies corresponding to the approximate summation of the coupled vibrational modes fundamental frequencies (Pavia et al, 2008). Difference bands arise from transitions from an excited state of one vibrational mode to a lower excited state of an adjacent vibrational mode and may be observed at frequencies that correspond to the difference in the coupled vibrational modes fundamental frequencies (Pavia et al, 2008).

Fermi resonance arises from interactions between overtones and fundamental transitions, and less frequently between combination bands and fundamental transitions, and describes changes in the frequency and intensity of respective absorption bands (Pavia et al, 2008). Fermi resonance occurs if there is a close match between the frequencies of the fundamental and overtone transition and if the coupled vibrational modes have identical symmetries (Pavia et al, 2008).

### 2.2.3 Infrared Absorption Frequencies of Biomolecules

The vibration of a molecule upon irradiation of infrared light is dependent on the energy imposed on its constituent atoms and hence may be characterised by the wavelength of applied electromagnetic waves which correspond to distinct infrared regions. The mid-infrared region is the pertinent spectral region for biomolecular identification where electromagnetic waves of 2.5-25μm wavelength promote fundamental transitions at 4000-400 $cm^{-1}$ (Williamson et al, 2012). The mid-infrared region can further be subdivided in to two distinct regions; the functional group and fingerprint region. The functional group region describes stretching vibrations of functional groups in molecules that resonate at characteristic frequencies between 4000-1450 $cm^{-1}$ (Byrn et al, 2017). In general, functional groups of double or triple bonds resonate at higher frequencies compared to those with single bonds. The fingerprint region describes bending vibrations of functional groups and interactions between vibrational modes at 1450-600cm-1, with acquired spectra in this region specific to the molecular composition of a particular molecule (Baker et al, 2014; Byrn et al, 2017). Together, evaluation of the functional group and fingerprint regions

permit the identification of molecular constituents of biological samples, as depicted in Figure 2.5.

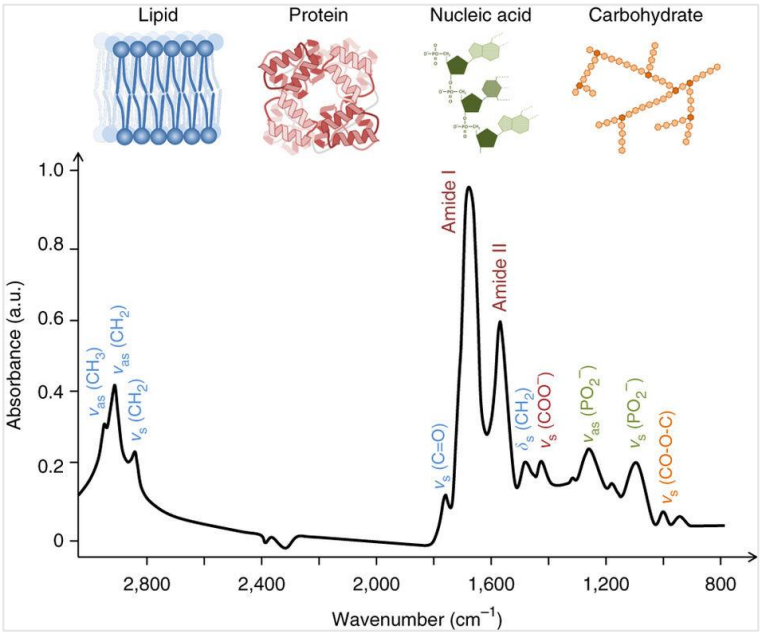


*Figure 2.5: An infrared spectrum characteristic of a biological sample. Reproduced. (Baker et al, 2014)*

Human blood serum is comprised of water (~93%) and a variety of biomolecules (~7%) which primarily constitute blood proteins (6-8g/dL) along with smaller quantities of lipids, carbohydrates, amino acids, nucleic acids and electrolytes (Sikaris, 2009; Busher et al, 1990; Krebs, 1950). Protein content of blood serum is comprised primarily of the globular protein albumin (3.5-5.0g/dL) with significant contributions from $\alpha_1$-Globulin, $\alpha_2$-Globulin, β-Globulin and γ-Globulin's (Busher et al, 1990; Spalding et al 2018). Consequently, the prominent absorption bands of serum spectra arise from characteristic vibrations of the amide group responsible for covalently bonding successive amino acids in protein. The amide group has a total of nine characteristic vibrations with amide A, amide I, amide II and amide III bands routinely

observed on infrared spectra (Stuart, 2004; Barth, 2007). The amide A mode is comprised of a fermi resonance doublet with the amide B mode and forms a strong absorption band at ~3300 $cm^{-1}$ assigned exclusively to $\nu$(NH) vibrations (Barth, 2007). The amide l mode induces a strong absorption band at 1600-1700 $cm^{-1}$ attributed to $\nu$(C=O) vibrations (~80%) and $\nu$(CN) (~10%) and δ(NH) modes (~10%) (Stuart, 2004). The amide l mode is the pertinent spectral band for identification of protein secondary structure with sensitive correlation between the wavenumber of absorption peaks and polypeptide backbone conformation (Barth, 2007). Alpha-helix conformation is characterised by a helical structure supported by hydrogen bond formation along the polypeptide backbone. Hydrogen bonding influences the amide I band position, with alpha-helix conformation observed at ~1657-1648$cm^{-1}$, and at a higher wavenumber than beta-sheet secondary structure (Stuart, 2004). Beta-sheet conformation features extensive hydrogen bonding in adjacent polypeptide backbones of beta-strands and, consequently, shifts the amide I band position to 1640-1610 $cm^{-1}$ (Stuart, 2004). The amide ll mode produces a strong absorption band at 1520-1560 $cm^{-1}$ assigned to δ(NH) (~60%) and $\nu$(CN) (~40%) vibrations and is less commonly employed for elucidation of protein secondary structure (Stuart, 2004; Barth, 2007). The amide lll mode produces a weak absorption band at 1200-1400 $cm^{-1}$ attributed predominantly to coupling of δ(NH) (~30%) and $\nu$(CN) (~30%) modes with smaller $\nu$(CC) and δ(CO) vibrations (Stuart, 2004; Barth, 2007).

Lipids are present in blood serum in the form of triglycerides, phospholipids and cholesteryl esters that have common chemical subunits in their molecular composition. Consequently, the prominent absorption bands of lipids on serum spectra arise from

vibrations of the hydrocarbon chain region in each class, with notable peaks in the 3100-2800cm-$^{1}$ region attributed to $\nu_s(CH_2)$, $\nu_{as}(CH_2)$ and $\nu_{as}(CH_3)$ modes (Baker et al, 2014, Stuart, 2004). Similarly, the hydrocarbon tail region instigates numerous weak bending vibrations in the 1485-1370cm$^{-1}$ region, most notably $\delta_{scissoring}(CH_2)$ and $\delta_s(CH_3)$ modes at ~1470 cm$^{-1}$ and ~1380 cm$^{-1}$ respectively (Stuart, 2004). Other characteristic lipid peaks may be observed at ~1735cm$^{-1}$, ~1242cm-1, ~1085cm$^{-1}$ and ~1200-1050cm$^{-1}$ that correspond to $\nu_s(C=O)$, $\nu_{as}(PO_2)$, $\nu_s(PO_2)$ and $\nu(COC)$ vibrational modes respectively (Liu et al, 2002).

Carbohydrates are present in blood serum primarily as hexose and pentose monosaccharides. Glucose is the major hexose monosaccharide of blood serum characterised by a prominent $\nu_s(CO)$ vibration at ~1035cm$^{-1}$ and numerous other vibrations in the 1100-900cm$^{-1}$ region assigned to $\nu(CC)$, $\delta(CH)$ and $\delta(COH)$ modes (Movasaghi et al, 2008; Wiercigroch et al, 2017). Major pentose monosaccharides of blood serum are ribose and deoxyribose which constitute the sugar-phosphate backbone of ribonucleic acid (RNA) and deoxyribonucleic acid (DNA) respectively with distinctive spectral features in the 800-1200cm-1 region (Movasaghi et al, 2008). In both pentose sugars, strong $\nu_s(OH)$ vibrations are observed with absorption peaks in the ~3400-3200 cm-$^{1}$ region (Wiercigroch et al, 2017).

Nucleic acids are present in blood serum in the free circulating form with increased concentrations compared to healthy individuals indicative of diseased states (Anker et al, 1999). Nucleic acids comprise single or double helical polynucleotide chains with

nucleotide monomers covalently bonded to one another through phosphodiester bonds. Consequently, the pronounced absorption bands of nucleic acids on serum spectra correspond to nitrogenous bases at 1800-1500cm$^{-1}$, 5-carbon sugar at 1100-900cm$^{-1}$ and phosphodiester linkages at 1244-1230cm$^{-1}$/1089-1084cm$^{-1}$ (Stuart, 2004; Wiercigroch et al, 2017). Furthermore, interactions between nucleic acid chemical structures may be observed at 1500-1250cm$^{-1}$, 1250-1000cm$^{-1}$ and 1000-800cm$^{-1}$ on infrared spectra (Stuart, 2004).

### 2.2.4 Sampling Modes

#### 2.2.4.1 Attenuated Total Reflectance

Attenuated total reflectance is a spectroscopic sampling modality characterised by total internal reflection of infrared electromagnetic waves incident on an internal reflection element (IRE) where resultant evanescent waves penetrate sample components to identify their molecular composition, as depicted in Figure 2.6.

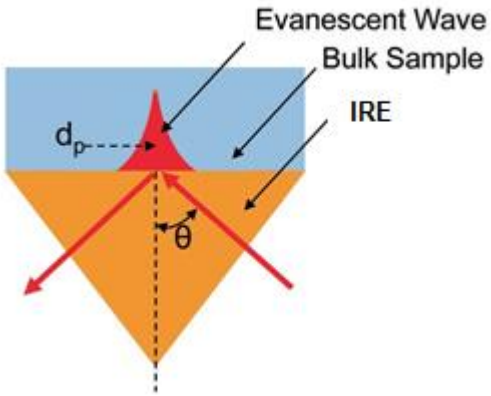


*Figure 2.6: Schematic of internal reflection element in ATR-FTIR configuration. Adapted. (Baker et al, 2016).*

The IRE comprises an infrared transparent material, commonly diamond, where the refractive index of the material must exceed the refractive index of the sample to satisfy total internal reflection of the incident beam. Materials with a high refractive index are chosen to minimise the critical angle, since the angle of incidence must exceed the critical angle to instigate total internal reflection (Baker et al, 2016). On occasions where the angle of incidence does not exceed the critical angle, both total internal reflection and external reflection will contribute to observed spectra (Baker et al, 2016). The critical angle, $\theta_c$, may be calculated as a function of the refractive index of the sample, $n1$, and the refractive index of the IRE, $n2$ (Baker et al, 2016).

$$\theta_c = \sin^{-1} \frac{n2}{n1} \qquad \text{(eq 2.13)}$$

Total internal reflection of infrared radiation at the interior surface of the IRE causes electromagnetic energy to oscillate perpendicular to the refractive boundary with the phase of oscillation giving the appearance of a wave propagating parallel to the surface of the IRE (Milosevic, 2013). The wave, known as an evanescent wave, arises as a consequence of energy conservation between incident and reflective beams during total internal reflection and has an exponentially decaying electric field (Milosevic, 2013). Therefore, the evanescent wave is confined to the surface of the IRE with a typical depth of penetration of ~1.0-2.0 microns in the fingerprint region (Baker et al, 2014). The penetration depth of the evanescent wave is defined as the distance from the external surface of the IRE where the electric field amplitude decreases by 1/e of its initial value. The penetration depth of the evanescent wave, $d_p$, may be calculated

given the wavelength of applied light, $\lambda$, the angle of incidence with respect to normal of the IRE, $\theta$, the refractive index of the sample, $n1$, and the refractive index of the IRE, $n2$.

$$d_p = \frac{\lambda}{2\pi(n_1^2 sin^2\theta - n_2^2)^{1/2}} \quad \text{(eq 2.14)}$$

Thus, the angle of incidence and refractive index of the IRE have significant influence on the amplitude of the evanescent wave where an increase in either parameter causes a decrease in the resultant penetration depth. Furthermore, it may be observed that the depth of penetration is dependent on the wavelength of incident light with the amplitude of the evanescent wave decreasing linearly over the mid-infrared region, causing spectral features in high wavenumber regions to have reduced absorption values compared to those observed in low wavenumber regions (Baker et al, 2016). The depth of penetration is also dependent on the refractive index of the sample, and since the refractive index of the sample varies in regions of high absorption due to anomalous dispersion, absorption peak maxima may be observed at lower wavenumbers relative to transmission experiments (Hancer et al, 2000; Grdadolnik, 2002). However, ATR correction methods are routinely employed to account for differences in wavenumbers prior to spectral analysis (Grdadolnik, 2002).

2.2.4.2 Transmission

Transmission FTIR is a spectroscopic sampling modality characterised by the projection of a spectrum of infrared radiation on to an optically transparent cell where the wavelength and intensity of transmitted infrared light permits molecular classification of sample constituents. Liquid cells comprise two infrared transparent windows, commonly manufactured from calcium fluoride, barium fluoride or zinc selenide, configured either side of a spacer which contains the liquid sample and defines the sample path length, as depicted in Figure 2.7.

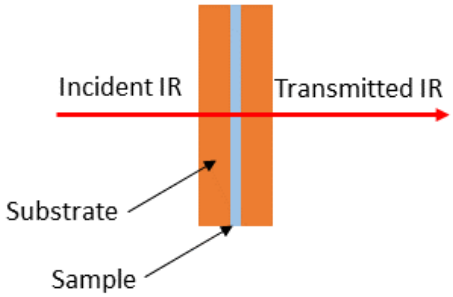


*Figure 2.7: Schematic of transmission FTIR configuration. Original Image.*

Infrared light absorbed by the sample, A, corresponds to the intensity of incident, Io, and transmitted light, I, and is a function of molar absorptivity, e, pathlength, l, and concentration, c, of the sample, in accordance with the Beer-Lambert law (Vitha, 2018).

$$A = log_{10}\left(\frac{I_O}{I}\right) = \varepsilon\, l\, c \qquad \text{(eq 2.15)}$$

Thus, the sample path length in transmission FTIR is not wavelength dependent in contrast to ATR-FTIR and instead permeates the sample producing spectra indicative of the bulk sample (Baker et al, 2016). Sample path length is imperative to acquisition of quality spectra and should be specified at 1-20μm to prevent signal saturation and non-linearity of the Beer-Lambert law, which is detrimental to spectroscopic analysis (Baker et al, 2016). In particular, liquid samples of aqueous media should have a significantly reduced sample path length, ~1um, to account for the strong infrared absorption of water molecules, which routinely obscure pertinent diagnostic bands inclusive of the amide l and C-H stretch regions on infrared spectra (Grdadolnik, 2002). This is often difficult to achieve in practice because of reproducibility issues with the spacer thickness and the presence of air bubbles in samples, and at such sample thickness surface interactions between the sample and optical window may influence infrared spectra (Grdadolnik, 2002). Furthermore, inconsistencies in the drying of biofluid films at such sample thickness may have a profound influence on the reproducibility of the analytical technique (Dubois et al, 2004). This highlights the difficulties in employing transmission FTIR for biofluid analysis where sampling techniques with reduced sample path lengths may be more appropriate, namely ATR-FTIR spectroscopy (Baker et al, 2016).

#### 2.2.4.3 Transflection FTIR

Transflection FTIR describes the projection of a spectrum of infrared light on to a sample located on an infrared reflective coated slide where a small proportion of

incident light is specularly reflected, with the majority transmitted to the underlying metal surface and then projected back through the sample, as depicted in Figure 2.8.

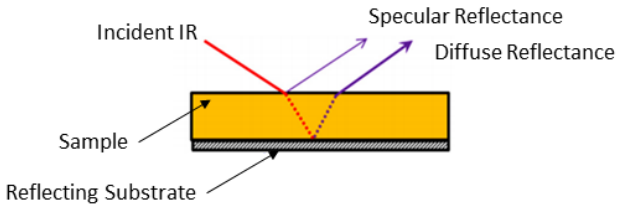


*Figure 2.8: Schematic of trans-flection FTIR configuration. Adapted. (Baker et al, 2016).*

The reflected infrared light is collected by surrounding mirrors and projected to an infrared detector that enables the production of infrared spectra indicative of the characteristic frequencies of sample constituents. The absorption of characteristic bands on infrared spectra is significantly larger than transmission and ATR-FTIR mode experiments attributable to the increased sample path length (Baker et al, 2016). However, transflection FTIR is not applicable for wet biofluid analysis since the increased sample path length causes increased absorption of infrared light by water molecules that may obscure diagnostic bands on infrared spectra. Similarly, transflection experiments suffer from electric field standing wave effects where the intensity of absorption bands varies across infrared spectra, with the phenomena strongly influenced by sample thickness of dried biofluid films (Baker et al, 2016; Hughes et al, 2014). Therefore, transflection mode will not be considered throughout the course of the project due to concerns with reproducibility of the technique given the difficulty in achieving consistent drying patterns with biological samples.

### 2.2.5 FTIR Spectrometer

#### 2.2.5.1 Overview

FTIR spectrometers comprise a bench top unit featuring a polychromatic light source, a Michelson interferometer, a sample aperture and an infrared detector connected to a desktop computer. The polychromatic light source generates a spectrum of infrared light in the mid-infrared region which is projected on to the Michelson interferometer and creates an interferogram which interrogates the sample residing above the aperture. Transmitted infrared light not absorbed by sample components is collected by the infrared detector with the resultant interferogram subjected to a Fourier transform operation on the instruments software. The FTIR spectrometer employed during the course of this project was the Perkin-Elmer Spectrum 2 configured with the Perkin-Elmer ATR top-plate accessory module for diamond control data, as depicted in Figure 2.9.

*Figure 2.9: Picture of Perkin-Elmer Spectrum 2 fitted with ATR top-plate accessory module*

2.2.5.2 Infrared Sources

The Perkin-Elmer Spectrum 2 FTIR spectrometer features a silicon carbide rod that emits black body radiation when heated by an electric current source. The silicon carbide rod behaves as a black body source where radiance is dependent on temperature (Griffiths et al, 2007). The silicon carbide rod, referred to as a Globar source, is commonly heated to ~1500°C for mid-infrared spectroscopy to produce electromagnetic waves with peak energy density in the mid-infrared region (Griffiths et al, 2007). The specified temperature also ensures that the infrared source is stable throughout operation and produces high signal to noise ratios for analysis while preventing signal saturation at the detector (Griffiths et al, 2007).

Quantum cascade lasers have recently demonstrated considerable promise as an alternative infrared source for mid-infrared spectroscopy. Quantum cascade lasers operate on the principle of inter-sub-band transitions and produces coherent light sources that emit photons of narrow line widths with increased power densities compared to Globar's (Schwaighofer et al, 2017). Quantum cascade lasers have demonstrated significant potential for FTIR-microscopy with reduced sampling time and the ability to produce discrete frequencies of mid-infrared light that can be engineered to correspond to pertinent diagnostic frequencies of particular samples (Kole et al, 2012). The discrete frequency approach would also circumvent the need for a Michelson interferometer in future spectrometers, meaning low cost, compact instruments. However, quantum cascade lasers are a relatively new technology in the field and the device was not available for use in the current project.

2.2.5.3 Michelson Interferometer

The Michelson interferometer is the primary component of FTIR spectrometers and its purpose is to create an interference pattern of a spectrum of infrared light to enable a mathematical operation, the Fourier-transform, to be applied to the resultant signal. Polychromatic light is collimated on to a beam splitter where, theoretically, incident light is divided in to two beams of equal intensity, with half reflected to a stationary mirror and half transmitted to a translatable mirror, depicted in Figure 2.10.

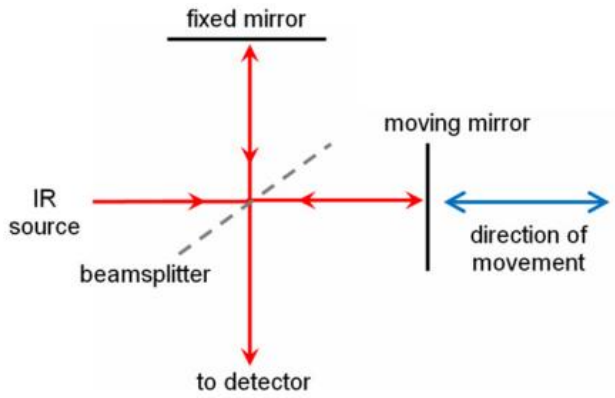


*Figure 2.10: A schematic of components of a Michelson Interferometer. Adapted. (Baker et al, 2016).*

The two light beams subsequently reflect off their respective mirrors and interact at the beam splitter creating an interference pattern dependent on the optical path difference of the two beams, which is determined by displacement of the translatable mirror. The optical path difference is defined as zero, referred to as zero path difference, when the translatable mirror is stationary. The energy intensity is at a maximum at the position of zero path difference, also referred to as the centre burst, due to constructive interference of the electromagnetic waves that have no phase difference and identical frequencies. Similarly, constructive interference is observed upon displacement of the translatable mirror provided the electromagnetic waves of

the two beams are in-phase and thus have a phase difference equivalent to 0, $2\pi$, $4\pi$… radians. Conversely, destructive interference is observed upon displacement of the translatable mirror provided the electromagnetic waves of the two beams are out of phase with a phase difference equivalent to $\pi$, $3\pi$, $5\pi$… radians.

Superposition of the two beams over the mid-infrared frequency range may be observed on an interferogram that plots amplitude of energy intensity with respect to displacement of the translatable mirror. The interference pattern recorded at the detector can then be transformed from the time to frequency domain to obtain an infrared spectrum through application of the Fourier-transform operation.

#### 2.2.5.4 Fourier Transform Approach to Infrared Spectroscopy

The Fourier-transform is a mathematical operation that enables a waveform represented in the time domain to be separated in to discrete sinusoidal waves of frequencies characteristic of the original signal in the frequency domain. In infrared spectroscopy, this technique is applied to interferogram signals which represent the intensity of superimposed electromagnetic waves in the time domain. The Fourier-transform is pertinent to infrared spectroscopy as it allows observation of multiple frequencies of infrared light absorbed by different sample constituents. The Fourier-transform approach is significantly faster than previous dispersive spectrometers and reduction in acquisition time enables measurements to be multiplexed, resulting in an improved signal to noise ratio on spectra, know as Fellgett's advantage (Griffiths et al, 2007). The Fourier-transform approach also enables increased quantities of infrared

light to reach the detector, with an improved signal to noise ratio, which in turn improves the analytical sensitivity of the technique, known as Jacquinot's advantage (Griffiths et al, 2007). Lastly, the Fourier-transform approach implements an internal calibration method, resulting in increased accuracy over previous dispersive systems, and is known as Connes advantage (Griffiths et al, 2007).

#### 2.2.5.5 Infrared Detectors

The Perkin-Elmer Spectrum 2 FTIR spectrometer features a lithium tantalate pyroelectric bolometer that responds to changes in temperature when infrared light is absorbed by sample constituents. The lithium tantalite detector offers a significant reduction in material cost and practicality when compared to the most widely employed mid-infrared detectors, deuterated triglycine sulfate (DTGS) (Bakeev, 2010). However, DTGS detectors have two to three times the sensitivity of lithium tantalate detectors (Bakeev, 2010). Photonic detectors are also widely used in infrared spectroscopy, commonly mercury cadmium telluride (MCT) detectors, which offer significant increases in sensitivity compared to DGTS detectors (Bakeev, 2010). However, MCT detectors are significantly more expensive and often cooled with liquid nitrogen (Bakeev, 2010), and, therefore, have not been chosen for the spectrometer in the project.

### 2.2.6 Sample Spectrum

Spectral quality is often characterised by the signal to noise ratio of infrared spectra, which is dependent on the analytical time and scan resolution, as summarised by the

FTIR trading rules. The first rule states that spectral quality increases at the expense of analytical time, where the resultant signal to noise ratio, SNR, is proportional to the square root of accumulated scans, N (Griffiths et al, 2007).

$$SNR \propto \sqrt{N} \qquad \text{(eq 2.16)}$$

The second rule states that spectral quality decreases as the scan resolution increases, attributed to the increase in spectral noise with the acquisition of additional information, where the signal to noise ratio, SNR, is proportional to scan resolution, RES (Griffith et al, 2007).

$$SNR \propto RES \qquad \text{(eq 2.17)}$$

### 2.2.7 Pre-Processing Methods

Pre-processing methods are routinely employed in FTIR spectroscopy prior to interpretation of sample data sets to compensate for spectral artefacts that do not represent the biochemical information of sample constituents. Baseline correction is extensively utilised in infrared spectroscopy to account for baseline drift, often attributed to scattering or reflection of infrared light upon interaction with sample components (Baker et al, 2014). Rubber-band baseline correction has been employed throughout the project and describes a baseline correction technique where a polynomial curve is fitted to a reference baseline and subtracted from the baseline of

the original spectrum to create a baseline corrected spectrum. Extended multiplicative scattering correction (EMSC) has also been employed throughout the project to account for the increased scattering of infrared light with silicon IRE's. Normalisation techniques further allow for removal of spectral artefacts that may arise from deviations in sample thickness and include vector normalisation, min-max normalisation and amideI/II pre-processing methods (Baker et al, 2014). Both vector normalisation and min-max normalisation have been used extensively throughout the project as a means for ensuring absolute absorption values are normalised prior to spectral analysis. Sample binning is another common pre-processing technique employed in infrared spectroscopy and averages the absorption of neighbouring wavenumbers with the number of wavenumbers averaged dependent on the selected binning parameter (Butler et al, 2018). Sample binning has been used in Chapters 4 and 5 in the current project with a binning parameter of 8 as a means to increase the signal to noise ratio of biological spectra at the expense of overall spectral resolution.

### 2.2.8 Derivative Spectra

First and second-order derivatives may also be employed on spectral data to remove contributions of baseline drift effects whilst accentuating differences in absorption peaks characteristic of sample constituents. The first-order derivative represents the rate of change of absorption of zero-order bands with respect to the change in frequency of infrared light. The first-order derivative operation resolves spectral features according to the full-width, half-height of absorption peaks on infrared spectra. The first-order derivative of an absorption peak may be observed on an

infrared spectrum as two bands of positive and negative amplitude positioned at frequencies that correspond to the inflection point of the zero-order band. Similarly, second order derivatives resolve spectral features according to the full-width, half-height of zero-order bands. The second derivative may be observed on an infrared spectrum as two positive and one negative peaks respectively, where the frequency of the negative band corresponds to the frequency of the zero-order absorption maxima, as depicted in Figure 2.11. Therefore, second-order derivatives are routinely used to resolve overlapping spectral features at the expense of increased noise on absorption infrared spectra and have been used throughout Chapter 5 for such purposes.

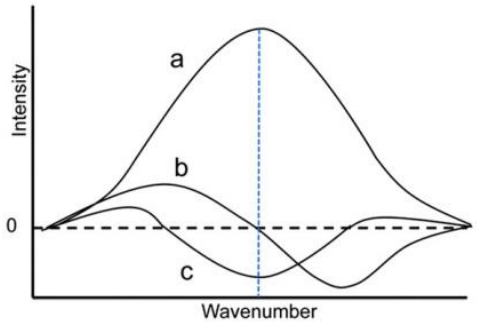


*Figure 2.11: Representation of (a) zero-order absorption band, (b) first-order derivative and (c) second-order derivative band.*

The one distinct disadvantage of employing derivatives to spectral data is the significant increase in high frequency noise observed on spectra with an increase in the order of the derivative, which consequently decreases the signal to noise ratio of derivative spectra (Baker et al, 2016). Therefore, second-order derivatives are often employed concurrently with a Savitzky-Golay low-pass filter to smooth high frequency noise and increase the signal to noise ratio on derivative spectra (Baker et al, 2016).

### 2.2.9 Multivariate Analysis

Principal component analysis is a multi-variate statistical technique fundamental to FTIR spectroscopy that reduces the dimensionality of data sets to allow easier interpretation of existing relationships in spectra. Briefly, principal component analysis subjects a pre-processed data matrix to an orthogonal linear transformation that ultimately transforms the matrix to a new space of reduced dimensions to establish covariance between spectral variables. The resultant covariance matrix is then decomposed in to a score matrix of eigenvalues and loading matrix of eigenvectors to allow covariance to be represented as principal components. The first principal component corresponds to the first eigenvector with a line of best fit in the direction that represents the greatest covariance in the data set, as depicted in Figure 2.12a, and therefore relates to the first eigenvalue with maximum covariance. The second principal component corresponds to the second eigenvector with a line of best fit in the orthogonal direction to the first eigenvector, as depicted in Figure 2.12b, and therefore relates to the eigenvalue that describes the second greatest covariance in the data set. The remaining principal components, which correspond to the number of dimensions in the transformed space, have eigenvectors that always points in an orthogonal direction to the preceding eigenvector. Consequently, successive principal components have an eigenvalue that represents decreasing covariance in the data. Generally, spectroscopist's are typically concerned with the primary principle components which describe the vast majority of covariance in the data set, and may be often visualised with PCA scores plots describing the first three principal components. PCA loading plots subsequently identify the wavenumber regions that describes most variance between classes by plotting the eigenvalues that correspond to the

eigenvectors of PCA scores plots. Overall, PCA has been employed extensively throughout the project as an exploratory method to determine the variance between spectral classes.

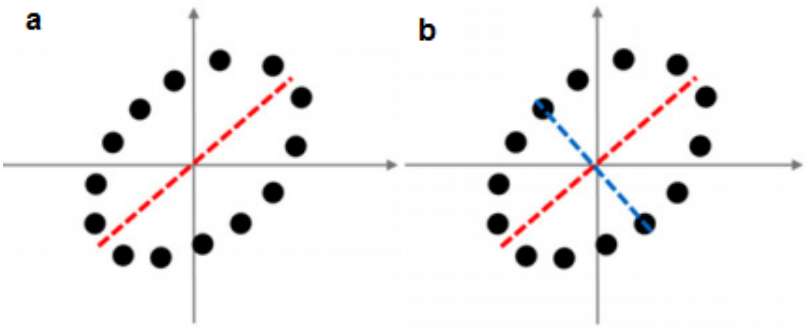


*Figure 2.12: Representation of (a) principal component 1 and (b) principal component 2 on an orthogonally transformed data set using PCA analysis. Reproduced. (Baker et al, 2016)*

## 2.3 Electrochemistry

### 2.3.1 Overview

The study of electron transfer events at the electrode electrolyte interface upon the application of electrical potentials is fundamental to the discipline of electrochemistry and permits qualitative and quantitative detection of electro-active species. The transfer of electrons between the target molecule and charged surface is termed a faradaic reaction where the resultant current is proportional to the applied potential (Hamann et al, 2007). The faradaic reaction proceeds with mass transport of the target molecule to the vicinity of the electrode surface where the population of chemical reactants overcome the electrical double layer to participate in electron transfer through quantum mechanical tunnelling (Hamann et al, 2007). The probability of electron transfer at the electrode electrolyte interface is dependent on the thermodynamics and kinetics of the faradaic reaction and is partly determined by the

relative energy levels of the electrode and target molecule (Sato, 1998). Accordingly, application of sufficient energy in the form of an anodic or cathodic potential may convert the chemical reactant to an oxidised or reduced species that represents the molecules loss of electrons during faradaic reactions (Hamann et al, 2007). Hence, the chemical reactant may transform between oxidised and reduced states during the faradaic reaction, in a process formally described by redox half reactions (Zoski, 2007).

$$O + e^- \rightarrow R \qquad \text{(eq 2.18)}$$

$$R \rightarrow O + e^- \qquad \text{(eq 2.19)}$$

2.3.2 Energy Levels

The energy levels of electro-active molecules and electrodes qualitatively predict the thermodynamic probability of electron transfer at the electrode electrolyte interface upon application of electrical potentials. The energy levels of electro-active molecules, characterised by molecular orbitals, describe the probability of valence electrons orbiting a particular region of space with quantised energy around the nuclei of the molecule (Atkins et al, 2010). The molecular orbital of highest energy occupied by valence electrons is called the highest occupied molecular orbit (HOMO), whilst the unoccupied anti-bonding orbital of lowest energy is referred to as the lowest unoccupied molecular orbit (LUMO) (Atkins et al, 2010). The HOMO and LUMO of the molecule, relative to the Fermi level of the solid electrode, is fundamental to the thermodynamic probability of electron transfer at the electrode electrolyte interface. Solids feature two distinct, continuous energy bands commonly referred to as the valence and conduction band that overlap for conducting solids and allow valence

electrons to freely move to the conduction band on application of electrical potentials (Girault, 2004). The Fermi level of solids represents the molecular orbital of highest energy occupied by valence electrons, analogous to the HOMO level of molecules, and consequently shifts on application of electrical potentials (Sato, 1998).

The application of an appropriately positive potential to the electrode reduces the intrinsic Fermi level of the solid to lower energy with respect to the HOMO of the electro-active molecule, such that it becomes thermodynamically conducive for electrons to participate in oxidation events. Oxidation reactions involve the transfer of valence electrons from the HOMO of the molecule to the electrode surface. Conversely, the application of sufficiently negative potentials to the electrode increases the intrinsic Fermi level of the solid to a greater energy relative to the LUMO of the electro-active species, such that it becomes thermodynamically conducive for electrons to participate in reduction reactions. Reduction reactions involve the transfer of valence electrons from the electrode surface to the LUMO of the electro-active molecule. Together, the application of sufficiently positive and negative potentials to the electrode surface enables oxidation and reduction reactions indicative of electro-active redox molecules, as depicted in Figure 2.13.

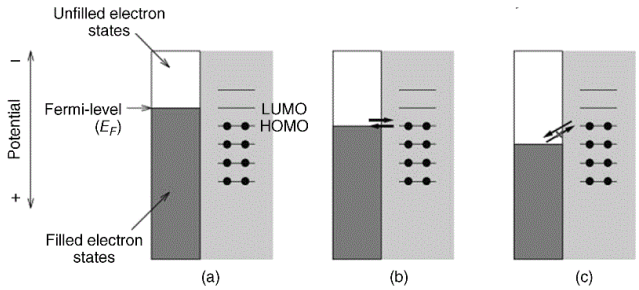


*Figure 2.13: The relationship of the Fermi level of the electrode with respect to the LUMO / HOMO of the molecule to induce electron transfer events.*

2.3.3 Kinetics of Electron Transfer

The number of electrons transferred during redox events and the resultant current flow measured at the electrode surface is governed by kinetics of electron transfer and mass transport to the electrode (Hamann et al, 2007). The kinetics of electron transfer describes the rate of current observed at the electrode upon application of anodic, $I_a$, and cathodic, $I_c$, potentials and is determined by the electrode area, $A$, the rate of electron transfer for the oxidation, $k_{ox}$, and reduction reaction, $k_{red}$, Faraday's constant, $F$, and the concentration of oxidised, $O$, and reduced, $R$, species present at the vicinity of the electrode surface (Hamann et al, 2007).

$$I_a = FAk_{ox}[R] \quad \text{(eq 2.20)}$$

$$I_c = -FAk_{red}[O] \quad \text{(eq 2.21)}$$

The kinetics of electron transfer is also dependent on the potential applied to the electrode and may be understood with consideration of the electron transfer rate constants and activation energy barrier. The electron transfer rate constant for the oxidised and reduced reaction may be qualitatively described with respect to the activation energy barrier, the universal Gas constant and temperature in Kelvin (Hamann et al, 2007).

$$k = k_o exp\left(\frac{-E_A}{RT}\right) \quad \text{(eq 2.22)}$$

The activation energy barrier describes the minimum energy required to convert chemical reactants to chemical products during redox events and is observed to

decrease with an increase in the applied potential, as depicted in Figure 2.14. The reduction in energy of the activation barrier may be attributed to the formation of the electrical double layer upon application of electrical potentials (Plieth, 2008; Vetter, 2013). Hence, the electron transfer rate constants for oxidation and reduction processes must be revised to account for observed changes in the energy of the activation barrier, in accordance with Butler-Volmer theory (Eliaz et al, 2019; Hamann et al, 2007).

$$k_a = k\ exp\left(\frac{(1-\beta)FV}{RT}\right) \quad \text{(eq 2.23)}$$

$$k_c = k\ exp\left(\frac{-\beta FV}{RT}\right) \quad \text{(eq 2.24)}$$

Thus, it can be observed that applied potential has a major influence on the rate of electron transfer that directly impacts the current measured at the electrode surface. However, the current response is not solely determined by the applied potential and, additionally, is dependent on the rate of mass transport to the electrode surface (Zoski, 2007).

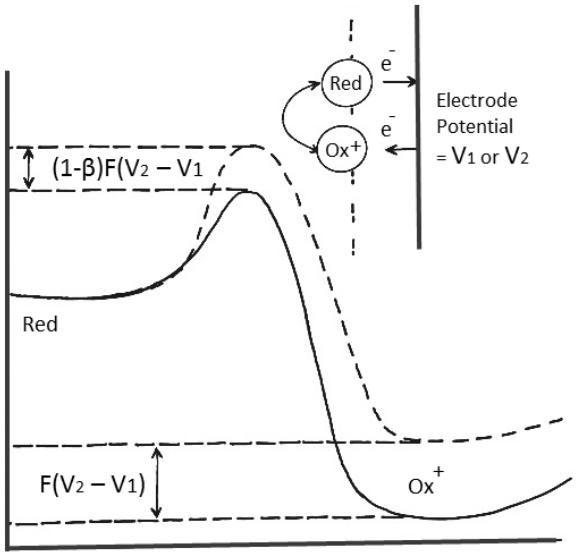


*Figure 2.14: The activation energy barrier of a redox reaction that is observed to vary with applied potential.*

### 2.3.4 Mass Transport

The current response at the electrode upon application of electrical potentials is also dependent on the availability of fresh reactants to participate in redox reactions and is governed by the rate of mass transport to the electrode (Hamann et al, 2007). Mass transport describes the movement of electro-active species from bulk solution to the electrode interface where reactants can either be absorbed or desorbed at the electrode surface to induce electron transfer events, depicted in Figure 2.15. Mass transport primarily occurs through diffusion in electrochemical reactions where molecules of high concentration in bulk solution spontaneously move to the electrode interface that feature the same molecule of low concentration. The electro-active species is present in reduced quantities at the electrode surface because of the conversion of reactants to products that leads to the formation of a concentration gradient in solution (Hamann et al, 2007). Mass transport of electro-active species to the electrode may less commonly occur through either natural of forced convection where molecules travel through the electrolytic solution because of a difference in density between particles or mechanical stirring respectively (Hamann et al, 2007).

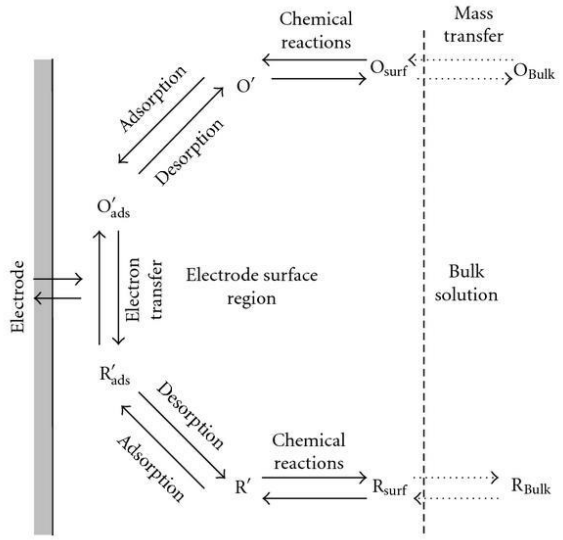


*Figure 2.15: The mass transport of electro-active species from bulk solution to the electrode surface. Reproduced. (Zoski, 2007)*

### 2.3.5 Electrical Double Layer

Appreciation of the electrical double layer is fundamental to the understanding of the interactions of molecules with the electrode surface and their influence on the current observed at the electrode. The electrical double layer arises due to the neutrally charged interface where the charged electrode surface is balanced by the accumulation of oppositely charged molecules in the electrolytic solution (Zoski, 2007). Consequently, molecules of opposite charge may participate in specific adsorption to the electrode surface, forming a compact layer confined to the electrode surface, commonly referred to as the inner Helmholtz layer (Zoski, 2007). Accordingly, molecules of opposite charge may subsequently experience electrostatic attraction to the compact layer, producing a second layer of charged particles adjacent to the inner Helmholtz layer, commonly referred to as the outer Helmholtz layer (Zoski, 2007). Together, the inner and outer Helmholtz plane constitute the Stern layer of ~1nm

thickness where the potential is observed to decrease linearly with distance from the electrode surface (Butt et al, 2013). The diffuse layer, adjacent to the Stern layer, represents the region where charged molecules experience electrostatic attraction to the outer Helmholtz layer, in conjunction with thermal motion away from the electrode surface. Consequently, the influence of the electrical potential decreases exponentially with distance from the electrode in the diffuse region, tending to zero in bulk solution, where it has no influence on the molecules of the electrolytic solution (Butt et al, 2013), as illustrated in Fig. 2.16.

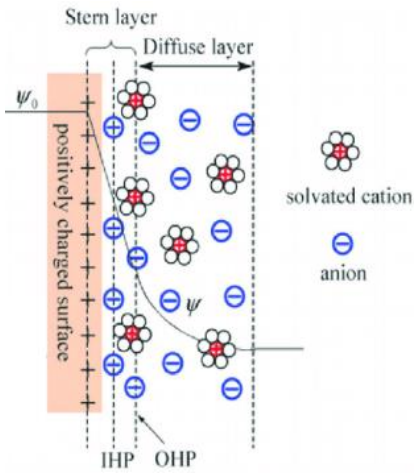


*Figure 2.16: Electrochemical behaviour at the electrical double layer interface. Reproduced. (Raza et al, 2018).*

### 2.3.6 Cyclic Voltammetry

Cyclic voltammetry is an electrochemical technique characterised by a triangular waveform where the potential is ramped linearly with time at the working electrode to allow the observation of redox reactions indicative of reversible electro-active species. Cyclic voltammetry measures current responses at the working electrode as a function of applied potential where the resultant voltammogram profile is governed by the rate

of mass transport and the rate of electron transfer kinetics associated with the electron-mediated chemical reaction (Elgrishi et al, 2017).

Initially, the working electrode measures a non-faradaic current response at the working electrode that describes the formation of the electrical double layer, as the initial applied cathodic potential is insufficient to promote reduction of target electro-active species. The cathodic potential increases linearly with time from an initial potential, E1, to a specified potential, E2, deemed sufficient to promote reduction of electro-active species, at a rate determined by the sweep rate, illustrated in Figure 2.17. The measured cathodic current increases sharply when the applied potential corresponds with the reduction potential of the target electro-active species, depicted in Figure 2.17. Thereafter, the cathodic current peaks representative of the transfer of one or more electrons to reactants present at the immediate electrode surface. The kinetics of electron transfer is strongly influenced by potential and further subsequent increases in the applied cathodic potential increases the rate of electron transfer during the electrochemical reaction. However, the conversion of reactants to products at the working electrode creates a concentration gradient where the concentration of fresh reactant is significantly higher in bulk solution relative to the electrode surface. The concentration gradient promotes diffusion controlled mass transport of fresh reactants from bulk solution to the working electrode surface where the rate of mass transport occurs on comparatively slow time scales relative to electron transfer kinetics. Consequently, the rate of mass transport decreases as the electrochemical reaction proceeds since additional conversion of reactants to products increases the diffusion layer and fresh reactants must travel greater distances from bulk solution to the

electrode surface over time. Therefore, mass transport is said to be the rate-limiting step in unstirred electrochemical reactions and results in a subsequent decrease in measured cathodic current upon application of higher cathodic potentials over time (Elgrishi et al, 2017).

In the corresponding oxidation reaction, the applied potential is reversed at the working electrode such that the potential is decreased linearly with time from the switching potential, E2, to the initial potential, E1, at a rate determined by the sweep rate, as depicted in Figure 2.17. Consequently, the reduced electro-active species previously present at the electrode surface are oxidised, with one or more electrons transferred from the analyte to the electrode surface. Accordingly, the current measured at the working electrode becomes increasingly anodic and reaches a peak anodic current upon oxidation of all electro-active species present at the electrode surface, as depicted in Figure 2.17. The conversion of reactants to products similarly results in the formation of a diffusion layer at the electrode surface that grows over time and decreases the rate of mass transport of fresh reactants to the working electrode over time. Therefore, anodic currents measured at the working electrode decrease over time upon application of increasingly anodic potentials, and subsequently returns to equilibrium at the initial potential, E1 (Elgrishi et al, 2017). Ultimately, the interplay between the rate of mass transport and the rate of electron transfer kinetics throughout the electrochemical reaction determines the resultant profile of the cyclic voltammogram.

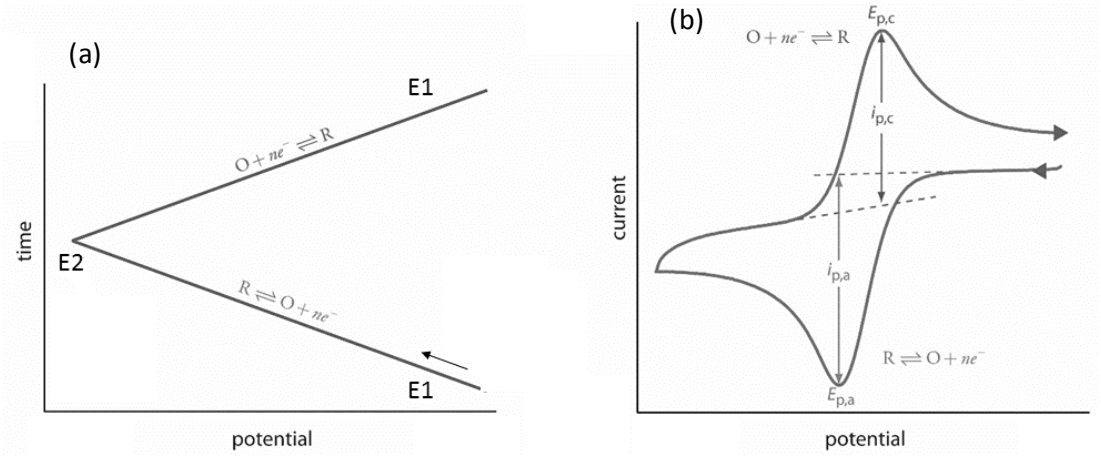


*Figure 2.17: (a) Applied Potential with respect to time and (b) resultant cyclic voltammogram.*

The characteristic shape of the oxidation and reduction peak on a CV is representative of the electro-active species participation in physical and electrochemical processes throughout the trace, as governed by Fick's first law of diffusion and the Nernst equation (Elgrishi et al, 2017; Hamann et al, 2007). Consideration of a one electron-transfer redox reaction may be employed to understand whether the chemical and electrochemical reaction is deemed reversible or irreversible, and to establish the associated rate of electron transfer kinetics. The faradaic reaction is considered electrochemically reversible, and exhibits fast electron transfer kinetics, when peak-to-peak separation, $\Delta E_p$, between the anodic, $E_{pa}$, and cathodic, $E_{pc}$, potential is appropriately small for an $n$ electron transfer reaction (Hamann et al, 2007).

$$\Delta E_p = E_{pa} - E_{pc} = \frac{59.2mV}{n} \qquad \text{(eq 2.25)}$$

The faradaic reaction may also be deemed electrochemically reversible when the difference between the peak potential, $E_p$, and potential at half of the maximum current, $E_{p/2}$, corresponds to the predicted value for an $n$ electron transfer reaction given the gas constant, $R$, temperature, $T$, and Faraday constant, $F$ (Hamann et al, 2007).

$$E_p - E_{p/2} = 2.218 \frac{RT}{nF} \quad \text{(eq 2.26)}$$

Additionally, the potential at half the maximum current, $E_{p/2}$, should correlate with the potential estimated midway between the anodic and cathodic potential, $E_{1/2}$, commonly referred to as the half-wave potential (Hamann et al, 2007).

$$E_{p/2} = E_{1/2} \pm 28.5mV \quad \text{(eq 2.27)}$$

The faradaic reaction may also be considered electrochemically reversible with fast electron transfer kinetics when the ratio of the peak anodic and cathodic current is equal to one (Hamann et al, 2007). This indicates that the electron transfer rate constant is greater than the rate of mass transport enabling equilibrium concentrations of redox species to be established at the vicinity of the working electrode, as predicted by the Nernst equation (Hamann et al, 2007). Accordingly, peak anodic and cathodic currents occur at potentials independent of the potential sweep scan rate, with a linear relationship between peak current and the square root of scan rate, as governed by the Randles-Sevcik equation (Hamann et al, 2007; Zoski, 2007).

$$i_p = 0.4463\ nFAC\left(\frac{nFvD}{RT}\right)^{1/2} \quad \text{(eq 2.28)}$$

Where $i_p$ corresponds to the peak current, $n$ is the number of electrons associated with the redox reaction, $F$ is the Faraday constant, $A$ is the electrode area, C is the concentration of electro-active species, $v$ is the scan rate, $D$ is the diffusion co-efficient, $R$ is the gas constant and $T$ is the temperature of the reaction.

It may further be observed from the Randles-Sevcik equation that peak currents for electrochemically reversible reactions have a proportional increase to the potential sweep scan rate, and may be attributed to the reduced diffuse layer at the electrode surface as a consequence of decreased scan times. In situations where the peak currents exhibit disproportionate responses to the potential sweep scan rate it indicates that the electrochemical reaction may be quasi-reversible.

### 2.3.7 Electrochemical Impedance Spectroscopy

#### 2.3.7.1 Overview

Electrochemical impedance spectroscopy is an electrochemical technique characterised by the application of small sinusoidal perturbations of constant amplitude and variable frequencies to an electrochemical system assumed linear and in an equilibrium state. Electrochemical impedance spectroscopy measures the current

response at the working electrode as a function of sinusoidal potential excitations to determine impedance measurements at frequencies representative of physical and electrochemical processes at the electrode/electrolyte interface (Randviir et al, 2013; Lasia, 2014). Consequently, electrochemical impedance spectroscopy may be employed to determine specific electrochemical parameters at time scales unattainable through conventional direct current techniques, namely solution resistance, charge transfer resistance, double layer capacitance and Warburg resistance. Additionally, electrochemical impedance spectroscopy may be employed to identify the binding of target molecules to functionalised electrode surfaces through monitoring of changes in the charge transfer resistance at the electrode interface, permitting label free, non-destructive quantitative detection of biomarkers in biological samples (Randviir et al, 2013).

The working electrode is subjected to an AC potential of constant amplitude, which is superimposed on to a specified DC bias potential, allowing the study of an electrochemical system in a chosen state of interest. The small AC perturbations are solely responsible for the current response obtained at the working electrode throughout the experiment, enabling the impedance of an electrochemical experiment in an equilibrium state to be determined over a specified frequency range.

Impedance, with reference to electrochemical impedance spectroscopy, describes the measure of physical or electrochemical phenomena ability to oppose the flow of current through an electrochemical circuit with respect to rate of change of applied

potential. Hence, for a linear electrochemical system, the impedance of a certain physical or electrochemical phenomenon may be determined by measuring the current response to an input potential at a characteristic frequency.

The applied potential, $V$, expressed as a sinusoid function, may be calculated at a given time point, $t$, with respect to the initial amplitude of the signal, $V_0$, and the angular frequency, $\omega$.

$$V(\omega,t) = V_0 \sin(\omega t) \qquad \text{(eq 2.29)}$$

The angular frequency, $\omega$, may be calculated from the temporal frequency, $f$, which is inversely related to the period of oscillation, $T$.

$$\omega = 2\pi f = \frac{2\pi}{T} \qquad \text{(eq 2.30)}$$

The measured current, $I$, expressed as a sinusoid function, exhibits an equivalent angular frequency, $\omega$, with a different phase, $\emptyset$, and magnitude, $I_0$, to the applied potential at a corresponding time point, $t$.

$$I(\omega,t) = I_0 \sin(\omega t - \emptyset) \qquad \text{(eq 2.31)}$$

Therefore, impedance, $Z$, may be calculated for a particular frequency, $\omega$, given the voltage, $V$, and current, $I$, at the corresponding time point, $t$, through the extension of Ohm's law.

$$Z\ (\omega, t) = \frac{V\ (\omega,t)}{I\ (\omega,t)} \qquad \text{(eq 2.32)}$$

2.3.7.2 Electrical Elements

The impedance of different physicochemical and electrochemical processes that occur throughout an electrochemical experiment may be represented by common circuit components, namely resistor, conductor and inductor elements, allowing prospective EIS measurements to be fitted to an equivalent electrical circuit. The resistor element solely comprises a real impedance component and therefore may be employed to describe impidimetric events where no phase shift occurs between the current response and the applied potential (Lasia, 2014). The impedance of a resistor element, $Z_R$, may be calculated given the potential, $V$, and current, $I$, and is equivalent to resistance, $R$.

$$Z_R = \frac{V}{I} = R \qquad \text{(eq 2.33)}$$

The capacitor element solely comprises an imaginary electrical component where the impedance is inversely proportional to the frequency of the applied potential. Consequently, the capacitor element may be employed to describe impidimetric processes that induce +90 degree phase shifts between the current response and the

applied potential (Lasia, 2014). The impedance of a capacitor element, $Z_C$, may be calculated with respect to the current, $I$, given the potential, $V$, of a particular frequency, $\omega$, and the capacitance, $C$.

$$Z_C(\omega, t) = \frac{V(\omega,t)}{I(\omega,t)} = \frac{1}{j\omega C} \quad \text{(eq 2.34)}$$

The inductor element solely comprises an imaginary impedance component, with a value proportional to the frequency of the applied potential. Hence, inductor elements may be implemented to represent impedimetric events resulting in -90 degree phase shifts between the current response and the applied potential (Lasia, 2014). The impedance of an inductor element, $Z_L$, may be calculated with respect to the current, $I$, given the potential, $V$, of a particular frequency, $\omega$, and the inductance, $L$.

$$Z_L(\omega, t) = \frac{V(\omega,t)}{I(\omega,t)} = j\omega L \quad \text{(eq 2.35)}$$

2.3.7.3 Electrical Circuits

The common circuit components employed to resemble individual physicochemical and electrochemical processes may be combined to form an equivalent electrical circuit representative of a simplified electrochemical experiment. Circuit elements may either be combined in a series or parallel configuration, with each having a profoundly different influence on the overall impedance of the circuit. Series circuits

describe two or more electrical elements connected such that the total current is equivalent at each component and the total voltage is the summation of the individual voltages of each component. Therefore, the total impedance of a series circuit, $R_{total}$, is equivalent to the summation of the impedance of each circuit element, $R_n$.

$$R_{total} = R_1 + R_2 + \cdots + R_n \qquad \text{(eq 2.36)}$$

Parallel circuits describe two or more circuit elements configured such that the total current is the summation of the individual currents observed at each component, and the total voltage is equivalent to the voltage observed at respective circuit elements. Hence, the total impedance of a parallel circuit, $R_{total}$, may be calculated by finding the reciprocal of the summation of the individual reciprocals of impedance associated with respective circuit elements, $R_n$.

$$\frac{1}{R_{total}} = \frac{1}{R_1} + \frac{1}{R_2} + \cdots + \frac{1}{R_n} \qquad \text{(eq 2.37)}$$

Therefore, it may be observed that circuit elements combined in parallel have reduced total impedance compared to identical circuit elements combined in a series configuration.

The Randles circuit, illustrated in Figure 2.18, consists of a resistor in series with a parallel RC circuit, and is the most routinely employed equivalent model to describe simplified electrochemical experiments where circuit elements represent the rate of the faradaic reaction at the electrode surface controlled by kinetic and mass transport processes (Randviir et al, 2013). The resistor element, $R_s$, represents the electrolytic solution resistance which is dependent on solution conductivity, temperature, electrode distance and cross-sectional sample area. The capacitor element, $C_{dl}$, represents charging of the electrical double layer which is dependent on the electrode area and electron transfer process during the faradaic reaction. Hence, the electrical double layer capacitance is modelled in parallel with the charge transfer resistance, $R_{ct}$, which describes the ability of electrons to be transferred from the electrolytic solution to the electrode surface during faradaic reactions. Together, the capacitor and resistor circuit elements describe the faradaic reaction as controlled by kinetic processes. Additionally, the charge transfer resistance is modelled in series with the resistor element, $R_W$, called the Warburg resistance which represents the rate of the faradaic reaction limited by mass transport processes, specifically diffusion of the electroactive species to the electrode surface.

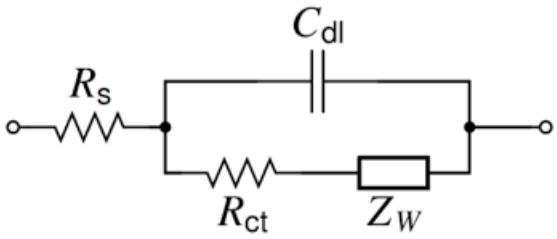


*Figure 2.18: Randles equivalent circuit*

Overall impedance of the faradaic reaction, as modelled by the Randles circuit, is dependent on the frequency of applied perturbations and is characterised by the behaviour of the individual circuit components. Firstly, solution resistance is independent of frequency, and as the frequency of the applied potential tends to high frequencies of the kinetically controlled faradaic reaction, the capacitance of the electrical double layer tends to zero. Hence, impedance at such frequencies may be described by the real impedance component, and corresponds to the solution resistance. Secondly, when the frequency of the applied potential tends to the low frequency limit of the kinetically controlled faradaic reaction, the capacitance tends to a maximum value, such that impedance may be described by the real impedance component and is equivalent to the summation of solution resistance and charge transfer resistance. Thirdly, the time constant of the parallel RC circuit is equivalent to the product of the electrical double layer capacitance and charge transfer resistance when the complex component of impedance is at maximum impedance. Additionally, when the frequency of the applied potential decreases beyond the low frequency limit of the kinetically controlled faradaic reaction, total impedance corresponds solely to the impedance of mass transport processes, and is equivalent to the Warburg resistance.

#### 2.3.7.4 Nyquist Plot

Impedance measurements calculated for different frequencies may be presented graphically as a Nyquist plot. Nyquist plots present the real component, Z', of impedance on the x-axis against the imaginary component, Z'', of impedance on the y-axis where each data point represents the impedance at a particular frequency, illustrated in Figure 2.19. Nyquist plots depict the magnitude of the impedance in an

electrochemical experiment and, hence, it is possible to deduce the different physical and electrochemical processes that occur over a range of frequencies. Nyquist plots, equivalent to the Randles circuit, constitute a semi-circle at high frequencies concerning kinetically controlled faradaic reactions and a straight line at low frequencies representative of diffusion controlled faradaic reactions (Randviir et al, 2013). Specifically, the diameter of the semi-circle curve and the gradient of the straight line determine the impedance of the charge transfer resistance and diffusion co-efficient values respectively (Randviir et al, 2013). Additionally, it is possible to determine the solution resistance by inspecting where the semi-circle curve intercepts the real axis, Z', with the impedance value on the real axis, Z', indicative of the solution resistance. Furthermore, it is possible to determine the capacitance of the electrical double layer by selecting a complex impedance, $Z''$, on the semi-circle of the Nyquist plot at a particular frequency, $f$, and solving for capacitance, $C_{dl}$.

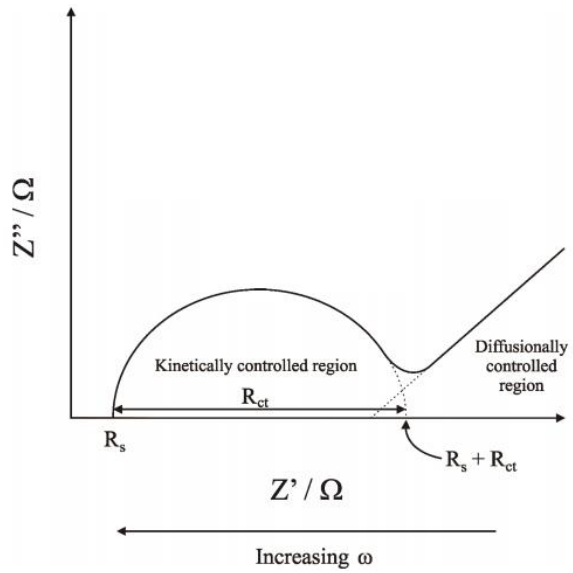


*Figure 2.19: Nyquist plot characteristic of Randles equivalent circuit. Reproduced. (Randviir et al, 2013)*

# 2 References


Anker, P., Mulcahy, H., Qi Chen, X. et al. (1999) Detection of Circulating Tumour DNA in the Blood (Plasma/Serum) of Cancer Patients. Cancer Metastasis Rev. 18: 65. doi: 10.1023/A:1006260319913

Atkins, P., de Paula, J. (2010) Atkins' Physical Chemistry. OUP Oxford, 2010. ISBN: 0199543372, 9780199543373 p.381-385

Bakeev, K. A. (2010) Process Analytical Technology: Spectroscopic Tools and Implementation Strategies for the Chemical and Pharmaceutical Industries. John Wiley & Sons, 2010. ISBN: 0470689609, 9780470689608 p.173-177

Baker, M. J., Hollywood, K. A., Hughes, C. (2016) Biophotonics: Vibrational Spectroscopic Diagnostics. *Morgan & Claypool Publishers, 2016.* ISBN: 1681741350, 9781681741352

Baker, M. J., Trevisan, J., Bassan, P., Bhargava, R., Butler, H. J., Dorling, K. M., … Martin, F. L. (2014). Using Fourier transform IR spectroscopy to analyze biological materials. *Nature protocols*, *9*(8), 1771–1791. doi:10.1038/nprot.2014.110

Barth, A. (2007). Infrared spectroscopy of proteins. *Biochimica et Biophysica Acta (BBA) - Bioenergetics*, 1767(9), 1073–1101. doi:10.1016/j.bbabio.2007.06.004

Busher, J. T. Walker H. K, Hall, W. D, Hurst, J. W, editors (1990) Clinical Methods: The History, Physical, and Laboratory Examinations. Editor *Annals of Internal Medicine, 113(7), 563*. doi:10.7326/0003-4819-113-7-563_2

Butler, H. J., Smith, B. R., Fritzsch, R., Radhakrishnan, P., Palmer, D., & Baker, M. J. (2018). *Optimised spectral pre-processing for discrimination of biofluids via ATR-FTIR spectroscopy. The Analyst.* doi:10.1039/c8an01384e

Butt, H-J., Graf, K., Kappl, M. (2013) Physics and Chemistry of Interfaces. john Wiley & Sons, 2013 ISBN: 3527412166, 9783527412167

Byrn, S. R., Zografi, G., Chen, X. (2017) Solid-State Properties of Pharmaceutical Materials. *John Wiley & Sons, 2017.* ISBN: 1118145305, 9781118145302.

Dubois, J., & Shaw, R. A. (2004). *Peer Reviewed: IR Spectroscopy in Clinical and Diagnostic Applications. Analytical Chemistry, 76(19), 360 A–367 A.* doi:10.1021/ac041647v

Elgrishi, N., Rountree, K. J., McCarthy, B. D., Rountree, E. S., Eisenhart, T. T., & Dempsey, J. L. (2017). *A Practical Beginner's Guide to Cyclic Voltammetry. Journal of Chemical Education, 95(2), 197–206*. doi:10.1021/acs.jchemed.7b00361

Eliaz, N., Gileadi, E. (2019) Physical Electrochemistry: Fundamentals, Techniques, and Applications. John Wiley & Sons, 2019. ISBN: 3527341390, 9783527341399 p. 254.

Girault, H. H. (2004) Analytical and Physical Electrochemistry. CRC Press, 2004. ISBN: 1439807841, 9781439807842. p.23-26

Grdadolnik, J. (2002) ATR-FTIR spectroscopy: Its advantages and limitations. *Acta Chimica Slovenica*. 49(3):631-642.

Griffiths, P. R., de Haseth, J. A. (2007) Fourier Transform Infrared Spectroscopy. Second Edition. *John Wiley & Sons Inc*, ISBN: 9780471194040

Hamann, C. H., Hamnett, A., Vielstich, W. (2007) Electrochemistry. Wiley, 2007. ISBN: 352731069X, 9783527310692

Hancer, M., Sperline, R. P., & Miller, J. D. (2000). *Anomalous Dispersion Effects in the IR-ATR Spectroscopy of Water. Applied Spectroscopy, 54(1), 138-143. Doi:10.1366/0003702001948222*

Kelter, P. B., Mosher, M. D., Scott, A. (2008) Chemistry: The Practical Science. *Cengage Learning, 2008.* ISBN: 0618000720, 9780618000722. p.320

Kole, M. R., Reddy, R. K., Schulmerich, M. V. K., Bhargava, R. (2012) Discrete Frequency Infrared Microscpectroscopy and Imaging with a Tuneable Quantum Cascade Laser. Analytical Chemistry. 84(23), 10366-10372. Doi:10.1021/ac302513f

Krebs, H. A. (1950). Chemical Composition of Blood Plasma and Serum. *Annual Review of Biochemistry*, 19(1), 409–430. doi:10.1146/annurev.bi.19.070150.002205

Krey, U., Owen, A. (2007) Basic Theoretical Physics: A concise Overview. *Springer Science & Business Media, 2007.* ISBN: 3540368051, 9783540368052

Larkin, P. (2011) Infrared and Raman Spectroscopy: Principles and Spectral Interpretation. *Elsevier, 2011.* ISBN: 0123870186, 9780123870186. p.18-22

Lasia, A. (2014) Electrochemical Impedance Spectroscopy and its Applications. Springer Science + Business Media New York 2014. ISBN: 978-1-4614-8932-0/978-1-4614-8933-7

Liu, K. Z., Shaw, R. A., Man, A., Dembinski, T. C., Mantsch, H. H. (2002) Reagent-free, simultaneous determination of serum cholesterol in HDL and LDL by infrared spectroscopy. *Clin Chem.* 48(3):499-506.

Lusch, D. P. (1999) Introduction to Microwave Remote sensing. Department of Geography. Michigan State University. Accessed September 2019. http://web.pdx.edu/~emch/ip2/RADAR.pdf

Milosevic, M. (2013). *On the Nature of the Evanescent Wave. Applied Spectroscopy, 67(2), 126–131.* doi:10.1366/12-06707

Misner, C. W., Thorne, K. S., Wheeler, J. A. (2017) Gravitation. Chapter 4: Electromagnetism and Differential Forms. p.111. *Princeton University Press, 2017.* ISBN: 0691177791, 9780691177793

Movasaghi, Z., Rehman, S., & ur Rehman, D. I. (2008). *Fourier Transform Infrared (FTIR) Spectroscopy of Biological Tissues. Applied Spectroscopy Reviews, 43(2), 134–179.* doi:10.1080/05704920701829043

Pavia, D. L., Lampma, G. M., Kriz, G. S., Vyvyan, J. A. (2008) Introduction to Spectroscopy. Cengage Learning, 2008. ISBN: 0495114782, 9780495114789. p.16, 17

Plieth, W. (2008) Electrochemistry for Materials Science. Elsevier, 2008. ISBN: 0080556256, 9780080556253 p185-187.

Prasad, P. N. (2004) Introduction to Biophotonics. John Wiley & Sons, 2004. ISBN: 0471465399, 9780471465393 p.125

Randviir, E. P., & Banks, C. E. (2013). *Electrochemical impedance spectroscopy: an overview of bioanalytical applications. Analytical Methods, 5(5), 1098.* doi:10.1039/c3ay26476a

Raza, W., Ali, F., Raza, N., Luo, Y., Kim, K.-H., Yang, J., … Kwon, E. E. (2018). *Recent advancements in supercapacitor technology. Nano Energy, 52, 441–473.* doi:10.1016/j.nanoen.2018.08.013

Sasic, S., Ozaki, Y. (2011) Raman, Infrared, and Near-Infrared Chemical Imaging. *John Wiley & Sons, 2011.* ISBN: 1118058259, 9781118058251

Sathyanarayana, D. N. (2015) Vibrational Spectroscopy: Theory and Applications. *New Age International, 2015.* p.9, 12

Sato, N. (1998) Electrochemistry at Metal and Semiconductor Electrodes. Elsevier, 1998. ISBN: 0080530737, 9780080530734

Schwaighofer, A., Brandstetter, M., & Lendl, B. (2017). *Quantum cascade lasers (QCLs) in biomedical spectroscopy. Chemical Society Reviews, 46(19), 5903–5924.* doi:10.1039/c7cs00403f

Sikaris K. (2009). The correlation of hemoglobin A1c to blood glucose. *Journal of diabetes science and technology*, *3*(3), 429–438. doi:10.1177/193229680900300305

Smith, B. C. (1998) Infrared Spectral Interpretation: A Systematic Approach. *CRC Press, 1998.* ISBN: 0849324637, 9780849324635. p.15, 18

Spalding, K., Bonnier, F., Bruno, C., Blasco, H., Board, R., Benz-de Bretagne, I., … Baker, M. J. (2018). Enabling quantification of protein concentration in human serum biopsies using attenuated total reflectance – Fourier transform infrared (ATR-FTIR) spectroscopy. *Vibrational Spectroscopy*, 99, 50–58. doi:10.1016/j.vibspec.2018.08.019

Stuart, B. (2004) Infrared Spectroscopy: Fundamentals and Applications. John Wiley & Sons. ISBN: 0-470-85427-8; 0-470-85428-6

Vetter, K. J. (2013) Electrochemical Kinetics: Theoretical Aspects. Elsevier, 2013. ISBN: 1483266397, 9781483266398.

Vitha, M. F. (2018) Spectroscopy: Principles and Instrumentation. John Wiley & Sons, 2018. ISBN: 1119436648, 9781119436645. p.43-48

Wiercigroch, E., Szafraniec, E., Czamara, K., Pacia, M. Z., Majzner, K., Kochan, K., … Malek, K. (2017). *Raman and infrared spectroscopy of carbohydrates: A review. Spectrochimica Acta Part A: Molecular and Biomolecular Spectroscopy, 185, 317–335.* doi:10.1016/j.saa.2017.05.045

Williamson, K. L., Masters, K. M. (2012) Techniques Labs for Macroscale and Microscale Organic Experiments. Cengage Learning, 2012. ISBN: 113338725X, 9781133387251. p.220.

Zoski, C. G. (2007) Handbook of Electrochemistry. Elsevier, 2007. ISBN: 0444519580, 9780444519580.

# Chapter 3: Development of Silicon IRE Device for Combined Spectroscopic and Electrochemical Analysis

## 3.1 Overview

This chapter will describe the development of a medical device to evaluate a novel silicon substrate for combined infrared spectroscopic and electrochemical detection of human blood serum and electro-active compounds respectively. Thereafter, the chapter will detail further product design iterations and additional engineering requirements necessary to enhance the novel silicon substrates performance before assessing its diagnostic applicability as an integrated spectroscopic and electrochemical medical device for the clinical setting.

## 3.2 Introduction

Development of an integrated spectroscopic and electrochemical medical device would facilitate molecular and reaction based detection of human serum samples in the point-of-care clinical setting. Infrared spectroscopy permits molecular classification of sample components based on infrared active vibrational modes. Hence, a medical device with an infrared spectroscopic platform would provide the capacity for qualitative detection of all infrared active biochemical constituents of a blood serum sample, such as proteins, carbohydrates, lipids and nucleic acid content (Baker et al, 2014). The ability to provide information rich biochemical fingerprints of blood serum samples would have significant benefits in clinical environments where analysis of single biomarkers is often elusive on further clinical investigation due to the heterogeneous nature of cancerous diseases. However, a recognised current

limitation of infrared spectroscopy is the inability to provide quantitative detection of specific biochemical signals within complex sample mediums at low-level biological concentrations (Bonnier et al, 2016). The addition of an electrochemical technique within the medical device would circumvent such issues and facilitate quantitative detection of specific biomarkers at biologically relevant concentrations (Kaim et al, 2009; O'Reilly et al, 2015). Therefore, an integrated device, that performs both infrared spectroscopic and electrochemical analysis, would provide significantly more diagnostic information with quantitative detection of specific biomarkers and qualitative detection of the global biochemical signatures of patient blood serum samples. Ultimately, a combined spectroscopic and electrochemical approach would facilitate the acquisition of advanced molecular content on biofluid samples inaccessible by either technique alone.

Previous combined infrared spectroscopic and electrochemical approaches predominantly focus on the fabrication of infrared transparent noble metal mini-grid working electrodes immersed in liquid samples housed between calcium fluoride windows (Chen et al, 1999). Proposed flow cells rely on the application of FTIR transmission mode for spectroscopic analysis where large sample path lengths often instigate significant absorption of aqueous media, routinely obscuring pertinent diagnostic bands in the amide I (~1650cm-1) region of infrared spectra (Garidel et al, 2006; Best et al, 2008). Additionally, the high cost of calcium fluoride substrates and the difficulty in obtaining ~1um sample thicknesses with appropriate spacers to negate signal saturation effects further compromises the accuracy, reproducibility and cost-effectiveness of the technique (Grdadolnik, 2002). Other well-reported integrated

infrared spectroscopic and electrochemical strategies employ indium tin oxide (ITO) electrodes that exhibit the desired optical transparency and electrical conductivity for combined analysis (Lopez-Naranjo et al, 2016). However, indium shortages have dramatically elevated raw material costs, in addition to high costs of technically challenging fabrication processes, which ultimately prevents translation to single-use, disposable components for point-of-care testing (Kulkarni et al, 2015; Cai et al, 2016; Hecht et al, 2011).

Development of an integrated device that employs ATR-FTIR configuration presents a promising alternative strategy for translation to the point-of-care setting with potential to circumvent aforementioned challenges. ATR-FTIR describes the projection of increasing frequencies of infrared electromagnetic radiation on to the interior surface of an internal reflection element (IRE) where total internal reflection of the incident beam causes attenuation of evanescent waves by chemical bonds present in sample constituents. Generated evanescent waves penetrate sample surfaces to depths of ~1-2µm in the finger print mid-infrared region and decay exponentially with respect to distance (Baker et al, 2014). Hence, adopting ATR-FTIR approaches may permit reduced absorption of infrared light by water molecules and consequently improve analysis of aqueous biological samples in the wet state (Grdadolnik, 2002; Minnes et al, 2017). Furthermore, ATR-FTIR is associated with significantly easier experimental configuration when compared to transmission experiments (Glassford et al, 2013), with minimal preparation required for biofluid samples (Hosafci et al, 2006), and therefore represents an attractive modality for combined spectroscopic and electrochemical diagnostic platforms.

Previous integrated ATR-FTIR and electrochemical approaches have focused on the development of electrically conductive films or doped substrates to improve the electrical conductivity of the IRE pertinent to spectroscopic analysis. Martin employed thin-layers of boron-doped diamond on top of IRE's for detection of electrolytic solutions (Martin et al, 2001); however, the high cost of boron-doped diamond substrates and the challenging chemical vapour deposition fabrication process make it unsuitable for point-of-care devices (Muzyka et al, 2019; Srikanth et al, 2012). Similarly, previous attempts from Kvarnström and Kellenberger to deposit thin conductive films of platinum and gold on top surfaces of germanium and zinc selenide substrates are not economically viable for point-of-care testing due to current costs of both IRE materials (Kvarnström et al, 2000; Kellenberger et al, 2012). Presently, IRE's comprise diamond, germanium, KRS-5 and zinc selenide materials, where the high material cost and insufficient electrical conductivity prevent use as disposable substrates for combined ATR-FTIR and electrochemical analysis. Recently, Schumacher found micro-fabrication of v-shaped grooves on silicon (100) substrates to be an economical alternative as an IRE with spectral acquisition over the entire mid-infrared wavenumber region (4000-450$cm^{-1}$) (Schumacher et al, 2010). Silicon is a low-cost, abundant material that possesses excellent mechanical and chemical properties and is well suited to high-volume manufacturing (Deen et al, 2012; Fatikow et al, 1997), thus presenting an economically viable opportunity to adopt grooved silicon substrates for point-of-care testing. Furthermore, Huang demonstrated that silicon substrates may perform as electrodes with careful consideration of specific dopant concentrations, which potentially enables optimisation of grooved silicon

IRE's for electrochemical analysis (Huang et al, 2008). Similarly, Ataka showed that gold nano-particle depositions on unprocessed silicon substrates permit simultaneous electrochemical and spectroscopic detection of biological samples (Ataka et al, 2013); thus offering a multitude of approaches to develop an IRE capable of dual electrochemical and spectroscopic analysis.

The current chapter shall firstly evaluate the spectroscopic and electrochemical performance of novel silicon (100) micro-fabricated v-groove substrates for detection of pooled human serum samples and electrochemical model complexes respectively. Subsequently, the chapter shall assess the spectroscopic and electrochemical performance of silicon in relation to substrate dopants and dopant concentrations. Thereafter, the chapter will evaluate the spectroscopic and electrochemical performance of deposited gold nano-particle film silicon substrates for detection of pooled human blood serum and biomarkers respectively. Lastly, the chapter shall explore different design possibilities for the medical device, with the aim of utilising recent technological advances to develop an integrated infrared spectroscopic and electrochemical platform for the point-of-care clinical setting.

## 3.3 Materials & Methods

### *3.3.1 Materials & Reagents*

Tris(2,2'-bipyridine) ruthenium(ll) hexafluorophosphate ($Ru(bpy)_3(PF_6)_2$), potassium ferri/ferrocyanide ($K_3[Fe(CN)_6]^{-3/4}$), phosphate-buffered saline (PBS), acetone, isopropyl alcohol (Sigma-Aldrich, USA) and deionised water (Millipore, USA) were

employed for electrochemical preparation and analysis. Pooled human blood serum, Virkon and 99.5% ethanol were additionally required for spectroscopic preparation and analysis. Silicon (100) P-type 1-3Ω.cm substrates were designed to feature V-shaped grooves in-house by another member of our research group, namely Mr Duncan Finlayson, and fabricated by Scottish Microelectronics Centre (SMC, United Kingdom). Degenerate P-type and N-type silicon (100) 0.001-0.005Ω.cm substrates were supplied from IDB Technologies (IDB Technologies, United Kingdom).

### *3.3.2 Electrochemical Set-Up*

Electrochemical experiments were performed on a PalmSens 3 potentiostat (PalmSens, The Netherlands) configured in a standard three-electrode arrangement with one reference, counter and working electrode. Electrochemical control measurements were performed with conventional electrodes constituting CH Instruments CHI111 silver/silver chloride wire reference electrode, CH Instruments CHI115 platinum wire counter electrode and CH Instruments CHI104 ø=3mm glassy carbon or CHI101 gold ø=2mm working electrodes (CH Instruments, USA). Electrochemical measurements were performed with one conventional reference and counter electrode as previously described and one novel working electrode comprising either a silicon substrate, degenerate P-type silicon substrate, degenerate N-type silicon substrate or 5-200nm thick gold films deposited on silicon substrates.

### *3.3.3 ATR-FTIR Set-Up*

Initial spectroscopic measurements were performed on Perkin Elmer Spectrum 2 spectrometers (PerkinElmer, Massachusetts, U.S.A) configured with Pike Technologies VeeMax accessory module (Pike Technologies, Wisconsin, U.S.A) with mirrors arranged at 45° angles. Subsequently, spectroscopic measurements were recorded on Perkin Elmer Spectrum 2 spectrometers configured with Quest ATR Specac accessory modules (Specac, United Kingdom) optimised with mirrors at 45° angles. Spectroscopic measurements tested the performance of each novel IRE that comprised either undoped silicon, degenerate P-type silicon, degenerate N-type silicon or 200-5nm gold thin film silicon substrates. Spectroscopic control measurements were performed with Quest ATR Specac accessory modules fitted with a Specac diamond IRE top plate.

### *3.3.4 Experimental Method*

Electrochemical experiments commenced with thorough cleaning of electrodes prior to analysis. Conventional macro disc electrodes were polished with 0.05 micron alumina on Buehler micro-cloth for 5 minutes per electrode and subsequently sonicated for 15 minutes in deionised water to remove remaining alumina particles. Silicon electrodes were cleaned with acetone in an ultrasonic bath for 5 minutes followed by consecutive rinses in isopropyl alcohol and deionised water. Electrochemical controls were conducted by submerging one working, counter and reference electrode in 3ml of 1mM $Ru(bpy)_3(PF_6)_2$ or 10mM $K_3[Fe(CN)_6]^{-3/4}$ in 0.1M PBS solutions. Electrochemical measurements were conducted with novel silicon

working electrodes and conventional counter and reference electrodes configured in designed flow cells described in detail in sections 3.3.5 and 3.3.6. Cyclic voltammetry was performed on all electrode substrates with the potential window specified as 0.8V and 1.3V for $Ru(bpy)_3(PF_6)_2$ and -0.4V and 0.6V for $K_3[Fe(CN)_6]^{-3/4}$ molecules. Other parameters were specified as a potential step of 0.01V and a scan rate of 0.025-1.0V/s depending on experiments. Chronoamperometry was also performed on electrodes with potentials of 1.2V and 0.2V for oxidation and reduction of $Ru(bpy)_3(PF_6)_2$ respectively, whilst potentials of 0.5V and 0.1V were selected for oxidation and reduction of $K_3[Fe(CN)_6]^{-3/4}$ respectively. Chronoamperometry experiments were conducted for 10s durations with currents recorded at 0.1s time intervals.

Spectroscopic experiments commenced with thorough cleaning of respective IRE's prior to pipetting of target samples. Diamond IRE's were consecutively wiped with ethanol and deionised water, whilst silicon IRE's were sonicated in acetone for 5 minutes and then rinsed with isopropyl alcohol and deionised water. Spectroscopic measurements conducted on diamond IRE's utilised 2µl of either human pooled serum, $Ru(bpy)_3(PF_6)_2$ or $K_3[Fe(CN)_6]^{-3/4}$ samples. Spectroscopic measurements conducted on silicon IRE's employed 3µl of either human pooled serum, $Ru(bpy)_3(PF_6)_2$ or $K_3[Fe(CN)_6]^{-3/4}$ samples to ensure full coverage of substrates. Pooled human serum was thawed and frozen in a -80°C freezer between analyses to prevent sample degradation. Both diamond and silicon IRE's were disinfected with Virkon and then consecutively wiped with ethanol and deionised water after analysis. ATR-FTIR was employed for all spectroscopic measurements with one background absorption spectrum collected prior to contact between the IRE and sample to account

for atmospheric conditions, therefore minimising variability between replicate measurements. Absorption spectra were obtained for samples in either the wet (0 minutes) or dry (30 minutes) state with spectral acquisition in the mid-infrared region (4000-450cm-1) at a resolution of 4$cm^{-1}$ with 16 co-added scans. Spectral pre-processing parameters included spectral selection between 4000-900$cm^{-1}$, rubber-band baseline correction and vector normalisation computed on Matlab 2016a software (Mathworks, Massachusetts, U.S.A).

### *3.3.5 Initial Device Design & Fabrication for Silicon Substrate*

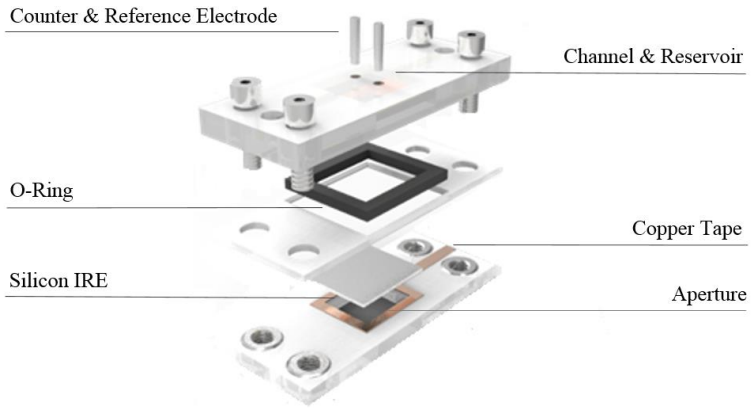


*Figure 3.1: Designed CAD model of flow cell for spectroscopic and electrochemical evaluation of novel silicon substrate.*

The device design comprised three polylactic acid (PLA) components that contained a liquid sample and novel silicon IRE that performed as an ATR crystal and working electrode for spectroscopic and electrochemical analysis. The lower PLA part was recessed to contain the silicon IRE and the aperture allowed the projection of mid-infrared light on to the bottom surface of the silicon substrate. The silicon IRE featured V-shaped grooves on the underside surface that facilitated spectral acquisition of

samples in intimate contact with the top silicon surface. The PLA part also featured an electrical connection to allow application of electrical potentials to the silicon IRE with the view to extending the substrates functionality to perform as a working electrode for electrochemical studies. The adjacent PLA part contained a PLA gasket that functioned as an O-ring when compressed to prevent sample leakage at the interface between the silicon and lower PLA components. The upper PLA part featured one straight microfluidic channel that allowed transportation of samples to the top surface of the silicon substrate for spectroscopic analysis. Additionally, the upper PLA part featured a sample reservoir and two entry points for insertion of one silver/silver chloride reference electrode and one platinum counter electrode for electrochemical analysis. All PLA parts were secured together with four M2.5 x 6mm hex socket cap screws that interfaced with four M2.5 nuts. To the best of our knowledge, no previous approach has utilised silicon substrates to function as an IRE and working electrode in a medical diagnostic device.

All three PLA components were manufactured through fused filament fabrication with an Ultimaker 2 3D printer configured with 0.4mm nozzle diameter (Ultimaker B.V., The Netherlands). Printing settings were selected to have 30mm/s print speed, 215°C nozzle temperature, 70°C build plate temperature, 100µm layer height and 100% fill density. All PLA components were designed with PTC Creo Parametric 3.0 (PTC, USA) and subsequently converted to Cura 2.1.2 software (Ultimaker B.V., The Netherlands) to facilitate device fabrication. Devices were inspected with scanning electron microscopy (SEM) to evaluate the quality of microfluidic channels and revealed the fabrication process produced channel geometries with a high degree of

surface roughness and irregularity, evident in figure 2c. Furthermore, the nature of the fabrication process produced porous features at join lines between deposited filaments, evident in figure 2c. Although adequate for initial testing with pipettes, sample leakage may occur at increased flow rates and pressures if flow injection analysis were to be used in future experiments. Therefore, it was deemed necessary to explore alternative fabrication methods to produce prototypes with fully sealed microfluidic channels.

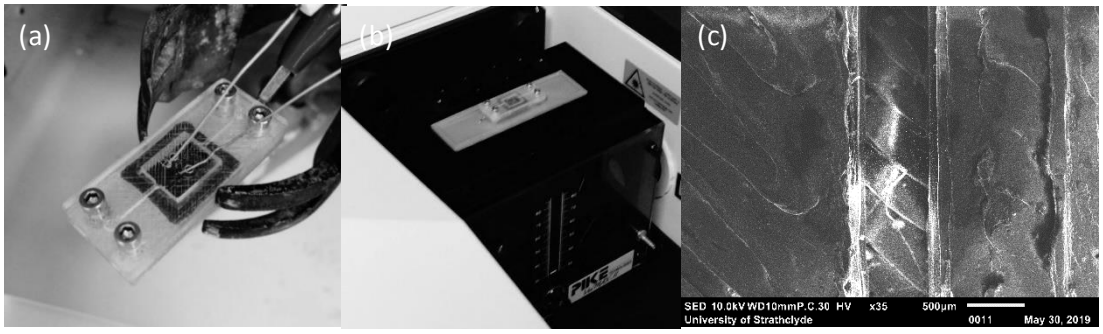


*Figure 3.2: Fabricated flow cell for (a) electrochemical and (b) spectroscopic analysis. (c) SEM image of microfluidic channels in flow cell.*

### *3.3.6 Revised Design & Fabrication for Silicon Substrate*

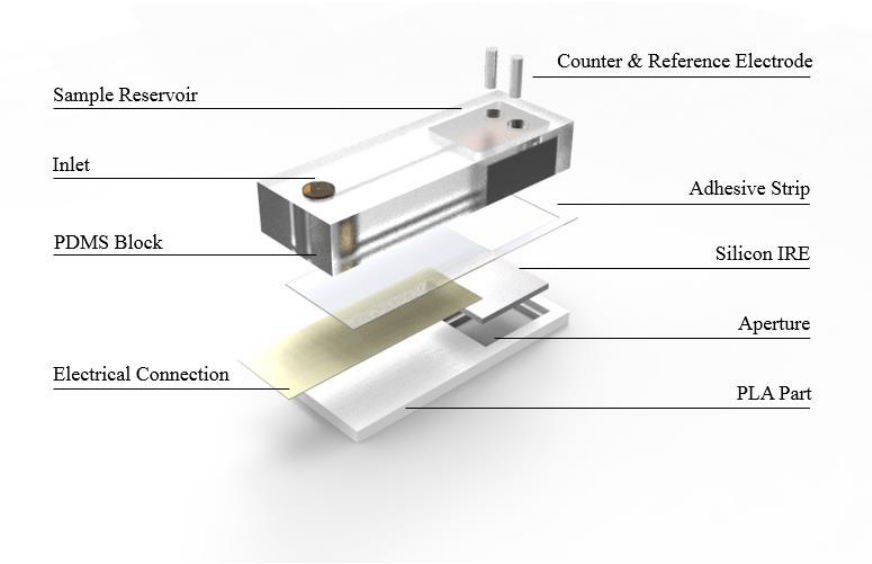


*Figure 3.3: CAD model of revised flow cell design for spectroscopic and electrochemical evaluation of novel silicon substrate.*

The revised design comprised one polydimethylsiloxane (PDMS) block with an inlet and straight microfluidic channel of 500µm nominal thickness for transportation of samples to a detection reservoir to contact the silicon component. Additionally, the PDMS block featured two insertion points for one counter and reference electrode and the TapeCase 9707 XYZ isotropic electrically conductive adhesive tape provided a stable electrical connection to the silicon substrate for electrochemical analysis. The lower PLA part housed the silicon component and featured an aperture to allow interaction of infrared light with the V-shaped grooves of silicon substrates to enable spectroscopic analysis. The 3M 467MP high performance adhesive transfer tape was cut to size and secured the PDMS and PLA parts preventing sample leakage at the interface between the silicon component and detection reservoir. Furthermore, the adhesive strip negated the use of screw and nut fastenings and was therefore deemed more suitable from both a fabrication and economical perspective.

Devices were fabricated from polydimethylsiloxane (PDMS) by employing a novel 3D printed methodology adapted from previous work of Saggiomo (Saggiomo et al, 2015). The methodology boasted rapid and inexpensive fabrication processes with PDMS chosen due to its biocompatibility and familiarity to current microfluidic applications. Microfluidic channel geometries were firstly 3D printed from acrylonitrile butadiene styrene (ABS) filament on an Ultimaker 2 3D printer with 0.25mm nozzle diameter, evident in figure 4a. Microfluidic channels were then suspended in designed and 3D printed molds that had been lined with acetate film to enable successful removal of PDMS, evident in figure 4b. PDMS was mixed

thoroughly in a 10:1 ratio of Sylgard 184 elastomer and cure agent and centrifuged for 5 minutes at 5,000rpm to remove visible air bubbles. Degassed PDMS was then poured in to each mold and cured in the oven at 50°C for 3 hours, evident in figure 4c and 4d. Thereafter, PDMS substrates were removed from molds, immersed in acetone for 24 hours to dissolve ABS features, and then flushed with acetone to remove residual ABS from enclosed channels, depicted in figure 4e. Device testing and SEM inspection confirmed that microfluidic features were suitable for electrochemical and spectroscopic studies and were fully enclosed and significantly improved compared to previous prototypes, evident from figures 3.4f, 3.4g and 3.4h respectively.

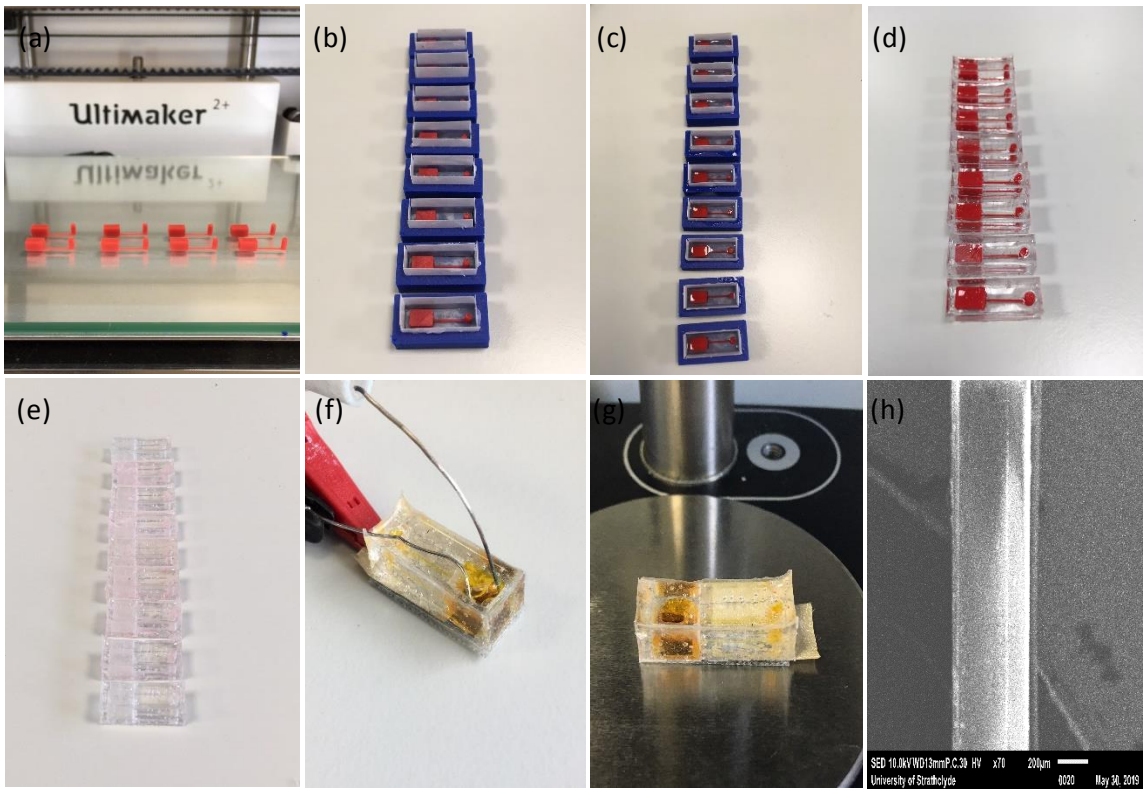


*Figure 3.4: (a) 3D printing of microfluidic features, (b) Suspension of microfluidic features in 3D printed molds, (c) PDMS cured and (d) removed from 3D printed molds, (e) microfluidic features dissolved with acetone, (f) electrochemical and (g) spectroscopic analysis of device prototype, (h) SEM image of device microfluidic channels.*

### *3.3.7 Gold Thin Film Fabrication Process*

Gold thin films were sputtered on the top surface of silicon substrates using a Leica EM ACE200 Sputter Coater. The sputtering process proceeded with Argon gas purging at a base vacuum pressure of $5x10^{-2}$ mbar, at a sputter current of 50mA, in directional mode with a quartz crystal detector employed to verify specified depositions of 5-200nm thickness. Silicon substrates to be evaporated were pre-treated with a buffered oxide etch that comprised a 6:1 ratio of 40% ammonium fluoride in water and 49% hydrofluoric acid in water to remove the native oxide and hydrogen terminate silicon surfaces. Subsequently, gold thin films of 10nm thickness were evaporated on silicon substrates with an Edwards 306 E-beam evaporator conducted by technicians from Level 7 clean room at the Technology and Innovation Centre, University of Strathclyde. Thereafter, evaporated gold thin films were annealed with a Jipelec JetFirst Rapid Thermal Annealer with a 5-minute ramp to 600°C, 1-minute hold at 600°C and programmed cool in nitrogen atmosphere at a flow rate of 50L per hour.

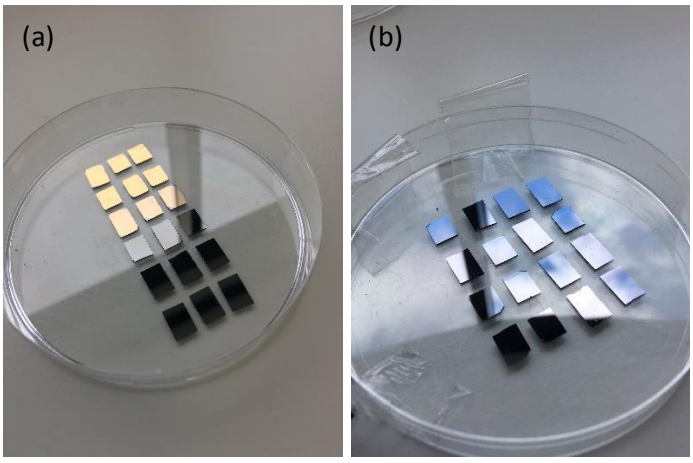


*Figure 3.5: Silicon IRE's (a) sputtered with gold of 200-5nm nominal thicknesses and (b) evaporated with gold of 10nm nominal thickness*

### 3.3.8 Data Analysis & Statistics

One-way ANOVA studies were conducted to determine statistical differences between mean oxidation and reduction maxima for different working electrode substrates for electrochemical analysis. Thereafter, Fisher least significant difference (LSD) post-hoc studies were conducted on statistically significant results when p-values <0.05 at 95% confidence intervals to evaluate the difference between means of individual data sets. Principal component analysis (PCA) studies were conducted with 17 principal components to determine the variance in spectra between the diamond IRE and novel silicon IRE's for spectroscopic analysis. Thereafter, one-way ANOVA studies were conducted on corresponding principal component scores to determine the statistical significance of diamond IRE and novel silicon IRE spectra where p-values of <0.05 at 95% confidence intervals indicate statistical significant results. Presented data indicates mean results ± one standard deviation with three sample repeats and three replicates measurements obtained for electrochemical and spectroscopic data sets.

## 3.4 Results & Discussion

### *3.4.1 Electrochemical Evaluation of Silicon Vs Conventional Electrodes*

#### *3.4.1.1 Initial Testing of 1mM $Ru(bpy)_3(PF_6)_2$ Molecules*

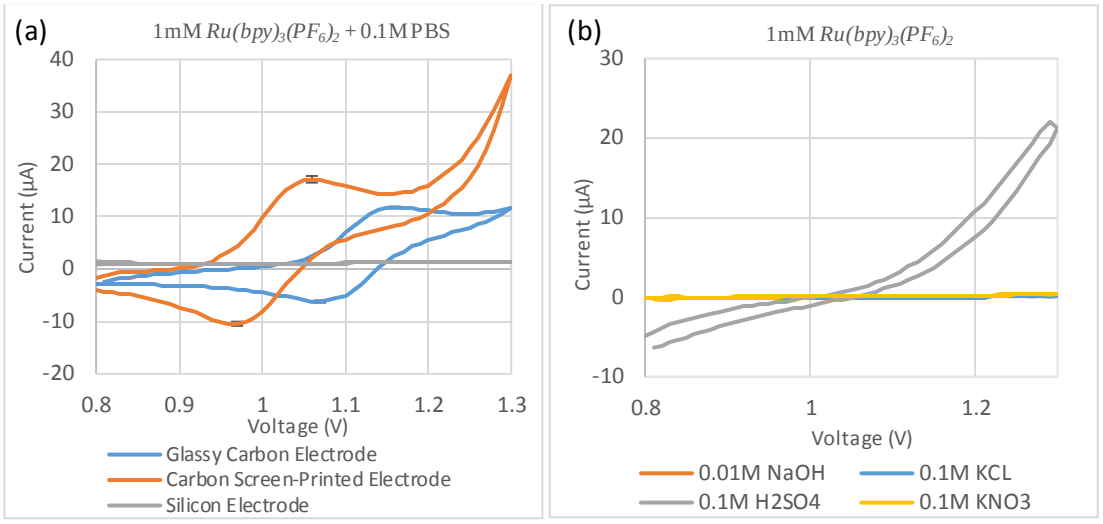


*Figure 3.6: (a) Cyclic voltammograms of different electrode substrates for detection of 1mM $Ru(bpy)_3(PF_6)_2$ + 0.1M PBS (n=3) (b) Cyclic voltammograms of silicon substrates for detection of 1mM $Ru(bpy)_3(PF_6)_2$ with different electrolytes.*

Conventional electrodes measured one-electron transfer redox reactions characteristic of $Ru(bpy)_3(PF_6)_2$, where the central ruthenium ion transitions between $Ru^{2+}$ and $Ru^{3+}$ oxidation states upon application of the analytes formal potential (Figure 3.6a) (Bond et al, 1999). Glassy carbon electrodes instigated oxidation of $Ru^{2+}$ to $Ru^{3+}$ at $E_{pa}$ = 1.160V where the one-electron transfer produced $I_{pa}$ = 6.272 ± 1.290µA. Thereafter, glassy carbon electrodes initiated reduction of $Ru^{3+}$ to $Ru^{2+}$ at $E_{pc}$ = 1.070V where the one-electron transfer measured $I_{pc}$ = 6.764 ± 0.891µA. Hence, redox reactions were electrochemically reversible at glassy carbon electrodes since $\Delta E_p$ = 90mV, in close accordance with the theoretical value of $\Delta E_p$ = 59.2mV specified for one-electron transfer reversible reactions (Hamann et al, 1998). Furthermore, glassy carbon electrodes produced $I_{pa}/I_{pc}$ = 0.927, in close agreement with the theoretical value of $I_{pa}/I_{pc}$ = 1.000 for ideal reversible electrochemical reactions (Hamann et al, 1998). Carbon screen-printed electrodes similarly observed the transition between $Ru^{2+}$ and $Ru^{3+}$ redox states, with oxidation events at $E_{pa}$ = 1.060V that measured $I_{pa}$ = 15.590 ±

1.437µA, whilst reduction events occurred at $E_{pc}$ = 0.970V and measured $I_{pc}$ = 10.356 ± 0.768µA. Likewise, carbon screen-printed electrodes observed electrochemically reversible behaviour with $\Delta E_p$ = 90mV consistent with previously mentioned theoretical values. However, $I_{pa}/I_{pc}$ = 1.510 was greater than glassy carbon electrodes, which implies that it is more difficult to transfer electrons from carbon screen-printed electrode surfaces to redox species, and suggests that electrochemical behaviour may in fact be quasi-reversible in nature (Hamann et al, 1998). Similarly, variation in oxidation and reduction potentials between carbon and glassy carbon electrodes may be attributed to differences in electrode material compositions. Silicon electrodes were unable to instigate oxidation or reduction reactions of $Ru(bpy)_3(PF_6)_2$ in PBS solutions. Similarly, silicon substrates were unable to promote redox reactions of $Ru(bpy)_3(PF_6)_2$ in NaOH, $H_2SO_4$, KCL or $KNO_3$ solutions (Figure 3.6b), confirming that the supporting electrolyte and solution pH were not responsible for poor electrochemical performance, which instead may be attributed to the significantly reduced electrical conductivity of the material. Silicon is categorised as a semi-conductor material where unlike conductors the valence band and conduction band do not overlap at the Fermi level, in accordance with band theory, resulting in a notable band gap of 1.12eV at 300K for intrinsic silicon substrates (Zhang, 2007). Consequently, the quantity of free charge carriers that transition to the conduction band upon thermal excitation by the application of electrical potentials is significantly reduced compared to conducting materials, and therefore restricts electron transfer events at the electrode electrolyte interface (Zhang, 2007). Hence, current silicon substrates subjected to standard electrochemical parameters are not suitable for characterisation of electrochemically active $Ru(bpy)_3(PF_6)_2$ molecules.

### *3.4.1.2 Varying Scan Rate for Detection of 1mM $Ru(bpy)_3(PF_6)_2$ Molecules*

Electrochemical current responses at the working electrode are influenced by analytical parameters of cyclic voltammetry experiments. Therefore, in the next experiment, all three respective electrodes were subjected to variable scan rates to determine whether silicon electrodes could induce redox reactions at faster scan rates, since it is known that current responses are proportional to square root of scan rate, in accordance with Randles-Sevcik equation (Hamann et al, 1998).

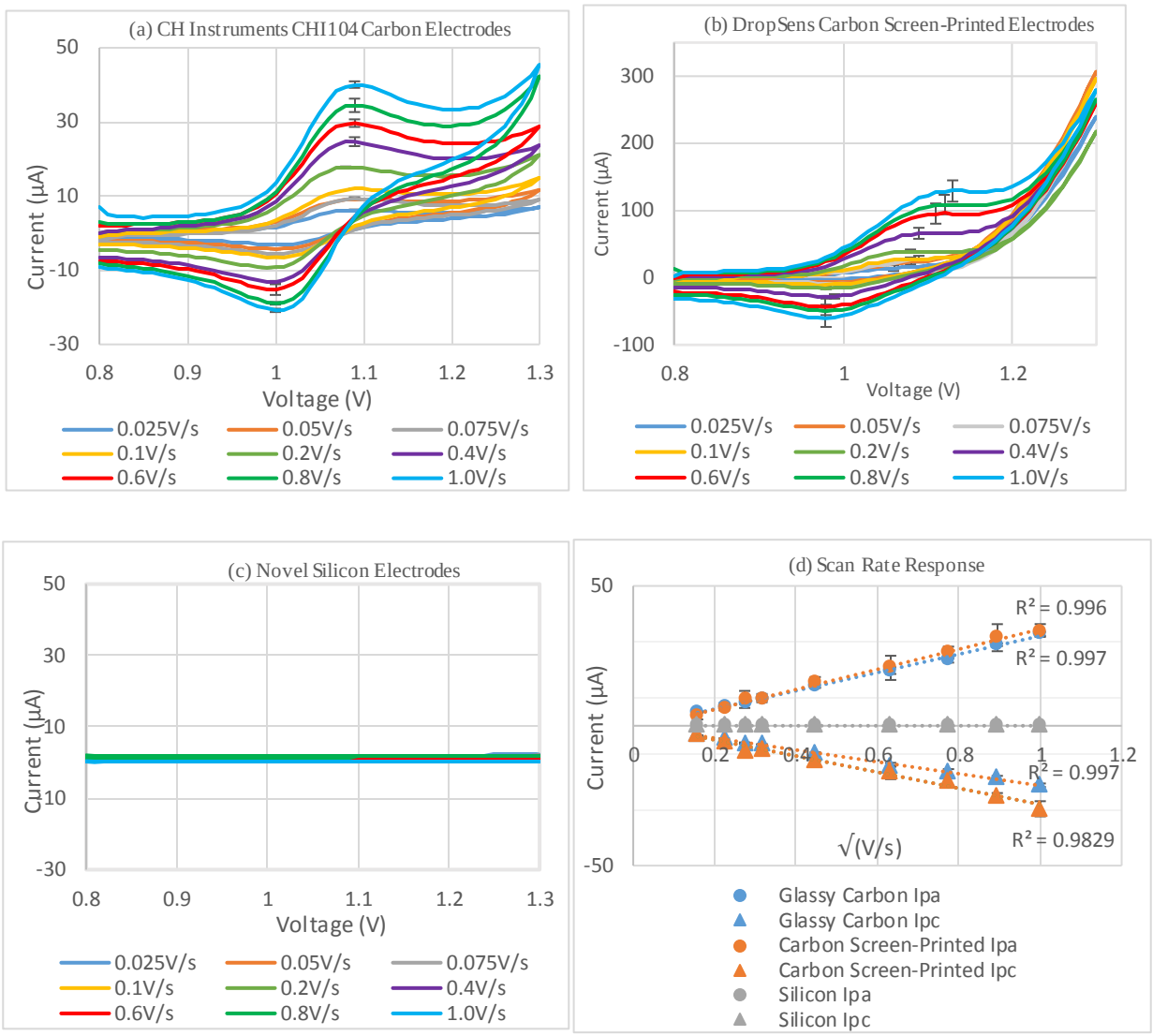


*Figure 3.7: Cyclic voltammograms of (a) glassy carbon electrodes, (b) carbon screen-printed electrodes, (c) silicon electrodes subjected to variable scan rates for detection of 1mM $Ru(bpy)_3(PF_6)_2$ + 0.1M PBS (n=3). (d) Plot of the current response of all three electrodes with respect to the square root of scan rate.*

Conventional electrodes exhibit strong positive linear relationships for peak current with respect to square root of scan rate, with $R^2 = 0.997$ for $I_{pa}$ and $I_{pc}$ of glassy carbon electrodes and $R^2 = 0.996$ and $R^2 = 0.983$ for $I_{pa}$ and $I_{pc}$ of carbon screen-printed electrodes (Figure 3.7d). Glassy carbon macro electrodes measured $I_{pa} = 6.153 \pm 0.234\mu A$ and $I_{pc} = -3.029 \pm 0.072\mu A$ for 0.025V/s that increased with cumulative scan rates to $I_{pa} = 40.079 \pm 0.880\mu A$ and $I_{pc} = -20.821 \pm 0.455\mu A$ for 1.0V/s (Figure 3.7a).

Oxidation and reduction potentials were constant with applied scan rates at $E_{pa}$ = 1.090V and $E_{pc}$ = 1.000V respectively, indicative of reversible redox reactions with fast electron transfer kinetics (Hamann et al, 1998). Similarly, carbon screen-printed electrodes measured $I_{pa}$ = 3.555 ± 1.291µA and $I_{pc}$ = -2.984 ± 1.046µA for 0.025V/s that increased proportionally with scan rate to $I_{pa}$ = 34.071 ± 2.284µA and $I_{pc}$ = -29.688 ± 2.712µA for 1.0V/s. Oxidation and reduction potentials shifted with increased scan rates from $E_{pa}$ = 1.060V and $E_{pc}$ = 0.990V at 0.025V/s to $E_{pa}$ = 1.130V and $E_{pc}$ = 0.980V at 1.0V/s, which suggests the presence of slower electron transfer kinetics compared to glassy carbon macro electrodes. In general, electrochemical behaviour at faster scan rates may be attributed to the reduced time for redox species to accumulate at working electrodes, which decreases the diffusion layer and increases the concentration gradient at the electrode surface, ultimately resulting in larger currents (Elgrishi et al, 2017). Hence, it is evident that electrochemical reactions with conventional electrodes are diffusion limited. Conversely, silicon electrodes were unable to obtain oxidation or reduction peaks when subjected to various scan rates (figure 3.7c), which implies that the applied thermal excitation did not cause sufficient quantities of free charge carriers to occupy the conductance band. Hence, current silicon substrates do not possess the necessary electrical conductivity to act as working electrodes to characterise $Ru(bpy)_3(PF_6)_2$ molecules.

### *3.4.1.3 Amperometric Detection of 1mM $Ru(bpy)_3(PF_6)_2$ Molecules*

Silicon electrodes were further evaluated with chronoamperometry as an alternative electrochemical technique to assess current responses over time and to evaluate

whether electrochemical behaviour was in any way indicative of redox reactions of $Ru(bpy)_3(PF_6)_2$ molecules.

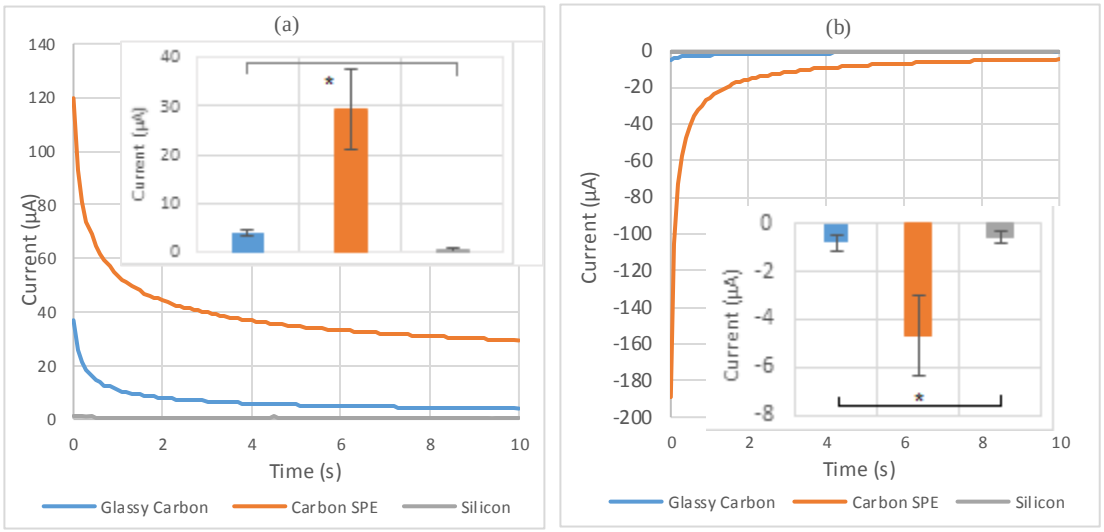


*Figure 3.8: Chronoamperometry responses of glassy carbon, screen-printed carbon and silicon electrodes when $Ru(bpy)_3(PF_6)_2$ molecules were subjected to (a) oxidation and (b) reduction potentials. Inset plots show (a) oxidation and (b) reduction current responses at 10 seconds. (n=3), * statistically significant at $P < 0.05$.*

Both conventional electrodes demonstrated current changes over time for detection of $Ru(bpy)_3(PF_6)_2$ when subjected to constant applied potentials. Glassy carbon electrodes measured current plateaus of $I_{pa}$ = 3.926 ± 0.699µA and $I_{pc}$ = -0.817 ± 0.332µA at 10 seconds that represents the time interval where the rate of the faradaic reaction is in equilibrium with the rate of diffusion to the electrode surface, in accordance with the Cottrell equation (Borland et al, 2007). Similarly, carbon screen-printed electrodes measured faradaic currents of $I_{pa}$ = 29.322 ± 8.281µA and $I_{pc}$ = -4.710 ± 1.669µA at 10 seconds. Hence, both electrodes were observed to instigate oxidation and reduction reactions of $Ru(bpy)_3(PF_6)_2$ molecules. Conversely, silicon electrodes did not produce significant changes in current over time with $I_{pa}$ = 0.453 ±

0.479µA and $I_{pc}$ = -0.596 ± 0.271µA recorded at 10 seconds. The high standard deviation of silicon electrode results were indicative of noise and not representative of redox reactions of $Ru(bpy)_3(PF_6)_2$ molecules.

*3.4.1.4 Initial Testing of 1mM* $K_3[Fe(CN)_6]^{-3/4}$ *Target Molecules*

Silicon electrodes were further evaluated in the presence of another common redox active couple, $K_3[Fe(CN)_6]^{-3/4}$, to assess whether the substrate could perform as an electrode for detection of a different electro-active molecule at a lower formal potential. However, identical experiments to those previously conducted with $Ru(bpy)_3(PF_6)_2$ all showed that it was not possible to detect $K_3[Fe(CN)_6]^{-3/4}$ species. Therefore, these results will not be discussed in detail to prevent repetition but can be found in Appendix A.

*3.4.2 ATR-FTIR Evaluation of Silicon Vs Conventional Substrates*

*3.4.2.1 Concentration Study of* $Ru(bpy)_3(PF_6)_2$ *Molecules*

Infrared spectra of wet $Ru(bpy)_3(PF_6)_2$ samples of different concentrations in water were obtained from diamond (Figure 3.9a) and silicon (Figure 3.9c) substrates. Both IRE's identified a broad absorption band in the ~3300cm$^{-1}$ region that may be attributed to $\nu_s$(OH) and $\nu_{as}$(OH) vibrations of water molecules (Falk et al, 1966). Similarly, both substrates identified an intense absorption band in the ~1650cm$^{-1}$ region assigned to $\delta_{in\text{-}plane}$(HOH) vibrations of water molecules (Falk et al, 1966). These spectroscopic peaks clearly dominate respective infrared spectra due to the strong permanent dipole moment, ~3.0D, and hydrogen bonding of water molecules (Morozenko et al, 2014). Consequently, spectral bands of $Ru(bpy)_3(PF_6)_2$ molecules

were significantly diminished for wet sample analysis and only visible at higher sample concentrations of 2-10mM for both substrates. Specifically, weak absorption bands were observed at 831cm$^{-1}$, 763cm$^{-1}$ and 556cm$^{-1}$ that may be tentatively assigned to $\nu_{as}(PF_6)$, $\nu_s(PF_6)$ and $\delta(PF_6)$ vibrations of hexafluorophosphate ions respectively (Lakshmi et al, 2015; Adeloye et al, 2012). The intensity of these absorption bands were observed to increase with concentration, as expected given the Beer-Lambert law, with weak positive correlations for diamond, $R^2$ = 0.9444 (Figure 3.9b), and silicon, $R^2$ = 0.7913 (Figure 3.9d), substrates.

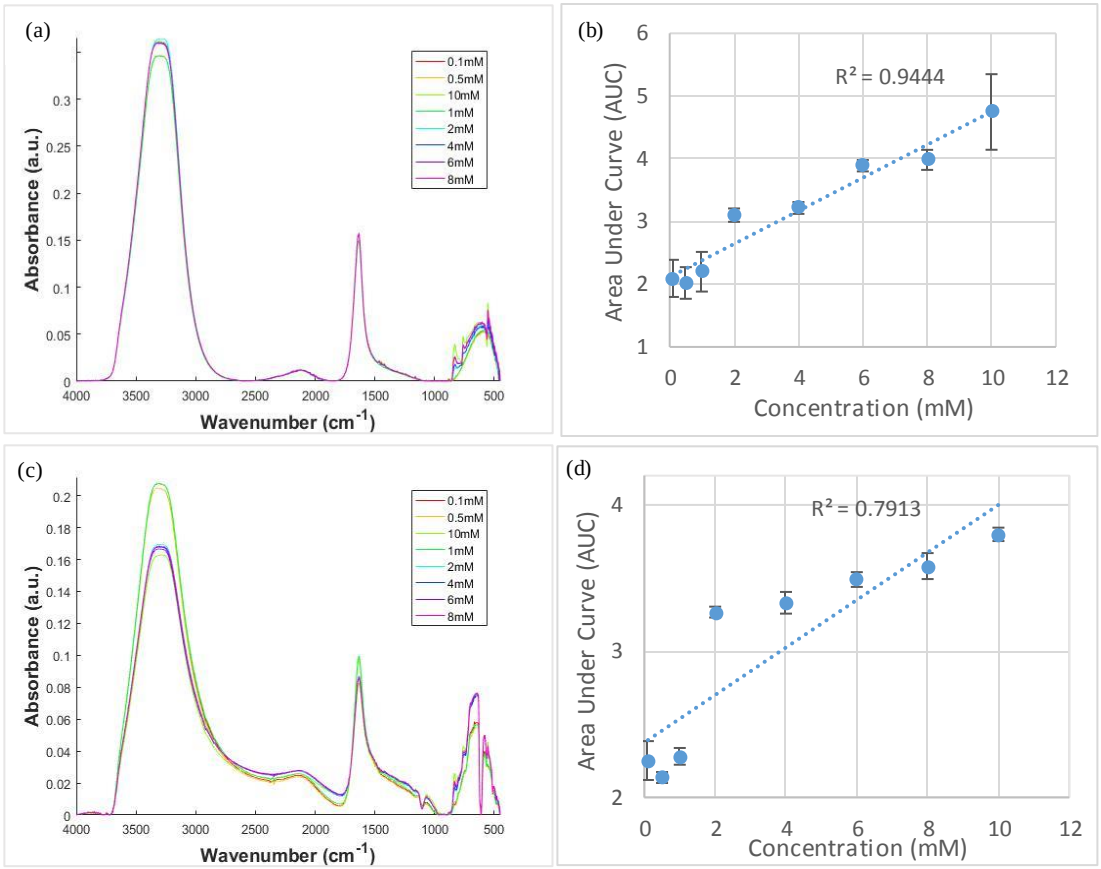


*Figure 3.9: Mean infrared spectra of wet $Ru(bpy)_3(PF_6)_2$ samples in water for concentrations ranging from 0.1-10mM obtained from (a) diamond and (c) silicon substrates. Pre-processing parameters employed consisted of rubber-band baseline correction and offset correction methods. Plots for (b) diamond and silicon (d) substrates show total area under the curve calculations for 831cm$^{-1}$, 763cm$^{-1}$ and 556cm$^{-1}$ peaks for given concentrations.*

Infrared spectra of air dried $Ru(bpy)_3(PF_6)_2$ samples of different concentrations revealed significantly more spectral information for diamond (Figure 3.10a) and silicon (Figure 3.10c) substrates. Infrared absorption peaks associated with $\nu_{as}(PF_6)$, $\nu_s(PF_6)$ and $\delta(PF_6)$ vibrations of hexafluorophosphate ions were accentuated in the absence of water molecules and allowed successful inspection of target molecules to 0.1mM concentrations. The correlation between absorption intensity of specified peaks and concentration improved significantly for dried samples obtained on both diamond, $R^2 = 0.9746$ (Figure 3.10b), and silicon, $R^2 = 0.9906$ (Figure 3.10d), substrates. Interestingly, novel silicon IRE's showed improved quantification of target molecules compared to diamond, which may be attributed to the greater sample volume required to cover the sensor surface. It was necessary to use 3uL per sample on silicon substrates to ensure adequate sensor coverage due to the hydrophobic nature of the aqueous sample, whilst 2uL per sample was sufficient for diamond substrates. Other infrared spectral signatures characteristic of $Ru(bpy)_3(PF_6)_2$ molecules were apparent on dried samples for both substrates, with several absorption peaks in the 1600-1400$cm^{-1}$ and 1200-1000$cm^{-1}$ regions attributed to ring mode $\nu$(CC) and in-plane $\delta$(CH) vibrations of aromatic rings respectively (Coates, 2000). Furthermore, diamond and silicon substrates identified a strong absorption band at 730$cm^{-1}$ related to the out-of-plane $\delta$(CH) vibration that corresponds to the mono-substituted aromatic ring of $Ru(bpy)_3(PF_6)_2$ (Ouellette et al, 2014; Coates, 2000). Importantly, however, both substrates were unable to identify the central ruthenium ion fundamental to electrochemical redox reactions because the absorption band for ruthenium at ~280$cm^{-1}$ is below the minimum recorded wavenumber on the infrared spectrometer (Venegas-Yazigi et al, 2003). Hence, it is not possible to conduct combined spectroscopic and

electrochemical experiments on $Ru(bpy)_3(PF_6)_2$ molecules, since it is not possible to observe in situ spectroscopic changes in the chemical structure of ruthenium when subjected to redox potentials.

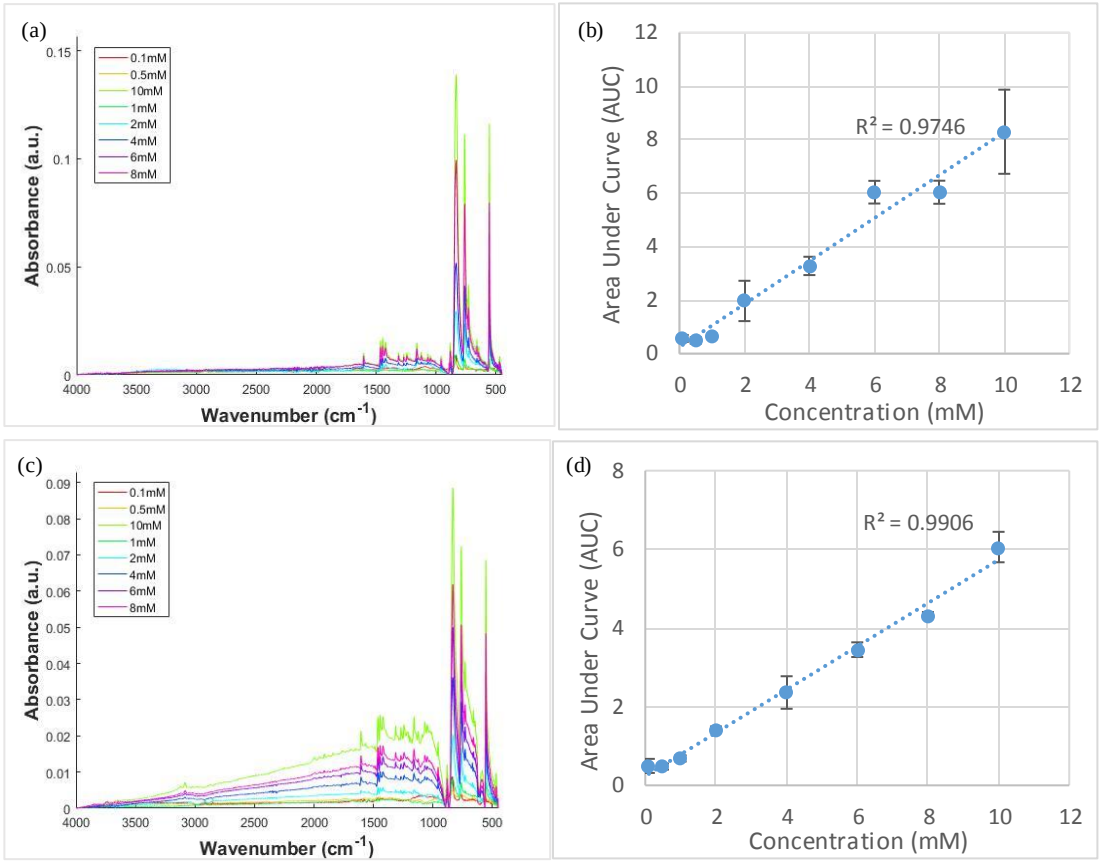


*Figure 3.10: Mean infrared spectra of air dried $Ru(bpy)_3(PF_6)_2$ samples for concentrations ranging from 0.1-10mM obtained from (a) diamond and (c) silicon substrates. Pre-processing parameters employed consisted of rubber-band baseline correction and offset correction methods. Plots for (b) diamond and silicon (d) substrates show total area under the curve calculations for 831cm$^{-1}$, 763cm$^{-1}$ and 556cm$^{-1}$ peaks for given concentrations.*

### *3.4.2.2 Concentration Study* of $K_3[Fe(CN)_6]^{-3/4}$ *Molecules*

Infrared spectra of wet $K_3[Fe(CN)_6]^{-3/4}$ samples of different concentrations showed markedly obscured spectral signatures of target molecules for diamond (Figure 3.11a) and silicon (Figure 3.11c) substrates. Instead, the strong dipole moment of water molecules dominated infrared spectra, with only two weak characteristic absorption

peaks present at 2115cm$^{-1}$ and 2038cm$^{-1}$ that correspond to respective $\nu_6$ vibrational modes of ferricyanide and ferrocyanide molecules assigned to $\nu$(C≡N) vibrations (Pharr et al, 1997; Reig et al, 2002; Sun-Kyung Park et al, 2002). Intensities of the absorption band at 2038cm$^{-1}$ were found to be proportional to sample concentration, for both diamond, $R^2 = 0.8973$ (Figure 3.11b), and silicon, $R^2 = 0.9259$ (Figure 3.11d) substrates. However, spectral bands were only observable at concentrations ≥2mM for both substrates, identical to previous experiments with ruthenium redox couples, which is not suitable for future cancer biomarker testing where biological molecules typically range from pg/ml to ng/ml concentrations (Rusling et al, 2010). Hence, the poor spectroscopic performance on wet samples of different molecules brings in to question the feasibility of an in situ combined infrared and electrochemical analysis of liquid serum samples.

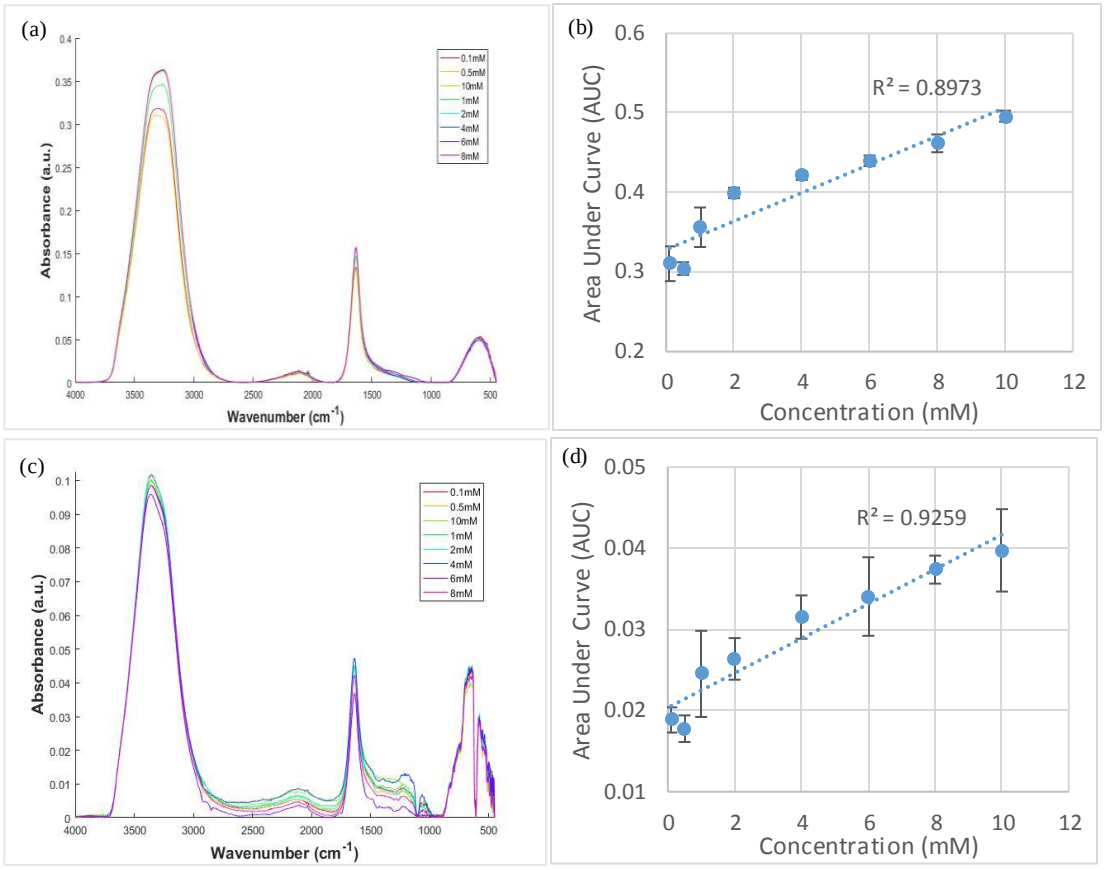


*Figure 3.11: Mean infrared spectra of wet $K_3[Fe(CN)_6]^{-3/4}$ samples for concentrations ranging from 0.1-10mM obtained from (a) diamond and (c) silicon substrates. Pre-processing parameters employed consisted of rubber-band baseline correction and offset correction methods. Plots for (b) diamond and silicon (d) substrates show total area under the curve calculations for the 2038cm$^{-1}$, absorption peak for given concentrations.*

Infrared spectra of air dried $K_3[Fe(CN)_6]^{-3/4}$ samples of different concentrations showed vastly improved spectral signatures characteristic of target molecules for both diamond (Figure 3.12a) and silicon (Figure 3.12c) substrates. Previously observed infrared bands at 2115cm$^{-1}$ and 2038cm$^{-1}$ were enhanced in the absence of water molecules, whilst strong spectral peaks representative of $K_3[Fe(CN)_6]^{-3/4}$ emerged at 2026cm$^{-1}$ and 585cm$^{-1}$, which may be assigned to ν(C≡N) and ν(FeC) vibrations respectively (Gaffar et al, 2001). Similarly, the presence of medium absorption peaks at 2072cm$^{-1}$ and 2093cm$^{-1}$ were indicative of interactions between $\nu_3 + \nu_{13}$ and $\nu_3 + \nu_9$

vibrational modes of $K_3[Fe(CN)_6]^{-3/4}$ respectively (Klyuev, 1965). Intensities of specified spectral peaks were significantly increased and found to be proportional to concentration for both diamond, $R^2 = 0.9278$ (Figure 3.12b), and silicon, $R^2 = 0.9466$ (Figure 3.12d), substrates, enabling successful quantification down to 0.1mM concentrations. Hence, infrared spectroscopic inspection of dried samples demonstrates markedly improved performance in comparison to wet sample analysis of redox couples, conflicting the requirements of electrochemistry where electron transfer events rely on diffusion of redox species in liquid samples. Therefore, future experiments must evaluate whether water molecules suppress spectral signatures of biological constituents of liquid serum samples in the same manner as previously tested molecules to assess the viability of a combined in situ infrared and electrochemical approach.

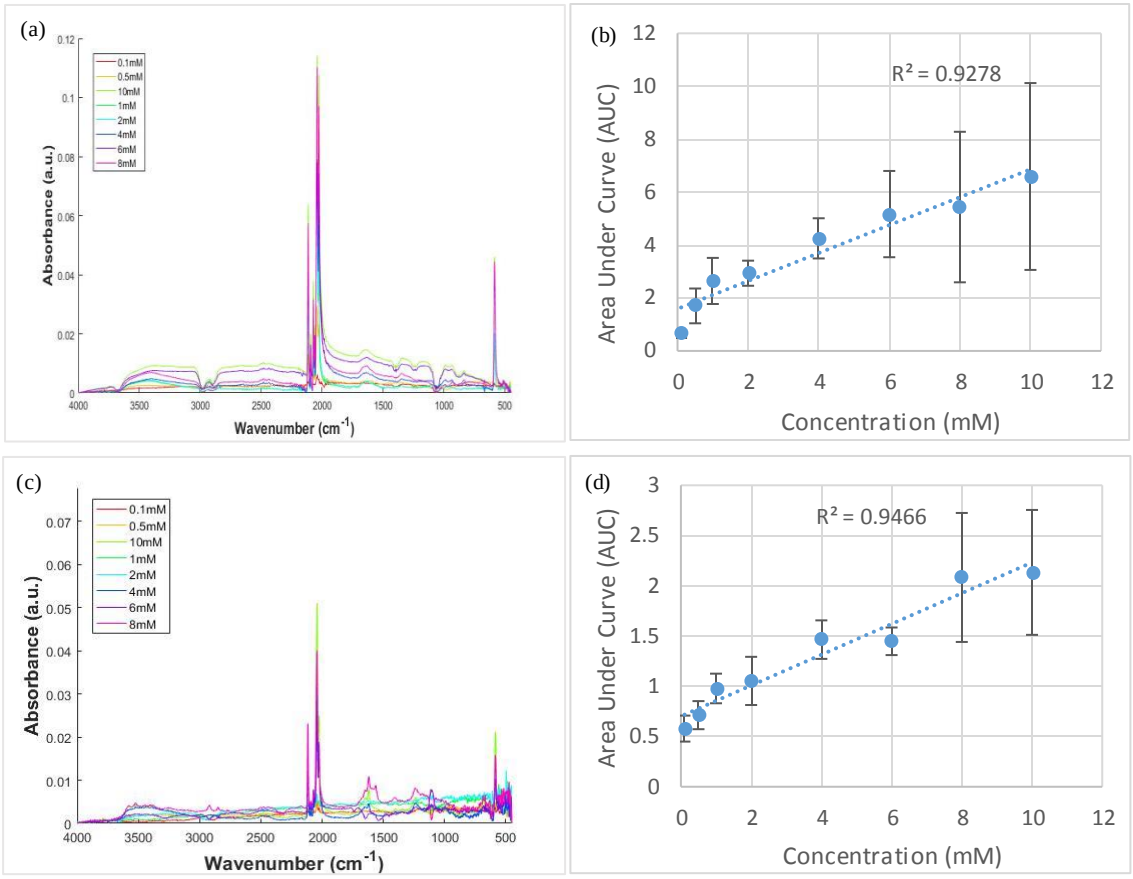


*Figure 3.12: Mean infrared spectra of air-dried* $K_3[Fe(CN)_6]^{-3/4}$ *samples for concentrations ranging from 0.1-10mM obtained from (a) diamond and (c) silicon substrates. Pre-processing parameters employed consisted of rubber-band baseline correction and offset correction methods. Plots for (b) diamond and silicon (d) substrates show total area under the curve calculations for* $2115cm^{-1}$, $2093cm^{-1}$, $2072cm^{-1}$, $2038cm^{-1}$, $2026cm^{-1}$ *and* $585cm^{-1}$ *peaks for given concentrations.*

### *3.4.2.3 Evaluation of Pooled Human Serum*

#### *3.4.2.3.1 Wet Sample Analysis*

Infrared spectra of raw, unprocessed human pooled serum in the wet state shows markedly increased absorption of infrared light by sample constituents over the entire mid-infrared wavenumber region for diamond in comparison to silicon substrates (Figure 3.13a). However, once spectral pre-processing procedures have been

employed in the form of rubber-band baseline correction and vector normalisation methods, relative intensities of spectral features were found to be comparable over the entire mid-infrared region for both substrates (Figure 3.13b). Diamond and silicon both observed strong absorption of water molecules in 3300cm$^{-1}$ and 1640cm$^{-1}$ regions attributed to previously assigned vibrational modes. Consequently, spectral peaks characteristic of macromolecular components of serum are significantly diminished, for example, weak absorption peaks at 1550cm$^{-1}$ and 1400cm$^{-1}$ may be assigned to amide II and $\nu_s(COO^-)$ vibrations of protein constituents (Baker et al, 2014). Similarly, weak infrared peaks at 1455cm$^{-1}$, 1250cm$^{-1}$ and 1050cm$^{-1}$ may be attributed to $\delta_s(CH_2)$, $\nu_{as}(PO_2)$ and $\nu_s(PO_2)$ vibrations representative of lipid and nucleic acid components of serum (Baker et al, 2014).

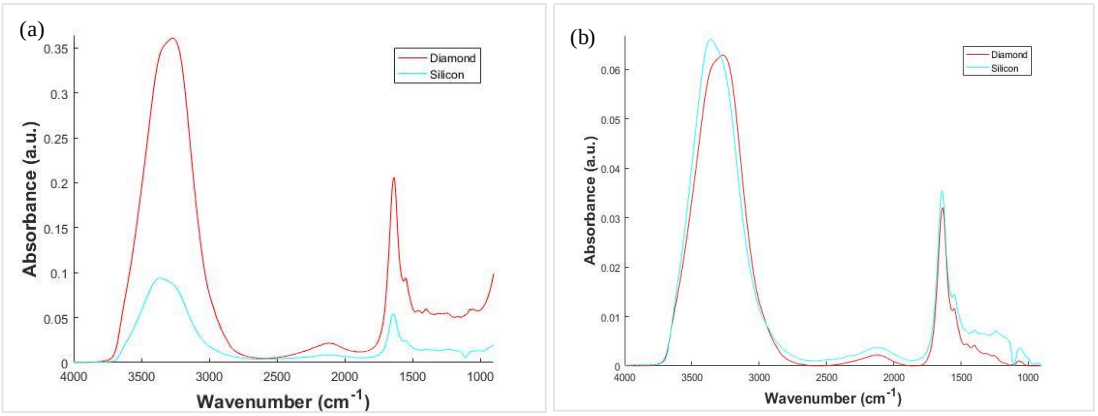


*Figure 3.13: Mean infrared spectra of human pooled serum from 4000-900cm$^{-1}$ with (a) no pre-processing parameters and (b) rubber-band baseline correction and vector normalisation pre-processing methods.*

The PCA scores plot (Figure 3.14a) indicates weak correlation of wet serum spectra between diamond and silicon substrates confirmed to be statistically different for PC1 ($t(15) = 63.73$, p-value $< 0.05$) scores but not for PC2 ($t(15) = -0.25$, p-value $= 0.806$) or PC3 ($t(12) = 0.00$, p-value $= 0.997$) scores. The PC1 loading plot (Figure 3.14b)

accounts for 96.8% of total variance and reveals spectral dissimilarity predominantly originates from differences in absorption intensities of infrared peaks at 3300cm$^{-1}$ and 1640cm$^{-1}$. Hence, spectral variation may be attributed to different quantities of water molecules that reside on substrate surfaces, expected given that 2µL and 3µL volumes were used to cover diamond and silicon substrates respectively. Overall, FTIR analysis of human blood serum samples in the wet state has shown significant concealing of biological bands pertinent to the molecular classification of sample constituents, due to the significant permanent dipole moment of water, ~3.0D, and the presence of hydrogen bonding (Morozenko et al, 2014). Thus, future work should consider separate spectroscopic and electrochemical analysis for detection of biofluids, since it is necessary to conduct electrochemical analysis on wet samples to facilitate diffusion controlled electron transfer, whilst spectroscopic analysis is significantly limited for wet biofluid samples. Alternatively, computational methods to remove ν(OH) and δ(OH) vibrations of water signatures would require development to achieve combined electrochemical and spectroscopic approaches, which has not yet been realised by our research group.

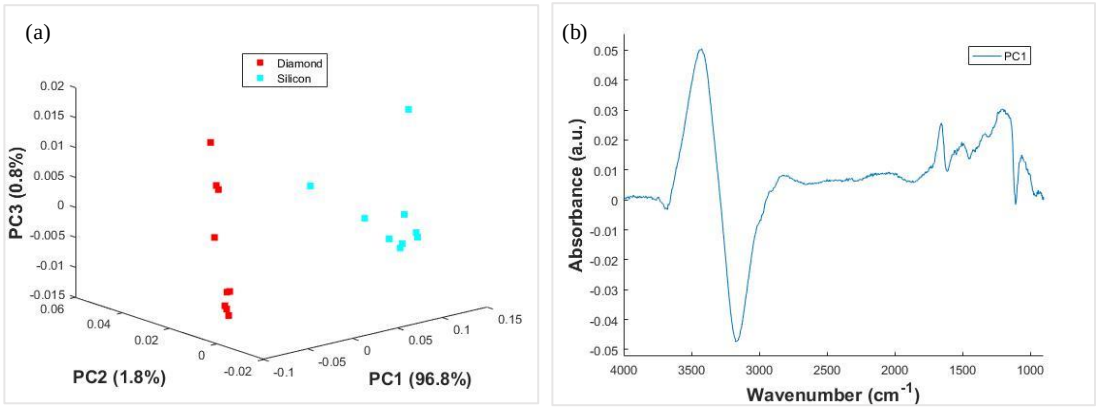


*Figure 3.14: (a) PCA scores plot of infrared spectra from 4000-900cm-1 with rubber-band baseline correction and vector normalisation pre-processing methods and (b) PC1 loadings of infrared spectra with identical pre-processing parameters.*

### *3.4.2.3.2 Dry Sample Analysis*

Infrared spectra of raw, unprocessed human pooled serum samples dried in air also showed significantly elevated absorption of infrared light by sample constituents over the entire mid-infrared wavenumber region for diamond in comparison to silicon substrates (Figure 3.15a). Whilst identical pre-processing methods were employed to scale absorption intensities between respective substrates, notable differences were still evident in specific spectral bands between diamond and silicon substrates (Figure 3.15b). Firstly, the prominent infrared peak observed at ~1650cm-1 attributed to the amide I vibration decreased for diamond relative to silicon, with resultant differences in the ratio of the amide I and amide II bands, which may be of diagnostic significance given that amide I and amide II vibrations are sensitive to protein conformation and secondary structure (Kong et al, 2007). Conversely, spectral peaks related to $\nu_s(COO^-)$, $\delta_s(CH_2)$, $\nu_{as}(PO_2)$ and $\nu_s(PO_2)$ vibrations were observed to increase for diamond

with respect to silicon. Spectral differences for diamond substrates may be a result of baseline distortion from Mie scattering artefacts, which may arise from incomplete coverage or surface imperfections of the diamond crystal employed for this experiment. Regardless, the novel silicon substrate has demonstrated the capability of detecting biological molecules present in human blood serum, which requires validation with large clinical sample sets to determine whether silicon IRE's may be employed for diagnostic applications.

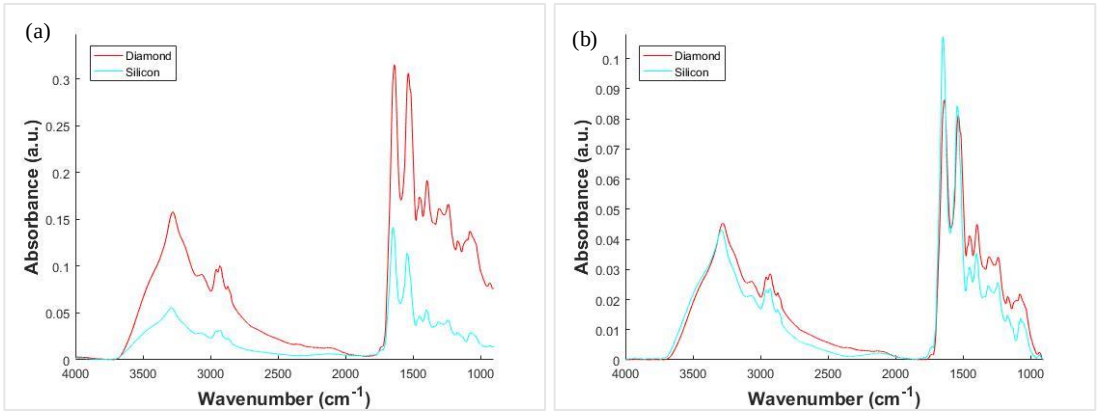


*Figure 3.15: Mean infrared spectra of air-dried human pooled serum from 4000-900cm$^{-1}$ acquired from silicon and diamond substrates (a) with no pre-processing parameters and (b) rubber-band baseline correction and vector normalisation pre-processing methods.*

The PCA plot confirms spectral differences between diamond and silicon substrates, with separation between both data sets deemed statistically significant for PC1 ($t(15) = 34.36$, p-value $<0.05$) but statistically similar for PC2 ($t(13) = 0.13$, p-value $= 0.902$) and PC3 ($t(11) = 0.10$, p-value $= 0.925$) scores. The PC1 loading plot representative of 97.0% of total variance confirms that spectral variation originates from intensity differences of infrared peaks in the fingerprint region as previously described. Additionally, the PC1 loading plot highlights a sharp depression in silicon spectra at

~1110cm$^{-1}$ not evident in diamond spectra, which may be attributed to intrinsic silicon lattice and ν(Si-O-Si) vibrations (Schumacher et al, 2010). Preliminary findings from mean spectra indicate that this spectral artefact does not obscure biological peaks related to human blood serum samples, although the overall shape of the $\nu_s(PO_2)$ band appears more prominent on silicon compared to diamond substrates as a consequence of the spectral distortion.

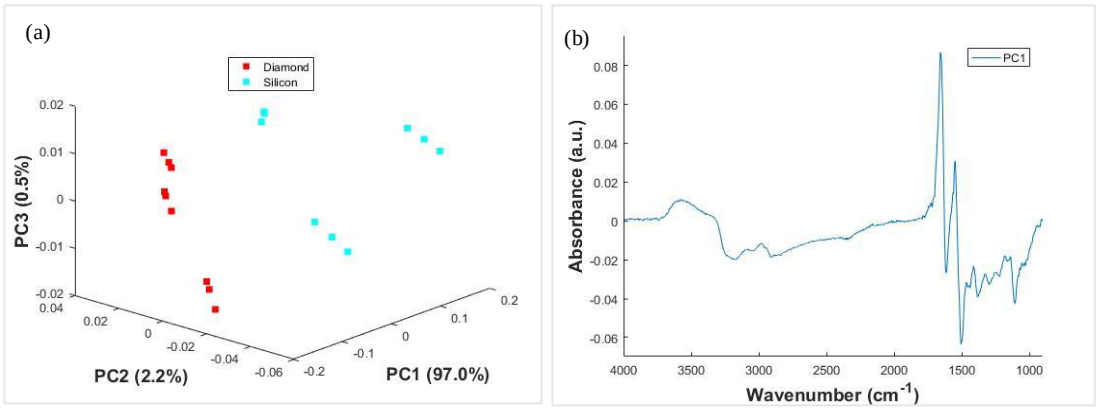


*Figure 3.16: PCA plot of mean infrared spectra of air-dried human pooled serum from 4000-900cm$^{-1}$ acquired from silicon and diamond substrates (a) with rubber-band baseline correction and vector normalisation pre-processing methods and (b) PC1 loading plot from PCA analysis.*

Infrared spectra of dried and wet human serum samples display distinctive spectroscopic patterns, with significantly increased absorption values for amide II, $\nu_s(COO^-)$, $\delta_s(CH_2)$, $\nu_{as}(PO_2)$ and $\nu_s(PO_2)$ peaks for dried spectra. Furthermore, additional infrared peaks emerged in the ~1650cm$^{-1}$ and 2800-3600cm$^{-1}$ regions for dried spectra previously obscured by $\delta_{in\text{-}plane}$(H-O-H) and $\nu_s/\nu_{as}$ (OH) vibrations of water molecules respectively. Specifically, amide I and amide A peaks at ~1650cm$^{-1}$ and 3310-3270cm$^{-1}$ respectively provide significant information on the secondary

structure and hydrogen bonding environment of protein constituents (Barth, 2007), with both peaks of significant clinical importance for disease diagnostics (Tiwari et al, 2016; Bassan et al, 2014; Pilling et al, 2017). Similarly, appearance of infrared peaks at ~2960cm$^{-1}$, ~2930cm$^{-1}$ and 2870cm$^{-1}$ correspond to $\nu_{as}(CH_3)$, $\nu_{as}(CH_2)$ and $\nu_s(CH_2)$ vibrations respectively that provides valuable information on lipid constituents of serum (Baker et al, 2014; Movasaghi et al, 2008) and demonstrate significant clinical importance for cancer diagnostics (Rigas et al, 1990). Hence, employment of infrared spectroscopy for serum sample analysis in the wet state to satisfy the requirements of electrochemistry will undoubtedly result in reduced spectral information pertinent to the classification of biological samples. Therefore, clear clinical benefits of an in situ combined spectroscopic and electrochemical approach must be demonstrated to outweigh the loss of spectral information, otherwise separate consecutive analysis of wet samples for electrochemistry and dry samples for spectroscopy may be preferential to maximise the biological information obtained from infrared spectra.

*3.4.2.3.3 Drying Study*

Drying studies were conducted on silicon and diamond substrates to determine the necessary time required to acquire optimum spectral information from human serum samples. Silicon spectra showed increased absorption of previously assigned biological bands over the entire mid-infrared wavenumber region with incremental reductions in water signatures over time from 0-30 minute time intervals (Figure 3.17a). Spectral features reached maximum absorption at 12 minutes and remained

unchanged over an extended period of time (Figure 3.17b), and, therefore was deemed sufficient to dry human serum samples.

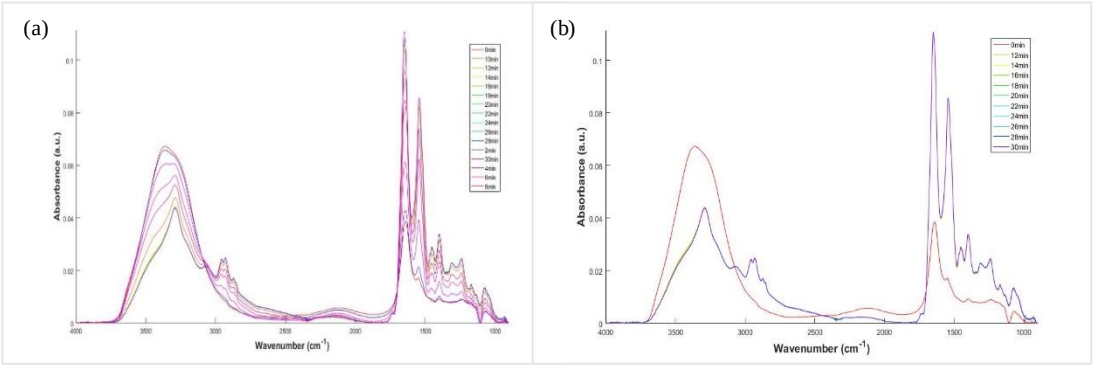


*Figure 3.17: Mean infrared spectra of human pooled serum from 4000-900cm$^{-1}$ with rubber-band baseline correction and vector normalisation pre-processing methods acquired from silicon substrates at (a) time intervals of 0-30 minutes and (b) time intervals of 0 minutes and 12-30 minutes.*

Diamond spectra also showed increased absorption of infrared peaks over time as serum samples dried in air at 0-30 minute time intervals (Figure 3.18a). Diamond spectra were deemed dry for spectroscopic analysis at 18 minutes, with the reduced drying time of silicon in comparison to diamond substrates attributed to the increased surface area of the sensor that allows larger sample volumes to interact with the surrounding environment (Figure 3.18b).

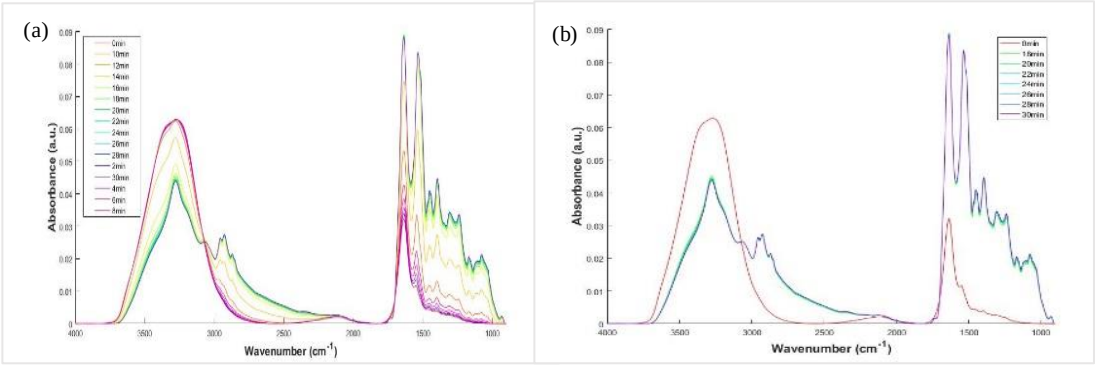


*Figure 3.18: Mean infrared spectra of human pooled serum from 4000-900cm$^{-1}$ with rubber-band baseline correction and vector normalisation pre-processing methods acquired from diamond substrates at (a) time intervals of 0-30 minutes and (b) time intervals of 0 minutes and 18-30 minutes.*

*3.4.2.3.4 Volume Study*

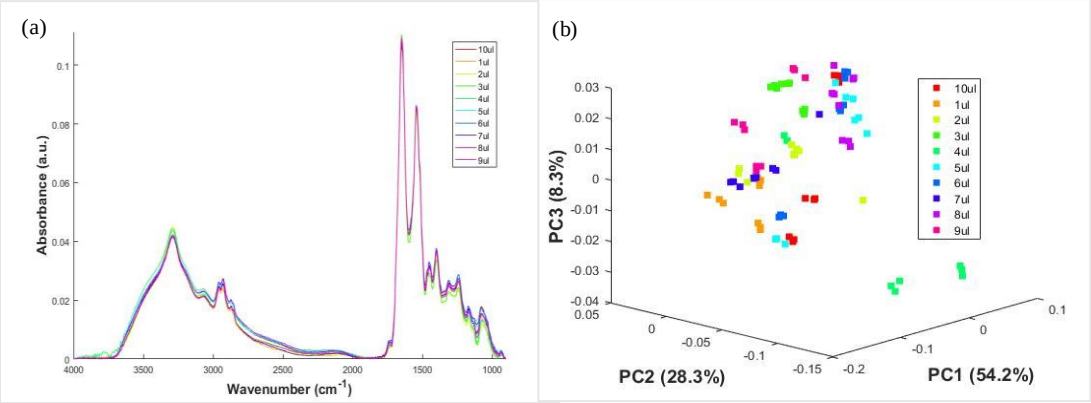


*Figure 3.19: Mean infrared spectra of human pooled serum from 4000-900cm$^{-1}$ with rubber-band baseline correction and vector normalisation pre-processing methods acquired from silicon substrates with (a) 1-10µL sample volumes and (b) PCA plot of described analysis.*

Sample volume studies were conducted on silicon substrates with human serum to assess whether increased quantities of biological molecules on sensor surfaces influenced spectral responses. All sample volumes from 1-10uL were observed to produce consistent infrared spectra characteristic of human pooled serum (Figure 3.19a) provided biological samples fully covered the silicon surface to negate Mie scattering artefacts. Further inspection found 3uL to be the optimum volume as it produced the lowest standard deviation over the infrared spectrum between sample replicates, however, it should be noted that all sample volumes with the exception of 4uL displayed inappreciable standard deviations. PCA scores plot (Figure 3.19b) shows spectral differences between sample volumes, deemed statistically significant for PC1 ($F(9,80) = 35.62$, p-value $< 0.05$), PC2 ($F(9,80) = 12.53$, p-value $< 0.05$) and PC3 ($F(9,80) = 6.96$, p-value $< 0.05$) scores. However, interval and PC1 loading plots, which accounts for 52.4% of total variance, both reveal small differences in absorption

of pertinent biological bands, including amide I, amide II, $\nu_{as}(CH_3)$ and $\nu_{as}(CH_2)$ vibrations, were not correlated to sample volume (Figure 3.20a,b). Furthermore, interval and PC2 loading plots representative of 28.3% of total variance show that spectral differences stemming from the amide A and amide I region along silicon lattice vibrations were not correlated to sample volume (Figure 3.20c,d). Overall, it is reassuring that different sample volumes do not promote considerable biological spectral variation on silicon substrates, and is expected for ATR-FTIR given the depth of penetration of evanescent waves is ~1-2 microns in the fingerprint region (Baker et al, 2014), and therefore unaffected by additional changes in sample thickness.

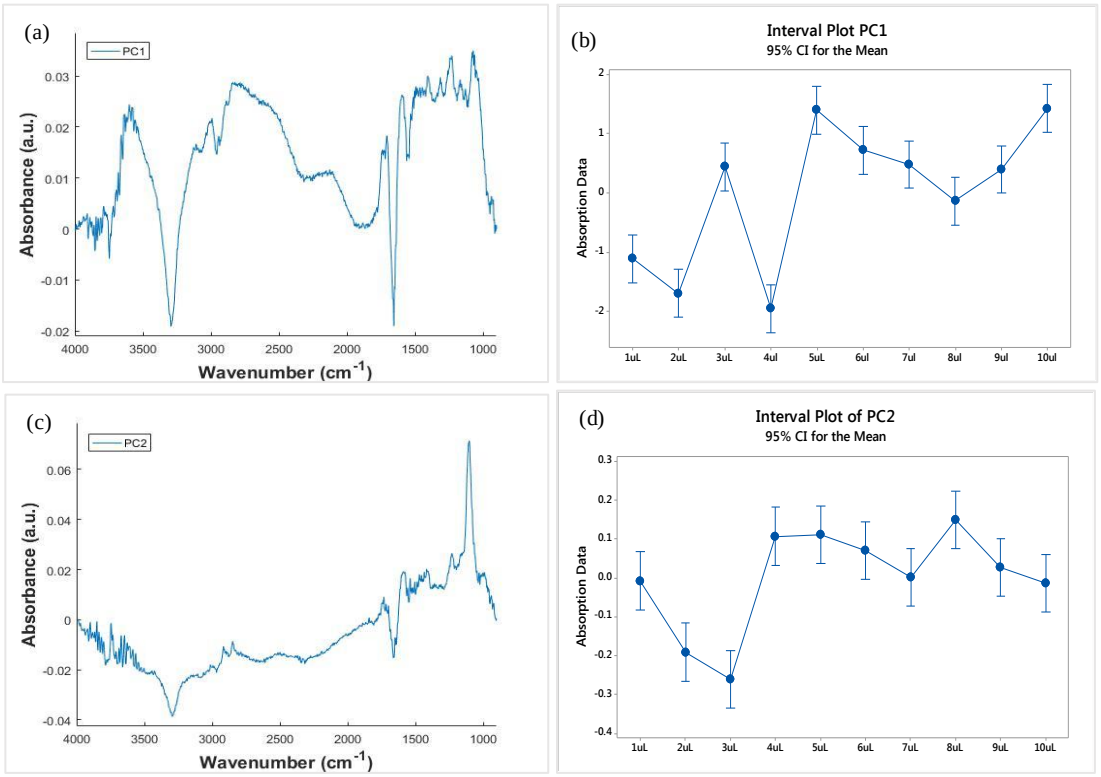


*Figure 3.20: (a) PC1 and (c) PC3 loading plots from PCA analysis of mean infrared spectra of human pooled serum from 4000-900cm$^{-1}$ with rubber-band baseline correction and vector normalisation pre-processing methods acquired from silicon substrates and (b,d) corresponding interval plots showing associated PC scores.*

### *3.4.2 Electrochemical Evaluation of Degenerate P-Type & N-Type Silicon*

#### *3.4.2.1 Testing of $Ru(bpy)_3(PF_6)_2$ Target Molecules*

Different silicon substrates with increased dopant concentrations were evaluated to assess whether respective materials with reduced resistivity were suitable for electrochemical detection of $Ru(bpy)_3(PF_6)_2$ molecules.

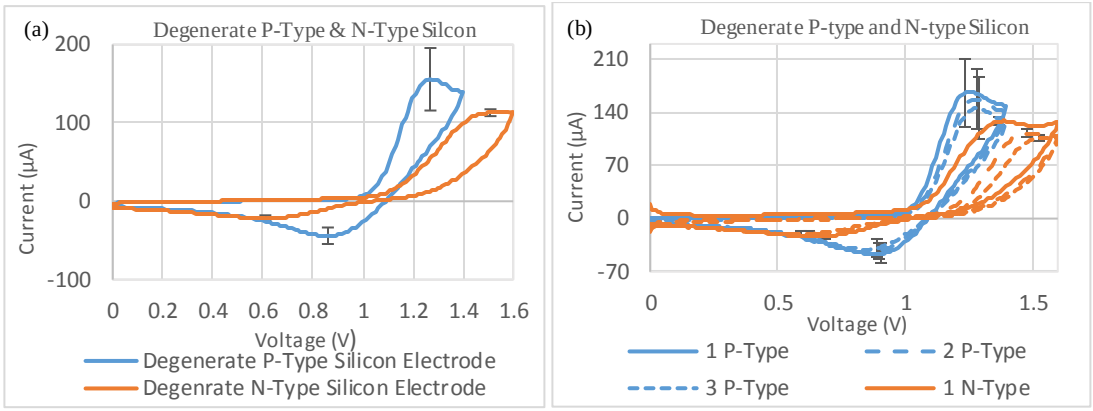


*Figure 3.21: (a) Mean cyclic voltammograms of degenerate P-type and N-type silicon (100) electrodes in $Ru(bpy)_3(PF_6)_2$ + 0.1M PBS and (b) cyclic voltammograms for each scan for degenerate P-type and N-type silicon (100) electrodes in $Ru(bpy)_3(PF_6)_2$ + 0.1M PBS.*

Degenerate silicon (100) P-type and N-type substrates observed one-electron transfer redox reactions characteristic of $Ru(bpy)_3(PF_6)_2$ molecules (Figure 3.21a). Degenerate P-type substrates established oxidation events with $I_{pa}$ = 155.717 ± 39.902µA at $E_{pa}$ = 1.269V and reduction events with $I_{pc}$ = -44.000 ± 10.532µA at $E_{pc}$ = 0.860V. Hence, degenerate P-type substrates produced $I_{pa}/I_{pc}$ = 3.539 and $\Delta E_p$ = 409mV indicative of irreversible electrochemical reactions with slow electron transfer kinetics (Hamman et al, 1998). Whilst responses of degenerate P-type electrodes were poorer compared to conventional carbon electrodes, electrochemical performance was significantly

improved compared to previously tested silicon sensors, due to the substrates increased electrical conductivity. Specifically, doping with trivalent boron acceptor impurities to degenerate levels vastly increases hole populations in silicon crystal lattices, which creates additional energy levels in the valence band and decreases the intrinsic band gap of silicon, ultimately enabling improved transfer of free charge carriers to the conduction band (Li, 2007).

Degenerate N-type substrates identified oxidation events with $I_{pa} = 113.062 \pm 4.384 \mu A$ at $E_{pa} = 1.509V$ and reduction events with $I_{pc} = -21.413 \pm 3.497 \mu A$ at $E_{pc} = 0.610V$. Similarly, degenerate N-type substrates displayed irreversible electrochemical behaviour since $I_{pa}/I_{pc} = 5.280$ and $\Delta E_p = 899mV$. The improved electrochemical behaviour of degenerate N-type substrates in comparison to previously tested silicon electrodes may also be attributed to the substrates increased electrical conductivity. Doping with pentivalent arsenic donor impurities to degenerate levels increases free electron populations in silicon crystal lattices, which consequently produces additional energy levels in the conduction band and reduces the band gap of silicon (Li, 2007). Both degenerate silicon substrates produced higher anodic and cathodic current responses in comparison to previously tested conventional carbon electrodes due to the increased electrode surface area of silicon electrodes, in accordance with the Randles-Sevcik equation (Hamann et al, 1998). Degenerate N-type electrodes observed oxidation events at greater anodic potentials compared to degenerate P-type substrates, which may be attributed to the position of the Fermi level of respective substrates relative to the redox potential of the electro-active species. Specifically, the Fermi level for P-type and N-type silicon substrates reside in close approximation to

the valence and conduction band respectively, and therefore implies that additional energy is required in the form of electrical potentials to equilibrate the Fermi level of N-type silicon with the redox potential of the electro-active species (Rajeshwar, 2007; Zhang, 2001). Interestingly, the performance of both substrates diminished with consecutive repeat measurements for all electrodes (Figure 3.21b), which may be attributed to the depletion layer of semiconductors. Specifically, quantities of free mobile charge carriers become redundant with stationary ionised charge in the space charge region of semiconductors following electrical conductivity, ultimately restricting the supply of free charge carriers to the electrode electrolyte interface (Zhang, 2001). Nevertheless, both substrates displayed significantly improved electrochemical performance compared to previously tested silicon electrodes, and issues regarding repeated long-term measurements is not of paramount importance since electrodes will be incorporated in to a disposable, one-time use diagnostic device. Therefore, future experiments will aim to characterise the performance of degenerate P-type and N-type substrates over a range of analytical parameters when exposed to $Ru(bpy)_3(PF_6)_2$ solutions of different concentrations.

### *3.4.2.2 Varying Scan Rate for Detection of 1mM $Ru(bpy)_3(PF_6)_2$ Molecules*

#### *3.4.2.2.1 Degenerate P-type Silicon Substrates*

Degenerate P-type silicon electrodes displayed strong positive correlations between current responses and the square root of scan rate, with $R^2 = 0.979$ and $R^2 = 0.990$ for $I_{pa}$ and $I_{pc}$ events respectively. Hence, electrodes measured $I_{pa} = 23.537 \pm 1.811\mu A$ and $I_{pc} = -4.961 \pm 0.762\mu A$ for 0.025V/s that increased with applied scan rate and reached

$I_{pa}$ = 178.889 ± 18.204µA and $I_{pc}$ = -45.630 ± 1.633µA for 1.0V/s. Both oxidation and reduction potentials were independent of scan rate at $E_{pa}$ = ~1.300V and $E_{pc}$ = ~0.720V, which indicates that electron transfer events were sufficiently fast such that electrochemical reactions were diffusion limited (Hamann et al, 1998). However, it is evident that kinetics of electron transfer were significantly reduced compared to conventional electrode materials tested previously, given the increased $\Delta E_p$ observed on cyclic voltammograms.

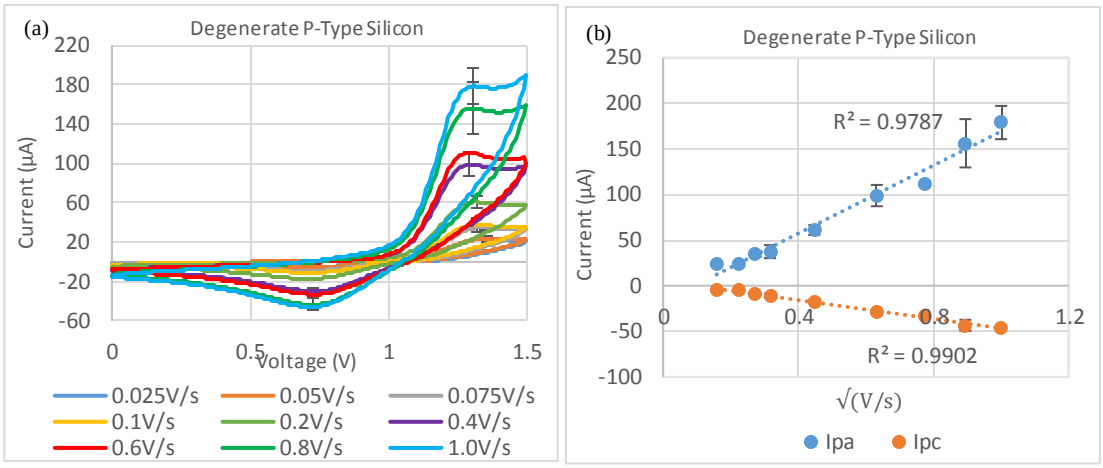


*Figure 3.22: (a) Cyclic voltammograms of degenerate P-type silicon electrodes subjected to varying scan rates from 0.025-1.0V/s in $Ru(bpy)_3(PF_6)_2$ + 0.1M PBS and (b) plots of peak current versus square root of scan rate for both oxidation and reduction currents for degenerate P-type silicon electrodes.*

### *3.4.2.2.2 Degenerate N-type Silicon Substrates*

Degenerate N-type silicon electrodes displayed weak positive correlations between current responses and the square root of scan rate, for $I_{pa}$ with $R^2$ = 0.968 and $I_{pc}$ with $R^2$ = 0.944 (Figure 3.23b). Consequently, electrodes recorded Ipa = 11.001 ± 5.729µA and $I_{pc}$ = -1.273 ± 1.340µA for 0.025V/s that increased proportionally with applied

scan rate to $I_{pa}$ = 239.490 ± 72.055µA and $I_{pc}$ = -36.332 ± 10.822µA for 1.0V/s (Figure 3.23a). Peak-to-peak potential separations were not observed to increase with scan rate and remained predominantly unchanged at Epa = ~1.540-1.560V and Epc = ~0.370-0.440V, which similar to p-type silicon substrates indicates that electrochemical reactions were diffusion limited (Hamann et al, 1998). However, $\Delta E_p$ was larger for degenerate N-type substrates in comparison to degenerate P-type substrates, which implies slower electron transfer events at the electrode interface (Zhang, 2001).

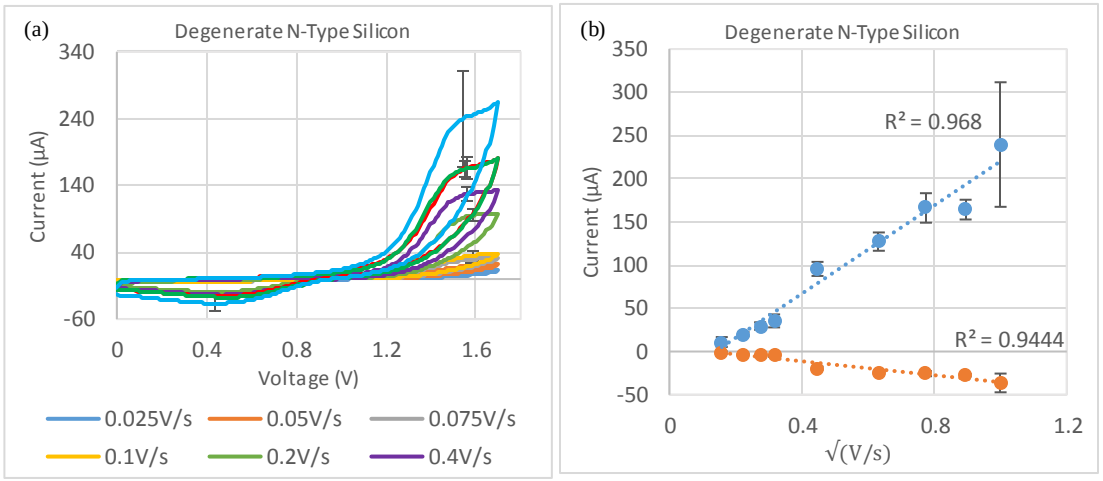


*Figure 3.23: (a) Cyclic voltammograms of degenerate N-type silicon electrodes subjected to varying scan rates from 0.025-1.0V/s in $Ru(bpy)_3(PF_6)_2$ + 0.1M PBS and (b) plots of peak current versus square root of scan rate for both oxidation and reduction currents for degenerate P-type silicon electrodes.*

### *3.4.2.3 Concentration study for Detection of $Ru(bpy)_3(PF_6)_2$ Molecules*

#### *3.4.2.3.1 Cyclic Voltammetry of Degenerate P-Type Silicon*

Degenerate P-type silicon substrates successfully identified the target redox couple from 1mM down to 0.05mM concentrations. Electrode current responses were

proportional to concentration with a strong positive linear relationship between concentration and current, for both $I_{pa}$ and $I_{pc}$ redox events at $R^2 = 0.982$ and $R^2 = 0.991$ respectively. Electrode behaviour is in agreement with theoretical expectations since the Randles-Sevcik equation states that measured current is directly proportional to species concentration and diffusion co-efficient of the species. Furthermore, mass transport of target molecules to the electrode in the case of unstirred solutions relies on diffusion, which is dependent on analyte concentration, in accordance with Fick's second law of diffusion. Significant standard deviations of peak oxidation currents may be attributed to the reduced substrate performance between repeat measurements as previously described and to manual cutting of electrodes resulting in deviations in electrode surface areas.

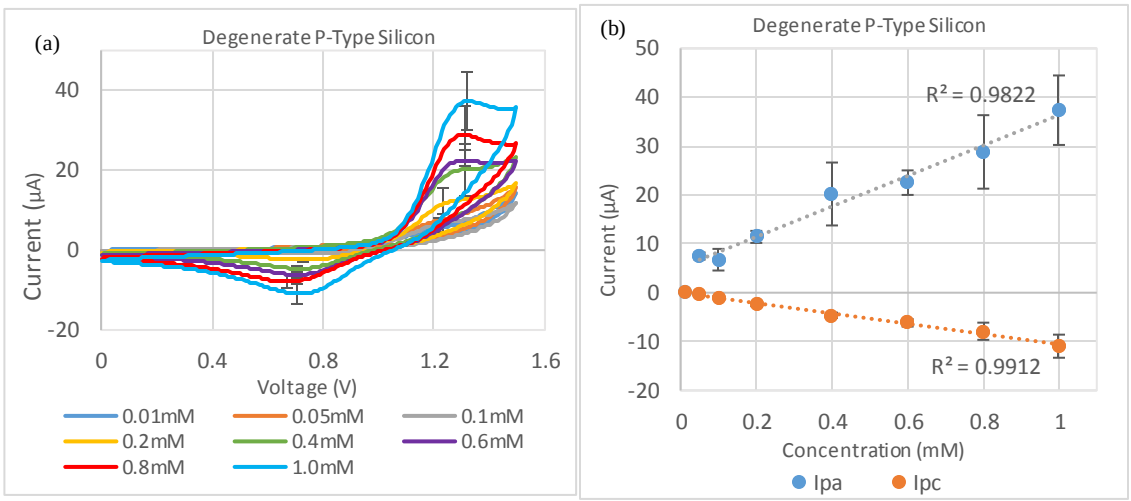


*Figure 3.24: (a) Concentration study of degenerate P-type electrodes in $Ru(bpy)_3(PF_6)_2$ + 0.1M PBS at 0.01-1.0mM concentrations and (b) plot of peak oxidation and reduction currents versus concentration of $Ru(bpy)_3(PF_6)_2$ + 0.1M PBS.*

*3.4.2.3.2 Cyclic Voltammetry of Degenerate N-Type Silicon*

Degenerate N-type silicon substrates characterised $Ru(bpy)_3(PF_6)_2$ species from 1mM to 0.1mM concentrations (Figure 3.25a,b). Electrodes were similarly observed to exhibit strong positive linear relationships between current and detectable concentrations, with $R^2 = 0.990$ and $R^2 = 0.984$ for $I_{pa}$ and $I_{pc}$ respectively. Degenerate N-type electrodes displayed poorer detection capabilities with a limit of detection of 0.1mM compared to 0.05mM for degenerate P-type substrates. Reduced performance of degenerate N-type silicon in detection of $I_{pa}$ currents may be understood with consideration of concentrations of surface charges and the position of the Fermi level of respective substrates relative to the energy levels of redox species. The probability of substrates favouring a particular charge transfer process is determined by their proximity to the redox energy levels of species. For P-type silicon, the Fermi level is located at the valence band and the surface concentration of hole majority carrier increases at positive potentials. Conversely, the Fermi level is located at the conduction band for N-type silicon and surface concentration of electron majority charge carriers decreases with increasingly positive potentials. Hence, the increased current response for P-type substrates implies that the Fermi level of P-type silicon is closer aligned to oxidation energy levels of $Ru(bpy)_3(PF_6)_2$ species. Consequently, charge transfer is observed to improve for P-type substrates and makes sense given that the surface concentration of majority charge carriers is greater for P-type silicon in comparison to N-type silicon at the applied potential.

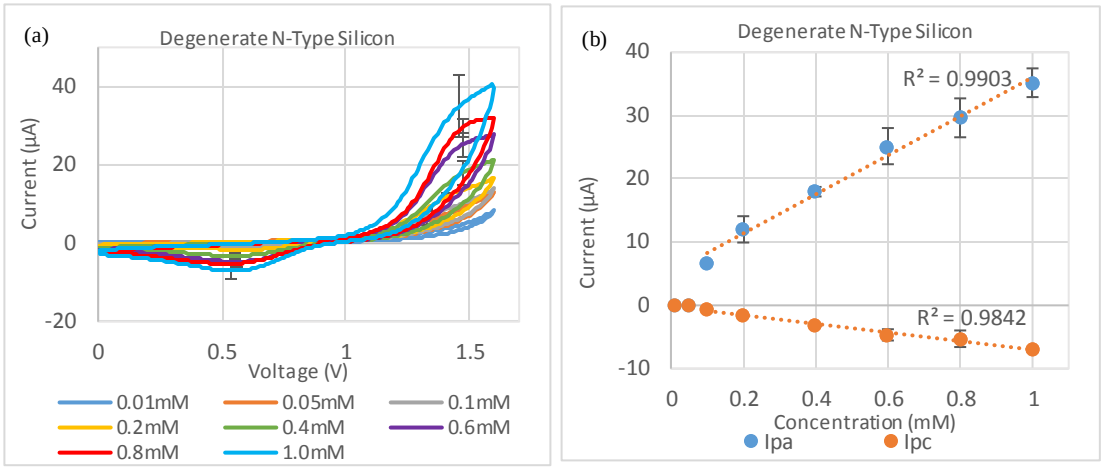


*Figure 3.25: (a) Concentration study of degenerate N-type electrodes in $Ru(bpy)_3(PF_6)_2$ + 0.1M PBS at 0.01-1.0mM concentrations and (b) plot of peak oxidation and reduction currents versus concentration of $Ru(bpy)_3(PF_6)_2$ + 0.1M PBS*

### *3.4.2.3.3 Differential Pulsed Voltammetry of Degenerate P-Type Silicon*

Differential pulsed voltammetry was employed with degenerate silicon substrates to further evaluate detection capabilities of electrodes and to assess whether smaller concentrations may be identified given the increased sensitivity of the technique (Scholz, 2015). Indeed, degenerate P-type electrodes observed oxidation events down to 0.01mM concentrations, lower than cyclic voltammetry results at 0.05mM (Figure 29a,b). Improved electrode responses reflect the nature of the technique where subtraction of currents measured at two potential pulse intervals negates capacitive currents that often obscure faradaic currents at low concentrations with cyclic voltammetry (Scholz, 2015). However, whilst current responses were proportional to concentration, electrodes were associated with poor linearity, $R^2$ = 0.870, and significant relative standard deviations, that ranged from 17.1-57.4% with a mean relative standard deviation of 43.7% across all electrodes. Significant standard deviations of peak oxidation currents may be attributed to poor substrate performance

between repeat measurements and deviations in electrode surface areas due to manual cutting procedures. Therefore, degenerate P-type electrodes were not deemed suitable for quantitative analysis of $Ru(bpy)_3(PF_6)_2$ despite significantly improved performance compared to original silicon electrodes.

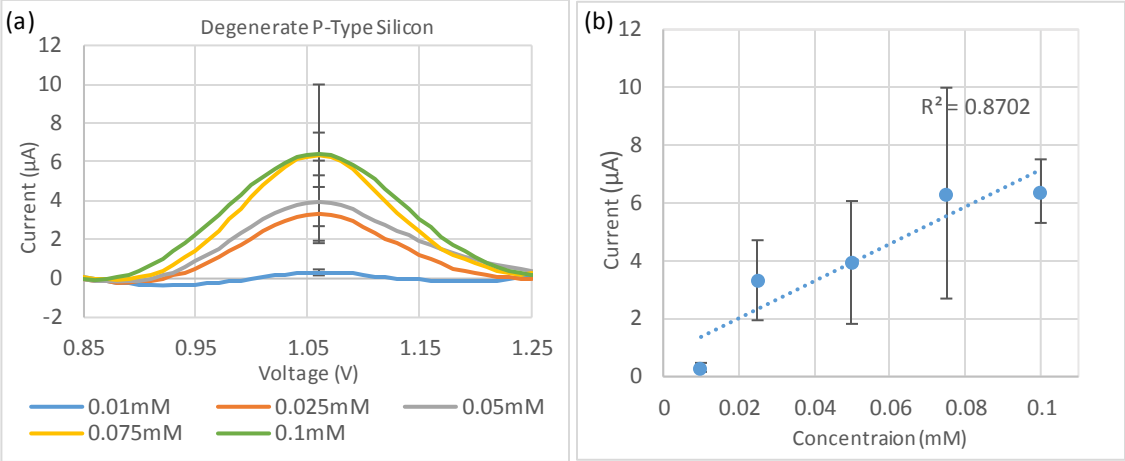


*Figure 3.26: (a) Differential pulse voltammetry results for degenerate P-type electrodes at 0.01-0.1mM concentrations of $Ru(bpy)_3(PF_6)_2$ + 0.1M PBS and (b) plot of peak oxidation current versus concentration of $Ru(bpy)_3(PF_6)_2$.*

### *3.4.2.3.4 Differential Pulsed Voltammetry of Degenerate N-Type Silicon*

Degenerate N-type silicon substrates identified $Ru(bpy)_3(PF_6)_2$ target molecules down to 0.025mM concentrations, with a strong positive correlation between current responses and concentration, $R^2 = 0.978$. Whilst electrode performance significantly improved compared to previous cyclic voltammetry results at 0.1mM, high standard deviations of acquired results ultimately makes substrates inadequate for quantitative detection of $Ru(bpy)_3(PF_6)_2$ redox species.

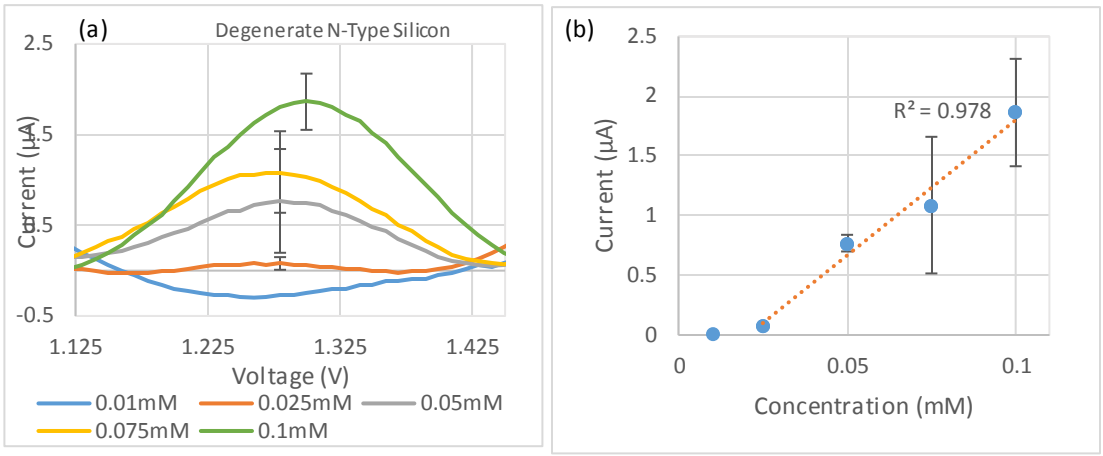


*Figure 3.27: (a) Differential pulse voltammetry results for degenerate N-type electrodes at 0.01-0.1mM concentrations of $Ru(bpy)_3(PF_6)_2$ + 0.1M PBS and (b) plot of peak oxidation current versus concentration of $Ru(bpy)_3(PF_6)_2$.*

### *3.4.3 ATR-FTIR Evaluation of Degenerate P-Type & N-Type Silicon*

Degenerate silicon (100) P-type and N-type substrates were unable to identify absorption peaks characteristic of serum samples in either dry or wet states and instead produced noise over the entire mid-infrared region (Figure 31a,b). Stotter previously found that increases in boron dopant concentrations to degenerate levels (~10x10^19 B/cm$^3$) for boron-doped diamond films on silicon significantly reduced the optical transparency of substrates to 0-10% over the entire mid-infrared region (Stotter et al, 2003). Specifically, it was found that reductions in optical transparency were due to increased absorption of dopant atoms and boron centre one-phonon transitions that arised from the presence of acceptor impurities in crystal lattice structures (Stotter et al, 2003). Sobaszek further demonstrated that increased dopant concentrations of boron-doped diamond films on silicon caused significant reductions in the refractive index of the material at higher wavelengths on spectra, resulting in subsequent

decreases in the infrared transparency of substrates (Sobaszek et al, 2015). Thus, it can be conjectured that the introduction of degenerate dopant concentrations to silicon substrates results in insufficient optical transparency to perform spectroscopic analysis on dried and wet serum in the mid-infrared region.

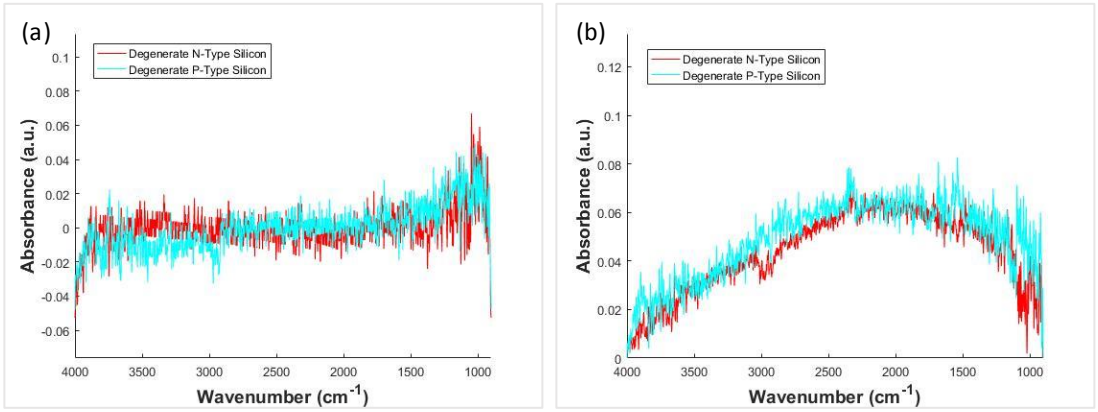


*Figure 3.28: Mean infrared spectra of human pooled serum in (a) dry and (b) wet states acquired with degenerate N-type and P-type silicon substrates.*

### *3.4.4 Evaluation of Sputtered Gold Film Silicon Substrates*

#### *3.4.4.1 Electrochemical Evaluation of 1mM $Ru(bpy)_3(PF_6)_2$ Molecules*

Silicon substrates sputtered with gold depositions of 5-200nm thickness were unable to detect redox peaks of $Ru(bpy)_3(PF_6)_2$ molecules. Instead, silicon substrates oxidised the gold deposited surfaces at high electrical potentials >1.0V with visible removal of the gold layer, evident from Figure 32b. Gold silicon substrates further identified one reduction peak at ~0.4V consistent with the reduction of gold oxide at substrate surfaces. Furthermore, the measured peaks were observed to increase with deposition thickness and traces varied significantly between repeat measurements, confirming

that electrochemical behaviour was inconsistent and correlated to the redox states of gold and removal of deposited layers from substrates surfaces. Hence, sputtered gold silicon substrates were unsuitable for detection of target $Ru(bpy)_3(PF_6)_2$ molecules due to the poor adhesion of gold thin films to silicon surfaces. The observed electrochemical behaviour is consistent with literature findings where previous studies recognise the poor adhesive qualities of gold thin films to silicon substrates when applied with physical vapour deposition techniques (Miyake et al, 2002; Ataka et al, 2007). Generally, gold is recognised to exhibit poor adhesion to silicon oxides and adhesion layers of either titanium or chromium should first be deposited to form an intermediate bond with silicon dioxide, to which gold forms a stable metallic bond with improved adhesion (Matarese et al, 2018). However, the use of an adhesion layer would significantly reduce the optical transparency of substrates for spectroscopic analysis. Interestingly, Miyake suggests, in the absence of an adhesion layer, gold adhesion to silicon may be significantly improved either through chemical deposition methods or pre-treatment of silicon substrates with hydrofluoric acid where hydrogen termination of the silicon surface allows silicide to be established between gold and silicon layers (Miyake et al, 2002).

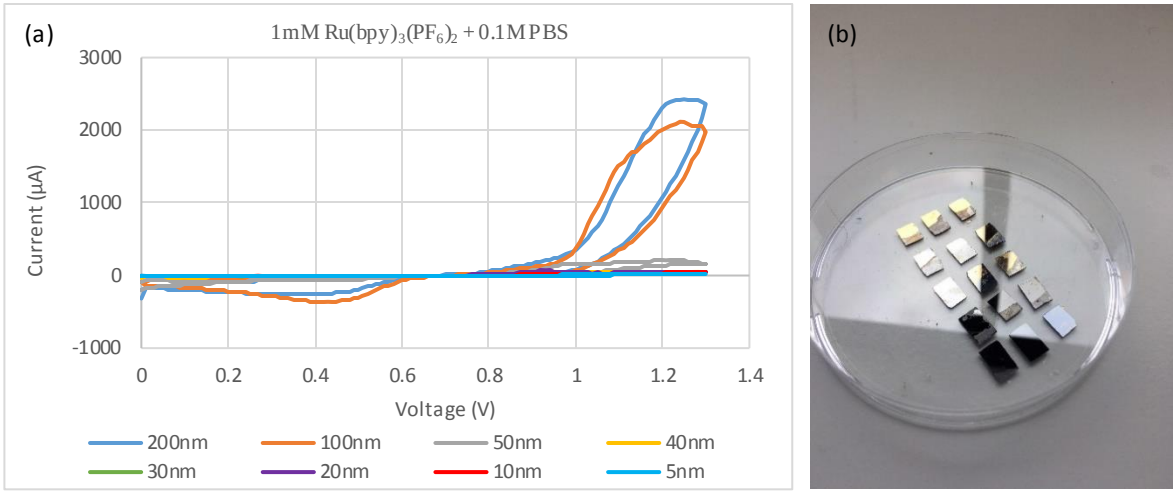


*Figure 3.29: (a) Cyclic voltammograms of silicon electrodes with different thicknesses of gold depositions from 5-200nm and (b) corresponding picture of silicon substrates following analysis showing removal of gold film.*

### *3.4.4.2 Electrochemical Evaluation of 10mM $K_3[Fe(CN)_6]^{-3/4}$ Molecules*

Gold thin film silicon substrates of different deposition thicknesses were evaluated for electrochemical detection of $K_3[Fe(CN)_6]^{-3/4}$ molecules to observe whether the application of lower electrical potentials would prevent delamination of gold from silicon surfaces. Electrochemical detection of 10mM $K_3[Fe(CN)_6]^{-3/4}$ molecules strongly depends on the film thickness of sputtered gold-silicon substrates (Figure 33a,b). Gold 200nm deposited electrodes measured greatest $I_{pa}$ and $I_{pc}$ responses characteristic of the one-electron transfer reversible redox reaction of $K_3[Fe(CN)_6]^{-3/4}$ species, significantly greater than 100nm thick depositions for both $I_{pa}$ ($t(12) = 2.46$, p-value $< 0.05$) and $I_{pc}$ ($t(10) = 2.84$, p-value $< 0.05$) events. Electrochemical behaviour markedly decreased with further reductions in gold deposition thickness, with reduced $I_{pa}$ ($t(13) = -6.65$, p-value $< 0.05$) and $I_{pc}$ ($t(12) = 13.37$, p-value $< 0.05$) responses for 50nm gold-silicon substrates. Similarly, electrode current responses were significantly different between 40nm, 30nm and 20nm substrates, with consecutive decreases in $I_{pa}$

(F(2,24) = 66.12, p-value < 0.05) and $I_{pc}$ (F(2,24) = 53.47, p-value < 0.05) as a function of film thickness. Further decreases in thickness prompted dramatic reductions in current intensities of both $I_{pa}$ (t(8) = 91.69, p-value < 0.05) and $I_{pc}$ (t(8) = -57.06, p-value < 0.05) events for 10nm gold-silicon substrates. Additionally, redox peaks narrowed in width for 10nm films whilst $E_{pa}$ = 0.360V and $E_{pc}$ = 0.180V remained consistent with 50-20nm substrates at $E_{pa}$ = 0.340-0.350V and $E_{pc}$ = 0.200-0.190V, indicative of diffusion differences at electrode surfaces. Specifically, 10nm gold films described mixed diffusion regimes with planar diffusion consistent with macro-electrodes and hemispherical diffusion contributions akin to microelectrodes, consistent with gold surfaces that feature micrometer dimensions (Hood et al, 2009). Thereafter, 5nm thick gold-silicon electrodes were unable to reproducibly detect oxidation or any reduction reactions from $K_3[Fe(CN)_6]^{-3/4}$ molecules.

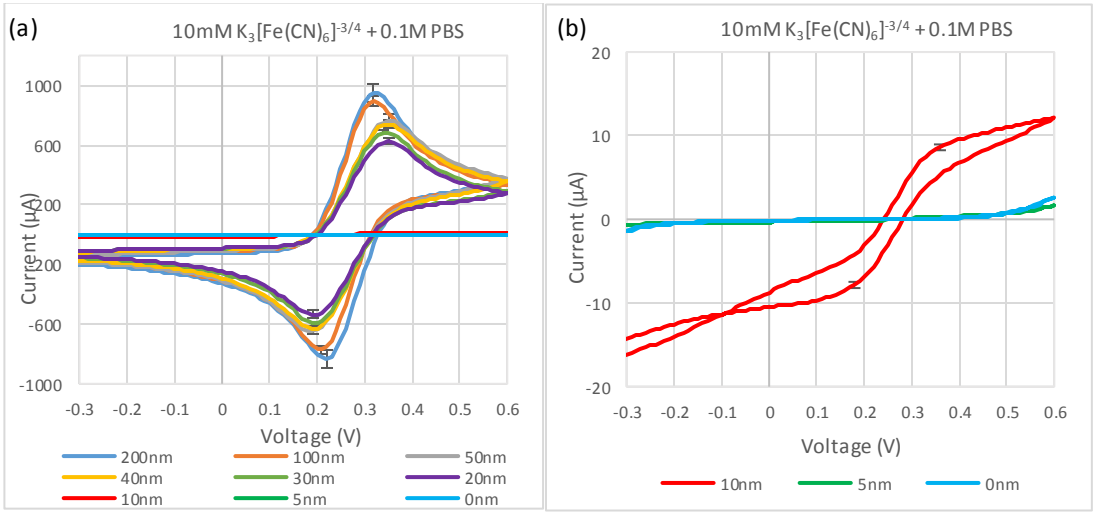


*Figure 3.30: (a) Cyclic voltammograms of silicon substrates sputtered with gold of 200-5nm thicknesses and tested in 10mM $K_3[Fe(CN)_6]^{-3/4}$ + 0.1M PBS (b) Inset of previous cyclic voltamogramms for silicon gold electrodes of 10-0nm thickness.*

Electrode observations reflect the growth stages of gold particles during depositions that directly influence electrical properties of fabricated thin-films. Gold atoms

condense on substrates to form individual nuclei that multiply and grow with sustained diffusion from continued sputtering (Smith et al, 1986). Prolonged nucleation of gold particles causes coalescence and the formation of metal islands on silicon surfaces, recognised to occur at depositions ≤5nm thickness (Smith et al, 1986). Hence, the significantly poor electrode behaviour of our 5nm thin-films may be attributed to discontinuous gold particles on silicon, which produces high sheet resistance and poor electrical conductivity (Svorcik et al, 2002). Subsequently, further coalescence promotes the transition from isolated metal islands to integrated metal structures with morphologies representative of inhomogeneous continuous metal films, previously reported at ≤10nm thickness (Smith et al, 1986; Svorcik et al, 2002). Svorcik found a dramatic change in sheet resistance of gold and significantly improved electrical conductivity at the transition between formation of a discontinuous and continuous thin-film, consistent with our observed results for 10nm thickness, albeit at an increased thickness compared to those reported by Svorcik (Svorcik et al, 2002). Similarly, dramatic increases in electrical conductivity for our 20nm gold-silicon electrodes may be attributed to additional coalescence during sputtering, which promotes formation of increasingly homogenous, continuous gold layers previously reported at ~15-20nm thickness (Smith et al, 1986; Yakubovsky et al, 2017). Electrical conductivity of thin-films is proportional to mean free path length that describes electron mobility through the conductive layer. The mean free path length increases with grain size of thin-films until characteristic of the bulk metal and the grain size increases with deposition thickness (Wanarattikan et al, 2019). Hence, further improved electrochemical behaviour of 30-200nm thick substrates may be attributed to morphologies of electrode surfaces where the increased grain size reduces electron

scattering and increases the mean free path length, ultimately improving electrical conductivity (Gould, 2006). Gradual increases in electrical conductivity observed for 30-200nm gold-silicon substrates were consistent with previously reported electrochemical behaviour in literature where upon the formation of a continuous thin-film sheet resistance decreases slowly until characteristic of bulk properties (Svorcik et al, 2002).

*3.4.4.3 ATR-FTIR Evaluation of Human Pooled Blood Serum*

Gold thin film silicon substrates of different deposition thicknesses were evaluated for spectroscopic characterisation of human pooled serum samples. Rubber-band baseline corrected mean spectra showed reduced absorption of biological peaks of human serum for sputtered gold thin-film substrates of all nominal thicknesses compared to diamond and uncoated silicon IRE's (Figure 35a). Specifically, amide I peak intensities decreased for gold 5nm thick deposits to 0.09846 ± 0.0261 AU compared to 0.11063 ± 0.00693 AU for silicon substrates, although intensities were not statistically different ($t(9) = 1.35$, p-value = 0.209), whilst 10nm depositions at 0.01217 ± 0.00295 AU were statistically different to bare silicon ($t(10) = 39.22$, p-value < 0.05). Gold depositions of 20-200nm nominal thickness were unable to identify any biological bands characteristic of human serum. Therefore, sputtered 5-10nm thick gold substrates were found to display a degree of optical transparency in the mid-infrared region, whilst ≥20nm thick depositions did not permit sufficient transmission of evanescent waves to identify sample components.

Vector normalised mean spectra further demonstrates optical transparency for 5-10nm gold-silicon substrates in comparison to silicon and diamond crystals, whilst depositions $\geq$ 20nm were omitted due to noise contributions accentuated by vector normalisation methods (Figure 34b). Gold 5-10nm thin-films produced significant Mie resonance scattering artefacts attributed to the surface morphologies of films, described in detail later. Nevertheless, both substrates successfully identified absorption bands characteristic of human serum over the entire mid-infrared wavenumber region. The PCA plot shows weak clustering between diamond, silicon, 5nm and 10nm gold-silicon substrates, albeit with significantly different PC1 ($F(3, 32) = 203.04$, p-value $< 0.05$), PC2 ($F(3,32) = 23.51$, p-value $< 0.05$) and PC3 ($F(3,32) = 113.84$, p-value $< 0.05$) scores. The PC1 loading plot, representative of 58.2% of total variance, indicates weak clustering of these substrates arises from the ability to detect absorption bands in the fingerprint region, particularly amide I, amide II and $\nu_s(COO)$ vibrations. Similarly, the PC2 loading plot, which accounts for 20.0% of total variance, reveals spectral variance originates from amide I, amide II, $\nu_s(COO)$ and $\nu_{as}(PO_2)$ vibrations in the fingerprint region and amide A, $\nu_{s/as}(CH_2)$ and $\nu_{as}(CH_3)$ vibrations in the 4000-2800cm$^{-1}$ region.

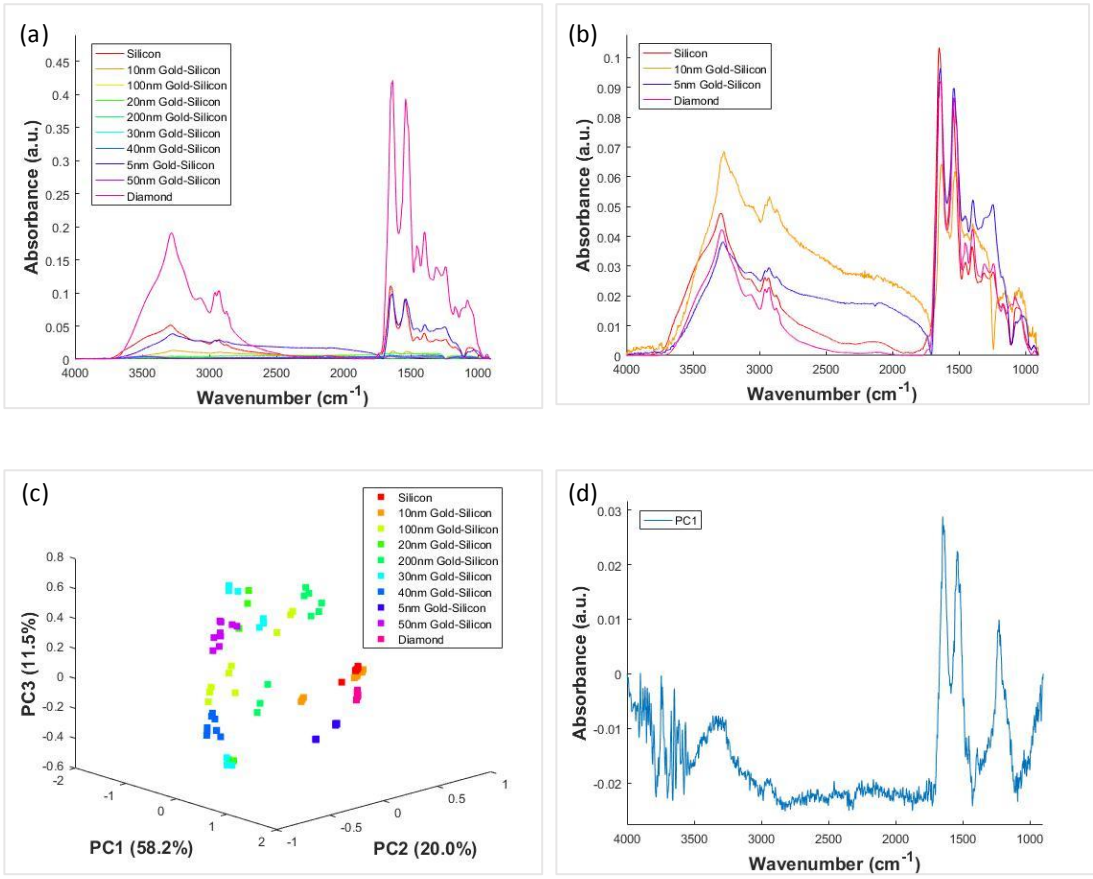


*Figure 3.31: (a) Infrared spectra of pooled blood serum for silicon gold substrates of different gold depositions of 200-5nm thickness along with silicon and diamond substrates with spectra baseline corrected (b) baseline corrected and vector normalised. Only 10-5nm gold silicon, silicon and diamond substrates have been shown due to noise (c) PCA plot of baseline corrected and vector normalised spectra and (d) associated PC1 loading plot describing spectral variance.*

Spectral observations reflect the growth stages of gold particles during film formation as previously described that directly influence the optical properties of thin-films. In particular, the complex refractive index, N, of gold is affected by deposition thickness and may be characterised by the real component, n, and imaginary extinction co-efficient, $k$.

$$N = n + ik \qquad \text{(eq 3.1)}$$

The real component, n, and extinction co-efficient, $k$, decrease and increase at wavelengths $\lambda \geq$ 0.5-0.7μm respectively as a function of film thickness, until representative of bulk gold (Smith et al, 1986; Yakubovsky et al, 2017). The extinction co-efficient represents the degree of light absorption by a material at a given wavelength and increased absorption with film thickness correlates with experimental findings and the significantly reduced transmission observed at ≥20nm thickness. Furthermore, reflectance of light, $R$, at the boundary between a non-absorbing material with refractive index, $n_0$, and absorbing thin-film is influenced by previously specified optical constants, $n_1$, and $k_1$, of the material for a given wavelength of light.

$$R = \frac{(n_0 - n_1)^2 + k_1^2}{(n_0 + n_1)^2 + k_1^2} \qquad \text{(eq 3.2)}$$

Therefore, reflectance of infrared light at the thin-film interface increases with deposition thickness, given that $n_1$ decreases and $k_1$ increases with film thickness until characteristic of bulk gold properties. Consequently, thin-films of increased thickness are associated with reduced transmission of infrared light, given that total energy of incident electromagnetic radiation, $I_0$, must equal the sum of absorption, $I_A$, reflectance, $I_R$, and transmission, $I_T$, of electromagnetic radiation, in accordance with energy conservation (Axelevitch et al, 2012).

$$I_0 = I_A + I_R + I_T \qquad \text{(eq 3.3)}$$

Experimental findings were consistent with theoretical predictions since transmission of mid-infrared light decreased with consecutive increases in film thickness, with significant reductions in transmission observed for depositions $\geq$ 20nm thickness. However, our results contradict some previous literature findings that demonstrate optical transparency of gold thin-films in the mid-infrared region at greater deposition thicknesses. In particular, Ataka found that biological spectra of protein monolayers could be detected using silicon hemispherical crystals coated with 10-200nm thick gold films (Ataka, 2013). Similarly, Zaitseva performed spectroscopic analysis on protein monolayers with gold films and found that optical transparency only reduced by 30% in the mid-infrared region for fabricated gold-silicon substrates, which according to the methodology equated to ~50nm average thickness (Zaitseva et al, 2010; Miyake et al, 2002). Both Ataka and Zaitseva employed electroless chemical deposition methods to fabricate gold thin-films where gold nano-particle plating solutions contact hydrogen terminated silicon substrates for 60-90 seconds to form gold island films (Miyake, 2002). Delgado found that electroless chemically prepared films had larger grain sizes in comparison to sputtered gold layers (Delgado et al, 2008), whilst Miyake found electroless deposited layers were discontinuous with prominent metal island structures (Miyake et al, 2002). Hence, discrepancies in results from such literature findings may be explained by different surface morphologies arising from contrasting deposition methods, which is recognised to strongly influence optical properties of gold thin-films (Kossoy et al, 2014).

*3.4.4.4. Reflectance Spectroscopy*

Gold thin film substrates were previously found to be reflective at ≥ 20nm thickness and therefore poses the question whether it would be beneficial to conduct spectral analysis in reflectance mode given the markedly improved electrochemical performance observed with increased deposition thickness.

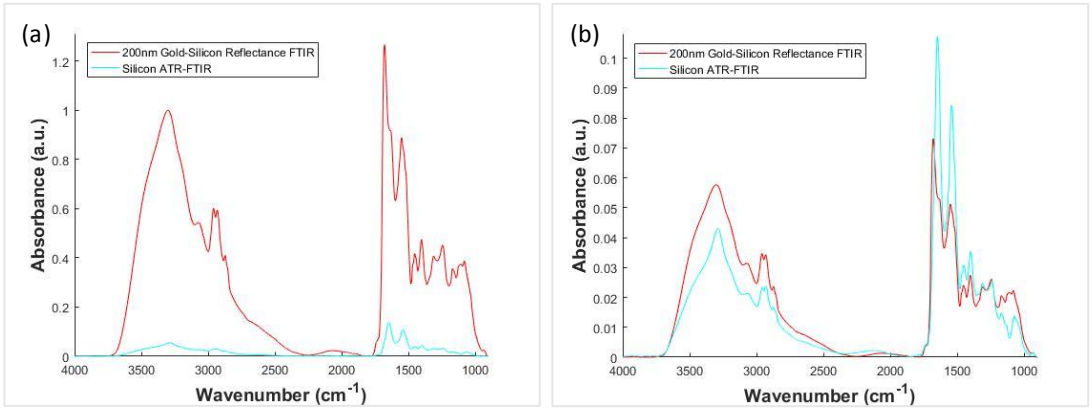


*Figure 3.32: (a) Comparison of mean infrared spectra of pooled human serum with ATR-FTIR and reflectance FTIR spectroscopy with baseline correction pre-processing and (b) baseline correction and vector normalisation pre-processing steps.*

Rubber-band baseline corrected spectra of human pooled serum for silicon and gold silicon substrates highlights the significant difference in absorbance of infrared light by molecules when subjected to reflectance FTIR and ATR-FTIR analysis. Increased absorption of infrared light by molecules for reflectance FTIR measurements may be attributed to the significantly longer sample path length, where the incident infrared beam travels through the sample thickness, reflects off the gold surface and travels back through the sample before reaching the detector. Conversely, ATR-FTIR interrogates the sample surface where the evanescent waves have a penetration depth of 1 to 2 microns in the fingerprint region (Baker et al, 2014). Vector normalisation of spectra reveals significant differences between spectral signatures of human pooled

serum for reflectance FTIR and ATR-FTIR techniques. Specifically, reflectance FTIR spectra shows accentuation of high wavenumber regions in comparison to ATR-FTIR spectra as a consequence of the electric standing wave effect observed at the gold surface (Mayerhofer et al, 2018).

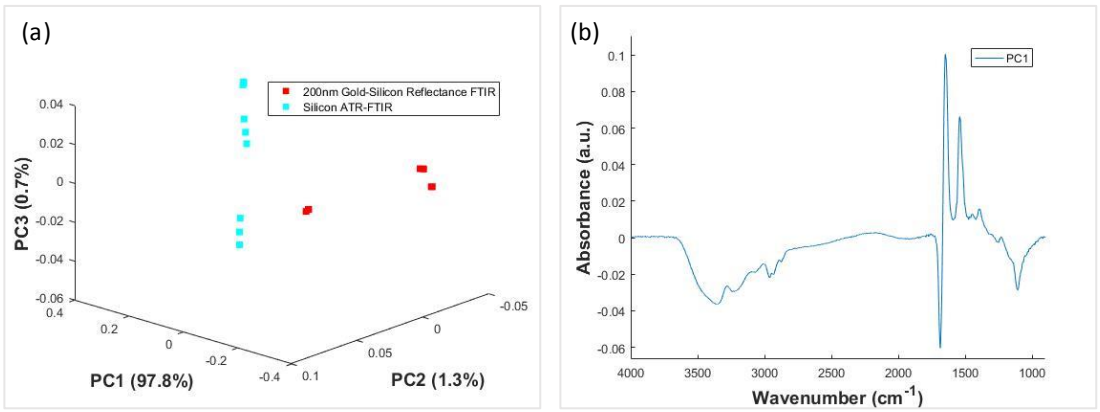


*Figure 3.33: (a) PCA plot of mean infrared spectra of human pooled serum obtained with ATR-FTIR and reflectance FTIR spectroscopy and (b) corresponding PC1 loading plot.*

### *3.4.5 Evaluation of Hydrogen Terminated Annealed Evaporated Gold Coated Silicon*

#### *3.4.5.1 SEM & Energy Dispersive X-Ray (EDX) Spectroscopy*

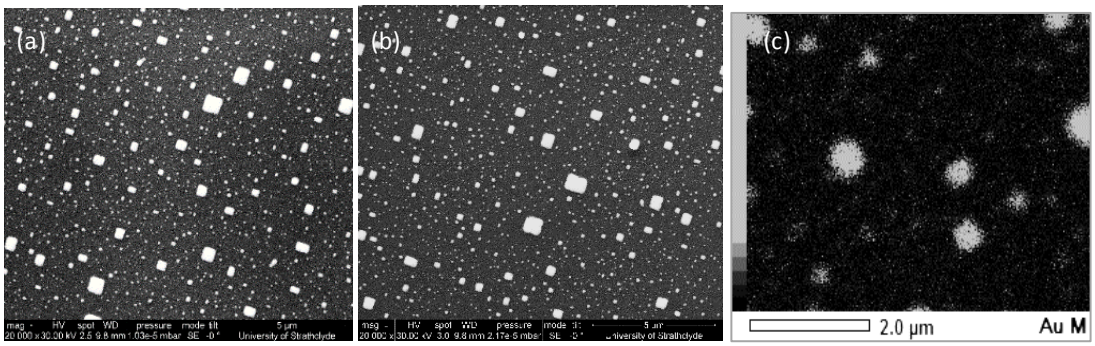


*Figure 3.34: (a,b) SEM and (c) EDX images of fabricated gold silicon fabricated substrates*

Inspection of gold thin film silicon substrates reveals inhomogeneous surface morphologies with gold particles of different grain sizes deposited on silicon. The thin

film microstructure depicts gold hillocks amongst gold particles of smaller grain sizes consistent with high evaporation rates and thermal annealing procedures employed during film formation. The presence of gold hillocks indicates possible gold island formation on silicon substrates that would explain the mixed diffusion regimes and significant optical transparency observed for electrochemistry and ATR-FTIR studies respectively described in detail below. EDX measurements confirm particles constitute gold elements given strong X-ray emissions at ~2.2eV and weak X-ray emissions at ~9.7eV represent characteristic energies of M and L lines of gold atoms and is consistent with previous literature findings (Rajarathinam et al, 2012). Similarly, strong X-ray emissions at ~1.7eV represent energies associated with silicon K lines and is consistent with previous studies reported in the literature (Baldwin et al, 2005). Interestingly, intensities of X-ray emissions are proportional to quantities of atomic elements found in samples, thereby indicating high levels of gold particles present on silicon substrates.

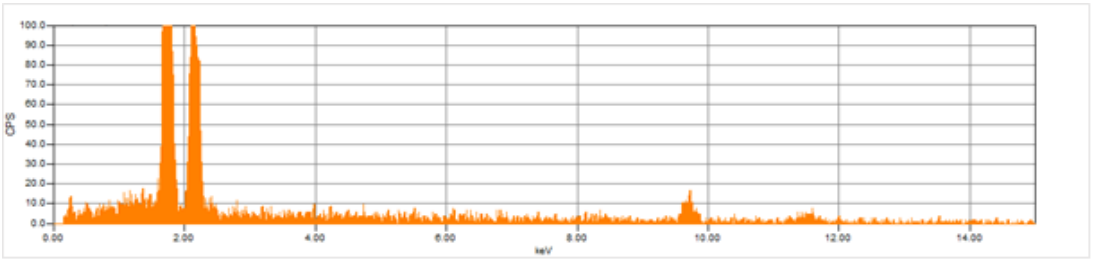


*Figure 3.35: EDX spectra of the top surface of fabricated gold-silicon components*

### *3.4.5.2 Atomic Force Microscopy (AFM) Analysis*

AFM inspection of gold thin film silicon substrates further confirms the presence of gold hillocks and particles of various grain sizes that correlates with previous SEM

and EDX findings. Topographical analysis of three randomly selected areas on a silicon gold substrate provided root mean square roughness, Rq, values of 23.85nm, 16.36nm and 18.91nm. Additionally, surface profiles indicate that gold hillocks have peak heights of 76.90nm, 90.79nm and 91.03nm respectively and vary considerably in width up to ~1.3µm maximally. Interestingly, topographical analysis also revealed areas of substrates with minimal gold coverage, depicted in purple below, which suggests surface morphologies of gold thin films are inhomogeneous and to a certain extent discontinuous in places.

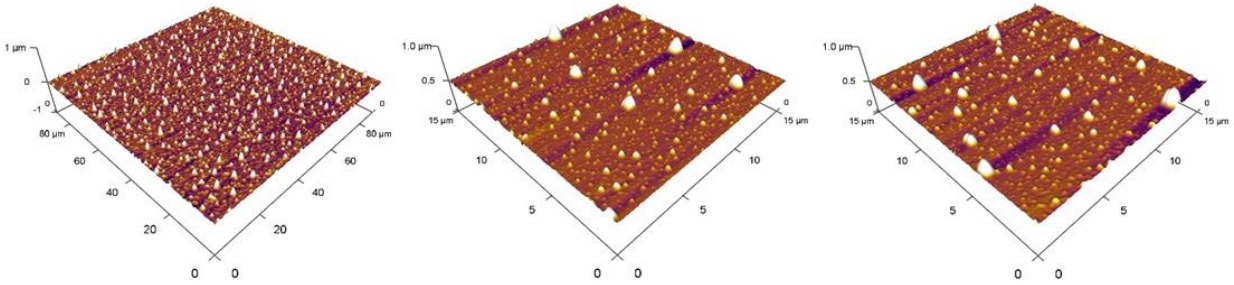

*Figure 3.36: Atomic force microscopy images of* three randomly selected areas on a fabricated silicon gold substrate.

### *3.4.5.3 Electrochemical Evaluation of Standard Redox-Active Target Molecules*

Gold silicon substrates were electrochemically evaluated with $K_3[Fe(CN)_6]^{-3/4}$ and $Ru(bpy)_3(PF_6)_2$ solutions to allow comparison of electrode performance to previously tested substrates. Gold silicon electrodes successfully identified $K_3[Fe(CN)_6]^{-3/4}$ molecules with oxidation and reduction events at $E_{pa}$ = 0.629V and $E_{pc}$ = 0.060V, where increased $\Delta E_p$ = 569mV indicates substantially slower electron transfer kinetics compared to traditional gold macro and screen-printed electrodes. However, peak current intensities improved in comparison to previously sputtered 10nm thick gold

thin film electrodes, likely due to thermal annealing procedures where heat treatment is recognised to increase particle grain sizes and therefore reduce grain boundaries, ultimately enhancing electrical properties of thin films (Wißmann et al, 2007). Gold silicon electrodes also successfully identified $Ru(bpy)_3(PF_6)_2$ molecules with redox peaks at $E_{pa}$ = 1.239-1.379V and $E_{pc}$ = 0.856-0.880V, with a similarly increased $\Delta E_p$ = 383-499mV compared to conventional electrodes. Furthermore, gold evaporated layers remained intact following electrochemical detection of $Ru(bpy)_3(PF_6)_2$ molecules in contrast to previously sputtered gold films that detached from silicon substrates when subjected to formal potentials of $Ru(bpy)_3(PF_6)_2$ molecules. Interestingly, removal of native silicon dioxide layer have been recognised to improve adhesion of gold particles to silicon due to the weak interaction between gold and silicon oxides (Wasserman et al, 1989). This is likely a contributory factor to the improved adhesion observed for evaporated films, since silicon substrates were pre-treated with buffered oxide etchant to remove silicon dioxide layers unlike previously sputtered films that were subjected to Piranha cleaning methods. Furthermore, thermal annealing procedures also significantly contribute to improved film adhesion where thermal heat treatment promotes interstitial mixing of gold atoms in to silicon lattices, and also increases the mechanical strength of gold films (Ghorbanpour et al, 2013). Lastly, overall electrode responses correlate with previously sputtered electrodes of similar deposition thickness and may be assigned to diffusion profiles at electrode surfaces discussed in detail below.

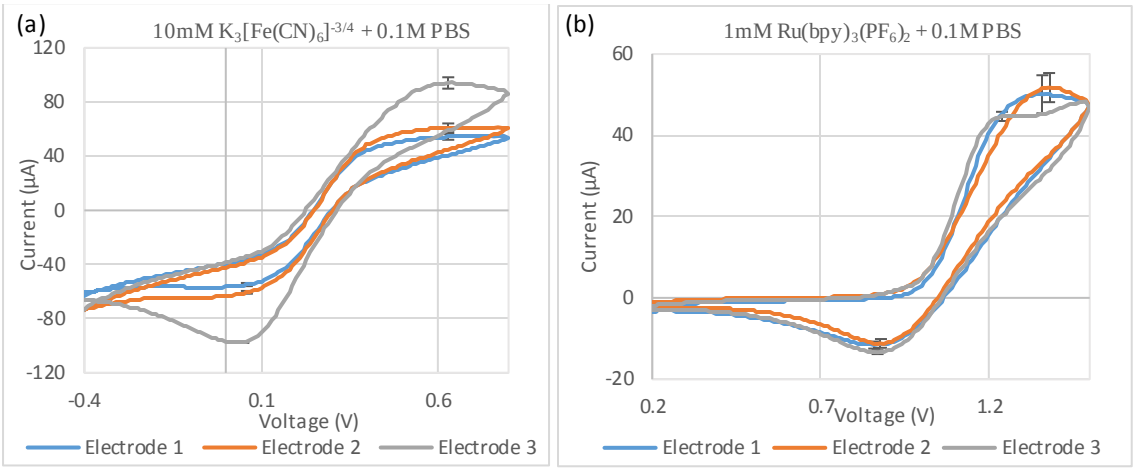


*Figure 3.37: (a) Cyclic voltammograms of $K_3[Fe(CN)_6]^{-3/4}$ + 0.1M PBS and (b) $Ru(bpy)_3(PF_6)_2$ + 0.1M PBS measured with three different fabricated silicon gold electrodes.*

### *3.4.5.4 Further Scan Rate Investigations to Establish Electrode Responses*

Cyclic voltammetry experiments were conducted over a wide range of scan rates to evaluate diffusion at gold silicon surfaces and validate electrochemical behaviour of electrodes. Both redox peaks were observed to increase from $I_{pa}$ = 16.028 ± 1.652µA and $I_{pc}$ = -15.958 ± 0.570µA at 10mV/s to $I_{pa}$ = 30.606 ± 1.636µA and $I_{pc}$ = -30.714 ± 0.147µA at 1V/s, which confirms the presence of planar diffusion at electrode surfaces, since strictly hemi-spherical diffusion regimes typical of microelectrodes produce steady-state current responses independent of specified scan rates (Wang, 2006). However, distinctive sigmoidal shapes of redox peaks do not reflect planar diffusion at electrode surfaces, instead indicative of increased mass transport of electro-active species to gold silicon substrates and the presence of hemi-spherical diffusion contributions. Consideration of AFM and SEM images reveal a multitude of gold hillocks that have increased perimeter-to-surface areas on electrode surfaces that would facilitate radial diffusion profiles and enhance mass transport of redox species

at edges of deposited particles. Indeed, electrochemical behaviour is consistent with previous literature findings that state the presence of mixed diffusion regimes at electrode surfaces with contributions from planar and hemi-spherical diffusion profiles (Simm et al, 2005; Wadhawan et al, 2003; Nirmaier et al, 2005).

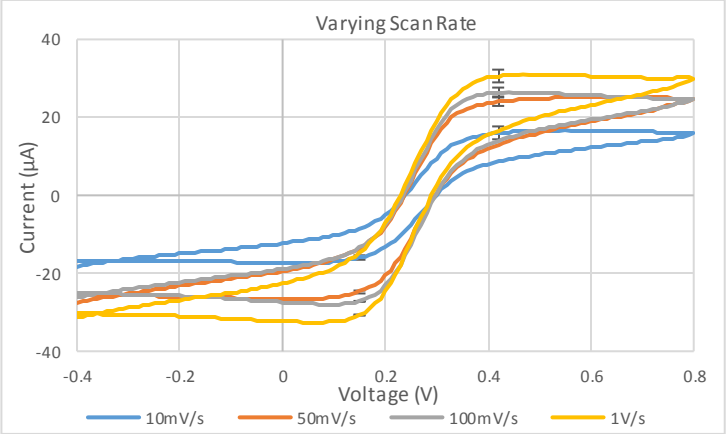


*Figure 3.38: Cyclic voltammograms of $K_3[Fe(CN)_6]^{-3/4}$ + 0.1M PBS measured with fabricated gold silicon electrodes over a range of scan rates.*

### *3.4.5.5 Application of Annealed Gold Silicon Electrode for Biomarker Detection*

Gold thin-film silicon electrodes were employed for detection of redox-active pyocyanin molecules to assess whether fabricated substrates had the capability to detect a clinical biomarker at biologically relevant concentrations. Pyocyanin is a virulence factor metabolite secreted exclusively by the gram-negative bacteria Pseudomonas aeruginosa responsible for a wide range of clinical infections, such as blood (Webster et al, 2014), wound (Muller et al, 2009) and lung infections of cystic fibrosis patients (Caldwell et al, 2009). Electrochemical pyocyanin detection would enable translation from high-performance liquid chromatography analysis of microbacterial isolates cultured over extended periods of time to real time point-of-

care testing, whilst spectroscopic analysis would facilitate further identification of additional biomolecular signatures indicative of pseudomonas aeruginosa infections.

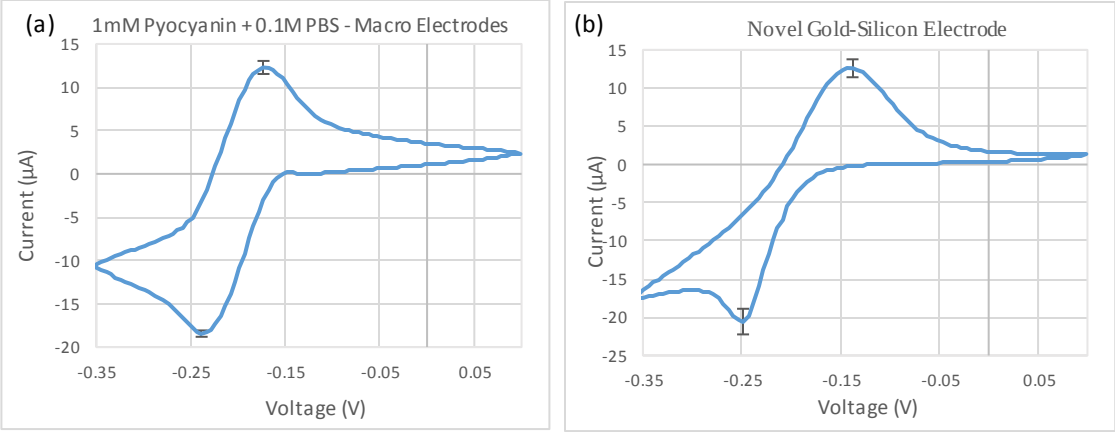


*Figure 3.39: Cyclic voltammetry of 1mM pyocyanin + 0.1M PBS for (a) gold macro disc and (b) novel gold-silicon electrodes.*

Gold-silicon electrodes identified the two-electron reversible redox reaction characteristic of pyocyanin whilst the irreversible phenolic oxidation of pyocyanin at increased positive potentials was not studied in this experiment (). Gold-silicon electrodes observed oxidised and reduced pyocyanin species with $I_{pa}$ = 13.7 ± 1.43 µA at $E_{pa}$ = -0.138V and $I_{pc}$ = -11.9 ± 1.63 µA at $E_{pc}$ = -0.249V respectively, consistent with previous studies reported at $E_{pa}$ = -0.18-0.20V and $E_{pc}$ = -0.20-0.25V (Sharp et al, 2010; Burkitt et al, 2017; Oziat et al, 2017). Gold-silicon electrodes displayed quasi-reversible chemical and electrochemical behaviour since $I_{pa}/I_{pc}$ = 1.15 and $\Delta E_p$ = 55.5mV, greater than theoretical $\Delta E_p$ = 28.5mV for a two-electron transfer reversible reaction at 25°C (Elgrishi et al, 2017). Conversely, gold macro disc electrodes displayed chemically and electrochemically reversible behaviour given that measured redox events of $I_{pa}$ = 12.5 ± 0.945 µA at $E_{pa}$ = -0.173V and $I_{pc}$ = -12.3 ± 0.715 µA at $E_{pc}$ = -0.239V resulted in $I_{pa}/I_{pc}$ = 1.02 and $\Delta E_p$ = 33.0mV. The reduced $I_{pa}/I_{pc}$ for gold-silicon electrodes may be attributed to the poorly defined reduction peak, whilst the

increase in $\Delta E_p$ further suggests the presence of slower electron transfer kinetics at the electrode surface as previously described.

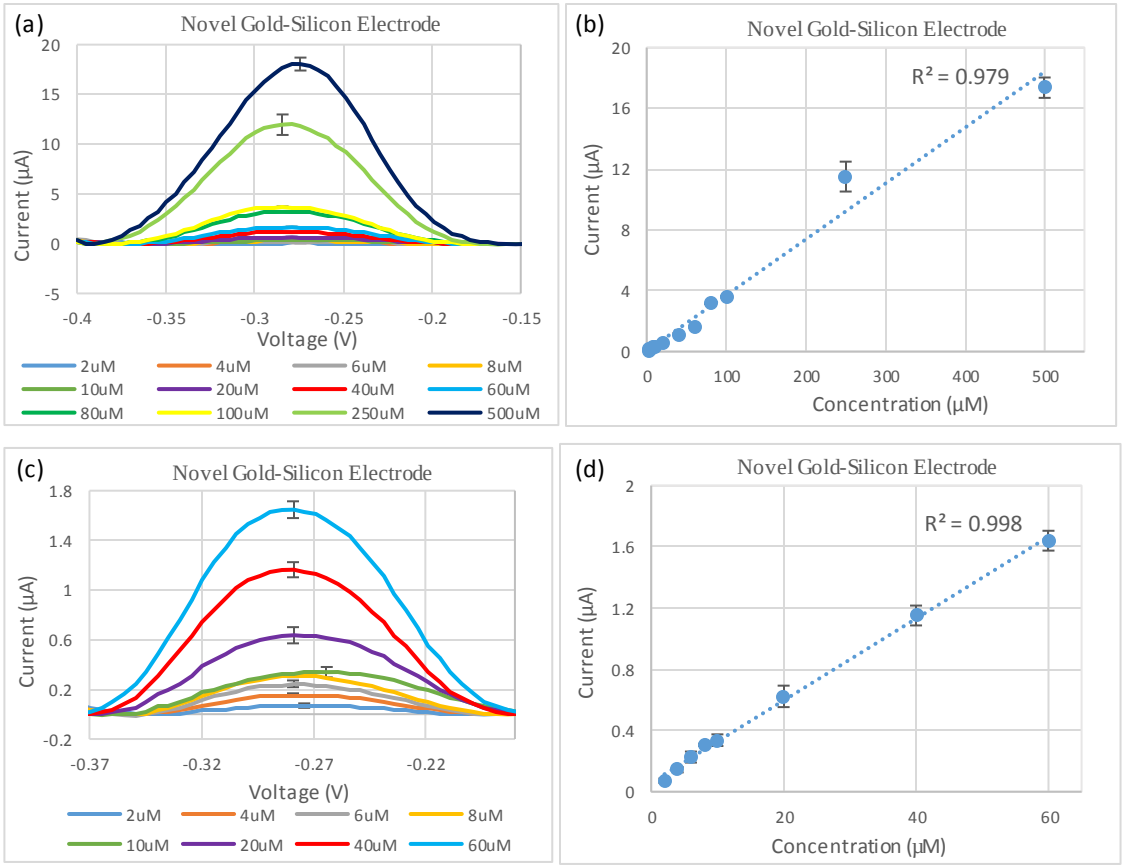


*Figure 3.40: (a,b) Differential pulsed voltammetry concentration studies showing oxidation of 500-2µM Pyocyanin + 0.1M PBS and (c,d) 60-2µM Pyocyanin + 0.1M PBS.*

Gold-silicon electrodes subjected to differential pulsed voltammetry measurements successfully identified oxidation of pyocyanin at $E_{pa}$ = -0.274-0.284V for 500-2µM concentrations (Figure 44a), with a strong positive correlation between current responses and concentration, $R^2$ = 0.979 (Figure 44b). Gold-silicon electrodes demonstrated enhanced quantification at 2-60µM concentrations with an improved linearity of $R^2$ = 0.998 (Figure 44c,d) comparable to previous reported literature

findings on paper-based carbon, conventional carbon and carbon-fibre electrodes (Alatraktchi et al, 2018, Webster et al, 2014, Sharp et al, 2010). Gold-silicon electrodes performed comparably to conventional macro gold electrodes that displayed identical experimental limits of detection of 2µM and similar linearity of $R^2$ = 0.976 (Figure 46). However, the average standard deviation for all concentrations was significantly higher for gold-silicon electrodes at 0.172µA compared to macro electrodes at 0.038µA, which may be attributed to differences in the surface topologies of evaporated gold layers and dimensions of silicon substrates given the manual dicing of silicon wafers.

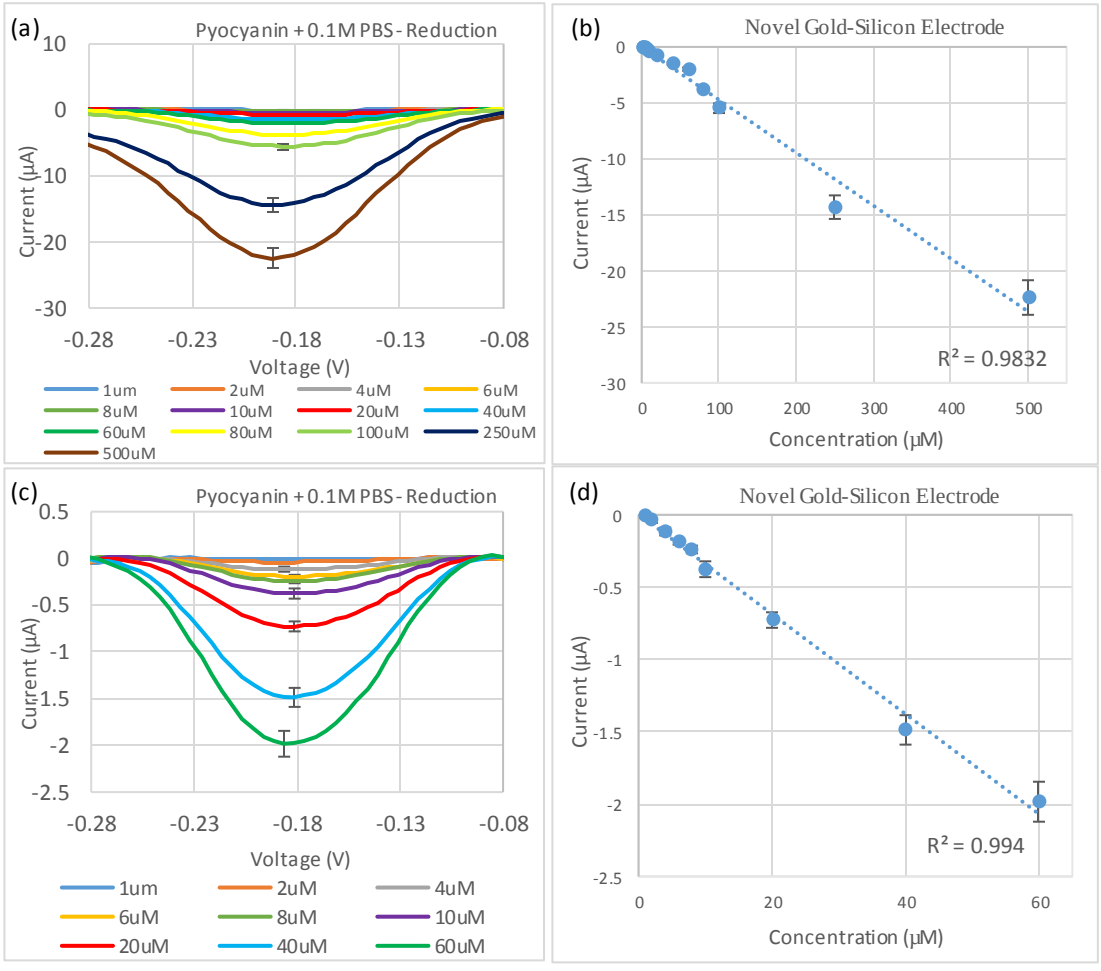


*Figure 3.41: (a,b) Differential pulsed voltammetry concentration studies showing reduction of 500-2µM Pyocyanin + 0.1M PBS and (c,d) 60-2µM Pyocyanin + 0.1M PBS.*

Gold-silicon electrodes showed quantification of reduced pyocyanin species at $E_{pc}$ = 0.181-0.191V for 1-500µM concentrations (Figure 45a), with a strong positive correlation for current responses over the specified concentration range, $R^2$ = 0.983 (Figure 45b). Gold-silicon electrodes performed better at 1-60µM concentrations with $R^2$ = 0.994, identical to conventional gold macro electrodes that displayed linearity of $R^2$ = 0.994 (Figure 45c). Additionally, the average standard deviation for gold-silicon electrodes of ± 0.281µA for all specified concentrations compare favourably to ± 0.596µA for conventional macro electrodes. Both electrode types displayed improved experimental limits of detection for $I_{pc}$ of pyocyanin samples at 1µM, which implies that the target molecule is easier to reduce than oxidise on electrode surfaces, evident from previous cyclic voltammetry experiments and literature findings (Alatraktchi et al, 2016). Overall, gold-silicon electrodes limit of detection of 1µM is applicable to clinical translation with pyocyanin concentrations of 0.95-123 µM reported for sputum from cystic fibrosis and bronchiectasis patients (Wilson et al, 1988), and typically below 10µM for wound infections (Hall et al, 2016). Therefore, gold-silicon electrodes have demonstrated significant capabilities for electrochemical detection of clinically relevant redox-active biomarkers, and further validated the performance of evaporated gold thin-film silicon electrodes.

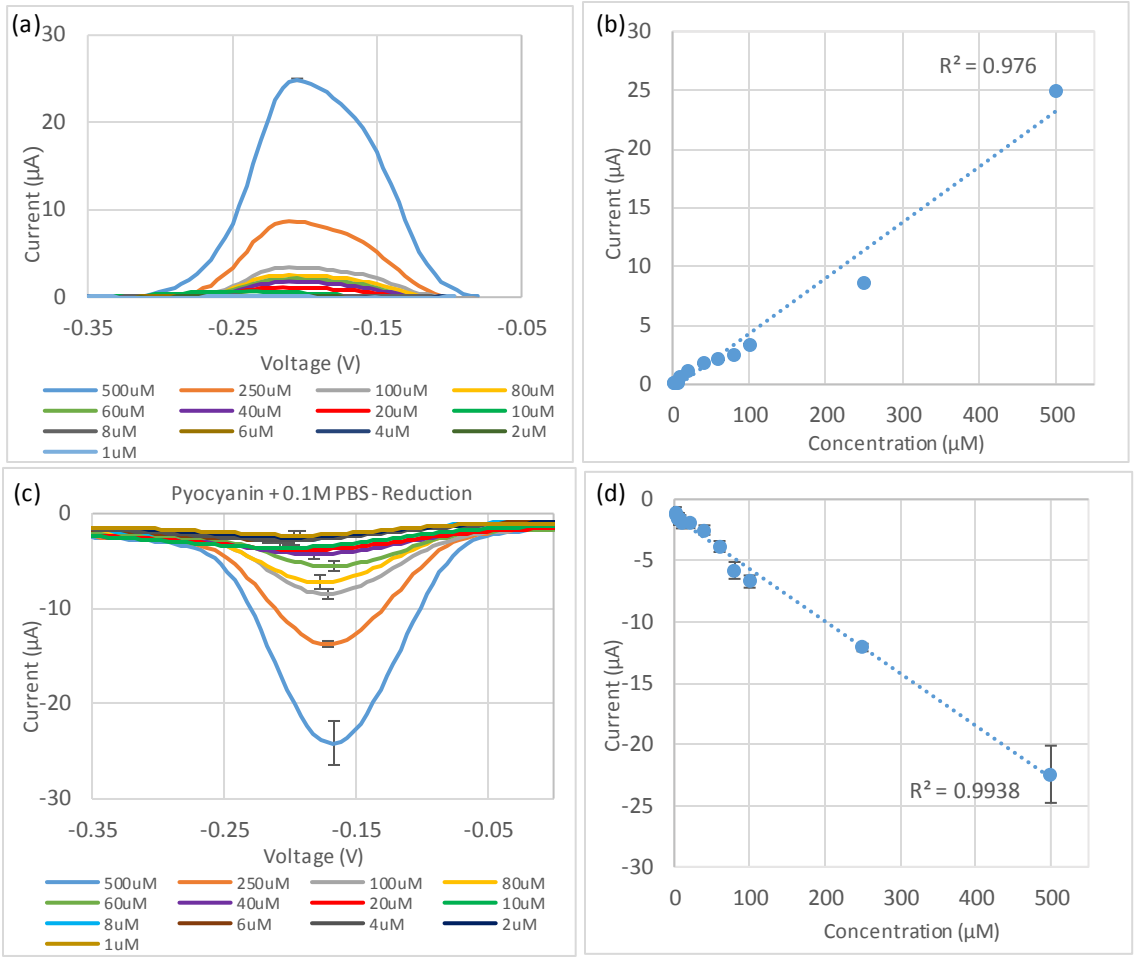


*Figure 3.42: (a,b) Differential pulsed voltammetry concentration studies showing (a,b) oxidation and (c,d) reduction of 500-2µM Pyocyanin + 0.1M PBS on macro gold disc electrodes.*

### *3.4.5.6 ATR-FTIR Evaluation of Human Pooled Blood Serum*

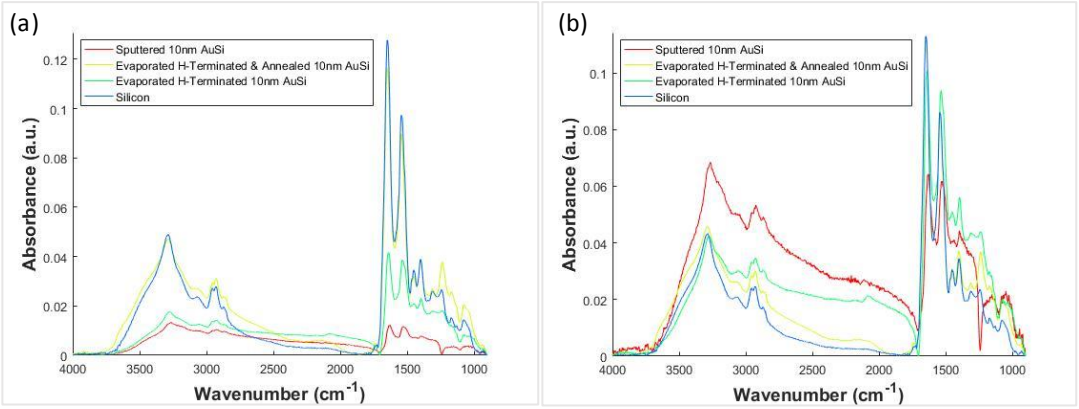


*Figure 3.43: (a) Infrared spectra of human pooled serum of different silicon gold and silicon substrates with baseline correction pre-processing and (b) baseline correction and vector normalisation pre-processing.*

Gold-silicon substrates displayed different degrees of optical transparency for detection of human pooled serum depending on the applied pre-treatment and deposition technique, as observed with baseline-corrected mean spectra (Figure 47a). Evaporated gold-silicon substrates of 10nm nominal thickness pre-treated with hydrofluoric acid and thereafter annealed identified infrared peaks characteristic of human serum with increased absorption intensities relative to other coated substrates. In particular, amide I band intensities for evaporated and annealed substrates measured 0.117 ± 0.014 AU, significantly greater than 0.040 ± 0.005 AU for evaporated films and 0.010 ± 0.002 AU for sputtered gold films ($F(2,24) = 371.88$, p-value $< 0.05$). However, optical transparency was still significantly reduced compared to silicon substrates, given amide I peak absorption intensities of 0.128 ± 0.003 AU for silicon crystals ($t(8) = 2.36$, p-value $< 0.05$). Nevertheless, evaporated and annealed substrates offered the greatest optical transparency whilst providing electrical conductivity, primarily attributed to changes in film surface morphologies when subjected to

annealing procedures. Thermal annealing promotes interstitial mixing of gold atoms with silicon lattices through diffusion, which ultimately compacts the gold film thickness, decreases the grain size of surface boundaries, with consequent increases in surface roughness (Alonzo-Medina et al, 2013). Interestingly, thermal annealing induces agglomeration of thin metal films that varies as a function of film thickness and for 10nm deposition thicknesses creates clusters of gold nano-particles whilst partially exposing underlying substrate surfaces (Boragno et al, 2009). Gold nano-particle clusters were clearly present on top surfaces of partially exposed silicon substrates, evident from both acquired SEM and AFM images and consistent with previous literature findings (Boragno et al, 2009), thereby improving optical transparency. Additionally, annealing procedures significantly decreased Mie scattering artefacts for both sputtered and evaporated films, indicated on vector normalised mean spectra (Figure 47b), similarly attributed to the increased compactness of gold particles and reduction of surface grain sizes. Furthermore, pre-treatment of silicon surfaces with hydrofluoric acid buffered oxide etch increased the optical transparency of gold-silicon substrates, which may be attributed to the removal of native silicon oxide layers previously found to reduce optical transparency as the thickness of the native oxide layer increases (Schumacher et al, 2010).

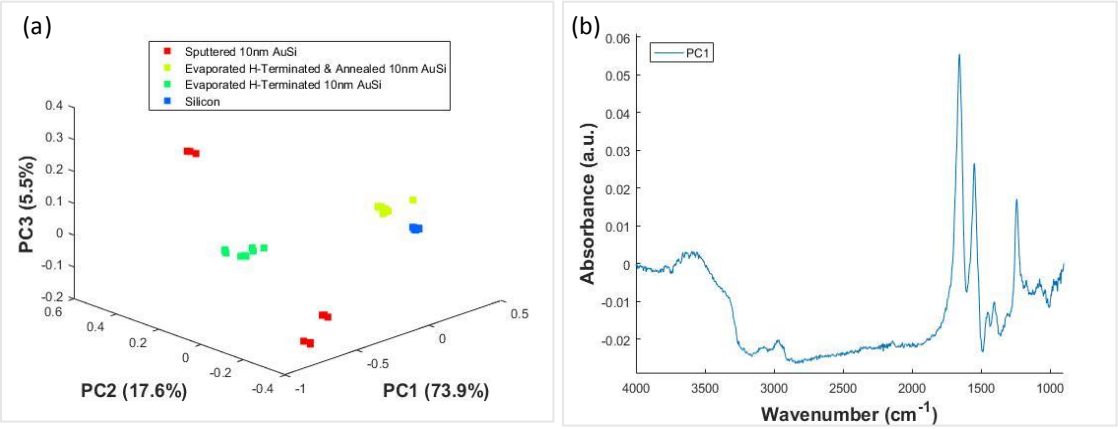


*Figure 3.44: (a) PCA plot of infrared spectra of human pooled serum of different silicon gold and silicon substrates with baseline correction and vector normalisation pre-processing steps with (b) associated PC1 loading plot.*

Gold 10nm evaporated and annealed substrates displayed similar absorption intensities to silicon crystals upon baseline-correction and vector normalisation of mean spectra, with respective amide I absorption intensities of 0.113 ± 0.002 AU for gold-silicon and 0.113 ± 0.0003 AU for silicon deemed statistically similar ($t(8) = 0.28$, p-value = 0.784). Indeed, the PCA plot shows weak clustering between gold-silicon and silicon substrates, although PC1 ($t(13) = 27.3$, p-value $< 0.05$) and PC3 ($t(8) = -8.99$, p-value $< 0.05$) score values were deemed statistically different, whilst PC2 score values were calculated to be statistically similar ($t(9) = -2.11$, p-value = 0.064). The PC1 loading plot, which accounts for 73.9% of total variance, reveals that spectral variance between gold 10nm evaporated annealed substrates and silicon crystals originates from differences in absorption at ~1400cm$^{-1}$ and ~1240cm$^{-1}$. Increased absorption intensities of gold-silicon substrates at ~1400cm$^{-1}$ and ~1240cm$^{-1}$ may indicate possible surface enhancement of biological molecules, since it is well recognised that interaction of evanescent waves with rough gold nano-particle films excites surface plasmon polaritons and consequently provides up to a ten-fold increase in the strength

of the electromagnetic field (Ataka et al, 2013). However, further analysis on greater quantities of gold-silicon substrates is required to conclusively assign spectral differences to surface enhancement of gold films and not simply to baseline artefacts unaccounted for by current spectral pre-processing methods. Lastly, the PC1 loading plot confirms that gold evaporated annealed substrates provide significantly improved absorption of amide I, amide II, and $\delta_s$ ($CH_2$) bands compared to other gold thin-film substrates, further validating their applicability for future ATR-FTIR studies of biological samples.

### *3.4.6 Electrochemical Evaluation of Human Pooled Blood Serum for Biomarkers*

Conventional macro-disc gold electrodes were employed for cyclic voltammetry studies of human pooled serum to establish whether electrochemical responses may be utilised for detection of clinically relevant biomarkers. Electrochemical human pooled serum responses were not found to produce redox signatures associated with clinical biomarkers relevant to the diagnostic aims of the project, evident from Figure 49. Hence, future work must consider surface functionalisation methods on electrode surfaces to specifically detect clinical biomarkers of interest, commonly achieved through implementation of either aptamers or antibody antigen recognition strategies (Jin et al, 2017; Yuan et al, 2016).

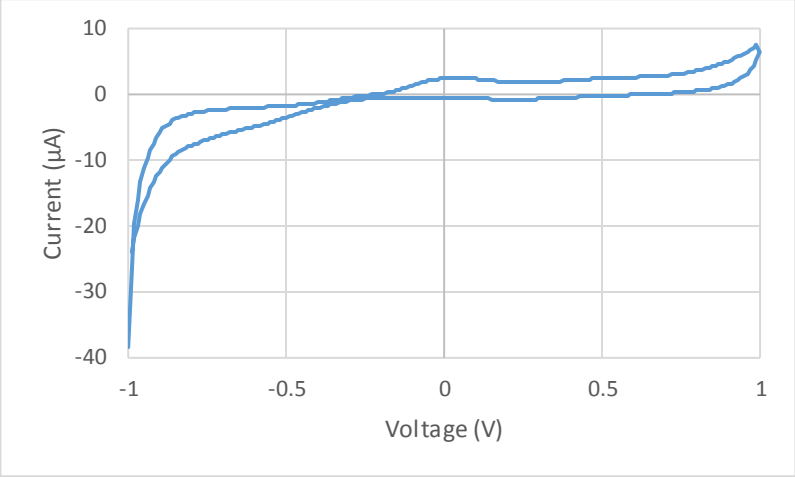


*Figure 3.45: Cyclic voltammogram of human blood serum measured by conventional gold macro electrodes.*

### *3.4.7 Future Design Possibilities*

#### *3.4.7.1 One-Well Approach*

The device may be designed with previously fabricated gold silicon substrates that demonstrated capabilities for both electrochemical and spectroscopic detection of biological molecules and would allow both techniques to be conducted in one sample well. The gold silicon substrates would interface with one reference and counter electrode that may be manufactured with current screen-printer technologies on plastic substrates in order to be economical for mass production. Additionally, it is recommended that samples should be pipetted directly on to the sample well to remove the need for microfluidic channels that currently only serve to transport samples to silicon substrates, thereby reducing both the cost and complexity of device manufacture.

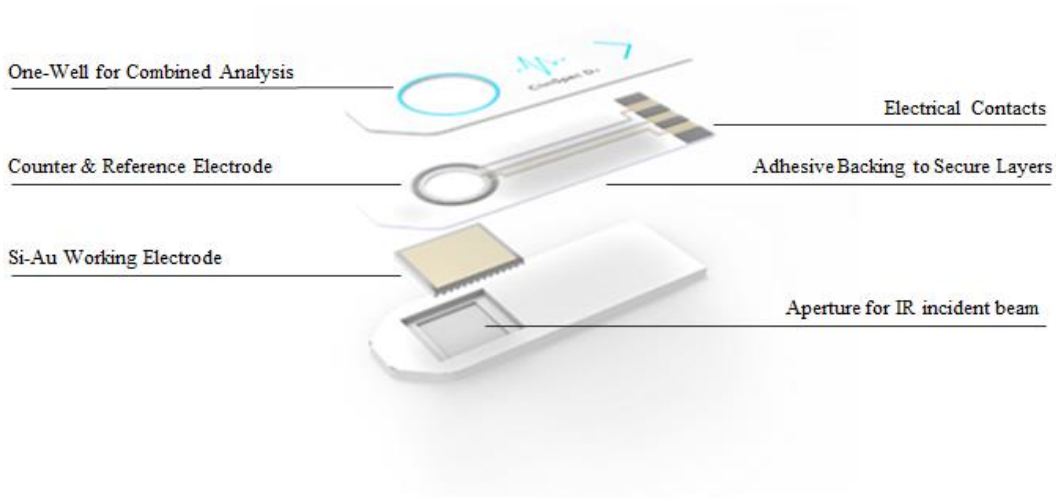


*Figure 3.46: Proposed future design for one-well integrated approach where ATR crystal also functions as the working electrode.*

In the short term, it is recommended that the device should perform electrochemical and spectroscopic analysis separately with electrochemistry performed on wet samples and spectroscopy performed on air-dried samples to prevent the molecular signature of water obscuring pertinent infrared absorption peaks of interest. In the long term, it is hoped that the spectroscopic signature of water may be computationally removed from wet sample spectra to reveal spectroscopic information of interest. Computational removal of water signatures from infrared spectra is currently underway by other members of our research group, and if successful, the proposed device design would facilitate simultaneous electrochemical and spectroscopic analysis of biological samples.

### *3.4.7.2 Two-Well Approach*

The alternative device design features two discrete sample wells for separate electrochemical and spectroscopic analysis in case either computational water removal does not prove successful or there is no demonstrable clinical utility for simultaneous

electrochemical and spectroscopic measurements for a given clinical application. In such cases, the device would contain the previously tested silicon IRE and a conventional three-electrode arrangement screen-printed on a plastic substrate. Adhesive transfer tape would similarly be employed to secure individual device layers due to its low-cost and industrial familiarity given its current use in the fabrication of glucose diagnostic strips.

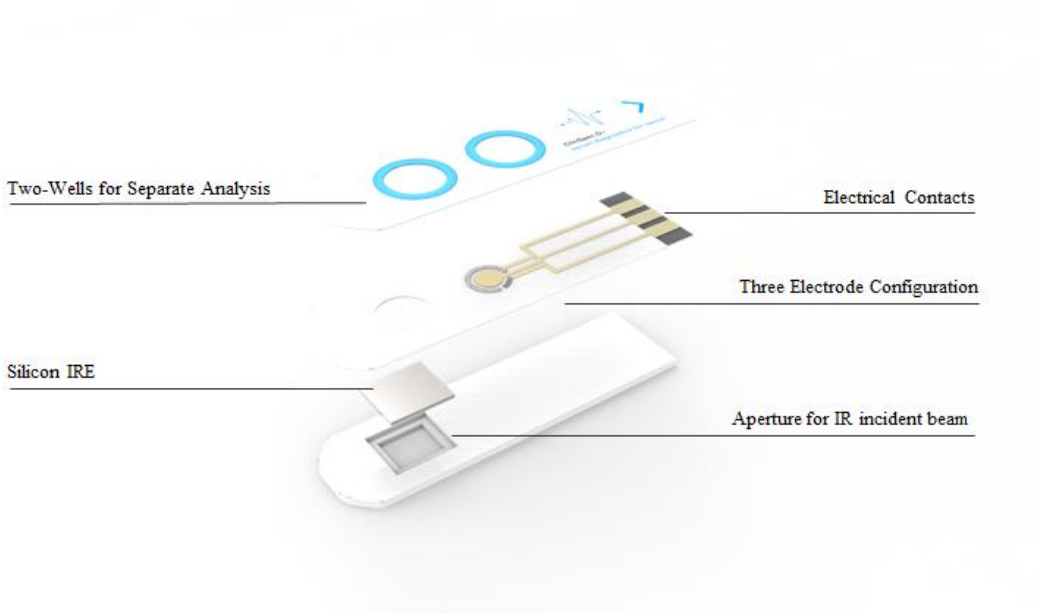


*Figure 3.47: Proposed future design for two-well approach with separate ATR crystal and electrode design.*

## 3.5 Conclusion

Various strategies have been employed for the development of silicon substrates that offer electrochemical and spectroscopic detection capabilities for the analysis of biological molecules. Silicon P-type 1-3Ω substrates successfully characterised standard redox-active molecules and human pooled serum samples for spectroscopic studies and were found to be comparable to current diamond IRE's. However, silicon

P-type 1-3Ω substrates were unable to perform electrochemical studies on standard redox-active molecules due to the poor electrical conductivity and insufficient dopant concentrations of substrates. Degenerately doped silicon P-type and N-type substrates successfully characterised redox-active molecules electrochemically due to vastly increased dopant concentrations and significantly improved electrical conductivity of substrates. However, degenerately doped silicon P-type and N-type substrates were unsuitable for spectroscopic analysis due to the significantly reduced optical transparency of substrates attributed to the absorption of infrared light by dopant atoms. Thereafter, silicon P-type 1-3Ω substrates sputtered with gold were found to have sufficient optical transparency for spectroscopic characterisation of human pooled serum provided depositions were below 20nm thickness. Sputtered gold silicon substrates also demonstrated electrochemical capabilities for detection of at depositions of 200-10nm thickness, although were not suitable for detection of molecules due to the poor adhesion of gold to silicon. Lastly, silicon P-type 1-3Ω substrates evaporated and annealed with gold of 10nm deposition thickness were found to be suitable for electrochemical detection of $K_3[Fe(CN)_6]^{-3/4}$, $Ru(bpy)_3(PF_6)_2$ and pyocyanin molecules and spectroscopic detection of human pooled serum samples. Hence, silicon P-type 1-3Ω substrates evaporated and annealed with gold of 10nm deposition thickness show considerable promise for development of a medical device with dual electrochemical and spectroscopic detection capabilities.

## *3.6 References*


Adeloye, A. O., Olomola, T. O., Adebayo, A. I., & Ajibade, P. A. (2012). *A High Molar Extinction Coefficient Bisterpyridyl Homoleptic Ru(II) Complex with trans-2-Methyl-2-butenoic Acid Functionality: Potential Dye for Dye-Sensitized Solar Cells. International Journal of Molecular Sciences, 13(3), 3511–3526.* doi:10.3390/ijms13033511

Alatraktchi, F. A., Noori, J. S., Tanev, G. P., Mortensen, J., Dimaki, M., Johansen, H. K., … Svendsen, W. E. (2018). *Paper-based sensors for rapid detection of virulence factor produced by Pseudomonas aeruginosa. PLOS ONE, 13(3), e0194157.*doi:10.1371/journal.pone.0194157

Alatraktchi, F., Breum Andersen, S., Krogh Johansen, H., Molin, S., & Svendsen, W. (2016). *Fast Selective Detection of Pyocyanin Using Cyclic Voltammetry. Sensors, 16(3), 408.*doi:10.3390/s16030408

Alonzo-Medina, G. M., González-González, A., Sacedón, J. L., & Oliva, A. I. (2013). *Understanding the thermal annealing process on metallic thin films. IOP Conference Series: Materials Science and Engineering, 45, 012013*. doi:10.1088/1757-899x/45/1/012013

Ataka, K., Heberle, J. (2007) Biochemical applications of surface-enhanced infrared absorption spectroscopy. Anal Bioanal Chem. 388;47-54.

Ataka, k., Stripp, S. T., Heberle, J. (2013) Surface-enhanced infrared absorption spectroscopy (SEIRAS) to probe monolayers of membrane proteins. *Biochimica et Biophysica 1828.* 2283-2293.

Axelevitch, A., Gorenstein, B., & Golan, G. (2012). *Investigation of Optical Transmission in Thin Metal Films. Physics Procedia, 32, 1–13.* doi:10.1016/j.phpro.2012.03.510

Baker, M. J., Trevisan, J., […], and Martin, F. L. (2014) Using Fourier transform IR spectroscopy to analyse biological materials. *Nat Protoc. 2014 Aug*.9(8);1771-1791.

Baker, M. J., Trevisan, J., Bassan, P., Bhargava, R., Butler, H. J., Dorling, K. M., … Martin, F. L. (2014). *Using Fourier transform IR spectroscopy to analyze biological materials. Nature Protocols, 9(8), 1771–1791.*doi:10.1038/nprot.2014.110

Baldwin, R. K., Zou, J., Pettigrew, K. A., Yeagle, G. J., Britt, R. D., & Kauzlarich, S. M. (2006). *The preparation of a phosphorus doped silicon film from phosphorus containing silicon nanoparticles. Chemical Communications, (6), 658.*doi:10.1039/b513330k

Barth, A. (2007). *Infrared spectroscopy of proteins. Biochimica et Biophysica Acta (BBA) - Bioenergetics, 1767(9), 1073–1101*. doi:10.1016/j.bbabio.2007.06.004

Bassan, P., Mellor, J., Shapiro, J., Williams, K. J., Lisanti, M. P., & Gardner, P. (2014). *Transmission FT-IR Chemical Imaging on Glass Substrates: Applications in Infrared Spectral Histopathology. Analytical Chemistry, 86(3), 1648–1653.*doi:10.1021/ac403412n

Best, S. P, Borg, S. J., Vincent, K. A. (2008) Spectroelectrochemistry. Chapter1: Introduction. Royal Society of Chemistry, 2008 ISBN: 1847558402, 9781847558404

Bond, A. M. (1999). *Voltammetric Determination of the Reversible Redox Potential for the Oxidation of the Highly Surface Active Polypyridyl Ruthenium Photovoltaic Sensitizer cis-Ru[sup (II)](dcbpy)[sub 2](NCS)[sub 2]. Journal of The Electrochemical Society, 146(2), 648.* doi:10.1149/1.1391657.

Bonnier, F., Brachet, G., Duong, R., Sojinrin, T., Respaud, R., Aubrey, N., … Chourpa, I. (2016). *Screening the low molecular weight fraction of human serum using ATR-IR spectroscopy. Journal of Biophotonics, 9(10), 1085–1097*. doi:10.1002/jbio.201600015

Boragno, C., Buatier de Mongeot, F., Felici, R., & Robinson, I. K. (2009). *Critical thickness for the agglomeration of thin metal films. Physical Review B, 79(15).* doi:10.1103/physrevb.79.155443

Borland LM, Michael AC. An Introduction to Electrochemical Methods in Neuroscience. In: Michael AC, Borland LM, editors. Electrochemical Methods for Neuroscience. Boca Raton (FL): CRC Press/Taylor & Francis; 2007. Chapter 1. Available from: https://www.ncbi.nlm.nih.gov/books/NBK1845/

Burkitt, R., Sharp, D. (2017) *Submicromolar quantification of pyocyanin in complex biological fluids using pad-printed carbon electrodes.* Electrochemistry Communications, 78. pp. 43-46. ISSN 1388-2481 DOI: https://doi.org/10.1016/j.elecom.2017.03.021

Cai, C., Jia, F., Li, A., Huang, F., Xu, Z., Qiu, L., … Wang, M. (2016). *Crackless transfer of large-area graphene films for superior-performance transparent electrodes. Carbon, 98, 457–462.*doi:10.1016/j.carbon.2015.11.041

Caldwell, C. C., Chen, Y., Goetzmann, H. S., Hao, Y., Borchers, M. T., Hassett, D. J., Young, L. R., Mavrodi, D., Thomashow, L., & Lau, G. W. (2009). Pseudomonas aeruginosa exotoxin pyocyanin causes cystic fibrosis airway pathogenesis. *The American journal of pathology, 175*(6), 2473–2488. https://doi.org/10.2353/ajpath.2009.090166

Chen, H. Y., Long, YT. (1999) Study of biomolecules by combining electrochemistry with UV/Vis, IR and surface enhanced Raman scattering spectroscopy by a novel flow microcell. *Analytica Chimica Acta.* 382: 171-177.

Coates, J. (2006). Interpretation of Infrared Spectra, A Practical Approach. Encyclopedia of Analytical Chemistry. doi:10.1002/9780470027318.a5606

Deen, J. M., Basu, P. K. (2012) Silicon Photonics: **Fundamentals and Devices.** John Wiley & Sons, 2012. ISBN: 1119940907, 9781119940906

Delgado, J. M., Orts, J. M., Perez, J. M., Rodes, A. (2008) Sputtered thin-film gold electrodes for in situ ATR-SEIRAs and SERS studies. *Journal of Electroanalytical Chemistry 617*. 130-140.

Elgrishi, N., Rountree, K. J., McCarthy, B. D., Rountree, E. S., Eisenhart, T. T., & Dempsey, J. L. (2017). *A Practical Beginner's Guide to Cyclic Voltammetry. Journal of Chemical Education, 95(2), 197–206*. doi:10.1021/acs.jchemed.7b00361

Falk, M., Ford, T. A. (1966) INFRARED SPECTRUM AND STRUCTURE OF LIQUID WATER. Canadian Journal of Chemistry. 44;1699-1707.

Fatikow, S., Rembold, U. (1997) Microsystem Technology and Microrobotics. Springer Science & Business Media, 1997. ISBN: 3540606580, 9783540606581.

Gaffar, M. A., & Abd-Elrahman, M. I. (2001). *Vibration Spectra of Ferrocyanide Ions in the Paraelectric Phase of K4[Fe(CN)6] . 3H2O. Physica Status Solidi (b), 225(2), 271–287*. doi:10.1002/1521-3951(200106)225:2<271::aid-pssb271>3.0.co;2-v

Garidel, P., Schott, H. (2006) Fourier-Transform Midinfrared Spectroscopy for Analysis and Screening of Liquid Protein Formulations Part 2: Detailed Analysis and Applications. *BioProcess International.*

Ghorbanpour, M., & Falamaki, C. (2013). *A novel method for the production of highly adherent Au layers on glass substrates used in surface plasmon resonance analysis: substitution of Cr or Ti intermediate layers with Ag layer followed by an optimal annealing treatment. Journal of Nanostructure in Chemistry, 3(1), 66*. doi:10.1186/2193-8865-3-66

Glassford, S. E., Byrne, B., & Kazarian, S. G. (2013). *Recent applications of ATR FTIR spectroscopy and imaging to proteins. Biochimica et Biophysica Acta (BBA) - Proteins and Proteomics, 1834(12), 2849–2858.* doi:10.1016/j.bbapap.2013.07.015

Gould, R. (2006) Thin Films, In: Kasap S., Capper P. (eds) Springer Handbook of Electronic and Photonic Materials. Springer, Boston, MA. ISBN 978-0-387-26059-4

Grdadolnik, J. (2002) ATR-FTIR SPECTROSCOPY: ITS ADVANTAGES AND LIMITATIONS. Acta Chim. Slov. 49: 631-642

Hall, S., McDermott, C., Anoopkumar-Dukie, S., McFarland, A., Forbes, A., Perkins, A., … Grant, G. (2016). *Cellular Effects of Pyocyanin, a Secreted Virulence Factor of Pseudomonas aeruginosa. Toxins, 8(8), 236*.doi:10.3390/toxins8080236

Hamann, C. H., Hamnett, A., Vielstich, W. (1998) Electrochemistry. 2nd Edition. Wiley. ISBN 0471043729

Hecht, D. S., Hu, L., & Irvin, G. (2011). *Emerging Transparent Electrodes Based on Thin Films of Carbon Nanotubes, Graphene, and Metallic Nanostructures. Advanced Materials, 23(13), 1482–1513.*doi:10.1002/adma.201003188

Hood, S. J., Kampouris, D. K., Kadara, R. O., Jenkinson, N., del Campo, F. J., Muñoz, F. X., & Banks, C. E. (2009). *Why "the bigger the better" is not always the case when utilising microelectrode arrays: high density vs. low density arrays for the electroanalytical sensing of chromium(vi). The Analyst, 134(11), 2301*. doi:10.1039/b911507b

Hoşafçı, G., Klein, O., Oremek, G., & Mäntele, W. (2006). *Clinical chemistry without reagents? An infrared spectroscopic technique for determination of clinically relevant constituents of body fluids. Analytical and Bioanalytical Chemistry, 387(5), 1815–1822.* doi:10.1007/s00216-006-0841-3

Huang, Y., Suni, I. I. (2008) Degenerate Si as an Electrode Material for Electrochemical Biosensors. Journal of The Electrochemical Society. 155(12);J350-J354

Jin, C., Qiu, L., Li, J., Fu, T., Zhang, X., & Tan, W. (2016). *Cancer biomarker discovery using DNA aptamers. The Analyst, 141(2), 461–466.* doi:10.1039/c5an01918d

Kaim, W., & Fiedler, J. (2009). *Spectroelectrochemistry: the best of two worlds. Chemical Society Reviews, 38(12), 3373.*doi:10.1039/b504286k

Kellenberger, A., Dmitrieva, E., & Dunsch, L. (2012). *Structure Dependence of Charged States in "Linear" Polyaniline as Studied by In Situ ATR-FTIR Spectroelectrochemistry. The Journal of Physical Chemistry B, 116(14), 4377–4385.*doi:10.1021/jp211595n

Klyuev, Y. A. (1965). *Vibrational spectra of crystalline potassium ferri- and ferrocyanide. Journal of Applied Spectroscopy, 3(1), 30–34.*doi:10.1007/bf00653885

Kong, J., & Yu, S. (2007). *Fourier Transform Infrared Spectroscopic Analysis of Protein Secondary Structures. Acta Biochimica et Biophysica Sinica, 39(8), 549–559.* doi:10.1111/j.1745-7270.2007.00320.x

Kossoy, A., Merk, V., Simakov, D., Leosson, K., Kéna-Cohen, S., & Maier, S. A. (2014). *Optical and Structural Properties of Ultra-thin Gold Films. Advanced Optical Materials, 3(1), 71–77.* doi:10.1002/adom.201400345

Kulkarni, G. U., Kiruthika, S., Gupta, R., & Rao, K. (2015). *Towards low cost materials and methods for transparent electrodes. Current Opinion in Chemical Engineering, 8, 60–68.*doi:10.1016/j.coche.2015.03.001

Kvarnström, C., Neugebauer, H., Ivaska, A., & Sariciftci, N. . (2000). *Vibrational signatures of electrochemical p- and n-doping of poly(3,4-ethylenedioxythiophene) films: an in situ attenuated total reflection Fourier transform infrared (ATR-FTIR) study. Journal of Molecular Structure, 521(1-3), 271–277.* doi:10.1016/s0022-2860(99)00442-1

Lakshmi, D. S., Cundari, T., Furia, E., Tagarelli, A., Fiorani, G., Carraro, M., & Figoli, A. (2015). *Preparation of Polymeric Membranes and Microcapsules Using an Ionic Liquid as Morphology Control Additive. Macromolecular Symposia, 357(1), 159–167.* doi:10.1002/masy.20140021

Li, S. S. (2007) Semiconductor Physical Electronics. Springer Science & Business Media. ISBN: 0387377662, 9780387377667

López-Naranjo, E. J., González-Ortiz, L. J., Apátiga, L. M., Rivera-Muñoz, E. M., & Manzano-Ramírez, A. (2016). *Transparent Electrodes: A Review of the Use of Carbon-Based Nanomaterials. Journal of Nanomaterials, 2016, 1–12.*doi:10.1155/2016/4928365

Martin, H. B., & Morrison, P. W. (2001). *Application of a Diamond Thin Film as a Transparent Electrode for In Situ Infrared Spectroelectrochemistry. Electrochemical and Solid-State Letters, 4(4), E17.*doi:10.1149/1.1353162

Matarèse, B. F. E., Feyen, P. L. C., Falco, A., Benfenati, F., Lugli, P., & deMello, J. C. (2018). *Use of SU8 as a stable and biocompatible adhesion layer for gold bioelectrodes. Scientific Reports, 8(1).* doi:10.1038/s41598-018-21755-6

Minnes, R., Nissinmann, M., Maizels, Y., Gerlitz, G., Katzir, A., & Raichlin, Y. (2017). *Using Attenuated Total Reflection–Fourier Transform Infra-Red (ATR-FTIR) spectroscopy to distinguish between melanoma cells with a different metastatic potential. Scientific Reports, 7(1).* doi:10.1038/s41598-017-04678-6

Miyake, H., Ye, S., Osawa, M. (2002) Electroless deposition of gold thin films on silicon for surface-enhanced infrared spectroelectrochemistry. *Electrochemistry Communications 4*. 973-977.

Morozenko, A., Leontyev, I. V., Stuchebrukhov, A. A., (2014) Dipole Moment and Binding Energy of Water in Proteins from Crystallographic Analysis. J. Chem. Theory Comput. 10(10);4618-4623.

Morozenko, A., Leontyev, I. V., Stuchebrukhov, A. A., (2014) Dipole Moment and Binding Energy of Water in Proteins from Crystallographic Analysis. J. Chem. Theory Comput. 10(10);4618-4623.

Muller, M., Li, Z., & Maitz, P. K. M. (2009). *Pseudomonas pyocyanin inhibits wound repair by inducing premature cellular senescence: Role for p38 mitogen-activated protein kinase. Burns, 35(4), 500–508.* doi:10.1016/j.burns.2008.11.010

Muzyka, K., Sun, J., Fereja, T. H., Lan, Y., Zhang, W., & Xu, G. (2018). *Boron Doped Diamond: Current Progress and Challenges in view of Electroanalytical Applications. Analytical Methods.*doi:10.1039/c8ay02197j

Niranjana, E., Kumara Swamy, B. E., Raghavendra Naik, R., Sherigara, B. S., & Jayadevappa, H. (2009). *Electrochemical investigations of potassium ferricyanide and dopamine by sodium dodecyl sulphate modified carbon paste electrode: A cyclic voltammetric study. Journal of Electroanalytical Chemistry, 631(1-2), 1–9.*doi:10.1016/j.jelechem.2009.02.011

Nirmaier, H.-P., & Henze, G. (1997). *Characteristic behavior of macro-, semimicro- and microelectrodes in voltammetric and chronoamperometric measurements. Electroanalysis, 9(8), 619–624.*doi:10.1002/elan.1140090808

O'Reilly, E. J., Conroy, P., Keyes, T. E., O'Kennedy, R., Forster, R. J., Dennany, L. (2015) Combining recombinant Antibody technology and highly sensitive electrochemiluminescence for the detection of the Cardiac Biomarker C-Reactive protein at sub fg Limits of Detection. *RSC Advances*. 5:68874-67877.

Ouellette, R. J., Rawn, D. J. (2014) Organic Chemistry : Structure, Mechanism, and Synthesis. Elsevier, 2014. ISBN: 0128010827, 9780128010822

Oziat, J., Gougis, M., Malliaras, G. G., & Mailley, P. (2017). *Electrochemical Characterizations of four Main Redox-metabolites of Pseudomonas Aeruginosa . Electroanalysis, 29(5), 1332–1340.* doi:10.1002/elan.201600799

Park, S. K., Lee, C. K., Lee, N. S. & Lee, S. H. (2002). Vibrational analysis of ferrocyanide complex ion based on density functional force field. *Bulletin of the Korean Chemical Society*, 22(2), 253-261.

Pharr, C. M., & Griffiths, P. R. (1997). *Infrared Spectroelectrochemical Analysis of Adsorbed Hexacyanoferrate Species Formed during Potential Cycling in the Ferrocyanide/Ferricyanide Redox Couple. Analytical Chemistry, 69(22), 4673–4679*. doi:10.1021/ac961120l

Pilling, M. J., Henderson, A., Shanks, J. H., Brown, M. D., Clarke, N. W., & Gardner, P. (2017). Infrared spectral histopathology using haematoxylin and eosin (H&E) stained glass slides: a major step forward towards clinical translation. The Analyst, 142(8), 1258–1268. doi:10.1039/c6an02224c

Rajarathinam, G., & Sarada. (2012). *Gold and silver nanoparticles from Trianthema decandra: synthesis, characterization, and antimicrobial properties. International Journal of Nanomedicine, 5375.* doi:10.2147/ijn.s36516

Rajeshwar, K. (2007). *Fundamentals of Semiconductor Electrochemistry and Photoelectrochemistry. Encyclopedia of Electrochemistry*. doi:10.1002/9783527610426.bard060001

Reig, F. (2002). FTIR quantitative analysis of calcium carbonate (calcite) and silica (quartz) mixtures using the constant ratio method. *Application to geological samples*. Talanta, 58(4), 811–821. doi:10.1016/s0039-9140(02)00372-7

Rigas, B., Morgello, S., Goldman, I. S., & Wong, P. T. (1990). Human colorectal cancers display abnormal Fourier-transform infrared spectra. *Proceedings of the National Academy of Sciences of the United States of America*, *87*(20), 8140–8144. doi:10.1073/pnas.87.20.8140

Rusling, J. F., Kumar, C. V., Gutkind, J. S., & Patel, V. (2010). Measurement of biomarker proteins for point-of-care early detection and monitoring of cancer. *The Analyst*, 135(10), 2496.doi:10.1039/c0an00204f

Saggiomo, V., & Velders, A. H. (2015). *Simple 3D Printed Scaffold-Removal Method for the Fabrication of Intricate Microfluidic Devices. Advanced Science, 2(9), 1500125.* doi:10.1002/advs.201500125

Scholz, F. (2015). *Voltammetric techniques of analysis: the essentials. ChemTexts, 1(4)*. doi:10.1007/s40828-015-0016-y

Schumacher, H., Kunzelmann, U., Vasiley, B., Eichhorn, K. J. ., Bartha, L. W. (2010) Applications of microstructured silicon wafers as internal reflection elements in attenuated total reflection Fourier transform infrared spectroscopy. *Appl. Spectrosc.* 64(9);1022-7

Sharp, D., Gladstone, P., Smith, R. B., Forsythe, S., & Davis, J. (2010). *Approaching intelligent infection diagnostics: Carbon fibre sensor for electrochemical pyocyanin detection. Bioelectrochemistry, 77(2), 114–119*.doi:10.1016/j.bioelechem.2009.07.008

Simm, A. O., Banks, C. E., Ward-Jones, S., Davies, T. J., Lawrence, N. S., Jones, T. G. J., … Compton, R. G. (2005). *Boron-doped diamond microdisc arrays: electrochemical characterisation and their use as a substrate for the production of microelectrode arrays of diverse metals (Ag, Au, Cu)via electrodeposition. The Analyst, 130(9), 1303.* doi:10.1039/b506956d

Smith, D. J., Petford-Long, A. K., Wallenberg, L. R., , Bovin, J. O. (1986) Dynamic Atomic-Level Rearrangements in Small Gold Particles. *Science*. Vol. 233, Issue 4766, pp. 872-875 DOI: 10.1126/science.233.4766.872

Sobaszek, M., Siuzdak, K., Skowronski, L., Bogdanowicz, R., Plucinski, J. (2015) Optically transparent boron-doped nanocrystalline diamond films for spectroelectrochemical measurements on different substrates. *Materials Science and Engineering*. 104;012024

Srikanth, V. V. S. S., Sampath Kumar, P., & Kumar, V. B. (2012). *A Brief Review on theIn SituSynthesis of Boron-Doped Diamond Thin Films. International Journal of Electrochemistry, 2012, 1–7.* doi:10.1155/2012/218393

Stotter, J., Haymond, S., Zak, J. K., Show, Y., Cvackova, Z., Swain, G. M. (2003) Optically Transparent Diamond Electrodes for UV-Vis and IR Spectroelectrochemistry. *The Electrochemical Society Interface*.

Svorcik, V., Zehentner, J., Rybka, V., Slepicka, P., & Hnatowicz, V. (2002). *Characterization of thin gold layers on polyethyleneterephthalate: transition from discontinuous to continuous, homogenous layer. Applied Physics A: Materials Science & Processing, 75(4), 541–544*. doi:10.1007/s003390101024

Tiwari, S., Raman, J., Reddy, V., Ghetler, A., Tella, R. P., Han, Y., … Bhargava, R. (2016). *Towards Translation of Discrete Frequency Infrared Spectroscopic Imaging for Digital Histopathology of Clinical Biopsy Samples. Analytical Chemistry, 88(20), 10183–10190*.doi:10.1021/acs.analchem.6b02754

Venegas-Yazigi, D., Campos-Vallette, M., Lever, A.B.P. Costamagna, J., R.O. Latorre, W., Hernández G. (2003) A FAMILY OF RYTHENIUM COMPLEXES CONTAINING THE NON-INNOCENT LIGAND O-BENZOQUINONEDIIMINE AN INFRARED STRUCTURAL INTERPRETATION. J. Chil. Chem. Soc., 48, N 3 ISSN 0717-9324

Wadhawan, J. D., Welford, P. J., Yunus, K., Fisher, A. C., & Compton, R. G. (2003). *Voltammetry at micro-mesh electrodes. Journal of the Brazilian Chemical Society, 14(4), 510–516*. doi:10.1590/s0103-50532003000400004

Wanarattikan, P., Jitthammapirom, P., Sakdanuphab, R., & Sakulkalavek, A. (2019). *Effect of Grain Size and Film Thickness on the Thermoelectric Properties of Flexible Sb2Te3 Thin Films. Advances in Materials Science and Engineering, 2019, 1–7*.doi:10.1155/2019/6954918

Wang, J. (2006) Analytical Electrochemistry. Third Edition. John Wiley and Sons. ISBN 047179029x / 9780471790297.

Wasserman, S. R., Biebuyck, H., & Whitesides, G. M. (1989). *Monolayers of 11-trichlorosilylundecyl thioacetate: A system that promotes adhesion between silicon dioxide and evaporated gold. Journal of Materials Research, 4(04), 886–892*. doi:10.1557/jmr.1989.0886

Webster, T. A., Sismaet, H. J., Conte, J. L., Chan, I. J., & Goluch, E. D. (2014). *Electrochemical detection of Pseudomonas aeruginosa in human fluid samples via pyocyanin. Biosensors and Bioelectronics, 60, 265–270*. doi:10.1016/j.bios.2014.04.028

Wilson, R., Sykes, D. A., Watson, D., Rutman, A., Taylor, G. W., Cole, P. J. (1988) Measurement of Pseudomonas aeruginosa phenazine pigments in sputum and assessment of their contribution to sputum sol toxicity for respiratory epithelium. Infect Immun. 56(9):2515-7.

Wißmann, P., & Finzel, H.-U. (2007). The Effect of Annealing on the Electrical Resistivity of Thin Gold Films. Electrical Resistivity of Thin Metal Films, 35–52. Springer Tracts in Modern Physics. Springer, Berlin, Heidelberg. doi:10.1007/3-540-48490-6_4

Yakubovsky, D. I., Arsenin, A. V., Stebunov, Y. V., Fedyanin, D. Y., & Volkov, V. S. (2017). *Optical constants and structural properties of thin gold films. Optics Express, 25(21), 25574*. doi:10.1364/oe.25.025574

Yuan, J. (2016). *Circulating protein and antibody biomarker for personalized cancer immunotherapy. Journal for ImmunoTherapy of Cancer, 4(1)*. doi:10.1186/s40425-016-0150-0

Zaitseva, E., Saavedra, M., Banerjee, S., Sakmar, TP., Vogel, R. (2010) SEIRA spectroscopy on a membrane receptor monolayer using lipoprotein particles as carriers. Biophys J. 6;99(7):2327-35.

Zanyar Movasaghi, Shazza Rehman & Dr. Ihtesham ur Rehman (2008): Fourier Transform Infrared (FTIR) Spectroscopy of Biological Tissues, Applied Spectroscopy Reviews, 43:2, 134-179

Zhang, X. G., (2007) Electrochemistry of Silicon and Its Oxide. Springer Science & Business Media, 2007. ISBN 0306479214, 9780306479212

# Chapter 4: Development of an electrochemical and spectroscopic platform for brain cancer diagnostics

## 4.1 Overview

This chapter will describe the development of an electrochemical immunosensor using different electrode technologies where the gold surface has been functionalised with appropriate surface chemistries and antibodies for the detection of IDH1-R132H mutated proteins present in spiked buffer samples. Subsequently, the electrochemical immunosensor shall be tested on human serum samples from patients diagnosed with grade IV glioblastoma multiforme, with known IDH1 status, to investigate whether it is possible to detect IDH1-R132H proteins in clinical serum samples. Thereafter, the capabilities of our novel silicon substrates will be evaluated for diagnosis of IDH1 moleular status in clinical patient samples using ATR-FTIR spectroscopy.

## 4.2 Introduction

Detection of isocitrate dehydrogenase 1 (IDH1) mutations from patient serum samples represents an attractive, non-invasive, biomolecular diagnostic modality for glioma classification that would have far reaching implications for patients and health care providers. Presently, clinical laboratories routinely employ enzyme-linked immunosorbent assays (ELISA's) to detect target protein biomarkers from human serum samples, which inform diagnostic and prognostic decisions in the clinical setting. Typically, ELISA's are performed in either a sandwich or competitive assay that allows quantification of enzyme labelled antibody-antigen complexes, with

sensitive and specific detection down to the pico molar concentration range (Ghindilis et al, 1998). However, sandwich ELISA assays require target antigens to bind firstly to primary antibodies immobilised on the walls of micro-well plates, and subsequently to secondary labelled antibodies, to obtain colorimetric or fluorometric signals proportional to analyte concentration (Kokkinos et al, 2016). Therefore, target antigens must possess multiple epitopes in the sandwich ELISA format for successive attachment to primary and secondary antibodies (Kokkinos et al, 2016), which is unsuitable for IDH1-R132H protein detection, since the target antigen exhibits one single point mutation (Cohen et al, 2013). Competitive ELISA assays may be employed for detection of single epitope antigens where unlabelled target antigens and labelled reference antigens compete for binding sites on immobilised primary capture antibodies (Kokkinos et al, 2016). However, the optical signal is inversely proportional to analyte concentration, with assay sensitivity significantly reduced to the nano-molar concentration range compared to sandwich assays (Ghindilis et al, 1997). Additionally, ELISA assays utilise large colorimetric or fluorometric micro-well plate readers to detect enzymatic signals, and other specialised laboratory equipment, which is not conducive to point of care testing (Chikkaveeraiah et al, 2012). Similarly, ELISA procedures describe complex, costly, time consuming, multi-stage processes that are best suited for automation of high volume biofluid tests, restricting its applicability to clinical laboratories. Alternatively, western blots may be utilised for protein biomarker detection, where sample protein constituents are separated with electrophoresis based on their molecular weights, and subsequently probed on membranes with primary capture and secondary labelled antibodies to obtain optical signals indicative of the target antigen. However, western blots are notoriously time consuming and labour

intensive procedures that require highly specialised technicians, and produce qualitative to semi-quantitative information on target molecules (Sanders et al, 2016), prompting the need for novel diagnostic strategies for IDH-R132H detection in the point-of-care clinical setting.

Electrochemical immunosensors have recently shown significant promise for cancer diagnostics with quantitative detection of antibody-antigen affinity interactions demonstrated in a variety of rapid, low-cost, portable formats. Typically, electrochemical immunosensors comprise a three-electrode configuration that converts physical antibody antigen binding events to electrical signals using a range of electrochemical techniques. Electrochemical impedance spectroscopy is particularly suited to immunosensing where the resistance to electron transfer at the working electrode is especially sensitive to molecular interactions with the sensor surface (Brett, 2008). Previously, electrochemical impedance spectroscopy has successfully demonstrated detection of various clinical biomarkers, including cancer proteins human prostatic acid phosphatase (PAP) and alpha-feto protein (AFP), with limits of detection of 11pM and 0.00172 ng/ml respectively (Lehr et al, 2014; Idris et al, 2018). Additionally, impedimetric immunosensors permit direct recognition of antibody antigen binding without the requirement for enzymatic or labelled secondary antibodies, which is attractive because labelling can negatively influence the binding properties of antibody antigen complexes resulting in variable signals (Daniels et al, 2007). Furthermore, label-free immunosensor platforms have been recognised to facilitate simpler, cheaper and faster device fabrication and, hence, easier clinical translation (Daniels et al, 2007). Similarly, voltammetric immunosensor devices,

whilst commonly reported with enzymatic, quantum dot or nano-particle electro-active labels, may be employed for label-free biomarker detection, with current decreases of the redox probe indicative of antigen binding. Previously, voltammetric immunosensors have displayed sensitive detection of protein serum biomarkers, such as dengue non-structural 1 antigen with a limit of detection of 0.03µg/ml (Parkash et al, 2014). Therefore, electrochemical impedance spectroscopy and voltammetry shall constitute the primary and secondary detection methods in this chapter for immunosensor development, with the view to reducing assay complexity and easier clinical translation. Conversely, amperometry has not be chosen for immunosensor development in this chapter because amperometric immunosensors, in general, rely on secondary enzymatic labels, electro-active mediators and co-factors, which introduces additional complexity and cost, with labels further consumed preventing later clinical validation (Mahato et al, 2018).

Electrochemical immunosensors further require the design of suitable surface chemistry strategies to develop a molecular probe that functions in conjunction with the chosen electrochemical technique. Generally, physisorption and chemisorption immobolisation methods are widely employed in the development of molecular probes, which greatly influences the stability and sensitivity of the immunosensor. Physisorption describes the physical adsorption of target molecules to the electrode surface through Van der Waal forces, resulting in simple, inexpensive, yet weakly bound molecular probes. Conversely, chemisorption permits attachment of target molecules to electrode surfaces through the formation of chemical bonds, which enables greater stability and versatility to probe development. Predominantly, alkane

thiol chemistry has been utilised on gold electrodes to develop self-assembled monolayers (SAM's) on immunosensors, which is widely recognised as a simple, inexpensive and biocompatible method to probe the biological environment (Suroviec, 2012; Vericat et al, 2010). Specifically, the sulphur atoms of the head groups chemisorb to gold electrode surfaces, forming a strong semi-covalent bond (~126kJ/mol) (Lavrich et al, 1998), whilst functional end groups may attach to antibodies using various coupling strategies. Ciani et al have previously reported successful attachment of SAM functional end groups to antibodies on impedimetric immunosensors through primary amine and thiol sites (Ciani et al, 2012). Conversely, Parkash utilised the carboxylic group of antibodies for immobilisation on impedemetric immunosensors with carbodiimide cross-linker chemistry (Parkash et al, 2014). Therefore, the current chapter will aim to assess the suitability of different antibody attachment sites, and molecular probes with physisorption and chemisorption methods for IDH1-R132H protein detection.

Electrochemical immunosensors further require selection of suitable electrode surfaces to develop molecular probes since it is well recognised that electrode surfaces greatly influence SAM properties and sensor responses (Butterworth et al, 2019). Therefore, this chapter will also assess the suitability of current electrode technologies, including screen-printed and macro-disc electrodes, as substrates for the development of SAM based immunosensors.

Lastly, ATR-FTIR studies shall be conducted on clinical serum samples of patients with either astrocytoma, oligodendroglioma or glioblastoma multiform tumour types with known IDH1 status to determine whether it is possible to discriminate patients based on IDH1 molecular status.

## 4.3 Materials & Methods

### *4.3.1 Electrochemical Set-up*

Electrochemical experiments were performed on a PalmSens 3 potentiostat (PalmSens, The Netherlands) that interfaced with either DropSens C223AT screen-printed electrodes, DropSens C223BT screen-printed electrodes (DropSens, Spain) or CH Instruments macro electrodes (CHI Instruments, USA). DropSens C223AT and DropSens C223BT electrodes comprised one silver reference electrode, one gold counter electrode and one gold 1.6mm diameter working electrode cured with high and low temperature ink respectively. CH Instruments electrodes comprised one CHI111 silver silver/chloride reference electrode, one CHI115 platinum wire counter electrode and one CHI101 gold 2.0mm diameter working electrode configured in a standard three-electrode arrangement.

*Fig. 4.1: Screen-Printed Electrode Arrangement*

*Fig. 4.2: Macro Disc Electrode Arrangement*

### *4.3.2 Materials*

Sulfosuccinimidyl 6-(3'-(2-pyridyldithio)propionamido)hexanoate (Sulfo-LC-SPDP), DL-dithiothreitol (DTT), 6-mercapto-1-hexanol (MCH), phosphate buffered saline (PBS), potassium ferricyanide, potassium ferrocyanide, sulphuric acid (98%), 30% hydrogen peroxide (Sigma-Aldrich), deionised water (Millipore) and isocitrate dehydrogenase 1 - R132H (IDH1-R132H) H-mab-1 antibodies (Merck) were employed for the cross-linker immunosensor protocol. Ethanol, 3-mercaptoproprionic acid (MPA), *N*-(3-Dimethylaminopropyl)-*N'*-ethylcarbodiimide hydrochloride (EDC), N-Hydroxysuccinimide (NHS), MES buffer (pH 5.0) and bovine serum albumin (BSA) (Sigma-Aldrich) were further required for the carbodiimide cross-linker protocol. Additionally, protein G (Sigma-Aldrich) was employed for protein G heterobifunctional cross-linker and physisorption protocols.

### *4.3.3 Antibody Selection*

Monoclonal H-mab1 IDH1-R132H antibodies from mouse species were selected for the proposed immunosensor based on publications from Kato (Kato et al, 2009) and

Takano (Takano et al, 2012). Kato showed that the clone H-mab1, formerly known as I-mab1, is specific to IDH1-R132H mutations and does not cross-react with IDH1-wild type, IDH1-R132S, IDH1-R132C, IDH1-R132G or IDH1-R132L mutations, confirmed by ELISA and Western blot tests. Similarly, Takano demonstrated in a study on 164 patients with gliomas that clone H-mab1 is specific to the IDH1-R132H mutation and successfully detected its presence in patients with primary grade IV (9.7%), secondary grade IV (63.6%), grade III (51.7%) and grade II (77.8%) gliomas. Recently, Kato published a review article on monoclonal antibody selection for IDH1 mutations (Kato, 2015), which contained a study by Preusser (Preusser et al, 2011) that showed clone H-mab1 performed identically to the other commercially available clone, H09, in 94 of 95 glioma patient samples. Clone H-mab1 has been selected for the proposed immunosensor over clone H09 due to its reduced cost and increased availability.

### *4.3.4 Patient Samples*

Electrochemical patient data sets consisted of 18 grade IV glioblastoma serum samples collected from The Walton Centre, Liverpool; 9 of which were confirmed as IDH1 wild-type status and 9 of which were confirmed as IDH1-R132H mutated status. Spectroscopic patient data sets comprised clinical serum samples from The Walton Centre and The Royal Preston hospital with a total of 47 IDH1 wild-type patients and 57 IDH1-R132H mutated patients of glioblastoma, astrocyte and oligodendroglioma tumour types. All patient information is disclosed in Appendix B.

### *4.3.5 Experimental Methodology*

#### *4.3.5.1 Electrochemical Cleaning*

DropSens C223AT/BT and CHI101 electrodes were thoroughly cleaned prior to antibody immobilisation to enable effective adsorption of SAM's to electrode surfaces. DropSens C223AT/BT electrodes were electrochemically cleaned in 0.1M sulphuric acid with potential cycling between 0V and +1.6V at a scan rate of 100mV/s for 10 scans to successively remove gold oxide. DropSens C223AT/BT electrodes were not subjected to mechanical or chemical cleaning procedures to ensure electrode surfaces remained intact prior to immobilisation protocols.

CH Instruments CHI101 electrodes were subjected to three distinct cleaning procedures. Firstly, electrodes were chemically cleaned in hot piranha solution comprised of a 3:1 ratio of 98% sulphuric acid and 30% hydrogen peroxide in water for 10 minutes to remove organic contaminants. Secondly, electrodes were mechanically cleaned with polish for 5 minutes using 0.05 micron alumina MicroPolish powder on a Microcloth pad from CH Instruments CHI120 polishing kit. Electrodes were subsequently sonicated for 15 minutes in distilled water to remove residual alumina contaminants. Thirdly, electrodes were electrochemically cleaned in 0.1M sulphuric acid by cycling the potential between -0.2V and +1.7V at a scan rate of 100mV/s for 10 scans to successively remove gold oxide.

*4.3.5.2 Heterobifunctional Cross-linker Methodology*

Gold working electrodes were functionalised with IDH1-R132H antibodies by adapting a protocol described previously by Ciani (Ciani et al, 2016) and Steel (Steel et al, 2017). Briefly, 6.66µL of 40 mM Sulfo-LC-SPDP in 1 X PBS and 3.33µL of 200µg/ml antibody solution in 5 X PBS were agitated at room temperature for 1 hour to allow formation of amide bonds between the N-hydroxysuccinimide (NHS) esters and lysine residues of the cross-linker and antibody respectively. Additionally, pyridyldithiol groups of the cross-linker react with cysteine residues of the antibody to enable the formation of reversible disulfide bonds that permit specific attachment of antibodies to gold. Subsequently, 10µL of 150mM DTT in 5 X PBS was added to the assay for 45 minutes to enable the reduction of disulfide bonds to sulfydryl groups for improved chemisorption to gold. Lastly, 20µL droplets of assay were pipetted on to working electrodes and incubated in a humidity chamber at 4 degrees Celsius for 15 hours to facilitate chemical bond formation between sulphur atoms of the cross-linker and gold surfaces.

Gold working electrodes were thoroughly rinsed with 1 X PBS solution following immobilisation to remove excess antibody solution unbound to the electrode surface. Electrodes were subsequently incubated with 20µL of 1mM MCH in 1 X PBS for 30 minutes to prevent non-specific binding at the electrode surface, and rinsed in 1 X PBS solution to remove unbound MCH particles. Thereafter, electrodes were immersed in measurement buffer of 10mM Ferri/Ferro potassium cyanide in 1 X PBS solution for

1 hour to obtain equilibrium impedance measurements prior to exposure of specified antigen concentrations.

Gold working electrodes were thoroughly rinsed with 1 X PBS and incubated with 20uL of either specific antigen (10,000 - 0.1ng/ml) in 1 X PBS or solely 1 X PBS for control measurements for 30 minutes in a humidity chamber at room temperature to facilitate antibody antigen interaction. Electrodes were subsequently rinsed in 1 X PBS and immersed in measurement buffer of 10mM ferri/ferro potassium cyanide in 1 X PBS for 30 minutes prior to acquisition of impedance measurements.

*4.3.5.3 BSA Methodology for Screen Printed Electrodes*

DropSens C223BT working electrodes were modified with IDH1-R132H antibodies by employing a protocol previously described by Badea (Badea et al, 2016). 10µL droplets of 5mg/ml BSA, 0.4M EDC and 0.1M NHS (2.5:1:1 ratio) were incubated on electrodes for 30 minutes at room temperature to facilitate cross-linking of BSA to gold. 10µL droplets of 0.4M EDC and 0.1M NHS (1:1 ratio) were then incubated on electrodes to facilitate antibody attachment to carboxylic groups of BSA. 10uL droplets of 5µg/ml IDH1-R132H antibody solution in 5 x PBS were subsequently left to react at room temperature for 1 hour on electrodes to facilitate successful conjugation to BSA. 10µL droplets of 1% ethanolamine were then incubated on electrodes for 30 minutes to block remaining bare gold surfaces and prevent non-specific binding events. 100mM MES (pH 5.0) and 1 x PBS were employed as buffer solutions for assays and were further used to rinse electrodes prior to incubation

procedures. All electrochemical measurements were obtained in an identical manner to procedures described in section 4.3.5.2.

*4.3.5.4 Carbodiimide Cross-linker Methodology*

CH Instruments CHI101 electrodes were functionalised with IDH1-R132H antibodies by modifying a protocol described previously by Molazemhosseini (Molazemhosseini et al, 2016). Briefly, electrodes were immersed in ethanolic solutions containing 1mM MPA at room temperature for 16 hours to enable chemical bond formation between sulphur atoms of MPA and gold. 20µl droplets of 0.25M EDC and 0.05M NHS (1:1 ratio) in 100mM MES buffer (pH 5.0) were incubated on electrodes for 2 hours to allow formation of stable succinimidyl esters. 10µL droplets of 200µg/ml IDH1-R132H antibody solution in 5 x PBS were then incubated on electrodes for 1 hour to allow amide bond formation and cross-linking of antibodies to carboxylic groups of MPA. 20µl droplets of 1% BSA in 1 x PBS were then incubated on electrodes for 30 minutes at room temperature to prevent non-specific adsorption upon antigen incubations. 100mM MES buffer (pH 5.0) was employed to rinse electrodes following each incubation stage. All electrochemical measurements were obtained with reference to methods outlined in section 4.3.5.2.

*4.3.5.5 Heterobifunctional Cross-linker Protein G Methodology*

CH Instruments CHI101 electrodes were functionalised with IDH1-R132H antibodies in a specific orientation by modifying surface chemistries described previously in the heterobifunctional cross-linker protocol. Briefly, 6.66µL of 40µg/ml protein G in 1 x

PBS and 3.33µL 40mM Sulfo-LC-SPDP (2:1 ratio) per electrode were agitated for 1 hour at room temperature to allow formation of amide bonds between the cross-linker and protein. 10µL of 150mM DTT in 5 x PBS per electrode was subsequently introduced to the assay for 45 minutes as previously described and then 20µL of assay was incubated on electrodes for 15 hours at 4 degrees Celsius to facilitate attachment of protein G to gold surfaces. 20µL of 40µg/ml IDH1-R132H antibodies in 5 x PBS were then incubated on electrodes for 1 hour to allow binding between protein G and the Fc region of antibodies to ensure specific orientation of antibodies on electrodes. 20µl of 0.1% BSA in 1 x PBS was then incubated for 30 minutes at room temperature on electrodes to prevent non-specific binding interactions. Remaining protocol procedures are identical to those described previously in section 4.3.5.2. However, the inclusion of protein G in the current assay, to the best of our knowledge, has not been formerly reported in the literature.

*4.3.5.6 Physisorbed Protein G Methodology*

CH Instruments CHI101 electrodes were functionalised with IDH1-R132H antibodies in accordance with a protocol previously described by Chammem (Chammem et al, 2015) and Hafaiedh (Hafaiedh et al, 2013). Briefly, clean electrodes were incubated with 20µL of 40µg/ml protein G in 1 x PBS for 2 hours at room temperature to facilitate physisorption of protein G to gold. Electrodes were subsequently rinsed in 1 x PBS and then incubated with 20µL of 40µg/ml IDH1-R132H antibodies in 1 x PBS for one hour at room temperature to allow orientated attachment between Fc region of antibodies and binding domains of protein G. Thereafter, electrodes were rinsed in 1

x PBS and incubated with 20µl of 1% BSA in 1 x PBS for 30 minutes at room temperature to prevent non-specific analyte interactions. All electrochemical measurements were obtained in an identical manner to procedures described previously in section 4.3.5.2, with the exception that measurement buffers consisted of 5mM Ferri/Ferro potassium cyanide in 1 x PBS solution.

### *4.3.6 Scanning Electron Microscopy Set-up*

Scanning electron microscopy (SEM) experiments were performed with JEOL JSM-IT100 InTouchScope configured in high vacuum mode with an acceleration voltage of 10-20kV, probe current of 0.30 and working distance of 10-14mm. Images were acquired from three random sites on working electrodes at x1700-10,000 magnification to provide accurate representations of substrates.

### *4.3.7 Atomic Force Microscopy Set-up*

Atomic force microscopy (AFM) experiments were conducted with the Asylum Research MFP-3D instrument with triangular AFM cantilevers configured in contact mode at a drive frequency of 75kHz, scan rate of 1.0016Hz, scan angle of 90 degrees and spring constant of 1N/m. Images were acquired from three random sites on working electrodes to provide accurate topographical information on substrates.

*4.3.8 Fluorescence Microscopy Set-up*

Fluorescence microscopy experiments were conducted on Nikon Eclipse LV100 configured with Photometrics CoolSNAP HQ monochrome camera. All images employed Nikon CFI TU Plan Fluor x20 magnification objective lens with bright field, Nikon Semrock BrightLine FITC-3540B-NTE and Nikon Semrock BrightLine TRITC-A-NTE cube filters. All images were acquired with MetaMorph software with parameters specified as frames to average of 4, binning of 1 and exposure times of 0.05 and 10 seconds for bright field and fluorescence respectively, and subsequently formatted with ImageJ software.

*4.3.9 ATR-FTIR Set-up*

ATR-FTIR experiments were performed on a Perkin Elmer Spectrum 2 spectrometer (Perkin Elmer, USA) configured with the Quest ATR Specac accessory module optimised with mirrors at a 45-degree angle (Specac, USA). For spectroscopic assay characterisation experiments, ATR-FTIR measurements were conducted on micro-fabricated silicon (100) internal reflection elements with 10nm evaporated gold films designed and fabricated in-house. For spectroscopic brain tumour experiments, ATR-FTIR measurements were conducted on micro-fabricated silicon (100) substrates developed by our group with no gold deposition, where further details can be found in our groups recent publication (Butler et al, 2019). All spectra were acquired in the 4000-450 $cm^{-1}$ wavenumber region at a resolution of 4 $cm^{-1}$ with 16 co-added scans.

*4.3.10 ATR-FTIR Methodology*

For assay characterisation experiments, background spectra were initially recorded for the gold-silicon substrates to account for environmental conditions. Thereafter, 5 µL volumes of respective assay steps were pipetted consecutively on the top surface of the gold-silicon substrate and allowed to incubate according to electrochemical protocols. The gold-silicon substrates were carefully washed with 1 X PBS to remove unreacted chemicals and air-dried prior to spectral acquisition. Pre-processing parameters employed on acquired spectra consisted of wavenumber selection between 4000-900 $cm^{-1}$, rubber-band base line correction and vector normalisation steps in MathWorks MATLAB R2016b (MathWorks, USA, Massachusetts). For brain cancer experiments, background spectra were recorded on the first silicon well of devices and did not contain patient serum samples. Patient samples were thawed from a -80 degree Celsius freezer to prevent protein denaturation and 3µL volumes were pipetted on to the remaining three silicon wells of devices and dried in an incubator for 1 hour at 25 degrees Celsius before conducting replicate measurements. Spectral pre-processing parameters consisted of Extended Multiplicative Scatter Correction (EMSC), truncation to the fingerprint region (1800-1000$cm^{-1}$), min-max normalisation and binning by a factor of 8 with PRFFECT version 2.0 on RStudio (R Foundation for Statistical Computing, Austria).

*4.3.11 Data Analysis & Statistics*

For electrochemical experiments, one-way ANOVA studies were conducted to determine statistical differences between percentage increases in mean charge transfer

resistances before and after antigen incubation for specified concentrations and controls. Similarly, one-way ANOVA studies were conducted to determine statistical differences between the percentage decrease in mean peak anodic current for specified concentrations and controls. In both cases, Fisher least significant difference (LSD) post-hoc studies were conducted on statistically significant results when p-values were $<0.05$ at 95% confidence intervals to analyse differences between mean values of individual data sets. All data sets consist of three repeat and three replicate measurements and stated results describe the mean value ± standard deviation.

For brain cancer experiments, pre-processed spectra were either subjected to unsupervised exploratory principal component analysis (PCA) or supervised classifications with Random Forest or Partial Least Squares (PLS) models. For supervised classifications, pre-processed spectra were separated in to either the test or training set in a 30%/70% split respectively to allow training of the model and testing of patient samples. Random Forest or Partial Least Squares (PLS) classifications were employed with five-fold cross-validation on the sample test set and repeated 50 times to determine the diagnostic accuracy of the classification. The diagnostic accuracy of the test is expressed in terms of test sensitivity and specificity representative of mean values ± standard deviation over 50 resamples. Test sensitivity describes the quantity of known patients within sample test sets that have been successfully identified with a particular disease, as indicated by equation 4.1. Test specificity describes the quantity of known control patients within the sample test set that have been correctly identified as controls, as indicated by equation 4.2.

$$Test\ Sensitivity = \frac{True\ Positives}{True\ Positives + False\ Negatives} \quad \text{(eq 4.1)}$$

$$Test\ Specificity = \frac{True\ Negatives}{True\ Negatives + False\ Positives} \quad \text{(eq 4.2)}$$

## 4.4 Results & Discussion

### *4.4.1 DropSens C223AT Screen Printed Electrodes*

#### *4.4.1.1 Electrochemical Cleaning*

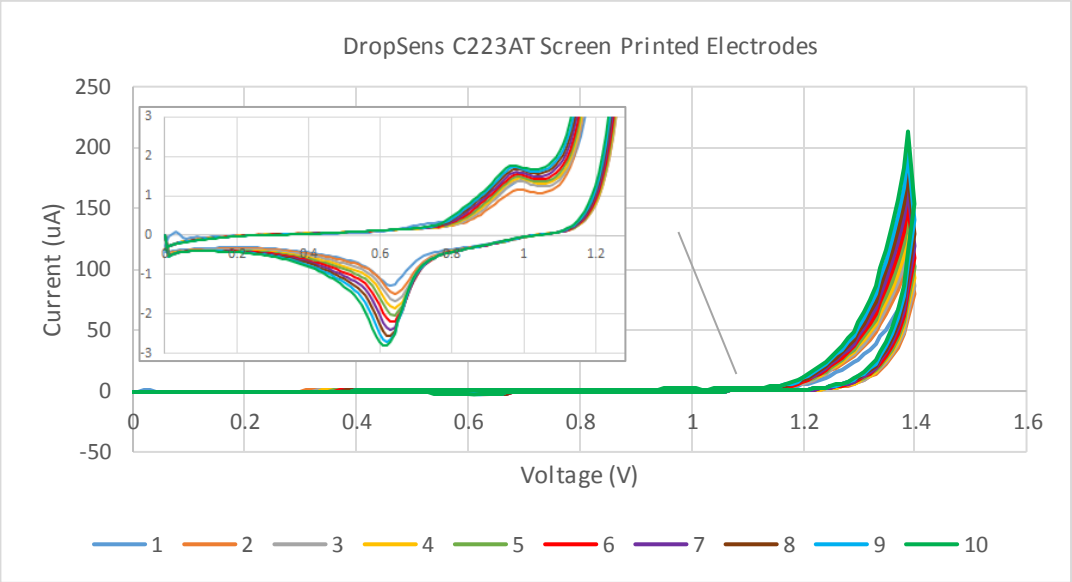


*Fig. 4.3: Electrochemical cleaning of DropSen C223AT screen printed electrodes in 0.1M H2SO4 with potential cycles from 0 to 1.4V at a scan rate of 100mV/s for 10 cycles (n=3).*

DropSens C223AT screen-printed electrodes subjected to the electrochemical cleaning procedure identified the one electron transfer redox reaction characteristic of clean gold surfaces (Fig. 4.3). Electrodes established one broad oxidation peak at ~0.969V,

and one sharp reduction peak at ~0.620V, consistent with gold oxide removal on screen-printed electrodes (Steel et al, 2017). Electrodes produced peak oxidation and reduction currents in the first scan of 1.407 µA ± 0.038 and -1.271 µA ± 0.635 respectively, which increased with consecutive scans to 1.703 µA ± 0.127 and -2.804 µA ± 0.500 in the tenth scan, indicative of progressive gold oxide removal at the electrode surface.

#### *4.4.1.2 Heterobifunctional Cross-linker Protocol*

##### *4.4.1.2.1 Electrochemical Characterisation of SAM*

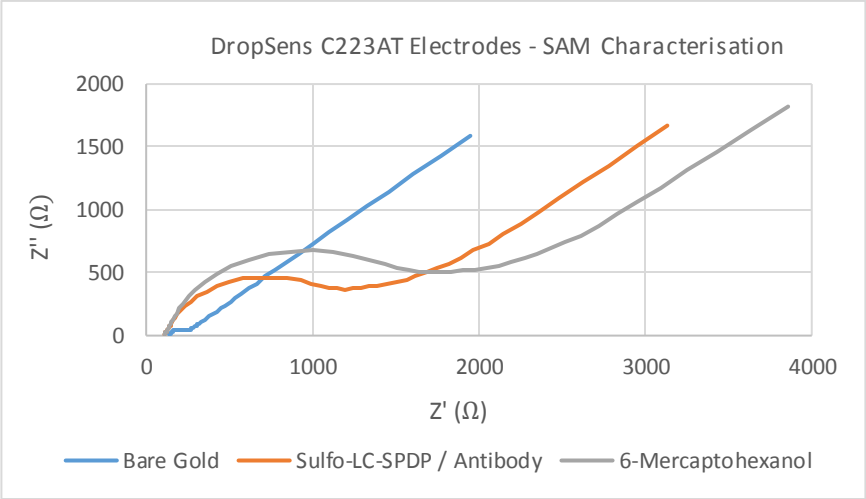


*Fig. 4.4: Nyquist plot of self-assembled monolayer characterisation on Dropsens C223AT screen printed electrodes (n=3).*

DropSens C223AT bare electrodes displayed low charge transfer resistance, Rct, values of 105.936Ω + 21.698, which suggests that electro-active species can readily interact with electrode surfaces through electron tunnelling prior to functionalisation (Fig. 4.4) (Akkerman et al, 2007). Additionally, bare electrodes displayed theta values of θ = 0.862 + 0.018 indicative of relatively smooth electrode surfaces (Badea et al, 2016). Sulfo-LC-SPDP antibody deposition produced significant increases in Rct to

1217.322Ω + 260.358 (t(8) = -14.82, p-value < 0.05) and significant decreases in theta to θ = 0.808 + 0.010 (t(8) = 7.96, p-value < 0.05), which suggests cross-linker attachment to gold restricts electron transfer events and produces rougher electrode surfaces (Badea et al, 2016). MCH deposition prompted additional significant increases in both Rct to 1724.889Ω + 356.190 (t(8) = -5.93, p-value = <0.05) and theta values to θ = 0.829 + 0.009 (t(8) = -23.45, p-value < 0.05). This indicates that thiol head groups successfully block remaining bare gold surfaces that further restricts electron transfer events and produces smoother SAM layers (Badea et al, 2016).

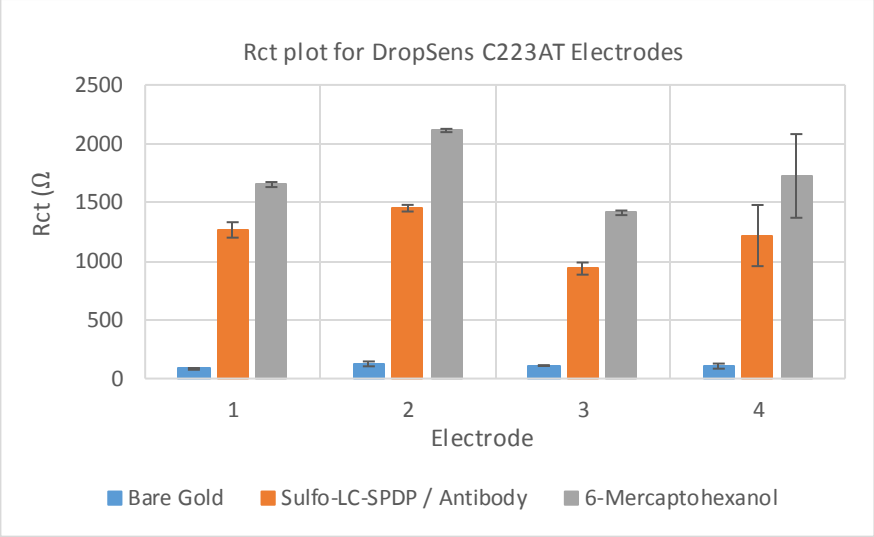


*Fig. 4.5: Charge transfer resistance, Rct, plot of self-assembled monolayer characterisation on Dropsens C223AT screen-printed electrodes (n=3).*

The degree of immobilisation varies significantly between all three electrode surfaces for both Sulfo-LC-SPDP antibody (F(2, 8) = 78.15, p-value < 0.05) and MCH (F(2, 8) = 1105.01, p-value < 0.05) assays (Fig. 4.5). Kwasny previously reported variation in SAM attachment between membrane electrodes with an identical assay protocol; however, fluctuations in starting Rct values did not appear to negatively influence sensor responses (Kwasny et al, 2018). Conversely, Steel found significant differences

in Rct values of SAM's on screen-printed electrodes were associated with reduced assay linearity (Steel et al, 2017). Therefore, concentration studies must be conducted on additional electrodes to determine the extent of SAM variation and to evaluate whether variation is detrimental to detection of IDH1-R132H antigens.

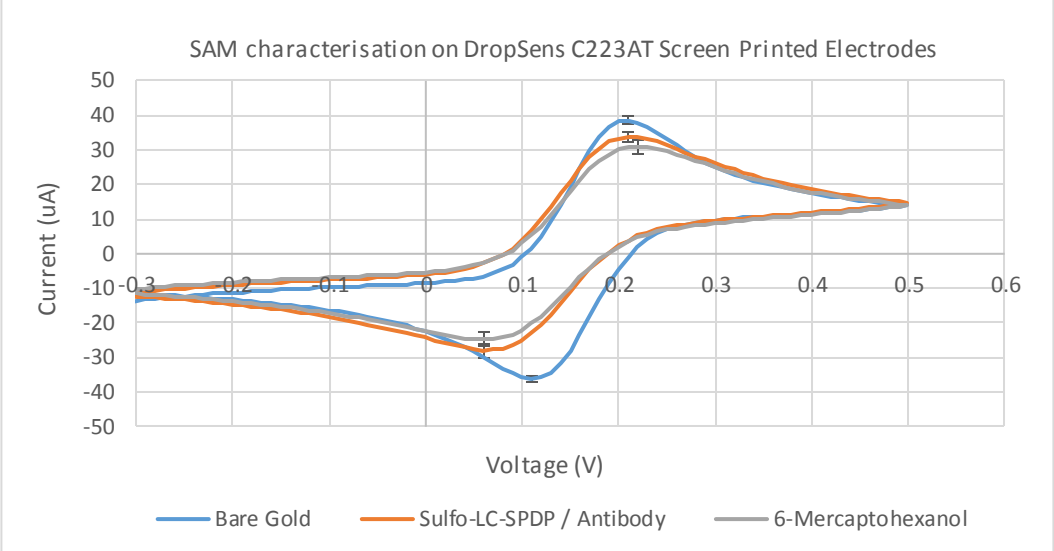


*Fig. 4.6: CV plot of Dropsens C223AT screen-printed electrodes following immobilisation procedures (n=3).*

Voltammetric responses reveal consecutive current decreases with successive molecular depositions indicative of successful self-assembled monolayer immobilisation on electrode surfaces (Islam et al, 2017). CV results for bare gold electrodes displayed one-electron redox reactions characteristic of ferri/ferro probes, with oxidation, ~0.21V, and reduction, ~0.11V, potentials giving a peak-to-peak potential separation of ~100mV, indicative of a quasi-reversible reaction (Elgrishi et al, 2018). Similarly, measured peak oxidation, 38.571µA + 1.156, and reduction, -36.063µA + 0.919, currents produced a peak anodic to cathodic current ratio of 1.069, indicative of a quasi-reversible reaction. Sulfo-LC-SPDP antibody depositions result

in statistically significant decreases in peak oxidation, 33.774µA + 1.331 (F(2,24) = 31.94, p-value < 0.05), and reduction, -27.830µA + 2.042 (F(2,24) = 125.85, p-value < 0.05) currents. This indicates increased electron transfer resistance between the redox probe and electrode, coherent with EIS data, and implies successful thiol attachment to gold. Similarly, shifts in reduction potentials to 0.060V increases peak-to-peak potential separation to ~150mV, which implies slower electron transfer kinetics due to thiol coupling to the electrode surface. MCH depositions further cause statistically significant decreases in peak oxidation, 30.931µA + 2.214 (F(2,24) = 31.94, p-value = <0.05), and reduction, -24.820µA + 2.051 (F(2,24) = 125.85, p-value < 0.05) currents, which indicates head group attachment of the alkane thiol to remaining bare gold surfaces.

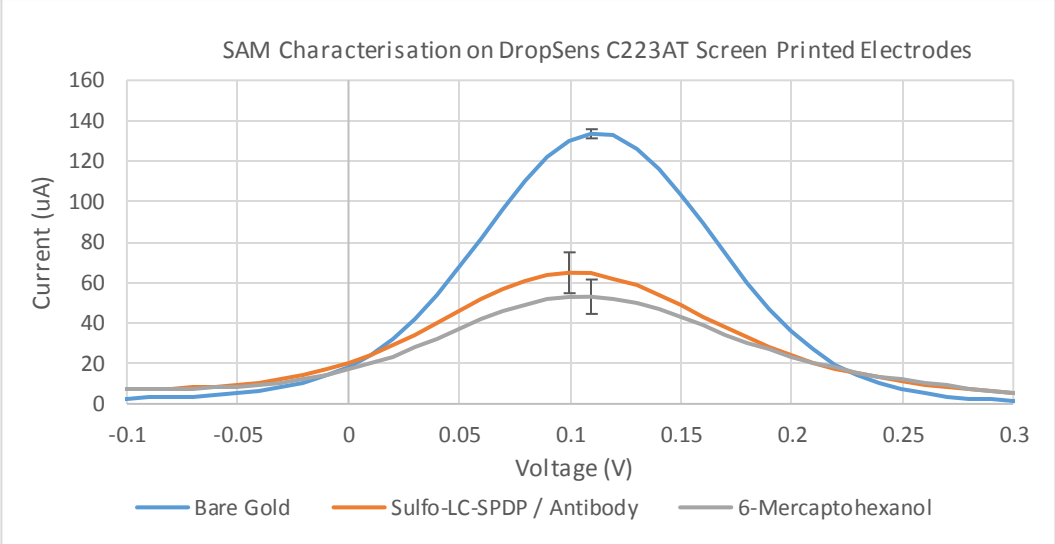


*Fig. 4.7: Differential pulsed voltammetry of self-assembled monolayer characterisation on Dropsens C223AT screen printed electrodes (n=3).*

DPV data is consistent with previous CV results where oxidation currents for bare gold electrodes, 133.558µA + 2.264, decrease significantly to 64.837µA + 10.107 upon deposition of Sulfo-LC-SPDP antibody assays (F(2,24) = 363.22, p-value < 0.05).

Deposition of MCH assays further produces statistically significant current decreases to 52.991µA + 8.503 ($F(2,24) = 363.22$, p-value $< 0.05$). Interestingly, current responses for all immobilisation stages are greater compared to previous CV results, attributed to increased sensitivity of the technique (Hussain et al, 2017). Therefore, DPV shall be employed for concentration studies given increased signal strengths to assess the feasibility of voltammetry for IDH1-R132H quantification.

#### *4.4.1.2.2 ATR-FTIR Characterisation of SAM*

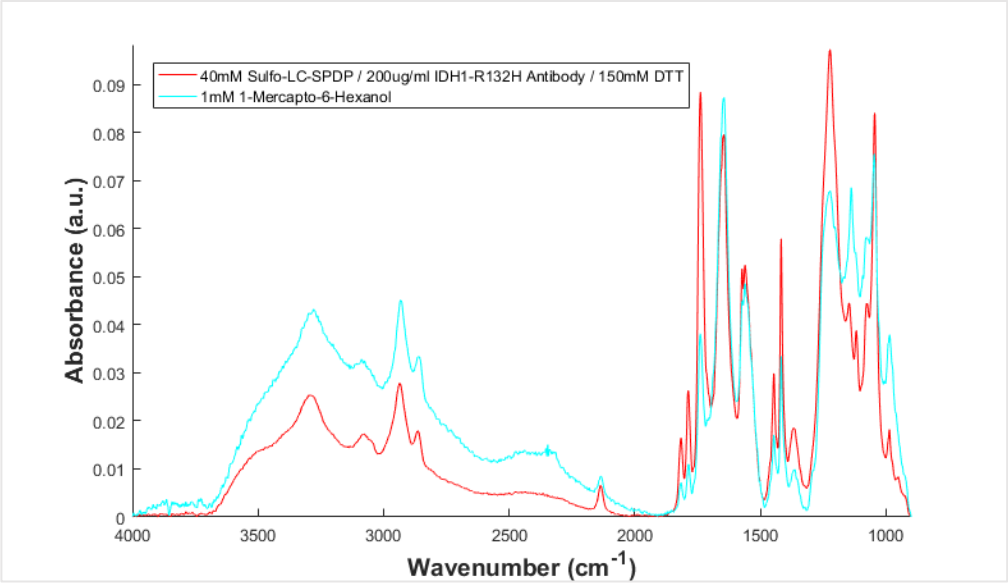


*Fig. 4.8: ATR-FTIR spectra of SAM deposition layers attached to gold coated silicon crystals with rubber-band baseline correction and vector normalisation pre-processing steps (n=3).*

Infrared spectra display distinctive absorption signatures representative of the molecular bonding environment present on functionalised gold-silicon ATR crystals following immobilisation with heterobifunctional cross-linker assays. Strong absorption bands were observed in ~3200-2800cm$^{-1}$ and ~1450-1375cm-1 regions that correlate with $\nu(CH_2)/\nu(CH_3)$ and $\delta(CH_2)/\delta(CH_3)$ vibrations attributed to the

hydrocarbon chain of Sulfo-LC-SPDP molecules and heavy chain region of antibodies. Similarly, intense absorption bands at ~1740cm-1, ~1417cm-1 and ~1220cm-1 may be assigned to $\nu$(C=O), $\nu$(S=O) and $\nu$(CN) vibrations respectively, indicative of the presence of Sulfo-LC-SPDP molecules. Likewise, strong absorption peaks at ~1650cm-1, ~1550cm-1 and ~1045cm-1 may be assigned to amide I, amide II and $\nu$(CO) vibrations that indicate antibody presence on electrodes. Subsequent blocking with MCH assays prompted suppression of above absorption peaks with concurrent increases in intensities of previously described $\nu(CH_2)/\nu(CH_3)$ and $\delta(CH_2)/\delta(CH_3)$ vibrations, and $\nu$(OH) vibrations associated with the tail group of MCH molecules. Therefore, spectroscopic evidence suggests successful immobilisation of heterobifunctional cross-linker assays to gold substrates.

*4.4.1.2.3 Fluorescence Microscopy Characterisation of SAM*

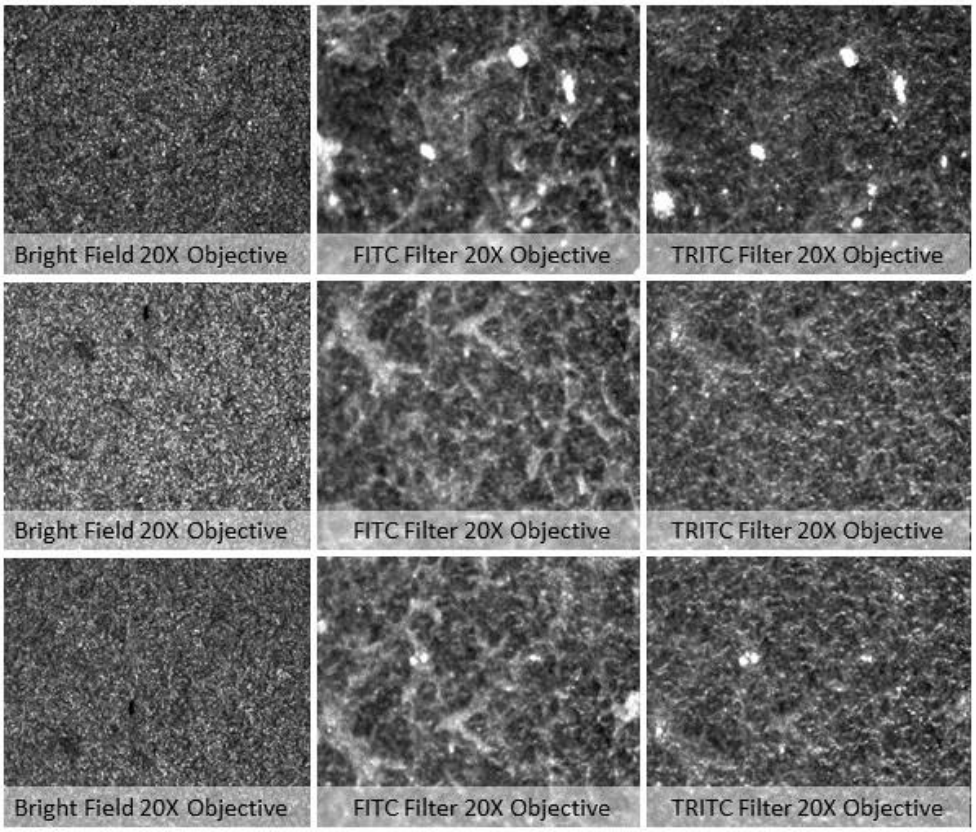


*Fig. 4.9: Fluorescence microscopy images of DropSens C223AT electrodes functionalised with FITC conjugated antibodies when subjected to bright field, FITC and TRITC light sources (n=3).*

Inspection of fluorescence microscopy images of DropSens C223AT electrodes reveals successful immobilisation of FITC conjugated antibodies to gold surfaces using proposed heterobifunctional cross-linker assays. Specifically, electrodes were observed to strongly fluoresce at 482nm ± 17 excitation wavelengths, with mean pixel intensities of 81.1 ± 39.7, 98.0 ± 35.0 and 97.4 ± 35.6 calculated from image 1b, 2b and 3b respectively. Conversely, electrodes were observed to weakly fluoresce at 542nm ± 16 excitation wavelengths, with reduced mean pixel intensities of 72.8, 91.1 and 88.5 for images 1c, 2c and 3c respectively, albeit decreases were not deemed statistically different ($F(1,4) = 1.02$, p-value = 0.370). Findings are consistent with fluorescence of FITC dyes that are recognised to have a peak absorption wavelength of 495nm (Holmes et al, 2001). Furthermore, the presence of FITC molecules

elucidates to the weak fluorescence signals observed at 540-525nm wavelengths, since FITC dyes still weakly fluoresce at TRITC wavelengths, attributed to bleed-through and the overlapping of FITC and TRITC excitation and emission spectra (Renier et al, 2007). Interestingly, FITC fluorescence intensities were not uniform over sensor surfaces, which indicates uneven antibody coverage on electrodes, consistent with previous studies that suggest inclusion of DTT in the assay may lead to aggregation on electrode surfaces (Kwasny et al, 2018). However, on closer inspection, hot spots appear in close proximity to defects within gold screen-printed layers, which suggests that the topography of electrode surfaces may influence antibody distribution.

*4.4.1.2.4 Concentration Study*

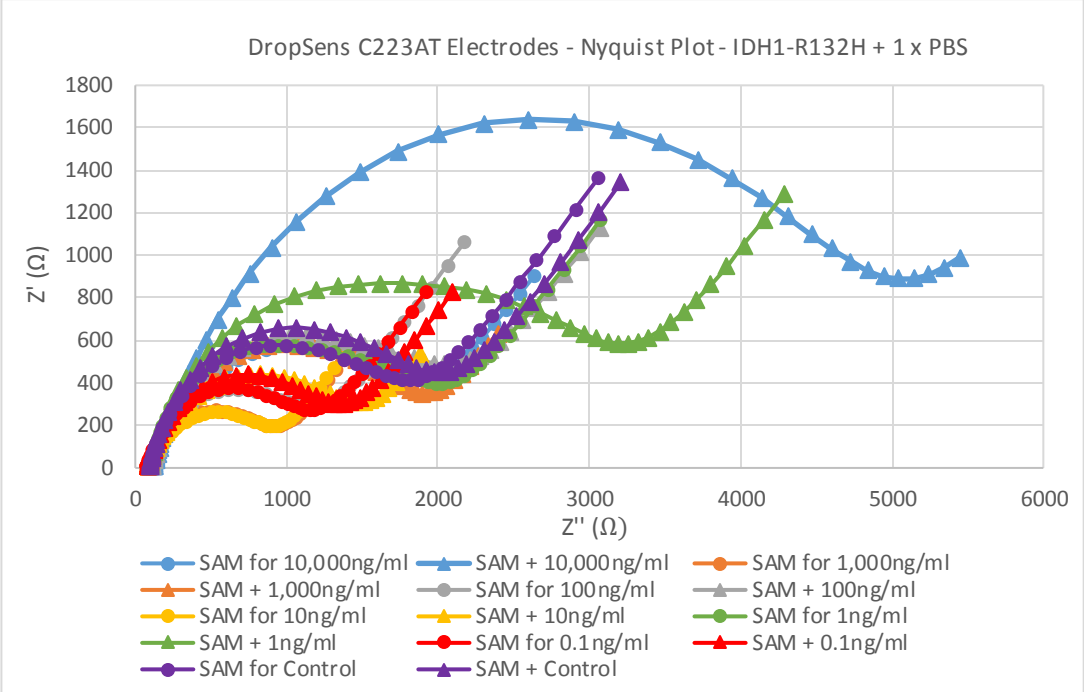


*Fig. 4.10: Nyquist plots for functionalised DropSens C223AT electrodes before and after incubation with specified antigen concentrations (n=3).*

DropSens C223AT electrodes produced starting impedimetric responses characteristic of SAM's that changed upon exposure to specified antigen concentrations (Fig. 4.10). Initially, Nyquist plots depict a semi-circle at high frequencies for functionalised electrodes representative of Rct between the redox couple and modified electrode surface. Furthermore, Nyquist plots depict 45-degree straight lines at low frequencies characteristic of Warburg resistance that describes diffusion of the redox probe at the electrode. Thereafter, exposure to samples of specified antigen concentrations causes increases in Rct, indicative of successful antibody-antigen affinity binding at the SAM, which restricts electron transfer between the redox probe and electrode. Similarly, Warburg resistances increase upon exposure to samples of specified antigen

concentrations, which suggests that additional molecules on SAM's from antibody-antigen interactions restrict diffusion of redox probes to the electrode surface.

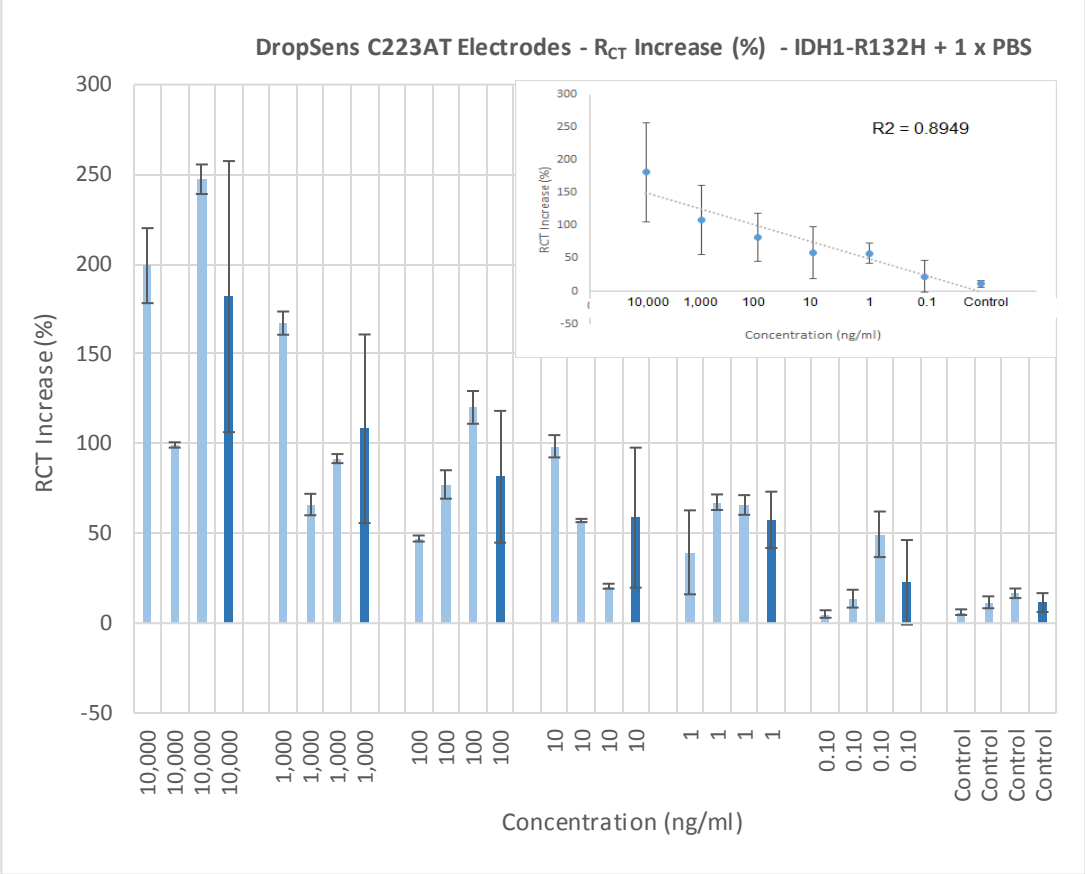


*Fig. 4.11: Rct plots for functionalised DropSens C223AT electrodes before and after incubation with specified antigen concentrations (n=3).*

Percentage increases of Rct for functionalised electrodes before and after antigen incubation were observed to have a weak positive correlation to target IDH1-R132H protein concentrations, with a Pearson co-efficient of $r^2$= 0.8949 (Fig 4.11). Specifically, functionalised electrodes recorded increased Rct values of 181.9% ± 75.5 for 10,000 ng/ml protein concentrations, significantly greater than 108.3% ± 52.5 for 1,000 ng/ml samples (F(1,16) = 7.51, p-value = <0.05). However, functionalised electrodes recorded increased Rct values of 81.5% ± 36.7 for 100ng/ml, which was not significantly different to 1,000ng/ml (F(1,16) = 2.05, p-value = 0.171). Similarly,

functionalised electrodes were unable to distinguish between 10ng/ml at 58.8% ± 39.0 and 1ng/ml at 57.6% ± 15.7 ($F(1,16) = 0.01$, p-value = 0.926). At 0.1ng/ml concentrations, percentage differences in Rct were negligible at 22.8% ± 23.6 compared to control measurements at 11.5% ± 5.26 ($F(1,16) = 2.34$, p-value = 0.146). Our findings are consistent, to a certain extent, with reported studies in the literature where Rct values are observed to increase proportionally to protein concentration. However, our immunosensor has a current limit of detection of 1ng/ml, significantly poorer compared to previous studies of similar methodologies, with Ciani (Ciani et al, 2012) and Steel (Steel et al, 2017) reporting detection limits of 100pg/ml and 50pg/ml respectively. Additionally, our results display considerable standard deviations for all concentrations, which indicates possible reproducibility issues with our current sensor.

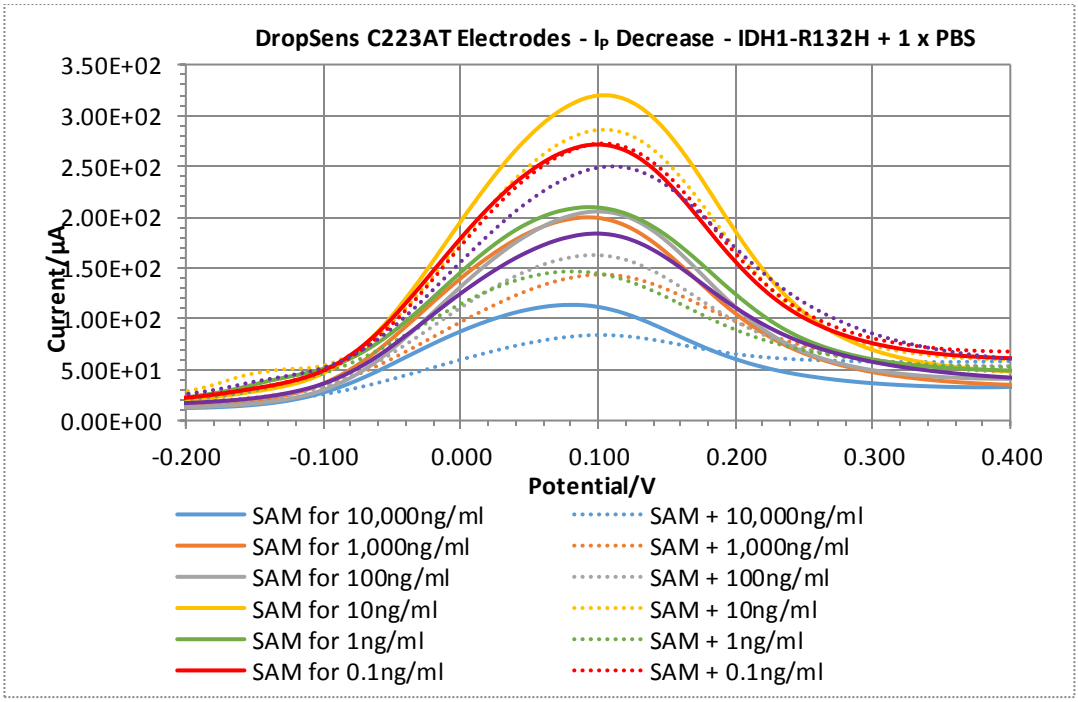


*Fig. 4.12: DPV plots for functionalised DropSens C223AT electrodes before and after incubation with specified antigen concentrations (n=3).*

DropSens C223AT electrodes functionalised with SAM's produced current responses characteristic of oxidation of the Ferri/Ferro probe (Shahrokhian et al, 2016). The electro-active species was converted from $Fe(CN)_6^{-4}$ to $Fe(CN)_6^{-3}$ on application of anodic potentials of ~0.1V resulting in a loss of one electron to the electrode surface through tunnelling. Oxidation currents were observed to decrease proportionally to antigen concentration upon incubation with samples of different antigen concentrations, which indicates that antigen binding to SAM's restricts electron transfer at the electrode surface, consistent with increased Rct values measured in previous impidimetric experiments. Interestingly, electrodes measured different intensities of oxidation currents before incubation with target antigens, which further suggests varying degrees of SAM immobilisation on electrode surfaces.

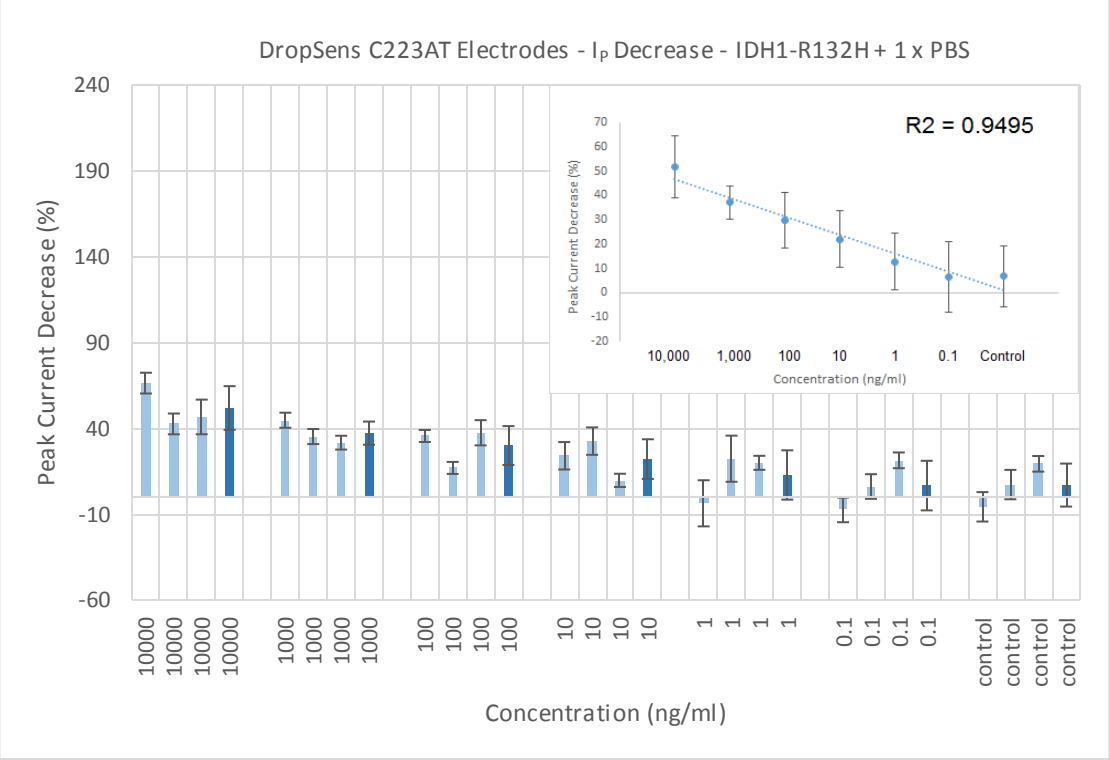


*Fig. 4.13: Percentage differences in peak oxidation currents for functionalised DropSens C223AT electrodes before and after incubation with specified antigen concentrations (n=3).*

Percentage decreases in anodic currents associated with oxidation of the redox couple at functionalised electrodes before and after antigen incubation were observed to have a weak positive correlation to IDH1-R132H protein concentration, with a Pearson co-efficient of $r^2 = 0.9495$ (Fig. 4.13). Electrodes measured current decreases of 51.8% ± 12.6 for 10,000ng/ml concentrations, and were found to be significantly greater than 37.2% ± 6.68 for 1,000ng/ml concentrations ($F(1,16) = 9.46$, p-value $< 0.05$). Conversely, electrodes measured current decreases of 29.9% ± 10.7 for 100ng/ml antigen concentrations, which were not statistically different to 10ng/ml at 22.1% ± 11.0 ($F(1, 16) = 2.39$, p-value = 0.142). Similarly, electrodes measured percentage current decreases of 12.8% ± 14.3 for 1ng/ml antigen concentrations which were not deemed statistically different to 0.1ng/ml at 6.62% + 13.2 ($F(1,16) = 0.91$, p-value = 0.354), or to control measurements at 6.92% ± 12.0 ($F(1,16) = 0.90$, p-value = 0.358). Interestingly, voltammetric results display an improved Pearsons co-efficient compared to impidimetric experiments, possibly attributed to the latter's incapacity to distinguish between specific and non-specific binding of the target molecule and electrolytic solution respectively (Bogomolova et al, 2009). However, considerable standard deviations still exist below ≤100ng/ml concentrations that indicate the current immunosensor is not capable of reproducibly detecting low antigen concentrations, which explains the poor linearity of our results and questions either the effectiveness of our functionalisation protocol or choice of electrode substrates.

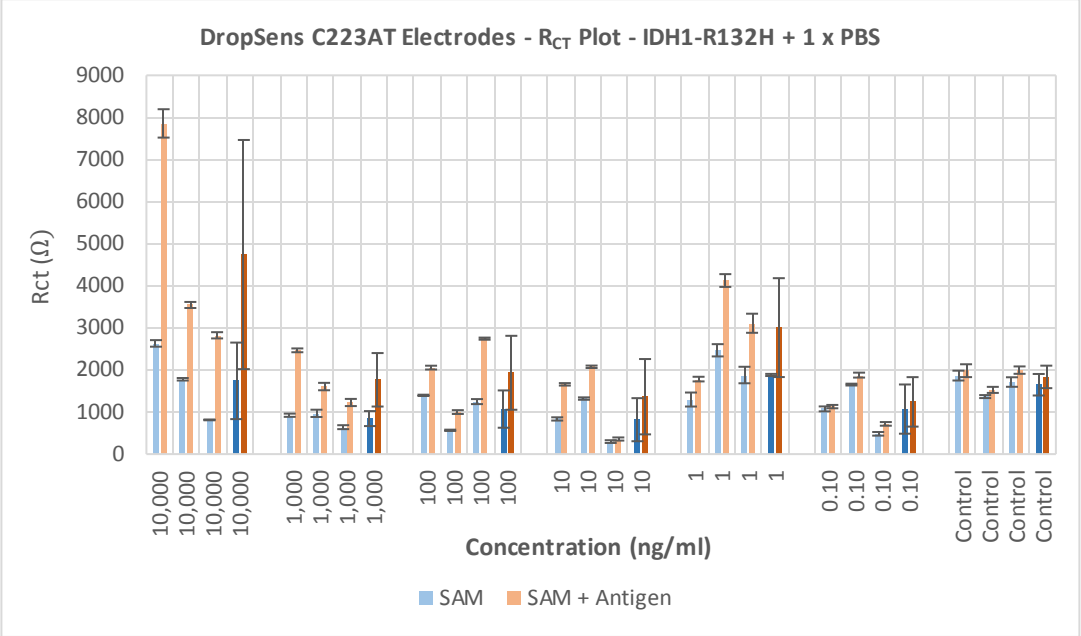


*Fig. 4.14: Rct plot for functionalised DropSens C223AT electrodes before and after incubation with specified antigen concentrations (n=3).*

The cross-linker assay may contribute to electrochemical variation observed in previous experiments, with distinct differences observed in Rct values between electrodes prior to antigen incubation (Fig. 4.14), raising the possibility of different degrees of SAM formation between electrodes. Mendes found reductions in Rct were associated with pinholes in SAM layers that permit interaction of electro-active species with electrode surfaces, and suggests possible defects in our SAM layers (Mendes et al, 2004). Interestingly, Kwasny previously removed DTT from the cross-linker assay to avoid the reduction of disulphide bonds in Sulfo-LC-SPDP, with the view that the greater affinity of thiols over dithiols may cause aggregation and negatively influence SAM coverage (Kwasny et al, 2018). However, Ciani demonstrated that inclusion of DTT was necessary to increase chemisorption of the assay and produce denser SAM layers on electrode surfaces (Ciani et al, 2012). Hence, any future removal of reducing agents from our assay requires further consideration. Additionally, our fluorescence

images show hot spots associated with uneven antibody distribution originate in close proximity to irregularities in electrode surfaces. Therefore, electrode surfaces may influence overall sensor performance, and elucidate to the variation observed in our impidimetric and voltammetric results, in agreement with previous findings of Steel (Steel et al, 2017) and Butterworth (Butterworth et al, 2019).

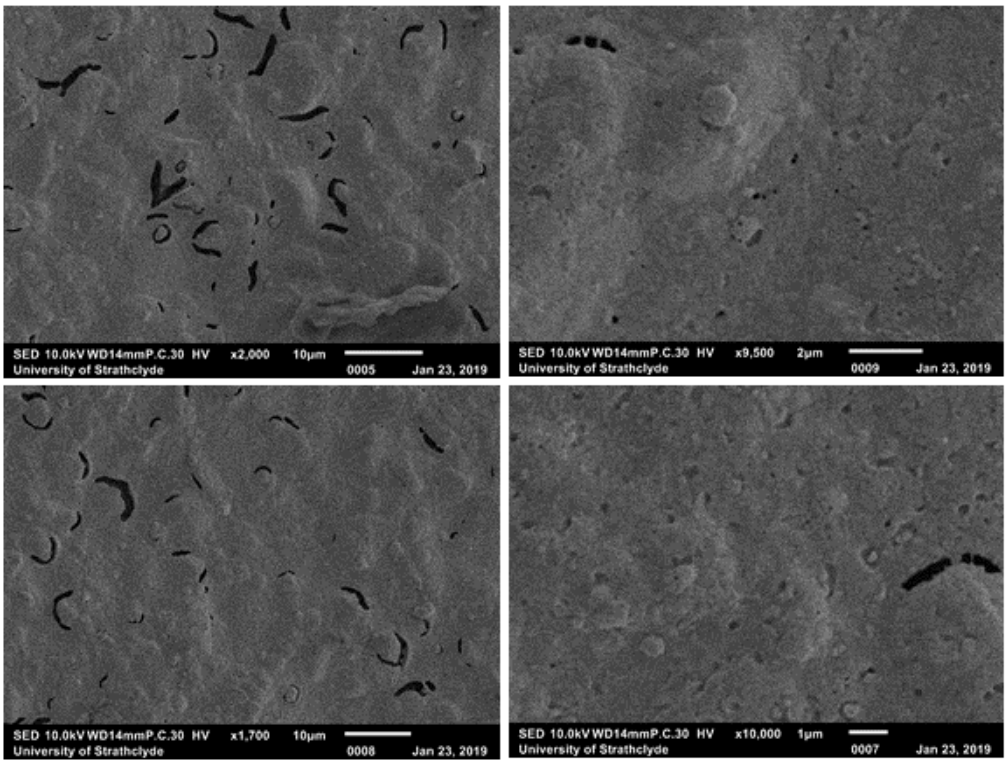


*Fig. 4.15: SEM images of bare gold DropSens C223AT electrodes.*

Closer inspection of DropSens C223AT electrodes show significant inconsistencies in gold deposits, with clusters of gold particles and defects across sensor surfaces, evident from obtained SEM images (Fig 4.15). Gold cluster formation is likely to arise because of aggregation of the screen-printed ink where gold particles mix with polymeric insulators and mineral binders to improve substrate adhesion (Li et al, 2012). Similarly, holes present in electrode surfaces may be attributed to the annealing of high temperature cure inks utilised in DropSens C223AT electrodes, since it is well

recognised that annealing at high temperatures may lead to crack formations in gold surfaces (Plaza et al, 2003).

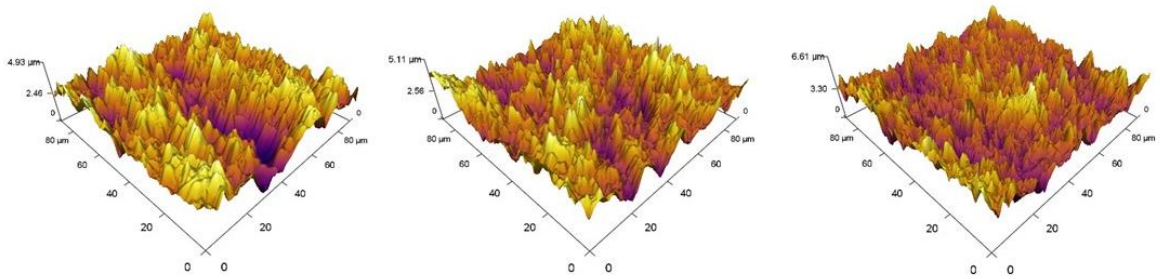


*Fig. 4.16: AFM images of bare gold DropSens C223AT electrodes.*

Topographical inspection of DropSens C223AT working electrodes further reveals significant surface roughness across cross-sectional areas, with root mean square roughness, Rq, calculated as 118.1nm, 166.8nm, 125.2nm respectively (Fig 4.16). Furthermore, peak features were calculated as 4.9um, 5.11um and 6.61um respectively. Interestingly, electrode surface roughness is associated with greater proportions of defects in SAM's, attributed to the poor organisation of thiols on rough gold, which is detrimental to both electron transfer rate constants and protein orientation (Jeuken, 2017). Therefore, identical assays should be performed on different electrode substrates to ascertain whether the electrode surface is the primary cause of variation in obtained electrochemical results.

### *4.4.2 DropSens C223BT Screen Printed Electrodes*

#### *4.4.2.1 Electrochemical Cleaning*

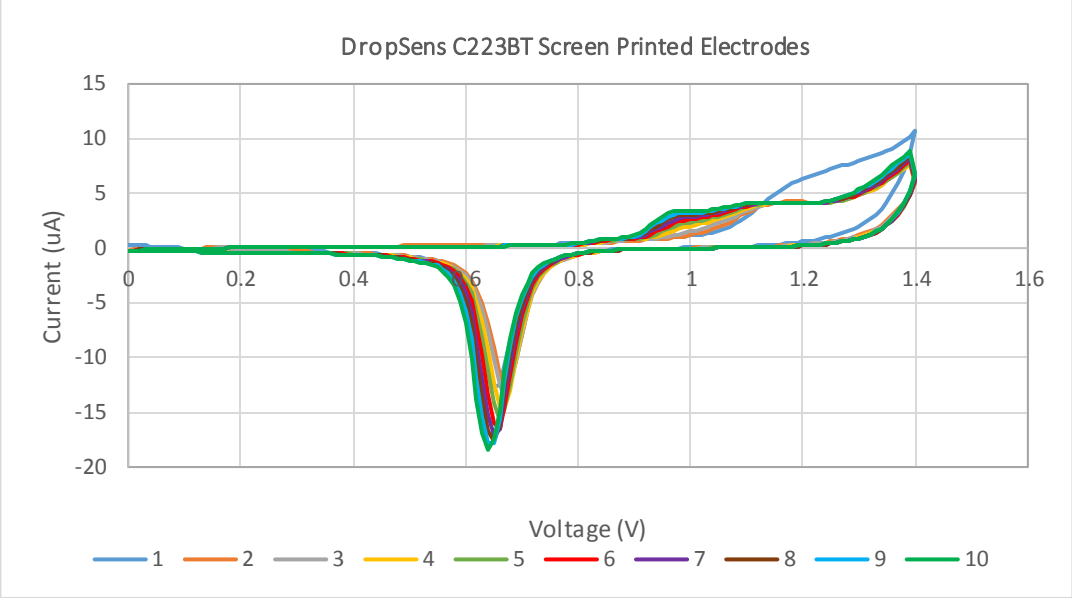


*Fig. 4.17: Electrochemical cleaning of DropSen C223BT screen printed electrodes in 0.1M H2SO4 with potential cycles from 0 to 1.4V at a scan rate of 100mV/s for 10 cycles (n=3).*

DropSens C223BT screen-printed electrodes subjected to the electrochemical cleaning procedure similarly identified one electron transfer redox reactions characteristic of gold surfaces (Fig. 4.17). Electrodes identified one broad Epa = ~1.199V in the first scan that progressively shifted to ~0.969V in the tenth scan, and one sharp Epc = ~0.640V, consistent with DropSens C223AT gold electrodes. Ipa and Ipc measured 6.339µA ± 2.218 and -12.653µA ± 4.044 respectively for the first scan, and similarly increased with gold oxide removal to 3.306µA ± 1.093 and 18.429µA ± 6.594 respectively in the tenth scan. Interestingly, peak reduction currents were significantly greater for DropSens C223BT electrodes compared to DropSens C223AT electrodes ($F(1,18) = 372.49$, p-value $< 0.05$), which indicates DropSens C223BT electrodes possess increased effective electro-active areas (Trasatti et al, 1992).

*4.4.2.2 Heterobifunctional Cross-linker Protocol*

*4.4.2.2.1 Electrochemical Characterisation of SAM*

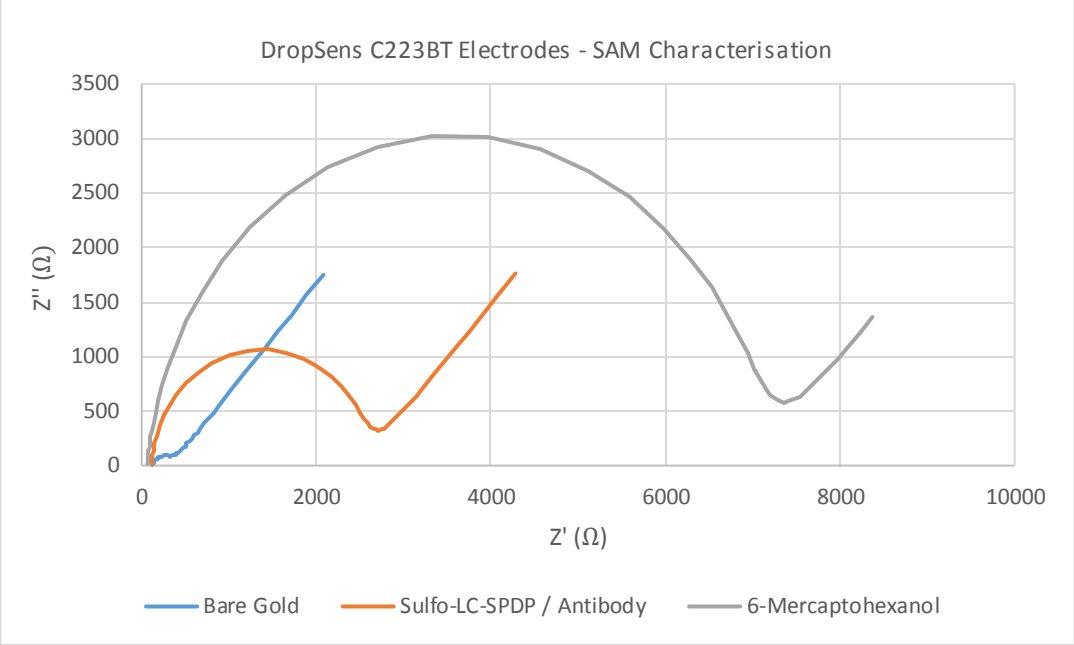


*Fig 4.18: Nyquist plots of SAM characterisation on Dropsens C223BT screen printed electrodes following immobilisation procedures (n=3).*

DropSens C223BT bare electrodes display low Rct values of 249.84 Ω + 75.932 comparable to previous DropSens C223AT electrodes. However, DropSens C223BT electrodes exhibit theta values of θ = 0.740 + 0.141, significantly lower than DropSens C223AT electrodes ($F(1,16) = 7.69$, p-value $< 0.05$), indicative of rougher bare electrode surfaces (Badea et al, 2016). Sulfo-LC-SPDP antibody depositions significantly increase Rct to 2415.889 Ω + 1033.332 ($F(1,16) = 50.01$, p-value $< 0.05$) and theta values to θ = 0.951 + 0.003 ($F(1,16) = 23.48$, p-value $< 0.05$), which suggests cross-linker attachment to gold results in reduced electrode surface roughness. MCH depositions significantly increase Rct to 6980.667 Ω + 2390.304 ($F(1,16) = 36.24$, p-value $< 0.05$) and decrease theta values to θ = 0.928 + 0.003 ($F(1,16) = 210.75$, p-

value < 0.05). Likewise, electrode responses indicate successful SAM attachment to gold surfaces, as previously described in section 4.4.1.2.1. Interestingly, impedance at each functionalisation stage is significantly greater compared to previous DropSens C223AT electrodes, which indicates formation of denser SAM's on electrode surfaces, possible explained by the increased effective electrochemical area found in section 4.4.2.1.

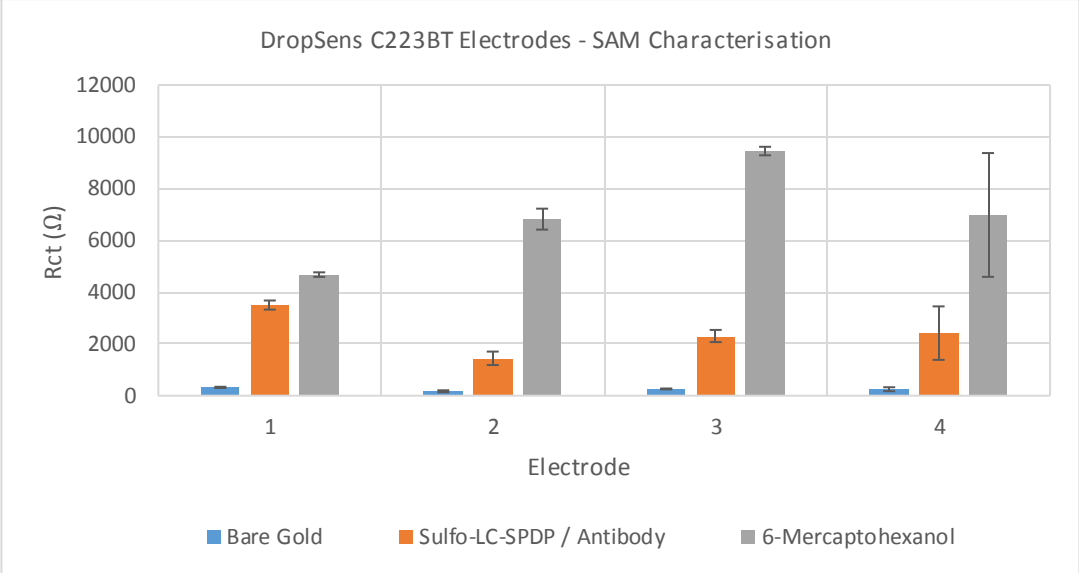


*Fig 4.19: Rct plot of self-assembled monolayer characterisation on Dropsens C223BT screen printed electrodes following immobilisation procedures (n=3).*

Immobilisation similarly varies significantly between all three electrode surfaces for both Sulfo-LC-SPDP antibody ($F(2,6) = 62.38$, p-value < 0.05) and MCH ($F(2,6) = 257.95$, p-value < 0.05) assays, consistent with previous DropSens C223AT electrodes. Interestingly, the degree of blocking varies between all three electrodes, which indicates the quantity of remaining bare gold surfaces is different on each electrode after Sulfo-LC-SPDP functionalisation. Therefore, preliminary results suggest that deposition of the cross-linker assay may in fact be the primary cause of variation in our previous results and not electrode surfaces.

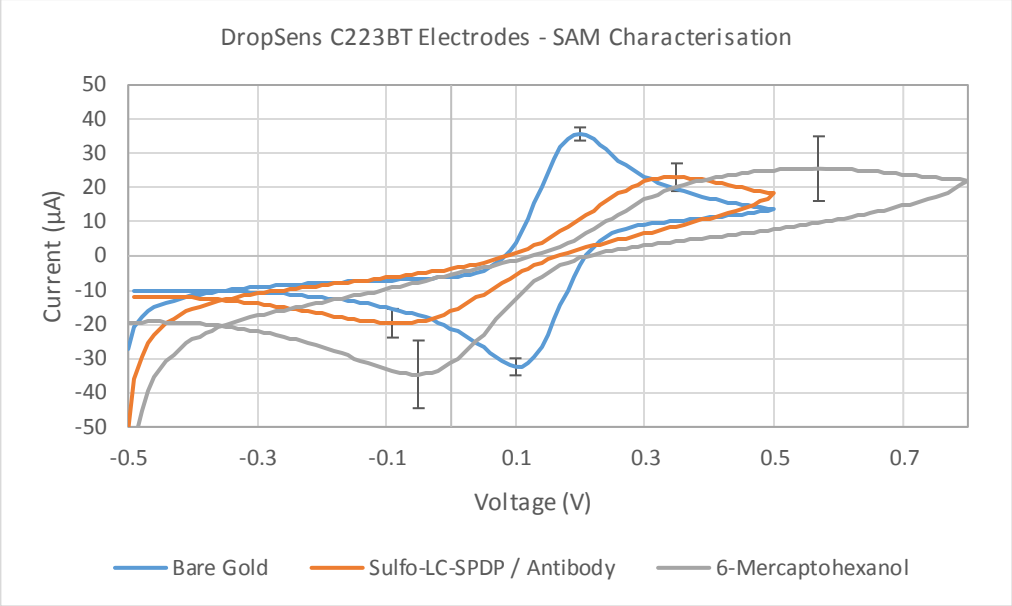


*Fig 4.20: Cyclic voltammogram of self-assembled monolayer characterisation on Dropsens C223BT screen printed electrodes following immobilisation procedures (n=3).*

CV results for bare gold electrodes similarly display one-electron quasi-reversible redox reactions consistent with DropSens C223AT. Bare gold electrodes measured Ipa = 35.670µA ± 1.931 and Ipc = -32.4205µA ± 2.493 at Epa = ~0.20V and Epc = ~0.10V respectively. Sulfo-LC-SPDP antibody depositions significantly reduced Ipa = 23.028µA ± 4.054 ($F(1,16) = 77.74$, p-value < 0.05), and Ipc = -19.678µA ± 4.199 ($F(1,16) = 79.20$, p-value < 0.05), indicative of successful immobilisation as previously described in section 4.4.1.2.1. Likewise, MCH assays increased peak-to-peak potential separation as a consequence of increased charge transfer resistance that suggests successful alkane thiol attachment to gold. However, MCH assays did not cause significant reductions in Ipa = 25.534µA ± 9.457 ($F(1,16) = 0.69$, p-value = 0.417) and instead produced increases in Ipc = -34.625µA ± 9.899 ($F(1,16) = 22.36$, p-value < 0.05). This response is not consistent with previous literature findings as one

would expect to observe further decreases in both redox peaks with additional deposition of molecules on gold (Ahmad et al, 2012). Thus, it can be conjectured that application of increasingly positive potentials at electrodes reduces the stability of the SAM, leading to pinholes that permits increased quantities of electro-active species to contact electrode surfaces, and would further validate the large standard deviation of our results.

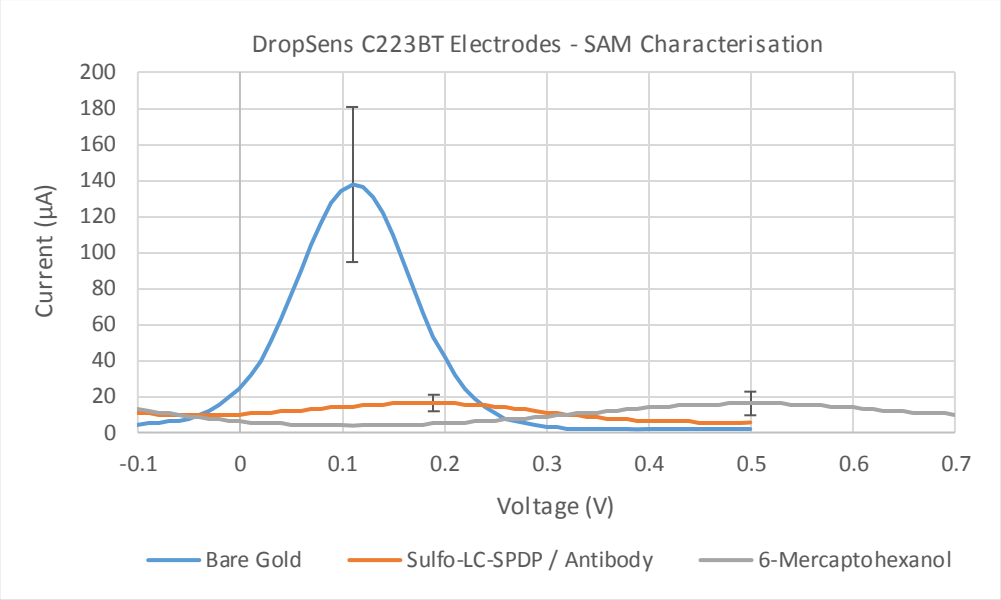


*Fig 4.21: DPV plot of self-assembled monolayer characterisation on Dropsens C223BT screen printed electrodes following immobilisation procedures (n=3).*

DPV results similarly show Ipa for bare gold electrodes of 137.588µA ± 43.027, that decrease to 16.366µA ± 4.579 following deposition of Sulfo-LC-SPDP antibody assays ($F(1,16) = 93.09$, p-value $< 0.05$). However, MCH assays do not cause significant reductions in Ipa = 16.133µA ± 6.548 ($F(1,16) = 0.01$, p-value $< 0.921$). Interestingly, current responses significantly reduced following immobilisation assays compared to DropSens C223AT electrodes, which again implies denser SAM

formation on electrode surfaces, and supports our previous impidimetric findings. Therefore, DropSens C223BT electrodes will not consider voltammetry as an appropriate detection method for future concentration studies based on the significantly poorer current responses.

*4.4.2.2.2 Fluorescence Microscopy Characterisation of SAM*

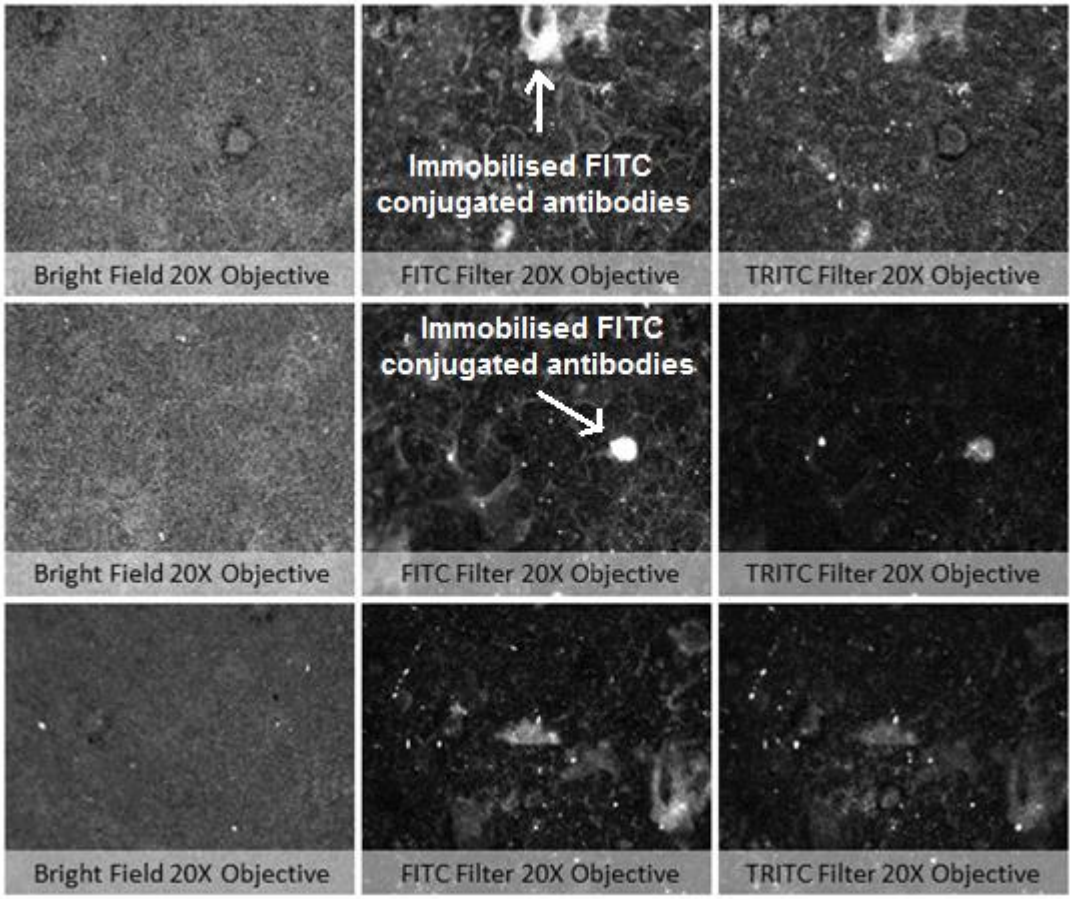


*Fig 4.22: Fluorescence microscopy images of functionalised DropSens C223BT electrodes with heterobifunctional cross-linker assays.*

Fluorescence microscopy of DropSens C223BT electrodes also show successful immobilisation of FITC conjugated antibodies to gold. Electrodes exhibited strong fluorescence at ~482nm ± 17nm excitation wavelength, with mean pixel intensities of

17361.218, 11969.437 and 32.477 for image 1b, 2b and 3b respectively. Electrodes subsequently displayed reduced fluorescence at 542nm ± 16 excitation wavelengths, with mean pixel intensities of 16,519.377, 5,748.349 and 30.354 for image 1c, 2c and 3c respectively. Thus, fluorescence intensities may be assigned to FITC dyes as previously described in section 4.4.1.2.3, and is consistent with DropSens C223AT electrodes. However, reductions in fluorescence at TRITC wavelengths were not deemed statistically significant ($F(1,4) = 0.11$, p-value = 0.755), presumably due to the appearance of small fluorescent particles at both FITC and TRITC wavelengths that relate to inconsistencies and contaminants in electrode surfaces, in agreement with control measurements. Interestingly, fluorescence intensities were poorly distributed across electrode surfaces compared to DropSens C223AT electrodes, which may possibly be explained by the rougher electrode surfaces indicated from theta values in section 4.4.2.2.1. Additionally, fluorescence intensities were significantly greater at hot spots on electrodes compared to DropSens C223AT electrodes, which suggests increased quantities of antibodies on gold surfaces, supported by our previous findings in section 4.4.2.2.1.

*4.4.2.2.3 Concentration Study*

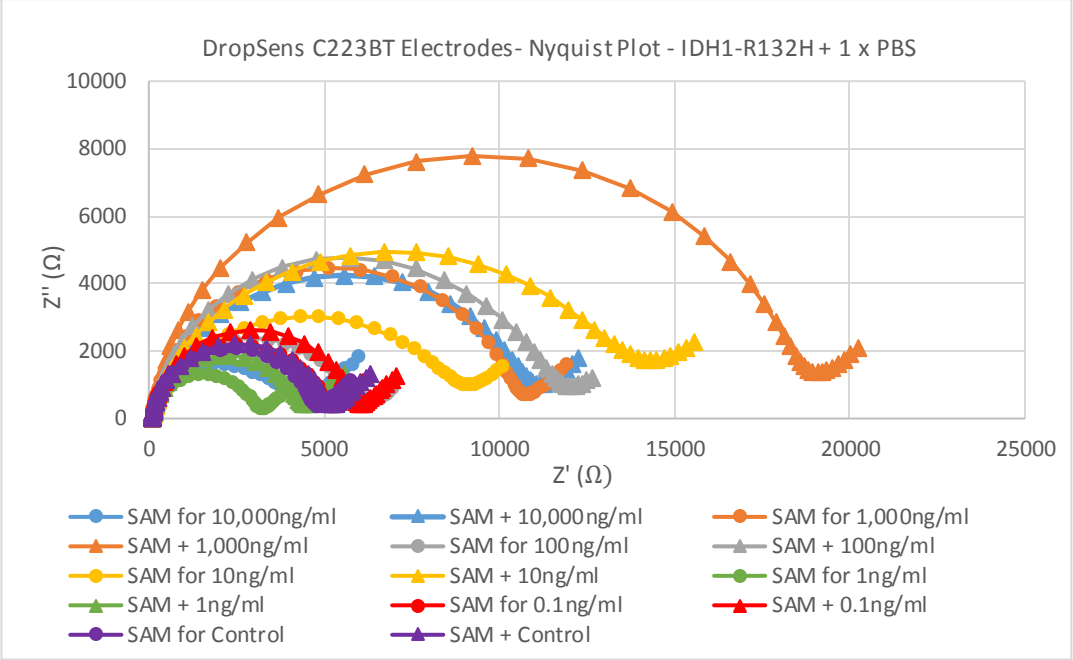


*Fig 4.23: Nyquist plot of functionalised DropSens C223BT electrodes before and after incubation with specified antigen concentrations (n=3).*

DropSens C223BT electrodes produce impedance responses typical of fitted Randles equivalent circuits. Impedance responses of electrodes before antigen incubation were characteristic of SAM formation, and were observed to increase upon exposure to antigen concentrations, indicative of antibody antigen interactions (Fig 4.23).

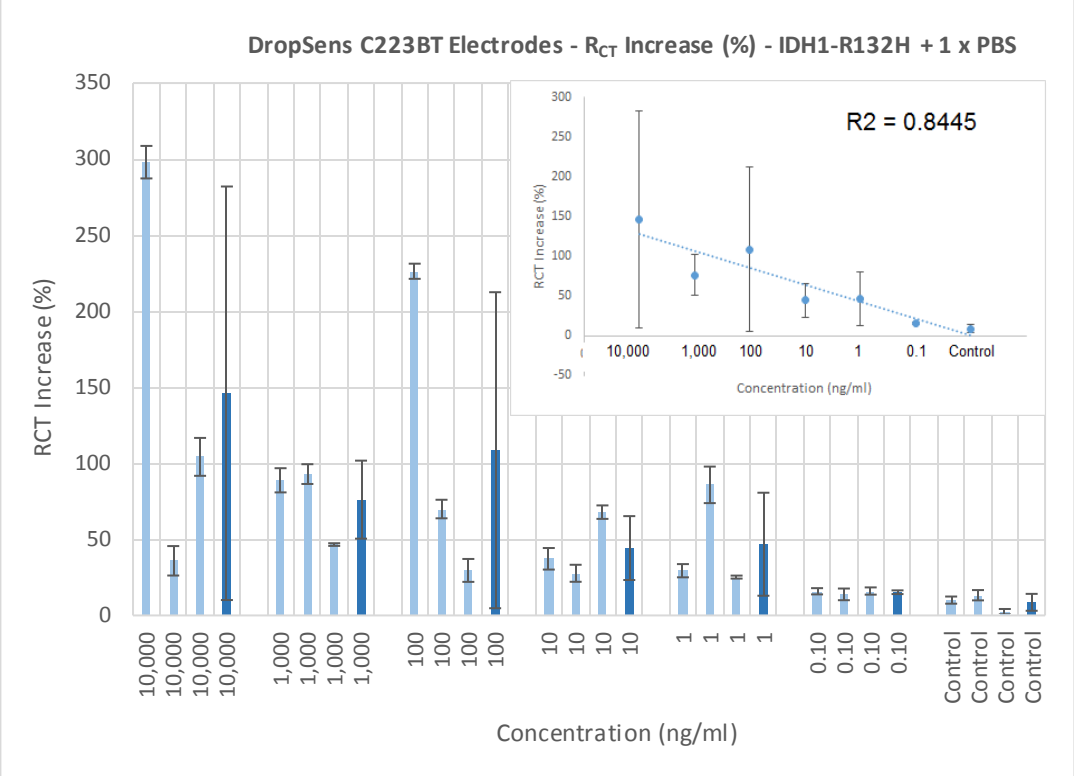


*Fig 4.24: Plot of percentage differences in Rct for functionalised DropSens C223BT electrodes before and after incubation with specified antigen concentrations (n=3).*

Percentage increases in Rct for functionalised electrodes before and after antigen incubation were observed to have a weak positive correlation to target IDH1-R132H protein concentrations, with a Pearson co-efficient of $r^2 = 0.8455$ (Fig 4.24). Percentage increases at 10,000ng/ml concentrations were markedly different between repeat measurements at 146.059% ± 135.947 and therefore not statistically different to 1,000ng/ml protein concentrations at 76.123% ± 25.651 ($F(1,16) = 3.04$, p-value = 0.100). Similarly, significant variations were observed in repeat measurements for 100ng/ml protein concentrations at 108.616% ± 103.886 that were not significantly different to 1,000ng/ml concentrations ($F(1,16) = 1.10$, p-value = 0.310). Likewise, whilst sensor reproducibility appeared to improve for 10ngml and 1ng/ml

concentrations, Rct values were not significantly different at 44.292% ± 20.999 and 46.823% ± 33.867 respectively ($F(1,16) = 0.05$, p-value = 0.833), attributed to the appreciable standard deviation of results. However, significant differences in Rct were found between 0.1ng/ml at 15.267% ± 1.223 and control measurements at 8.621% ± 5.556 ($F(1,16) = 11.22$, p-value < 0.05), indicating a current limit of detection of 0.1ng/ml that is consistent with previous literature findings described in section 4.4.1.2.4. However, the appreciable standard deviation is unacceptable for diagnostic purposes and may help to explain the poor linearity of our results for specified antigen concentrations.

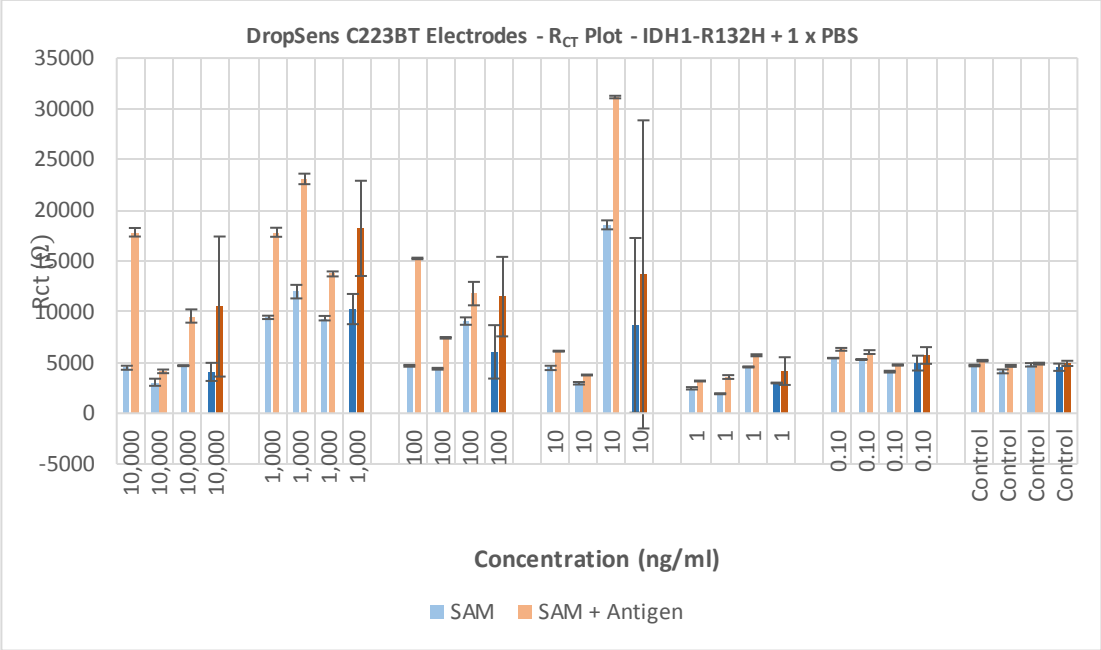


*Fig 4.25: Rct plot for functionalised DropSens C223BT electrodes before and after incubation with specified antigen concentrations (n=3).*

DropSens C223BT electrodes do not appear conducive to consistent SAM formation, with significant differences observed in starting Rct values prior to antigen incubation. This is consistent with our previously reported results for DropSens C223AT

electrodes and therefore indicates that the current assay may be the primary cause of variation rather than electrode substrates. However, significantly greater fluctuations in initial Rct were observed for DropSens C223BT electrodes, which may conflictingly suggest that poorer still electrode surfaces may explain the increased variation compared to DropSens C223AT electrodes.

*4.4.2.2.4 Scanning Electron Microscopy*

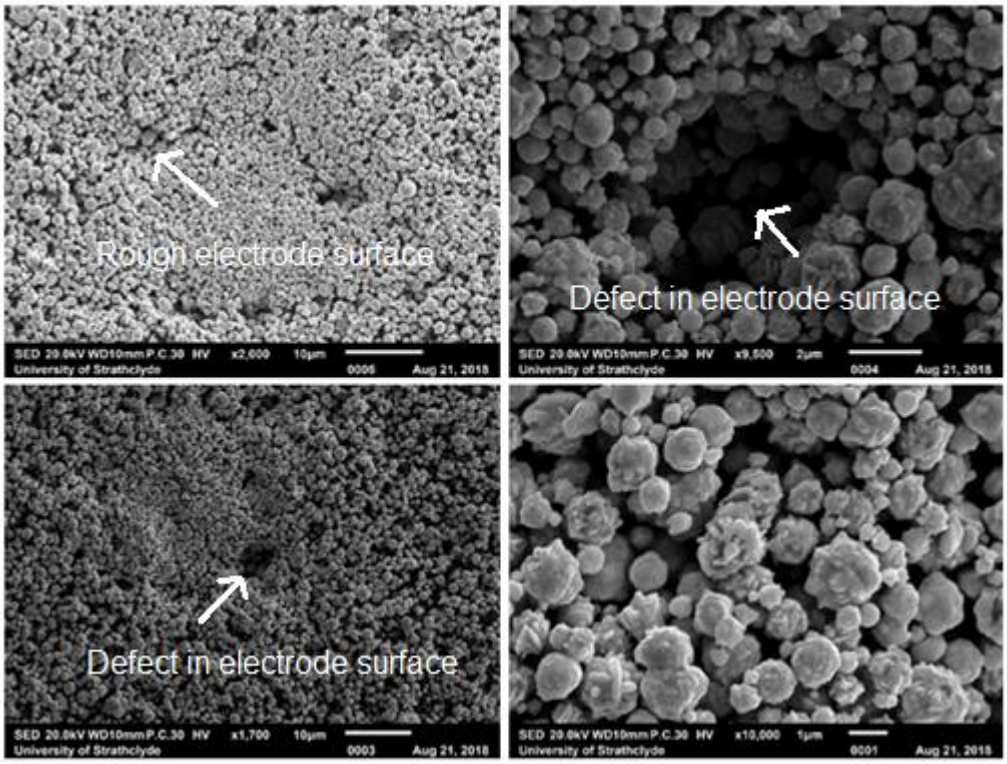


*Fig 4.26: SEM images for bare gold DropSens C223BT electrodes.*

Closer inspection of DropSens C223BT electrodes show markedly different surface characteristics to DropSens C223AT electrodes. Firstly, electrodes appear to consist of aggregates of screen-printed ink particles that leads to the formation of rougher, inhomogeneous gold surfaces. Secondly, electrodes display significantly larger defects

that vary considerably in shape across electrode surfaces. These observations are consistent with previous findings of Butterworth (Butterworth et al, 2019), and is likely attributed to differences in composition of the low cure temperature ink, and the reduced annealing temperature, which decreases the coalescence of gold particles on electrode surfaces (Zoski, 2007).

*4.4.2.2.5 Atomic Force Microscopy*

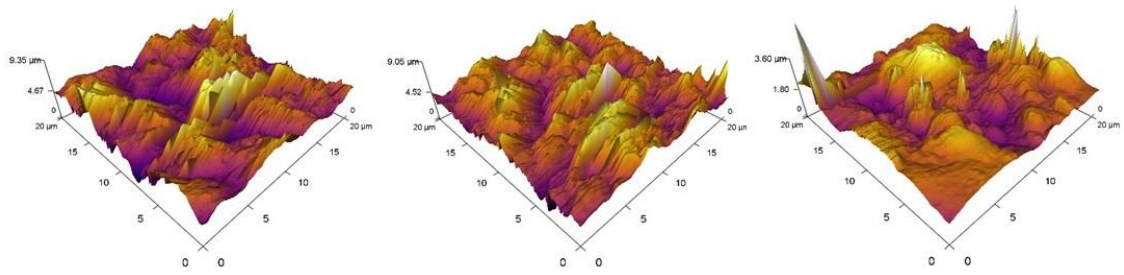


*Fig 4.27: AFM images for bare gold DropSens C223BT electrodes.*

Atomic force microscopy of DropSens C223BT working electrodes shows the significant electrode surface roughness, with root mean square roughness, Rq, calculated as 754.9nm, 521nm, 330.9nm respectively. Furthermore, peak topological features measured 9.35µm, 9.05µm and 3.60µm respectively, and were not consistent over the sensor surface. Overall, the surface roughness of DropSens C223BT electrodes is significantly greater compared to DropSens C223AT electrodes, which helps explain both the increased variation in SAM formation and standard deviation of our electrochemical results. Therefore, future work shall attempt to modify the electrode surface through application of a chemically cross-linked BSA layer, with the aim to fill voids and reduce surface roughness prior to antibody attachment, in line with the work of Badea (Badea et al, 2016).

*4.4.2.2.6 BSA Methodology Results*

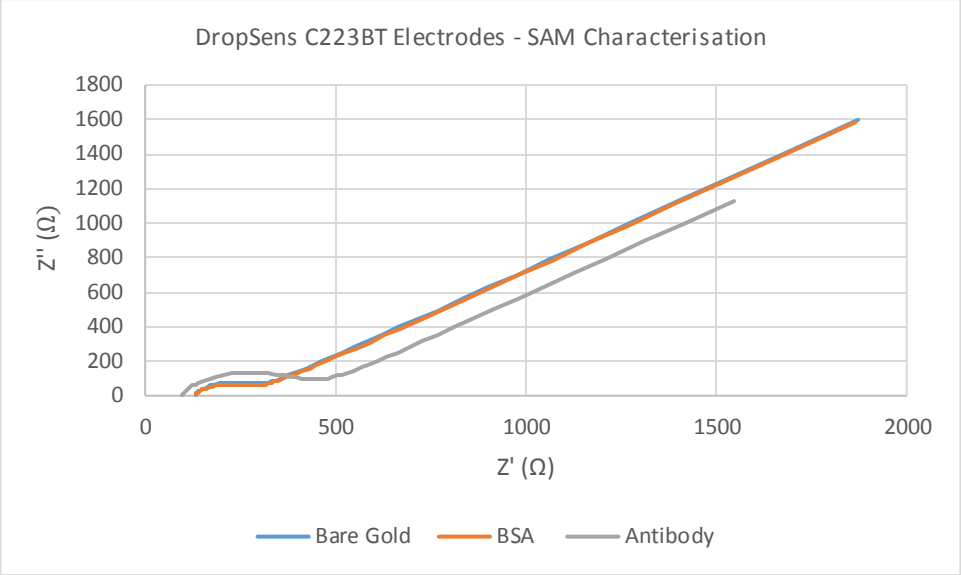


*Fig 4.28: Nyquist plot depicting SAM characterisation of DropSens C223BT electrodes following BSA immobilisation procedures (n=3).*

DropSens C223BT bare electrodes display low Rct values of 150.5667 Ω + 7.057 and theta values of θ = 0.890 + 0.008. BSA cross-linked assays did not significantly increase Rct values at 162.989 Ω + 26.656 ($F(1,16) = 223$, p-value = 0.155), which indicates poor attachment to electrode surfaces. However, theta values decreased significantly to θ = 0.807 + 0.018 ($F(1,16) = 11757$, p-value < 0.05), which indicates that minimal BSA attachment to electrodes resulted in poorer overall surface roughness, contrasting the aim of the study. Antibody depositions caused significant increases in Rct to 330.911 Ω + 45.487 ($F(1,16) = 116.74$, p-value < 0.05) and decreases in theta to θ = 0.826 + 0.018 ($F(1,16) = 4.67$, p-value < 0.05), contradicting previous literature findings. Badea reported that covalent bonding of antibodies neutralised the negative charge of BSA layers and resulted in pronounced decreases in Rct values (Badea et al, 2016). However, our BSA layers were poorly formed on

electrodes that explains the conflicting increase in Rct, and suggests antibodies are simply physisorbed to gold electrode surfaces.

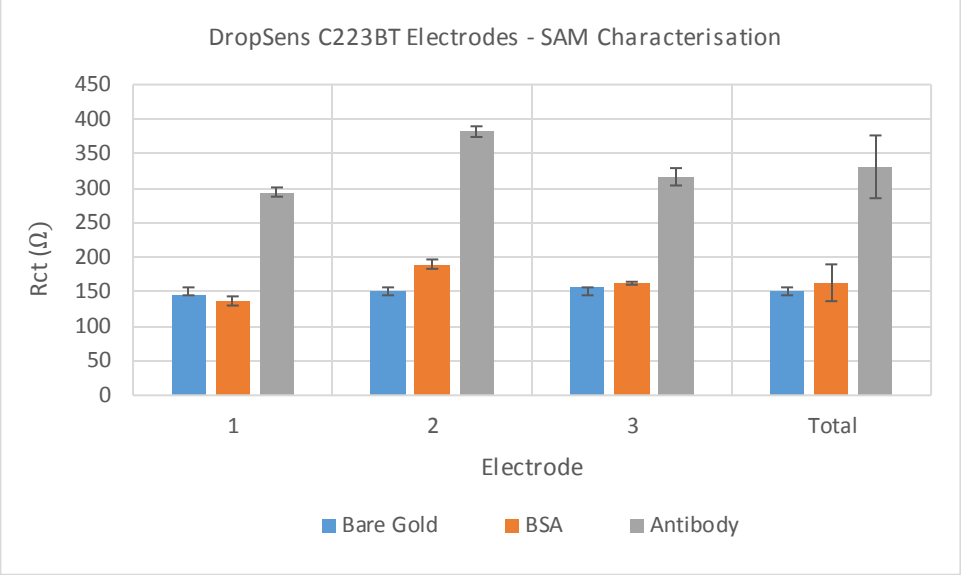


*Fig 4.29: Rct plot showing SAM characterisation of DropSens C223BT electrodes following BSA immobilisation procedures (n=3).*

Immobilisation varies significantly between all three electrodes for BSA ($F(2, 8) = 67.47$, p-value $< 0.05$) and antibody ($F(2, 8) = 71.02$, p-value $< 0.05$) assays. However, Rct values between electrodes is relatively small and therefore variation in electrode surfaces does not account for the significant differences in immobilisation compared to literature findings.

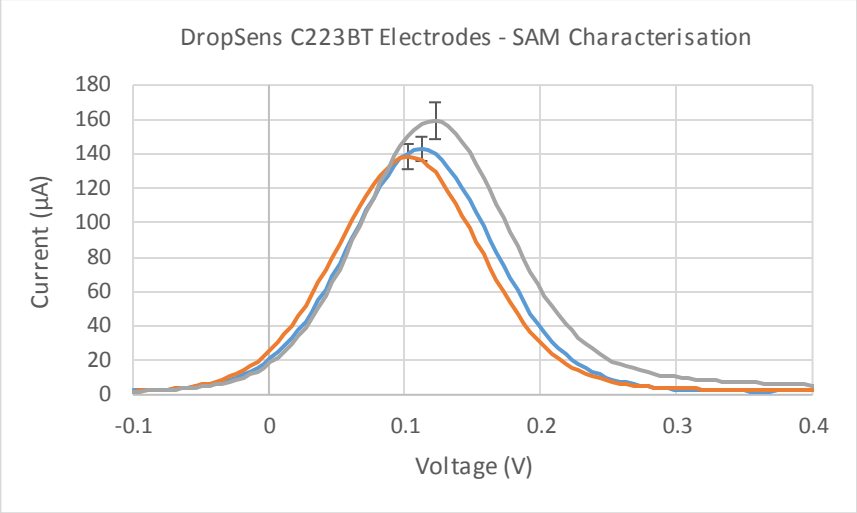


*Fig 4.30: DPV plot that shows SAM characterisation of DropSens C223BT electrodes following BSA immobilisation procedures (n=3).*

DPV results similarly show no significant reductions for BSA modified electrodes at Ipa = 138.438 µA + 7.328 compared to bare gold electrodes at Ipa = 142.912 µA ± 7.047 ($F(1,16) = 2.28$, p-value = 0.150), consistent with our impedance findings. However, antibody-modified electrodes caused Ipa = 159.275 µA + 10.698 ($F(1,16) = 27.46$, p-value < 0.05), which contradicts our impedance findings and highlights that the quantity of antibodies on the surface is not sufficient to restrict electron transfer events. Therefore, preliminary SAM characterisation results indicate that the current assay protocol is not appropriate for immobilisation of IDH1-R132H antibodies, although future testing of electrodes against controls is required to validate such claims.

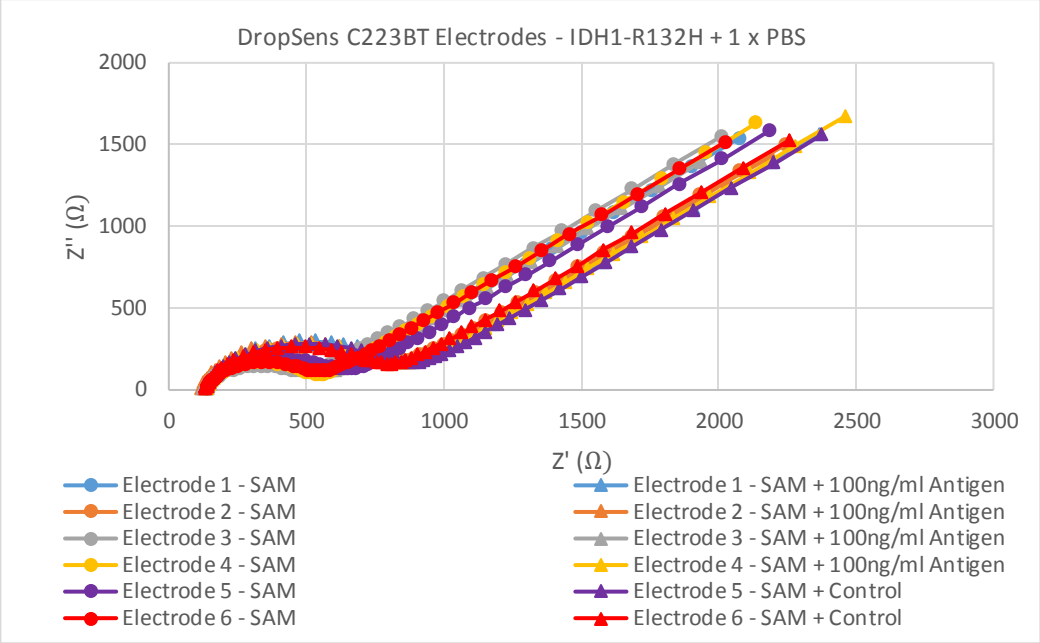


*Fig 4.31: Nyquist plot of functionalised DropSens C223BT electrodes before and after incubation with specified antigen concentrations (n=3).*

Nyquist plots show starting electrode impedance responses characteristic of SAM formation that when incubated with 100ng/ml antigen produced increases in Rct of 44.50% + 32.15. However, such differences were not statistically different to Rct values of 51.46% + 10.86 for controls ($F(1,16) = 0.26$, p-value = 0.618), which indicates increases are likely associated with random non-specific binding events of phosphate buffer saline to electrodes rather than antibody antigen interactions. This may be attributed to both the absence of blocking in the functionalisation protocol and the poorly formed BSA layer that allows minimal antibody attachment to electrodes. Furthermore, carbodiimide cross-linking of BSA to gold is dependent on successful EDC NHS coupling that permits amide bond formation between proteins. However, EDC NHS coupling is recognised to be more efficient at acidic pH ranges from 4.0 to 6.0 with a higher reaction yield (Hermanson, 2010), therefore, identical experiments with 0.1M MES buffer at optimal pH of 5.0 were conducted to increase cross-linking

efficiency of BSA to electrode surfaces. However, buffer modifications were ineffective and the assay was not deemed appropriate for detection of IDH1-R132H antigens, therefore, future work will consider the previously described heterobifunctional cross-linker protocol on new electrode substrates.

### *4.4.3 CH Instruments CH101 Disc Electrodes*

#### *4.4.3.1 Electrochemical Cleaning*

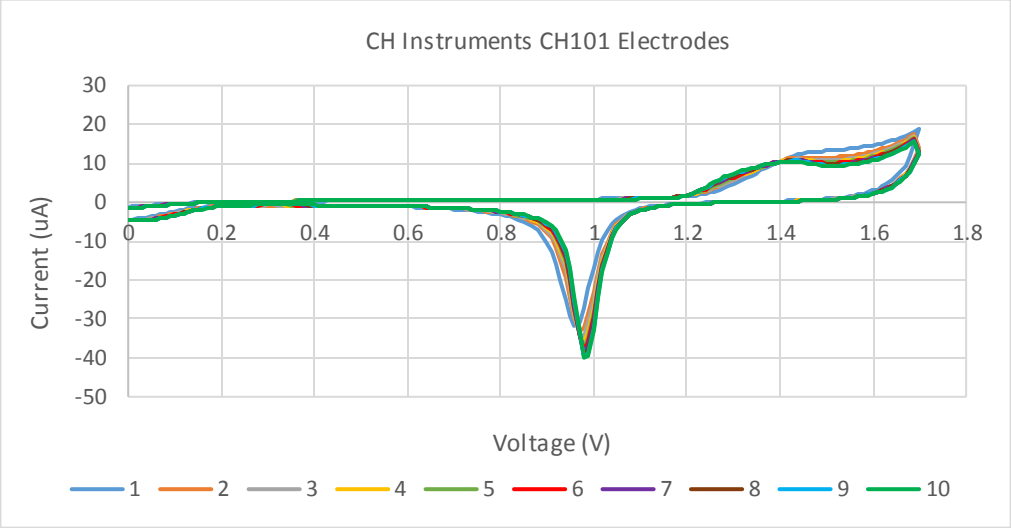


*Fig 4.32: Electrochemical cleaning of CH Instruments CHI101 macro disc electrodes in 0.1MH2SO4 with potential cycles from 0 to 1.7V at a scan rate of 100mV/s for 10 cycles (n=3).*

CH Instruments CHI101 electrodes subjected to the electrochemical cleaning procedure detected one electron transfer redox reactions characteristic of gold surfaces (Fig. 4.32). The first scan measured one broad oxidation peak, Ipa = 13.273µA ± 3.190 at Epa = 1.489V, and one sharp reduction peak, Ipc = -31.762µA ± 7.650 at Epc = 0.959V. By the tenth scan, oxidation currents decreased, Ipa = 10.584µA ± 2.010 at

Epa = 1.439V, with a concurrent increase in reduction currents, Ipc = -39.958µA ± 9.052 at Epc = ~0.979V, consistent with gold oxide removal as previously described in section 4.4.1.1. Interestingly, peak reduction currents for all scans were significantly greater for CH Instruments CHI101 electrodes compared to both DropSens C223AT & C223BT electrodes ($F(2,87) = 321.96$, p-value $< 0.05$), which suggests macro disc electrodes possess increased effective electro-active areas, as would be expected for greater electrode geometries given the Randles-Sevcik equation (Hamann et al, 1998).

### *4.4.3.2 Heterobifunctional Cross-linker Protocol*

#### *4.4.3.2.1 SAM Characterisation*

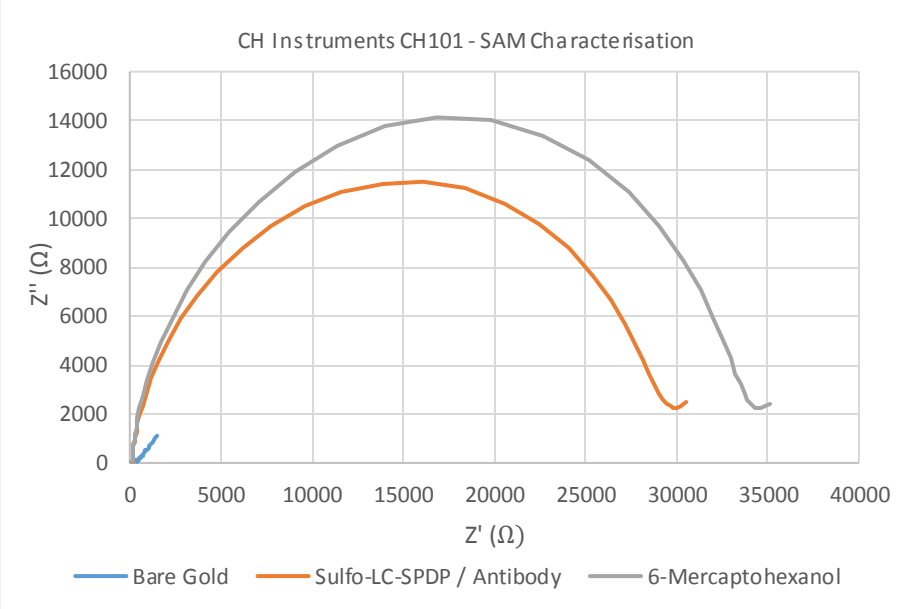


*Fig 4.33: Nyquist plot of SAM characterisation of CH Instruments CHI101 macro disc electrodes following immobilisation procedures (n=3).*

Bare gold electrodes exhibit reasonably smooth electrode surfaces with theta values of θ = 0.863 + 0.007 and low Rct values of 246.5 Ω + 53.712, similar to previous DropSens C223AT and C223BT electrodes. Sulfo-LC-SPDP antibody assays were successfully chemisorbed to gold with significant increases in Rct to 28500.00 Ω + 16398.39 ($F(1,16) = 35.62$, p-value $< 0.05$) and theta values to θ = 0.951 + 0.003 ($F(1,16) = 380.57$, p-value $< 0.05$). MCH depositions successfully occupied remaining bare gold surfaces, albeit increases in Rct at 6980.667 Ω + 2390.304 were not statistically significant ($F(1,16) = 0.39$, p-value $= 0.544$) and theta values decreased to θ = 0.928 + 0.003 ($F(1,16) = 5.23$, p-value $< 0.05$). Interestingly, impedance responses of electrodes at each functionalisation stage were significantly greater compared to previous DropSens C223AT and C223BT electrodes, due to the increased diameter of the working electrode resulting in the formation of denser SAM's on electrode surfaces.

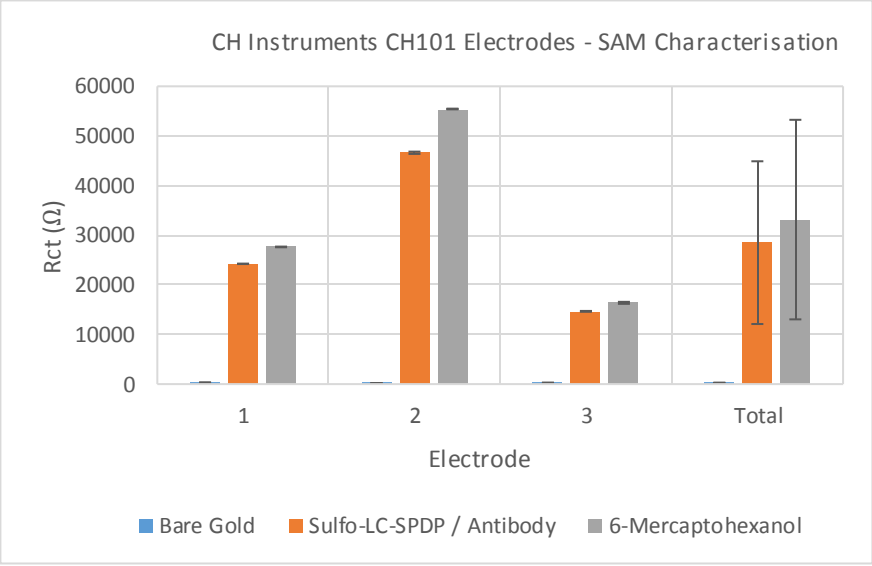


*Fig 4.34: Rct plot of SAM characterisation of CH Instruments CHI101 macro disc electrodes following immobilisation procedures (n=3).*

Immobilisation varies significantly between all three electrodes for both Sulfo-LC-SPDP antibody ($F(2,6) = 62.38$, p-value $< 0.05$) and MCH ($F(2,6) = 257.95$, p-value $< 0.05$) depositions, consistent with previous DropSens C223AT and C223BT electrodes. Interestingly, SAM formation is significantly more inconsistent on macro-disc electrodes compared to screen-printed electrodes, possibly due to increases in the electrode diameter that may accentuate variation associated with depositions of the cross-linker assay.

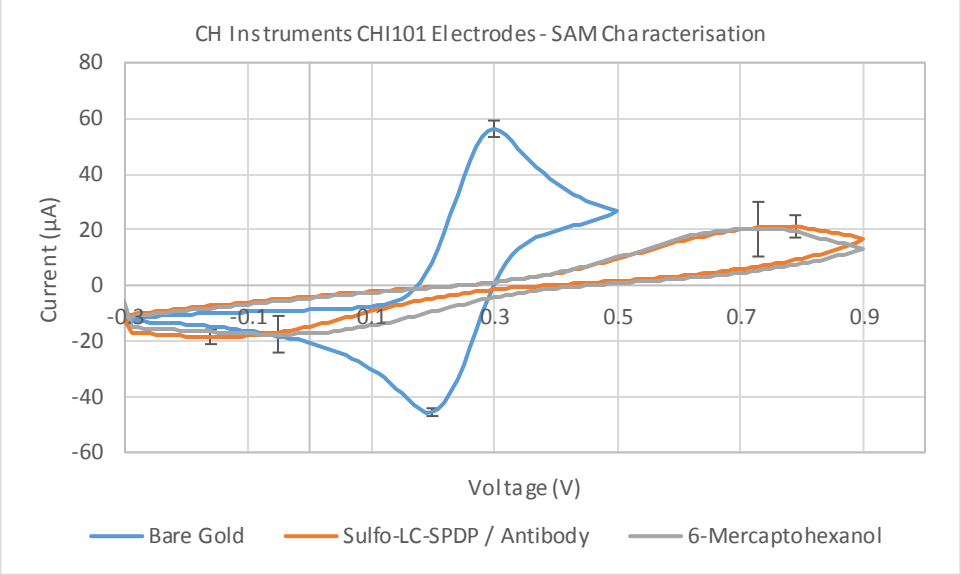


*Fig 4.35: CV plot of SAM characterisation of CH Instruments CHI101 macro disc electrodes following immobilisation procedures (n=3).*

Bare gold electrodes display one-electron quasi-reversible redox reactions consistent with previous DropSens C223AT and C223BT electrodes. Ipa measured 56.236 µA ± 2.954 at shifted potentials of Epa = ~0.30V and Ipc measured -45.559 µA ± 1.405 at shifted potentials of Epc = ~0.20V. Sulfo-LC-SPDP antibody immobilisation markedly decreased Ipa = 21.186 µA ± 4.026 ($F(1,16) = 510.41$, p-value $< 0.05$) at Epa = ~0.789V and Ipc = -18.470 µA ± 2.637 ($F(1,16) = 920.31$, p-value $< 0.05$) at Epc = ~0.160V, indicative of significantly slower electron transfer kinetics and

increased charge transfer resistances due to chemical bonding between sulphur and gold atoms. MCH depositions did not cause additional statistically significant reductions in Ipa = 20.173 µA ± 9.817 ($F(1,16) = 0.11$, p-value = 0.747) or Ipc = -17.567 µA ± 6.581 ($F(1,16) = 0.19$, p-value = 0.668), presumably because the extent of Sulfo-LC-SPDP antibody immobilisation restricts the availability of remaining bare surfaces for chemical bond formation between sulphur atoms of MCH and gold substrates. Furthermore, the large standard deviations of Ipa and Ipc results for MCH assays questions the stability of the SAM when subjected to increasingly positive potentials, as discussed in section 4.4.2.2.1.

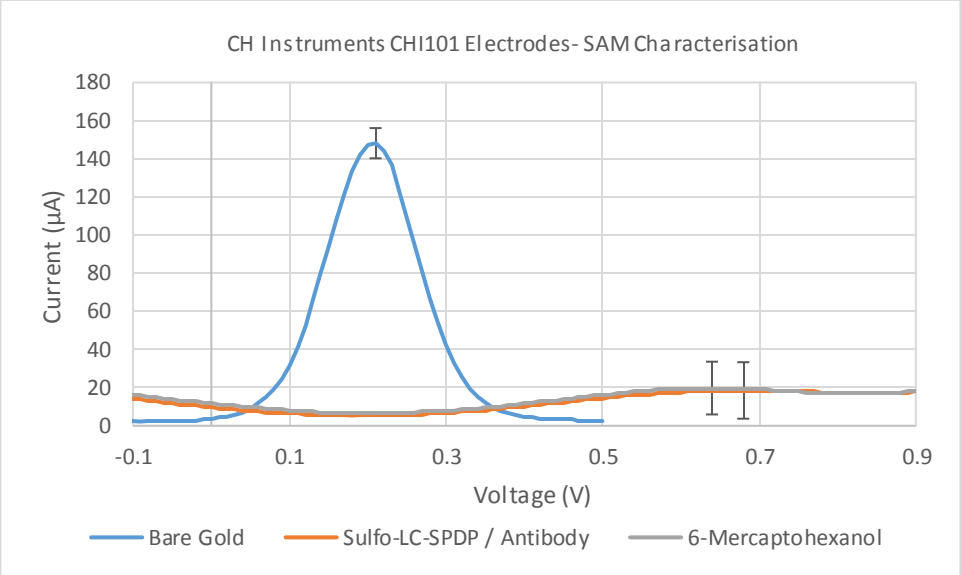


*Fig 4.36: DPV plot of SAM characterisation of CH Instruments CHI101 macro disc electrodes following immobilisation procedures (n=3).*

Bare gold electrodes give rise to Ipa = 148.173µA ± 7.918, which similarly decrease to Ipa = 18.53µA ± 14.813 upon immobilisation of Sulfo-LC-SPDP antibody molecules ($F(1,16) = 428.92$, p-value < 0.05). MCH assays do not cause further reductions in Ipa = 19.785 ± 13.829 ($F(1,16) = 0.05$, p-value = 0.833) and shows that

thiol attachment of MCH to gold did not further restrict electron transfer at electrode surfaces. Overall, assay depositions were associated with significantly reduced current responses and large standard deviations, which indicates that voltammetry is not a viable analytical method for future concentration studies of IDH1-R132H antigens.

*4.4.3.2.2 Fluorescence Microscopy Characterisation of SAM*

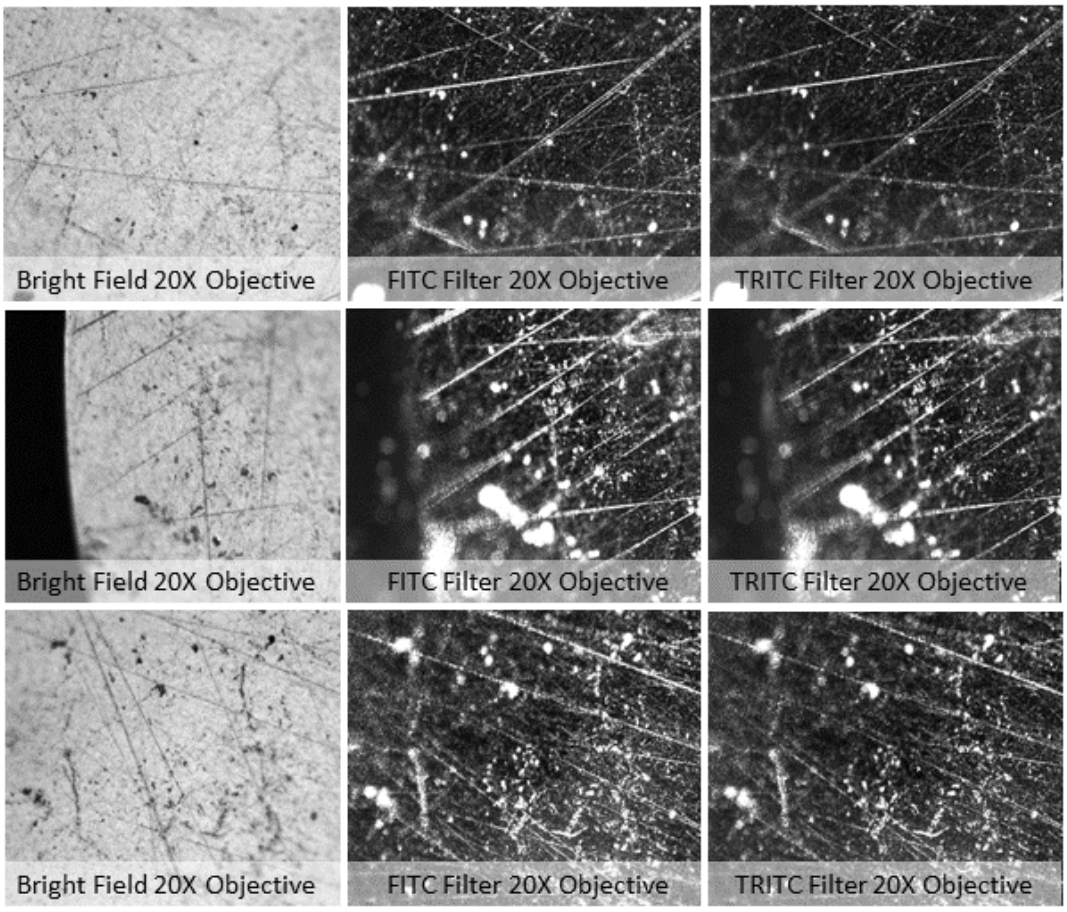


*Fig 4.37: Fluorescence microscopy images of CH Instruments CHI101 macro disc electrodes functionalised with FITC conjugated antibodies.*

Fluorescence microscopy experiments reveal successful immobilisation of the cross-linker assay to CH Instruments CHI101 electrodes. Fluorescence signals were observed to be greater at FITC wavelengths compared to TRITC wavelengths, albeit

differences in fluorescence intensities were not statistically significant ($F(1,4) = 1.35$, p-value = 0.310). FITC wavelengths produced mean pixel intensities of 64.509, 80.810 and 86.588 for images 1b, 2b and 3b respectively; compared to mean pixel intensities at TRITC wavelengths of 56.778, 70.821 and 74.520 for images 1c, 2c and 3c respectively, indicative of immobilised FITC conjugated antibodies as previously described in section 4.4.1.2.3. Interestingly, fluorescence was greater on macro-disc electrodes compared to previous screen-printed electrodes, which suggests improved antibody surface coverage on electrode substrates, most likely due to denser SAM formation. However, hot spots of increased fluorescence were still observed on electrode surfaces that on first inspection correlate with dark spotted artefacts in bright field images. Therefore, fluorescence fluctuations suggest that antibodies may accumulate in greater quantities at aberrations in electrode surfaces, further evident through the increased fluorescence observed at scratched surfaces, and consistent with previous findings for screen-printed electrodes.

### *4.4.3.2.3 Concentration Study*

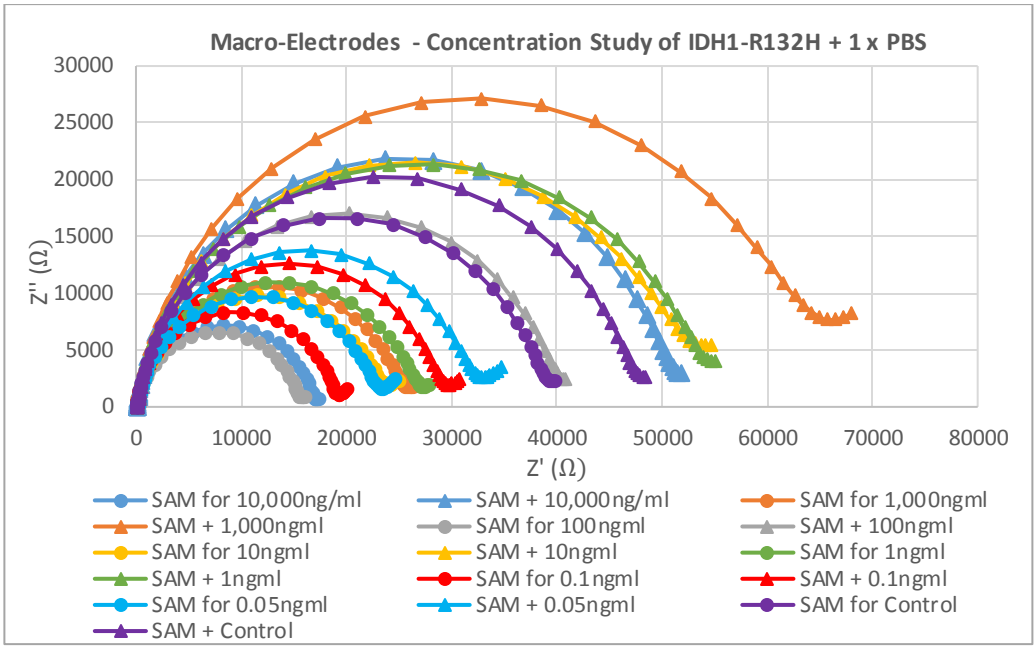


*Fig 4.38: Nyquist plot of functionalised CH Instruments CHI101 macro disc electrodes before and after incubation with specified antigen concentrations (n=3).*

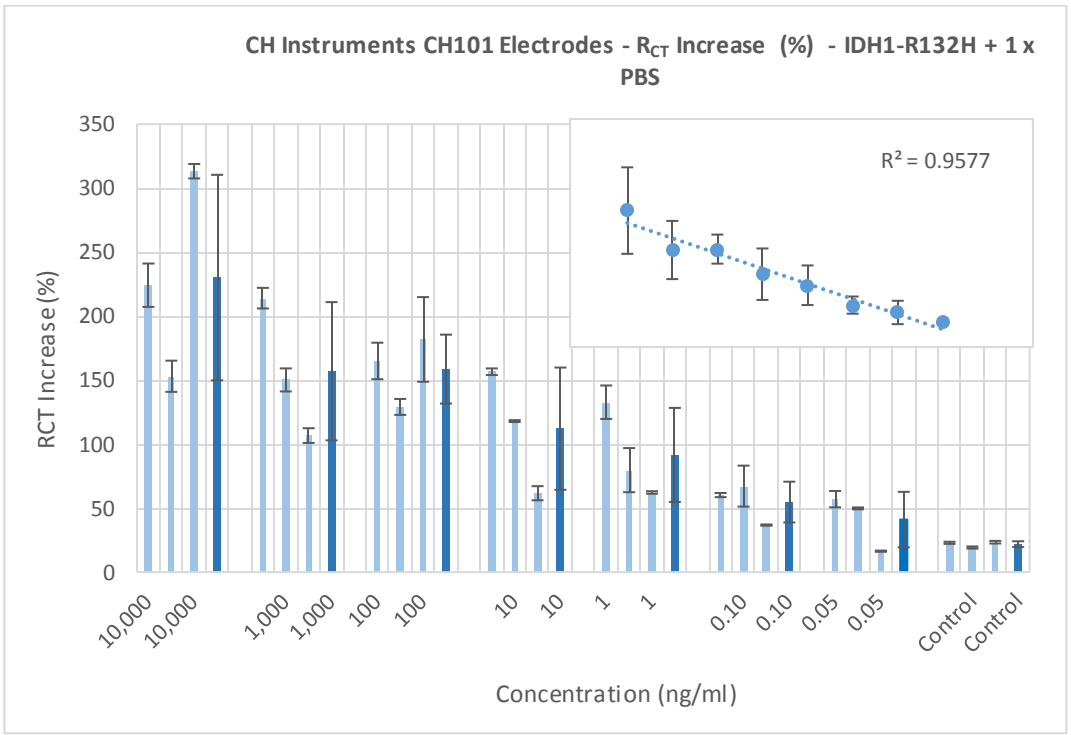


*Fig 4.39: Plot of percentage difference in Rct for functionalised CH Instruments CHI101 macro disc electrodes before and after incubation with specified antigen concentrations (n=3).*

Nyquist plots showed starting impedances of functionalised CH Instruments CHI101 electrodes to be consistent with SAM formation that increased upon exposure to antigen concentrations (Fig. 4.38). Largest percentage increases in $R_{ct}$ were observed for 10,000ng/ml concentrations at 230.143% ± 80.271, significantly greater than 1,000ngml concentrations at 156.971% ± 53.993 ($F(1,16) = 6.71$, p-value < 0.05). At 100ng/ml concentrations, percentage increases in $R_{ct}$ of 158.622% ± 26.936 were not statistically different to 1,000ng/ml concentrations ($F(1,16) = 0.01$, p-value = 0.930), but were statistically different to 10ng/ml concentrations at 112.077% ± 47.743 ($F(1,16) = 7.51$, p-value < 0.05). Likewise, electrodes could not distinguish between 10ng/ml concentrations and 1ng/ml concentrations at 91.562% ± 36.742 ($F(1,16) = 1.33$, p-value = 0.266), but responses were statistically different to 0.1ng/ml concentrations at 54.718% ± 15.940 ($F(1,16) = 8.82$, p-value < 0.05). Lastly, electrodes were able to successfully distinguish between 0.05ng/ml concentrations at 41.060% ± 21.687 and control measurements at 21.839% ± 2.271 ($F(1,16) = 9.05$, p-value < 0.05), resulting in a current limit of detection for the sensor of 0.05ng/ml. The current limit of detection is markedly improved compared to previously tested DropSens C223AT and C223BT electrodes at 1ng/ml and 0.1ng/ml respectively, which implies that the choice of electrode substrate may influence the overall sensor response. CH Instruments CHI101 electrodes have increased diameters compared to screen-printed electrodes, enabling the formation of denser SAM's with increased antibody surface coverage, evident through previous characterisation and fluorescence results. Consequently, electrodes display increased sensitivity over the range of specified antigen concentrations, evident through the larger percentage increases in Rct compared to screen-printed electrodes. However, standard deviations of our

current results are significantly increased compared to previous studies of Ciani, despite the employment of identical electrode substrates and assay protocols (Ciani et al, 2012). Therefore, it may be conjectured that the specific antibody performance and nature of antibody antigen interaction may also influence sensor responses.

Antibodies selected for our current experiment recognise a single amino acid arginine to histidine substitution at the 132$^{nd}$ amino acid in the beta sheet structure of IDH1 situated in the small domain of the protein momomer (Dang et al, 2009). Conversely, Ciani employed antibodies for detection of TREM-1 proteins, which typically recognise multiple epitopes and significantly longer amino acid sequences of the target protein, such as amino acids 74-90 in the V-type domain of TREM-1 (Boster Biological Technology, CA, USA). Therefore, one would expect it to be increasingly difficult to achieve detection of our target antigen with comparative sensitivity and reproducibility to previous studies, and may partly explain the increased standard deviation of our results. Additionally, our assay utilises Sulfo-LC-SPDP where N-hydroxysuccinimide (NHS) esters react with primary amines located on both Fc and Fab sections of the heavy side chains of IDH1-R132H antibodies. Hence, Sulfo-LC-SPDP is not conjugated to a specific location on the primary antibody structure, introducing variability in the orientation of the hypervariable regions of the antibody with respect to the electrode surface, which negatively influences sensor sensitivity (Trilling et al, 2013). Furthermore, our assay utilises DTT to reduce disulphide bonds in the spacer arm of Sulfo-LC-SPDP, but may also unintentionally reduce the intramolecular disulphide bonds located within IDH1-R132H antibodies, compromising antibody structure and resultant sensitivities (Ciani et al, 2012). Lastly,

Sulfo-LC-SPDP antibody conjugation precedes immobilisation of thiols of Sulfo-LC-SPDP to gold, possibly introducing further variability in the distribution of molecules on electrode surfaces, given the disparity in their respective molecular weights at 527.57 Da for Sulfo-LC-SPDP and 43,000 Da for IDH1-R132H antibodies.

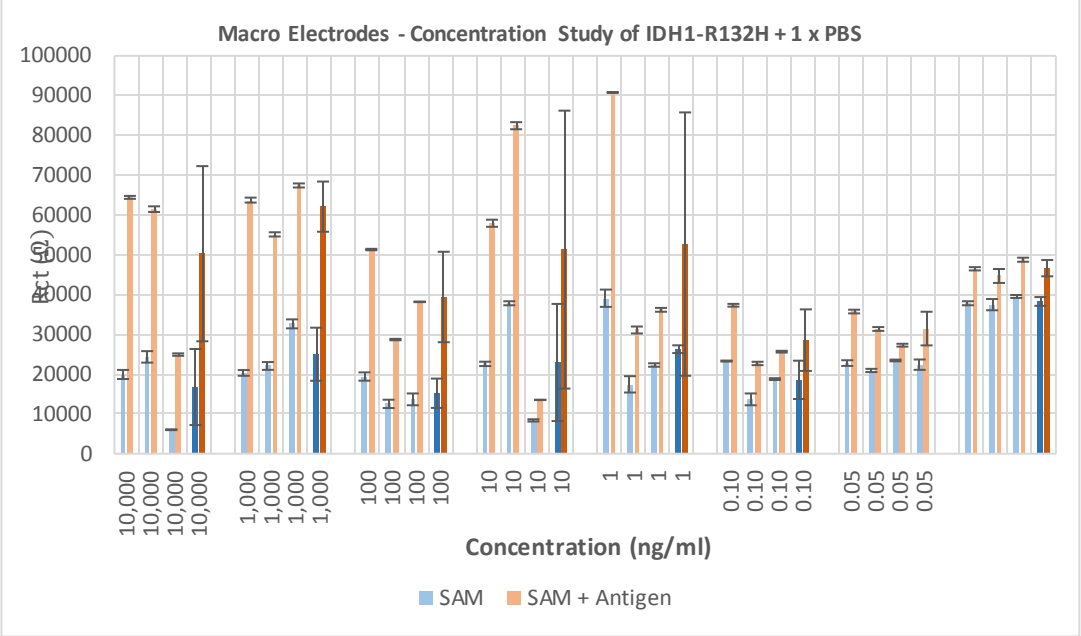


*Fig 4.40: Rct plot of functionalised CH Instruments CHI101 macro disc electrodes before and after incubation with specified antigen concentrations (n=3).*

Significant differences in immobilisation prior to antigen incubation were also observed between electrodes, consistent with our findings for screen-printed electrodes and previous literature studies described in section 4.4.1.2.4, and further implies that electrode-electrode variation may originate from the assay protocol. Corrigan postulates that micro-molar concentrations of SAM assays is excessive for standard incubation times and may lead to the formation of unordered SAM's that feature micelles and multi-layer assemblies (Corrigan et al, 2018). Furthermore, Kwasny suggests that unreacted thiols should be removed with a de-salting column

prior to incubation and that the inclusion of DTT may cause clusters on electrode surfaces due to their high reactivity (Kwasny et al, 2018). Hence, the current assay protocol clearly contributes to electrode variability and reproducibility issues observed in our current results. Therefore, future work should consider different immobilisation strategies, such as protein G protocols for improved antibody orientation (Trilling et al, 2013), or alkane thiol EDC NHS surface chemistries for improved control of SAM formation prior to antibody attachment (Molazemhosseini et al, 2016).

*4.4.3.3 SEM Images*

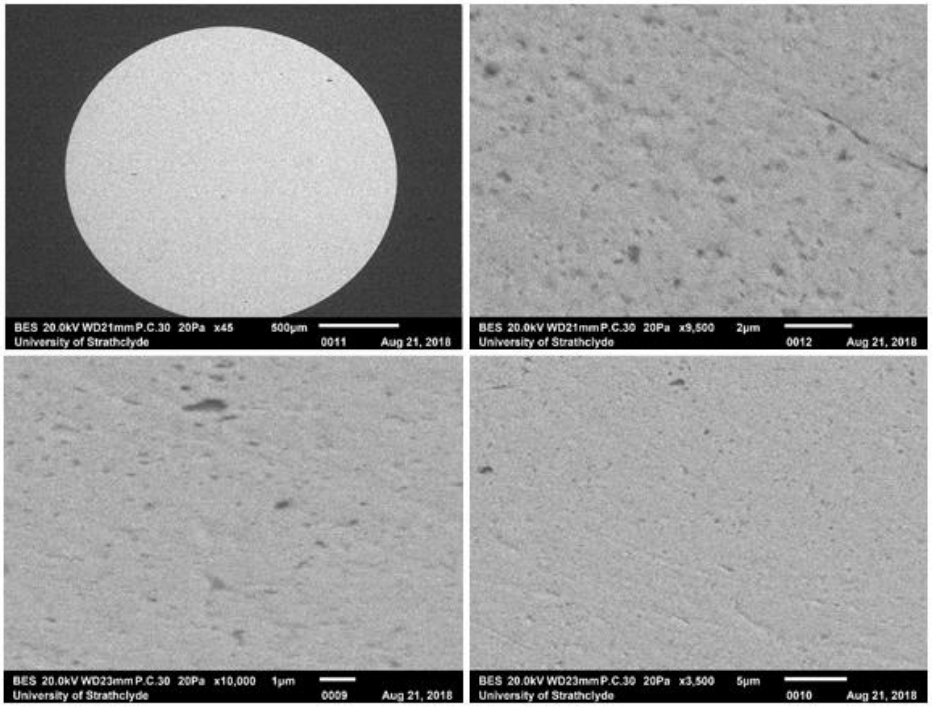


*Fig 4.41: SEM images of bare gold CH Instruments CHI101 macro disc electrodes.*

Inspection of CH Instruments CHI101 electrodes show substantially different surface properties to previous screen-printed electrodes. Electrodes comprise polycrystalline gold structures rather than colloidal gold deposits on screen-printed electrodes, leading to the formation of improved surface morphologies. However, electrodes still display

degrees of surface roughness, with the presence of holes and scratches across electrodes attributed to mechanical polishing procedures (Carvalhal et al, 2005). Likewise, the presence of impurities may either be attributed to residual alumina contaminants from polishing (Carvalhal et al, 2005), or to the considerable annealing temperatures that attract impurities to gold electrode surfaces during fabrication (Bard et al, 1996). Regardless, CH Instruments CHI101 electrodes exhibit smoother electrode surfaces with improved performance for SAM purposes compared to screen-printed alternatives (Butterworth et al, 2019), consistent with our current findings.

#### *4.4.3.4 AFM Images*

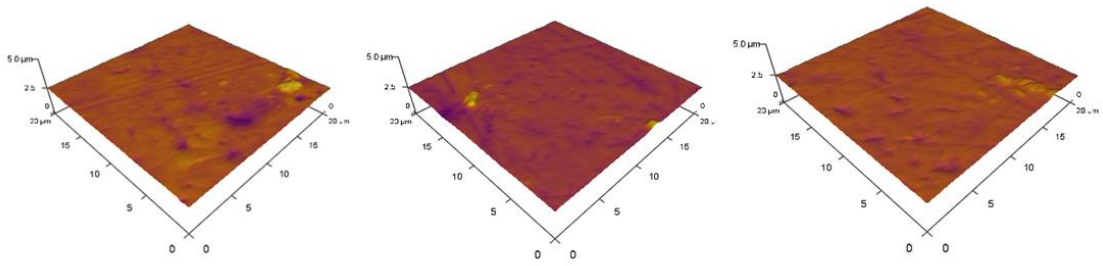

*Fig 4.42: AFM images of bare gold CH Instruments CHI101 macro disc electrodes.*

Atomic force microscopy of CHI 101 gold working electrodes showed superior surface topology in comparison to all other evaluated electrodes, with calculated root mean squared surface roughness of 19.43nm, 14.32nm and 26.01nm for all three electrodes respectively. Additionally, the surface topology is consistent with previous SEM images with evidence of surface scratches and pitting presumably from the mechanical polishing process. However, peak morphological features were still significantly lower than all other electrodes at 354.94nm, 382.71nm and 276.83nm, which indicates the electrode surfaces are far more consistent for surface functionalisation, as would be

expected for polycrystalline gold electrodes. Superior surface properties should translate to improved formation of self-assembled monolayers and consequently improved antibody immobilisation, which may explain the increased sensitivity and linearity of our results with current CHI 101 macro electrodes.

### *4.4.3.5 MPA Protocol*

#### *4.4.3.5.1 Electrochemical Characterisation of SAM*

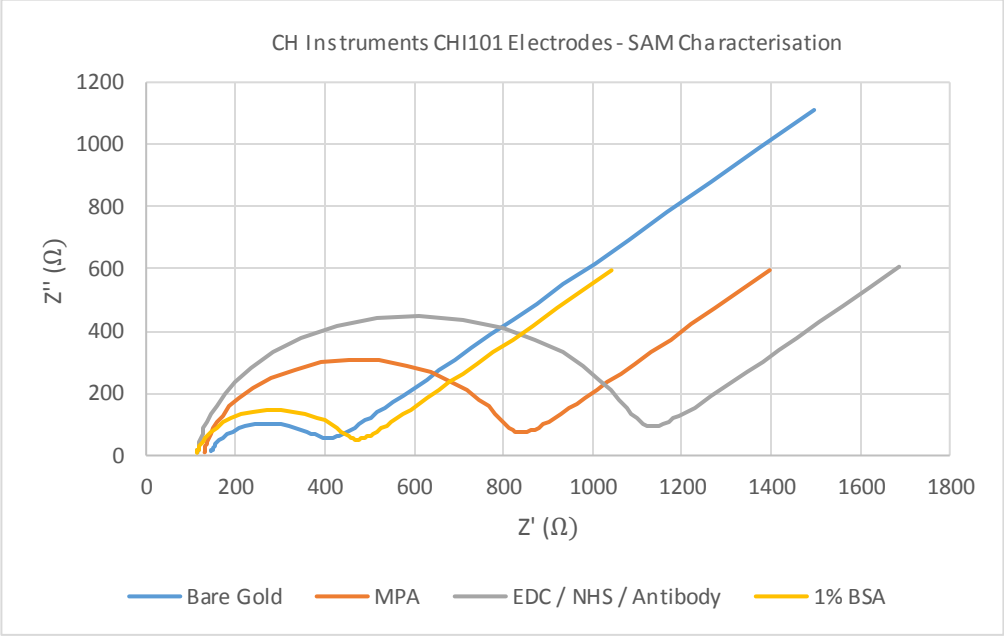


*Fig 4.43: Nyquist plot of SAM characterisation of functionalised CH Instruments CHI101 macro disc electrodes following MPA immobilisation procedures (n=3).*

Functionalised electrodes are not consistent with previous literature findings of Molazemhosseini who employs identical assay protocols (Molazemhosseini et al, 2016). Electrodes displayed significant increases in Rct from 246.5 Ω ± 53.712 for bare gold electrodes to 672.4 Ω ± 102.834 following immobilisation with MPA ($F(1,16) = 144.92$, p-value $< 0.05$). However, the degree of thiol head group

attachment of MPA to gold is significantly poorer compared to literature values of ~10,000Ω for identical concentrations, which indicates poor SAM formation on electrode surfaces. Electrodes further displayed significant increases in Rct at 966.911 Ω ± 119.210 upon carbodiimide cross-linking of antibodies to SAM's ($F(1,16) = 41.10$, p-value < 0.05), which indicates attachment of antibodies to carboxylic acids of MPA molecules. However, blocking of electrode surfaces significantly reduced Rct to 335.567 Ω ± 152.493 ($F(1,16) = 123.80$, p-value < 0.05). This behaviour is not reported in the previous assay protocol and one would anticipate further increases in Rct given the additional barrier molecules and their net charges at the electrode interface (Molazemhosseini et al, 2016). Covalent attachment of antibodies to carboxylic acids of MPA results in a neutral charge at the electrode surface. Hence, immobilisation of BSA with an isoelectric point of 4.7 should impart net negative charges at the electrode surface when immersed in measurement buffer (pH 7.4), which should induce electrostatic repulsion of anions and subsequently increase Rct values (Badea et al, 2016). Therefore, the observed behaviour questions the stability of the SAM and implies that antibodies were not successfully conjugated to MPA and instead simply detached from electrode surfaces following extensive wash steps.

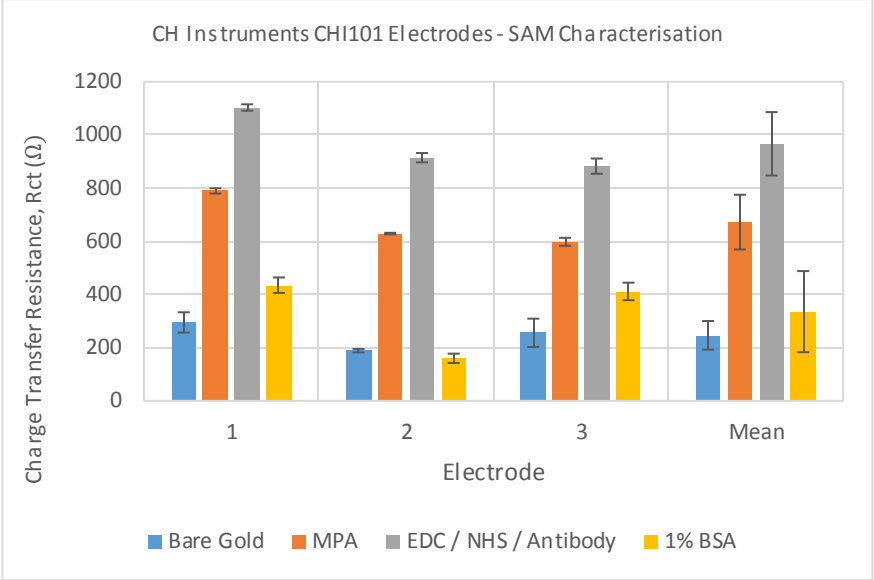


*Fig 4.44: Rct plot of SAM characterisation of functionalised CH Instruments CHI101 macro disc electrodes following MPA immobilisation procedures (n=3).*

The degree of chemisorption of thiol head groups of MPA molecules to gold surfaces significantly differs between all three electrodes ($F(2,6) = 286.94$, p-value $< 0.05$) and consequently affects the distribution of antibodies on substrates ($F(2,6) = 540.27$, p-value $< 0.05$). Likewise, electrode blocking promotes statistical differences in the immobilisation of BSA molecules to gold surfaces, with decreased Rct values for electrode 2 compared to electrode 1 and 3 ($F(2,6) = 93.31$, p-value $< 0.05$). However, all electrodes were consistent in their decreased Rct response upon blocking indicative of antibody detachment and thus preliminary evidence suggests that the current assay is not suitable for detection of IDH1-R132H proteins.

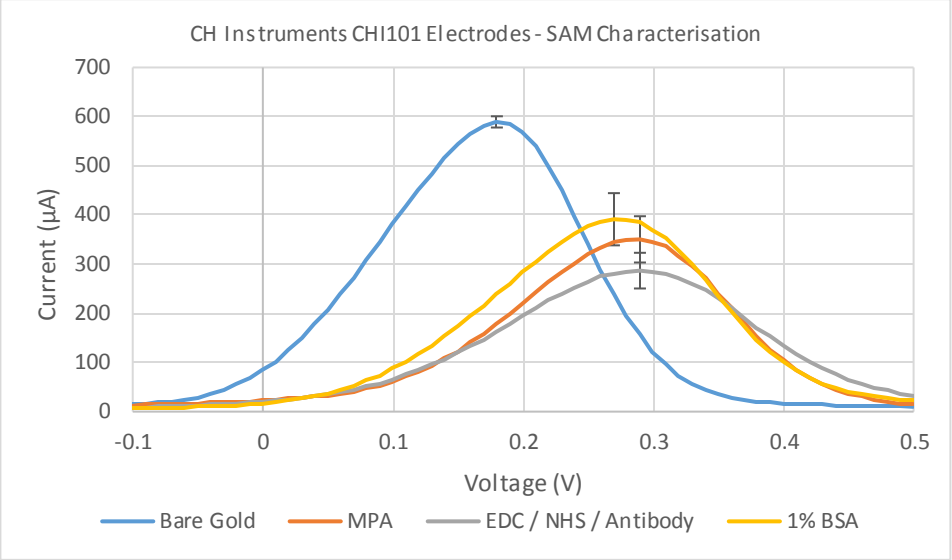


*Fig 4.45: DPV plot of SAM characterisation of functionalised CH Instruments CHI101 macro disc electrodes following MPA immobilisation procedures (n=3).*

MPA modified electrodes prompted significant reductions in Ipa = 350.3 µA ± 42.0 ($F(1,16) = 263.63$, p-value < 0.05), which highlights increased difficulty for $[Fe(CN)_6]^{-3/4}$ anions to transfer electrons to electrode surfaces, further evidence of successful thiol-gold chemisorption. Similarly, EDC/NHS/antibody depositions instigate significant reductions in Ipa = 286.8 µA ± 48.1 ($F(1,16) = 8.91$, p-value < 0.05), which implies that antibody attachment to MPA molecules acts as an additional barrier to electron transfer events. However, the magnitude of current responses is lower than previous studies and suggests poorer attachment of both depositions to electrodes (Molazemhosseini et al, 2016). Furthermore, BSA assays significantly increased Ipa = 391.3 µA ± 46.4 ($F(1,16) = 21.97$, p-value < 0.05), which conflicts previous literature findings, but is consistent with our previous impedance results. The increased current response demonstrates that greater quantities of $[Fe(CN)_6]^{-3/4}$ anions lose electrons to electrode substrates upon application of oxidation potentials of ~0.270V, and further

suggests the formation of pinholes or unintentional removal of SAM constituents from gold substrates (Bard et al, 1996).

*4.4.3.5.2 Initial Electrode Testing*

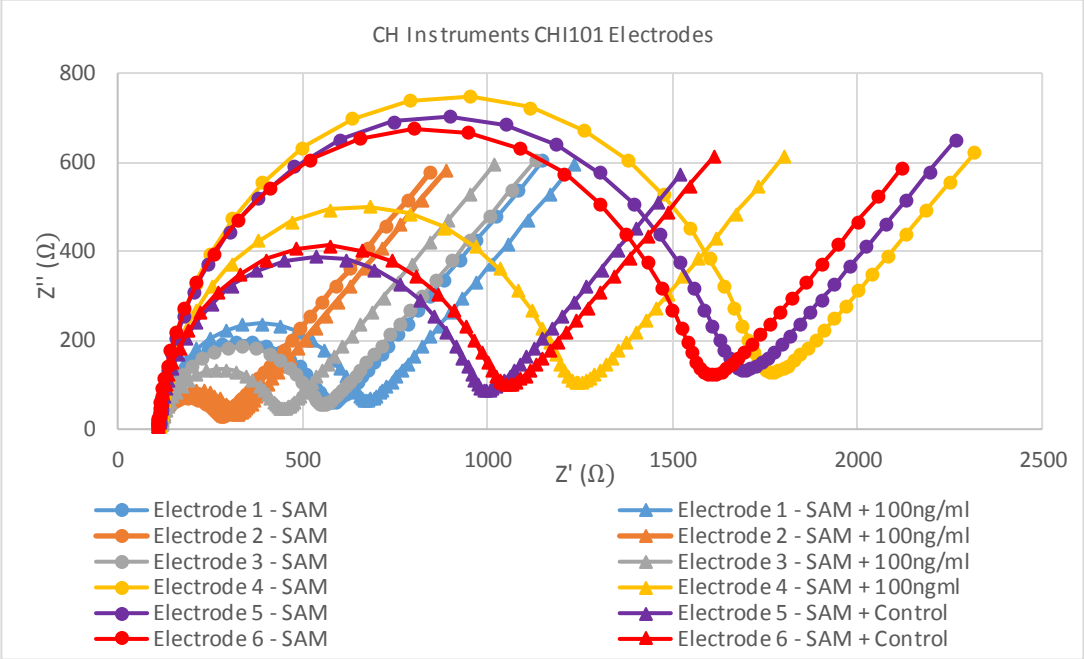


*Fig 4.45: Nyquist plot of functionalised CH Instruments CHI101 macro disc electrodes before and after incubation with specified antigen concentrations (n=3).*

Electrode testing reveals significant differences between responses of all four electrodes incubated with specific antigen concentrations ($F(3,8) = 160.91$, p-value $< 0.05$), which indicates that the current assay protocol is not reproducible between electrodes. Electrodes incubated with specific antigen did show statistically different responses to control measurements at $-2.26\Omega \pm 27.85$ and $-40.20\Omega \pm 9.59$ respectively ($F(3,8) = 10.25$, p-value $< 0.05$). However, Nyquist plots clearly show that electrodes with greater starting Rct values decrease following incubation with antigen concentrations, which is not representative of antigen binding and implies that SAM

layers detach with respect to time, in agreement with our previous characterisation results. Similarly, electrodes with markedly reduced starting Rct values show small increases upon exposure to antigen concentrations, which likely indicates that already detached SAM layers non-specifically absorb phosphate buffered saline (Riquelme et al, 2016). Therefore, future work shall not consider carbodiimide cross-linker assays and instead focus on different attachment methods for antibody-SAM conjugation, including protein G for orientated attachment at Fc domains of antibodies.

### *4.4.3.6 Sulfo Protein G Protocol*

#### *4.4.3.6.1 Electrochemical Characterisation of SAM*

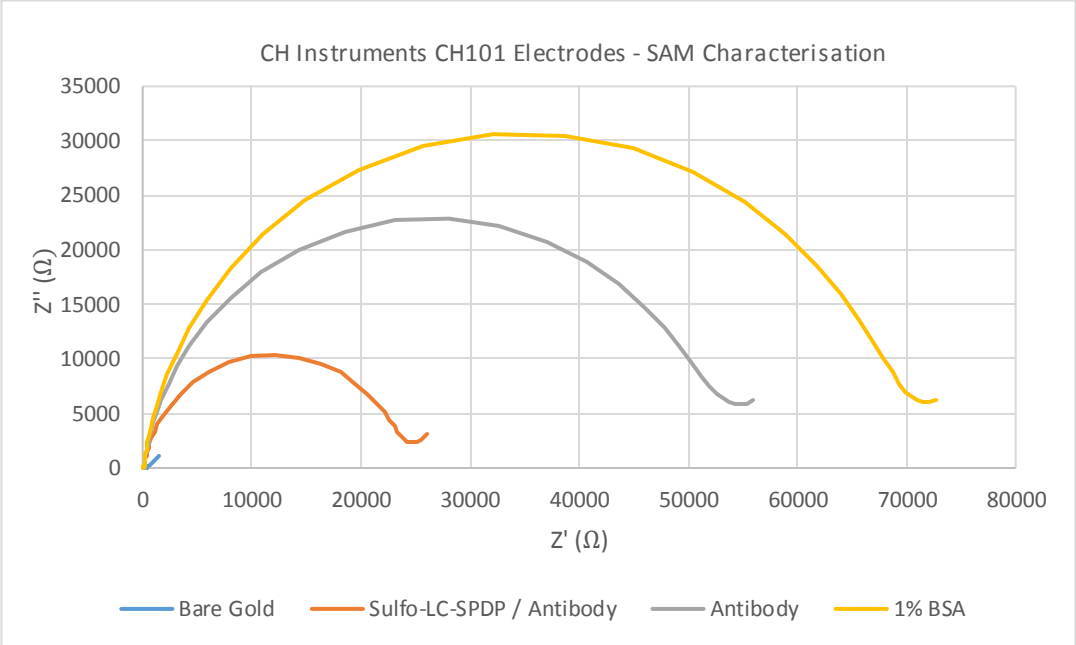


*Fig 4.46: Nyquist plot of SAM characterisation of CH Instruments CHI101 macro disc electrodes following Sulfo-LC-SPDP protein G immobilisation assays (n=3).*

Bare gold electrodes functionalised with Sulfo-LC-SPDP / protein G assays displayed significantly increased Rct values at 23,266.67Ω ± 3573.63 ($F(1,16) = 490.98$, p-value

< 0.05), which indicates successful attachment of the thiol spacer arm to electrode surfaces. Interestingly, impedance responses were reduced compared to previous Sulfo-LC-SPDP / antibody depositions, which may be attributed to the higher molecular weight of selected antibodies compared to protein G molecules. Antibody depositions subsequently increased Rct to 51,453.33Ω ± 4,037.26 ($F(1,16) = 323.22$, p-value < 0.05), which indicates successful coupling of protein G to Fc domains of antibodies. Lastly, BSA depositions significantly increased Rct to 68,465.56 ± 4,308.014 ($F(1,16) = 98.41$, p-value < 0.05), which indicates successful blocking of remaining bare gold surfaces. Overall, Rct responses on functionalised electrodes were greater than previous experiments due to the additional high molecular weight proteins present on gold surfaces.

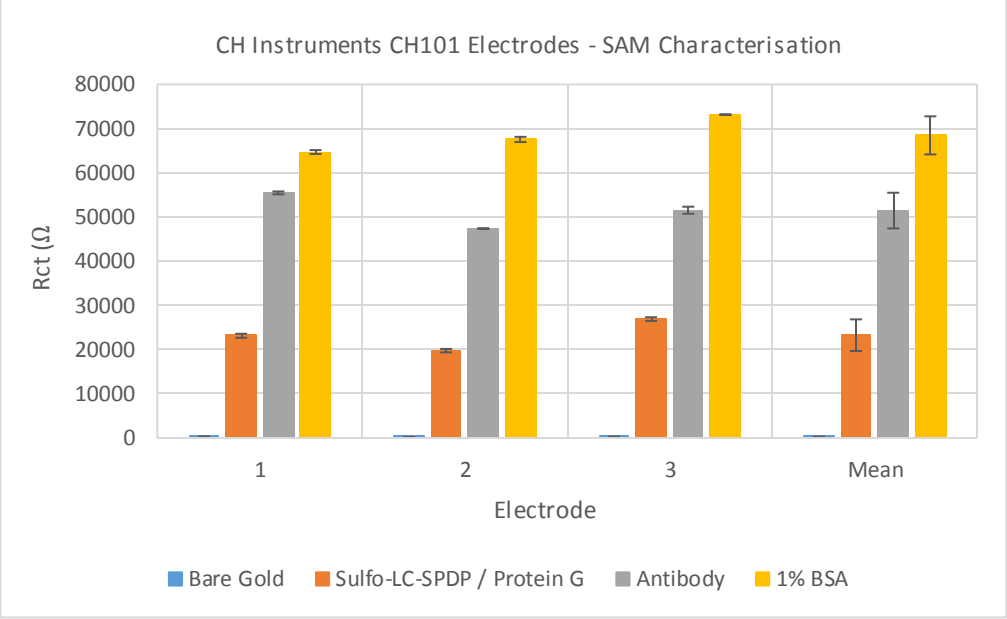


*Fig 4.47: Rct plot of SAM characterisation of CH Instruments CHI101 macro disc electrodes following Sulfo-LC-SPDP protein G immobilisation assays (n=3).*

Functionalisation varied across all electrodes for Sulfo-LC-SPDP / protein G depositions ($F(2,6) = 216.63$, p-value < 0.05), which indicates possible reproducibility

issues with thiol chemisorption to gold using the current assay, in agreement with our previous results. Consequently, impedance responses were significantly different between electrodes for both antibody ($F(2,6) = 196.26$, p-value $< 0.05$) and BSA ($F(2,6) = 304.93$, p-value $< 0.05$) depositions, which again implies differences in the quantities of respective molecules on electrode surfaces.

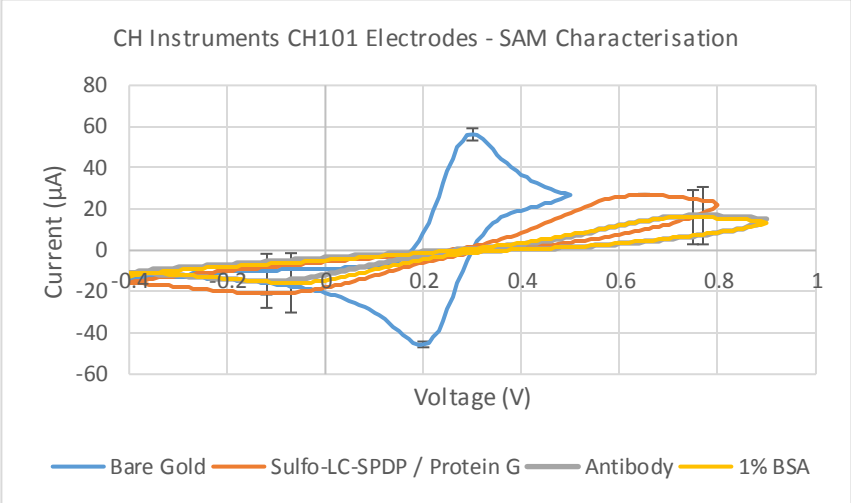


*Fig 4.48: CV plot of SAM characterisation of CH Instruments CHI101 macro disc electrodes following Sulfo-LC-SPDP protein G immobilisation assays (n=3).*

Sulfo-LC-SPDP / protein G modified electrodes significantly decreased Ipa = 26.953 µA ± 0.475 ($F(1,16) = 797.58$, p-value $< 0.05$) at ~0.649V and Ipc = -20.774 µA ± 0.604 ($F(1,16) = 2565.36$, p-value $< 0.05$) at ~0.120V, indicative of successful chemisorption as described in section 4.4.1.2.1. Antibody depositions subsequently decreased Ipa = 16.851 µA ± 13.905 ($F(1,16) = 14.02$, p-value $< 0.05$) at ~0.769 and Ipc = -14.744 µA ± 13.096 ($F(1,16) = 9.95$, p-value $< 0.05$) at ~0.120V, which implies that successful attachment of antibodies to protein G surfaces further restricts electron transfer events of $[Fe(CN)_6]^{-3/-4}$ at electrode surfaces. BSA assays were associated with negligible decreases in Ipa = 16.126 µA ± 13.148 ($F(1,16) = 0.32$, p-value $= 0.581$) and marginal increases in Ipc = -15.717 µA ± 14.390 ($F(1,16) = 6.83$, p-value $< 0.05$),

likely attributed to the saturation of molecules from previous depositions on electrode surfaces.

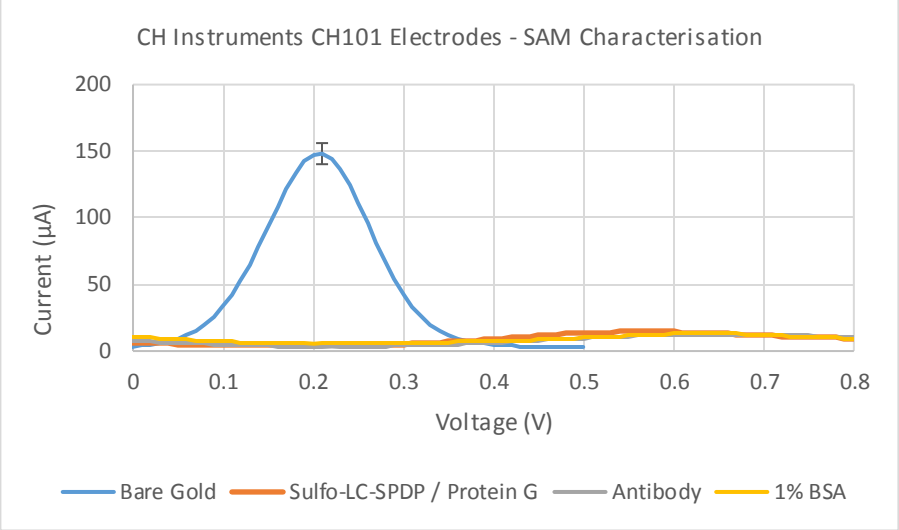


*Fig 4.49: DPV plot of SAM characterisation of CH Instruments CHI101 macro disc electrodes following Sulfo-LC-SPDP protein G immobilisation assays (n=3).*

Sulfo-LC-SPDP / protein G modified electrodes prompted significant reductions in Ipa = 14.582 µA ± 0.175 ($F(1,16) = 851.37$, p-value < 0.05), further indicative of thiol attachment of the spacer arm of Sulfo-LC-SPDP to gold. Similarly, antibody depositions prompted significant reductions in Ipa = 12.497 µA ± 0.145 ($F(1,16) = 14.73$, p-value < 0.05), suggestive of antibody conjugation to protein G molecules. However, BSA depositions caused marginal increases in Ipa = 13.126 µA ± 0.621 ($F(1,16) = 2.62$, p-value = 0.125), which implies minimal BSA attachment to gold due to significant binding of previous molecules, in agreement with our previous findings.

*4.4.3.6.2 Fluorescence Microscopy Characterisation of SAM*

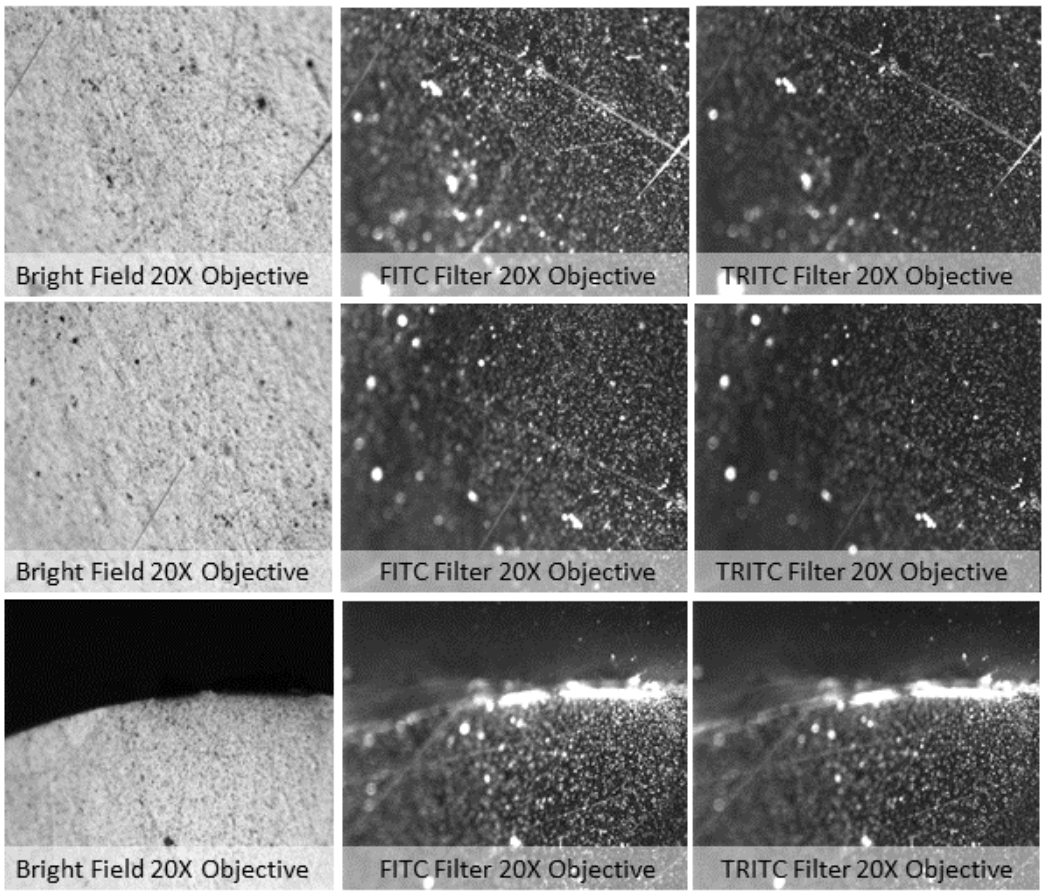


*Fig 4.50: Fluorescence microscopy images of CH Instruments CHI101 macro disc electrodes functionalised with FITC conjugated antibodies.*

Fluorescence microscopy images depict successful immobilisation of antibodies to electrode surfaces. FITC wavelengths produced mean pixel intensities of 23,309.58, 19,845.07 and 21,406.12 for images 1b, 2b and 3b respectively. Intensities were significantly greater than TRITC wavelengths at 17,499.96, 14,998.51 and 19,845.07 for images 1c, 2c and 3c respectively ($F(1,4) = 11.57$, p-value $< 0.05$), which reflects immobilisation of FITC conjugated antibodies as previously described in section 4.4.1.2.3. Interestingly, fluorescence intensities appear more uniform across electrode surfaces, which suggests that addition of protein G assays produces better distribution of antibodies on gold substrates. However, hot spots were still observed, albeit to a

lesser extent, on electrodes that suggests smaller proportions of antibody aggregates still exist on sensor surfaces.

#### *4.4.3.6.3 ATR-FTIR Characterisation of SAM*

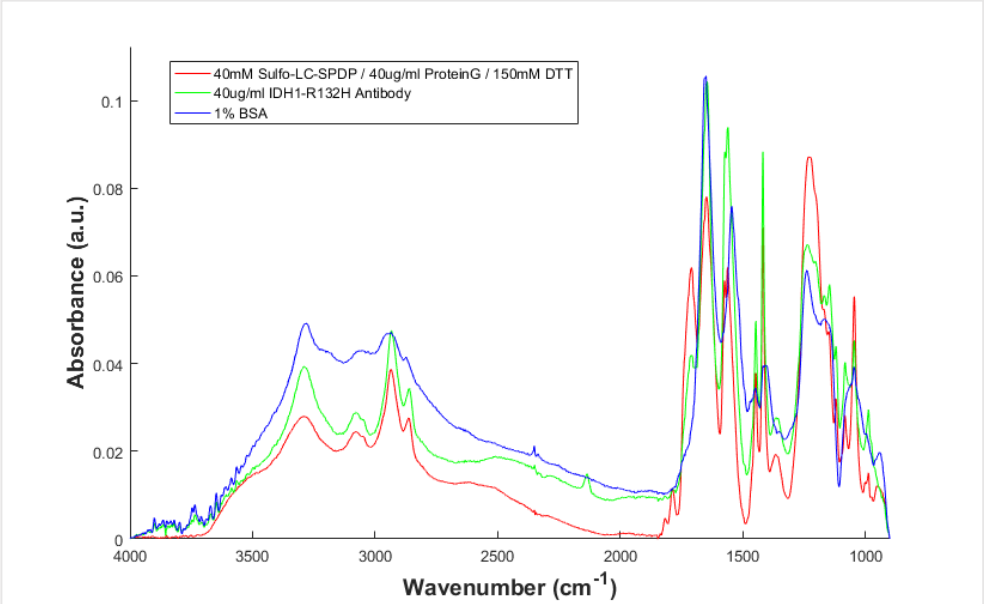


*Fig 4.51: ATR-FTIR spectra of SAM depositions attached to gold coated silicon crystals with spectra cut between 4000-900cm$^{-1}$, rubber-band baseline correction and vector normalisation pre-processing steps (n=3).*

Infrared spectra were representative of attachment of the heterobifunctional cross-linker protein G assay to gold-coated silicon ATR substrates. Sulfo-LC-SPDP protein G assays prompted strong absorption peaks consistent with assignments previously described in section 4.4.1.2.2, with the exception of broadening of the peak at ~1230cm$^{-1}$, tentatively assigned to $\nu$(CN) vibrations of amines. Antibody depositions suppressed the $\nu$(C=O) and $\nu$(CN) vibrations with concurrent increases in intensities of the amide I, amide II, $\nu(CH_2)/\nu(CH_3)$ and $\delta(CH_2)/\delta(CH_3)$ vibrations, representative of amine and hydrocarbon groups found on heavy chains of antibodies. Thereafter, BSA assays further suppressed absorption bands associated with previous

immobilisation steps whilst retaining strong intensities in amide I and amide II regions indicative of successful blocking on sensor surfaces.

#### *4.4.3.6.4 Concentration Study*

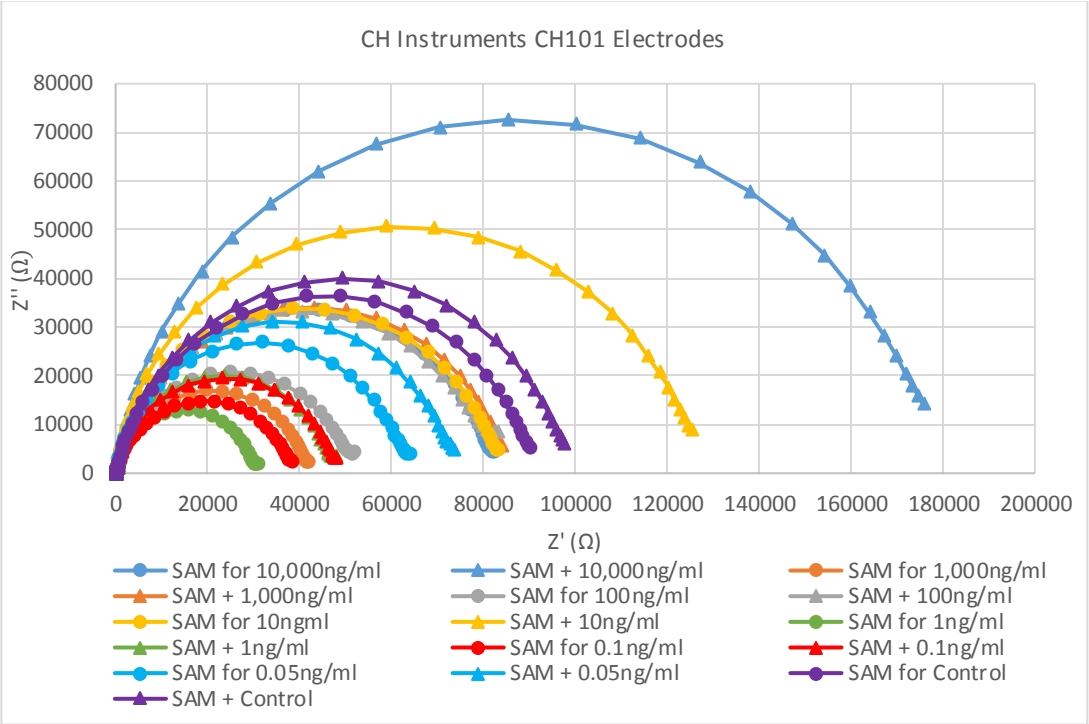


*Fig 4.52: Nyquist plot of functionalised electrodes before and after incubation with specified antigen concentrations (n=3).*

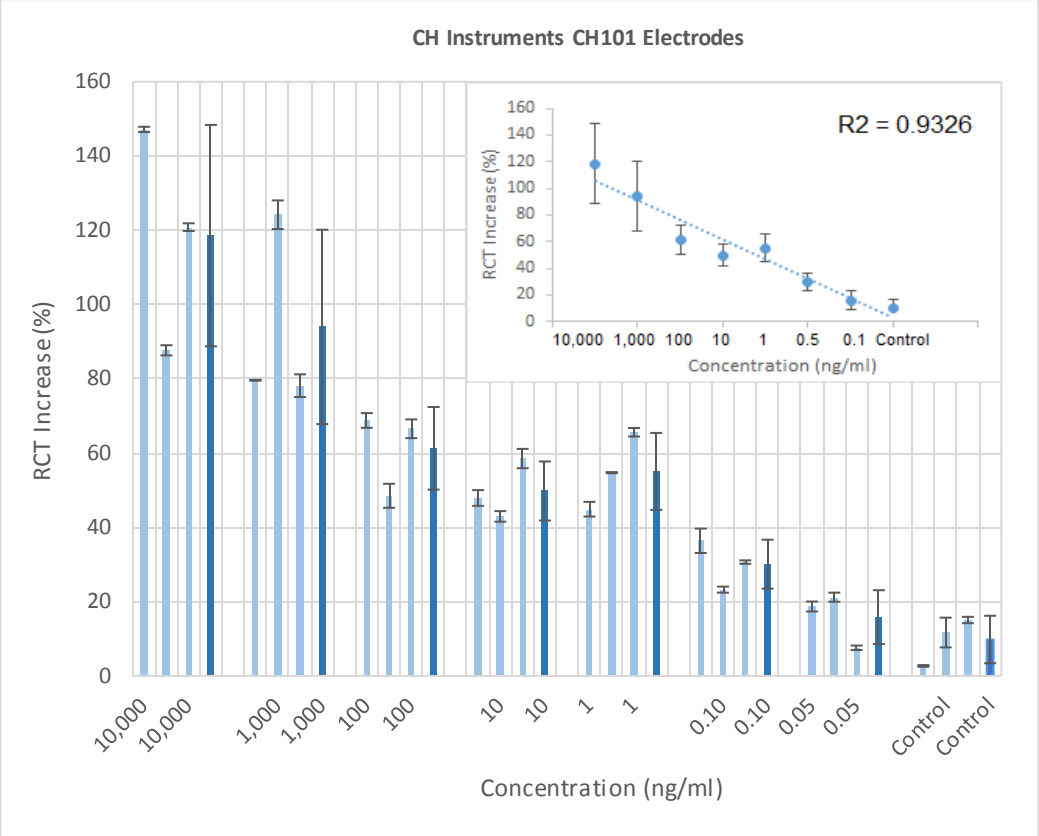


*Fig 4.53: Plot of the percentage difference in Rct for functionalised electrodes before and after incubation with specified antigen concentrations (n=3).*

Nyquist plots depict electrode impedance responses characteristic of SAM formation that increase upon incubation with spiked buffer samples, with a weak positive correlation to antigen concentration ($R^2 = 0.934$) (Fig. 4.53). Percentage differences in Rct for 10,000ng/ml concentrations were 118.58% ± 29.81, significantly greater than 94.01% ± 26.16 for 1,000ng/ml concentrations ($F(1,16) = 4.58$, p-value $< 0.05$). Similarly, percentage differences in Rct for 100ng/ml concentrations were 61.31% ± 11.12, statistically greater than 49.82% ± 7.96 for 10ng/ml concentrations ($F(1,16) = 7.98$, p-value $< 0.05$). However, 10ng/ml concentrations were not significantly different to 55.10% ± 10.36 for 1ng/ml concentrations, which highlights the poor linearity of our sensor. Percentage differences in Rct for 0.1ng/ml concentrations were

30.11% ± 6.59, significantly greater than 0.05ng/ml concentrations at 15.848% ± 7.251 ($F(1,16) = 24.14$, p-value $< 0.05$), which in turn were not different to control values at 9.83% ± 6.39 ($F(1,16) = 4.33$, p-value $= 0.054$). Therefore, the sensors current limit of detection was observed to be 0.1ng/ml, greater than our previous findings of 0.05ng/ml for the heterobifunctional cross-linker study. Furthermore, percentage differences in Rct were reduced for specified concentrations compared to our previous studies, which suggests the sensor is not as responsive upon antigen exposure and further explains the poorer limit of detection. Keighley previously found that denser peptide nucleic acid modified electrodes with larger starting impedance values were significantly less responsive to target DNA hybridisation (Keighley et al, 2008), and may partly explain the poor linearity of our results compared to our previous heterobifunctional cross-linker study.

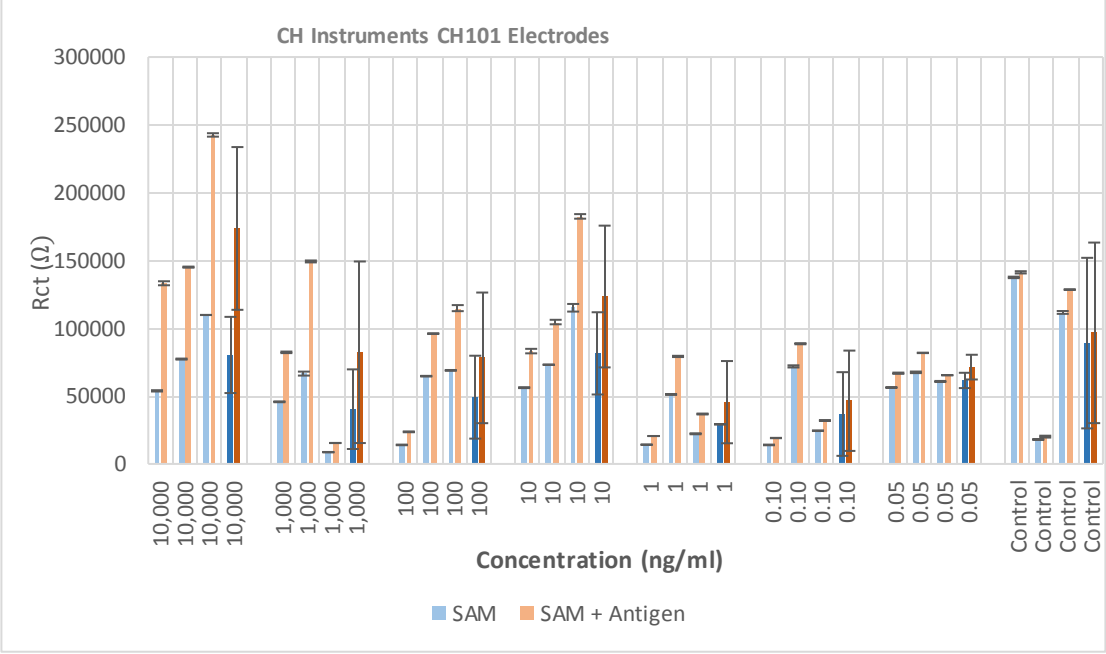


*Fig 4.54: Plot of Rct values for functionalised electrodes before and after incubation with specified antigen concentrations (n=3).*

The degree of SAM formation significantly varies between electrodes prior to antigen incubation, which implies the presence of different quantities of antibodies and other SAM constituents on electrode surfaces, which would naturally further explain the poor linearity of our results. Hence, the current assay is still not conducive to reproducible SAM formation, despite efforts to control antibody orientation through inclusion of protein G molecules, and suggests that either Sulfo-LC-SPDP or DTT may be responsible for observed variation on electrode substrates, as described in section 4.4.3.2.3. Therefore, future studies shall explore physisorption methods of protein G to gold, with the view that the absence of thiols and reducing agents may produce less dense SAM's with greater responsiveness and improved reproducibility.

### *4.4.3.7 Protein G Physisorption Protocol*

#### *4.4.3.7.1 Electrochemical Characterisation of SAM*

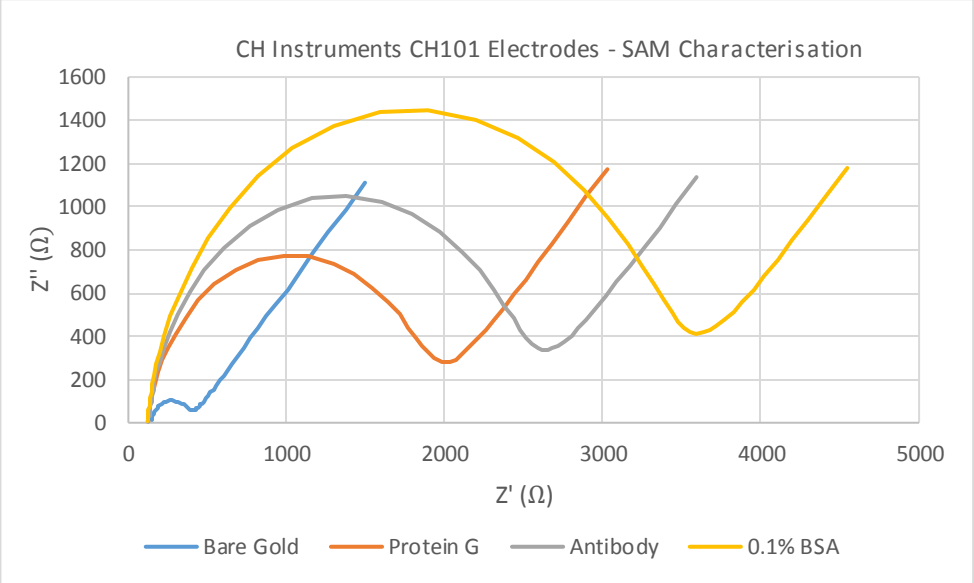


*Fig 4.55: Nyquist plot of SAM characterisation of electrodes following immobilisation procedures (n=3)*

Bare gold electrodes incubated with protein G assays were found to have significantly increased Rct values at 1743.67Ω ± 80.36 ($F(1,16) = 2319.58$, p-value $< 0.05$), which implies successful physisorption of protein G to electrode substrates (Hafaiedh et al, 2013). Interestingly, protein G assays displayed markedly reduced Rct values compared to the previous heterobifunctional cross-linker assays, which partly represents the reduced concentration of SAM constituents, and partly reflects the weaker Van der Waals forces (20-40kJ/mol) that hold molecules to electrode surfaces (Allen, 1988), as opposed to chemisorption of alkane thiols to gold (~126kJ/mol) (Lavrich et al, 1998). Antibody assays subsequently prompt significant increases in Rct to 2347.56Ω ± 107.15 ($F(1,16) = 4.75$, p-value $< 0.05$), which indicates successful, orientated conjugation of protein G to Fc domains of antibodies. Thereafter, BSA depositions significantly increase Rct values to 3274.22Ω ± 333.52 ($F(1,16) = 23.57$, p-value $< 0.05$), which implies successful blocking of bare gold electrode surfaces. Overall, impidimetric behaviour of electrodes following immobilisation procedures were consistent with previous literature findings, albeit the degree of SAM formation was found to be greater and reduced compared to studies of Hafaiedh (Hafaiedh et al, 2013) and Chammem (Chammem et al, 2015) respectively.

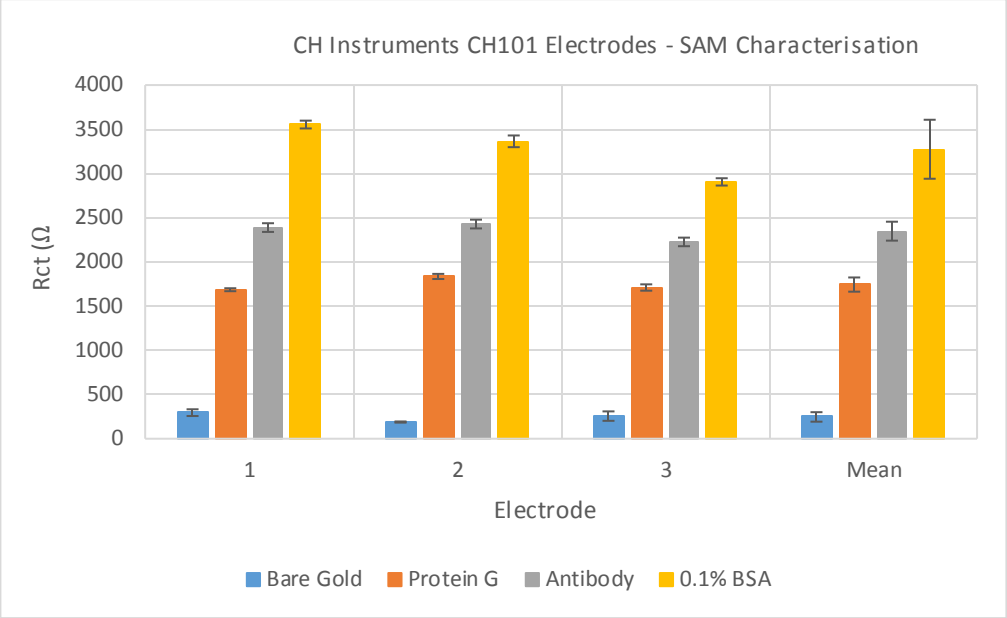


*Fig 4.56: Plot of Rct values for electrodes following immobilisation procedures (n=3)*

The degree of SAM formation does not statistically differ across electrodes for protein G ($F(2,6) = 0.78$, p-value $= 0.499$) or antibody ($F(2,6) = 1.41$, p-value $= 0.314$) depositions and highlights that the current assay has improved reproducibility compared to the previous heterobifunctional cross-linker assay. This further reinforces earlier suspicions that either Sulfo-LC-SPDP or DTT may be responsible for the large electrode-electrode variation observed in the previous assay. Nevertheless, BSA depositions were significantly different between all three electrodes for the current assay ($F(2,6) = 113.01$, p-value $< 0.05$), with the relative standard deviation of 10.19% greater than 6.29% for the previous Sulfo-LC-SPDP protein G assay. Therefore, fluctuations in SAM formation clearly still exists between electrodes, although crucially antibodies for detection of target antigens are more consistent between sensor substrates.

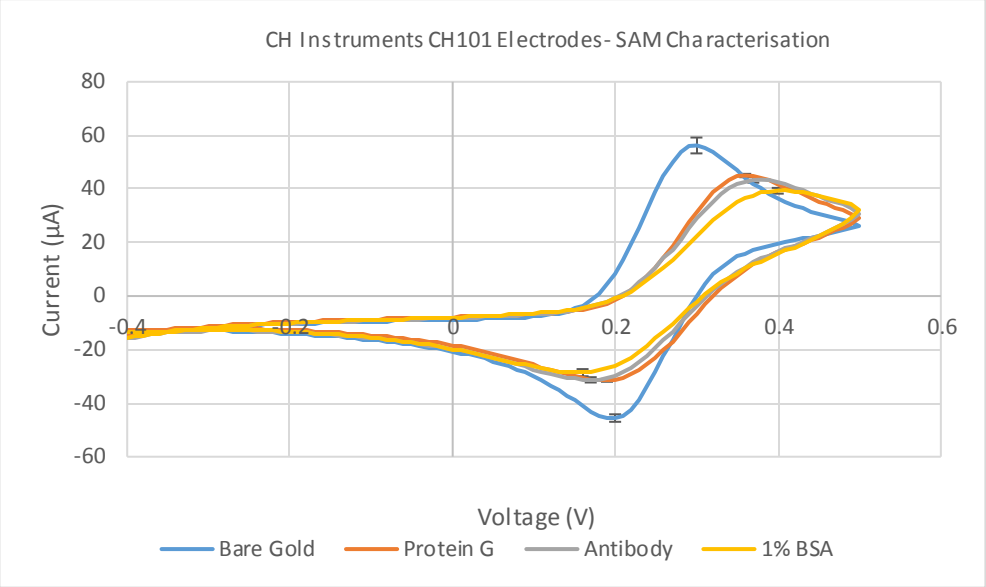


*Fig 4.57: CV plot for electrodes following immobilisation procedures (n=3)*

Voltammetric behaviour of electrodes following functionalisation assays is consistent with previous literature findings of Chammem (Chammem et al, 2015). Protein G depositions prompt significant decreases in Ipa = 45.001 µA ± 0.630 ($F(1,16) = 94.61$, p-value $< 0.05$) and Ipc = -31.480 ± 0.527 ($F(1,16) = 871.13$, p-value $< 0.05$), indicative of molecular attachment to electrode surfaces as previously described in section 4.4.1.2.1, and in agreement with our impedance results. Antibody depositions cause further reductions in Ipa = 43.400 µA ± 1.060 ($F(1,16) = 3.07$, p-value $= 0.099$) and Ipc = -31.294 µA ± 0.992 ($F(1,16) = 0.19$, p-value $= 0.665$), although results were not statistically significant and indicates reduced antibody attachment compared to the Sulfo-LC-SPDP protein G assay, expected given the reduced concentrations of both protein G and antibody assays. BSA depositions prompt further significant decreases in Ipa = 39.316 µA ± 1.080 ($F(1,16) = 17.34$, p-value $< 0.05$) and Ipc = -28.616 µA ± 1.334 ($F(1,16) = 22.23$, p-value $< 0.05$), which indicates successful blocking of electrode surfaces. Overall, electrode responses at redox potentials were markedly improved compared to previous cross-linker assays and showed increased availability

of $[Fe(CN)_6]^{-3/4}$ anions to participate in redox events, which consequently implies less dense SAM formation on electrode surfaces. Furthermore, standard deviations for respective functionalisation depositions were significantly reduced compared to the previous Sulfo-LC-SPDP protein G protocol, which indicates that current SAM's exhibit improved reproducibility when subjected to the potential range of interest.

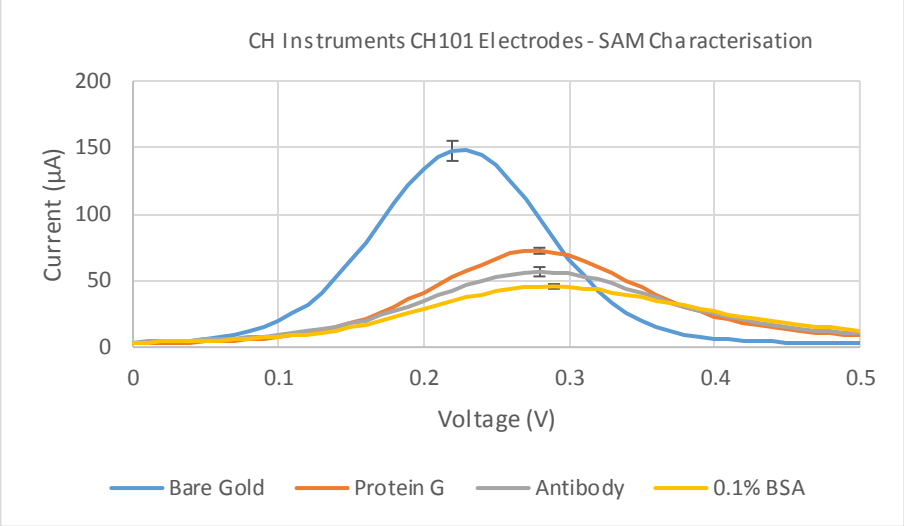


*Fig 4.58: DPV plot for electrodes following immobilisation procedures (n=3)*

Functionalised electrodes exhibit similar behaviour to CV results when subjected to pulsed potential waveforms. All immobilisation procedures were associated with significant reductions in peak oxidation currents; protein G assays to Ipa = 68.837 µA ± 2.258 ($F(1,16) = 287.97$, p-value $< 0.05$), antibody assays to Ipa = 55.127 µA ± 3.502 ($F(1,16) = 287.97$, p-value $< 0.05$) and BSA assays to Ipa = 44.360 µA ± 1.752 ($F(1,16) = 72.60$, p-value $< 0.05$). Therefore, physisorption of molecules to electrode surfaces was deemed successful for respective immobilisation assays, in agreement with our previous impedance findings.

*4.4.3.7.2 Fluorescence Microscopy Characterisation of SAM*

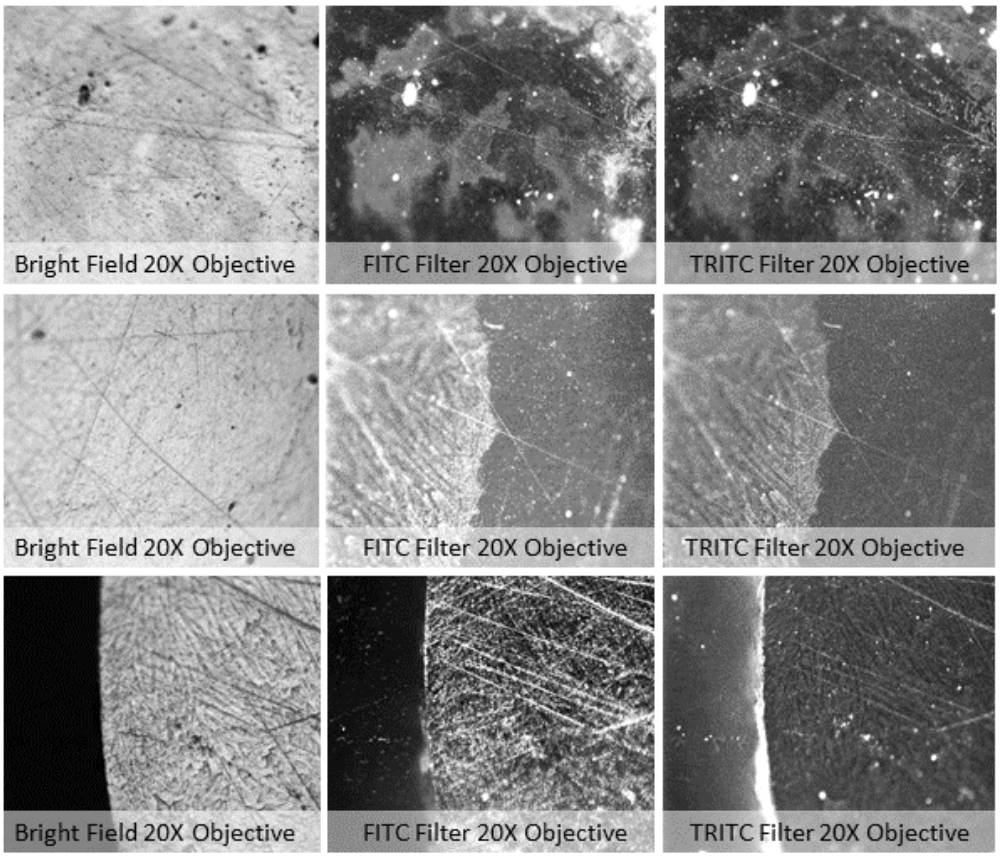


*Fig 4.59: Fluorescent microscopy images of electrodes functionalised with FITC conjugated antibodies at different excitation wavelengths (n=3).*

Fluorescence microscopy images show successful immobilisation of FITC conjugated antibodies to electrode surfaces. Fluorescence intensities were greater at FITC wavelengths, albeit not statistically different to TRITC wavelengths ($F(1,4) = 0.78$, p-value = 0.427), with mean pixel intensities of 102.033, 157.563 and 92.363 for images 1b, 2b and 3b respectively. Conversely, TRITC wavelengths produced mean pixel intensities of 86.065, 118.981 and 85.707 for images 1c, 2c and 3c respectively. Interestingly, fluorescence intensities appear more uniform at specific locations on electrode substrates, which suggests the location of protein G attachment to gold surfaces. Additionally, electrodes exhibit neighbouring areas of significantly reduced

fluorescence, which indicates the absence of protein G molecules at such areas on electrode surfaces and, hence, no binding of fluorescently tagged antibodies.

*4.4.3.7.3 ATR-FTIR Characterisation of SAM*

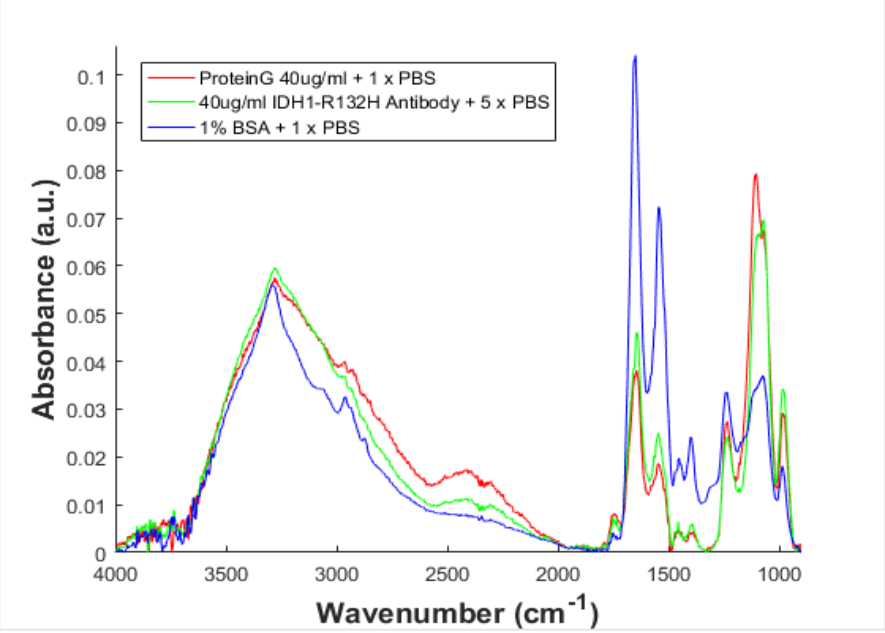


*Fig 4.60: ATR spectra of SAM depositions immobilised on gold coated silicon ATR crystals with spectra cut between 4000-900cm$^{-1}$, rubber-band baseline correction and vector normalisation pre-processing steps (n=3).*

Infrared spectra were characteristic of the physisorption of protein G assays to gold-coated silicon ATR crystals. Protein G depositions produced significant absorption in the amide I, amide II and amide III regions, and $\nu$(CN) vibrations at ~1230cm-1 which indicates protein attachment to sensor surfaces. Subsequently, antibody incubations prompt marginal increases in the intensities of amide I, amide II and amide III bands, consistent with coupling of low concentrations of antibodies to protein G molecules. Thereafter, BSA depositions produced significant increases in the absorption of amide I, amide II and amide III bands, which is expected given increased BSA concentrations,

and further implies that significant areas of bare gold were blocked with protein molecules upon immobilisation.

*4.4.3.7.4 Concentration Study*

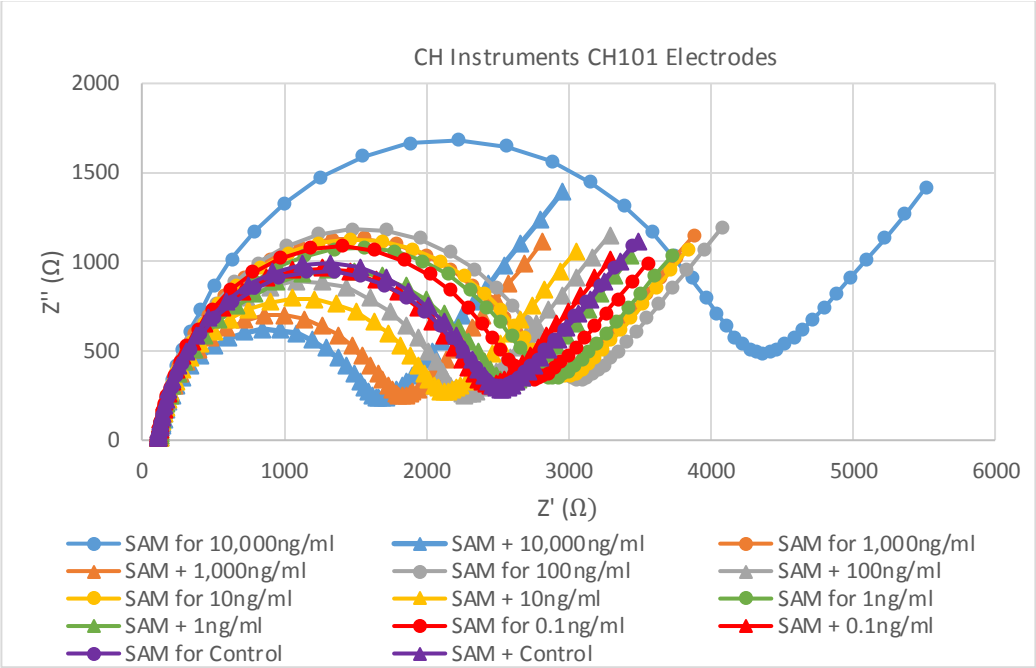


*Fig 4.61: Nyquist plot of functionalised electrodes before and after incubation with specified antigen concentrations (n=3).*

Nyquist plots depict electrode impedance values characteristic with SAM formation that subsequently decrease upon exposure to specified antigen concentrations, consistent with previous literature findings of Hafaiedh (Hafaiedh et al, 2013) and Chammem (Chammem et al, 2015). The observed Rct decrease upon antigen incubation is contrary to previous experiments and may be explained by electrostatic interactions between antibodies and antigens, which perturb antibody chains and consequently affect antibody conformation with respect to sensor surfaces (Chammem et al, 2015). Russell similarly observed Rct decreases upon exposure to interleukin-6 antigens and postulates that antigen affinity binding may create pinholes in SAM

layers that enables redox species to permeate the sensor surface (Russell et al, 2018). Regardless, electrode responses were consistent over the course of the experiment, and, on initial inspection, appeared proportional to specified antigen concentrations.

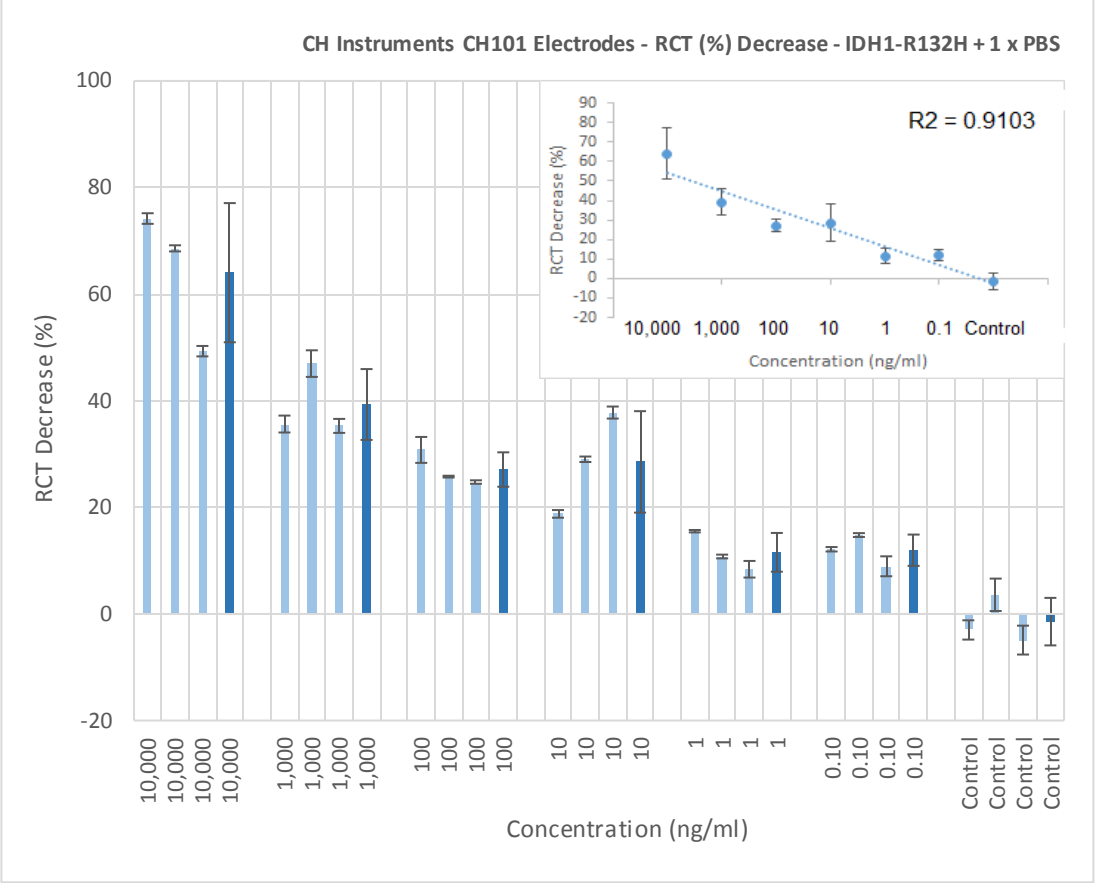


*Fig 4.62: Plot of the percentage difference in Rct values for functionalised electrodes before and after incubation with specified antigen concentrations (n=3).*

Percentage differences in Rct before and after incubation with IDH1-R132H target proteins were observed to have a weak positive correlation to specified antigen concentrations, with a Pearsons co-efficient of 0.9103 (Fig. 4.62). The largest decreases in Rct correlated with 10,000ng/ml concentrations at -64.025% ± 13.054 and were significantly greater than 1,000ng/ml concentrations at -39.295% ± 6.649 ($F(1,16) = 33.53$, p-value $< 0.05$). However, 100ng/ml concentrations were associated

with Rct decreases of -27.097% ± 3.227 that were not statistically significant to 10ng/ml concentrations at -28.525% ± 9.515 ($F(1,16) = 0.24$, p-value = 0.633), which highlights the poor linearity of the sensor. Similarly, no statistical differences were found between 1ng/ml concentrations at -11.564% ± 3.634 and 0.1ng/ml concentrations at -11.960% ± 2.934 ($F(1,16) = 0.08$, p-value = 0.783). However, 0.1ng/ml concentrations were significantly different from control measurements at 1.440% ± 4.458 ($F(1,16) = 0.08$, p-value = 0.783), which results in a current limit of detection of 0.1ng/ml protein concentration. Overall, current sensor responses to target antigens were reduced compared to our previous heterobifunctional cross-linker assays, surprising given the formation of less dense SAM's on electrode surfaces that have previously been shown to be more sensitive to target analytes (Butterworth et al, 2019; Keighley et al, 2008). Similarly, current sensor sensitivity was significantly poorer compared to previous studies of Hafaeidh who report limits of detection of 100fg/ml (Hafaeidh et al, 2013). However, sensor sensitivity was comparable to previous studies of Chemmam who report limits of detection of 1ng/ml, albeit in significantly more complex media, which suggests that antibody performance and antigen epitopes strongly influence sensor performance (Chemmam et al, 2015). Nevertheless, sensor linearity was significantly poorer with similarly high standard deviations compared to our previous heterobifunctional cross-linker assays using identical monoclonal antibodies. Reduced linearity was not expected since it was anticipated that antibodies with variable regions correctly orientated on electrode surfaces would allow more reproducible capture of target proteins at antigen binding sites, and hence suggests that antibody orientation is not the primary source of variability in the current assay.

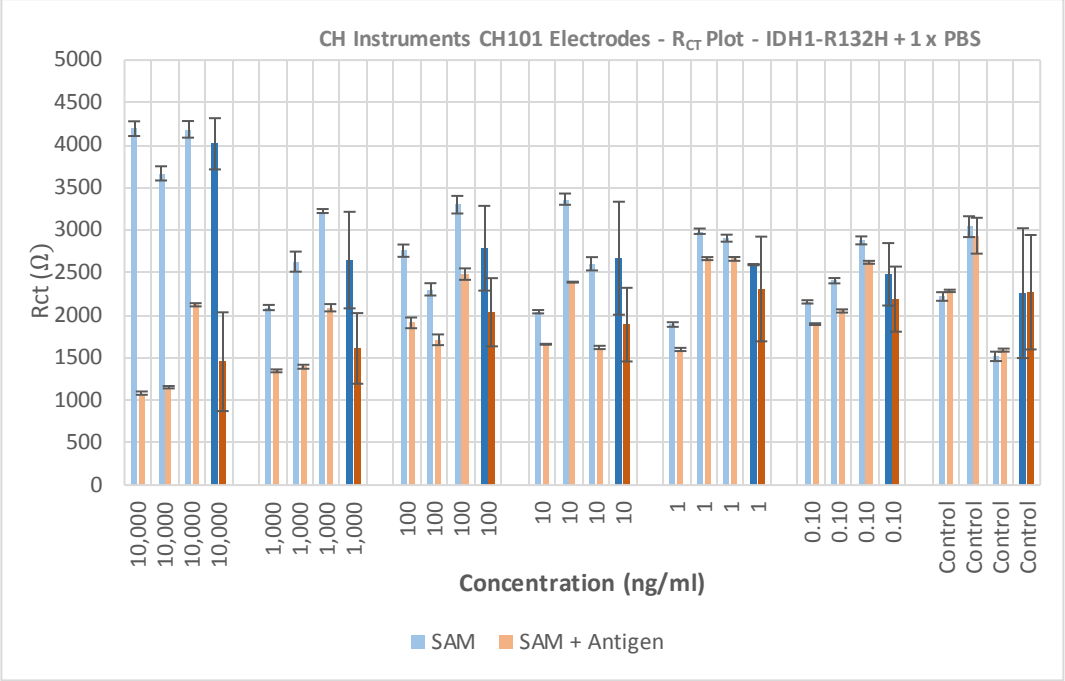


*Fig 4.63: Plot of Rct values for functionalised electrodes before and after incubation with specified antigen concentrations (n=3).*

Electrode variation in Rct values prior to antigen incubation may partly be responsible for the poor linearity of our sensor and is surprising given the markedly improved consistency of protein G and antibody depositions between electrodes, as characterised in section 4.4.3.7.1. Hence, it may be conjectured that the weak electrostatic forces attracting physisorbed molecules to sensor surfaces may subsequently be overcome with stringent wash steps that consequently permits degrees of detachment of SAM constituents. Differences in SAM films would likely prompt uneven distribution of antibodies on electrode surfaces that would correlate with poor reproducibility of target antigen binding, and would further corroborate our previous fluorescence findings. Hence, the current functionalisation protocol is not suitable for quantitative analysis of clinical serum samples, and it is recommended that future studies implement new chemisorption strategies to conjugate protein G to small alkane-thiol's,

given previous attempts with long chained cross-linker molecules did not have the required sensitivity or linearity.

### *4.4.3.8 Patient Samples*

CH Instruments CH101 electrodes were functionalised with the original heterobifunctional cross-linker assay as significant time-constraints prevented future development of new immobilisation protocols and it exhibited the greatest sensor linearity and limit of detection of tested assays.

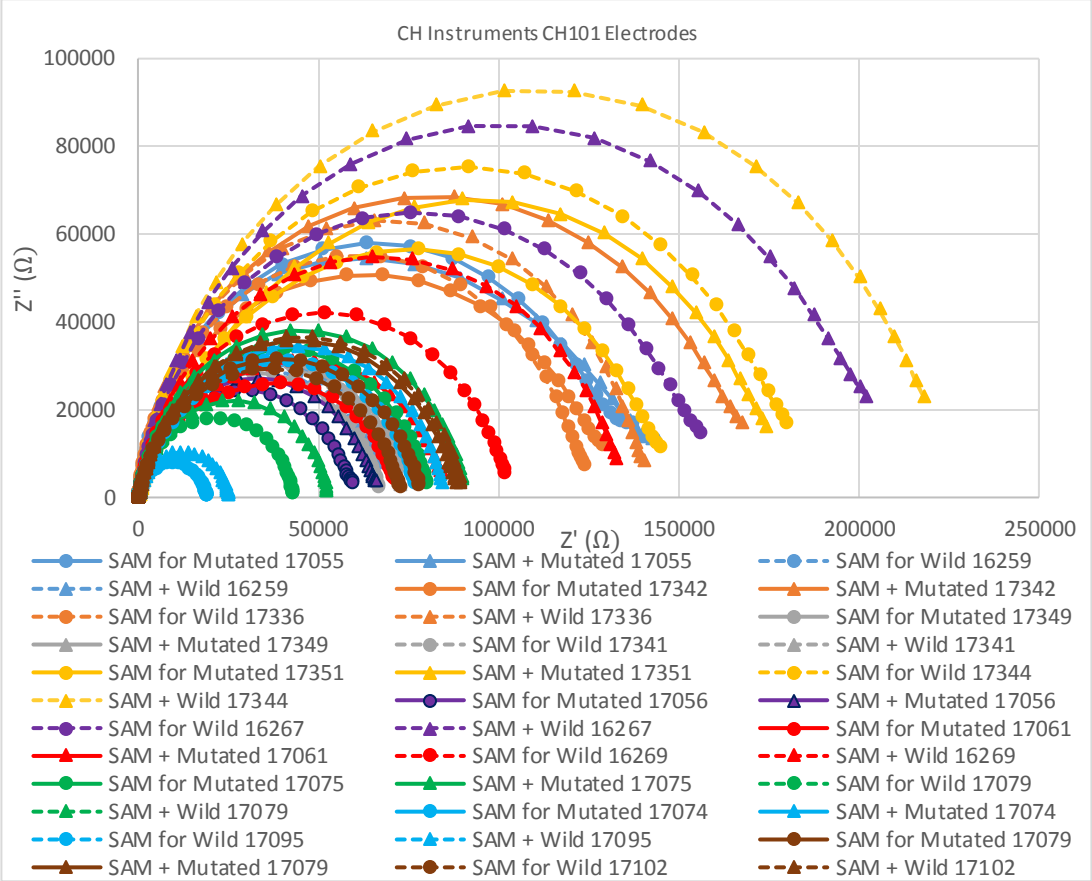


*Fig 4.64: Nyquist plot of functionalised electrodes before and after incubation with patient samples of either confirmed IDH1-R132H or IDH1-Wild type status (n=3).*

Nyquist plots depict impedance responses of functionalised electrodes before and after incubation with clinical human serum samples of patients with glioblastoma multiforne, that have confirmed IDH1-R132H or IDH1-Wild type status through previous immunohistochemical staining of resected tissue samples (Fig. 4.64). Overall impedance responses were observed to be greater than previous testing of the heterobifunctional cross-linker assay, which may possibly be attributed to the oxidation of thiols in MCH or DTT compounds to dithiols during long-term storage.

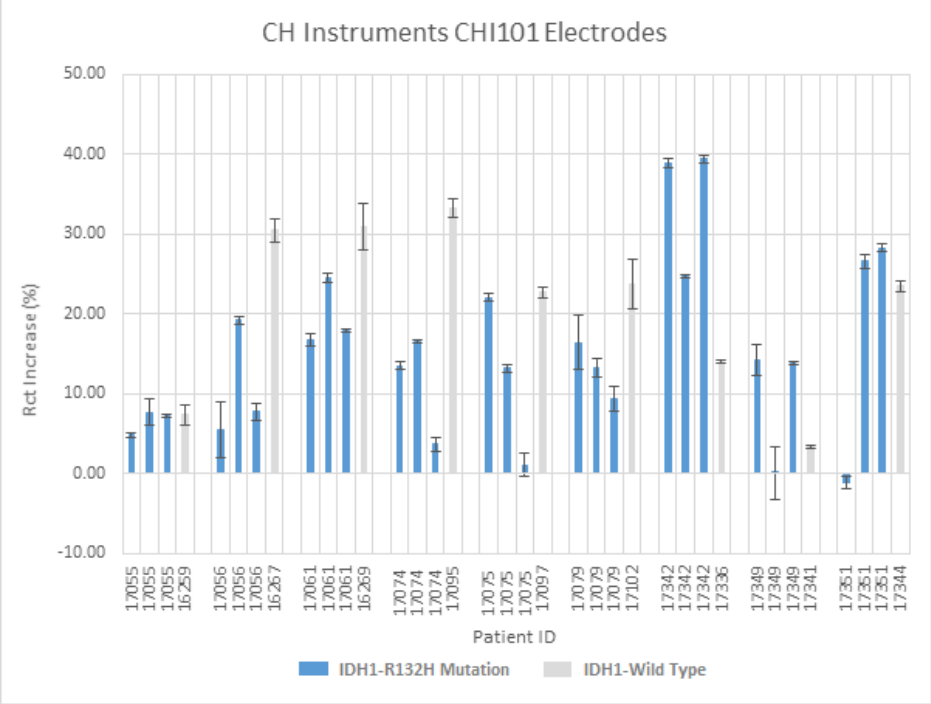


*Fig 4.65: Plot of percentage differences in Rct values for functionalised electrodes before and after incubation with patient samples of either confirmed IDH1-R132H or IDH1-Wild type status (n=3).*

Differences in Rct values were not statistically different for patients with IDH1-R132H and IDH1-wild type status at 15.04% ± 8.30 and 21.06% ± 10.63 respectively ($F(1,16) = 1.79$, p-value = 0.199), with no noticeable trend for either patient category. Hence, variation in electrode responses between patients were likely a result of non-specific binding events of serum constituents that naturally fluctuate in persons (Krebs, 1950;

Kamm et al, 1972), rather than antigen affinity binding at electrode surfaces. Furthermore, the high standard deviation between electrodes for identical patient samples questions the current reproducibility of our sensor, and was likely a consequence of different degrees of immobilisation on electrode surfaces (Fig. 4.65). Future work should consider the inclusion of tris(2-carboxyethyl)phosphine (TCEP) for deposition of SAM and blocking assays, as it has previously been reported to increase reproducibility of SAM formation and the magnitude of sensor responses for DNA probes following target binding (Corrigan et al, 2017). Additionally, the structure of TCEP does not contain a thiol functional group and, thus, cannot competitively chemisorb with free thiol cross-linker molecules to gold substrates (Hermanson, 2013).

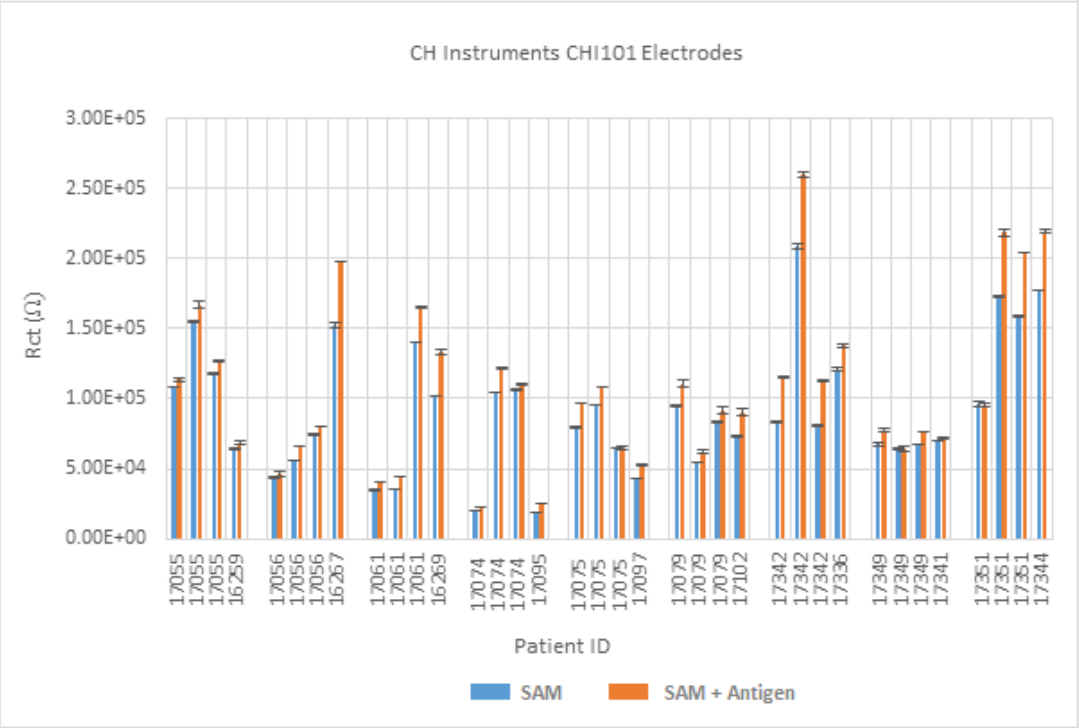


*Fig 4.65: Plot of Rct values for functionalised electrodes before and after incubation with patient samples of either confirmed IDH1-R132H or IDH1-Wild type status (n=3).*

Therefore, findings indicate that the current sensor does not possess the required sensitivity and reproducibility to detect IDH1-R132H mutations in clinical serum samples. Boisselier previously reported sensitivity issues for detection of small size DNA of IDH1-R132H mutations from clinical glioma plasma samples, citing the reduced concentration of DNA strands in the circulatory system, with detection in 60% of patients harbouring IDH1-R132H mutations (Boisselier et al, 2012). Hence, our current findings may alternatively indicate that IDH1-R132H mutant proteins were not in fact present in patient serum samples, which is plausible given that IDH1 proteins are located in the cytosol of cells (Frezza et al, 2010). Furthermore, the blood-brain barrier poses a significant challenge to IDH1 protein entry in to the circulatory system, considering tight junctions of densely packed endothelial cells prevent the passage of solutes and large molecules, and especially since IDH1 mutants are large proteins with molecular weights of ~44kDa (Holdhoff et al, 2013; Matteo et al, 2017). Therefore, future studies should conduct Western blot analysis to confirm the presence of IDH1 proteins in patient serum samples, since current reviews on blood-based glioma biomarkers have not reported such findings in the literature (Holdhoff et al, 2013). Additionally, future work should instead consider detection of the oncometabolite D-2-hydroxyglutarate (D2HG), with high concentrations of the biomarker correlated to IDH1 mutations in various cancer studies (Gross et al, 2010; Borger et al, 2014). Furthermore, D2HG is significantly smaller than IDH1 proteins with a molecular weight of 148.11Da, and thus has an increased chance to permeate the blood-brain barrier, with previous reports of entry in to the circulatory system at low concentrations (Horbinski, 2013). However, Pickard found the blood-brain barrier still prompts significant reductions in D2HG levels, reported to be at 500µM-10mM concentrations

in brain tumours compared to 0.36-3.48μM in blood plasma (Pickard et al, 2016). Additionally, Capper found in a study of 16 patients that elevated D2HG levels for patients harbouring IDH1-R132H mutations at 1.64μmol/l were not statistically significant compared to patients with wild-type status at 1.30μmol/l (Capper et al, 2011). Likewise, Lombardi found in a study of 84 patients similarly low D2HG concentrations between the blood plasma of both IDH1 groups; although when combined with detection of D2HG in urine, the resultant ratio was statistically significant between IDH1 classes (Lombardi et al, 2015). These findings are in agreement with the work of Fathi (Fathi et al, 2016) and, therefore, future endeavours should focus on identification of D2HG from patient plasma, in conjunction with urine samples, if the goal of IDH1-R132H detection from clinical blood samples is to be realised. Additionally, future efforts should consider strategies to increase assay sensitivity given the reduced concentrations of D2HG reported in blood plasma, possibly through inclusion of secondary antibody steps or molecular amplification with gold-nano-particles (Pei et al, 2001; Wang, 2007). Alternatively, detection of different biomarkers of glioma that have previously been identified in patient serum samples should be explored to prove the feasibility of our device, such as detection of the cell-free circulating DNA of $O^6$-methylguanine-DNA methyltransferase (MGMT) (Lavon et al, 2010; Wang et al, 2015).

### *4.4.4 ATR-FTIR Spectroscopy Results*

#### *4.4.4.1 ATR-FTIR Analysis of IDH1 Status for All Brain Tumour Types*

Clinical serum samples of brain cancer patients were subjected to Random Forest and PLS classifications to determine whether ATR-FTIR has the capacity to stratify patients with respect to IDH1 molecular status. Random Forest classification showed subtle differences between mean patient spectra truncated to the fingerprint region (1800-1000cm-1) that permitted successful identification of 10 out of 17 IDH1-R132H and 14 out of 14 IDH1 wild-type patients from one sample test set, as shown in the confusion matrix in Table 4.1. Further spectroscopic validation on 50 randomly assigned sample test sets provided an accurate assessment of the capabilities of the diagnostic model with sensitivity and specificity of 83.1 ± 9.30% and 85.8 ± 10.7% respectively, as indicated in Table 4.2. Random Forest identified absorption signatures significant to discrimination at 1685cm$^{-1}$, 1677cm$^{-1}$, 1669cm$^{-1}$, 1693cm$^{-1}$ and 1549cm$^{-1}$, which primarily corresponds to vibrations within the shoulder of the amide I region and to a lesser extent the amide II region, as indicated in Figure 4.66 (Barth, 2007). Additionally, smaller contributions pertinent to classification have been identified at 1053cm$^{-1}$, 1060cm$^{-1}$ and 1068cm$^{-1}$ assigned to $\nu$(C-O) vibrations of carbohydrates and nucleic acids (Movasaghi et al, 2011). Interestingly, the single arginine to histidine amino acid substitution that represents the only molecular difference between both IDH1 proteins has not been identified by the Random Forest classification. Absence of clear changes in amino acid vibrations of arginine ($\nu_s(CN_3H_5)$ at ~1614-1663cm$^{-1}$) and histidine ($\nu_s$(CN) at ~1229cm$^{-1}$) implies that discrimination of IDH1 status is instead based on other molecular constituents associated with the underlying differences in disease pathophysiology (Barth, 2007). As previously discussed, IDH1

mutated proteins instigate production of the onco-metabolite, D2HG, which is well recognised to interfere with normal epigenetic and metabolic cellular function and hyper-methylation of histone and DNA content (Kaminska et al, 2019). Therefore, it is possible that these global cellular differences contribute to secretion of different biomolecules into the blood circulatory system that may reflect the spectral signatures observed in the Random Forest model. Previously, Uckermann performed ATR-FTIR studies on resected glioma tissue of known IDH1 status and discovered spectral differences at 1050$cm^{-1}$, 1103$cm^{-1}$, 1362$cm^{-1}$, 1441$cm^{-1}$, 1485$cm^{-1}$ and 1558-1553$cm^{-1}$ assigned to changes in lipid, protein and carbohydrate content (Uckermann et al, 2018). Interestingly, the two peaks identified at 1050$cm^{-1}$ and 1558-1553$cm^{-1}$ were consistent with our current findings. Reitman also demonstrated through metabolic profiling of IDH1-R132H mutated cells that the point mutation is associated with significant changes in 143 biomolecules expressed or regulated by mutant cells, with at least two-fold concentration differences in 28 biomolecules (Reitman et al, 2011). In particular, Reitman showed that the amino acid expression profile of IDH1-R132H cells is significantly different from IDH1 wild-type cells, not limited to increases in glycine, serine and threonine, with notable decreases in aspartate and glutamate (Reitman et al, 2011). Others have supported these findings (Ohka et al, 2014), and may partly explain differences in intensities of the amide I and amide II peaks for IDH1-R132H mutated patients that represent absorption of protein molecules. Therefore, it is plausible that our current Random Forest spectroscopic findings reflect changes in global biomolecular environments stemming from IDH1-R132H mutations.

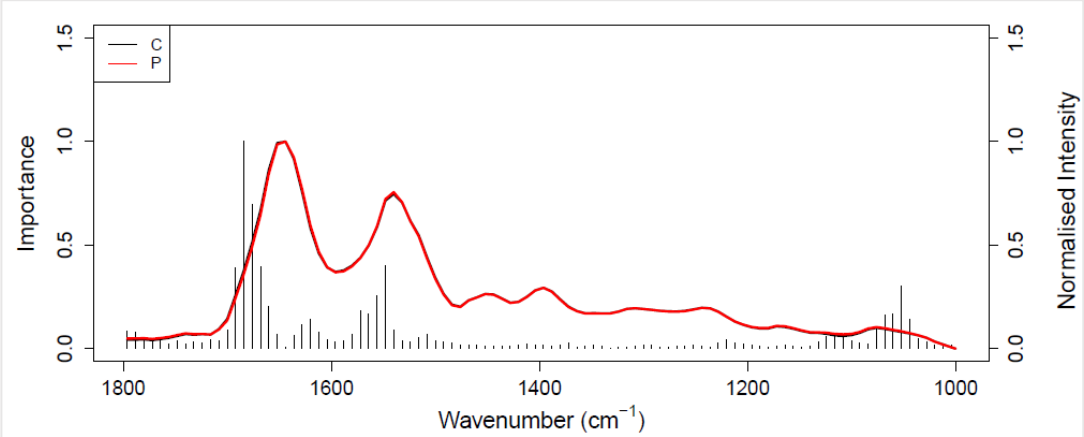


*Figure 4.66: Comparison of mean pre-processed ATR-FTIR spectra truncated to 1800-1000cm-1 of blood serum from brain cancer patients with IDH1 wild-type, denoted C, and IDH1-R132H molecular status, denoted P. Gini plot superimposed on mean spectra indicates significant wavenumbers for discrimination between patient groups as calculated by Random Forest model.*

| **Confusion Matrix** | | | **Patient Group** | **Patient ID** | **Misclassified Spectra** |
|---|---|---|---|---|---|
| | Reference | | IDH1-R132 | 15158 | 9/9 |
| Predictor | C | P | IDH1-R132 | 16076 | 9/9 |
| C | 14 | 7 | IDH1-R132 | 16234 | 9/9 |
| P | 0 | 10 | IDH1-R132 | 17453 | 9/9 |
| | | | IDH1-R132 | 1839 | 9/9 |
| | | | IDH1-R132 | 1955 | 9/9 |
| | | | IDH1-R132 | 908909 | 9/9 |

*Table 4.1: Confusion matrix describing the number of IDH1 wild-type, denoted C, and IDH1-R132H patients, denoted P, correctly identified by the Random Forest classifier in one sample set relative to known clinical status. Misclassified patients and number of spectra misclassified by the Random Forest model have been stated for both patients groups.*

| **Accuracy (n = 50)** | **Sensitivity (n =50)** | **Specificity (n = 50)** |
|---|---|---|
| 0.843 ± 0.061 | 0.831 ± 0.093 | 0.858 ± 0.107 |

*Table 4.2: Diagnostic performance of Random Forest model when re-analysed with 50 randomly generated sample test sets. Results presented as mean ± standard deviation.*

All identical brain tumour patients with known IDH1 status were also subjected to PLS classification as a comparative investigation to determine the optimum available model for classification of IDH1 molecular status in patients. Initial analysis on one sample test set showed improved diagnostic performance for PLS with identification of 14 out of 17 IDH1-R132H mutated patients and 13 out of 14 IDH1 wild-type patients, as illustrated in the confusion matrix of Table 4.3. However, validation on 50 randomly constructed sample test sets showed decreases in sensitivity to 80.4 ± 10.9% and specificity to 81.2 ± 11.8% compared to Random Forest classifications, as indicated in Table 4.4. Nevertheless, PLS scores reveal significant separation between IDH1-R132H and IDH1 wild-type patients on PLS1 versus PLS2, primarily attributed to variance in amide I and amide II regions of PLS1, as indicated from scores and loading plots in Figures 4.67/4.69. Similarly, the PLS2 versus PLS3 scores plot shows that separation between IDH1-R132H and IDH1 wild-type originates from variance in PLS3, as indicated in Figures 4.68/4.71, which predominantly describes differences in absorption at 1180cm$^{-1}$ and 1240cm$^{-1}$ assigned to $\nu$(CO) and $\nu_{as}(PO_2)$ vibrations (Movasaghi et al, 2011; Barth, 2007). Overall, the PLS classifier has been less discriminatory and shown reduced diagnostic capabilities compared to the Random Forest model, although it is extremely re-assuring that both disparate analyses identified identical biomolecular signatures responsible for stratification.


*Figure 4.67: PLS-DA plot showing spectral variance of mean ATR-FTIR spectra for PLS1 versus PLS2 components. Red and black circles correspond to individual spectra from serum samples of brain cancer patients with IDH1 wild-type and IDH1-R132H status respectively.*

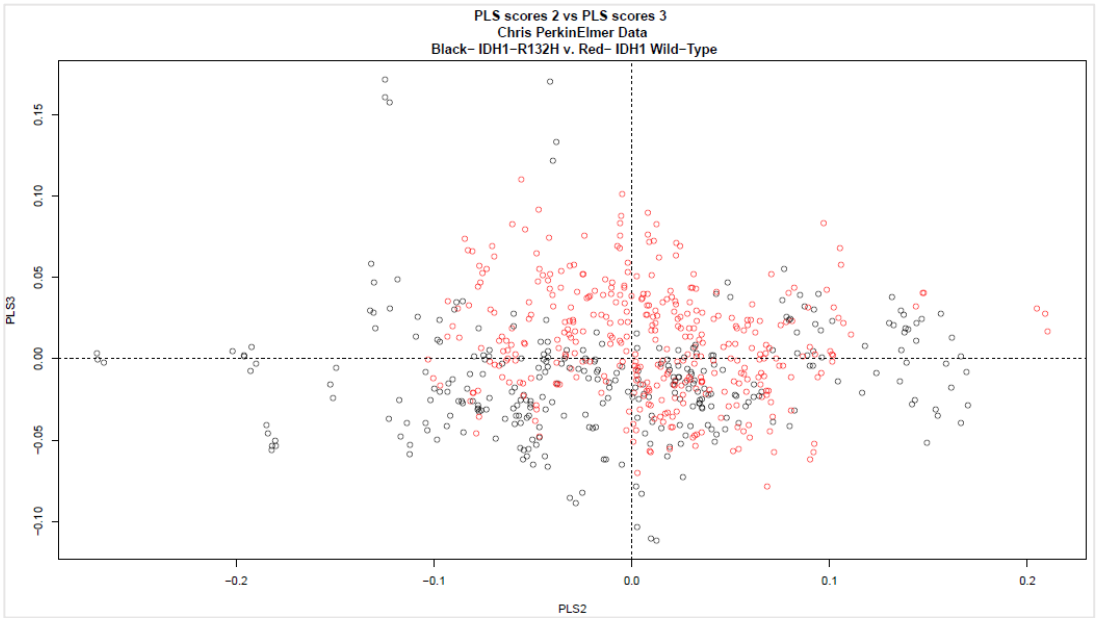


*Figure 4.68: PLS-DA plot showing spectral variance of mean ATR-FTIR spectra for PLS2 versus PLS3 components. Red and black circles correspond to individual spectra from serum samples of brain cancer patients with IDH1 wild-type and IDH1-R132H status respectively.*

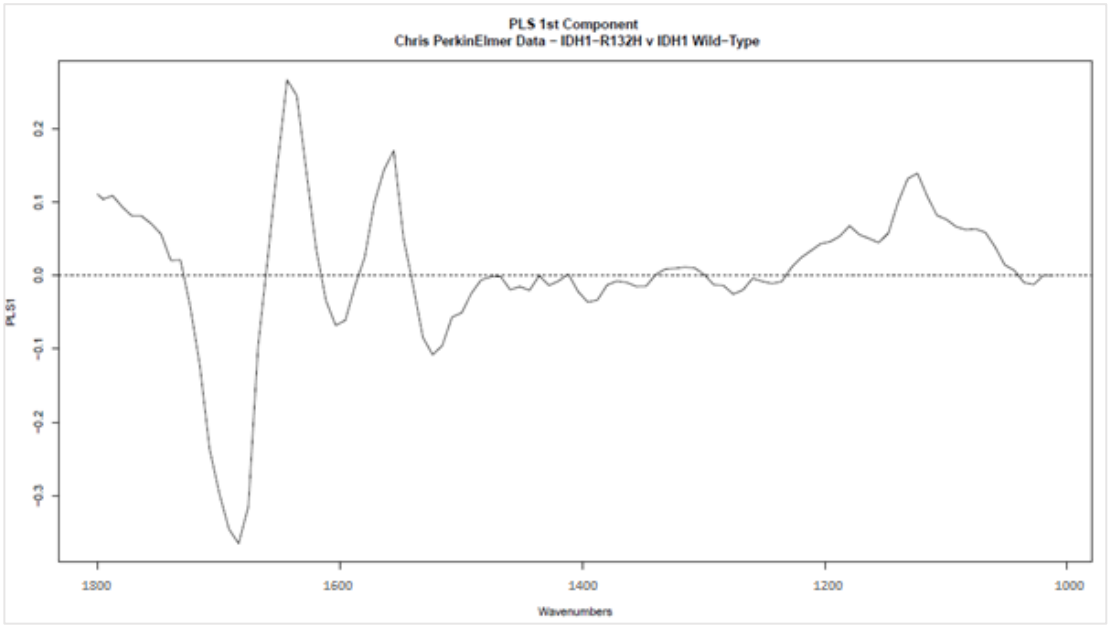


*Figure 4.69: PLS-DA loading plot showing the origin of spectral variance of mean ATR-FTIR spectra for PLS1 when evaluating IDH1 wild-type and IDH1-R132H molecular status.*

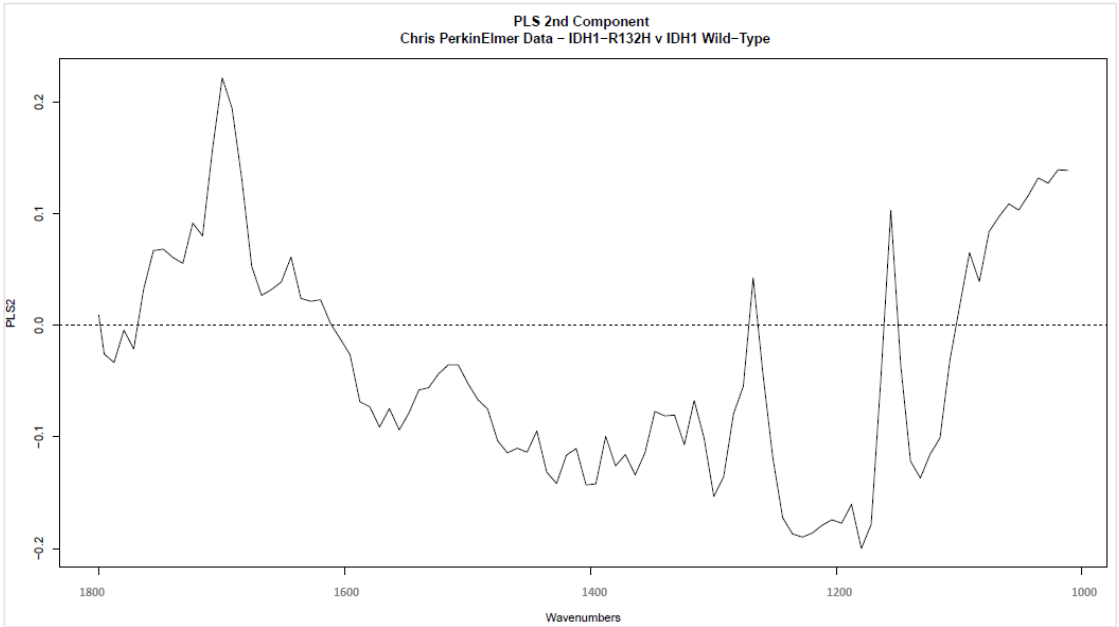


*Figure 4.70: PLS-DA loading plot showing the origin of spectral variance of mean ATR-FTIR spectra for PLS2 when evaluating IDH1 wild-type and IDH1-R132H molecular status.*

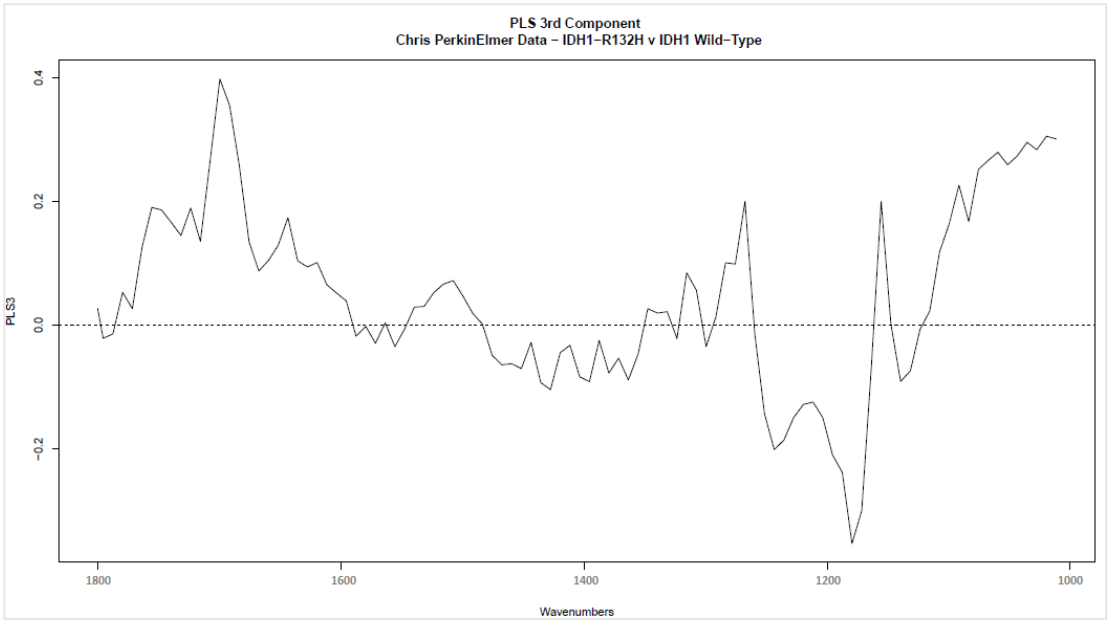


*Figure 4.71: PLS-DA loading plot showing the origin of spectral variance of mean ATR-FTIR spectra for PLS3 when evaluating IDH1 wild-type and IDH1-R132H molecular status.*

| **Confusion Matrix** | | | **Patient Group** | **Patient ID** | **Misclassified Spectra** |
|---|---|---|---|---|---|
| | Reference | | IDH1 Wild-Type | 1091 | 8/9 |
| Predictor | C | P | IDH1-R132H | 16076 | 9/9 |
| C | 13 | 3 | IDH1-R132H | 16227 | 7/9 |
| P | 1 | 14 | IDH1-R132H | 908909 | 9/9 |

*Table 4.3: Confusion matrix describing the number of IDH1 wild-type, denoted C, and IDH1-R132H patients, denoted P, correctly identified by the PLS classifier in one sample set relative to known clinical status. Misclassified patients and number of spectra misclassified by the PLS model have been stated for both patients groups.*

| **Accuracy (n = 50)** | **Sensitivity (n =50)** | **Specificity (n = 50)** |
|---|---|---|
| 0.808 ± 0.065 | 0.804 ± 0.109 | 0.812 ± 0.118 |

*Table 4.4: Diagnostic performance of PLS model when re-analysed with 50 randomly generated sample test sets. Results presented as mean ± standard deviation.*

*4.4.4.2 ATR-FTIR Analysis of IDH1 Status for Astrocytomas*

Random Forest and PLS models were further performed on clinical serum samples of brain cancer patients that solely had an astrocytoma tumour of either IDH1-R132H or IDH1 wild-type status to ensure previous analyses were not influenced by variation in tumour type. Previously, it has been well documented that certain protein serum biomarkers, such as interleukin-6 and YKL40, show progressively elevated levels with tumour severity (Shan et al, 2015; Iwamoto et al, 2014), and since the majority of grade IV glioblastoma samples were IDH1 wild-type, it was important to establish that separation between IDH status was not attributable to tumour grade. Mean absorption spectra truncated to the fingerprint region showed that similar wavenumbers in amide I and amide II regions and numerous vibrational modes in the ~1150-1050cm- region were deemed significant for discrimination between IDH1-R132H and IDH1 wild-type astrocytoma patients, illustrated in Figure 4.72. The comparable spectral signature with previous analysis is comforting and implies that previous band assignments were not subject to bias from other tumour types. Furthermore, the increased perceived significance of these bands for discrimination suggests that these spectral biomarkers strongly represent the biochemical differences between IDH1-R132H and IDH1 wild-type patients and have become more apparent once other tumour types have been removed from the classification. The Random Forest model successfully classified 7 out of 9 IDH1-R132H mutated and all 8 IDH1 wild-type astrocytoma patients from one sample test set, as indicated in Table 4.5. Further validation on 50 randomly constructed test sets produced a sensitivity of 79.2 ± 15.9% and specificity of 85.7 ± 11.8%, as indicated in Table 4.6, which is promising considering the reduced sample population compared to previous analysis. It is anticipated that the sensitivity and specificity of the model would increase with significantly larger sample populations,

as it would allow better understanding of spectral differences between patient classes and ultimately improve model training. To this extent, it should be noted that the results of separate investigations solely featuring glioblastoma or oligodendroglioma tumours have not been shown as the extremely low sample population and unbalanced classes produced results with poor statistical significance.

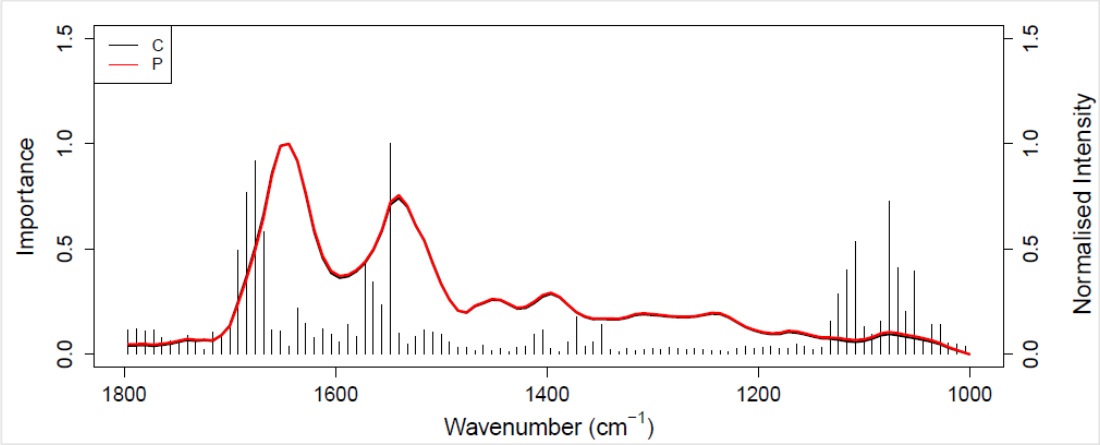


*Figure 4.72: Comparison of mean pre-processed ATR-FTIR spectra truncated to 1800-1000cm-1 of blood serum from astrocytoma brain cancer patients with IDH1 wild-type, denoted C, and IDH1-R132H molecular status, denoted P. Gini plot superimposed on mean spectra indicates significant wavenumbers for discrimination between patient groups as calculated by Random Forest model.*

| **Confusion Matrix** | | | **Patient Group** | **Patient ID** | **Misclassified Spectra** |
|---|---|---|---|---|---|
| | Reference | | IDH1-R132H | 16174 | 9/9 |
| Predictor | C | P | IDH1 Wild-Type | 16234 | 8/9 |
| C | 8 | 2 | | | |
| P | 0 | 7 | | | |

*Table 4.5: Confusion matrix describing the number of IDH1 wild-type, denoted C, and IDH1-R132H patients, denoted P, correctly identified by the Random Forest classifier in one sample set relative to known clinical status. Misclassified patients and number of spectra misclassified by the Random Forest model have been stated for both patients groups.*

| Accuracy (n = 50) | Sensitivity (n =50) | Specificity (n = 50) |
|---|---|---|
| 0.822 ± 0.077 | 0.792 ± 0.159 | 0.857 ± 0.118 |

*Table 4.6: Diagnostic performance of Random Forest model when re-analysed with 50 randomly generated sample test sets. Results presented as mean ± standard deviation*

Absorption spectra of astrocytoma patient samples were further subjected to PLS analysis to determine whether diagnostic accuracy could be improved with a different classification model. Initial analysis on a single sample test set successfully identified all 9 IDH1-R132H patients and 6 out of 8 IDH1 wild-type patients, as indicated in Table 4.7. Further validation on 50 sample test sets yielded an overall diagnostic accuracy of 88.6 ± 6.70% with sensitivity of 89.0 ± 11.3% and specificity of 88.2 ± 10.1%, as indicated in Table 4.8. Furthermore, PLS scores plots indicated significant separation between IDH1-R132H and IDH1 wild-type patients on both PLS1 versus PLS2 and PLS2 versus PLS3, attributed to PLS1 and PLS2 components, illustrated in Figures 4.73-4.76. Closer inspection of PLS loading plots show that differences in amide I and amide II regions primarily contribute to the separation observed on PLS1 axes, whilst $\nu_{as}(PO_2)$, $\nu(CO)$ and amide III vibrations primarily contribute to separation on PLS2 axes (Movasaghi et al, 2011). Overall, it is interesting that these additional molecular signatures contribute to differentiation of patient classes and highlights the major strength of spectroscopic approaches for diagnosis of IDH1-R132H molecular status in glioma patients.

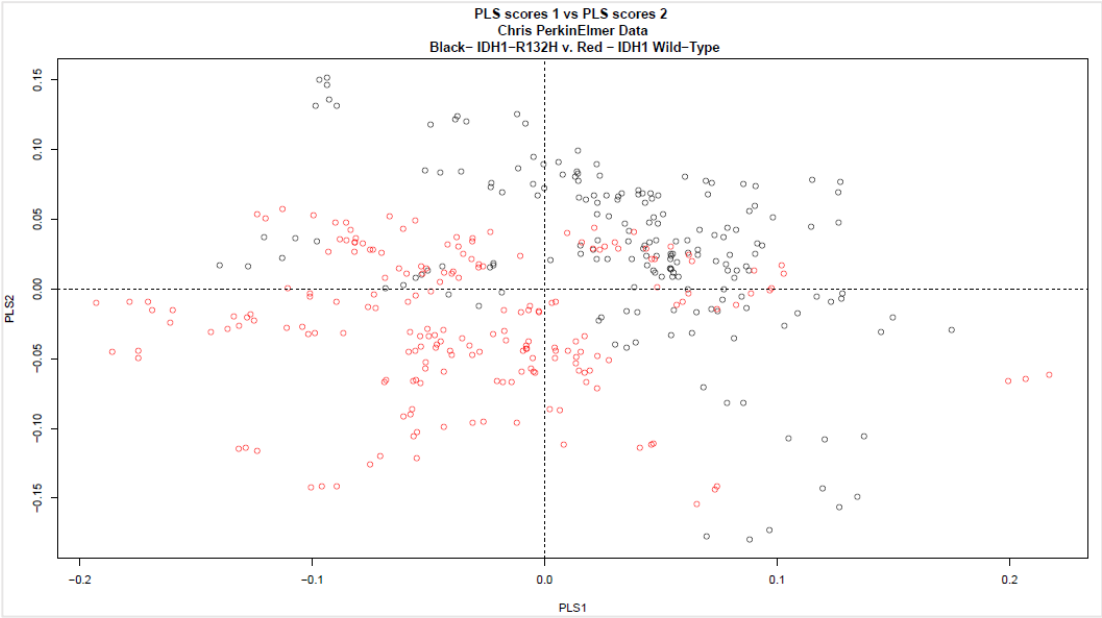


*Figure 4.73: PLS-DA plot showing spectral variance of mean ATR-FTIR spectra for PLS1 versus PLS2 components. Red and black circles correspond to individual spectra from serum samples of astrocytoma brain cancer patients with IDH1 wild-type and IDH1-R132H status respectively.*

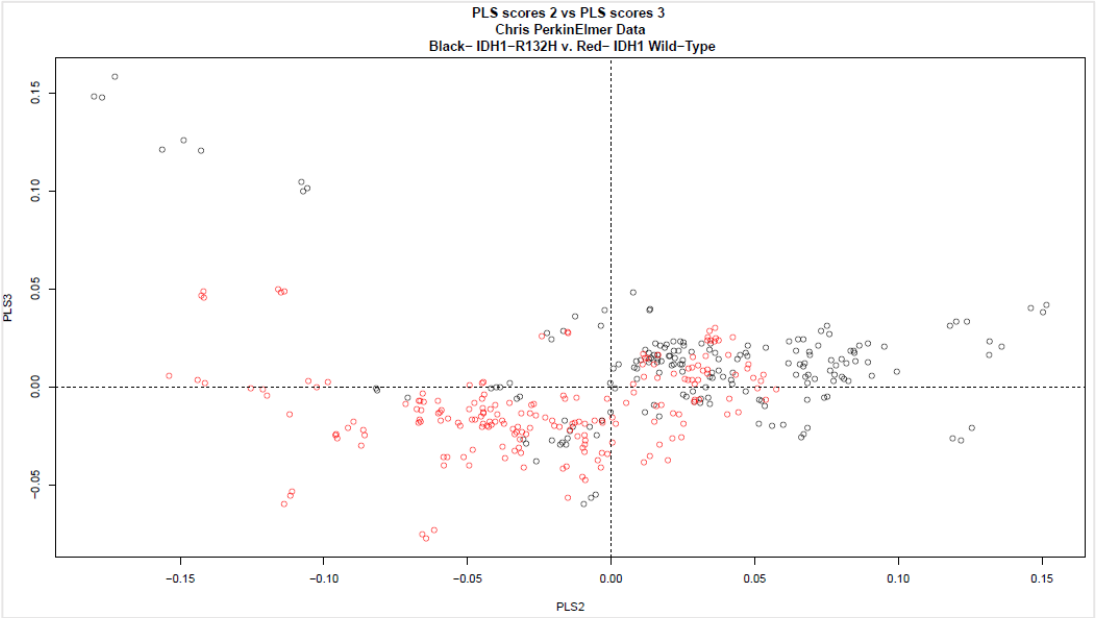


*Figure 4.74: PLS-DA plot showing spectral variance of mean ATR-FTIR spectra for PL2 versus PLS3 components. Red and black circles correspond to individual spectra from serum samples of astrocytoma brain cancer patients with IDH1 wild-type and IDH1-R132H status respectively.*

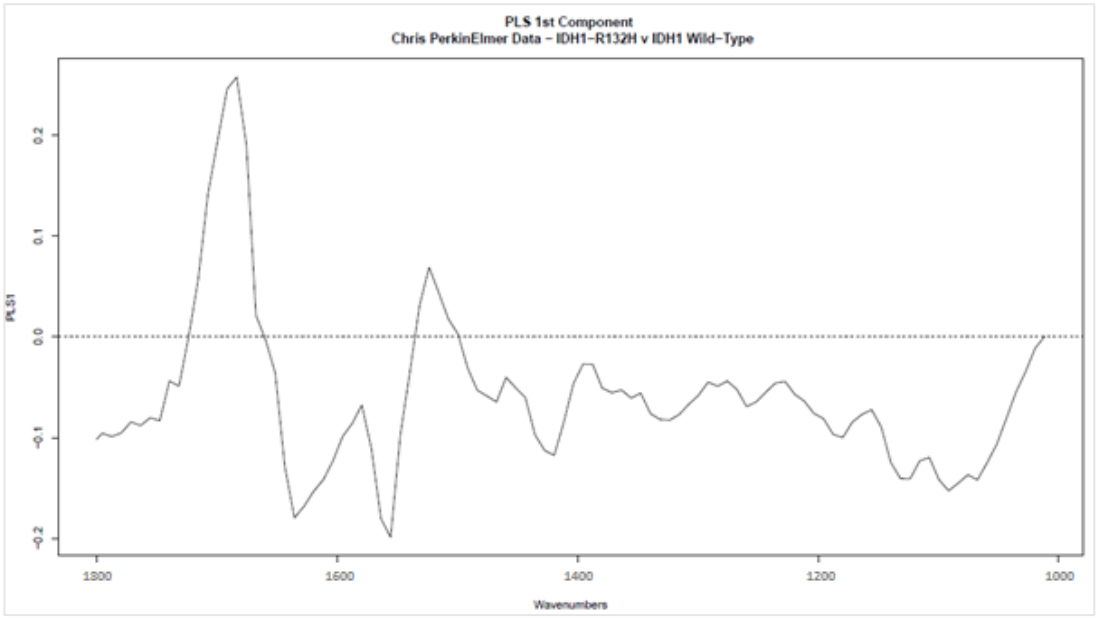


*Figure 4.75: PLS-DA loading plot showing the origin of spectral variance of mean ATR-FTIR spectra for PLS1 when evaluating IDH1 wild-type and IDH1-R132H molecular status of astrocytoma brain cancer patients.*

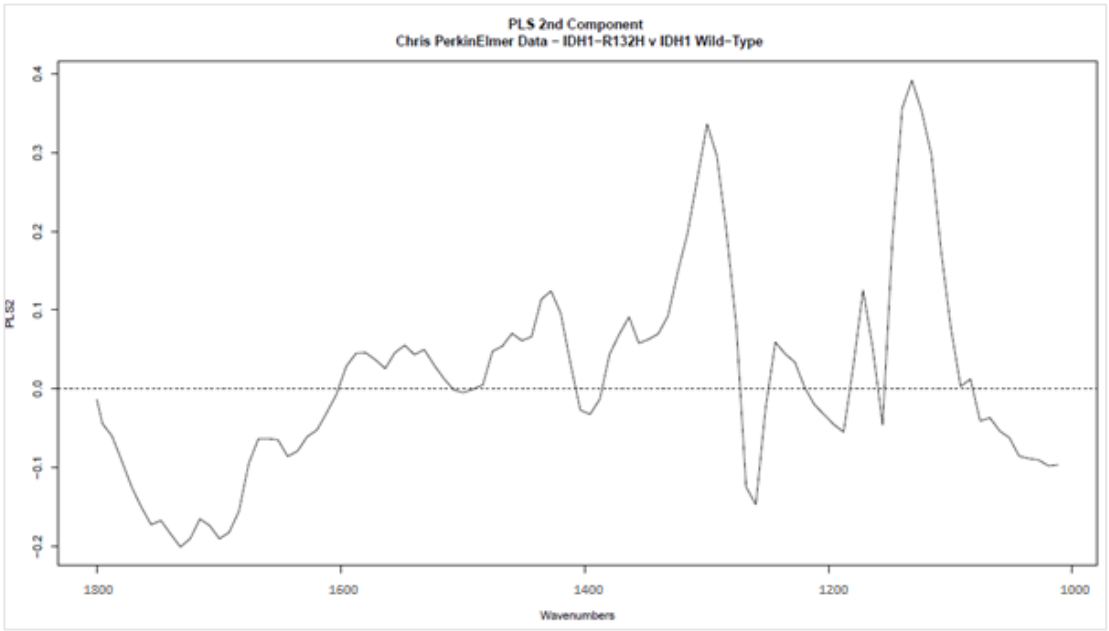


*Figure 4.76: PLS-DA loading plot showing the origin of spectral variance of mean ATR-FTIR spectra for PLS2 when evaluating IDH1 wild-type and IDH1-R132H molecular status of astrocytoma brain cancer patients.*

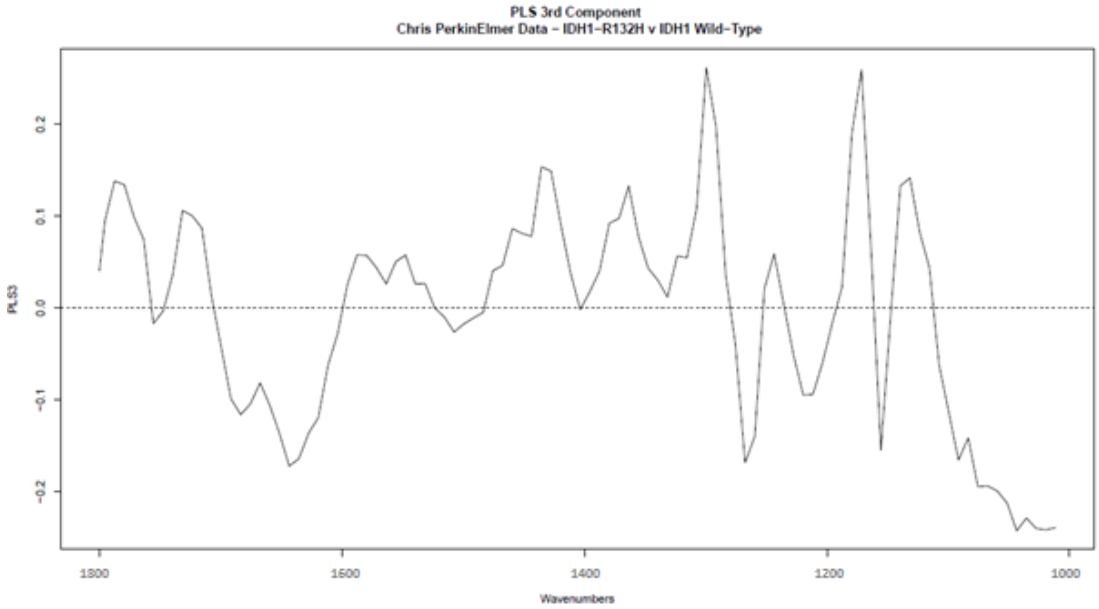


*Figure 4.77: PLS-DA loading plot showing the origin of spectral variance of mean ATR-FTIR spectra for PLS3 when evaluating IDH1 wild-type and IDH1-R132H molecular status of astrocytoma brain cancer patients.*

| **Confusion Matrix** | | | **Patient Group** | **Patient ID** | **Misclassified Spectra** |
|---|---|---|---|---|---|
| | Reference | | IDH1 Wild-Type | 15222 | 6/9 |
| Predictor | C | P | IDH1 Wild-Type | 16165 | 9/9 |
| C | 6 | 0 | | | |
| P | 2 | 9 | | | |

*Table 4.7: Confusion matrix describing the number of IDH1 wild-type, denoted C, and IDH1-R132H patients, denoted P, correctly identified by the PLS classifier in one sample set relative to known clinical status. Misclassified patients and number of spectra misclassified by the PLS model have been stated for both patients groups.*

| **Accuracy (n = 50)** | **Sensitivity (n =50)** | **Specificity (n = 50)** |
|---|---|---|
| 0.886 ± 0.067 | 0.890 ± 0.11.3 | 0.882 ± 0.10.1 |

*Table 4.8: Diagnostic performance of PLS model when re-analysed with 50 randomly generated sample test sets. Results presented as mean ± standard deviation.*

*4.4.4.3 ATR-FTIR Analysis of IDH1 Status with Spiked Serum Samples*

Pooled serum samples that had either been spiked with IDH1-R132H or IDH1 wild-type proteins were also subjected to spectroscopic testing with silicon IRE's to determine whether it was possible to identify differences in the spectral signatures of proteins at high to physiologically relevant concentrations. Mean spectra of IDH1-R132H and IDH1 wild-type proteins with concentrations from 10,000-0.1ng/ml showed similar spectroscopic profiles over the entire mid-infrared wavenumber region with the exception of the 1050-1100cm$^{-1}$ region where variation may be attributed to interstitial oxygen vibrations within silicon, indicated in Figure 4.78 (Karabudak et al, 2012). The lack of emerging spectral differences at increasing concentrations of IDH1-R132H and IDH1 wild-type proteins is further confirmed on PCA scores plots where no clear separation is observed between classes on PC1, PC2 or PC3 axes, as indicated in Figure 4.79. Therefore, it may be concluded that direct spectroscopic detection of IDH1-R132H molecules is not possible with current silicon components within a complex sample medium such as human blood serum.

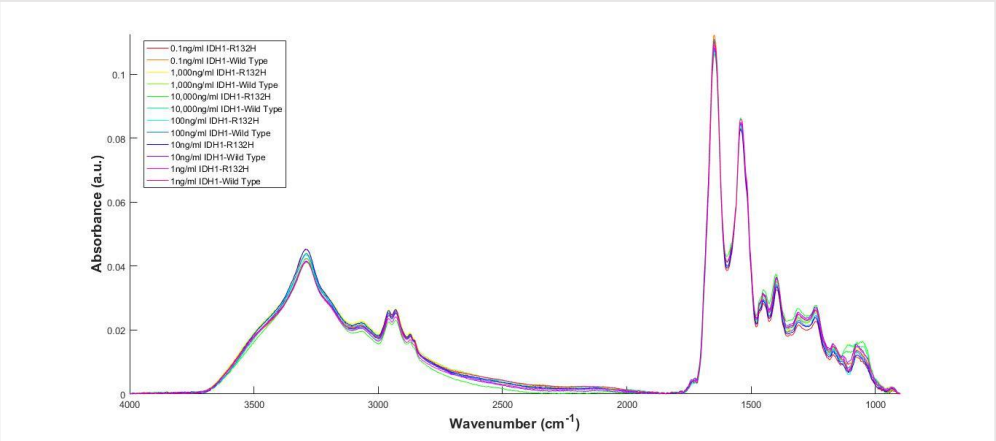


*Figure 4.78: Mean pre-processed spectra of human pooled serum spiked with either IDH1-R132H or IDH1 wild-type proteins at 10,000-0.1ng/ml concentrations. Spectra were acquired on silicon IRE's.*

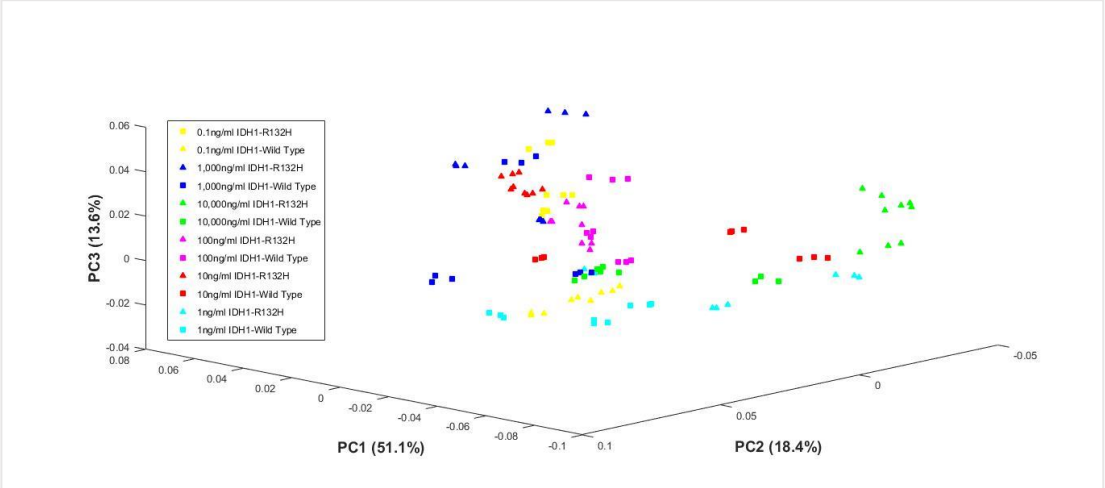


*Figure 4.79. PCA scores plot of mean pre-processed spectra of human pooled serum spiked with either IDH1-R132H or IDH1 wild-type proteins at 10,000-0.1ng/ml concentrations.*

ATR-FTIR investigations of IDH1-R132H and IDH1 wild-type proteins spiked in pooled blood serum were repeated on diamond ATR crystals to determine whether the inability to identify IDH1 molecules in previous analysis may be attributed to the silicon substrate. Mean pre-processed absorption spectra showed no obvious concentration dependent differences in the spectroscopic signatures of serum at 0.1-10,000ng/ml protein concentration, as indicated in Figure 4.80. Instead, differences in intensities of spectral bands did not correlate with concentration and were likely due to sampling errors associated with incomplete coverage of the diamond ATR crystal. This is further evident on the PCA scores plot where no clustering is observed for IDH1-R132H and IDH1 wild-type spiked samples with no obvious separation for different concentrations on either PC1, PC2 or PC3 axes, as indicated in Figure 4.81. Therefore, the inability to directly identify IDH1 molecules in previous analyses is not attributable to the spectroscopic performance of the silicon substrate, and instead suggests that simply the spectroscopic technique does not have the ability to identify

single amino acid substitutions of relatively low concentration proteins within a complex sample medium such as blood serum.

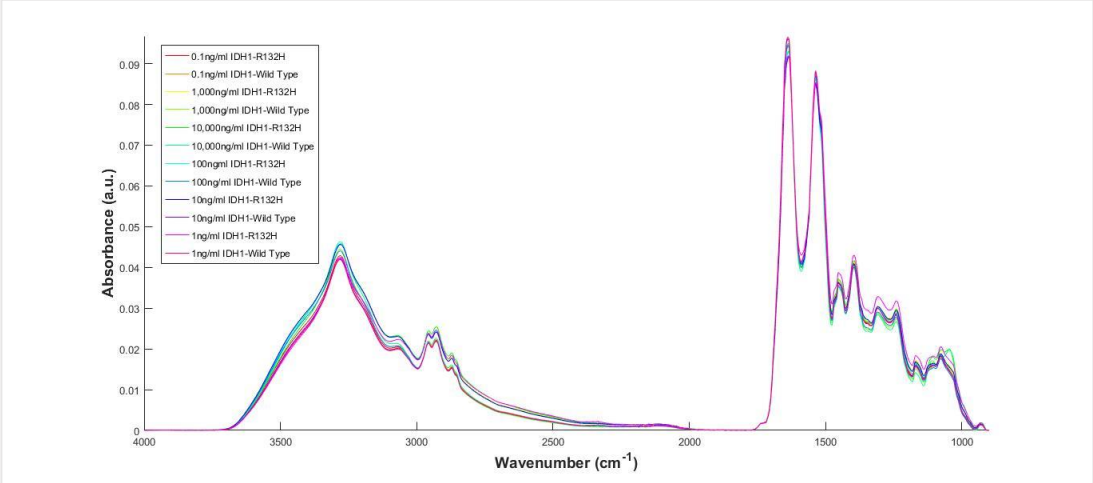


*Figure 4.80. Mean pre-processed spectra of human pooled serum spiked with either IDH1-R132H or IDH1 wild-type proteins at 10,000-0.1ng/ml concentrations. Spectra were acquired on diamond ATR crystals.*

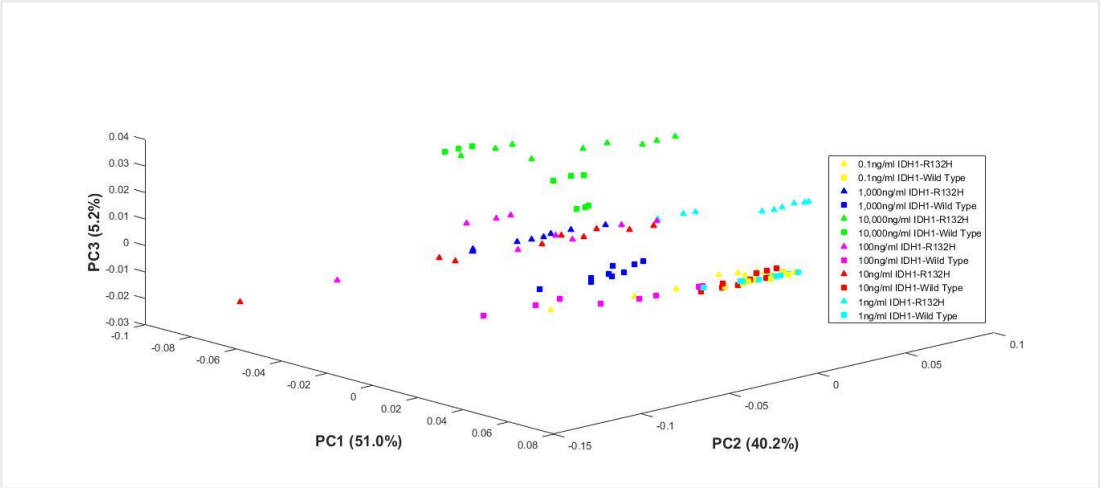


*Figure 4.81. PCA scores plot of mean pre-processed spectra of human pooled serum spiked with either IDH1-R132H or IDH1 wild-type proteins at 10,000-0.1ng/ml concentrations.*

## 4.5 Conclusion

Development of electrochemical immunosensors for detection of IDH1-R132H proteins entailed employment of various immobilisation strategies for conjugation of

antibodies and SAM constituents to electrode substrates. Heterobifunctional cross-linker assays were found most appropriate for detection of spiked buffer samples of specified antigen concentrations, with superior linearity and limit of detection compared to protein G and carbodiimide cross-linker assays. However, quantification of spiked buffer samples was not possible due to the insufficient linearity and reproducibility of sensors, attributed to inconsistent SAM formation and the challenges of non-specific adsorption associated with impidimetric sensing. Protein G assays were found to improve SAM reproducibility between electrodes, although surprisingly orientated antibodies did not contribute to improved sensor performance, attributed to detachment of weakly bound SAM constituents from substrates. Furthermore, the topography of gold surfaces was found to influence SAM development and sensor performance, with polycrystalline gold electrodes found to be favourable compared to tested screen-printed electrodes, due to the reduced inconsistencies and roughness of electrode surfaces. Lastly, functionalised electrodes were not able to detect IDH1-R132H proteins from clinical glioblastoma multiforme samples, attributed to insufficient assay sensitivity or the absence of mutant proteins in blood serum, with the blood-brain barrier thought to pose a significant challenge for entry in to the circulatory system. Indeed, ATR-FTIR spectroscopy was further unable to directly identify the presence of IDH1 proteins in either spiked buffer or patient samples. However, ATR-FTIR spectroscopy has demonstrated significant promise for the indirect detection of IDH1 molecular status through detection of global molecular changes associated with the IDH1-R132H mutation. Overall, future electrochemical studies should conduct Western blot analysis to confirm the presence of IDH1-R132H mutant proteins in clinical serum samples, or alternatively consider detection of the

oncometabolite D2HG reported in low concentrations in blood plasma that correlates with IDH1-R132H mutated status. Future ATR-FTIR studies should be conducted on significantly larger sample populations to understand the true detection capabilities of ATR-FTIR spectroscopy for detection of IDH1-R132H proteins.

## 4.6 References


Ahmad, A., Moore, E. (2012) Electrochemical immunosensor modified with self-assembled monolayer of 11-mercaptoundecanoic acid on gold electrodes for detection of benzo[*a*]pyrene in water. *Analyst*. 137:5839-5844.
Akkerman, H. B., Naber, R. C. G., Jongbloed, B., van Hal, P. A., Blom, P. W. M., de Leeuw, D. M., de Boer, B. (2007) Electron tunneling through alkanedithiol self-assembled monolayers in large-area molecular junctions. *PNAS*. 104(27):11161-11166.

Allen, K. W. (1988) PHYSICS AND ADHESION. Phys Technol. 19:234

Badea, M., Floroian, L., Restani, P., Cobzac, SC., Moga, M. (2016) Ochratoxin A Detection on Antibody- Immobilized on BSA-Functionalized Gold Electrodes. *PLoS One*. 11(7):e0160021.

Bard, A. J., Rubenstein, I. (1996) Volume 19 of Electroanalytical Chemistry: A Series of Advances. *CRC Press, 1996*. ISBN 082479379X, 9780824793791.

Barth, A. (2007). *Infrared spectroscopy of proteins. Biochimica et Biophysica Acta (BBA) - Bioenergetics, 1767(9), 1073–1101*. doi:10.1016/j.bbabio.2007.06.004

Bogomolova, A., Komarova, E., Reber, K., Gerasimov, T., Yavuz, O., Bhatt, S., Aldissi, M. (2009) Challenges of Electrochemical Impedance Spectroscopy in Protein Biosensing. Anal. Chem. 81(10):3944-3949.

Boisselier, B., Gallego Perez-Larrava, J., Rossetto, M., Labussiere, M., Ciccarino, P., Marie, Y., Delattre, JY., Sanson, M. (2012) Detection of IDH1 mutation in the plasma of patients with glioma. *Neurology. 79(16):1693-8*.

Borger, D. R., Goyal, L., Yau, T., (2014) Circulating oncometabolite 2-hydroxyglutarate is a potential surrogate biomarker in patients with isocitrate dehydrogenase-mutant intrahepatic cholangiocarcinoma. *Clin Cancer Res*. 20:1884–1890.

Brett, C. M. A. (2008) Electrochemical Impedance Spectroscopy for Characterization of Electrochemical Sensors and Biosensors. *ECS Transactions*. 13(13):67-80.

Butler, H. J., Brennan, P. M., Cameron, J. M., Finlayson, D., Hegarty, M. G., Jenkinson, M. D., … Baker, M. J. (2019). *Development of high-throughput ATR-FTIR technology for rapid triage of brain cancer. Nature Communications, 10(1)*. doi:10.1038/s41467-019-12527-5

Butterworth, A., Blues, E., Williamson, P., Cardona, M., Gray, L., Corrigan, D. K. (2019) SAM Composition and Electrode Roughness Affect Performance of a DNA Biosensor for Antibiotic Resistance. *Biosensors*. 9,22.

Capper, D., Simon, M., Langhans, C-D., Okun, J. G., Tonn, J. C., Weller, M., von Deimling, A., Hartmann, C. (2012) 2-Hydroxyglutarate concentration in serum from patients with gliomas does not correlate with IDH1/2 mutation status or tumor size. *International Journal of Cancer*. 131(3):766-768.

Carvalhal, R. F., Freire, R. S., Kubotaa, L. T. (2005)Polycrystalline Gold Electrodes: A Comparative Study of Pretreatment Procedures Used for Cleaning and Thiol Self-Assembly Monolayer Formation. *Electroanalysis*. 17,14.

Chammem, H., Hafaid, I, Bohli, N., Garcia, A., Meilhac, O., Abdelghani, A., Mora, L. (2015) A disposable electrochemical sensor based on protein G for High-Density Lipoprotein (HDL) detection. *Talanta*. 144:466-473

Chikkaveeraiah, B. V., Bhirde, A., Morgan, N. Y., Eden, H. S., Chen, X. (2012) Electrochemical Immunosensors for Detection of Cancer Protein Biomarkers. *ACS Nano*. Vol. 6: Issue. 8: Pages 6546-6561.

Ciani, I., Schulze, H., Corrigan, D. K., Henihan, G., Giraud, G., Terry, J. G., Walton, A. J., Pethig, R., Ghazal, P., Crain, J., Campbell, C. J., Bachmann, T. T., Mount, A. R. (2012) Development of immunosensors for direct detection of three wound infection biomarkers at point of care using electrochemical impedance spectroscopy. *Biosensors and Bioelectronics*. 31(1): 413-418.

Cohen, A. L., Holmen, S. L., Colman, H. (2013) IDH1 and IDH2 mutations in gliomas. *Curr Neurol Neurosci Rep*. 13(5):345

Corrigan, D. K., Schulze, H., Ciani, I., Henihan, G., Mount, A. R., Bachmann, T. T. (2017) Improving performance of a rapid electrochemical MRSA assay : optimisation of assay conditions to achieve enhanced discrimination of clinically important DNA sequences under ambient conditions. *Journal of Electroanalytical Chemistry*. 786:58-62.

Corrigan, D. K., Vezza, V., Schulze, H., Bachmann, T. T., Mount, A. R., Walton, A. J., Terry, J. G. (2018) A Microelectrode Array with Reproducible Performance Shows Loss of Consistency Following Functionalization with a Self-Assembled 6-Mercapto-1-hexanol Layer. *Sensors*. 18, 1891.

Dang, L., White, D. W., Gross, S., Bennett, B. D., Bittinger, M. A., Driggers, E. M., Fantin, V. R., Jang, H. G., Jin, S., Keenan, M. C., Marks, K. M., Prins, R. M., Ward, P. S., Yen, K. E., Liau, L. M., Rabinowitz, J. D., Cantley, L. C., Thompson, C. B., Vander Heiden, M. G., Su, S. M. (2009) Cancer-associated IDH1 mutations produce 2-hydroxyglutarate. *Nature*. 462(7274): 739.

Daniels, J. S., Pourmand, N. (2007) Label-Free Impedance Biosensors: Opportunities and Challenges. *Electroanalysis*. 19(12): 1239-1257.

Elgrishi, N., Rountree, K. J., McCarthy, B. D., Rountree, E. S., Eisenhart, T. T., Dempsey, J. L. (2018) A Practical Beginner's Guide to Cyclic Voltammetry. *J. Chem. Educ. 95* (2):197–206.

Fathi, A. T., Nahed, B. V., Wander, S. A., Lafrate, A J., Borger, D. R., Hu, R., Thabet, A., Cahill, D. P., Perry, A. M., Joseph, C. P., Muzikansky, A., Chi, A. S. (2016) Elevation of Urinary 2-Hydroxyglutarate in IDH-Mutant Glioma. *Oncologist*. 21(2):214-9.

Frezza, C., Tennant, D. A., Gottlieb, E. (2010) IDH1 Mutations in Gliomas: When an Enzyme Loses Its Grip. Cancer Cell. 17(1):7-9.

Ghindilis, A. L., Atanasov, P., Wilkins, M., Wilkins, E. (1998) Immunosensors: electrochemical sensing and other engineering approaches. *Biosensors & Bioelectronics*. Vol. 13, No. 1, pp. 113-131.

Gross, S., Cairns, R. A., Minden, M. D., Driggers, E. M., Bittinger, M. A., Jang, H. G., Sasaki, M., Jin, S., Schenkein, D. P., Su, S. M., Dang, L., Fantin, V. R., et al. Cancer-associated metabolite 2-hydroxyglutarate accumulates in acute myelogenous leukemia with isocitrate dehydrogenase 1 and 2 mutations. *J Exp Med*. 207:339–44.

Hafaiedh, I., Chammem, H., Abdelghani, A., Ait, E., Feldman, L., Meilhac, O., Mora, L. (2013) Supported protein G on gold electrode: characterization and immunosensor application. *Talanta*. 116:84-90

Hamann, C. H., Hamnett, A., Vielstich, W. (1998) Electrochemistry. 2nd Edition. Wiley. ISBN 0471043729.

Hermanson, G. T. (2010) Bioconjugate Techniques. 2nd Edition. Academic Press, 2010. ISBN 0080568726, 9780080568720.

Hermanson, G. T. (2013) Bioconjugate Techniques. 3rd Edition Revised. *Academic Press, 2013*. ISBN 0123822408, 9780123822406.

Holdhoff, M., Yovino, S. G., Boadu, O., Grossman, S. A. (2013) Blood-based biomarkers for malignant gliomas. *J Neurooncol*. 113(3):345-352.

Holmes, K. L., Lantz, L. M. (2001) Protein labeling with fluorescent probes. *Methods Cell Biol*. 63():185-204.

Horbinski, C. (2013) What do we know about IDH1/2 mutations so far, and how do we use it? *Acta Neuropathol*. 125(5):621-636.

Hussain, G., Silvester, D. S. (2017) Comparison of Voltammetric Techniques for Ammonia Sensing in Ionic Liquids. *Electroanalysis*. 30(1)

Idris, A. O., Mabuba, N., Arotiba, O. A., (2018) Towards cancer diagnostics – an α-feto protein electrochemical immunosensor on a manganese(IV) oxide/gold nanocomposite immobilisation layer. *RSC Adv*. 8: 30683-30691.

Islam, F., Haque, M., H., Yadav, S., Islam, M. N., Gopalan, V., Nguyen, N-T., Lam, A. K., Shiddiky, M. J. A. (2017) An electrochemical method for sensitive and rapid detection of FAM134B protein in colon cancer samples. *Nature Scientific Reports*. 7:133

Iwamoto, F. M., & Hormigo, A. (2014). Unveiling YKL-40, from Serum Marker to Target Therapy in Glioblastoma. *Frontiers in oncology*, *4*, 90. doi:10.3389/fonc.2014.00090

Jeuken, L. J. C. (2017) Biophotoelectrochemistry: From Bioelectrochemistry to Biophotovoltaics. *Springer, 2017*. ISBN 3319506676, 9783319506678.

Kaminska, B., Czapski, B., Guzik, R., Król, S. K., & Gielniewski, B. (2019). Consequences of *IDH1/2* Mutations in Gliomas and an Assessment of Inhibitors Targeting Mutated IDH Proteins. *Molecules (Basel, Switzerland)*, *24*(5), 968. doi:10.3390/molecules24050968

Kamm, C. R., Smith, A. G (1972) Nucleic Acid Concentrations in Normal Human Plasma. *Clinical Chemistry*. Vol. 18. No. 6.

Karabudak, E., Kas, R., Ogieglo, W., Rafieian, D., Schlautmann, S., Lammertink, R. G. H., … Mul, G. (2012). Disposable Attenuated Total Reflection-Infrared Crystals from Silicon Wafer: A Versatile Approach to Surface Infrared Spectroscopy. Analytical Chemistry, 85(1), 33–38. doi:10.1021/ac302299g

Kato, Y. (2015) Specific monoclonal antibodies against IDH1/2 mutations as diagnostic tools for gliomas. *Brain Tumor Pathol*. 32(1):3-11.

Kato, Y., Jin, G., Kuan, CT., McLendon, RE., Yan, H., Bigner, DD. (2009) A monoclonal antibody IMab-1 specifically recognizes IDH1R132H, the most common glioma-derived mutation. *Biochem Biophys Res Commun*. 390(3):547-51.

Keighley, S. D., Li, P., Estrela, P., Migliorato, P. (2008) Optimization of DNA immobilization on gold electrodes for label-free detection by electrochemical impedance spectroscopy. *Biosensors and Bioelectronics*. 23(8):1291-1297.

Kokkinos, C., Economou, A., Prodromidis, M. I. (2016) Electrochemical immunosensors: Critical survey of different architectures and transduction strategies. *Trends in Analytical Chemistry*. *79:88-105*.

Krebs, H. A. (1950) CHEMICAL COMPOSITION OF BLOOD PLASMA AND SERUM. *Annu. Rev. Biochem*. 19:409-430.

Kwasny, D., Tehrani, S. E., Almeida, C., Schjodt, I., Dimaki, M., Svendsen, W. E. (2018) Direct Detection of *Candida albicans* with a Membrane Based Electrochemical Impedance Spectroscopy Sensor. *Sensors (Basel)*. 18(7):2214.

Lavon, I. Refael, M., Zelikovitch, B., Shalom, E., Siegal, T. (2010) Serum DNA can define tumor-specific genetic and epigenetic markers in gliomas of various grades. *Neuro Oncol*. 12(2): 173-180.

Lavrich, D. J., Wetterer, S. M., Bernasek, S. L., Scoles, G. (1998) Physisorption and Chemisorption of Alkanethiols and Alkyl Sulfides on Au(111). *Phys. Chem. B*. 102, 3456-3465.

Lehr, J., Fernandes, F. C. B., Bueno, P. R., Davis, J. J., (2014) Label-free Capacitive Diagnostics: Exploiting Local Redox Probe State Occupancy. Anal. Chem. 86(5):2559-2564.

Li, M., Li, Y-T., Li, D-W., Long, YT. (2012) Recent developments and applications of screen-printed electrodes in environmental assays—A review. *Analytica Chimica Acta*. 734:31-44

Lombardi, G., Corona, G., Bellu, L., Della Puppa, A., Pambuku, A., Fiduccia, P., Bertorelle, R., Gardiman, M., D'Avella, D., Toffoli, G., Zagonel, V. (2015) Diagnostic Value of Plasma and Urinary 2-Hydroxyglutarate to Identify Patients With Isocitrate Dehydrogenase-Mutated Glioma *Oncologist*. 20(5):562-567

Mahato, K., Kumar, S., Srivastava, A., Maurya, P. K., Singh, R., Chandra, P. (2018) Chapter 14. Electrochemical Immunosensors: Fundamentals and Applications in Clinical Diagnostics. Handbook of Immunoassay Technologies: Approaches, Performances, and Applications. *Academic Press, 2018*. ISBN 012811794X, 9780128117941.

Matteo, D. A., Grunseth, A. J., Gonzalez, E. R., Anselmo, S. L., Kennedy, M. A., Moman, P., Scott, D. A., Hoang, A., Sohl, C. D. (2017) Molecular Mechanisms of Isocitrate Dehydrogenase 1 (IDH1) Mutations Identified in Tumors: The Role of Size and Hydrophobicity at Residue 132 on Catalytic Efficiency. *The American Society for Biochemistry and Molecular Biology*. 12;292(19):7971-7983

Mendes, R. K., Freire, R. S., Fonseca, C. P., Neves, S., Kubota, L. T. (2004) Characterization of self-assembled thiols monolayers on gold surface by electrochemical impedance spectroscopy. *J Braz. Chem. Soc*. 15,6.

Molazemhosseini, A., Magagnin, L., Vena, P., Liu, CC. (2016) Single-Use Disposable Electrochemical Label-Free Immunosensor for Detection of Glycated Hemoglobin (HbA1c) Using Differential Pulse Voltammetry (DPV). *Sensors*. 16(7):1024

Movasaghi, Z., Rehman, S., & ur Rehman, D. I. (2008). *Fourier Transform Infrared (FTIR) Spectroscopy of Biological Tissues. Applied Spectroscopy Reviews, 43(2), 134–179*. doi:10.1080/05704920701829043

Ohka F, Ito M, Ranjit M, Senga T, Motomura A, Motomura K, et al. (2014) Quantitative metabolome analysis profiles activation of glutaminolysis in glioma with IDH1 mutation. Tumour Biol. 35:5911-20.

Parkash, O., Yean, C. Y., Shueb, R. H., (2014) Screen Printed Carbon Electrode Based Electrochemical Immunosensor for the Detection of Dengue NS1 Antigen. *Diagnostics*. 4:165-180.

Pei, R., Cheng, Z., Wang, E., Yang, X. (2001) Amplification of antigen-antibody interactions based on biotin labeled protein-streptavidin network complex using impedance spectroscopy. *Biosens Bioelectron.* 16(6):355-61.

Pickard, A. J., Sohn, A. S. W., Bartenstein, T. F., He, S., Zhang, Y., Gallo, J. M. (2016) Intracerebral Distribution of the Oncometabolite D-2-Hydroxyglutarate in Mice Bearing Mutant Isocitrate Dehydrogenase Brain Tumors: Implications for Tumorigenesis. *Front Oncol.* 6:211

Plaza, J. L., Jacke, S., Chen, Y., Palmer, R. E. (2003) Annealing effects on the microstructure of sputtered gold layers on oxidized silicon investigated by scanning electron microscopy and scanning probe microscopy. *Philosophical Magazine*. 83(9): 1137-1142.

Preusser, M., Wohrer, A., Stary, S., Hoftberger, R., Streubel, B., Hainfellner, JA. (2011) Value and limitations of immunohistochemistry and gene sequencing for detection of the IDH1-R132H mutation in diffuse glioma biopsy specimens. *J Neuropathol Exp. Neurol.* 70(8):715-23.

Reitman, Z. J., Jin, G., Karoly, E. D., Spasojevic, I., Yang, J., Kinzler, K. W., … Yan, H. (2011). Profiling the effects of isocitrate dehydrogenase 1 and 2 mutations on the cellular metabolome. *Proceedings of the National Academy of Sciences of the United States of America*, *108*(8), 3270–3275. doi:10.1073/pnas.1019393108

Renier, W., Joubert, A., Bencokova, Z., Gastaldo, J., Massart, C., Foray, N. (2007) Consequences of the bleed-through phenomenon in immunofluorescence of proteins forming radiation-induced nuclear foci. *Int J Radiat Biol.* 83(8):543-9.

Riquelme, M. V., Zhao, H., Srinivasaraghavan, V., Pruden, A., Vikesland, P., Agah, M. (2016) Optimizing blocking of nonspecific bacterial attachment to impedimetric biosensors. *Sensing and Bio-Sensing Research.* 8:47-54

Russell, C., Ward, A. C., Vezza, V., Hoskisson, P., Alcorn, D., Steensona, P., Corrigan, D. K. (2019) Development of a needle shaped microelectrode for electrochemical detection of the sepsis biomarker interleukin-6 (IL-6) in real time. *Biosensors and Bioelectronics.* 126:806–814.

Sanders, B. J., Kim, D. C., Dunn, R. C. (2016) Recent Advances in Microscale Western Blotting. *Anal Methods.* 8(39): 7002-7013.

Shahrokhian, S., Salimiana, R., Kalhora, H. R. (2016) A simple label-free electrochemical DNA biosensor based on carbon nanotube–DNA interaction. *RSC Adv.* 6:15592–15598.

Shan, Y., He, X., Song, W., Han, D., Niu, J., & Wang, J. (2015). Role of IL-6 in the invasiveness and prognosis of glioma. *International journal of clinical and experimental medicine*, *8*(6), 9114–9120.

Steel, L., Ward, A. C., Jeffrey, C., Alcorn, D., Corrigan, D. K. (2017) Towards Simple, Rapid Point of Care Testing for Clinically Important Protein Biomarkers of Sepsis. *SCIOL Biotechnol*. 1:1-8.

Suroviec, A. H. (2012) Determining Surface Coverage of Self-Assembled Monolayers on Gold Electrodes. *Chem. Educator*. 17:83-85.

Takano, S., Kato, Y., Yamamoto, T., Kaneko, MK., Ishikawa, E., Tsuiimoto, Y., Matsuda, M., Nakai, K., Yanagiya, R., Morita, S., Tsuboi, K., Matsumura, A. (2012) Immunohistochemical detection of IDH1 mutation, p53, and internexin as prognostic factors of glial tumors. *J Neurooncol*. 108(3):361-73.

Trasatti, S., Petril, O. A. (1992) Real surface area measurements in electrochemistry. *Journal of electroanalytical chemistry*. 327(1):353-376.
Trilling, A. K., Beekwilder, J., Zuilhof, H. (2013) Antibody orientation on biosensor surfaces: a minireview. *Analyst*. 138(6):1619-27.

Vericat, C., Vela, M. E., Benitez, G., Carro, P., Salvarezza, R. C. (2010) Self-assembled monolayers of thiols and dithiols on gold: new challenges for a well-known system. *Chem. Soc. Rev.* 39:1805-1834.

Wang, J. (2007) Nanoparticle-Based Electrochemical Bioassays of Proteins. *Electroanalysis*. 19(7-8).

Wang, Z., Jiang, W., Wang, Y., Guo, Y., Cong, Z., Du, F., Song, B. (2015) *MGMT* promoter methylation in serum and cerebrospinal fluid as a tumor-specific biomarker of glioma. *Biomed Rep*. 3(4): 543-548.

Zoski, C. G. (2007) Handbook of Electrochemistry. *Elsevier, 2007*. ISBN 0444519580, 9780444519580.

# Chapter 5: Development of an electrochemical and spectroscopic platform for Hodgkin's Lymphoma cancer diagnostics.

## 5.1 Overview

This chapter will describe the development and testing of an electrochemical immunosensor for detection of the biomarker CCL17/TARC from spiked and clinical serum samples of Hodgkin's lymphoma patients. Subsequently, the analytical capabilities of our novel silicon substrates will be evaluated for the diagnosis of Hodgkin's lymphoma from clinical serum samples with ATR-FTIR spectroscopy.

## 5.2 Introduction

Development of an in-vitro medical diagnostic device with the capacity to provide a biomolecular fingerprint of clinical serum samples, concurrently with sensitive and specific detection of the chemokine CCL17/TARC, may have potential to facilitate earlier diagnostic strategies for classical Hodgkin's lymphoma. In the UK, ~2,100 people are diagnosed with Hodgkin's lymphoma per year, with a high survival rate in the patient group of 80% at 10 years post diagnosis (Cancer Research UK, 2019). However, Hodgkin's lymphoma remains responsible for ~330 deaths in the UK per year, with poorer patient overall survival found to correlate with systemic diagnostic delays and consequently late instigation of chemotherapy treatments (Cancer Research UK, 2019; Brooks et al, 2015). Presently, only ~35% of Hodgkin's lymphoma patients receive diagnosis through the "two-week wait" clinical pathway, whilst ~17% of patients receive diagnosis following emergency presentation, where over half attend

Accident and Emergency departments (Cancer Research UK, 2019). One of the major challenges for clinicians that often delays early diagnosis of Hodgkin's lymphoma in suspected patients concerns difficulties in differentiating symptoms of the cancer from routinely observed infectious diseases. In particular, classical Hodgkin's lymphoma which comprises ~90% of Hodgkin's lymphoma cases is primarily characterised by a localised painless lymphadenopathy and in ~25-40% of cases additional systemic symptoms, such as fatigue, and "B-symptoms", including fever, weight loss and night sweats (Shanbhag et al, 2017; Kuppers et al, 2012; Townsend et al, 2012). Unsurprisingly, these symptoms are not exclusive to Hodgkin's lymphoma and, particularly in the absence of "B-symptoms", may be misinterpreted in primary care settings for suspected glandular fever. Clinical confusion may culminate in significant diagnostic delays for suspected patients and prevents timely access to ABVD chemotherapy and/or radiotherapy treatments. In excess of 40% of Hodgkin's lymphoma patients visit their doctor on three or more occasions prior to referral for clinical diagnosis, whilst one study found 12% of patients waited in excess of 8 weeks for instigation of ABVD chemotherapy (Shephard et al, 2015; Lyratzopoulos et al, 2012; Brooks et al, 2015). Furthermore, current guidelines recommend a six-week wait period for patients reporting to primary care with lymphadenopathy <2cm diameter, in the absence of "B-symptoms", before justifying additional clinical investigations (Shephard et al, 2015). Since less than half of Hodgkin's lymphoma patients report "B-symptoms", it is unsurprising that a study from the Haematological Malignancy Research Network reported a median time to diagnosis for Hodgkin's lymphoma of 87 days in the UK (Howell et al, 2013). Hence, an accessible and rapid diagnostic triage strategy would be beneficial for primary care to ensure suspected classical

Hodgkin's lymphoma patients with lymphadenopathy receive timely referral for confirmatory diagnosis through a lymph node biopsy; thereby improving the current clinical diagnostic pathway.

Recently, our collaborators, lead by Professor Jarrett at the University of Glasgow, and others have identified elevated concentrations of the chemokine CCL17/TARC in serum samples of classical Hodgkin's lymphoma patients (Lake et al, 2018; Niens et al, 2008; Weihrauch et al, 2005; Plattel et al, 2016). Classical Hodgkin's lymphoma is characterised by a neoplasm comprised of a small proportion of Reed-Sternberg cells found within a large population of mixed inflammatory cells, which express cytokines and chemokines to promote further recruitment of inflammatory cells. The chemokine, CCL17/TARC, released from Reed-Sternberg cells is responsible for recruitment of inflammatory T cells to the site of the neoplasm, where CCL17/TARC binds to the glycoprotein, CD4, found on T cell surfaces during disease pathophysiology. Hence, presence of the chemokine CCL17/TARC in serum represents a sensitive and specific biomarker for classical Hodgkin's lymphoma shown to correlate with disease progression (Niens et al, 2008; Plattel et al, 2016). Interestingly, the serum concentration of CCL17/TARC has further been shown to correlate with patient response to ABVD chemotherapy, with markedly reduced levels observed in patients if responsive to therapeutic treatment. Therefore, CCL17/TARC further represents a potential prognostic biomarker that has demonstrated the ability to predict relapsed patients earlier compared to current positron emission tomography (PET) techniques (Farina et al, 2014). To this extent, our collaborators have provided clinical serum samples before and during treatment, with confirmed CCL17/TARC concentration

determined from previous ELISA testing, with the aim to develop a diagnostic and prognostic medical device for classical Hodgkin's lymphoma.

Development of an integrated ATR-FTIR and electrochemical device boasts several benefits, predominantly the ability to provide both qualitative identification of the entire macromolecular composition of serum in addition to quantitative detection of specific biomarkers of interest, as described in detail previously. Therefore, the aim of this chapter is to translate and develop work previously undertaken in chapter 4 for detection of CCL17/TARC in order to establish a suitable electrochemical and spectroscopic diagnostic platform for classical Hodgkin's lymphoma. Electrochemical work shall focus on electrochemical impedance spectroscopic, voltammetric and amperometric techniques to characterise modified assays and detect CCL17/TARC from spiked and clinical patient samples. Inclusion of an amperometric detection scheme not described in previous chapters will allow the development of a "sandwich assay" with the aim of nullifying previously observed non-specific binding events, and will further serve as a comparison between the analytical performance of a "labelled" and "unlabelled" electrochemical approach. Spectroscopic work shall focus on the evaluation of previously described silicon components to determine whether the proposed device is suitable for diagnosis of classical Hodgkin's lymphoma with ATR-FTIR spectroscopy

## 5.3 Materials & Methods

### *5.3.1 Electrochemical Instrumentation*

Electrochemical experiments were conducted on a PalmSens3 potentiostat (PalmSens, The Netherlands) alongside one CH Instruments CHI101 gold working, CHI111 silver silver/chloride reference and CHI115 platinum counter electrode positioned in a three-electrode configuration.

### *5.3.2 ATR-FTIR Instrumentation*

Spectroscopic experiments were conducted on a Perkin-Elmer 2 spectrometer (Perkin-Elmer, Massachusetts, U.S.A) together with a Quest ATR Specac accessory module with mirrors specified at 45° angles (Specac, United Kingdom). The Quest ATR Specac accessory module was operated in conjunction with a custom-built top plate to allow automatic positioning of silicon substrates between replicate measurements.

### *5.3.3 Materials*

Sulfosuccinimidyl 6-(3'-(2-pyridyldithio)propionamido)hexanoate (Sulfo-LC-SPDP), DL-dithiothreitol (DTT), 6-mercapto-1-hexanol (MCH), phosphate buffered saline (PBS), potassium ferricyanide, potassium ferrocyanide, sulphuric acid (95%), 30% hydrogen peroxide, 2-Iminothiolane hydrochloride, tris(2-carboxyethyl)phosphine (TCEP), Protein G and bovine serum albumin (BSA) were purchased for development of electrochemical immunosensors (Sigma-Aldrich, United Kingdom). Similarly, human CCL17/TARC Quantikine ELISA and DuoSet ELISA Ancillary Re-agent 1 kits were purchased for development of electrochemical immunosensors (R&D

Systems, Inc. Minneapolis, USA). Lastly, Amicon Ultra-0.5mL 3KDa centrifugal filters were purchased for the removal of unreacted chemicals during assay functionalisation procedures (Sigma-Aldrich, United Kingdom).

### *5.3.4 Patient Samples*

Patient samples were provided from our collaborators at the University of Glasgow and comprised of clinical serum samples from patients diagnosed with classical Hodgkin's lymphoma following a lymph node biopsy. Samples were originally collected from haematology clinics from patients before or during treatment as part of two studies, namely Investigation of the cause of Hodgkin lymphoma (ITCH) and Biomarkers and classical Hodgkin lymphoma (BACH). All samples provided by our collaborators consisted of serum aliquots from 60 healthy volunteers, 100 Hodgkin's lymphoma patients prior to treatment and 39 Hodgkin's lymphoma patients during treatment. Additional serum sample aliquots from 40 healthy volunteers were provided from Tissue Solutions to ensure classes within data sets contained equal numbers of samples for accurate spectroscopic analysis.

### *5.3.5 Experimental Methodology*

#### *5.3.5.1 Electrochemical Cleaning*

Gold working electrodes were chemically cleaned in hot piranha solution, a mixture that contained 15mL of sulphuric acid and 5mL of 30% hydrogen peroxide in water, for 10 minutes to remove organic chemicals bonded to electrode surfaces. Thereafter,

electrodes were mechanically cleaned consecutively with 0.05 micron alumina MicroPolish powder on a Microcloth pad for 5 minutes, then sonicated in distilled water for 15 minutes to remove alumina particles. Subsequently, gold working electrodes were electrochemically cleaned in 0.5M sulphuric acid by applying cyclic potentials between -0.2V and +1.5V at scan rates of 100mV/s for 20 scans to remove gold oxide formation.

*5.3.5.2 Thiolated Protein G Assay*

The surface of working electrodes were functionalised with Protein G molecules that were modified such that the amine groups of lysine amino acids were replaced with thiol groups through the addition of 2-iminothiolane, as previously described by Oh (Oh et al, 2002) and Fowler (Fowler et al, 2007). In our case, 100µL of 1mg/ml 2-iminothiolane in 1 X PBS was added to 100µL of 0.1mg/ml protein G in 1 X PBS and allowed to react at 4°C for 30 minutes. Subsequently, unreacted 2-iminothiolane was removed with an Amicon Ultra-0.5mL 3KDa centrifugal filter as detailed in the instructions to prevent sulphur groups of excess 2-iminothiolane molecules attaching to gold electrode surfaces. The modified protein G filtrate was reconstituted with 1 X PBS to a working concentration of 40ug/ml and 20uL of the resultant solution was pipetted on to respective working electrode surfaces and left to react overnight at 4°C. Thereafter, working electrodes were rinsed thoroughly with 1 X PBS and 20uL droplets of 40µg/ml Human TARC capture antibody in 1 X PBS were then added to functionalised electrode surfaces for 2 hours at room temperature. Working electrodes were rinsed in 1 X PBS and then blocked with 20µL of 1% BSA in 1 X PBS for 30 minutes at room temperature. Functionalised electrodes were then immersed in

measurement buffer of 10mM Ferri/Ferro potassium cyanide in 1 X PBS to obtain background measurements prior to the addition of antigen solutions. Electrodes were then consecutively incubated with specified antigen concentrations in 1 X PBS for 1 hour, rinsed with 1 X PBS solution and placed in measurement buffer of 10mM Ferri/Ferro potassium cyanide in 1 X PBS for 15 minutes before obtaining impedance measurements.

*5.3.5.3 Heterobifunctional Cross-linker Assay*

Functionalisation of working electrode surfaces were conducted in a similar manner to the protocol previously described in section 4.3.5.2, with a few notable modifications. Firstly, Amicon Ultra-0.5mL 3KDa centrifugal filters were used to discard of unreacted Sulfo-LC-SPDP and DTT molecules, since they both feature free sulphur atoms that may inadvertently attach to electrode surfaces. Secondly, the addition of 5mM TCEP to the blocking solution reduced MCH molecules that may have unintentionally oxidised during long-term storage, therefore ensuring the blocking solution comprised free thiols to attach to gold surfaces. Working electrodes were immersed in buffer measurement solution of 10mM Ferri/Ferro potassium cyanide in 1 X PBS following functionalisation for 30 minutes to obtain baseline impedance measurements. Thereafter, working electrodes were consecutively incubated with different specified antigen concentrations in 1 X PBS for 1 hour, thoroughly rinsed with 1 X PBS and washed in 10mM Ferri/Ferro potassium cyanide in 1 X PBS for 30 minutes before obtaining impedance measurements associated with specific antigen concentrations.

*5.3.5.4 Heterobifunctional Cross-linker Sandwich Assay*

Initial functionalisation of working electrodes were conducted in an identical manner to the protocol described above in section 5.3.5.3. Subsequently, working electrodes were incubated overnight with 20µL of 100ng/ml biotinylated Human TARC detection antibody at 4°C upon antigen binding to primary capture antibodies. Electrodes were rinsed with 1 X PBS and incubated in the dark for 20 minutes with 20µL of streptavidin conjugated horseradish-peroxidase, where the stock solution had previously been diluted x40 in 1 x PBS. Working electrodes were then thoroughly washed with 1 X PBS to remove unbound streptavidin conjugated horseradish-peroxidase and individually placed in 500µL substrate solution comprised of equal volumes of stabilised 3,3',5,5'-Tetramethylbenzidine and stabilised hydrogen peroxide solution. Lastly, amperometric measurements were obtained by subjecting working electrodes to a constant potential of -0.2V for 120 seconds with 0.1 second time intervals.

*5.3.5.5 ATR-FTIR Methodology*

Serum samples were firstly removed from -80°C long-term storage and exposed to a room temperature environment until sufficiently thawed. Serum samples were pipetted in 3uL volumes on to three consecutive wells on silicon substrates and spread with the pipette tip to ensure the total surface area of the well was completely covered with serum to prevent scattering artefacts. Silicon substrates were then batch dried with placement of slides in an incubator for 1 hour at 34°C to ensure consistent drying between all samples. Individual silicon substrates were then aligned on the top plate and one background spectrum was recorded on the bare well not exposed to the serum

sample to account for atmospheric conditions. Thereafter, the top plate moved consecutively to align respective wells with the infrared beam and three repeat measurements were recorded per well, therefore producing nine spectra per sample slide. Spectra were collected in the mid-infrared wavenumber region, 4000-450cm$^{-1}$, at a resolution of 4cm$^{-1}$ with 16 co-added scans. Lastly, sample slides were stored in long-term sample boxes to allow the possibility of sample re-analysis if required at a future date.

### *5.3.6 Data Analysis & Statistics*

Statistical analyses on electrochemical impedance measurements were conducted with one-way ANOVA studies on percentage differences in $R_{ct}$ before and after antigen incubation to establish the significance between healthy and Hodgkin's lymphoma patient samples. Similarly, one-way ANOVA studies were conducted on amperometric measurements by evaluating differences in the output current at 120 second time intervals to establish significance between healthy and Hodgkin's lymphoma patient samples. Post-hoc studies with Fisher least significant difference (LSD) were performed on statistically significant results in instances where p-values were $<0.05$ at 95% confidence intervals to identify differences between mean values of data classes. Additionally, four-parameter logistic regression analyses were performed on the percentage difference in $R_{ct}$ before and after antigen incubation, and output currents at 120-second time intervals for all spiked sample concentrations to identify relationships between concentration and output signal. All amperometric data and electrochemical impedance concentration data consisted of three replicate and one

repeat measurements. Patient sample studies with electrochemical impedance spectroscopy consisted of three replicate and three repeat measurements. All stated electrochemical results describe mean values ± standard deviation.

Infrared spectra were computed with PRFFECT version 2.0 on RStudio (R Foundation for Statistical Computing, Austria). Spectra were pre-processed before statistical analysis with Extended Multiplicative Scatter Correction (EMSC), truncated at specific wavenumbers specified in results section, normalised with min-max normalisation and binned by a factor of 8 across chosen wavenumbers. Spectra were subsequently assigned to either the testing or training dataset with a 0.3:0.7 split respectively, and analysed with a selected model, either Random Forest, Partial Least Squares (PLS) or Partial Least Squares-Discriminatory Analysis (PLS-DA), with five-fold cross validations and fifty resamples selected for respective models. Stated sensitivity and specificity values for models represent the mean ± standard deviation over fifty resamples.

## 5.4 Results & Discussion

### *5.4.1. Electrochemical Cleaning*

Electrodes observed growth of a sharp reduction peak characteristic of progressive electrochemical cleaning of the gold surface, as indicated in Figure 5.1, and was consistent with previous experiments in chapter 4 and literature findings (Haag et al, 2015). The first scan measured cathodic peaks of $I_{pc}$ = -37.284 ± 5.571µA at $E_{pc}$ = 0.729V that increased with successive scans to $I_{pc}$ = -64.546 ± 5.715µA at $E_{pc}$ = 0.749V

by the twentieth scan. Interestingly, the intensity of the reduction peak at the final scan was markedly increased compared to similar experiments in chapter 4, which indicates that electrode surfaces display improved gold oxide removal with additional scans.

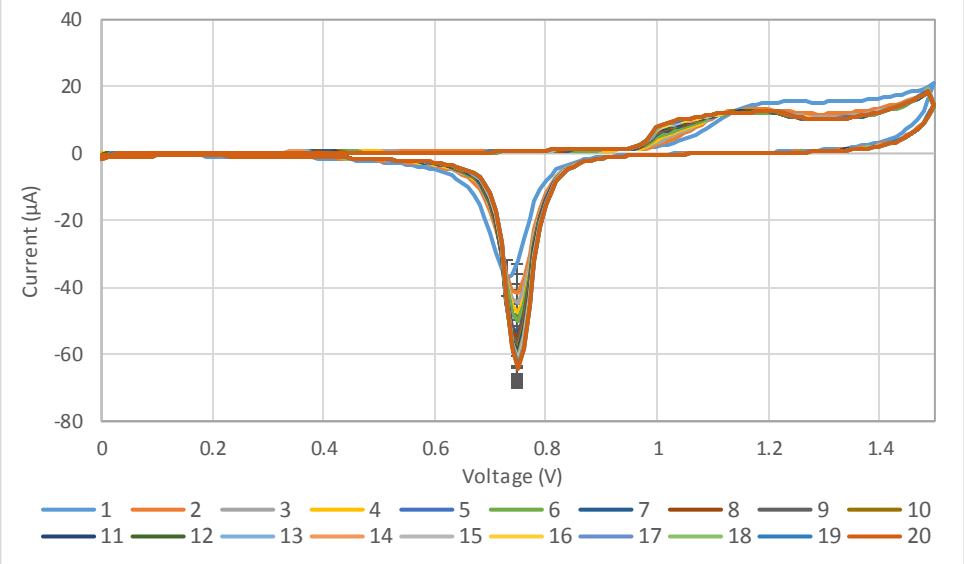


*Fig 5.1: Electrochemical cleaning of working electrodes in 0.1M $H_2SO_4$ from 0 to 1.5V for 20 scans (n=3) prior to assay functionalisation procedures.*

### *5.4.2 Thiolated Protein G Protocol*

#### *5.4.2.1 SAM Characterisation*

Electrochemically cleaned electrodes prior to assay functionalisation measured $R_{ct}$ = 113.1 ± 21.7Ω, which indicates clean gold surfaces where electrons can readily tunnel from the measurement buffer to electrodes. Functionalisation with thiolated protein G produced $R_{ct}$ = 5867.3 ± 325.9Ω, confirming successful attachment of protein G to electrode surfaces, as indicated in Figure 5.2a. Interestingly, $R_{ct}$ values of current protein G assays increased dramatically compared to physisorbed protein G assays previously described in chapter 4, which suggests that inclusion of sulphur atoms on modified protein G molecules facilitates improved attachment to gold surfaces.

Thereafter, capture antibody depositions measured $R_{ct}$ = 1.10x10$^4$ ± 409.9Ω, indicative of successful affinity binding between protein G and antibody molecules. Lastly, BSA depositions measured $R_{ct}$ = 2.10x10$^4$ ± 2462.5Ω, which highlights that remaining bare gold surfaces were successfully blocked on electrodes with attachment of BSA molecules. Experimental findings measured significantly larger $R_{ct}$ values compared to literature findings describing physisorption methods of protein G assays to electrodes (Hafaiedh et al, 2013), which was anticipated given increased strength of the chemisorbed sulphur-gold bond as previously described in chapter 4.

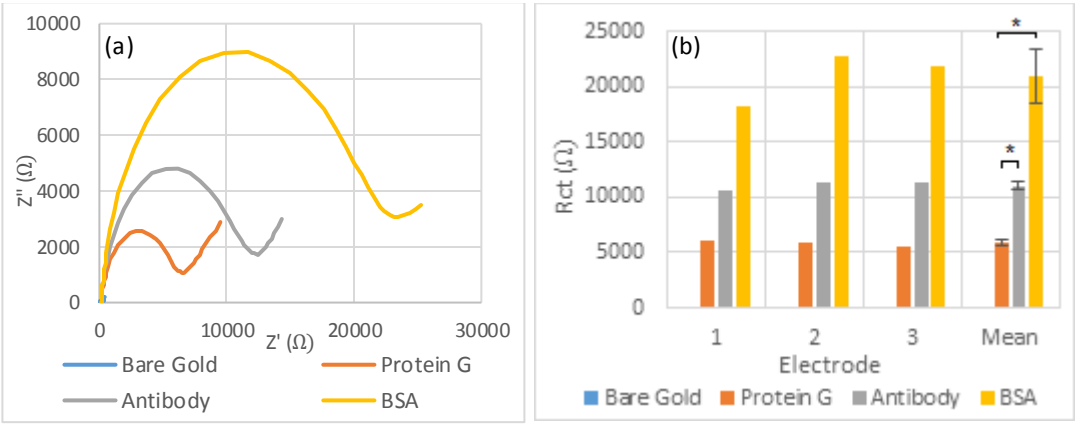


*Fig 5.2: (a) Nyquist plot for self-assembled monolayer characterisation of thiolated protein G assays following respective depositions on electrodes (n=3) (b) Plot of measured charge transfer resistance for self-assembled monolayer characterisation of the thiolated protein G assay on electrodes (n=3). * indicates statistical significance where p-value < 0.05 at 95% confidence intervals.*

Impidimetric behaviour describing increases in $R_{ct}$ for respective assay depositions were deemed statistically significant for all assay functionalisation procedures ($F(3,11) = 148.61$, p-value $< 0.05$), as shown in Figure 5.2b. Relative standard deviation of protein G depositions between all three electrodes measured 5.55%, which indicates the use of centrifugal filters enables a good degree of consistency of protein G attachment between electrode surfaces. Consequently, the degree of antibody

binding to protein G molecules was observed to be consistent between electrodes, evident by a relative standard deviation of 3.71%. Lastly, electrode blocking is associated with a higher degree of variability between electrodes compared to previous functionalisation steps, with a relative standard deviation for BSA depositions of 11.7%.

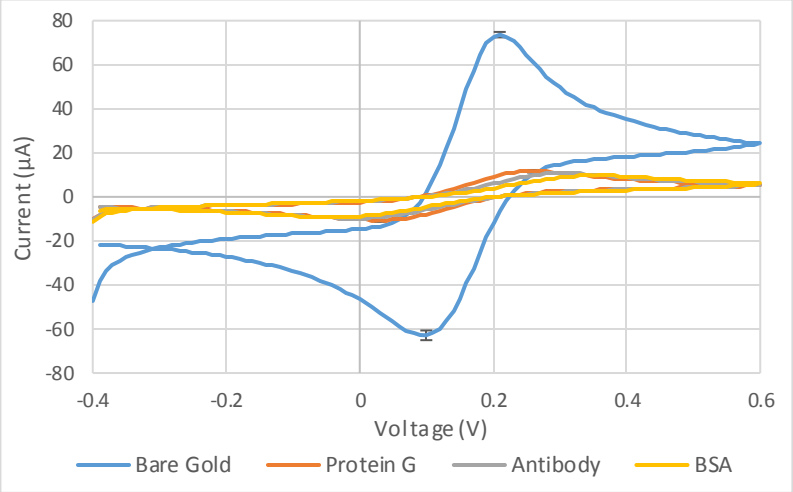


*Fig 5.3: Cyclic voltammogram of electrode responses after respective depositions of the thiolated protein G assay (n=3).*

Electrochemically cleaned electrodes prior to immobilisation of thiolated protein G molecules promoted oxidation, $I_{pa}$ = 73.6 ± 1.24µA, and reduction, $I_{pc}$ = -62.9 ± 2.20µA, of the electrochemical probe, $[Fe(CN)6]^{-3/4}$, at $E_{pa}$ = 0.210V and $E_{pc}$ = 0.100V respectively. The significant redox peak intensities highlight that electrode surfaces can readily instigate one-electron transfer reactions of $[Fe(CN)6]^{-3/4}$ at appropriate potentials, which correlates with previous $R_{ct}$ findings. Functionalisation with protein G molecules reduces the availability for redox reactions of $[Fe(CN)6]^{-3/4}$ at electrode surfaces, evident through reduced $I_{pa}$ = 11.6 ± 0.579µA, and, $I_{pc}$ = -10.6 ± 0.771µA and increased $\Delta E_p$ where $E_{pa}$ = 0.260V and $E_{pc}$ = 0.030V, as indicated in Figure 5.3. Immobilisation of capture antibodies further increases the surface concentration of

molecules at the vicinity of the electrodes, thereby reducing the quantity of one-electron transfer reactions where $I_{pa}$ = 10.8 ± 0.375μA and $I_{pc}$ = -9.75 ± 0.381μA at $E_{pa}$ = 0.300V and $E_{pc}$ = -0.010V respectively. Similarly, deposition of BSA molecules causes additional decreases in redox peak currents of $I_{pa}$ = 9.73 ± 0.196μA and $I_{pc}$ = -9.15 ± 0.230μA at $E_{pa}$ = 0.350V and $E_{pc}$ = -0.040V, where further $\Delta E_p$ separation highlights slower electron transfer kinetics at electrode surfaces. Electrode responses were deemed statistically significant between all assay steps for $I_{pa}$ ($F(3,36) = 17400.52$, p-value $< 0.05$) and between all assay procedures for $I_{pc}$ ($F(3,36) = 4494.03$, p-value $< 0.05$) with the exception of the antibody deposition. Electrode responses were in good agreement with previous literature findings for protein G assays on electrodes (Hafaiedh et al, 2013; Chammem et al, 2015), although $I_{pa}$ and $I_{pc}$ intensities were markedly lower presumably due to improved binding of protein G molecules to electrode surfaces due to thiolation procedures, consistent with previous impidimetric experiments.

### *5.4.2.2 Initial Assay Testing*

Electrodes were exposed to spiked solutions that contained either no antigen or high antigen concentrations of 12,500pg/ml to evaluate whether the proposed immunosensor has the capacity to identify CCL17/TARC molecules, as indicated in Figure 5.4a, b. Electrodes measured small reductions in $R_{ct}$ = -2.52% ± 1.83 after incubation with controls that were deemed negligible compared to baseline values ($t(3,3) = 2.33$, P-value = 0.145). Electrodes measured significant decreases in $R_{ct}$ for antigenic solutions = -86.8% ± 1.82 ($t(3,3) = -358.38$, P-value $< 0.05$) compared to

controls, which indicates potential for detection of CCL17/TARC in clinical samples. However, electrochemical behaviour of immunosensors must firstly be validated with concentration studies in spiked buffer samples to determine whether signals respond proportionally to the biomarker over a range of clinically relevant concentrations.

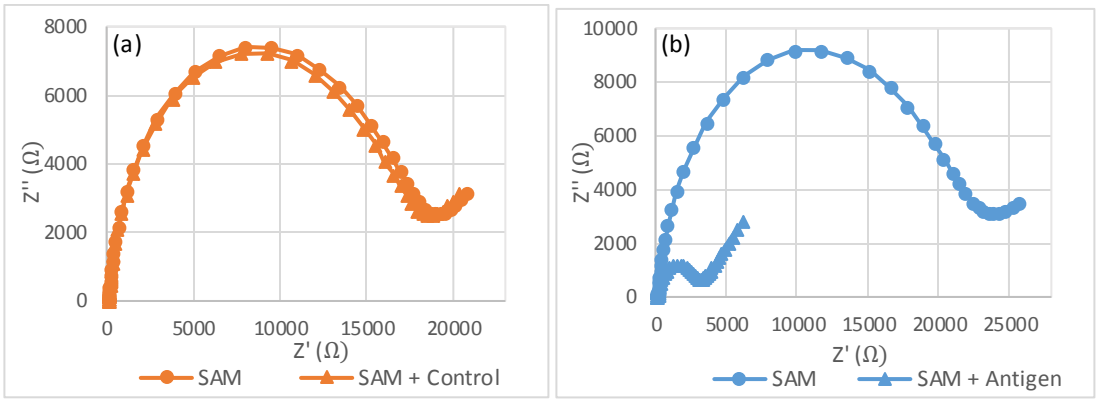


*Figure 5.4: (a) Nyquist plots of functionalised electrode responses before and after incubation with control samples (b) and before and after incubation with spiked samples of 12,500pg/ml CCL17/TARC concentration (n=3).*

### *5.4.2.3 Concentration Study*

Immunosensors were successively incubated with spiked buffer solutions that contained increased quantities of antigen over two separate experiments to determine sensitivity and reproducibility of electrode responses to CCL17/TARC concentrations. Nyquist plots consistently displayed decreases in $R_{ct}$ at electrodes following incubation with antigenic solutions, deemed statistically significant from baseline SAM measurements for experiment one ($F(7, 16) = 88.75$, p-value $< 0.05$) and experiment two ($F(6, 14) = 18.58$, p-value $< 0.05$), as indicated in Figures 5.5a and 5.5b respectively.

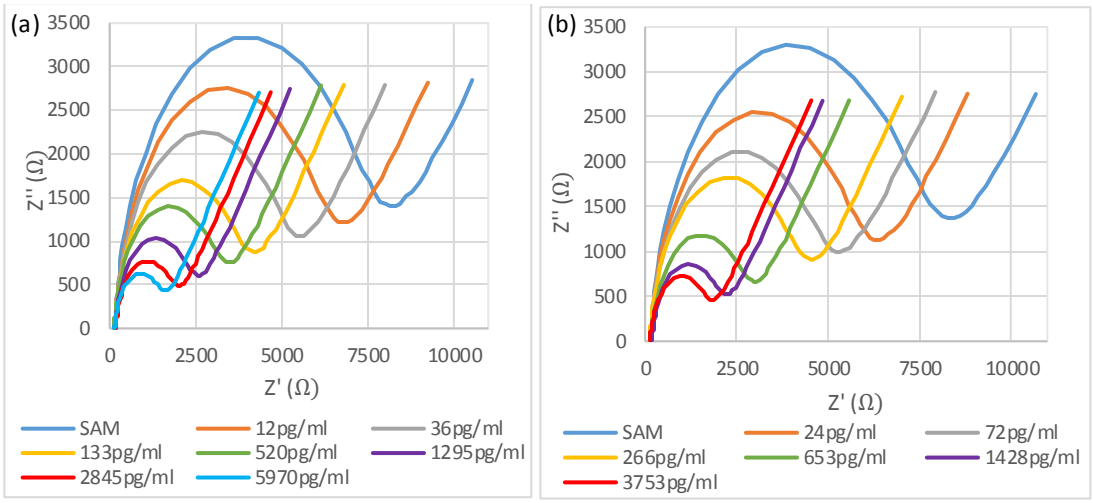


*Fig 5.5: (a) Nyquist plots of functionalised electrodes following incubations with different CCL17/TARC concentrations from 12-5,970pg/ml in experiment one (b) and from 24-3,753pg/ml in experiment two*

Further examination of immunosensor behaviour identified a positive relationship between measured $R_{ct}$ and CCL17/TARC concentration, with $R^2 = 0.987$, as indicated in Figure 5.6. However, electrodes showed considerable intra-assay variability, particularly at lower CCL17/TARC concentrations of 12-520pg/ml. Associated co-efficient of variation ranged from 15.4-43.2% and implies electrodes cannot reproducibly detect differences in antigen concentrations of 12-520pg/ml. Conversely, electrodes displayed improved repeatability and lower co-efficient of variation from 3.23-7.58% for 653-5970pg/ml CCL17/TARC concentrations, as would be expected for higher antigen concentrations. However, minimal changes in $R_{ct}$ for additional incubations with spiked samples of high antigen levels implies electrode responses were not linear over the entire concentration range. Therefore, careful consideration must be given to the dilution of clinical samples to ensure electrodes can reproducibly distinguish between CCL17/TARC concentrations in Hodgkin's lymphoma patients, since the chemokine is known to range from 632-250,000pg/ml in provided patient samples. Additionally, the inclusion of secondary antibodies and reporter molecules

should be considered to determine whether a "labelled" electrochemical approach may improve reproducibility and sensitivity of the proposed immunosensor.

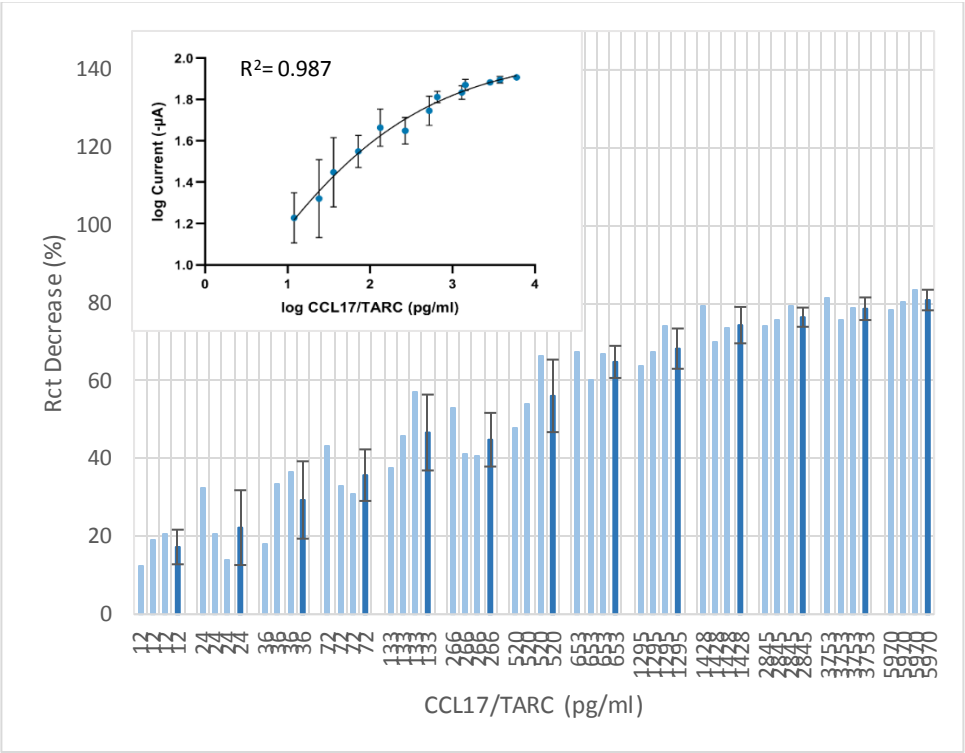


*Fig 5.6: Plot of differences in $R_{ct}$ measured at electrodes before and after incubation with spiked samples of specified CCL17/TARC concentrations. Light blue bars show individual electrode responses whilst dark blue bars show mean electrode responses for respective CCL17/TARC concentrations. Inset plot shows logarithmic CCL17/TARC versus logarithmic $R_{ct}$ where mean responses for concentrations have been fitted with a four-parameter logistic regression model. (n=3).*

## *5.4.3 Thiolated Protein G Sandwich Assay*

### *5.4.3.1 Electrochemical Detection of TMB Oxidation States*

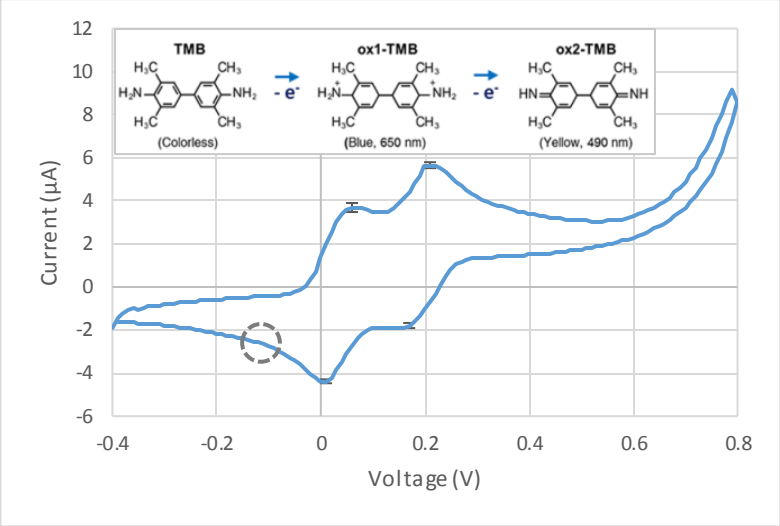


*Fig 5.7: Characterisation of TMB solution when subjected to two one-electron transfer redox reactions with cyclic voltammetry (n=3). Image overlay showing overview of TMB reaction reproduced from Lee et al, 2018. Selected potential for future amperometry experiments at $E_{pc}$ = -0.2V indicated with grey dashed circle.*

Bare electrodes were subjected to cyclic voltammetry experiments in substrate solutions of hydrogen peroxide and TMB to determine whether it was possible to electrochemically detect oxidised TMB reactants commonly associated with labelled sandwich assay approaches. Electrodes identified the two-electron transfer oxidation reaction characteristic of TMB similarly observed in standard ELISA experiments (Lee et al, 2018), as indicated in Figure 5.7. In ELISA protocols, horseradish peroxidase labels bind to secondary antibodies in the presence of captured antigen, where the label enzymatically reacts with a substrate solution comprised of hydrogen peroxide and TMB. Consequently, TMB is subjected to a one-electron transfer oxidation reaction that produces a blue reactant product measurable at $\lambda = 650$nm with ELISA plate readers. The blue oxidised product may also be observed electrochemically with voltammetry where $I_{pa}$ = 3.689 ± 0.209µA at $E_{pa}$ = 0.060V. Thereafter, the oxidised TMB product may undergo a second oxidation reaction in the presence of sulphuric acid with the yellow reactant product commonly measured at $\lambda$ = 490nm with ELISA plate readers. Similarly, the yellow oxidised product may be

detected electrochemically with voltammetry where $I_{pa}$ = 5.656 ± 0.137µA at $E_{pa}$ = 0.210V. The magnitude of oxidised reactant products may be electrochemically measured with amperometry by reducing oxidised species at the working electrode through application of an appropriate $E_{pc}$. The oxidised reactants gain an electron in the reverse one-electron transfer reactions where $I_{pc}$ = -1.790 ± 0.119µA at $E_{pc}$ = 0.170V and $I_{pc}$ = -4.379 ± 0.091µA at $E_{pc}$ = 0.010V. Therefore, a reduction potential of $E_{pc}$ = -0.200V has been chosen for future amperometric experiments to reduce oxidised blue TMB products since the applied potential is isolated from and does not coincide with oxidation potentials, $E_{pa}$, of TMB.

### *5.4.3.2 Amperometric Detection*

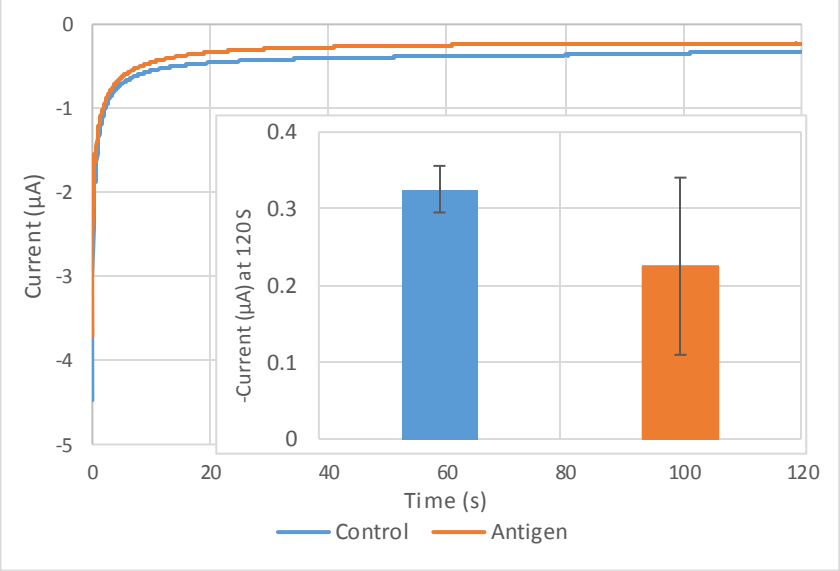


*Fig 5.8: Amperometric current-time curves for functionalised electrodes following incubation with control samples containing no antigen and spiked samples containing 1,550pg/ml antigen concentration. Inset bar graph shows current responses at 120 seconds for electrodes exposed to control samples and antigen samples (n=3).*

The proposed electrochemical assay was modified to include secondary antibodies and HRP labels in an attempt to employ a labelled sandwich assay to improve sensitivity and reproducibility of the electrochemical immunosensor. Electrodes identified one-electron oxidation reactions characteristic of the blue oxidation product of TMB following the application of a constant $E_{pc}$ = -0.2V at working electrode surfaces (Lee et al, 2018), as indicated in Figure 5.8. Surprisingly, control measurements not exposed to target antigen solutions produced significant signal responses with $I_{pc}$ = 0.326 ± 0.030µA at 120 seconds. Conversely, electrodes incubated with spiked solutions of 1,550pg/ml antigen concentration detected smaller signal responses of $I_{pc}$ = 0.225 ± 0.116µA at 120 seconds. Electrodes were tested with 1,550pg/ml antigen solutions as this is the proposed clinical cut-off for CCL17/TARC for differentiation between healthy individuals and Hodgkin's lymphoma patients pre-treatment (Lake et al, 2018). Enhanced signal responses obtained from control measurements may be attributed to protein G molecules on electrode surfaces, which inadvertently capture secondary antibodies due to their affinity for all IgG molecules. Hence, streptavidin conjugated HRP labels bind to biotinylated secondary antibodies, in all cases whether attached to protein G or antigen molecules, and converts TMB to a one-electron oxidation product in the presence of hydrogen peroxide. Previous studies have minimised signals from remaining active sites of protein G molecules by blocking with high concentrations of antibodies that do not interfere with subsequent assay procedures (Fowler et al, 2007). However, this approach was not considered practical due to the considerable quantities of antibodies applied to electrode surfaces and their high associated cost. Furthermore, the reduced signal acquisition following incubation with high antigen concentrations is counter-intuitive and may be partly explained by

previous findings where antigen antibody interactions were believed to displace protein G molecules from electrode surfaces (Hafaiedh et al, 2013; Chammem et al, 2015). Hence, secondary antibodies and HRP labels would be unable to attach to target antigens and would only attach to remaining protein G molecules on electrode surfaces, ultimately leading to reduced signal acquisition. Therefore, the current approach should not been considered for future amperometric experiments for detection of CCL17/TARC with a "labelled" electrochemical sandwich assay.

### *5.4.4 Heterobifunctional Cross-linker Protocol*

#### *5.4.4.1 SAM Characterisation*

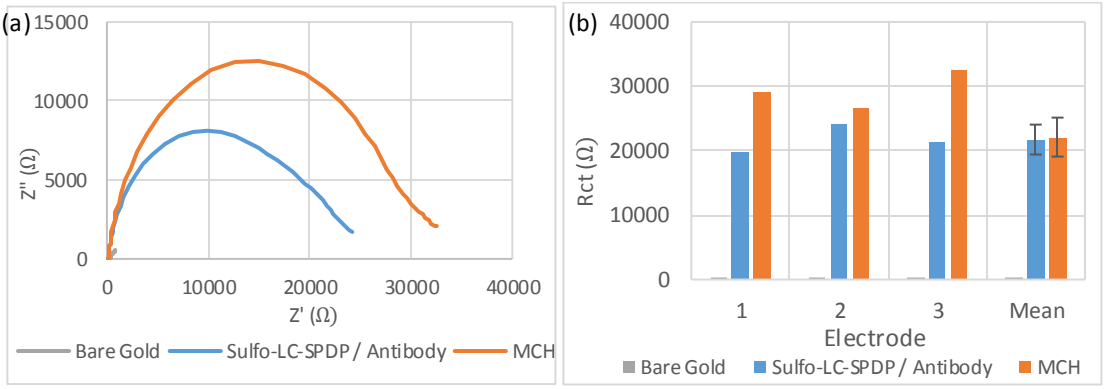


*Fig 5.9: (a) Nyquist plots for functionalised electrodes following* heterobifunctional cross-linker assay depositions (n=3) *b) Plot of measured charge transfer resistance for self-assembled monolayer characterisation of the* heterobifunctional cross-linker assay *on electrodes (n=3).*

Gold working electrodes measured significant increases in $R_{ct}$ following respective assay depositions, which indicated successful functionalisation of heterobifunctional cross-linker assays, shown in Figure 5.9a and 5.9b. Electrodes measured $R_{ct}$ = 106.99 ± 54.313Ω that significantly increased to $R_{ct} = 2.17\text{x}10^{4} \pm 2.32\text{x}10^{3}\Omega$ ($F(1,4) = 260.00$, p-value $< 0.05$) upon exposure to CCL17/TARC antibody / Sulfo-LC-SPDP solutions,

implying successful attachment of primary antibodies given the reduced ability for the $[Fe(CN)6]^{-3/4}$ couple to transfer electrons to electrodes. Similarly, electrodes measured significant increases in $R_{ct}$ = 2.21x10$^4$ ± 3.02x10$^3$Ω following MCH depositions (F(1,4) = 12.41, p-value < 0.05), which suggests chemisorption of sulphur atoms in the head groups of thiols to gold substrates and, hence, successful electrode blocking.

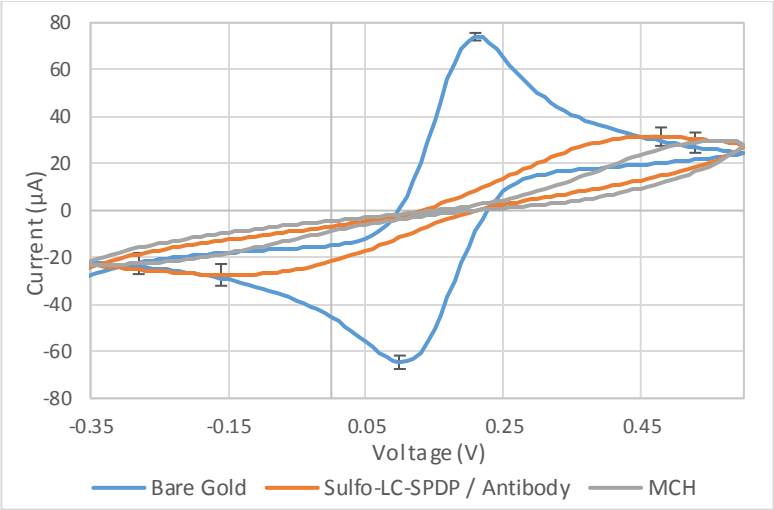


*Fig 5.10: Cyclic voltammograms depicting one-electron transfer redox reactions of* $Fe(CN)6^{-3/4}$ following heterobifunctional cross-linker assay depositions (n=3).

Cyclic voltammetry experiments further demonstrated successful functionalisation of assay procedures to electrode surfaces, as indicated in Figure 5.10. Bare gold electrodes observed one-electron reversible reactions characteristic of $Fe(CN)6^{-3/4}$ with $I_{pa}$ = 74.075 ± 1.613µA at $E_{pa}$ = 0.210V and $I_{pc}$ = -64.641 ± 2.856µA at $E_{pc}$ = 0.100V. CCL17/TARC antibody / Sulfo-LC-SPDP depositions decreased the readiness for electron transfer to occur at electrode surfaces, where $I_{pa}$ = 31.496 ± 3.930µA at $E_{pa}$ = 0.480V and $I_{pc}$ = -27.398 ± 4.645µA at $E_{pc}$ = -0.160V, due to formation of the SAM and antibody film. Similarly, MCH procedures decreased the availability for redox reactions of $Fe(CN)6^{-3/4}$, where $I_{pa}$ = 28.936 ± 4.324µA at $E_{pa}$ =

0.529V and $I_{pc}$ = -22.584 ± 4.484μA at $E_{pc}$ = -0.280V. The consecutive increases in ΔE at respective assay stages, from ΔE = 0.110V, and ΔE = 0.640V, to ΔE = 0.809V, further highlights slower electron transfer kinetics as would be expected given increased quantities of molecules at electrode surfaces.

### *5.4.4.2 Initial Testing of Electrodes*

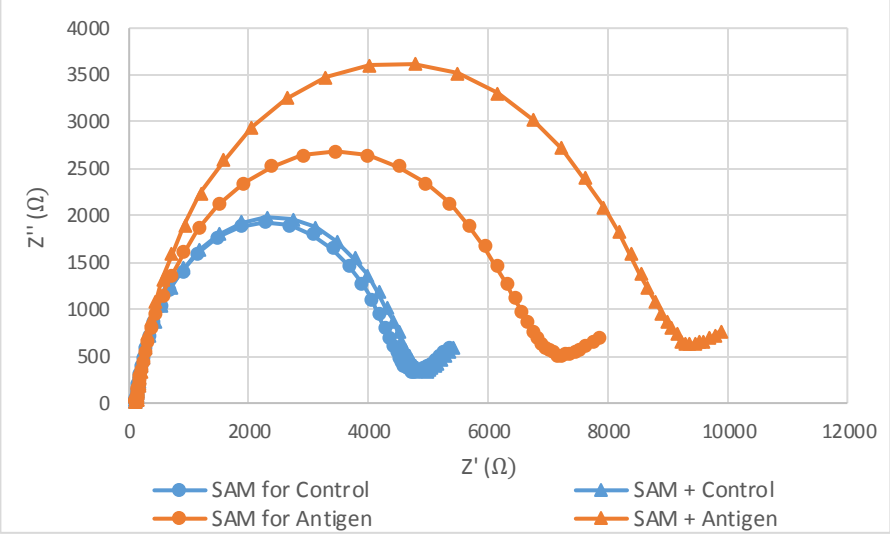


*Fig 5.11: Functionalised electrodes were measured before and after incubation with either control samples that contained no target antigen or spiked buffer samples that contained 97pg/ml CCL17/TARC concentrations* (n=3).

Electrodes measured electrical parameters at functionalised surfaces before and after incubation with spiked samples to determine whether it was possible to discriminate between control and antigenic CCL17/TARC solutions. Electrodes measured SAM layers with $R_{ct}$ = 4,442.33 ± 527.77Ω that increased marginally upon incubation with control samples to $R_{ct}$ = 4,604.33 ± 665.07Ω. Conversely, electrodes measured starting impedance values of $R_{ct}$ = 6,741.33 ± 3,467.20Ω that were associated with a greater increase in $R_{ct}$ = 8,817.33 ± 3,341.913Ω following incubation with spiked antigenic solutions of 97pg/ml concentration. Percentage differences in $R_{ct}$ were deemed statistically significant between controls at 3.46 ± 3.32% and 97pg/ml CCL17/TARC

concentration at 36.35 ± 16.64% (t(4) = -3.36, p-value <0.05), and implies that the proposed immunosensor has the capacity to identify the presence of target antigens in spiked samples. However, the co-efficient of variation associated with antigenic measurements was significant at 45.79%, and highlights the need to perform a concentration study to establish the true analytical performance of the current assay.

### *5.4.4.3 Concentration Study*

Two concentration studies were performed where spiked solutions of different antigen concentrations were consecutively incubated on electrodes to measure repeatability and sensitivity of the proposed immunosensor. Electrodes showed increases in Rct at the electrode/electrolyte interface for all electrodes in experiments one and two following incubation procedures relative to initial impedance values of SAM layers, as indicated in Figures 5.12a and 5.12b.

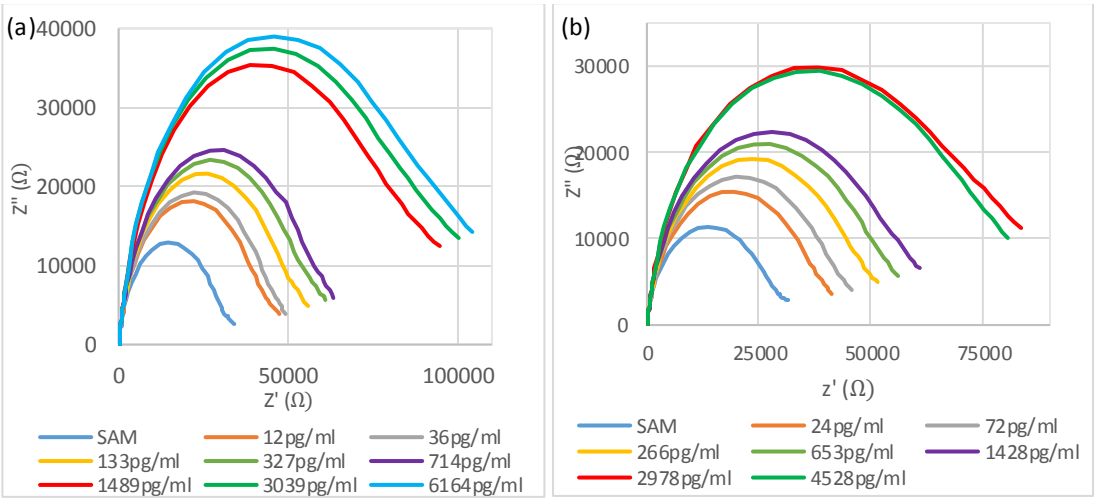


*Fig 5.12: Nyquist plots show electrode responses for (a) experiment one and (b) experiment two before and after exposure to spiked samples of specified CCL17/TARC concentrations (n=3).*

Immunosensor responses demonstrated recognition of CCL17/TARC upon exposure to antigenic solutions, although increases in $R_{ct}$ were weakly correlated with CCL17/TARC concentration, with $R^2 = 0.939$, as indicated in Figure 5.13. The weak positive relationship between impedance and antigen concentration may be attributed to significant intra-assay variability, where the co-efficient of variance ranged from 5.42-44.5% and 7.54-24.0% for experiments one and two respectively. The poor repeatability observed between electrodes makes it difficult to distinguish between antigen concentrations, particularly at lower CCL17/TARC levels with no significant difference between 12-72pg/ml ($F(3,8) = 0.72$, p-value = 0.567), 133-327pg/ml ($F(2,6) = 1.27$, p-value = 0.322) and 653-1428pg/ml ($F(2,6) = 0.99$, p-value = 0.425) concentrations. Sensor responses were more pronounced at CCL17/TARC concentrations $\geq$ 1489pg/ml, however, it was similarly not possible to differentiate between 1489-6164pg/ml ($F(2,6) = 0.19$, p-value = 0.835) and 2978-4528pg/ml ($F(1,4) = 0.05$, p-value = 0.826) concentrations for respective experiments. Furthermore, changes in $R_{ct}$ were markedly different between experiments, which further highlights repeatability issues between electrodes, and questions the quantitative detection capabilities of the proposed sensor. Nevertheless, electrodes were tested on clinical samples to determine whether it was possible to discriminate between serum of healthy volunteers and Hodgkin's lymphoma patients, given the significant difference in CCL17/TARC concentration between patient groups.

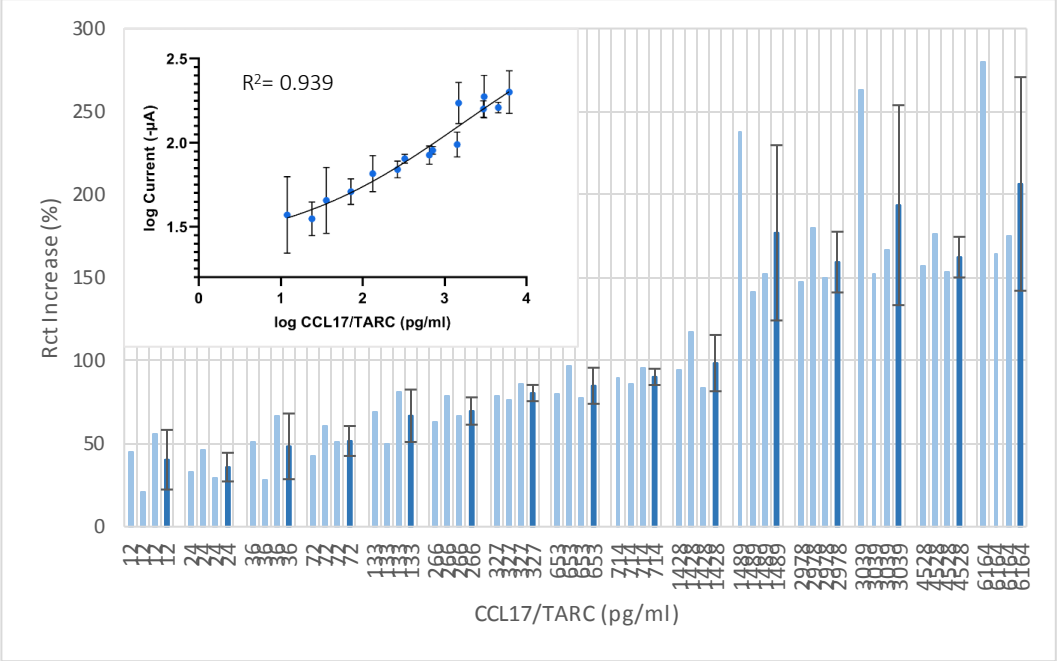


*Fig 5.13: Bar plots show differences in $R_{ct}$ before and after antigen incubation with specified CCL17/TARC concentrations. Inset shows four-parameter logistic regression analysis of $R_{ct}$ responses for specified CCL17/TARC concentrations (n=3).*

### 5.4.4.4 Patient Samples

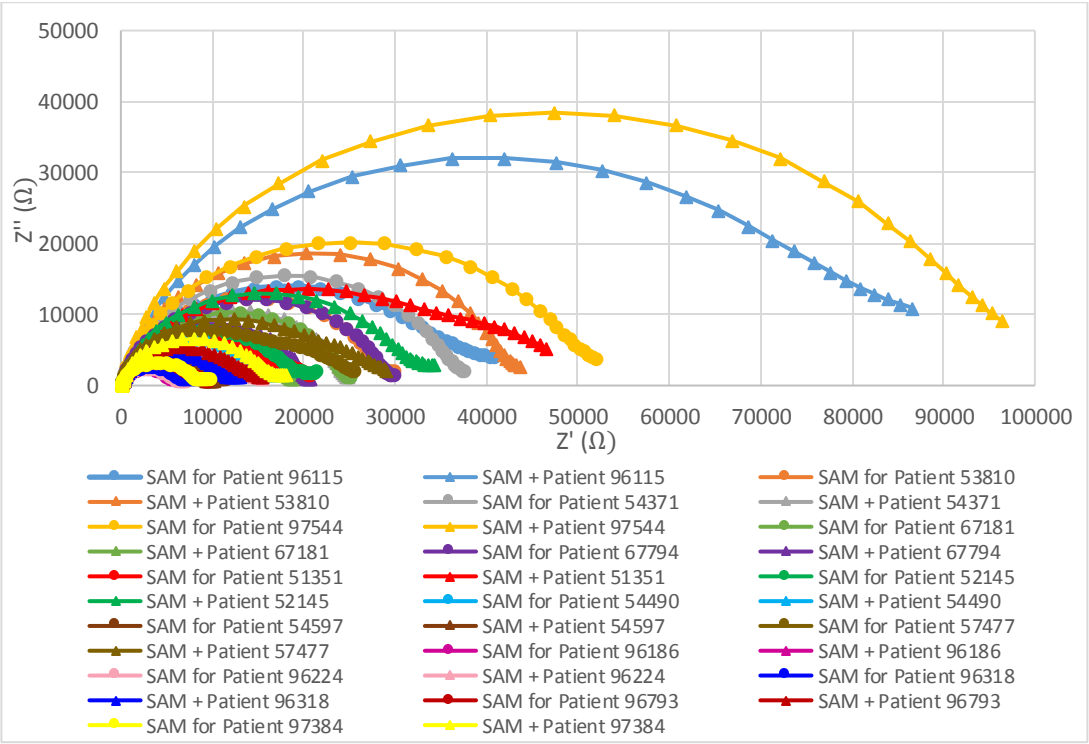


*Fig 5.14: Nyquist plots show functionalised electrode responses before and after incubation with specified diluted patient samples (n=3).*

Electrodes were measured before and after exposure to diluted x10 clinical serum samples to determine whether it was possible to identify CCL17/TARC affinity interactions at functionalised surfaces, as shown in Figure 5.14. Nyquist plots showed considerable variation in impedance prior to sample exposure that suggests variability in SAM formation at electrode surfaces. Electrodes incubated with diluted serum from healthy volunteers did not exhibit consistent impidimetric responses, with three and two electrodes showing increases and decreases in $R_{ct}$ values respectively. Observed variability may be attributed to non-specific binding of serum constituents to SAM layers in the case of electrodes showing increased responses, whilst removal or disruption of SAM layers following incubation or washing procedures may explain decreased responses. Electrodes incubated with diluted serum from Hodgkin's lymphoma patients also showed inconsistent impidimetric responses, although generally $R_{ct}$ values were observed to increase relative to healthy volunteers, indicative of different degrees of antigen binding to functionalised electrode surfaces.

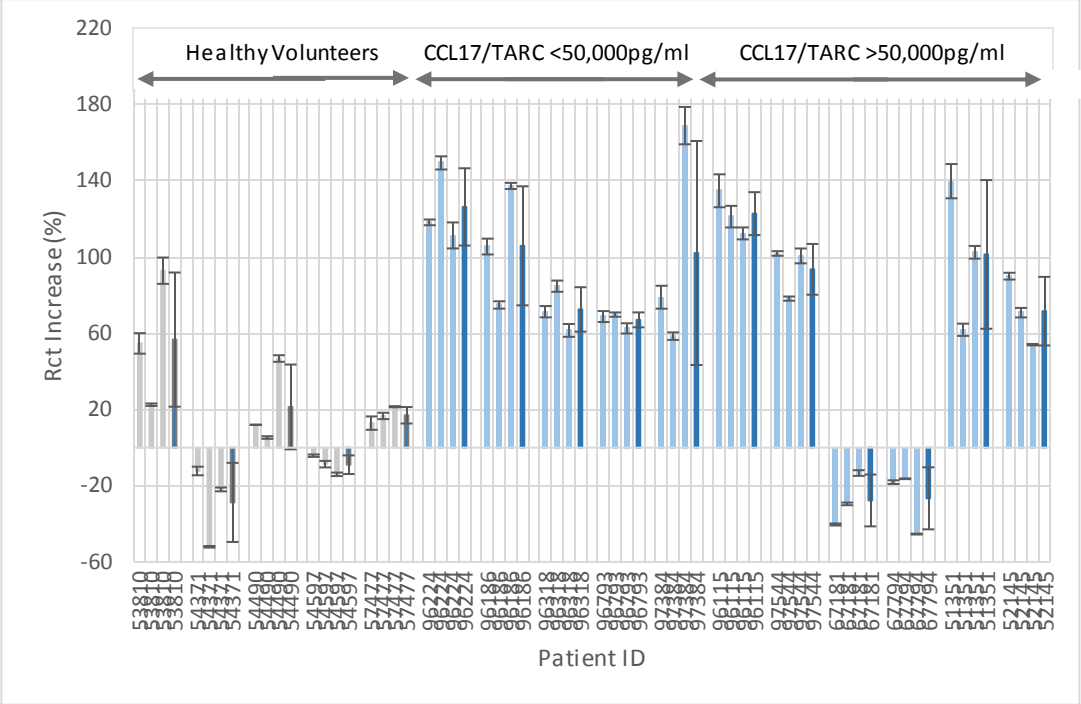


*Fig 5.15: Plots show the difference in charge transfer resistance, $R_{ct,}$ for electrodes following exposure to healthy volunteer and Hodgkin's lymphoma patient samples (n=3). Light grey and blue bars show mean responses per electrode for healthy volunteer and Hodgkin's lymphoma patient samples respectively, whilst dark grey and blue bars show mean responses per healthy volunteer and Hodgkin's lymphoma samples (n=3).*

Electrode behaviour became more apparent when percentage differences in $R_{ct}$ values were plotted before and after sample incubation for respective electrodes, as shown in Figure 5.15. Electrode responses for the healthy volunteer group showed significant variability both between patients and between electrodes for the same patient, which implies observed responses cannot solely be attributed to biochemical differences in blood serum between patients. Instead, several non-biochemical factors may contribute to electrochemical variability, primarily differences in SAM formation, non-specific binding of serum constituents, and washing inconsistencies, which are known causes of reproducibility issues for impedance based immunosensors (Radhakrishnan et al, 2014; Daniels et al, 2007). Electrodes displayed significant increases in $R_{ct}$ values after incubation with serum from patients with Hodgkin's

lymphoma compared to healthy volunteers for all patients with the exception of patients 67181 and 67794 ($F(2,58) = 14.27$, p-value $< 0.05$), both of which were not significantly different to healthy controls ($F(2,22) = 3.34$, p-value $= 0.054$). However, electrochemical responses did not appear proportional to known serum concentrations of CCL17/TARC in patients, with increased $R_{ct}$ for patients categorised <50,000pg/ml in comparison to patients with >50,000pg/ml CCL17/TARC concentration. Therefore, the technique has the capacity to characterise a certain degree of binding of CCL17/TARC to electrode surfaces and may have limited potential to provide qualitative assessment of CCL17/TARC status in patient samples. However, poor measurement consistency between healthy controls and significant variability in $R_{ct}$ for patient samples means the technique requires significant optimisation and in present form should not be considered for clinical applications. One possible explanation for inconsistencies between patients may arise from the sample dilution protocol prior to electrochemical analysis. Currently, 20µL of serum from each patient has been diluted in 180µL of 1 x PBS (1:10 dilution), with 25µL of the resultant solution incubated on each electrode. Perhaps, larger volumes with a greater initial volume of serum would reduce potential dilution errors and increase sample consistency so that diluted samples accurately reflect provided clinical samples. Additionally, differences in electrode responses for the same patient indicates significant intra assay variability where the coefficient of variance ranged from 5.83-104.23% for patients 96793 and 54490. Repeatability concerns highlight that the analytical performance of the sensor is not appropriate for clinical measurements and may be caused by non-specific binding events that obscure the true signal associated with CCL17/TARC binding and/or assay reproducibility issues regarding SAM

formation and antibody orientation, all of which have been discussed extensively in the previous chapter. Furthermore, the inability to detect two patients, 67181 and 67794, with known CCL17/TARC concentrations >50,000pg/ml is concerning and highlights major inter assay variability issues with the current "unlabelled" approach. All repeat measurements for both patients were conducted on the same day and therefore raises the possibility of considerable batch-to-batch assay variation.

*5.4.4.5 Reproducibility Study*

A reproducibility study was conducted over the course of experiments to determine whether SAM formation varied on electrodes between assay batches on different days that may inadvertently contribute to differences in analytical performance, as shown in Figure 5.16. Functionalisation of electrode surfaces varied considerably over the 9-day period, with inter assay variation calculated as $R_{ct}$ = 7,320.11 ± 8164.74Ω and $R_{ct}$ = 17,523.80 ± 15,19948Ω for Sulfo-LC-SPDP/antibody and blocking depositions respectively. It is recognised that thiol SAM formation on gold occurs in a two-step procedure where the density and packing of molecules may be influenced by several external and internal factors. Initially, formation of SAM's proceed with a high growth phase where the vast majority of molecular adsorption at the electrode surface occurs within seconds to minutes. The high growth phase is heavily influenced by surface cleanliness of the substrate, concentration of adsorption molecules, immersion time, temperature and humidity (Watson et al, 2015; Wang et al, 2014); thus fluctuations in experimental conditions may likely explain $R_{ct}$ variability between days. Thereafter, SAM formation continues with a slow growth phase where SAM density and

morphology is primarily determined by hydrogen bonding and Van der Waals forces between chains of alkane thiol molecules (Vericat et al, 2010; Watson et al, 2015). Hence, it is possible to improve the order, stability and density of SAM formation by selecting molecules of increased chain lengths, and should be considered for future experiments to improve SAM reproducibility on electrodes between days. Generally, intra assay variation decreased for Sulfo-LC-SPDP/antibody steps compared to the previous chapter and may be attributed to inclusion of centrifugation filters in the current protocol. However, intra assay variation was still considerable on certain days for Sulfo-LC-SPDP/antibody depositions, where the co-efficient of variation ranged from 12.1-67.3% on day 9 and 8 respectively. This suggests free thiol groups in unreacted DTT and Sulfo-LC-SPDP molecules in the assay are not solely responsible for large differences in initial $R_{ct}$ values, as previously believed, and that the influence of environmental conditions such as temperature and humidity requires further investigation. Intra assay variation was also considerable for $R_{ct}$ of electrodes following blocking procedures, where co-efficient of variation ranged from 10.1-52.9%, which indicates either blocking duration or selection of blocking agents should be revised to improve reproducibility in future studies. Overall, initial $R_{ct}$ associated with SAM formation on electrodes is highly variable between days, and, to a lesser extent, between electrodes on the same day. Therefore, it may be unwise to utilise $R_{ct}$ values in calculations to determine antigen binding to electrodes and may partly explain discrepancies in our current results.

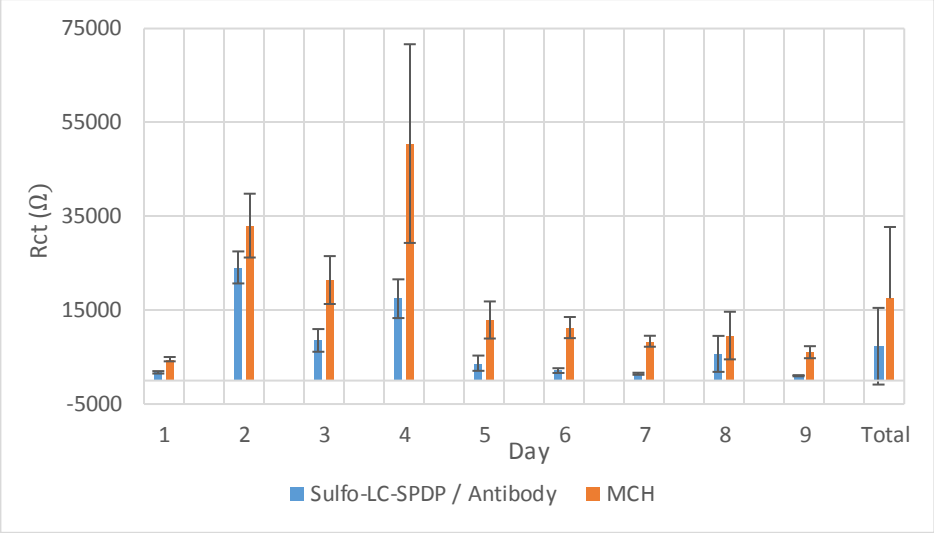


*Fig 5.16: Reproducibility plot showing variation of assay depositions between electrodes per day and on different days over the course of a nine day period (n=5).*

### *5.4.5 Heterobifunctional Cross-linker Sandwich Assay*

Electrochemical sandwich immunoassays function on the principle that attachment of secondary antibodies and labelled molecules generate sensitive and specific signals proportional to target antigen concentrations. With this in mind, the assay protocol was modified to determine whether a "labelled" electrochemical approach improves current diagnostic performance given the different detection scheme and analytical technique.

*5.4.5.1 Concentration Study*

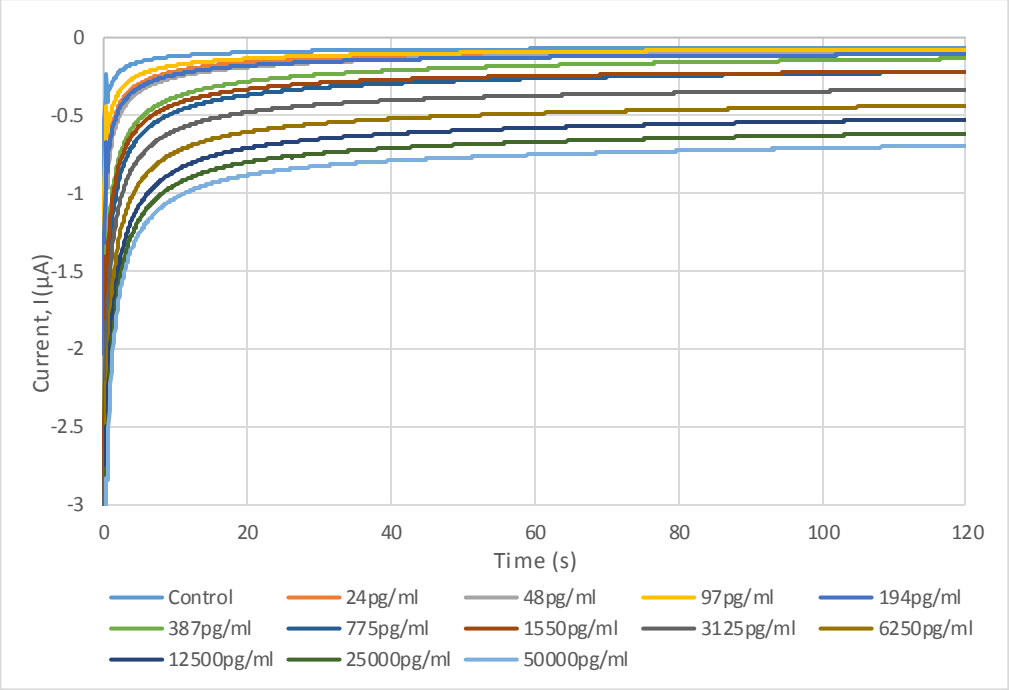


*Fig 5.17: Amperometric current-time curves that show reduction of oxidised TMB products at Epc = -0.2V for functionalised electrodes following incubation with different target antigen concentrations (n=3).*

Electrodes promoted reduction of oxidised TMB products at the vicinity of functionalised surfaces through the application of $E_{pc}$ = -0.2V, indicated in Figure 5.17, and were consistent with previous literature findings for detection of other biomarkers (San et al, 2016). The quantity of oxidised TMB products could also be observed through colorimetric observation where the colour of the solution directly correlated with concentration of bound antigen, evident from the colour of solutions in Figure 5.18. Amperometric current-time curves showed reduction of oxidised TMB products over time, where consumption of reactants with time produced a constant concentration gradient and steady-state currents, represented by the plateau at ~60 seconds onwards in Figure 5.17. Steady-state currents obtained at 120 seconds were

not characteristic of a linear assay over the specified concentration range, as indicated in Figure 5.19, which is unsurprising given the wide range of tested concentrations.


*Fig 5.18: Pictures of functionalised electrodes following previous amperometric measurements where gradual increases in the intensity of blue substrate solutions indicates the presence of increased antigen concentrations.*

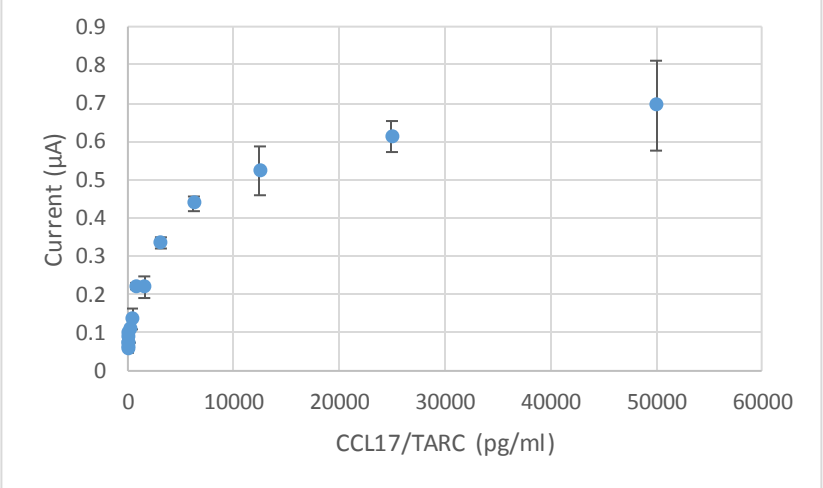


*Fig 5.19: Plot of amperometric current responses at 120 seconds for electrodes following incubation with different target antigen concentrations (n=3).*

Current responses and CCL17/TARC concentrations were plotted on logarithmic scales and fitted with a four-parameter logistic regression model to determine a better understanding of the relationship between current and target antigen concentration. The four-parameter logistic regression model was deemed suitable for electrochemical

analysis as it better reflects biological systems that do not display linear behaviour indefinitely, and has previously been employed in other electrochemical immunoassays (Bettazzi et al, 2018), and was recommended for the ELISA protocol which is also a surface based technique. Steady-state currents displayed a strong positive relationship with CCL17/TARC concentration, with $R^2 = 0.979$ for antigen concentrations deemed significantly different from controls, as indicated in Figure 5.20. Generally, electrode responses displayed reduced coefficient of variance for statistically significant measurements compared to previous impidimetric data. Co-efficient of variation ranged from 3.74-20.0% over statistically significant antigen concentrations and suggests the current assay detection scheme has improved reproducibility. The high co-efficient of variation for 24pg/ml, 48pg/ml, 97pg/ml and 194pg/ml samples at 18.4%, 18.6%, 24.8% and 32.3% respectively indicates the immunoassay cannot reproducibly detect these antigen concentrations, confirmed since currents were not statistically different to controls ($F(4,10) = 2.00$, p-value = 0.171). Nevertheless, the current sandwich assay showed statistically significant discrimination between control and spiked samples when CCL17/TARC concentration $\geq$387pg/ml ($F(12,26) = 80.57$, p-value $< 0.05$), which is promising since the proposed clinical cut-off value for concentrations of CCL17/TARC in serum for suspected Hodgkin's lymphoma patients is 1,150pg/ml (Lake et al, 2018). Therefore, the current sandwich assay has been tested on previous clinical serum samples to determine whether electrodes could distinguish between patient groups above and below the proposed clinical cut-off. The patient study further served as a comparative analysis between "labelled" and "unlabelled" electrochemical detection schemes to determine the optimal approach for future studies.

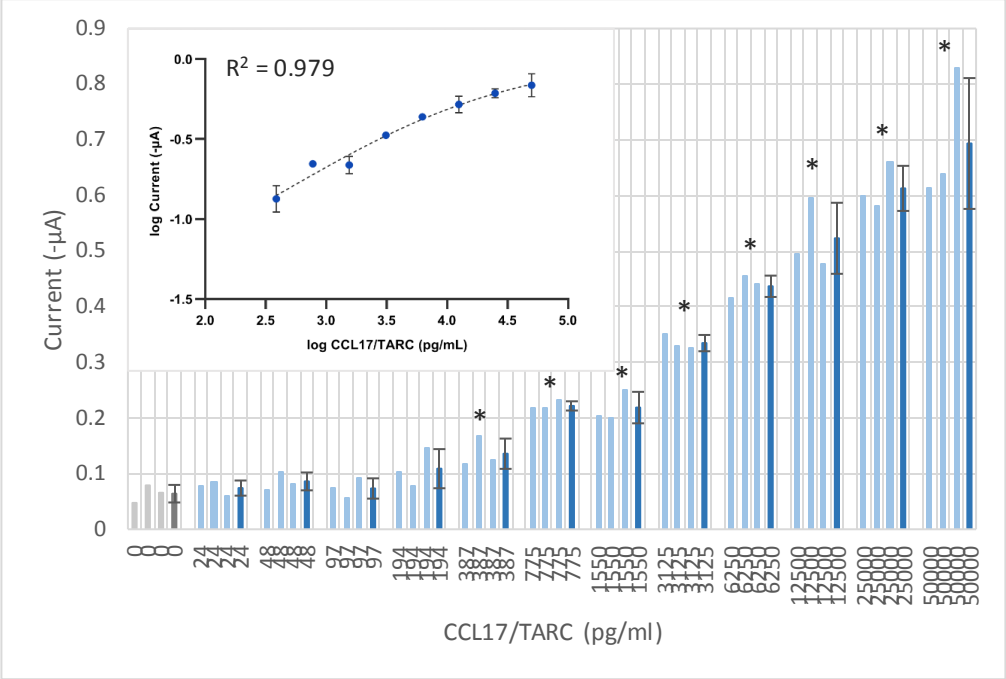


*Fig 5.20: Plot of current responses for electrodes following incubation with different target antigen concentrations (n=3). Asterisk's indicate significantly different responses from control measurements where P < 0.05 at 95% C.I.'s. Light grey and blue bars show responses per electrode for healthy volunteer and Hodgkin's lymphoma patient samples respectively, whilst dark grey and blue bars show mean responses per healthy volunteer and Hodgkin's lymphoma patients. Inset plot shows calibration curve for current responses versus log CCL17/TARC concentration for statistically significant responses fitted with a four-parameter logistic regression model.*

## *5.4.5.2 Sandwich Assay Patient Samples*

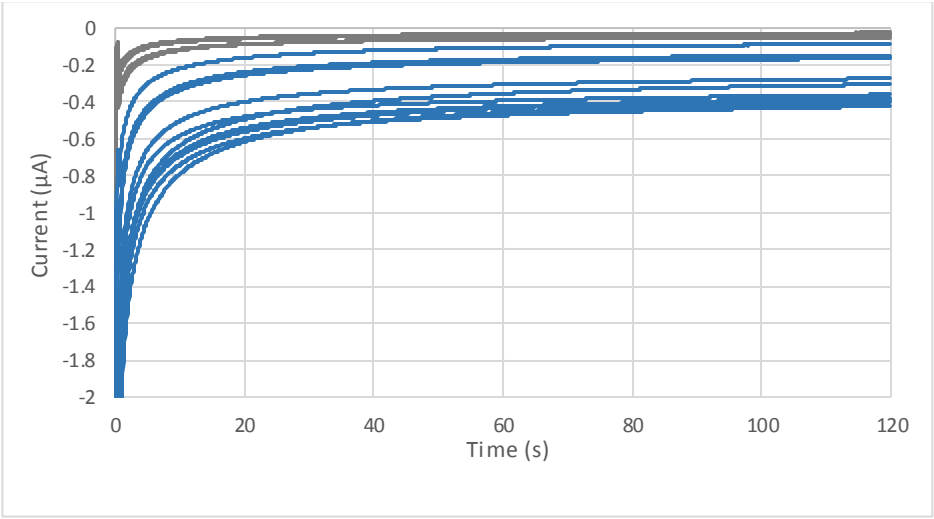


*Fig 5.21: Amperometric current-time plots show reduction of oxidised TMB products at electrodes following incubation with diluted serum samples of healthy volunteers, indicated in grey, and Hodgkin's lymphoma patients, indicated in blue (n=3).*

Immunosensors successfully characterised reduction of oxidised TMB products at electrode surfaces with significant differences in steady-state current responses observed between patients, as indicated in Figure 5.21. All patient samples clinically diagnosed with Hodgkin's lymphoma were associated with significantly increased steady-state reduction currents compared to healthy volunteer samples ($F(11, 36) = 69.04$, p-value $< 0.05$). Furthermore, Hodgkin's lymphoma patients that were categorised in to either <50,000pg/ml and >50,000pg/ml classes displayed distinct steady-state currents, with significantly increased current responses for patients > 50,000pg/ml ($F(1, 31) = 60.54$, p-value $< 0.05$). Therefore, electrode responses were found to respond proportionally to the concentration of CCL17/TARC present in serum, as anticipated since the quantity of oxidised TMB product should directly correlate with quantities of antigen bound to electrode surfaces. The presence of CCL17/TARC binding to electrode surfaces was further validated through colorimetric observation where the reagent solution turned progressively blue for increased antigen concentration, as indicated in Figure 5.22.


*Fig 5.22: Pictures of electrodes immersed in substrate solution following amperometric measurements where colorimetric change indicates the presence of CCL17/TARC in samples. Left picture depicts healthy control patient with little to no colour change. Middle picture depicts electrodes for Hodgkin's lymphoma patient where CCL17/TARC concentration is known to be <50,000pg/ml. Right picture shows electrodes for Hodgkin's lymphoma patient where CCL17/TARC concentration is known to be <50,000pg/ml.*

Present findings have demonstrated significant potential for clinical translation of the "labelled" electrochemical approach for detection of CCL17/TARC from serum samples. However, closer inspection of current responses shown in Figure 5.23 indicates a significant degree of intra assay variability between electrodes for a large proportion of patients, particularly for samples 96224, 96793, 96115 and 97544 where co-efficient of variance equals 25.9%, 29.8%, 23.2% and 18.9% respectively. Generally, immunoassays report co-efficient of variance <10% for clinical applications (Trombetta et al, 2018; Liew et al, 2007; DuPont et al, 2005), and therefore considerable optimisation is required to reduce repeatability errors and establish clinical confidence for prospective results. Whilst the co-efficient of variance for immunoassays is partly determined by antibody affinity and target antigen concentrations (Reed et al, 2002), other patient samples displayed lower values ranging from 6.08-14.5% for patients 67794 and 96318 respectively, and provides realistic evidence that this may be achievable in future studies. Immunosensor responses also highlight significant inter assay variability where measured currents were lower for patient 67794 compared to patient 97384 despite previous knowledge of increased CCL17/TARC concentration in blood serum of patient 67794. The sources of intra and inter assay variability most likely originate from sampling errors regarding dilution of clinical samples, experimental errors from washing procedures and/or differences in surface roughness and cleanliness between electrodes, and must be resolved in future studies before clinical translation can be realised.

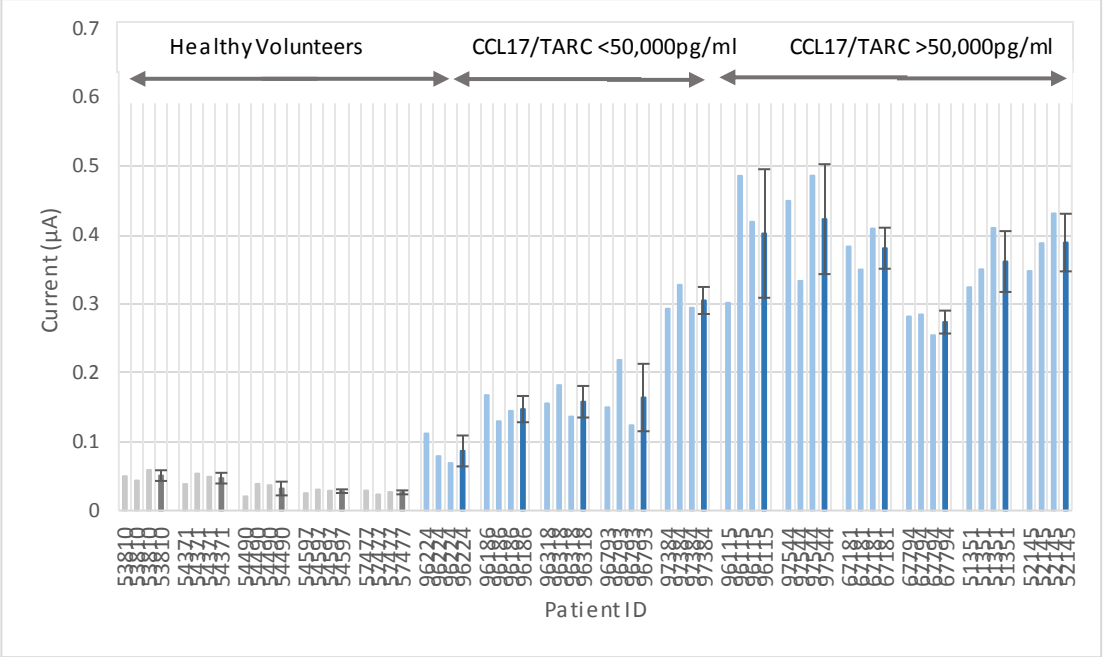


*Fig 5.23: Current responses for electrodes following incubation with diluted serum samples from healthy volunteers and Hodgkin's lymphoma patients. (n=3). Light grey and blue bars show responses per electrode for healthy volunteer and Hodgkin's lymphoma patient samples respectively, whilst dark grey and blue bars show mean responses per healthy volunteer and Hodgkin's lymphoma patients*

### *5.4.6 Comparison of Electrochemical and ELISA Results*

All three analytical methods provided vastly different capabilities for detection of CCL17/TARC from clinical serum samples, as indicated in Figure 5.24. Concentrations of CCL17/TARC in patients determined from the amperometric sandwich assay approach were substantially reduced for all patient samples compared to ELISA methods. Consequently, immunosensors did not have the capability to predict the concentration of CCL17/TARC for patient 96224 with Hodgkin's lymphoma, since the diluted sample concentration did not accurately represent the known clinical concentration. Furthermore, immunosensors measured currents of 0.087 ± 0.022µA for patient 96224, which did not correspond to the statistically significant lower limit of previous concentration studies, and therefore it was not

possible to interpolate the concentration from the calibration curve. Inaccuracies in the predictions of CCL17/TARC concentrations in serum samples with the amperometric sandwich assay approach is a major concern and must be resolved before clinical translation can be realised. Potential differences in dilution protocols between our laboratory and that of the Beatson Institute for Cancer Research may explain observed discrepancies in predicted concentrations between amperometric and ELISA techniques. Additionally, different sample volumes between both techniques may also contribute to inconsistencies in predicted concentrations, since micro-well plates for ELISA tests contain 100µL of diluted sample per well compared to 25µL for respective electrodes. Furthermore, volume differences of substrate solutions may contribute to analytical errors, where 500µL of substrate solution compared to 100µL for ELISA may dilute signals at electrode surfaces. Lastly, differences in primary antibody concentrations of 2µg/ml and 50µg/ml for ELISA and electrochemical protocols respectively may contribute to the disparity in observed responses, since it is recognised that excessive primary antibody concentrations may negatively influence antibody-antigen affinity interactions and assay sensitivity due to steric hindrance (Deshpande, 2012). Therefore, primary antibody titration experiments and extensive sample dilution studies must be conducted to improve diagnostic performance and enable future clinical translation.

Electrochemical impedance spectroscopy also substantially under predicted CCL17/TARC concentration in patient samples. However, in contrast to amperometric findings, obtained concentrations did not exhibit a similar trend to ELISA experiments, and predicted concentrations did not correlate with known clinical levels of

CCL17/TARC in patients. Instead, electrochemical impedance spectroscopy identified patient 96224 as having the highest CCL17/TARC concentration in the patient group at 14,589.16pg/ml, despite both ELISA and amperometric methods identifying the patient to have the lowest CCL17/TARC level at 2976pg/ml and 1063pg/ml respectively. Furthermore, electrochemical impedance spectroscopy predicted healthy volunteer patient 53810 to have a significant CCL17/TARC concentration of 1095.53pg/ml, close to the clinical cut-off of 1550pg/ml, despite no detection of antigen from either ELISA or amperometric measurements, or evidence of classical Hodgkin's lymphoma from clinical information. The increase in signal response for these patients highlights difficulties concerning non-specific binding for impedancebased immunosensors, where falsely elevated signals may arise from unintentional attachment of abundant serum proteins to electrode surfaces. Conversely, electrochemical impedance spectroscopy was unable to identify the presence of CCL17/TARC molecules in serum of patients 67181 and 67794, despite significant clinical levels >50,000pg/ml as registered by ELISA testing. Therefore, electrochemical impedance spectroscopy should not currently be considered for further clinical testing of patient samples, due to the poor quantitative and qualitative detection capabilities of the technique compared to previously validated ELISA methods.

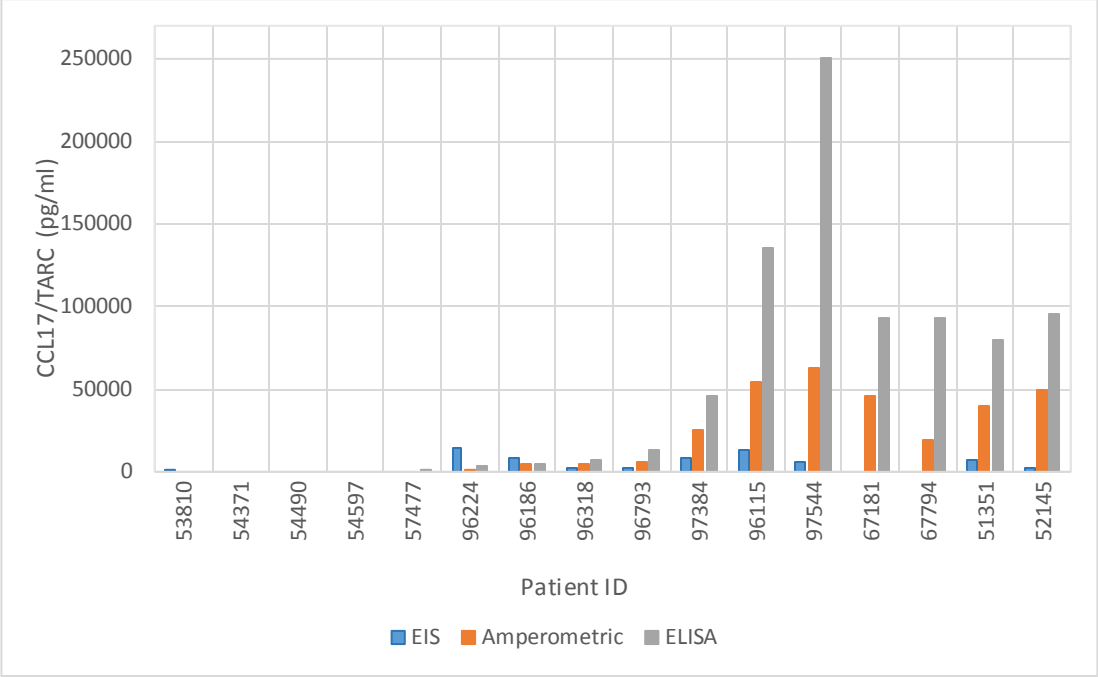


*Fig 5.24: Predicted mean CCL17/TARC concentration for tested patient samples based on impedance and amperometric signals and interpolation from respective calibration curves. Both techniques have been compared to known concentrations from previous ELISA experiments by our collaborators.*

### *5.4.7 ATR-FTIR Results*

#### *5.4.7.1 Age Study*

Spectra of blood serum samples from healthy volunteers in the non-cancerous control group were compared to establish whether patient age influences spectral signatures, as indicated in Figure 5.25a. Exploratory, unsupervised principal component analysis found no obvious clustering of spectral variance for persons in either <40 or ≥40 years of age categories, as indicated in Figure 5.25b and 5.25c, which suggests no marked differences between spectral signatures of patients with different age ranges. Indeed, PC1 ($F(1, 535) = 0.00$, p-value = 0.985) and PC3 ($F(1, 535) = 2.54$, p-value=0.112) scores on PC scores plots were not statistically significant between classes. However, PC2 ($F(1,535) = 22.60$, p-value <0.05) scores between patients <40 or ≥40 years of

age were deemed statistically different, although the small scale on PC2 axes should be highlighted. PC2 loading plots shows spectral variance originates from dissimilarities in amide I and amide II bands, as indicated in Figure 5.25d, which indicates minor differences in protein content between patient <40 or ≥40 age groups. However, spectral differences should be considered with caution since no distinct clustering is observed on PC2 versus PC3 scores plots. Furthermore, data classes comprise 126 spectra from patients ≥40 years of age in comparison to 411 spectra from patients <40 years of age to reflect the greater number of younger individuals contained within our Hodgkin's lymphoma sample set. Nevertheless, it is imperative that Hodgkin's lymphoma and healthy volunteer data sets contain a good balance of persons <40 or ≥40 years of age to account for possible spectral differences. This is particularly important as more patients are recruited over the course of the study and for possible clinical translation, since Hodgkin's lymphoma exhibits a bimodal age distribution with highest incidence rates at 20-24 and 75-84 years of age in the UK (Cancer Research UK, 2019).

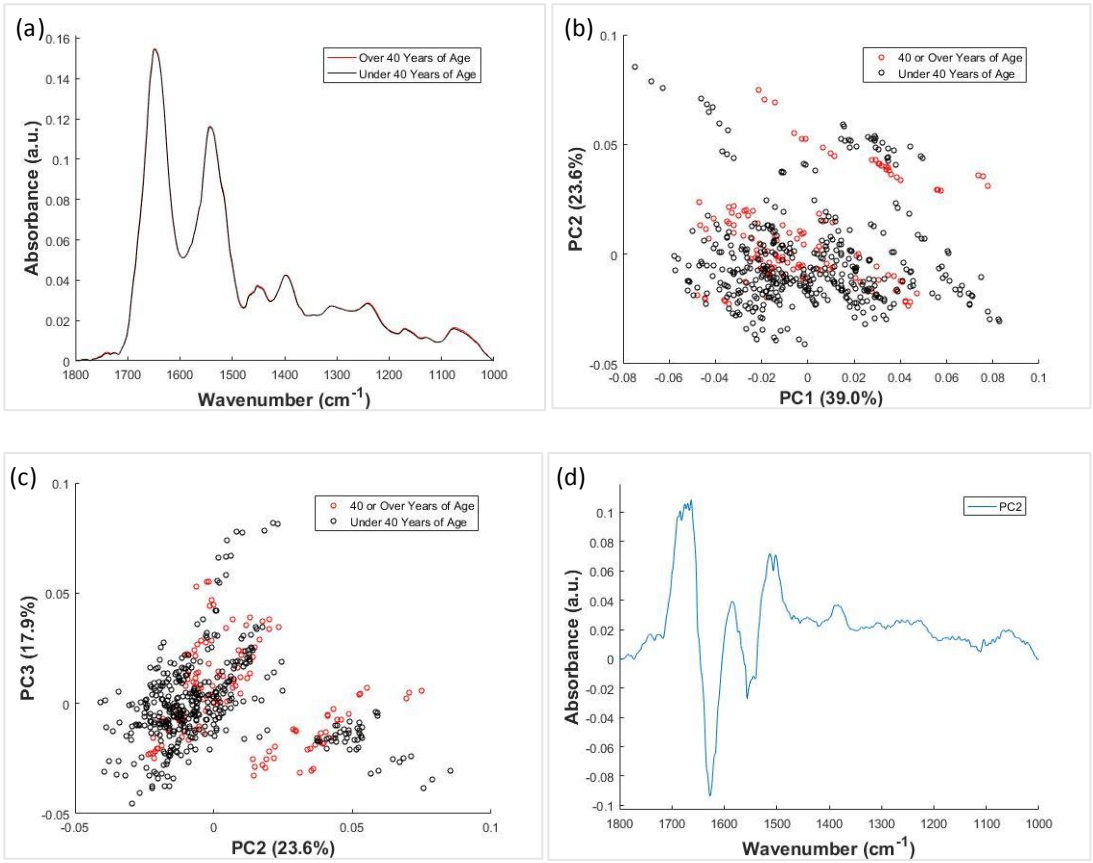


*Fig 5.25: (a) Mean ATR-FTIR spectra of blood serum of patients assigned to either <40 or ≥40 years of age categories. Spectra have been truncated from 1800-1000cm-1 and pre-processed with rubber-band baseline correction and vector normalisation procedures. PC scores plots showing the variance of mean, pre-processed patient spectra with (b) PC1 vs PC2 and (c) PC2 vs PC3 plots. (d) PC2 loading plot showing possible spectral differences between persons <40 or ≥40 years of age.*

### *5.4.7.2 Gender Study*

Spectra of blood serum samples from healthy volunteers in the non-cancerous control group were categorised according to gender and similarly compared to determine whether gender type influences spectral responses, as indicated in Figure 5.26a. Exploratory principle component analysis showed no strong correlation between spectral differences in the fingerprint region between male and female participants for all PC scores plots, shown in Figure 5.26b and 5.26c. PC's were statistically similar for PC1 ($F(1, 517) = 0.78$, p-value = 0.378) and PC3 ($F(1, 517) = 0.56$, p-value =

0.453) scores, although PC2 scores were deemed statistically different ($F(1,517) = 32.95$, p-value $<0.05$) between patient gender. This reflects previous analysis with similar spectral variance on PC2 loading plots that originate from amide I and amide II regions, indicated in Figure 5.26d. Still, no obvious separation can be observed on PC2 versus PC3 scores plots and statistical differences may possibly be attributed to greater quantities of female participants in the current batch of control samples, with a total of 348 female and 170 male spectra. Therefore, it is crucial in future studies that more male healthy volunteer patients are recruited to ensure a similar ratio of female and male participants exist within each patient group to prevent patient gender mismatch that may lead to possible confounding factors for spectroscopic studies. This is particularly important for diagnosis of Hodgkin's lymphoma given cases comprise slightly more male (57%) than female (43%) patients in the UK (Cancer Research UK, 2019).

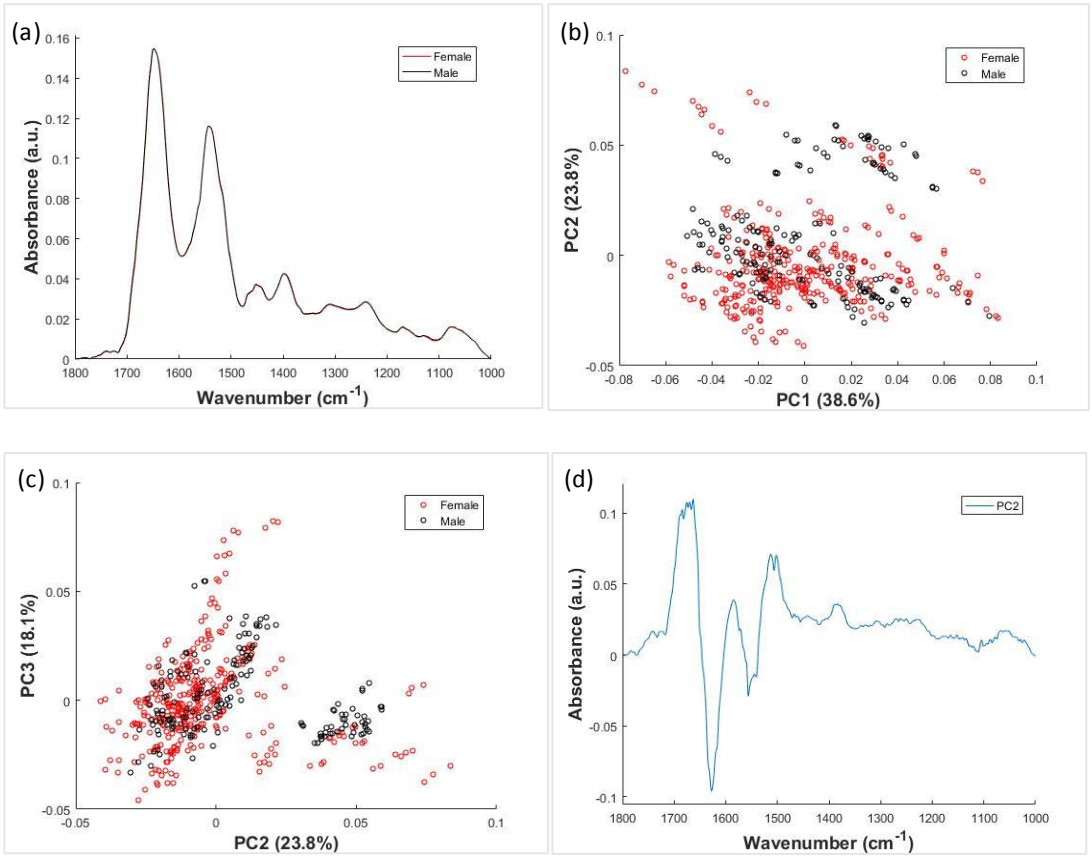


*Fig 5.26: (a) Mean, pre-processed ATR-FTIR spectra of blood serum of male and female patients highlighted in black and red respectively. Spectra have been truncated from 1800-1000cm-1 and pre-processed with rubber-band baseline correction and vector normalisation procedures. PC scores plots display spectral variance between male and female patients with (b) PC1 vs PC2 and (c) PC2 vs PC3 scores plots. (d) PC2 loading plot highlights spectral differences between patient gender on PC2 axes of PC scores plots.*

### *5.4.8 ATR-FTIR Diagnostic Studies*

#### *5.4.8.1 Random Forest Model: Absorption Spectra (4000-1000cm$^{-1}$)*

Absorption spectra of blood serum from all patient samples were subjected to supervised analysis with a Random Forest classifier to determine the diagnostic capabilities for discrimination between Hodgkin's lymphoma and healthy, non-cancerous control samples. Mean absorption spectra for Hodgkin's lymphoma and control samples truncated between 4000-1000cm-1 show similar spectral signatures

that reflect the abundant macromolecular constituents of blood serum, as indicated in Figure 5.27. Strong absorption peaks found at ~3300cm$^{-1}$, ~1650cm$^{-1}$ and ~1550cm$^{-1}$ in both patient groups correlate with amide A, amide I and amide II vibrational modes respectively (Barth, 2007), dominated by the high protein concentrations of albumin and α-, β- and γ-immunoglobulins present in blood serum (Bonnier et al, 2016). Similarly, distinctive absorption bands at ~3100-2800cm$^{-1}$ and ~1470cm$^{-1}$ regions describe $\nu_s(CH_2)$, $\nu_{as}(CH_2)$, $\nu_s(CH_3)$, $\nu_{as}(CH_3)$ and $\delta_s(CH_2)$ vibrational modes respectively (Stuart, 2004), associated with hydrocarbon chains of triglycerides, phospholipids and cholesterol found in blood serum samples. Likewise, weak absorption bands at ~1240cm$^{-1}$ and ~1085cm$^{-1}$ represent $\nu_{as}(PO_2)$ and $\nu_s(PO_2)$ modes of phospholipid and nucleic acid constituents of blood serum (Stuart, 2004). On closer inspection subtle spectral differences were observed in the shape and intensity of such bands between Hodgkin's lymphoma and healthy patients, which indicates different overall biomolecular profiles of blood serum for both patient groups. Interestingly, wavenumbers pertinent to identification of Hodgkin's lymphoma were primarily found within the fingerprint region (1800-1000cm$^{-1}$), with vibrations in the functional group region (4000-1800cm$^{-1}$) considered less significant for discrimination between patient groups, as highlighted by the importance plot in Figure 5.24.

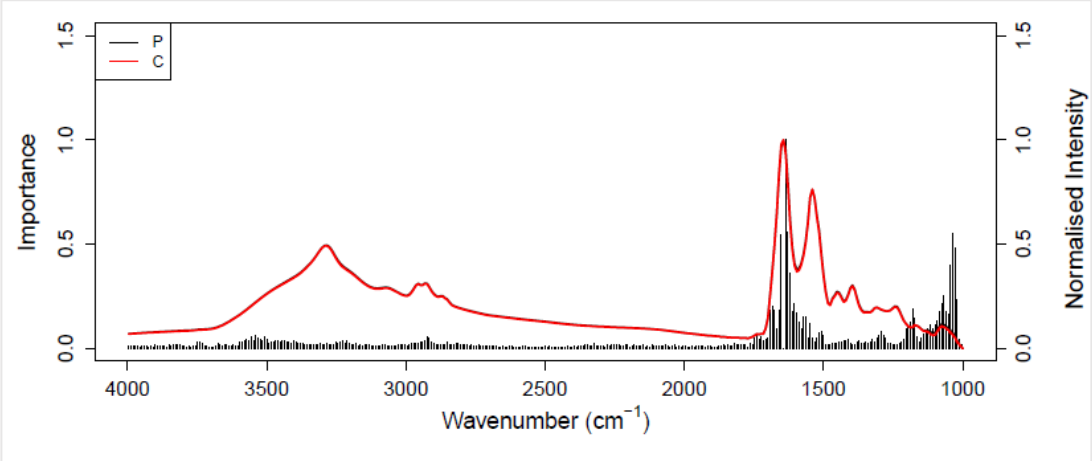


*Fig 5.27: Comparison of mean pre-processed ATR-FTIR spectra of blood serum truncated from 4000-1000cm$^{-1}$ from healthy volunteers, denoted C, and patients with Hodgkin's lymphoma, denoted P. Gini plot superimposed on mean spectra indicates significant wavenumber regions for discrimination between both patient groups as calculated by Random Forest model.*

Spectral differences identified by the training set over the full wavenumber region were subsequently validated on the sample test set to determine the diagnostic utility of spectral features for detection of Hodgkin's lymphoma. Successful diagnosis was predicted for 24 of 29 Hodgkin's lymphoma patients and 28 of 30 healthy volunteers contained within one sample test set, represented by the confusion matrix in Table 5.1. Misclassified spectra for patients misdiagnosed in both Hodgkin's lymphoma and healthy volunteer classes within the sample test set may be observed in Table 5.1. Validation was repeated with 50 randomly constructed sample test sets to gain an accurate representation of the diagnostic performance of the test, leading to relatively high accuracy, sensitivity and specificity, as indicated in Table 5.2. However, since earlier observations identified the fingerprint region to be the most significant for discrimination between Hodgkin's lymphoma patients and healthy volunteers, future studies shall conduct identical analysis with spectra truncated at 1800-1000cm$^{-1}$ to determine whether it is possible to improve diagnostic performance with reduced

quantities of wavenumbers that better describe differences between both patient classes.

| Confusion Matrix | | | Patient Group | Patient ID | Misclassified Spectra |
|---|---|---|---|---|---|
| | Reference | | Hodgkin's Lymphoma | 56162 | 9/9 |
| Predictor | P | C | Hodgkin's Lymphoma | 57211 | 9/9 |
| | | | Hodgkin's Lymphoma | 64606 | 7/9 |
| P | 24 | 5 | Hodgkin's Lymphoma | 64672 | 7/9 |
| | | | Hodgkin's Lymphoma | 97793 | 6/9 |
| C | 5 | 25 | Healthy Volunteer | 54061 | 5/9 |
| | | | Healthy Volunteer | 54597 | 5/9 |
| | | | Healthy Volunteer | 56559 | 6/9 |
| | | | Healthy Volunteer | 63627 | 9/9 |
| | | | Healthy Volunteer | 63766 | 5/9 |

*Table 5.1: Confusion matrix describing the number of healthy volunteers, denoted C, and Hodgkin's lymphoma patients, denoted P, correctly identified by the Random Forest classifier in one sample set relative to the known clinical status. Misclassified patients and number of spectra misclassified by the Random Forest model have been stated for both patients groups.*

| Accuracy (n = 50) | Sensitivity (n = 50) | Specificity (n = 50) |
|---|---|---|
| 0.826 ± 0.057 | 0.824 ± 0.079 | 0.827 ± 0.076 |

*Table 5.2: Diagnostic performance of Random Forest model when re-analysed with 50 randomly generated sample test sets. Results presented as mean ± standard deviation.*

*5.4.8.2 Random Forest Model: Absorption Spectra (1800-1000cm$^{-1}$)*

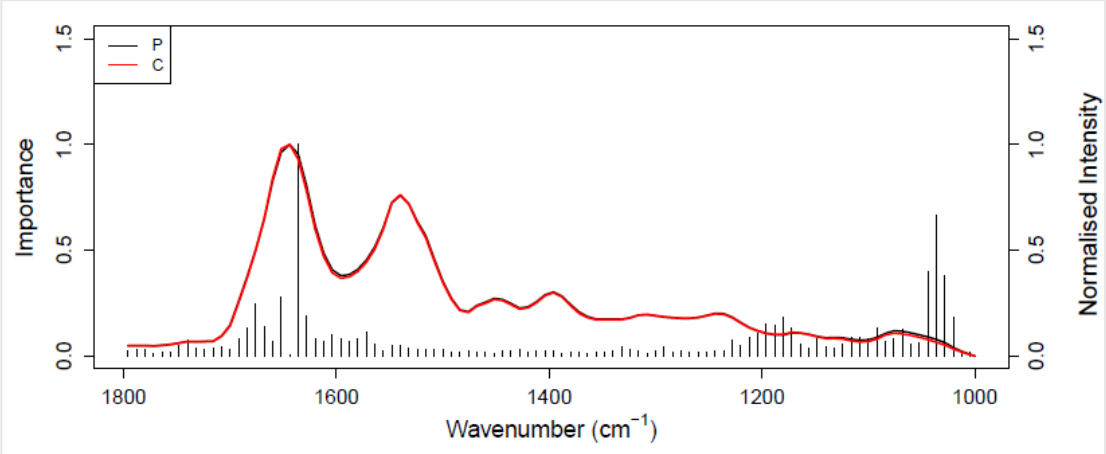


*Fig 5.28: Comparison of mean pre-processed ATR-FTIR spectra truncated to 1800-1000cm$^{-1}$ of blood serum from healthy volunteers, denoted C, and patients with Hodgkin's lymphoma, denoted P. Gini plot superimposed on mean spectra indicates significant wavenumbers for discrimination between patient groups as calculated by Random Forest model.*

Mean absorption spectra for Hodgkin's lymphoma and control samples truncated between 1800-1000cm-1 show spectral signatures characteristic of macromolecular constituents of blood serum, as indicated in Figure 5.28 and previously described. Spectral differences pertinent to the classification of Hodgkin's lymphoma primarily concerned the shape and intensity of the amide I band, suggestive of differences in the protein content of blood serum of Hodgkin's lymphoma patients. Additionally, absorption profiles of ν(CO), $\nu_s(PO_2)$ and ν(CC) vibrational modes were distinct between patient groups, suggestive of possible differences in carbohydrate, phospholipid and nucleic acid content in blood serum of Hodgkin's lymphoma patients. It is well-recognised that malignant Reed-Sternberg cells associated with Hodgkin's lymphoma express several proteins in the form of cytokines and chemokines to communicate with inflammatory cells, with increased concentrations of CCL17/TARC (Plattel et al, 2012), Galectin-1 (Ouyang et al, 2013), Interleukin-6

(Kurzrock et al, 1993), CD30 (Wang et al, 2018) and CD163 (Jones et al, 2013) reported in blood serum of Hodgkin's lymphoma patients. Additionally, endothelial cells found in the tumour environment have been shown to express increased concentrations of glycoproteins ICAM-1 and VCAM-1 (Syrigos et al, 2004); all of which may play a contributory role to differences in absorption of the amide I band between patient groups. Similarly, the presence of circulating tumour DNA fragments either associated with mutations in TNFAIP3, ITPKB, GNA13, B2M genes, or Epstein-Barr virus have previously been reported in blood plasma and serum of Hodgkin's lymphoma patients (Spina et al, 2018; Welch et al, 2017), and may influence differences in the $\nu_s(PO_2)$ mode between patient groups. However, it should be noted individual stated biomarkers for Hodgkin's lymphoma may be present in biological concentrations below the detection capabilities of ATR-FTIR for serum diagnostics. For instance, CCL17/TARC concentration in our samples range from ~1-250ng/ml and is thought to be below the quantification limit for protein detection of ATR-FTR in whole blood serum, as reported by others (Spalding et al, 2018, Bonnier et al, 2016). Instead, infrared spectra represent global changes in the biochemical serum profiles of patient groups, and therefore identified spectral differences may relate to other non-specific, general biomarkers of disease present in higher concentrations. For instance, low serum albumin concentrations <4g/dL in Hodgkin's lymphoma patients is common (Gobbi et al, 1985), as well as in other cancers, with hypoalbuminemia shown to be of prognostic significance for Hodgkin's lymphoma (Kojouri et al, 2004; Zhu et al, 2011). Serum albumin information is limited for our patient samples, although of patients where albumin concentrations have been provided, 24 of 32 patients were recognised to have hypoalbuminemia. Therefore,

differences in serum albumin content between Hodgkin's lymphoma patients and healthy controls may contribute to spectral differences in the amide I region, especially since serum albumin is abundant relative to other Hodgkin's lymphoma biomarkers and has previously been quantified in whole blood serum with ATR-FTIR (Spalding et al, 2018, Bonnier et al, 2016). However, spectra represent collective vibrations of vast quantities of infrared-active molecules present in interrogated serum samples, and therefore it is not possible to definitively assign differences in spectroscopic signatures to a specific biomolecule given the complexity of the sample matrix. Furthermore, medication information and the clinical history of the patient remain unknown for patients assigned to respective patient categories, and may contribute to the spectral differences identified between Hodgkin's lymphoma patients and healthy volunteers.

<table>
<tr><th colspan="3">Confusion Matrix</th><th>Patient Group</th><th>Patient ID</th><th>Misclassified Spectra</th></tr>
<tr><td></td><td colspan="2">Reference</td><td>Hodgkin's Lymphoma</td><td>52269</td><td>9/9</td></tr>
<tr><td rowspan="2">Predictor</td><td rowspan="2">P</td><td rowspan="2">C</td><td>Hodgkin's Lymphoma</td><td>53003</td><td>5/9</td></tr>
<tr><td>Hodgkin's Lymphoma</td><td>96050</td><td>8/9</td></tr>
<tr><td rowspan="2">P</td><td rowspan="2">25</td><td rowspan="2">4</td><td>Hodgkin's Lymphoma</td><td>97964</td><td>9/9</td></tr>
<tr><td>Healthy Volunteer</td><td>54134</td><td>9/9</td></tr>
<tr><td rowspan="2">C</td><td rowspan="2">4</td><td rowspan="2">26</td><td>Healthy Volunteer</td><td>54388</td><td>9/9</td></tr>
<tr><td>Healthy Volunteer</td><td>63627</td><td>9/9</td></tr>
<tr><td colspan="3"></td><td>Healthy Volunteer</td><td>63862</td><td>9/9</td></tr>
</table>

*Table 5.3: Confusion matrix describing the number of healthy volunteers, denoted C, and Hodgkin's lymphoma patients, denoted P, correctly identified by the Random Forest classifier in one sample set relative to the known clinical status. Misclassified patients and number of spectra misclassified by the Random Forest model have been stated for both patients groups.*

| Accuracy (n = 50) | Sensitivity (n = 50) | Specificity (n = 50) |
|---|---|---|
| 0.843 ± 0.053 | 0.832 ± 0.066 | 0.853 ± 0.081 |

*Table 5.4: Diagnostic performance of Random Forest model when re-analysed with 50 randomly generated sample test sets. Results presented as mean ± standard deviation.*

Spectral differences established by the Random Forest classifier training set over the fingerprint region (1800 - 1000cm$^{-1}$) were similarly tested blindly on one randomly selected sample test set, with marginal increases in diagnostic performance observed compared to spectral analysis over the full wavenumber region. The confusion matrix indicates 25 of 29 Hodgkin's lymphoma patients and 26 of 30 healthy volunteers were successfully predicted in the sample test set, as highlighted in Table 5.3. Interestingly, one healthy volunteer, 63627, was misdiagnosed both in current and previous analysis, which indicates the wavenumber selection criteria in this case does not influence misdiagnosis, presumably because the spectral features responsible for misclassification reside in the fingerprint region. Minor increases in diagnostic accuracy, sensitivity and specificity were observed for spectral analysis confined to the fingerprint region when validated with 50 randomly selected sample test sets, as detailed in Table 5.4. However, misclassification of Hodgkin's lymphoma patients and healthy volunteers remained significant and suggests either that the computational model has insufficient performance for detection of Hodgkin's lymphoma with high sensitivity and specificity, or that identified spectral signatures do not accurately represent the entire patient group leading to misdiagnosis. Furthermore, misclassification of patients may arise from spectral artefacts within particular patient data sets given that for some patients not all recorded spectra were misdiagnosed.

Therefore, further investigations on misdiagnosed spectra must firstly be conducted to rule out the possibility of non-biochemical differences accounting for patient misclassification, followed by further exploration of spectroscopic signatures responsible for diagnosis.

Clinically diagnosed Hodgkin's lymphoma patients that were identified as healthy by the Random Forest classifier in the sample test set were compared to the mean spectroscopic signature of Hodgkin's Lymphoma patients excluding misdiagnosed cases to understand possible explanations for misdiagnosis, indicated in Figure 5.29a. Overall, mean spectral signatures of misdiagnosed patients were not markedly different from spectra of successfully diagnosed Hodgkin's lymphoma patients, which indicates misdiagnosis does not appear to be associated with obvious spectral artefacts from experimental errors. On closer inspection, subtle spectral differences were observed in amide I and amide II bands that reflects the distribution of misdiagnosed patients on PC1 and PC2 axes of PC scores plots, as shown in Figure 5.26b and identified by PC1 and PC2 loading plots. However, misdiagnosed patients were within the overall distribution of variance for Hodgkin's lymphoma patients on PC1 and PC2 axes of PC scores plots, which suggests subtle differences in amide I and amide II band profiles exist within the patient group. Nevertheless, the amide I and amide II bands of patient 52269 correlated with the outer extremity of Hodgkin's lymphoma data on the PC1 axes, and consequently the Random Forest classifier may find difficulty in discriminating between Hodgkin's lymphoma and healthy status for this patient and may partly explain diagnostic inaccuracies within the sample test set. Additionally, spectral signatures of misdiagnosed patients with Hodgkin's lymphoma show

considerable variation within the 1140-1060cm$^{-1}$ region, highlighted in Figure 5.29a. Spectral variation correlates with variance observed for misdiagnosed patients on PC3 axes of PC scores plots, shown in Figure 5.29c and 5.29d, following consideration of PC3 loadings. Patients 52269, 53003 and patient 97964 were found on opposite outer extremities of data points on PC3 axes of PC scores plots, thus the Random Forest model may face similar challenges in associating variance on PC3 with Hodgkin's lymphoma. Whilst Random Forest deems the 1140-1060cm$^{-1}$ wavenumber region less significant for discrimination between Hodgkin's lymphoma and healthy controls compared to the amide I band, variability in this region may partly explain the relatively large standard deviations for specificity and sensitivity of the diagnostic test.

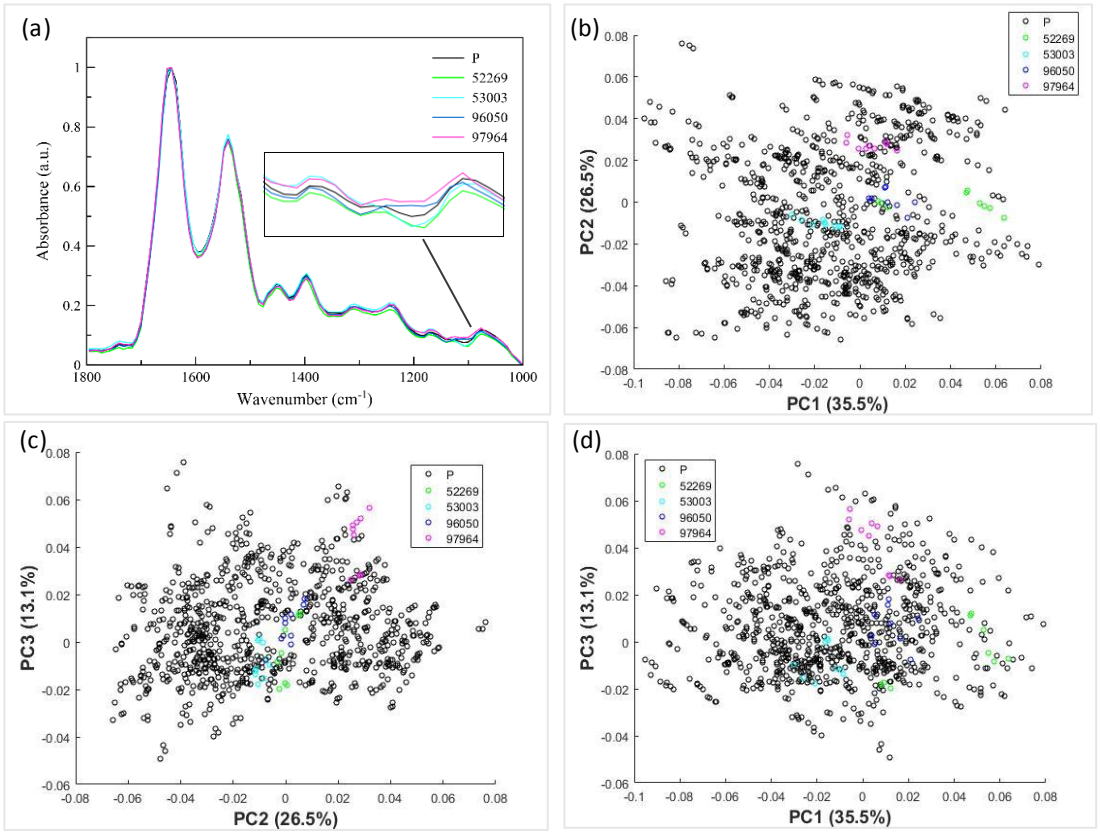


*Fig 5.29: (a) Mean pre-processed spectra of Hodgkin's lymphoma patients misclassified relative to mean, pre-processed Hodgkin's lymphoma spectra excluding misclassified patients and (b)resultant PC scores plots showing PC1 versus PC2, (c) PC2 versus PC3 and (d) PC1 versus PC3.*

Healthy volunteers diagnosed with Hodgkin's Lymphoma by the Random Forest classifier were similarly compared to mean spectra of the healthy volunteer group minus the misdiagnosed cases to determine potential sources of diagnostic error, as indicated in Figure 5.30a. Mean spectra of misdiagnosed healthy patients were similarly found to have subtle differences in amide I and amide II band shapes with these spectral features primarily responsible for the variance distribution in PC1 and PC2 axes of PC plots, shown in Figure 5.30b, as identified from PC1 and PC2 loading plots. Patients 54134, 54388 and 63862 were found on the extremity of healthy control data on the PC2 axes of PC scores plots, shown in Figure 5.30b and 5.30c, and therefore the Random Forest model may face increasing difficulty in correlating the amide I and amide II band profiles of these patients with healthy individuals. Interestingly, mean spectra of misdiagnosed healthy volunteers similarly showed variability in the 1140-1060cm$^{-1}$ wavenumber region, as shown in Figure 5.30a, and implies spectral variation is not exclusive to differences in the biochemical profile within Hodgkin's lymphoma patients. Instead, fluctuations in blood sugar levels may represent a likely cause of spectral variation across both patient groups, since it is well-documented that ν(CO) peaks occur within this spectral region (Bonnier et al, 2013; Movasaghi et al, 2008). Introduction of noise by silicon substrates is an additional and significant possible source of variation in the 1140-1060cm$^{-1}$ region. It is recognised that silicon dopants, interstitial oxygen ν(Si-O), and ν(O-Si-O) vibrations feature prominently in this spectral region and may thus interfere with the biochemical signatures of sample constituents (Karabudak et al, 2012; Schumacher et al, 2010). Hence, deviation in silicon composition across and between silicon wafers and

inaccuracies in the precision of groove geometries during manufacture may account for spectral variation in the 1140-1060cm$^{-1}$ region between silicon test devices.

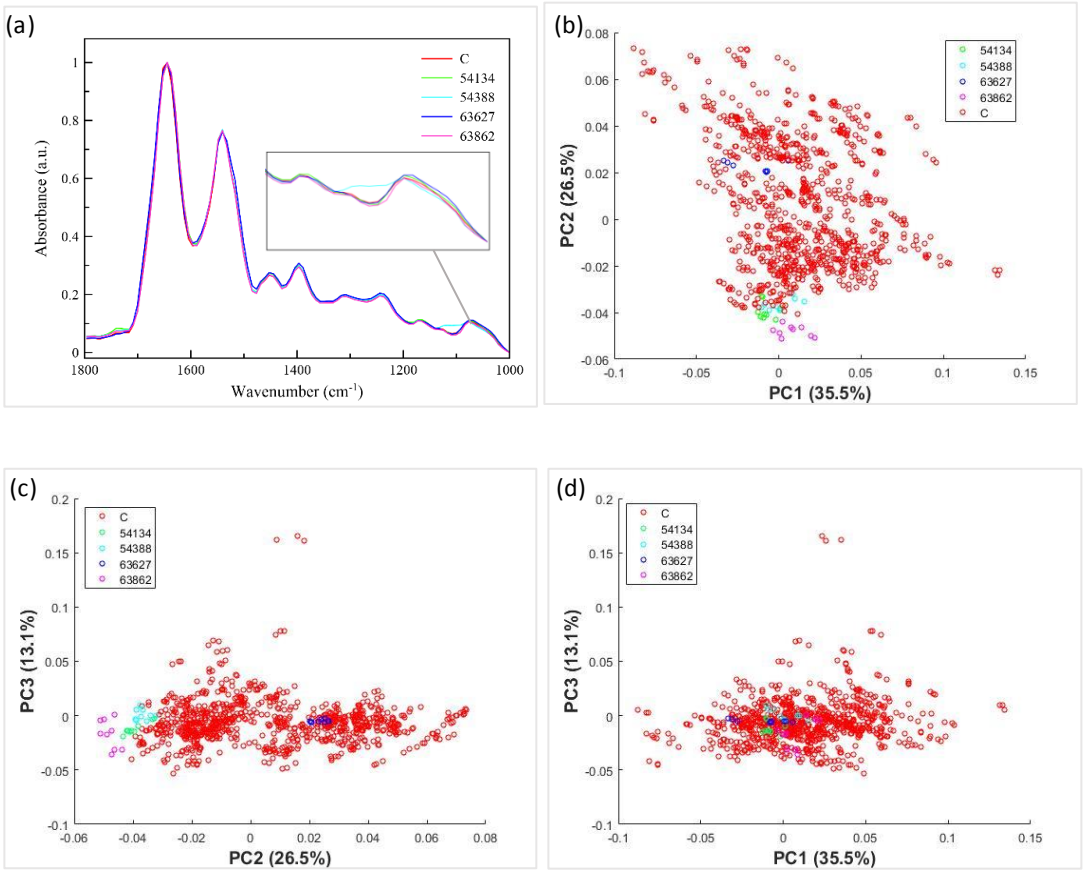


*Fig 5.30: (a) Mean pre-processed spectra of healthy volunteer patients misclassified relative to mean, pre-processed spectra of correctly identified healthy volunteer patients and (b)resultant PC scores plots showing PC1 versus PC2, (c) PC2 versus PC3 and (d) PC1 versus PC3.*

### *5.4.8.3 Random Forest: Absorption Spectra - Modified Fingerprint Region*

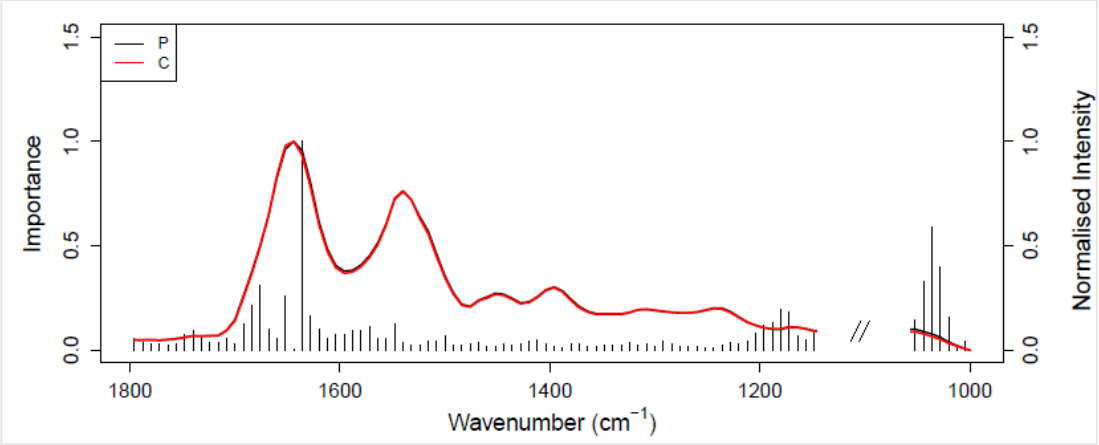


*Fig 5.31: Mean pre-processed ATR-FTIR spectra of modified fingerprint region truncated to 1800-1000cm$^{-1}$ with removal of variable 1140-1060cm$^{-1}$ region. Comparison of blood serum from healthy volunteers, denoted C, and patients with Hodgkin's lymphoma, denoted P. Gini plot superimposed on mean spectra indicates significant wavenumbers for discrimination between patient groups as calculated by Random Forest model.*

Hodgkin's lymphoma and healthy volunteer patients were subjected to an identical Random Forest classification with exception that the variable spectral region associated with silicon vibrations has been removed in an attempt to improve diagnostic performance, indicated in Figure 5.31. However, removal of the variable 1140-1060cm$^{-1}$ region failed to prevent misclassification of 6 of 29 patients with Hodgkin's lymphoma and 6 of 30 healthy volunteers, as indicated in Table 5.5, which suggests this spectral region is not primarily responsible for diagnostic error in the sample test set. Additionally, test sensitivity decreased and was found to have a larger standard deviation following validation on 50 resample test sets, as indicated in Table 5.6, which indicates a degree of biochemical information is likely contained in the 1140-1060cm$^{-1}$ region that contributes to diagnosis. Reduced test sensitivity is unsurprising given $\nu_s(PO_2)$ vibrations occur in this spectral region and may provide information on differences in phospholipid and nucleic acid content between patient groups (Fabian et al, 1995; Fujioka et al, 2004; Fukuyama et al, 1999; Baker et al,

2014). Test specificity remained unchanged with a marginal decrease in standard deviation as anticipated given the removal of a variable spectral region from spectroscopic analysis.

| Confusion Matrix | | | Patient Group | Patient ID | Misclassified Spectra |
|---|---|---|---|---|---|
| | Reference | | Hodgkin's Lymphoma | 56162 | 8/9 |
| Predictor | P | C | Hodgkin's Lymphoma | 64672 | 7/9 |
| | | | Hodgkin's Lymphoma | 66845 | 9/9 |
| P | 23 | 6 | Hodgkin's Lymphoma | 96817 | 6/9 |
| | | | Hodgkin's Lymphoma | 97553 | 5/9 |
| C | 6 | 24 | Hodgkin's Lymphoma | 97964 | 7/9 |
| | | | Healthy Volunteer | 54371 | 5/9 |
| - | | | Healthy Volunteer | 54490 | 6/9 |
| | | | Healthy Volunteer | 56559 | 6/9 |
| | | | Healthy Volunteer | 63495 | 8/9 |
| | | | Healthy Volunteer | 63669 | 6/9 |
| | | | Healthy Volunteer | R527108 | 9/9 |

*Table 5.5: Confusion matrix describing the number of healthy volunteers, denoted C, and Hodgkin's lymphoma patients, denoted P, correctly identified by the Random Forest classifier in one sample set relative to the known clinical status. Misclassified patients and number of spectra misclassified by the Random Forest model have been stated for both patients groups.*

| Accuracy (n = 50) | Sensitivity ( n = 50) | Specificity ( n = 50) |
|---|---|---|
| 0.835 ± 0.052 | 0.822 ± 0.089 | 0.848 ± 0.068 |

*Table 5.6: Diagnostic performance of Random Forest model when re-analysed with 50 randomly generated sample test sets. Results presented as mean ± standard deviation.*

*5.4.8.4 Exploring Spectral Signatures in Amide I Region*

Infrared spectroscopy is sensitive to hydrogen and amide-bonding environments associated with the polypeptide chains of protein molecules and therefore allows investigation of the secondary structure of proteins contained within an interrogated sample. In particular, the amide I band is routinely employed for analysis of protein secondary structure where the absorption signature represents the summation of overlapped vibrations whose relative positions and intensities depend on the interaction between dipole moments of amide bonds that constitute the backbone of protein molecules (Barth, 2007). Therefore, mean amide I absorption peaks for Hodgkin's lymphoma and healthy control groups were subjected to deconvolution methods in an attempt to better understand the nature of identified spectral differences in amide I bands of respective patient groups. Second derivative spectra of Hodgkin's lymphoma patients highlighted an increase and decrease in relative intensities of two peaks centred at ~1657cm$^{-1}$ and ~1637cm$^{-1}$ respectively compared to second derivative spectra of healthy volunteers, as depicted in Figure 5.32a and 5.32b. The spectral feature observed at ~1637cm$^{-1}$ may be tentatively assigned to the presence of β-sheet protein secondary structure (Goormaghtigh et al, 1994; Barth et al, 2007) and, hence, an increase in the intensity of this band suggests increased presence of β-sheet secondary structure in blood serum of Hodgkin's lymphoma patients. Similarly, the resolved peak at ~1657cm$^{-1}$ may be tentatively assigned to the presence of α-helix secondary structure (Goormaghtigh et al, 1994; Barth et al, 2007), with a decrease in absorbance indicative of global changes in α-helix protein secondary structure within blood serum samples of Hodgkin's lymphoma patients. Curve fitting analysis further highlighted distinct spectral signatures in the amide I region of patient groups, where

fitted curves represent the summation of resolved peaks and were found to be in good agreement with absorption spectra, as depicted in Figure 5.33a and 5.33b. Constructed peaks reflect second derivative spectra and allow easier visualisation of the differences in α-helix and β-sheet conformation between patient groups, as indicated by shaded peaks within fitted curve plots. However, it must be emphasised that the overall shape and precise wavenumbers of spectral features in second derivative spectra are dependent on sample binning and smoothing parameters, for which there is currently no standardised methodology, therefore secondary structure assignments should be considered with this in mind.

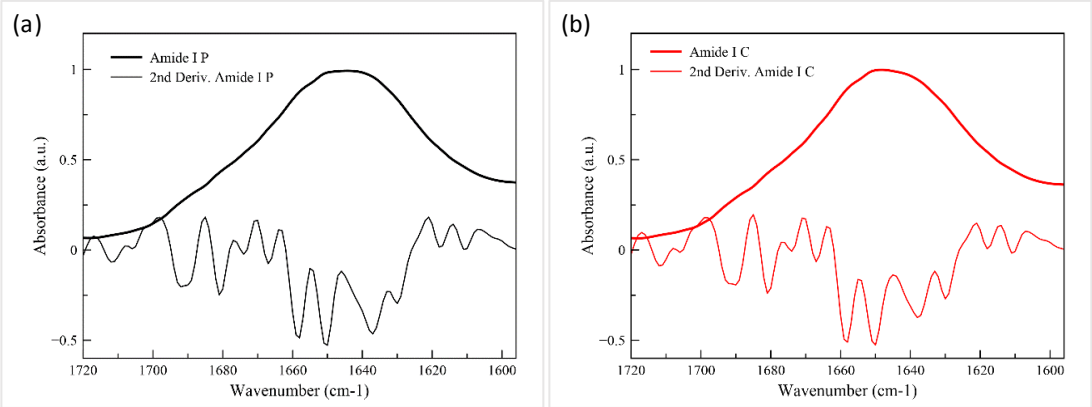


*Fig 5.32: Second derivative spectra from mean, pre-processed absorption spectra of the amide I band for (a) Hodgkin's lymphoma patients, denoted P, and (b) healthy volunteers, denoted C.*

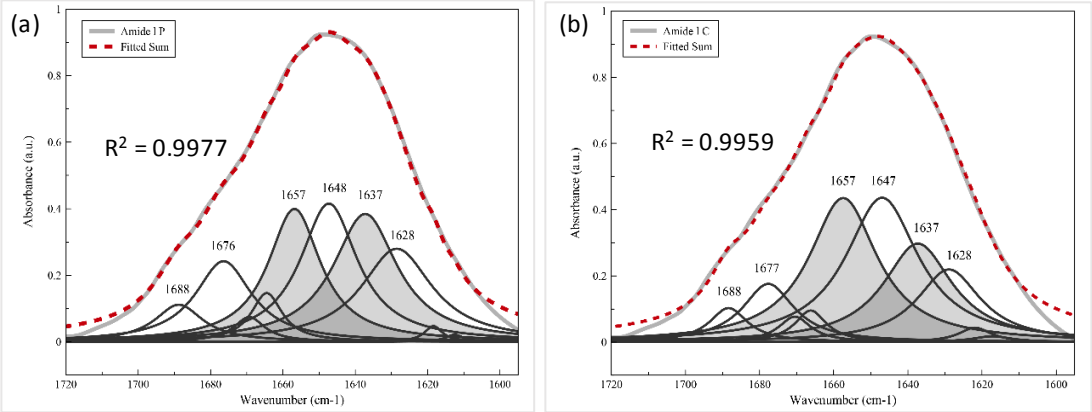


*Fig 5.33: Curve fitting analysis showing the summation of resolved second-derivative peaks relative to absorption spectra for (a) Hodgkin's lymphoma patients, denoted P, and (b) healthy volunteers, denoted C. Shaded grey peaks highlight primary differences in resolved peaks between both patient groups.*

Protein secondary structure changes observed between mean spectra of respective patient groups may speculatively reflect biochemical changes in serum content associated with Hodgkin's lymphoma. In particular, increased absorption in β-sheet secondary structures correlates with known secondary structures of previously specified protein biomarkers recognised to be present in blood serum during disease pathophysiology, as depicted in Figure 5.34. However, blood serum is a complex sample medium comprised of over 20,000 protein molecules (Bonnier et al, 2014) which naturally fluctuate between persons. Thus, the assumption that protein content is consistent in persons within respective patient groups and that any differences between patient groups may be confidently assigned to a particular protein biomarker is a significant generalisation. In reality, ATR-FTIR spectroscopy does not have the capacity to definitively correlate secondary structure changes with individual proteins within such a complex sample medium as blood serum. One proposed method to enhance spectroscopic protein signatures for elucidation of disease status is to centrifugal filter the high molecular weight protein fraction and in doing remove

albumin and immunoglobulin proteins that dominate the infrared spectrum (Bonnier et al, 2016). However, such an approach may not be practical for spectroscopic identification of protein biomarkers of Hodgkin's lymphoma, since CCL17/TARC, Galectin-1, CD30, CD163 and interleukin-6 display a range of molecular weights at 8KDa, 14.5KDa, 120KDa, 130KDa and 26KDa respectively. (Wirnsberger et al, 2006; Camby et al, 2006; Sauder et al, 2017; Etzerodt et al, 2013; Luo et al, 2016). Instead, validation of speculated protein biomarkers responsible for differences in absorption in the amide I band should be implemented in future studies with traditional analytical techniques such as SDS-PAGE, western blotting or proteomic mass spectroscopy, to firstly enhance our understanding of the sample medium and secondly to provide analytical confidence to clinicians regarding observed spectroscopic signatures and their diagnostic utility.

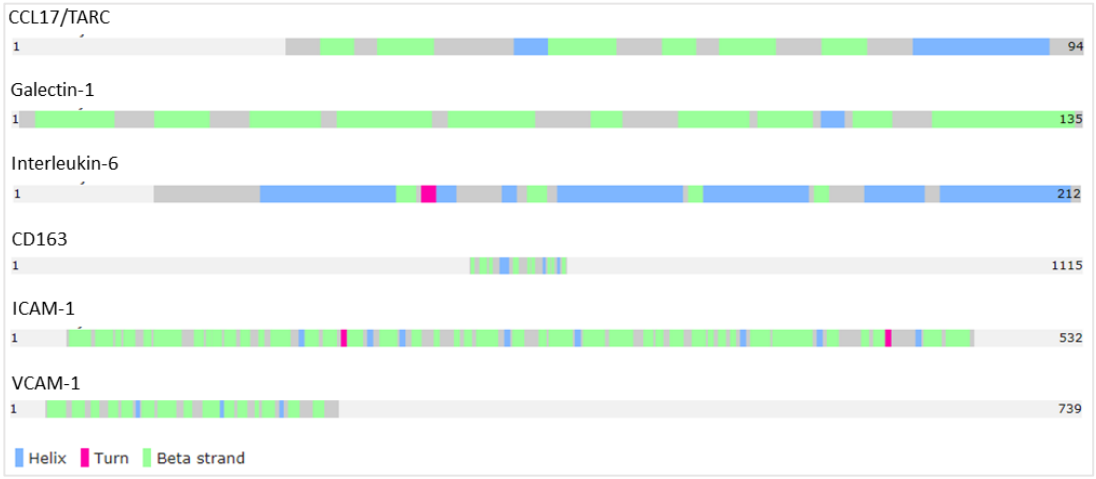


*Fig 5.34: Protein secondary structures of protein biomarkers reported to be elevated in serum of Hodgkin's lymphoma patients. Graphic collated from individual Uniprot profiles of specified molecules (Uniprot.org, 2019).*

*5.4.8.5 Random Forest Model: 2nd Derivative Spectra (1800-1000cm-1)*

Mean second derivative spectra of serum from Hodgkin's lymphoma and healthy volunteer patients truncated between 1800-1000cm$^{-1}$ were subjected to Random Forest analysis to determine whether second derivative spectra produce higher sensitivities and specificities given the significant spectral differences previously observed upon second derivation of the amide I bands. Mean spectra showed narrowing of absorption peaks and accentuation of spectral variation between both patient groups, shown in Figure 5.35, as anticipated for second derivative spectra. Resolved spectral signatures displayed comparable sensitivity to absorption spectra analysis over the fingerprint region, although specificity was poor for discrimination between classes, with 25 of 29 Hodgkin's lymphoma and 15 of 30 healthy patients successfully predicted in the sample test set, as outlined in the confusion matrix in Table 5.7. Similarly, second derivative spectra displayed poor diagnostic capabilities when subsequently validated on 50 randomly constructed sample sets, as show in Table 5.8, which may be attributed to the marked reduction in signal-to-noise associated with second derivative spectra (Rieppo et al, 2012), thus confirming that second derivative spectra over the entire fingerprint region is not suitable for Hodgkin's lymphoma diagnosis.

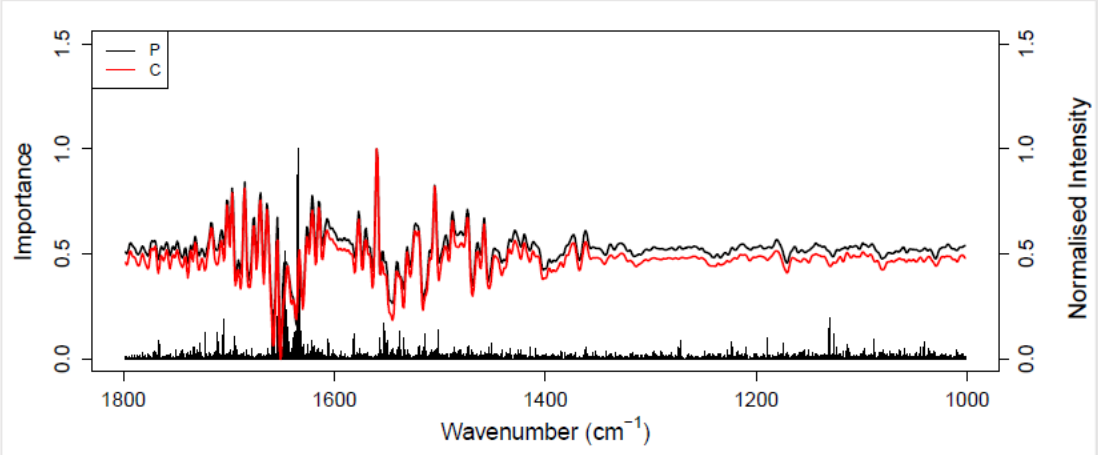


*Fig 5.35: Second derivative, mean, pre-processed spectra of blood serum from healthy volunteers, denoted C, and Hodgkin's lymphoma patients, denoted P. Gini plot superimposed on spectra shows the importance of individual wavenumbers for discrimination represented by the intensity of bars.*

| **Confusion Matrix** | | | **Patient Group** | **Patient ID** | **Misclassified Spectra** |
|---|---|---|---|---|---|
| | Reference | | Hodgkin's Lymphoma | 47764 | 5/9 |
| Predictor | P | C | Hodgkin's Lymphoma | 97488 | 7/9 |
| | | | Hodgkin's Lymphoma | 97793 | 8/9 |
| P | 25 | 15 | Hodgkin's Lymphoma | 98138 | 8/9 |
| | | | Healthy Volunteer | 53810 | 9/9 |
| C | 4 | 15 | Healthy Volunteer | 56559 | 5/9 |
| | | | Healthy Volunteer | 63615 | 6/9 |
| - | | | Healthy Volunteer | 63741 | 7/9 |
| | | | Healthy Volunteer | R526936 | 8/9 |
| | | | Healthy Volunteer | R526942 | 8/9 |
| | | | Healthy Volunteer | R526958 | 7/9 |
| | | | Healthy Volunteer | R526998 | 6/9 |
| | | | Healthy Volunteer | R527034 | 6/9 |
| | | | Healthy Volunteer | R527082 | 6/9 |
| | | | Healthy Volunteer | R527090 | 7/9 |
| | | | Healthy Volunteer | R527108 | 9/9 |

| | | | |
|---|---|---|---|
| | Healthy Volunteer | 63627 | 7/9 |
| | Healthy Volunteer | 54119 | 6/9 |
| | Healthy Volunteer | 54134 | 5/9 |

*Table 5.7: Confusion matrix describing the number of healthy volunteers, denoted C, and Hodgkin's lymphoma patients, denoted P, correctly identified by the Random Forest classifier in one sample set relative to the known clinical status. Misclassified patients and number of spectra misclassified by the Random Forest model have been stated for both patients groups.*

| **Accuracy (n = 50)** | **Sensitivity ( n = 50)** | **Specificity ( n = 50)** |
|---|---|---|
| 0.698 ± 0.051 | 0.811 ± 0.086 | 0.586 ± 0.120 |

*Table 5.8: Diagnostic performance of Random Forest model when re-analysed with 50 randomly generated sample test sets. Results presented as mean ± standard deviation.*

Mean second derivative spectra of serum from Hodgkin's lymphoma and healthy volunteer patients were also analysed with Random Forest exclusively in the 1665-1625cm$^{-1}$ region associated with biological changes in protein secondary structure, as shown in Figure 5.36, in an attempt to increase signal-to-noise of second derivative spectra. Interestingly, differences in the four prominent resolved spectral peaks between the two classes in the amide I region resulted in improved specificity, albeit at the expense of reduced sensitivity, with 20 of 29 Hodgkin's lymphoma and 20 of 30 healthy patients successfully identified in the sample test set, shown in Table 5.9. The change in diagnostic performance was further reflected when validated with 50 random sample sets, with significantly improved specificity and reduced sensitivity, outlined in Table 5.10. It is unsurprising that a vastly reduced wavenumber range produced poorer diagnostic sensitivity compared to previous tests since the current analysis does not consider amide II, $\delta_s(CH_2)$, $\nu_s(COO)$, $\nu_{as}(PO_2)$ and $\nu_s(PO_2)$ vibrations

recognised from previous importance plots to contribute to diagnosis of Hodgkin's lymphoma. However, current test results indicate that profiles and intensities of four predominant peaks within the amide I band serve as important and specific spectroscopic signature for discrimination between Hodgkin's lymphoma and healthy volunteers. Nevertheless, second derivative spectra have shown poorer diagnostic capabilities when compared to absorption spectra and thus will not be subject to further analysis or considered for future experiments.

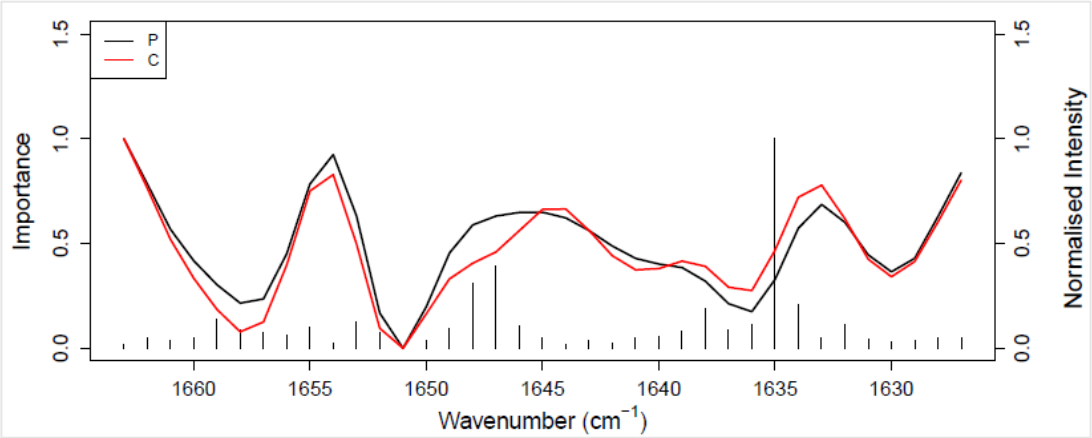


*Fig 5.36: Second derivative, mean, pre-processed spectra of blood serum truncated between 1665-1625cm$^{-1}$ from healthy volunteers, denoted C, and Hodgkin's lymphoma patients, denoted P. Gini plot superimposed on spectra shows the importance of individual wavenumbers for discrimination represented by the intensity of bars.*

| **Confusion Matrix** | | | **Patient Group** | **Patient ID** | **Misclassified Spectra** |
|---|---|---|---|---|---|
| | Reference | | Hodgkin's Lymphoma | 49142 | 9/9 |
| Predictor | P | C | Hodgkin's Lymphoma | 55377 | 9/9 |
| | | | Hodgkin's Lymphoma | 61717 | 5/9 |
| P | 20 | 10 | Hodgkin's Lymphoma | 66845 | 8/9 |
| | | | Hodgkin's Lymphoma | 96050 | 7/9 |
| C | 9 | 20 | Hodgkin's Lymphoma | 96259 | 7/9 |
| | | | Hodgkin's Lymphoma | 97183 | 7/9 |

| | | | |
|---|---|---|---|
| - | Hodgkin's Lymphoma | 97279 | 8/9 |
| | Hodgkin's Lymphoma | 97488 | 9/9 |
| | Healthy Volunteer | 53871 | 9/9 |
| | Healthy Volunteer | 54194 | 5/9 |
| | Healthy Volunteer | 54388 | 7/9 |
| | Healthy Volunteer | 63802 | 5/9 |
| | Healthy Volunteer | 63874 | 5/9 |
| | Healthy Volunteer | 64550 | 7/9 |
| | Healthy Volunteer | R526957 | 6/9 |
| | Healthy Volunteer | R526985 | 5/9 |
| | Healthy Volunteer | R527082 | 5/9 |
| | Healthy Volunteer | R527108 | 9/9 |

*Table 5.9: Confusion matrix describing the number of healthy volunteers, denoted C, and Hodgkin's lymphoma patients, denoted P, correctly identified by the Random Forest classifier in one sample set relative to the known clinical status. Misclassified patients and number of spectra misclassified by the Random Forest model have been stated for both patients groups.*

| Accuracy | Sensitivity | Specificity |
|---|---|---|
| 0.709 ± 0.058 | 0.709 ± 0.109 | 0.709 ± 0.106 |

*Table 5.10: Diagnostic performance of Random Forest model when re-analysed with 50 randomly generated sample test sets. Results presented as mean ± standard deviation.*

*5.4.8.6 Partial Least Squares Model: Absorption Spectra (1800-1000cm$^{-1}$)*

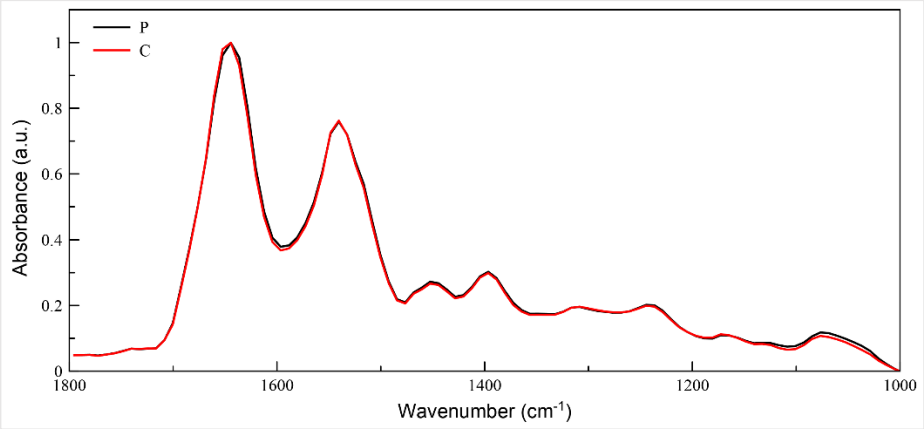


*Fig 5.37: Mean, pre-processed absorption spectra of blood serum truncated to 1800-1000cm$^{-1}$ from healthy volunteers, denoted C, and Hodgkin's lymphoma patients, denoted P.*

Hodgkin's lymphoma and healthy volunteer spectra were pre-processed with identical parameters and subsequently subjected to PLS analysis to determine whether diagnostic performance may be improved with a different classification model. Mean pre-processed spectra truncated to the fingerprint region showed modest spectral differences between both data classes in three discrete wavenumber regions; ~1650cm$^{-1}$, ~1450cm$^{-1}$ and ~1150-1000cm$^{-1}$, as indicated in Figure 5.37. Distinct spectral signatures were represented in PLS-DA scores plots where PLS1 versus PLS2 scores showed a significant degree of separation between patient groups, as indicated in Figure 5.38. The PLS1 loading plot primarily attributed separation on PLS1 axes to differences in absorption at ~1120-1150cm$^{-1}$ and 1240cm$^{-1}$ representative of ν(CO), ν(CC) and $\nu_{as}(PO_2)$ modes respectively (Movasaghi et al, 2008), as indicated in Figure 5.40. The PLS2 loading plot indicates separation on PLS2 axes predominantly arises from absorption intensities at ~1650cm$^{-1}$, ~1550cm$^{-1}$ and to lesser extents ~1300cm$^{-1}$ and 1090-1020cm$^{\sim -1}$, which encompasses amide I, amide II, amide III, $\nu_s(PO_2)$, ν(CO)

and ν(COH) modes respectively (Bonnier et al, 2014; Fujioka et al, 2004; Wood et al, 1998, Yoshida et al, 1997), as indicated in Figure 5.41. Interestingly, identical spectral signatures were identified with previous Random Forest classifications and appear pertinent to the diagnosis of Hodgkin's lymphoma. The PLS-DA scores plot of PLS2 versus PLS3 does not show a similar extent of clustering between classes, although a degree of separation is noticeable on PLS2, shown in Figure 5.39, and relates to previous assignments from the PLS2 loading plot. Conversely, PLS3 does not separate data classes with a random distribution of variance on PC3 axes. The PLS3 loading implies a degree of variation in absorption of amide I, amide II, ν(CO) and ν(CC) modes exist within each patient group, as shown in Figure 5.42.

Overall, spectral signatures found in the training set successfully identified 23 of 29 Hodgkin's lymphoma and 28 of 30 healthy volunteers, as shown by the confusion matrix in Table 5.11. Validation on 50 sample test sets resulted in decreased sensitivity and increased specificity values in comparison to Random Forest classifications, as indicated in Table 5.12. Possible explanation for the difference in diagnostic performance between PLS and Random Forest models may be the importance placed on different wavenumber regions. In particular, PLS1 shows patients may be separated according to absorption in lower wavenumber regions, ~1120-1150cm$^{-1}$ and 1240cm$^{-1}$, in contrast to Random Forest where increased importance is placed on the amide I band for discrimination. Specific computational frameworks responsible for diagnostic discrepancies between models is beyond the scope of current analyses, however, these inconsistencies must be carefully considered in future studies to establish

spectroscopic signatures deemed most important for discrimination between Hodgkin's lymphoma and healthy volunteers.

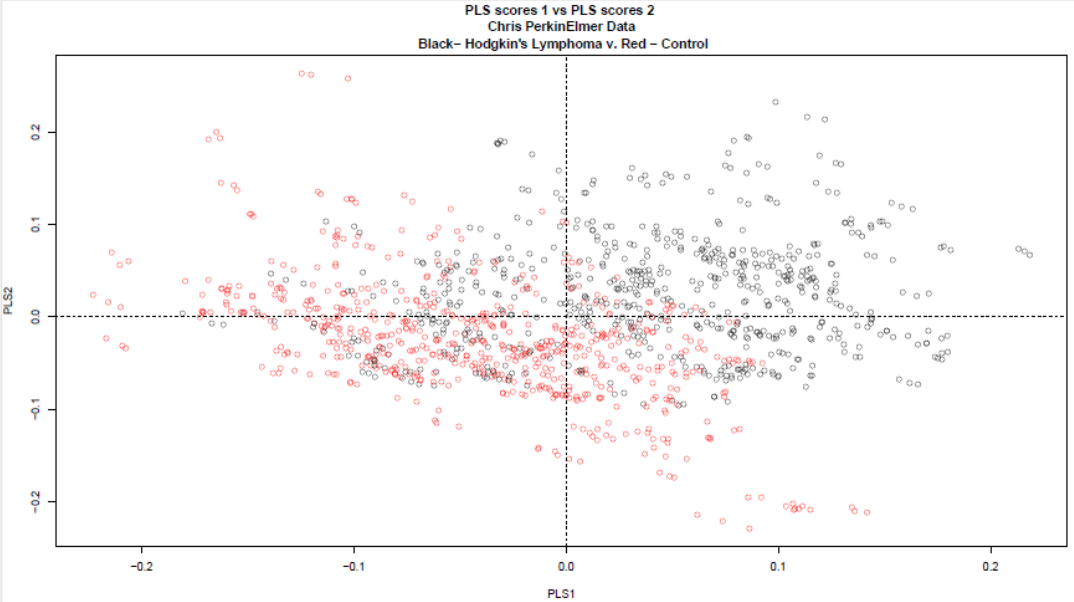


*Fig 5.38: PLS-DA plot showing spectral variance for PLS1 versus PLS2. Red and black circles correspond to individual spectra from blood serum of healthy volunteers and Hodgkin's lymphoma patients respectively.*

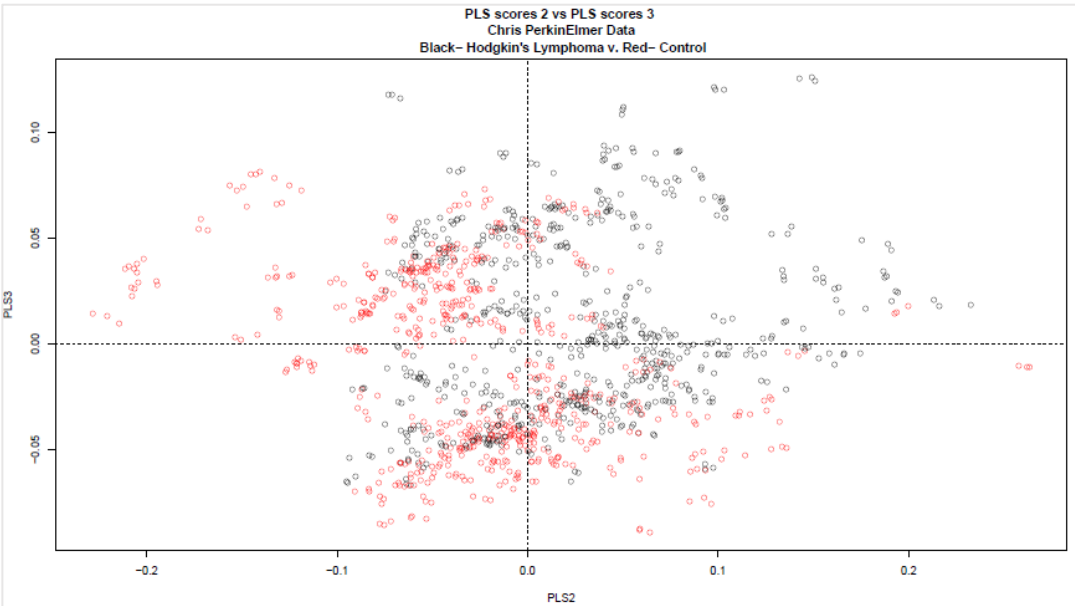


*Fig 5.39: PLS-DA plot showing spectral variance for PLS2 versus PLS3. Red and black circles correspond to individual spectra from blood serum of healthy volunteers and Hodgkin's lymphoma patients respectively.*

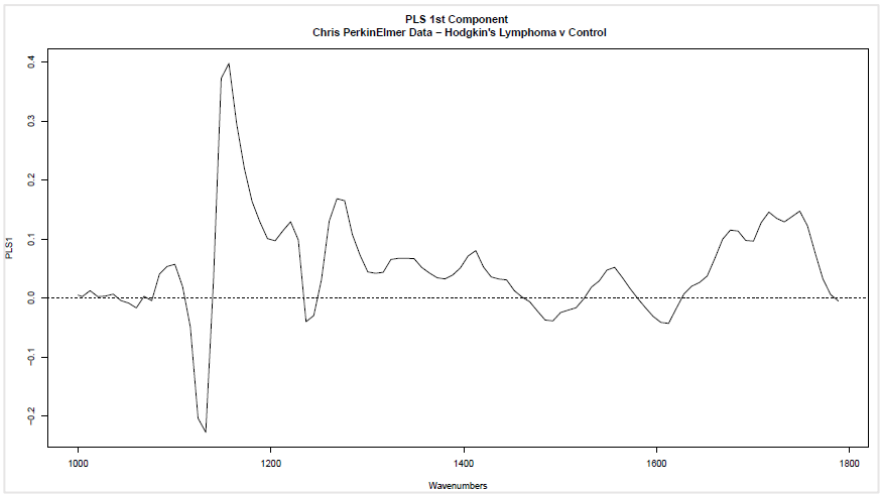


*Fig 5.40: PLS1 loading for PLS-DA analysis comparing serum of healthy volunteers and Hodgkin's lymphoma patients.*

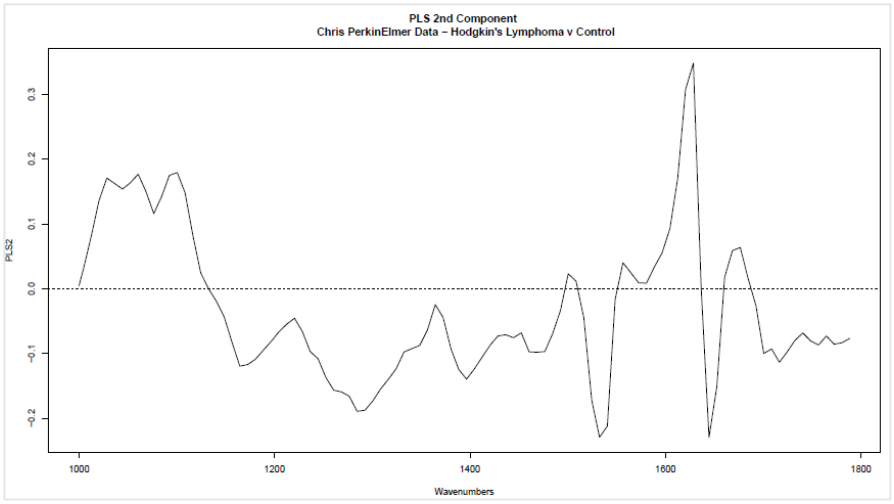


*Fig 5.41: PLS2 loading for PLS-DA analysis comparing serum of healthy volunteers and Hodgkin's lymphoma patients.*

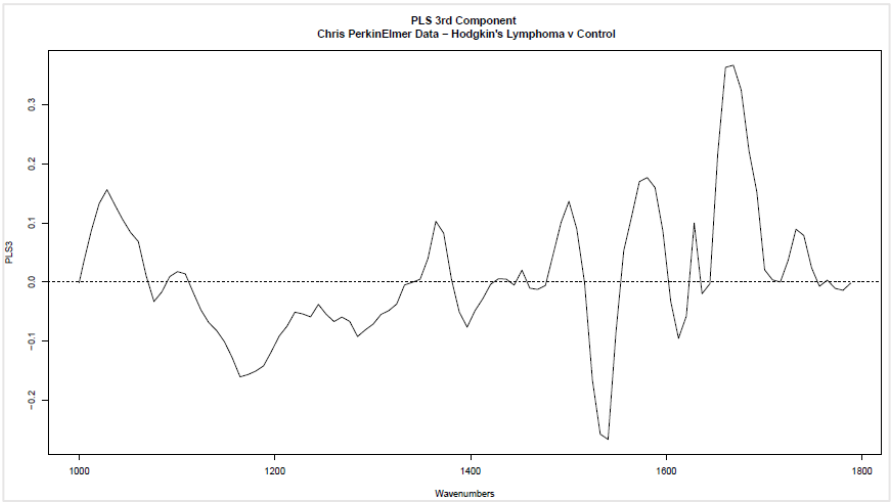


*Fig 5.42: PLS3 loading for PLS-DA analysis comparing serum of healthy volunteers and Hodgkin's lymphoma patients.*

| Confusion Matrix | | | Patient Group | Patient ID | Misclassified Spectra |
|---|---|---|---|---|---|
| | Reference | | Hodgkin's Lymphoma | 52121 | 9/9 |
| Predictor | P | C | Hodgkin's Lymphoma | 55177 | 6/9 |
| P | 23 | 2 | Hodgkin's Lymphoma | 56162 | 7/9 |
| C | 6 | 28 | Hodgkin's Lymphoma | 57211 | 8/9 |
| | | | Hodgkin's Lymphoma | 96259 | 9/9 |
| | | | Hodgkin's Lymphoma | 97348 | 6/9 |
| | | | Healthy Volunteer | 63627 | 5/9 |
| | | | Healthy Volunteer | 63681 | 9/9 |

*Table 5.11: Confusion matrix describing the number of healthy volunteers, denoted C, and Hodgkin's lymphoma patients, denoted P, correctly identified by the Partial Least Squares regression classifier in one sample set relative to the known clinical status. Misclassified patients and number of spectra misclassified by the Partial Least Squares regression model have been stated for both patients groups.*

| Accuracy ( n = 50) | Sensitivity (n = 50) | Specificity (n = 50) |
|---|---|---|
| 0.860 ± 0.044 | 0.764 ± 0.087 | 0.955 ± 0.042 |

*Table 5.12: Diagnostic performance of the Partial Least Squares regression model when re-analysed with 50 randomly generated sample test sets. Results presented as mean ± standard deviation.*

Overall, ATR-FTIR has shown promise for early detection of Hodgkin's lymphoma, with discrimination between clinical patient samples and healthy volunteers achieved with sensitivities and specificities up to 83.2 ± 6.6% and 85.3 ± 8.1% respectively with Random Forest classification. Spectral signatures pertinent to diagnosis primarily originate amide I, ν(CO), $\nu_s(PO_2)$ and ν(CC) vibrational modes, which may reflect changes in protein, phospholipid, nucleic acid and carbohydrate profiles in the blood serum of patients with Hodgkin's lymphoma. The rich biochemical content gathered on molecular bonds present within clinical serum samples highlights a critical strength and weakness of infrared spectroscopy for biofluid diagnostics. On one hand, ATR-FTIR boasts inexpensive, rapid, label-free acquisition of a biomolecular fingerprint of all macromolecular constituents within blood serum, yet on the other hand, the vast quantity of molecular information creates significant challenges for assignment of vibrational modes to specific clinical biomarkers. The lack of specificity for identification of particular chemokines and cytokines raises an important clinical question regarding future translation; what molecular information do clinicians require to inform diagnosis and facilitate successful triage of suspected patients with Hodgkin's lymphoma? If clinicians consider the differences in biomolecular profiles of blood serum adequate between patient groups for triage to clinical pathways, then ATR-FTIR represents significant promise for clinical translation. Conversely, if clinicians consider additional molecular specificity on clinical biomarkers essential for diagnosis, then an integrated ATR-FTIR and electrochemical platform has demonstrated significant potential for triage of classical Hodgkin's lymphoma patients, provided the diagnostic device is cost-effective for health care services. In

this regard, a health economics study must be conducted to identify required specificities and sensitivities for accurate clinical diagnosis whilst proving economically attractive to health care, as recently demonstrated with great success by others (Gray et al, 2018). Lastly, it is vital preliminary ATR-FTIR results are validated on a larger sample population to determine the true diagnostic capabilities of the proposed test. To this extent, significant limitations of the present study include the non-disclosure of medication information, previous or current clinical conditions, and collection of blood in a non-fasted state, which may represent confounding factors for spectroscopic diagnosis of Hodgkin's lymphoma.

### *5.4.8.7 Hodgkin's Lymphoma Pre-Treatment Vs On-Treatment Patient Samples*

#### *5.4.8.7.1 Random Forest Model: Absorption Spectra (1800-1000cm$^{-1}$)*

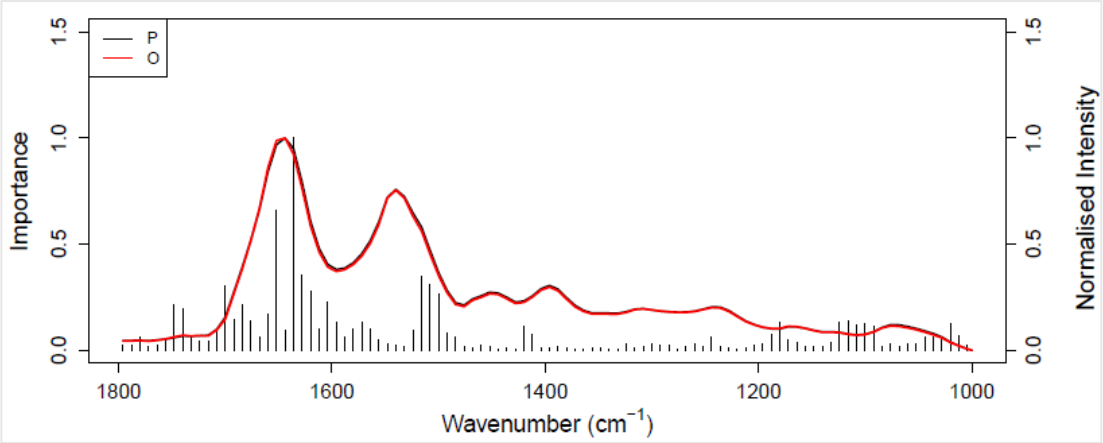


*Fig 5.43: Comparison of mean, pre-processed spectra of blood serum from Hodgkin's lymphoma patients pre-treatment, denoted P, and on-treatment, denoted O. Gini plot superimposed on spectra highlights importance of wavenumbers for discrimination between both patient classes.*

Serum samples collected from Hodgkin's lymphoma patients pre-treatment and during chemotherapy were subjected to a supervised classification to determine whether infrared spectroscopy could be employed to assess a patient's response to therapeutic treatment. Only paired patient samples have been employed in this study where the concentration of the biomarker CCL17/TARC decreased significantly during chemotherapy and suggested successful treatment response. Mean spectra truncated to the fingerprint region indicate the most important wavenumber region for discrimination between patient samples pre-treatment and during chemotherapy is at ~1640cm$^{-1}$ within the amide I band, shown in Figure 5.43. Interestingly, this spectral region was also shown to be most important for distinguishing between Hodgkin's lymphoma and healthy volunteers, and therefore may possibly have predictive significance when assessing patient responses to chemotherapy. Spectral differences were also observed at ~1500cm$^{-1}$ and at that correspond to amide II and $\nu(PO_2)$ modes

respectively and further suggests possible global change in protein content alongside nucleic acid and/or phospholipid content during chemotherapy. However, Random Forest classifications performed poorly with a significant quantity of patients misclassified in respective patient groups within the sample test set, shown in Table 5.13. Further validation on 50 random sample test sets produced low test sensitivity and specificity values of 58.2% and 60.2% respectively, as indicated in Table 5.14.

| **Confusion Matrix** | | | **Patient Group** | **Patient ID** | **Misclassified Spectra** |
|---|---|---|---|---|---|
| | Reference | | Pre-Treatment | 96224 | 9/9 |
| Predictor | P | C | Pre-Treatment | 96259 | 5/9 |
| P | 8 | 6 | Pre-Treatment | 96349 | 6/9 |
| C | 4 | 5 | Pre-Treatment | 97964 | 9/9 |
| - | | | On-Treatment | 97413 | 9/9 |
| | | | On-Treatment | 97419 | 8/9 |
| | | | On-Treatment | 97804 | 6/9 |
| | | | On-Treatment | 97981 | 8/9 |
| | | | On-Treatment | 98037 | 6/9 |
| | | | On-Treatment | 98202 | 9/9 |

*Table 5.13: Confusion matrix describing the number of Hodgkin's lymphoma patients pre-treatment, denoted P, and on-treatment, denoted O, correctly identified by the Random Forest model in one sample set relative to the known clinical status. Misclassified patients and number of spectra misclassified by the Random Forest model have been stated for both patients groups*

| **Accuracy (n = 50)** | **Sensitivity (n = 50)** | **Specificity (n = 50)** |
|---|---|---|
| 0.592 ± 0.093 | 0.582 ± 0.142 | 0.602 ± 0.147 |

*Table 5.14: Diagnostic performance of the Random Forest model when re-analysed with 50 randomly generated sample test sets. Results presented as mean ± standard deviation.*

Therefore, it has not been possible to discriminate between serum profiles of Hodgkin's lymphoma patients pre-treatment and during successful response to chemotherapy. Furthermore, even if discrimination had been demonstrated between Hodgkin's lymphoma patients pre-treatment and during treatment, spectral differences would not necessarily represent successful treatment response, and may reflect the presence of active drug compounds or possible side-effects of chemotherapy agents. To demonstrate, serum of Hodgkin's lymphoma patients during chemotherapy where treatment has been deemed successful were compared to previous healthy volunteer samples. Random Forest classification showed clear differences between serum profiles of Hodgkin's lymphoma patients during successful response to chemotherapy and healthy volunteers, with spectral distinction in the amide I band indicative of changes in protein content compared to healthy status, as shown in Figure 5.44. Furthermore, the Random Forest classifier was able to accurately discriminate between blood serum of Hodgkin's lymphoma patients on-treatment and those considered healthy, with high sensitivity and specificity, as shown in Table 5.15. Therefore, present findings show ATR-FTIR should not be considered as a predictive or prognostic tool for monitoring patient responses to chemotherapy treatment. Instead, techniques that have the ability to detect changes in concentrations of recognised specific predictive and prognostic biomarkers, such as CCL17/TARC, should be considered during chemotherapy treatment.

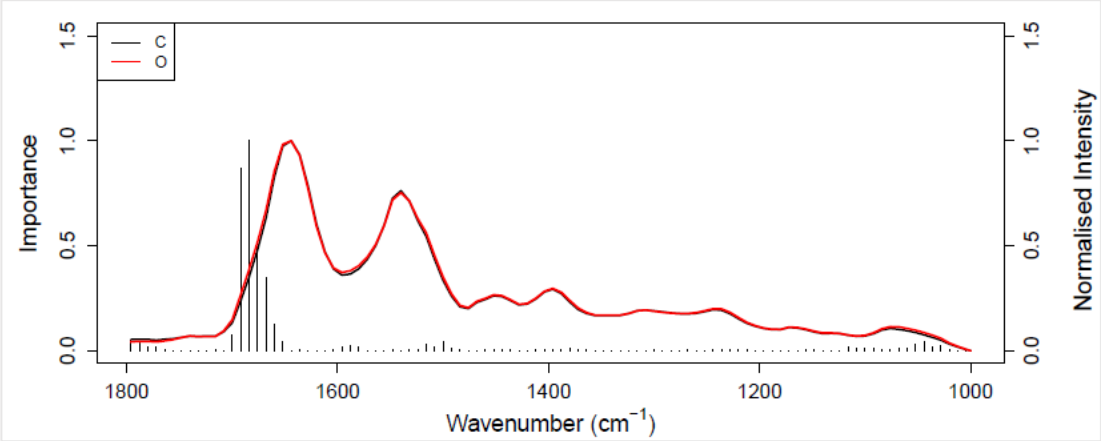


*Fig 5.44: Comparison of mean, pre-processed spectra of blood serum from Hodgkin's lymphoma patients on-treatment, denoted O, versus healthy volunteers, denoted C. Gini plot superimposed on spectra highlights importance of wavenumbers for discrimination between both patient classes.*

| **Confusion Matrix** | | | **Accuracy (n = 50)** | **Sensitivity (n = 50)** | **Specificity (n = 50)** |
|---|---|---|---|---|---|
| | Reference | | 0.970 ± 0.036 | 0.940 ± 0.072 | 1.00 ± 0.000 |
| Predictor | P | C | | | |
| P | 11 | 0 | | | |
| C | 0 | 11 | | | |

*Table 5.15: Confusion matrix describing the number of Hodgkin's lymphoma patients on-treatment, denoted O, and healthy volunteers, denoted C, correctly identified by the Random Forest model in one sample set relative to known clinical status. The diagnostic performance of the Random Forest model when re-analysed with 50 randomly generated sample test sets has also been included where results state mean ± standard deviation.*

## 5.5 Conclusion

Development of an integrated electrochemical and spectroscopic medical device has demonstrated significant potential for early diagnosis of classical Hodgkin's lymphoma. The proposed electrochemical platform features a "labelled" heterobifunctional cross-linker sandwich assay which has shown sensitive detection of

the biomarker, CCL17/TARC, specific to Hodgkin's lymphoma. In particular, functionalised electrodes showed successful discrimination between serum samples of healthy volunteers and Hodgkin's lymphoma patients, as well as quantitative detection of serum CCL17/TARC concentration, which has considerable potential for use as an early diagnostic triage tool within the clinical setting. Conversely, the "label-free" heterobifunctional cross-linker assay showed poor diagnostic capabilities with significant inter- and intra-assay variability, attributed to non-specific binding effects and reproducibility issues concerning SAM formation, and therefore should not be considered at present for clinical translation. ATR-FTIR has also shown significant potential for early diagnosis of classical Hodgkin's lymphoma, where the molecular fingerprint of samples enabled discrimination between patient groups with high accuracy, sensitivity and specificity with Random Forest classifications. However, ATR-FTIR was unable to discriminate between classical Hodgkin's lymphoma patients pre-treatment and during successful treatment, and should therefore not be considered as a prognostic tool to monitor patient responses to chemotherapy, but instead serve as a complimentary diagnostic tool to account for disease heterogeneity. Future studies should now be conducted on significantly larger sample populations to validate both analytical techniques and a health economics study should be considered in an attempt to realise clinical translation of the device within health care settings.

## 5.6 References


Baker, M. J., Trevisan, J., Bassan, P., Bhargava, R., Butler, H. J., Dorling, K. M., … Martin, F. L. (2014). *Using Fourier transform IR spectroscopy to analyze biological materials. Nature Protocols, 9(8), 1771–1791.* doi:10.1038/nprot.2014.110

Barth, A. (2007). Infrared spectroscopy of proteins. Biochimica et Biophysica Acta (BBA) - Bioenergetics, 1767(9), 1073–1101. doi:10.1016/j.bbabio.2007.06.004

Bettazzi, F., Romero Natale, A., Torres, E., & Palchetti, I. (2018). Glyphosate Determination by Coupling an Immuno-Magnetic Assay with Electrochemical Sensors. Sensors, 18(9), 2965. doi:10.3390/s18092965

Bonnier, F., Brachet, G., Duong, R., Sojinrin, T., Respaud, R., Aubrey, N., … Chourpa, I. (2016). *Screening the low molecular weight fraction of human serum using ATR-IR spectroscopy. Journal of Biophotonics, 9(10), 1085–1097*. doi:10.1002/jbio.201600015

Bonnier, F., Petitjean, F., Baker, M. J., & Byrne, H. J. (2013). Improved protocols for vibrational spectroscopic analysis of body fluids. Journal of Biophotonics, 7(3-4), 167–179. doi:10.1002/jbio.201300130

Brooks, E. G., Connors, J. M., Sehn, L. H., Gascoyne, R. D., Savage, K. J., Shenkier, T. N., … Villa, D. (2015). Impact of time from diagnosis to initiation of curative-intent chemotherapy on clinical outcomes in patients with classical Hodgkin lymphoma. Leukemia & Lymphoma, 57(4), 872–879. doi:10.3109/10428194.2015.1086919

Camby, I., Le Mercier, M., Lefranc, F., & Kiss, R. (2006). Galectin-1: a small protein with major functions. Glycobiology, 16(11), 137R–157R. doi:10.1093/glycob/cwl025

Cancer Research UK. (2019). Cancer Research UK. Accessed 26 September 2019. https://www.cancerresearchuk.org/health-professional/cancer-statistics/statistics-by-cancer-type/hodgkin-lymphoma#heading-One

Chammem, H., Hafaid, I., Bohli, N., Garcia, A., Meilhac, O., Abdelghani, A., & Mora, L. (2015). A disposable electrochemical sensor based on protein G for High-Density Lipoprotein (HDL) detection. Talanta, 144, 466–473. doi:10.1016/j.talanta.2015.06.009

Daniels, J. S., & Pourmand, N. (2007). *Label-Free Impedance Biosensors: Opportunities and Challenges. Electroanalysis, 19(12), 1239–1257*. doi:10.1002/elan.200603855

Deshpande, S. S. (2012) Enzyme Immunoassays: From Concept to Product Development. Chapter 9: Assay Development, Evaluation and Validation. Pages 295-299. Springer Science & Business Media, 2012. ISBN 1461311691, 9781461311690.

duPont, N. C., Wang, K., Wadhwa, P. D., Culhane, J. F., & Nelson, E. L. (2005). *Validation and comparison of luminex multiplex cytokine analysis kits with ELISA: Determinations of a panel of nine cytokines in clinical sample culture supernatants. Journal of Reproductive Immunology, 66(2), 175–191.* doi:10.1016/j.jri.2005.03.005

Etzerodt, A., & Moestrup, S. K. (2013). *CD163 and Inflammation: Biological, Diagnostic, and Therapeutic Aspects. Antioxidants & Redox Signaling, 18(17), 2352–2363.* doi:10.1089/ars.2012.4834

Fabian, H., Jackson, F. H., M., Murphy, L., Watson, P.H., Fichtner, I., and Mantsch, H.H. (1995) A comparative infrared spectroscopic study of human breast tumors and breast tumor cell xenografts. Biospectroscopy, 1 (1): 37–45.

Farina, L., Rezzonico, F., Spina, F., Dodero, A., Mazzocchi, A., Crippa, F., … Corradini, P. (2014). Serum Thymus and Activation-Regulated Chemokine Level Monitoring May Predict Disease Relapse Detected by PET Scan after Reduced-Intensity Allogeneic Stem Cell Transplantation in Patients with Hodgkin Lymphoma. Biology of Blood and Marrow Transplantation, 20(12), 1982–1988. doi:10.1016/j.bbmt.2014.08.016

Fowler, J. M., Stuart, M. C., & Wong, D. K. Y. (2007). *Self-Assembled Layer of Thiolated Protein G as an Immunosensor Scaffold. Analytical Chemistry, 79(1), 350–354.* doi:10.1021/ac061175f

Fujioka, N., Morimoto, Y., Arai, T., and Kikuchi, M. (2004) Discrimination between normal and malignant human gastric tissues by Fourier transform infrared spectroscopy. Cancer Detection & Prevention, 28: 32–36.

Fukuyama, Y., Yoshida, S., Yanagisawa, S., and Shimizu, M. (1999) A study on the differences between oral squamous cell carcinomas and normal oral mucosas measured by Fourier transform infrared spectroscopy. Biospectroscopy, 5: 117–126.

Gobbi, P. G., Gendarini, A., Crema, A., Cavalli, C., Attardo-Parrinello, G., Federico, M., … Ascari, E. (1985). Serum albumin in Hodgkin's disease. Cancer, 55(2), 389–393. doi:10.1002/1097-0142(19850115)55:2<389::aid-cncr2820550216>3.0.co;2-f

Goormaghtigh, E., Cabiaux, V., & Ruysschaert, J.-M. (1994). *Determination of Soluble and Membrane Protein Structure by Fourier Transform Infrared Spectroscopy. Physicochemical Methods in the Study of Biomembranes, 329–362.* doi:10.1007/978-1-4615-1863-1_8

Gray, E., Butler, H. J., Board, R., Brennan, P. M., Chalmers, A. J., Dawson, T., … Baker, M. J. (2018). Health economic evaluation of a serum-based blood test for brain tumour diagnosis: exploration of two clinical scenarios. BMJ Open, 8(5), e017593. doi:10.1136/bmjopen-2017-017593

Haag, A.-L., Nagai, Y., Lennox, R., & Grütter, P. (2015). Characterization of a gold coated cantilever surface for biosensing applications. EPJ Techniques and Instrumentation, 2(1), 1. doi:10.1140/epjti/s40485-014-0011-5

Hafaiedh, I., Chammem, H., Abdelghani, A., Ait, E., Feldman, L., Meilhac, O., & Mora, L. (2013). *Supported protein G on gold electrode: Characterization and immunosensor application. Talanta, 116, 84–90.* doi:10.1016/j.talanta.2013.04.059

Howell, D. A., Smith, A. G., Jack, A., Patmore, R., Macleod, U., Mironska, E., & Roman, E. (2013). Time-to-diagnosis and symptoms of myeloma, lymphomas and leukaemias: a report from the Haematological Malignancy Research Network. BMC Blood Disorders, 13(1). doi:10.1186/2052-1839-13-9

Jones, K., Vari, F., Keane, C., Crooks, P., Nourse, J. P., Seymour, L. A., … Gandhi, M. K. (2012). Serum CD163 and TARC as Disease Response Biomarkers in Classical Hodgkin Lymphoma. Clinical Cancer Research, 19(3), 731–742. doi:10.1158/1078-0432.ccr-12-2693

Karabudak, E., Kas, R., Ogieglo, W., Rafieian, D., Schlautmann, S., Lammertink, R. G. H., … Mul, G. (2012). Disposable Attenuated Total Reflection-Infrared Crystals from Silicon Wafer: A Versatile Approach to Surface Infrared Spectroscopy. Analytical Chemistry, 85(1), 33–38. doi:10.1021/ac302299g

Kojouri, K., El-Khoury, C., Pant, S., Kohrt, N., Selby, G. B., Ozer, H., Kamble, R., Kharfan-Dabaja, M. A. (2004) Prognostic Significance of Hypoalbuminemia in Patients with Relapsed/Refractory Hodgkin's Lymphoma (R/R-HL) Undergoing Salvage Autologous Bone Marrow/Peripheral Stem Cell Transplantation (auto-BM/PSCT). Blood. 104:5204.

Küppers, R., Engert, A., & Hansmann, M.-L. (2012). Hodgkin lymphoma. Journal of Clinical Investigation, 122(10), 3439–3447. doi:10.1172/jci61245

Kurzrock, R., Redman, J., Cabanillas, F., Jones, D., Rothberg, J., Talpaz, M. (1993) Serum interleukin 6 levels are elevated in lymphoma patients and correlate with survival in advanced Hodgkin's disease and with B symptoms. *Cancer Res.* 53(9):2118-22.

Lake, A. Nixon, I. J., Beattie, P., Ah-See, K., Culligan, D., Heaney, N., McKay, P, Hilmi, O. J. Jarrett, R. F. (2018) P031 (0145) EVALUATION OF CCL17 (TARC) AS A DIAGNOSTIC BIOMARKER FOR CLASSICAL HODGKIN LYMPHOMA. Hemasphere. Volume 2 – Issue S3 – p14-15. doi: 10.1097/01.HS9.0000547881.48587.85

Lee, G.-Y., Park, J.-H., Chang, Y. W., Cho, S., Kang, M.-J., & Pyun, J.-C. (2018). Chronoamperometry-Based Redox Cycling for Application to Immunoassays. ACS Sensors, 3(1), 106–112. doi:10.1021/acssensors.7b00681

Liew, M., Groll, M. C., Thompson, J. E., Call, S. L., Moser, J. E., Hoopes, J. D., … Spendlove, R. S. (2007). Validating a custom multiplex ELISA against individual commercial immunoassays using clinical samples. BioTechniques, 42(3), 327–333. doi:10.2144/000112332

Luo, Y., & Zheng, S. G. (2016). Hall of Fame among Pro-inflammatory Cytokines: Interleukin-6 Gene and Its Transcriptional Regulation Mechanisms. Frontiers in Immunology, 7. doi:10.3389/fimmu.2016.00604

Lyratzopoulos, G., Neal, R. D., Barbiere, J. M., Rubin, G. P., & Abel, G. A. (2012). Variation in number of general practitioner consultations before hospital referral for cancer: findings from the 2010 National Cancer Patient Experience Survey in England. The Lancet Oncology, 13(4), 353–365. doi:10.1016/s1470-2045(12)70041-4

Movasaghi, Z., Rehman, S., & ur Rehman, D. I. (2008). Fourier Transform Infrared (FTIR) Spectroscopy of Biological Tissues. Applied Spectroscopy Reviews, 43(2), 134–179. doi:10.1080/05704920701829043

Niens, M., Visser, L., Nolte, I. M., van der Steege, G., Diepstra, A., Cordano, P., … van den Berg, A. (2008). Serum chemokine levels in Hodgkin lymphoma patients: highly increased levels of CCL17 and CCL22. British Journal of Haematology, 140(5), 527–536. doi:10.1111/j.1365-2141.2007.06964.x

Oh, B.-K., Lee, W., Kim, Y.-K., Lee, W. H., & Choi, J.-W. (2004). Surface plasmon resonance immunosensor using self-assembled protein G for the detection of Salmonella paratyphi. Journal of Biotechnology, 111(1), 1–8. doi:10.1016/j.jbiotec.2004.02.010

Ouyang, J., Plutschow, A., von Strandmann, E. P., Reiners, K. S., Ponader, S., Rabinovich, G. A., … Shipp, M. A. (2013). *Galectin-1 serum levels reflect tumor burden and adverse clinical features in classical Hodgkin lymphoma. Blood, 121(17), 3431–3433.* doi:10.1182/blood-2012-12-474569

Plattel, W. J., Alsada, Z. N. D., van Imhoff, G. W., Diepstra, A., van den Berg, A., & Visser, L. (2016). Biomarkers for evaluation of treatment response in classical Hodgkin lymphoma: comparison of sGalectin-1, sCD163 and sCD30 with TARC. British Journal of Haematology, 175(5), 868–875. doi:10.1111/bjh.14317

Radhakrishnan, R., Suni, I. I., Bever, C. S., & Hammock, B. D. (2014). Impedance Biosensors: Applications to Sustainability and Remaining Technical Challenges. ACS Sustainable Chemistry & Engineering, 2(7), 1649–1655. doi:10.1021/sc500106y

Reed, G. F., Lynn, F., & Meade, B. D. (2002). Use of Coefficient of Variation in Assessing Variability of Quantitative Assays. Clinical and Vaccine Immunology, 9(6), 1235–1239. doi:10.1128/cdli.9.6.1235-1239.2002.

Rieppo, L., Saarakkala, S., Närhi, T., Helminen, H. J., Jurvelin, J. S., & Rieppo, J. (2012). *Application of second derivative spectroscopy for increasing molecular specificity of fourier transform infrared spectroscopic imaging of articular cartilage. Osteoarthritis and Cartilage, 20(5), 451–459.* doi:10.1016/j.joca.2012.01.010

San, L., Zeng, D., Song, S., Zuo, X., Zhang, H., Wang, C., … Mi, X. (2016). An electrochemical immunosensor for quantitative detection of ficolin-3. Nanotechnology, 27(25), 254003. doi:10.1088/0957-4484/27/25/254003

Sauder, M. B., O'Malley, J. T., & LeBoeuf, N. R. (2017). *CD30 + Lymphoproliferative Disorders of the Skin. Hematology/Oncology Clinics of North America, 31(2), 317–334.* doi:10.1016/j.hoc.2016.11.006

Schumacher, H., Künzelmann, U., Vasilev, B., Eichhorn, K.-J., & Bartha, J. W. (2010). *Applications of Microstructured Silicon Wafers as Internal Reflection Elements in Attenuated Total Reflection Fourier Transform Infrared Spectroscopy. Applied Spectroscopy, 64(9), 1022–1027.* doi:10.1366/000370210792434404

Shanbhag, S., & Ambinder, R. F. (2017). Hodgkin lymphoma: A review and update on recent progress. CA: A Cancer Journal for Clinicians, 68(2), 116–132. doi:10.3322/caac.21438

Shephard, E. A., Neal, R. D., Rose, P. W., Walter, F. M., & Hamilton, W. T. (2015). Quantifying the risk of Hodgkin lymphoma in symptomatic primary care patients aged ≥40 years: a case–control study using electronic records. British Journal of General Practice, 65(634), e289–e294. doi:10.3399/bjgp15x684805

Spalding, K., Bonnier, F., Bruno, C., Blasco, H., Board, R., Benz-de Bretagne, I., … Baker, M. J. (2018). *Enabling quantification of protein concentration in human serum biopsies using attenuated total reflectance – Fourier transform infrared (ATR-FTIR) spectroscopy. Vibrational Spectroscopy, 99, 50–58.* doi:10.1016/j.vibspec.2018.08.019

Spina, V., Bruscaggin, A., Cuccaro, A., Martini, M., Di Trani, M., Forestieri, G., … Rossi, D. (2018). Circulating tumor DNA reveals genetics, clonal evolution, and residual disease in classical Hodgkin lymphoma. Blood, 131(22), 2413–2425. doi:10.1182/blood-2017-11-812073

Stuart, B. (2004) Infrared Spectroscopy: Fundamentals and Applications. *2004 John Wiley & Sons, Ltd.* ISBN: 0-470-85427-8 / 0-470-85428-6

Syrigos, K. N., Salgami, E., Karayiannakis, A. J., Katirtzoglou, N., Sekara, E., Roussou, P. (2004) Prognostic significance of soluble adhesion molecules in Hodgkin's disease. Anticancer Res. 24(2C):1243-7.

Townsend, W., & Linch, D. (2012). Hodgkin's lymphoma in adults. The Lancet, 380(9844), 836–847. doi:10.1016/s0140-6736(12)60035-x

Trombetta, B. A., Carlyle, B. C., Koenig, A. M., Shaw, L. M., Trojanowski, J. Q., Wolk, D. A., … Arnold, S. E. (2018). The technical reliability and biotemporal stability of cerebrospinal fluid biomarkers for profiling multiple pathophysiologies in Alzheimer's disease. PLOS ONE, 13(3), e0193707. doi:10.1371/journal.pone.0193707

Vericat, C., Vela, M. E., Benitez, G., Carro, P., & Salvarezza, R. C. (2010). *Self-assembled monolayers of thiols and dithiols on gold: new challenges for a well-known system. Chemical Society Reviews, 39(5), 1805.* doi:10.1039/b907301a

Wang, Y., Nowakowski, G. S., Wang, M. L., & Ansell, S. M. (2018). Advances in CD30- and PD-1-targeted therapies for classical Hodgkin lymphoma. Journal of Hematology & Oncology, 11(1). doi:10.1186/s13045-018-0601-9

Wang, Y., Solano Canchaya, J. G., Dong, W., Alcamí, M., Busnengo, H. F., & Martín, F. (2014). Chain-Length and Temperature Dependence of Self-Assembled Monolayers of Alkylthiolates on Au(111) and Ag(111) Surfaces. The Journal of Physical Chemistry A, 118(23), 4138–4146. doi:10.1021/jp412285v

Watson, S., Nie, M., Wang, L., & Stokes, K. (2015). Challenges and developments of self-assembled monolayers and polymer brushes as a green lubrication solution for tribological applications. RSC Advances, 5(109), 89698–89730. doi:10.1039/c5ra17468f

Weihrauch, M. R., Manzke, O., Beyer, M., Haverkamp, H., Diehl, V., Bohlen, H., … Schultze, J. L. (2005). Elevated Serum Levels of CC Thymus and Activation-Related Chemokine (TARC) in Primary Hodgkin's Disease: Potential for a Prognostic Factor. Cancer Research, 65(13), 5516–5519. doi:10.1158/0008-5472.can-05-0100

Welch, J., Schwartz, C. L., Higman, M., Chen, L., Buxton, A., Kanakry, J. A., … Ambinder, R. F. (2017). Epstein-Barr virus DNA in serum as an early prognostic marker in children and adolescents with Hodgkin lymphoma. Blood advances, 1(11), 681–684. doi:10.1182/bloodadvances.2016002618

Wirnsberger, G., Hebenstreit, D., Posselt, G., Horejs-Hoeck, J., & Duschl, A. (2006). IL-4 induces expression of TARC/CCL17 via two STAT6 binding sites. European Journal of Immunology, 36(7), 1882–1891. doi:10.1002/eji.200635972

Wood, B.R., Quinn, M.A., Tait, B., Ashdown, M., Hislop, T., Romeo, M., and McNaughton, D. (1998) FTIR microspectroscopic study of cell types and potential confounding variables in screening for cervical malignancies. Biospectroscopy, 4: 75–91.

Yoshida, S., Miyazaki, M., Sakai, K., Takeshita, M., Yuasa, S., Sato, A., Kobayashi, T., Watanabe, S., and Okuyama, H. (1997) Fourier transform infrared spectroscopic analysis of rat brain microsomal membranes modified by dietary fatty acids: possible correlation with altered learning behavior. Biospectroscopy, 3 (4): 281–290.

Zhu, Y., Zhao, W., Xia, Y., Huang, J. (2011) Clinical significance of serum albumin in classical Hodgkin's lymphoma. Chinese Journal of Clinical Oncology. Vol 38. 10.3969/j.issn.1000-8179.2011.18.010

## Chapter 6: Conclusion

The need for earlier diagnosis of cancer in the clinical diagnostic pathway is well recognised and an imperative evolving strategy for health care services to improve patient outcomes and streamline clinical pathways. To this extent, brain cancer is in dire need of low-cost, earlier diagnostic approaches to complement the primary care setting, which would reduce diagnostic delays, better inform clinical referrals and remove financial and practical constraints placed on current imaging modalities. Similarly, patients with Hodgkin's lymphoma would benefit from introduction of a low-cost device capable of distinguishing between unexplained lymphadenopathy of infectious disease or malignant origin, especially for younger patients, allowing prompt referral for lymph node biopsies. Detection of serum-based molecular biomarkers would facilitate earlier diagnosis of Hodgkin's lymphoma that would allow timely access to chemotherapy and radiotherapy for patients as well as subsequent monitoring of treatment response. Similarly, molecular biomarker approaches would facilitate earlier diagnosis of brain cancer patients, particularly, detection of IDH1 status would provide clinically relevant information regarding prognosis that may inform surgical planning and treatment strategies. Consequently, earlier diagnosis translates to improved patient outcomes and is a pressing need for health care services given that no country in the UK currently meets the "62-day" cancer waiting time target for initiation of first-line treatment following referall. Therefore, the primary objective of the project has been to develop a medical device with the capacity for detection of molecular biomarkers that may inform earlier diagnosis of brain cancer and Hodgkin's lymphoma in the clinical setting.

The proposed medical device focused on the integration of ATR-FTIR spectroscopy and electrochemistry for serum-based cancer diagnostics. Blood serum was selected for the project as it represents a convenient, highly accessible, minimally invasive sample medium well suited for integration in to clinical workflows with minimal disruption to the current diagnostic pathway. Furthermore, electrochemistry was chosen for the ability to quantitatively detect specific biomarkers at clinically relevant concentrations, whilst ATR-FTIR spectroscopy was chosen for its ability to qualitatively assess the entire biochemical signature of serum, together providing access to vast quantities of biochemical information relevant to clinical decision making.

Development of a combined electrochemical and ATR-FTIR spectroscopy device focused on the design and engineering of a silicon based component capable of performing both analytical techniques. Initially, it was shown that original silicon components were not suitable for electrochemical analysis attributable to the poor conductivity of substrates. Thereafter, silicon was shown to be suitable for electrochemical analysis provided the silicon component was doped to degenerate concentrations, with boron-doped substrates showing superior electrochemical performance. However, silicon substrates doped to degenerate levels were not suitable for ATR-FTIR spectroscopy, since dopants were not transparent to infrared light. Subsequent device development focused on fabrication of optically transparent gold films deposited on silicon, and were found to provide sufficient conductivity $\geq$ 10nm and optical transparency $\leq$ 10nm. However, initial fabricated gold layers poorly adhered to the oxide layer of silicon substrates and, hence, it was not possible to

successfully conduct electrochemical experiments. Therefore, silicon pre-treatment with buffered oxide etchant and post evaporation treatment with annealing were employed to improve overall adhesion properties and successfully demonstrated potential for an integrated component. In particular, pre-treated and annealed gold-silicon components demonstrated electrochemical detection of the model biomarker pyocyanin at 500-2µM concentrations with a linearity of $R^2$ = 0.979-0.983 for oxidation and reduction events respectively. Similarly, the revised gold-silicon component showed spectroscopic characterisation of human pooled serum, albeit differences in absorption in amide I, ~1400cm-1 and ~1240cm-1 regions were observed in comparison to bare silicon substrates. Whilst proposed gold-silicon components have demonstrated capabilities for an integrated electrochemical and spectroscopic approach, the inability to perform spectroscopic analysis in the wet sample state has ultimately restricted its use in the current project. Therefore, the remainder of the project employed separate electrochemical and spectroscopic detection methods with hope that future research within our group would enable translation to an integrated approach with developed gold-silicon components.

Clinical serum samples were subjected to electrochemical and ATR-FTIR spectroscopic analysis with aim of detecting IDH1 molecular status in brain cancer patients. Initial electrochemical experiments tested the viability of different assay functionalisation strategies for immobilisation of IDH1-R132H antibodies on electrode surfaces. The heterobifunctional cross-linker assay with Sulfo-LC-SPDP showed superior performance for identification of IDH1-R132H proteins in spiked buffer solutions with a linearity of $R^2$ = 0.958 and detection capabilities down to

0.05ng/ml protein concentration on gold macro electrodes. Interestingly, the composition and topology of electrode substrates were found to have a profound influence on the performance of electrochemical immunosensors, thought to be attributable to differences in SAM formation and antibody distribution on electrode surfaces. However, gold macro elecrodes functionalised with Sulfo-LC-SPDP and IDH1-R132H antibodies were unable to identify IDH1 molecular status in clinical patient samples, believed either to be attributable to insignificant concentrations of IDH1-R132H proteins in serum samples or the poor analytical performance of the technique. The electrochemical immunosensor utilised electrochemical impedance spectroscopy throughout IDH1 studies and was susceptible to non-specific binding effects and issues surrounding reproducibility, ultimately restricting its applicability for clinical diagnostics. Conversely, ATR-FTIR spectroscopy successfully identified IDH1 molecular status in brain cancer patients of different tumour types with sensitivity of 83.1 ± 9.3% and specificity of 85.8 ± 10.7% with Random Forest classification. Similalrly, ATR-FTIR spectroscopy successfully identified IDH1 moecular status in astrocytoma patients with sensitivity of 89.0 ± 11.3% and specificity of 88.2 ± 10.1% with PLS classification. Both spectroscopic studies showed indirect detection of IDH1 status through global changes to biomolecular profiles of serum samples as a consequence of the IDH1 mutation, and highlights the strength of a spectroscopy based approach for complex disease diagnostics.

Clinical serum samples were similarly subjected to electrochemical and ATR-FTIR spectroscopic analysis with the aim of detecting the chemokine CCL17/TARC that may lead to earlier diagnosis for Hodgkin's lymphoma patients. Electrochemical

studies that employed an "unlabelled" approach with electrochemical impedance spectroscopy showed poor assay performance for spiked buffer samples of CCL17/TARC at 6,164-12pg/ml concentrations with a linearity of $R^2$ = 0.939 and significant standard deviation. Similarly, the "unlabelled" approach was unable to accurately identify elevated CCL17/TARC concentrations in serum samples of Hodgkin's lymphoma patients, believed to be attributable to poor inter-assay reproducibility. Conversely, subsequent electrochemical studies that employed amperometric detection with a "labelled" assay demonstrated superior detection capabilities for CCL17/TARC molecules in spiked buffer samples with a linearity of $R^2$ = 0.979 and limit of detection of 387pg/ml. Similarly, the "labelled" approach successfully identified increased concentrations of CCL17/TARC in clinical serum samples that permitted accurate diagnosis of all 11 Hodgkin's lymphoma patients relative to healthy controls. Additionally, ATR-FTIR spectroscopy successfully demonstrated the ability to distinguish between Hodgkin's lymphoma patients and healthy controls through analysis of global changes to biochemical constituents of serum samples. Specifically, ATR-FTIR demonstrated diagnosis of Hodgkin's lymphoma with a sensitivity of 83.2 ± 6.6% and specificity of 85.3 ± 8.1% with Random Forest classification, primarily attributable to differences in the secondary structure of proteins within clinical serum samples. Overall, an integrated electrochemical and spectroscopic approach has demonstrated significant clinical potential for earlier and minimally invasive detection of Hodgkin's lymphoma in health care settings.

## Chapter 7: Future Work

The current project has demonstrated signinficant potential for earlier cancer diagnostics through detection of a targeted biomarker with electrochemistry and a molecular sample fingerprint with ATR-FTIR spectroscopy. However, several technical and clinical challenges remain in the quest for early serum-based cancer diagnostics and must be overcome before clinical translation can be realised.

The proposed electrochemical platform has demonstrated clinically sufficient detection capabilities of CCL17/TARC for Hodgkin's lymphoma, but consistently under predicted the biomarkers concentration relative to ELISA methods. The discreprancy in biomarker concentration with current clinically employed techniques must be addressed to facilitate clinical translation and, therefore, in the short-term future work should focus on sample dilution and volume studies in an attempt to better characterise biomarker concentration in clinical serum samples. To this extent, long-term future work should consider fabrication of electrode arrays where by antibody immobilisation is restricted to specific electrodes leaving surrounding bare gold electrodes direct access to detect TMB products. We believe that such an approach would enable detection of TMB products with increased sensitivity as the functionalised SAM layer would be on a different electrode from the detection electrode and, therefore, would not provide an obstacle for TMB detection at the electrode surface. Furthermore, electrode arrays have recently demonstrated improved detection capabilities for "sandwich" immunosensors in a separate approach where by the polarity of the potential is switched on two different electrodes, which ultimately

provides an increased signal intensity and therefore should be considerd for future work. Additionally, micro electrodes have previously demonstrated improvements in analytical sensitivity for biomarker detection, and therefore fabrication of micro electrode arrays should strongly be considered in future work.

The proposed spectroscopic platform has demonstrated potential to stratify glioma patients based on IDH1 molecular status that would have significant clinical applicability for brain cancer diagnostics. However, the sample population for the current study was relatively small as immunohistochemistry IDH1 testing was not performed on a significant number of patients in the cinical setting. Therefore, future work should consider a larger, multi-centre study with significantly greater sample populations to validate current results. Similarly, the spectroscopic study for Hodgkin's lymphoma diagnostics was conducted on 200 patient serum samples and, therefore, should be scaled up to significantly larger sample populations to better account for patient demographics and differences in blood collection and processing from different clinical environments. Additionally, the recent emergence of surfaced enhanced infrared spectroscopy and nano-spectroscopy should be considered as research tools in future studies where the high analytical sensitivity may provide insights and a means to better identify and understand spectral biomarkers at low biological concentrations in clinical serum samples.

From a clinical perspective for future Hodgkin's lymphoma studies, it would be beneficial to concurrently detect CCL17/TARC and the Epstein-Barr virus from

patient samples, since the Epstein-Barr virus is associated with ~40% of Hodgkin's lymphoma patients and has prognostic and diagnostic value for determination of tumour type. Therefore, future work for Hodgkin's lymphoma should consider development of electrode arrays functionalised with both antibody and DNA probes for detection of multiple biomarkers that may better inform clinical diagnostic decisions.

From a clinical perspective for brain cancer studies, it is currently unclear whether IDH1-R132H protein molecules are present at sufficient levels for diagnostic purposes. Therefore, future studies should consider other proteomic techniques, such as mass spectrometry, to confirm and validate the presence of IDH1 molecules in clinical blood serum samples. Additionally, future studies should seek to develop highly sensitive DNA electrochemical sensors for IDH1 mutations, since circulating tumour DNA associated with the IDH1 gene has previously been identified in blood plasma of glioma patients. Furthermore, future work should seek to develop electrode arrays to detect a panel of biomarkers for diagnosis of glioma. Whilst the present diagnostic pathway only recognises mutations of IDH and ATRX and 1p/19q co-deletion as molecular biomarkers, other research studies have shown that other systemic biomarkers, such as interleukin-6, are significantly increased with tumour grade. Therefore, there is an argument that detection of other biomarkers alongside currently clinically recognised biomarkers may provide additional diagnostic information and warrants consideration in future works. To this extent, the current project has contributed to the award of a research grant by Cancer Research UK to explore clinical biomarkers for glioma through electrochemical and spectroscopic

detection techniques and, therefore, significant work in this area is expected to be conducted in the immediate future.

# Appendices

## Appendix A: Additional electrochemical testing of silicon substrates

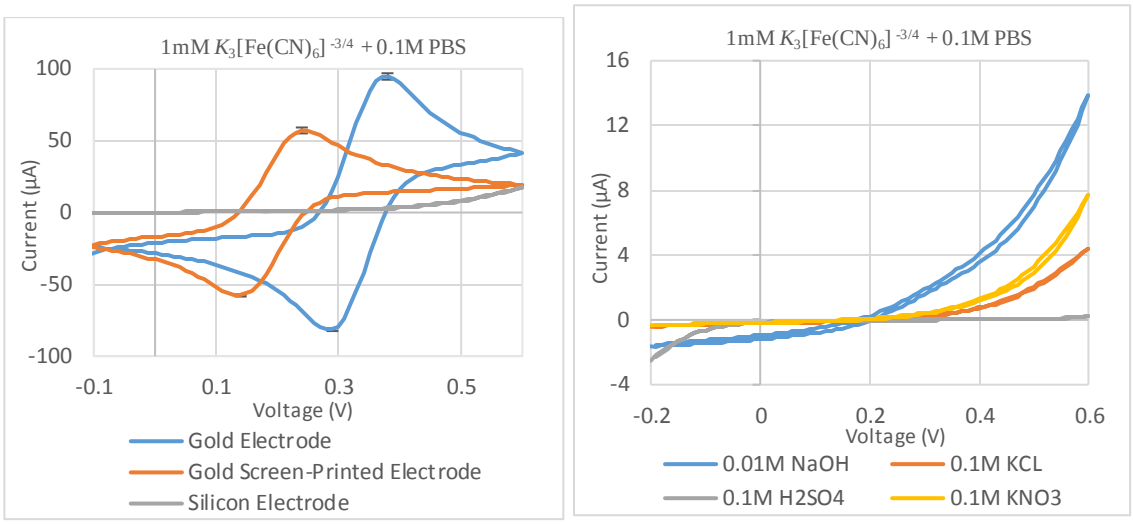


*Figure A.1: Cyclic voltammograms of gold macro, gold screen-printed and silicon electrodes for detection of (a) $K_3[Fe(CN)_6]^{-3/4}$ molecules in PBS solutions and (b) other supporting electrolytic solutions.*

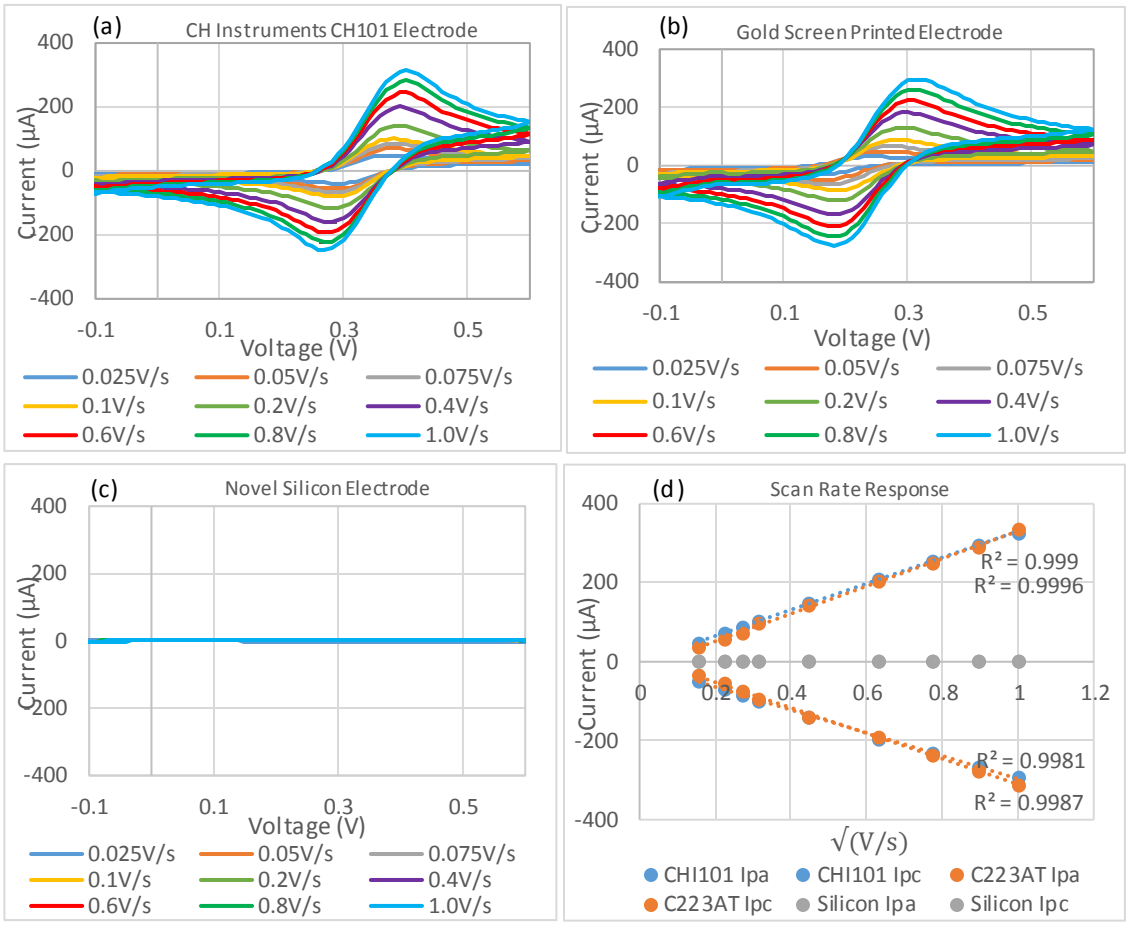


*Figure A.2: Cyclic voltammograms of (a) gold macro electrodes, (b) gold screen-printed electrodes, (c) silicon electrodes subjected to variable scan rates for detection of 1mM $K_3[Fe(CN)_6]^{-3/4}$ + 0.1M PBS (n=3). (d) Plot of the current response of all three electrodes with respect to the square root of scan rate.*

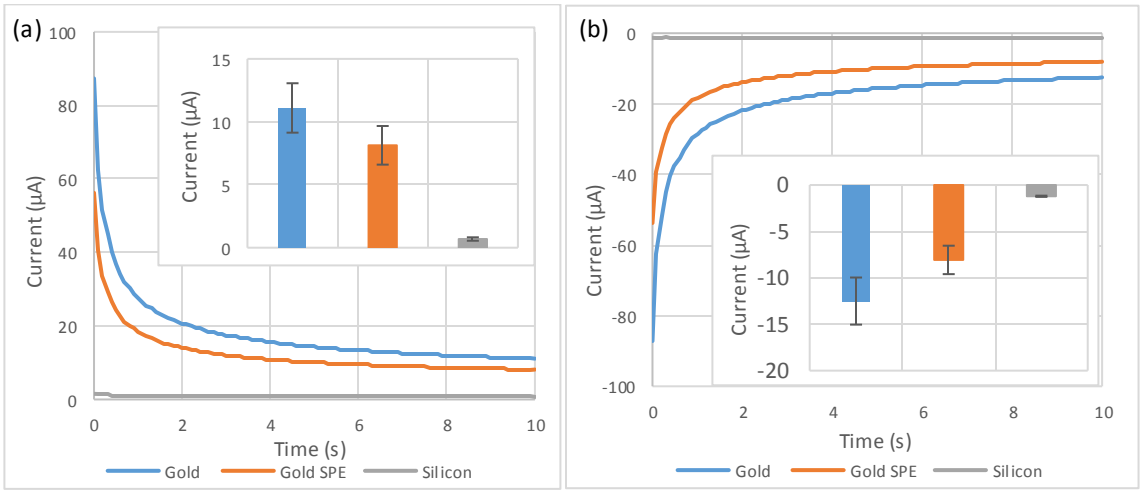


*Figure A.3: Chronoamperometry responses of gold macro, screen-printed gold and silicon electrodes when $K_3[Fe(CN)_6]^{-3/4}$ molecules were subjected to (a) oxidation and (b) reduction potentials.*

## Appendix B: Clinical information for analysed glioma patients.

| WRTB | Tumour Type | WHO Grade | IDH1 | N/A |
|---|---|---|---|---|
| 15008 | Oligodendroglioma | II | Positive | |
| 15017 | Oligodendroglioma | II | Positive | |
| 15023 | Astrocytoma | II | Positive | |
| 15024 | Oligodendroglioma | II | Positive | |
| 15045 | Oligodendroglioma | II | Positive | |
| 15048 | Astrocytoma | III | Negative | |
| 15052 | Astrocytoma | II | Negative | |
| 15099 | Glioma | III | Negative | |
| 15100 | Astrocytoma | III | Negative | |
| 15105 | Oligodendroglioma | II | Positive | |
| 15118 | Astrocytoma | II | Positive | |
| 15158 | Astrocytoma | II | Positive | |
| 15167 | Astrocytoma | III | Negative | |
| 15184 | Oligodendroglioma | II | Positive | |
| 15193 | Oligodendroglioma | II | Positive | |
| 15198 | Astrocytoma | II | Negative | |
| 15201 | Oligoastrocytoma | II | Negative | |
| 15204 | Glioblastoma | IV | Positive | |
| 15205 | Astrocytoma | II | Positive | |
| 15209 | Glioma | II | Positive | |
| 15210 | Glioma | II | Negative | |
| 15216 | Oligodendroglioma | III | Positive | |
| 15218 | Oligoastrocytoma | III | Negative | |
| 15222 | Astrocytoma | II | Negative | |
| 15236 | Astrocytoma | I | Negative | |
| 15241 | Astrocytoma | II | Negative | |
| 15245 | Astrocytoma | II | Negative | |
| 15278 | Oligodendroglioma | II | Negative | |
| 15280 | Astrocytoma | III | Negative | |
| 15284 | Astrocytoma | III | Negative | |
| 15293 | Astrocytoma | II | Negative | |
| 15300 | Oligodendroglioma | II | Positive | |
| 15302 | Oligoastrocytoma | II | Positive | |
| 15312 | Astrocytoma | II | Positive | |
| 15320 | Astrocytoma | II | Positive | |
| 15327 | Astrocytoma | II | Negative | |
| 15328 | Astrocytoma | II | Positive | |
| 15329 | Astrocytoma | II | Positive | |

| | | | | |
|---|---|---|---|---|
| 15332 | Glioblastoma | IV | Positive | |
| 15343 | Astrocytoma | II | Positive | |
| 15344 | Astrocytoma | III | Negative | |
| 15346 | Astrocytoma | II | Negative | |
| 16016 | Anaplastic Astrocytoma | III | Positive | |
| 16027 | Oligodendroglioma | II | Positive | |
| 16037 | Oligodendroglioma | II | Positive | |
| 16048 | Oligoastrocytoma | II | Positive | |
| 16062 | Astrocytoma | II | Negative | |
| 16074 | Anaplastic Oligodendroglioma | III | Negative | |
| 16076 | Oligodendroglioma | II | Positive | |
| 16082 | Astrocytoma | II | Negative | |
| 16109 | Oligodendroglioma | II | Positive | |
| 16143 | Anaplastic Astrocytoma | III | Negative | |
| 16150 | Astrocytoma | II | Negative | |
| 16165 | Astrocytoma | II | Negative | |
| 16167 | Astrocytoma | II | Negative | |
| 16174 | Astrocytoma | II | Positive | |
| 16187 | Anaplastic Astrocytoma | III | Positive | |
| 16192 | Astrocytoma | III | Negative | |
| 16216 | Oligodendroglioma | II | Positive | |
| 16218 | Astrocytoma | II | Positive | |
| 16226 | Oligodendroglioma | III | Positive | |
| 16227 | Astrocytoma | II | Positive | |
| 16234 | Astrocytoma | II | Positive | |
| 16245 | Astrocytoma | II | Positive | |
| 16263 | Oligodendroglioma | | Positive | |
| 17005 | Astrocytoma | II | Positive | |
| 17010 | Astrocytoma | II | Positive | |
| 17086 | Oligodendroglioma | II | Positive | |
| 17091 | Astrocytoma | II | Positive | |
| 17104 | Astrocytoma | II | Positive | |
| 17153 | Anaplastic Astrocytoma | III | Positive | |
| 17172 | Oligodendroglioma | II | Positive | |
| 17234 | Anaplastic Astrocytoma | III | Negative | |
| 17292 | Astrocytoma | II | Positive | |
| 17345 | Anaplastic Astrocytoma | III | Positive | |
| 17357 | Astrocytoma | II | Positive | |
| 17400 | Oligodendroglioma | II | Positive | |
| 17447 | Astrocytoma | II | Positive | |
| 17453 | Anaplastic Astrocytoma | III | Positive | |
| 17452 | Astrocytoma | I | Negative | |
| 17464 | Anaplastic Astrocytoma | III | Positive | |

| | | | | |
|---|---|---|---|---|
| 17474 | Anaplastic Astrocytoma | III | Positive | |
| 1088 | Glioblastoma | IV | Negative | |
| 1090 | Glioblastoma | IV | negative | |
| 1091 | Glioblastoma | IV | negative | |
| 1098 | Glioblastoma | IV | negative | |
| 1100 | Glioblastoma | IV | negative | |
| 1101 | Glioblastoma | IV | negative | |
| 1131 | Glioblastoma | IV | negative | |
| 1134 | Glioblastoma | IV | negative | |
| 1135 | Glioblastoma | IV | negative | |
| 1167 | Glioblastoma | IV | negative | |
| 1839 | Glioblastoma | IV | Positive | |
| 1955 | Glioblastoma | IV | Positive | |
| 2310 | Glioblastoma | IV | Positive | |
| | | | | |
| **WCFT Number** | **WRTB Number** | **Tumour Type** | **WHO Grade** | **IDH1 Mutation** |
| **83397** | **17073** | Glioblastoma | IV | Wildtype |
| | **17083** | Glioblastoma | IV | |
| **196052** | **17196** | Glioblastoma | IV | Wildtype |
| | **17208** | Glioblastoma | IV | |
| | **17210** | Glioblastoma | IV | |
| **365772** | **17095** | Glioblastoma | IV | Wildtype |
| | **17097** | Glioblastoma | IV | |
| | **17102** | Glioblastoma | IV | |
| **397519** | **16259** | Glioblastoma | IV | Wildtype |
| | **16267** | Glioblastoma | IV | |
| | **16269** | Glioblastoma | IV | |
| **907899** | **17055** | Glioblastoma | IV | Mutated |

| | | | | |
|---|---|---|---|---|
| | **17056** | Glioblastoma | IV | |
| | **17061** | Glioblastoma | IV | |
| **908909** | **17074** | Glioblastoma | IV | Mutated |
| | **17075** | Glioblastoma | IV | |
| | **17079** | Glioblastoma | IV | |
| **921486** | **17326** | Glioblastoma | | Wildtype |
| | **17328** | Glioblastoma | IV | |
| | **17333** | Glioblastoma | | |
| **921549** | **17343** | Glioblastoma | | Wildtype |
| | **17347** | Glioblastoma | IV | |
| | **17350** | Glioblastoma | | |
| **921775** | **17336** | Glioblastoma | | Wildtype |
| | **17341** | Glioblastoma | IV | |
| | **17344** | Glioblastoma | IV | |
| **922364** | **17342** | Glioblastoma | IV | Mutated |
| | **17349** | Glioblastoma | IV | |
| | **17351** | Glioblastoma | IV | |
| **923131** | **17352** | Glioblastoma | IV | Wildtype |
| | **17364** | Glioblastoma | IV | |
| | **17370** | Glioblastoma | IV | |
| **923382** | **17369** | Glioblastoma | IV | Wildtype |
| | **17383** | Glioblastoma | IV | |

| | | | | |
|---|---|---|---|---|
| | **17384** | Glioblastoma | IV | |
| 91424 | n/a | Glioblastoma | IV | Positive |
| 34151 | n/a | Glioblastoma | IV | Negative |

## Appendix C: Clinical information for analysed Hodgkin's lymphoma patients.

| Pat ref | Clinical Info | Sex | Age | CCL17 result |
|---|---|---|---|---|
| 10089 | Healthy volunteer | F | 45 | no serum result |
| 10154 | Healthy volunteer | F | 35 | no serum result |
| 10157 | Healthy volunteer | M | 47 | no serum result |
| 10174 | Healthy volunteer | F | 25 | no serum result |
| 10280 | Healthy volunteer | M | 35 | 242 |
| 10632 | Healthy volunteer | M | 25 | 426 |
| 10644 | Healthy volunteer | M | 19 | 230 |
| 10647 | Healthy volunteer | M | 57 | 446 |
| 10661 | Healthy volunteer | F | 18 | 378 |
| 10713 | Healthy volunteer | F | 54 | 199 |
| 9269 | Pre treatment HL | M | 64 | 79960 |
| 9366 | Pre treatment HL | F | 35 | 95473 |
| 10374 | Pre treatment HL | F | 49 | 100319 |
| 11696 | Pre treatment HL | F | 23 | 85257 |
| 11854 | Pre treatment HL | F | 47 | 93670 |
| 11906 | Pre treatment HL | F | 29 | 93340 |
| 36513 | Pre treatment HL | F | 18 | 135239 |
| 36514 | Pre treatment HL | M | 46 | 5289 |
| 36524 | Pre treatment HL | M | 34 | 2976 |
| 36519 | Pre treatment HL | M | 23 | 13876 |
| 36532 | Pre treatment HL | F | 21 | 7644 |
| 36530 | Pre treatment HL | F | 34 | 1600 |
| 36547 | Pre treatment HL | F | 78 | 1946 |
| 36548 | Pre treatment HL | M | 49 | 13179 |
| 36529 | Pre treatment HL | F | 57 | 5360 |
| 36512 | Pre treatment HL | M | 32 | 7475 |
| 36515 | Pre treatment HL | F | 85 | 8091 |
| 36564 | Pre treatment HL | M | 59 | 2108 |
| 36565 | Pre treatment HL | F | 25 | 30900 |
| 36536 | Pre treatment HL | F | 27 | 3246 |
| 36521 | Pre treatment HL | F | 79 | 2828 |
| 36516 | Pre treatment HL | M | 35 | 52164 |
| 36540 | Pre treatment HL | M | 53 | 9644 |
| 36566 | Pre treatment HL | M | 36 | 5087 |
| 36520 | Pre treatment HL | F | 21 | 45771 |
| 36574 | Pre treatment HL | M | 45 | 41565 |
| 36575 | Pre treatment HL | F | 32 | 16214 |
| 36554 | Pre treatment HL | M | 26 | 6946 |
| 36580 | Pre treatment HL | F | 32 | 250000 |
| 36526 | Pre treatment HL | M | 21 | 59622 |
| 36569 | Pre treatment HL | M | 25 | 27767 |
| 36523 | Pre treatment HL | F | 69 | 9054 |
| 36586 | Pre treatment HL | F | 19 | 6271 |
| 36558 | Pre treatment HL | M | 18 | 2960 |
| 36590 | Pre treatment HL | M | 28 | 18904 |
| 36539 | Pre treatment HL | F | 37 | 62700 |

| | | | | |
|---|---|---|---|---|
| 36591 | Pre treatment HL | M | 39 | 11093 |
| 36525 | Pre treatment HL | M | 77 | 632 |
| 36578 | Pre treatment HL | F | 74 | 2672 |
| 36567 | Pre treatment HL | F | 34 | 4463 |
| 36593 | Pre treatment HL | M | 41 | 43285 |
| 36600 | Pre treatment HL | M | 76 | 17380 |
| 36560 | Pre treatment HL | F | 35 | 34353 |
| 36572 | Pre treatment HL | M | 36 | 5968 |
| 36581 | Pre treatment HL | F | 46 | 6184 |
| 36585 | Pre treatment HL | M | 66 | 8633 |
| 36577 | Pre treatment HL | M | 18 | 5715 |
| 36573 | Pre treatment HL | M | 22 | 12665 |
| 36604 | Pre treatment HL | M | 60 | 3999 |
| 36518 | Pre treatment HL HI CCL17 | F | 20-24 | 17691 |
| 10854 | Pre treatment HL HI CCL17 | F | 25-29 | 29254 |
| 11721 | Pre treatment HL HI CCL17 | F | 85-89 | 49603 |
| 11783 | Pre treatment HL HI CCL17 | F | 40-44 | 1833 |
| 11810 | Pre treatment HL HI CCL17 | M | 60-64 | 3235 |
| 11837 | Pre treatment HL HI CCL17 | F | 65-69 | 29330 |
| 11914 | Pre treatment HL HI CCL17 | M | 40-44 | 13043 |
| 10581 | Pre treatment HL HI CCL17 | F | 20-24 | 1262 |
| 10597 | Pre treatment HL HI CCL17 | F | 55-59 | 136895 |
| 10578 | Pre treatment HL HI CCL17 | M | 25-29 | 1698 |
| 10607 | Pre treatment HL HI CCL17 | M | 40-44 | 72317 |
| 10612 | Pre treatment HL HI CCL17 | F | 25-29 | 8493 |
| 10639 | Pre treatment HL HI CCL17 | M | 50-54 | 1396 |
| 10622 | Pre treatment HL HI CCL17 | M | 55-59 | 4774 |
| 10687 | Pre treatment HL HI CCL17 | M | 40-44 | 24680 |
| 10709 | Pre treatment HL HI CCL17 | F | 35-39 | 11708 |
| 12037 | Pre treatment HL HI CCL17 | M | 35-39 | 31920 |
| 10368 | Pre treatment HL HI CCL17 | M | 35-39 | 58715 |
| 10392 | Pre treatment HL HI CCL17 | M | 65-69 | 19002 |
| 10402 | Pre treatment HL HI CCL17 | M | 20-24 | 7630 |

| | | | | |
|---|---|---|---|---|
| 10414 | Pre treatment HL HI CCL17 | F | 15-19 | 41522 |
| 10428 | Pre treatment HL HI CCL17 | F | 20-24 | 14074 |
| 10480 | Pre treatment HL HI CCL17 | F | 35-39 | 9397 |
| 10499 | Pre treatment HL HI CCL17 | F | 55-59 | 67586 |
| 8989 | Pre treatment HL LO CCL17 | M | 60-64 | 254 |
| 9235 | Pre treatment HL LO CCL17 | M | 70-74 | 805 |
| 10720 | Pre treatment HL LO CCL17 | M | 25-29 | 728 |
| 36517 | Pre treatment HL LO CCL17 | F | 75-79 | 437 |
| 36508 | Pre treatment HL LO CCL17 | M | 85-89 | 194 |
| 9378 | Pre treatment HL HI CCL17 | F | 30-34 | 2222 |
| 9481 | Pre treatment HL HI CCL17 | M | 25-29 | 14598 |
| 9496 | Pre treatment HL HI CCL17 | F | 35-39 | 18242 |
| 9518 | Pre treatment HL HI CCL17 | F | 30-34 | 20867 |
| 10019 | Pre treatment HL HI CCL17 | M | 70-74 | 17828 |
| 10056 | Pre treatment HL HI CCL17 | F | 25-29 | 50333 |
| 36522 | Pre treatment HL LO CCL17 | F | 80-84 | **145** |
| 36555 | Pre treatment HL LO CCL17 | F | 75-79 | **216** |
| 36527 | Pre treatment HL LO CCL17 | M | 70-74 | **44** |
| 36571 | Pre treatment HL LO CCL17 | M | 55-59 | **36** |
| 36557 | Pre treatment HL LO CCL17 | F | 65-69 | **481** |
| 36563 | Pre treatment HL LO CCL17 | M | 50-54 | **533** |
| 8483 | Pre treatment HL LO CCL17 | M | 50-54 | 275 |
| 10119 | Pre treatment HL LO CCL17 | M | 40-44 | 449 |
| 10222 | Pre treatment HL HI CCL17 | F | 40-44 | 27170 |
| 10259 | Pre treatment HL HI CCL17 | F | 35-39 | 26520 |
| 10268 | Pre treatment HL LO CCL17 | F | 35-39 | 393 |

| | | | | |
|---|---|---|---|---|
| 10313 | Pre treatment HL HI CCL17 | M | 30-34 | 67756 |
| 10355 | Pre treatment HL HI CCL17 | M | 45-49 | 19923 |
| 10364 | Pre treatment HL HI CCL17 | M | 35-39 | 51187 |
| 9353 | Pre treatment HL HI CCL17 | F | 15-19 | 13170 |
| 10088 | Healthy volunteer | F | 40-44 | 202 |
| 10100 | Healthy volunteer | F | 20-24 | 134 |
| 10102 | Healthy volunteer | M | 20-24 | 396 |
| 10103 | Healthy volunteer | F | 45-49 | 379 |
| 10104 | Healthy volunteer | F | 25-29 | 480 |
| 10111 | Healthy volunteer | M | 50-54 | 367 |
| 10116 | Healthy volunteer | F | 65-69 | 231 |
| 10117 | Healthy volunteer | F | 40-44 | 269 |
| 10118 | Healthy volunteer | M | 30-34 | 296 |
| 10120 | Healthy volunteer | F | 25-29 | 375 |
| 10121 | Healthy volunteer | F | 35-39 | 27 |
| 10122 | Healthy volunteer | F | 30-34 | 155 |
| 10130 | Healthy volunteer | F | 25-29 | 231 |
| 10134 | Healthy volunteer | F | 25-29 | 92 |
| 10146 | Healthy volunteer | F | 35-39 | 441 |
| 10147 | Healthy volunteer | M | 20-24 | 173 |
| 10148 | Healthy volunteer | F | 30-34 | 45 |
| 10150 | Healthy volunteer | F | 25-29 | not detected |
| 10152 | Healthy volunteer | F | 45-49 | not detected |
| 10153 | Healthy volunteer | F | 30-34 | not detected |
| 10382 | Healthy volunteer | F | 30-34 | 104 |
| 10383 | Healthy volunteer | M | 45-49 | 164 |
| 10573 | Healthy volunteer | F | 25-29 | 407 |
| 10631 | Healthy volunteer | F | 25-29 | 215 |
| 10633 | Healthy volunteer | M | 20-24 | 366 |
| 10634 | Healthy volunteer | - | 25-29 | 298 |
| 10635 | Healthy volunteer | F | 25-29 | 277 |
| 10641 | Healthy volunteer | F | 15-19 | 152 |
| 10642 | Healthy volunteer | M | 45-49 | 131 |
| 10643 | Healthy volunteer | M | 55-59 | 164 |
| 10645 | Healthy volunteer | F | 15-19 | 423 |
| 10646 | Healthy volunteer | F | 35-39 | 331 |
| 10648 | Healthy volunteer | M | 20-24 | 283 |
| 10650 | Healthy volunteer | F | 20-24 | 394 |
| 10651 | Healthy volunteer | M | 20-24 | 411 |
| 10652 | Healthy volunteer | M | 35-39 | 520 |
| 10653 | Healthy volunteer | F | 20-24 | 330 |
| 10654 | Healthy volunteer | M | 20-24 | 270 |
| 10655 | Healthy volunteer | M | 40-44 | 599 |
| 10656 | Healthy volunteer | F | 25-29 | 266 |
| 10657 | Healthy volunteer | F | 20-24 | 207 |
| 10658 | Healthy volunteer | M | 15-19 | 233 |
| 10659 | Healthy volunteer | - | 30-34 | 351 |

| | | | | |
|---|---|---|---|---|
| 10660 | Healthy volunteer | F | 30-34 | 420 |
| 10663 | Healthy volunteer | F | 20-24 | 823 |
| 10664 | Healthy volunteer | F | 20-24 | 322 |
| 10666 | Healthy volunteer | F | 35-39 | 449 |
| 10667 | Healthy volunteer | F | 25-29 | 424 |
| 10668 | Healthy volunteer | F | 20-24 | 135 |
| 10669 | Healthy volunteer | F | 30-34 | 177 |
| 526942 | Healthy volunteer | M | 39 | no serum result |
| R526950 | Healthy volunteer | M | 37 | no serum result |
| R526951 | Healthy volunteer | M | 35 | no serum result |
| R526956 | Healthy volunteer | M | 33 | no serum result |
| R526957 | Healthy volunteer | M | 43 | no serum result |
| R526958 | Healthy volunteer | M | 33 | no serum result |
| R526961 | Healthy volunteer | M | 32 | no serum result |
| R526962 | Healthy volunteer | M | 44 | no serum result |
| R526970 | Healthy volunteer | M | 39 | no serum result |
| R526974 | Healthy volunteer | M | 49 | no serum result |
| R526976 | Healthy volunteer | M | 40 | no serum result |
| R526985 | Healthy volunteer | M | 31 | no serum result |
| R526998 | Healthy volunteer | M | 37 | no serum result |
| 526916 | Healthy volunteer | M | 39 | no serum result |
| 526917 | Healthy volunteer | M | 36 | no serum result |
| 526935 | Healthy volunteer | M | 38 | no serum result |
| 526936 | Healthy volunteer | M | 42 | no serum result |
| 526982 | Healthy volunteer | M | 48 | no serum result |
| 526990 | Healthy volunteer | M | 40 | no serum result |
| 527000 | Healthy volunteer | M | 50 | no serum result |
| 527070 | Healthy volunteer | M | 31 | no serum result |
| 527109 | Healthy volunteer | M | 46 | no serum result |
| 527114 | Healthy volunteer | M | 33 | no serum result |
| 527127 | Healthy volunteer | M | 29 | no serum result |
| 527033 | Healthy volunteer | F | 44 | no serum result |
| 527051 | Healthy volunteer | M | 47 | no serum result |
| 527075 | Healthy volunteer | M | 34 | no serum result |
| 527077 | Healthy volunteer | M | 31 | no serum result |
| 527081 | Healthy volunteer | M | 33 | no serum result |
| 527089 | Healthy volunteer | M | 35 | no serum result |
| 527090 | Healthy volunteer | M | 45 | no serum result |
| 527094 | Healthy volunteer | M | 45 | no serum result |
| 527106 | Healthy volunteer | M | 31 | no serum result |
| 527072 | Healthy volunteer | M | 32 | no serum result |
| 527098 | Healthy volunteer | M | 37 | no serum result |
| 527108 | Healthy volunteer | F | 41 | no serum result |
| 527034 | Healthy volunteer | M | 33 | no serum result |
| 527045 | Healthy volunteer | M | 35 | no serum result |
| 527074 | Healthy volunteer | M | 30 | no serum result |
| 527082 | Healthy volunteer | M | 33 | no serum result |
| 36513 | On treatment HL | F | 18 | 721 |
| 36514 | On treatment HL | M | 46 | 264 |
| 36524 | On treatment HL | M | 34 | 820 |
| 36519 | On treatment HL | M | 23 | 394 |

| | | | | |
|---|---|---|---|---|
| 36532 | On treatment HL | F | 21 | 294 |
| 36532 | On treatment HL | F | 21 | 294 |
| 36547 | On treatment HL | F | 78 | 205 |
| 36548 | On treatment HL | M | 49 | 945 |
| 36529 | On treatment HL | F | 57 | 773 |
| 36512 | On treatment HL | M | 32 | 491 |
| 36515 | On treatment HL | F | 85 | 745 |
| 36564 | On treatment HL | M | 59 | 731 |
| 36565 | On treatment HL | F | 25 | 208 |
| 36536 | On treatment HL | F | 27 | 178 |
| 36521 | On treatment HL | F | 79 | 348 |
| 36516 | On treatment HL | M | 35 | 394 |
| 36540 | On treatment HL | M | 53 | 257 |
| 36566 | On treatment HL | M | 36 | 136 |
| 36520 | On treatment HL | F | 21 | 831 |
| 36540 | On treatment HL | M | 53 | 257 |
| 36574 | On treatment HL | M | 45 | 213 |
| 36575 | On treatment HL | F | 32 | 77 |
| 36554 | On treatment HL | M | 26 | 154 |
| 36569 | On treatment HL | M | 25 | 154 |
| 36523 | On treatment HL | F | 69 | 285 |
| 36586 | On treatment HL | F | 19 | 124 |
| 36558 | On treatment HL | M | 18 | 351 |
| 36590 | On treatment HL | M | 28 | 274 |
| 36539 | On treatment HL | F | 37 | 533 |
| 36591 | On treatment HL | M | 39 | 124 |
| 36525 | On treatment HL | M | 77 | 1690 |
| 36578 | On treatment HL | F | 74 | 258 |
| 36567 | On treatment HL | F | 34 | 208 |
| 36600 | On treatment HL | M | 76 | 505 |
| 36560 | On treatment HL | F | 35 | 190 |
| 36572 | On treatment HL | M | 36 | 109 |
| 36581 | On treatment HL | F | 46 | 45 |
| 36560 | On treatment HL | F | 35 | 190 |
| 36585 | On treatment HL | M | 66 | 301 |
| 36581 | On treatment HL | F | 46 | 45 |
| 36577 | On treatment HL | M | 18 | 473 |
| 36573 | On treatment HL | M | 22 | 287 |
| 36604 | On treatment HL | M | 60 | 381 |
| 36572 | On treatment HL | M | 36 | 109 |
| 36577 | On treatment HL | M | 18 | 473 |
| 36585 | On treatment HL | M | 66 | 301 |
| 36573 | On treatment HL | M | 22 | 287 |
| 36604 | On treatment HL | M | 60 | 381 |